

eman ta zabal zazu



Universidad del País Vasco Euskal Herriko Unibertsitatea

Characterization of the biological and molecular activity of PML in breast cancer

Doctoral thesis

Leire Arreal López

2020

Characterization of the biological and molecular activity of PML in breast cancer

Doctoral thesis

*Report of the experimental work to apply for the grade of Doctor in Biological Sciences, into the Doctorate Programme of Molecular Biology and Biomedicine of the University of the Basque Country. The work here in has been performed by Leire Arreal López at the Center for Cooperative Research in Biosciences (CICbioGUNE) under the mentorship of **Dr. Arkaitz Carracedo Pérez** and **Dr. Natalia Martín-Martín**.*

Leire Arreal López

2020

Supported by:

µg: Microgram	DMEM: Dulbecco's Modified Eagle Medium
µL: Microliter	DMF: N,N-dimethylformamide
µm: Micrometer	DMSZ: Leibniz-Institut-Deutsche Sammlung von Mikroorganismen und Zellkulturen GmbH
µM: Micromolar	DNA: Desoxyribonucleic Acid
AKT: Protein Kinase B, PKB	Dox: Doxycycline
APL: Acute promyelocytic leukemia	DSB: Double-strand breaks
ATO: Arsenic trioxide	EDA: Exploratory data analysis
ATCC: American Type Culture Collection	EGFR: Epidermal growth factor receptor
ATM: Ataxia telangiectasia mutated	ER: Estrogen receptor
ATR: Ataxia telangiectasia Rad-3 related kinase	ER+: Estrogen receptor positive
AURKA: Aurora kinase A	ER-: Estrogen receptor negative
BCa: Breast cancer	ERK2: Extracellular signal-regulated kinase 2
BrdU: 5-bromodeoxyuridine	FAO: Fatty acid oxidation
CAM: Chorioallantoic membrane	FOXA1: Forkhead box A1
CDC25A: Cell division cycle 25 homolog A	FBS: Fetal Bovine Serum
CDKN1A: Cyclin Dependent Kinase Inhibitor 1A, p21 ^{WAF1/Cip1}	FDR: false discovery rate
CDKN2A: cyclin-dependent kinase inhibitor 2A, p16 ^{INK4a}	FSC: Forward scatter
cDNA: Complementary DNA	GAPDH: Glyceraldehyde-3-Phosphate Dehydrogenase
CHK2: Checkpoint kinase-2	GAS: IFN-γ activation site
CK2: Casein kinase 2	GEO: Gene Expression Omnibus
CDK: Cyclin-dependent kinase	GLM: Generalized linear model
CDKI: Cyclin-dependent kinase inhibitor	H3K9Me3: Lysine 9-trimethylated histone H3
CM: Conditioned media	HER2: Human epidermal growth factor receptor 2
CML: Chronic myeloid leukemia	HDAC7: Histone deacetylase 7
CRISPR: Clustered regularly interspaced short palindromic repeats	HIF1α: Hypoxia-inducible factor 1 alpha
DCF-DA: 2',7'-dichlorofluorescein diacetate	HMGA: high-mobility group A
DCIS: Ductal carcinoma <i>in situ</i>	HP1: Heterochromatin protein 1
DDR: DNA damage response	HSC: Hematopoietic stem cells
DepMap: Cancer Dependency Map Project at the Broad Institute	IARC: International Agency for Research in Cancer
dH2O: Distilled water	IDC NOS: Invasive ductal carcinoma, not otherwise specified

Abbreviations

IFN: Interferons	PICS: PTEN-loss induced cellular senescence
IHC: Immunohistochemistry	PIK3CA: phosphatidylinositol-4,5-bisphosphate 3-kinase catalytic subunit α
ISRE: IFN- α /- β stimulated response element	PIM1: Proviral integration site for Moloney murine leukemia virus-1
KDa: Kilodalton	PML: Promyelocytic leukemia protein/gene
KRT: Cytokeratin	PML-NB: PML nuclear bodies
LC-MS: liquid chromatography-mass spectrometry	PMSF: Phenylmethylsulfonyl fluoride
LCIS: Lobular carcinoma <i>in situ</i>	PPARD: Peroxisome-proliferator activated δ
LIC: Leukemia-initiating cell	PR: Progesterone receptor
MAPK: mitogen-activated protein kinase	PR+: Progesterone receptorpositive
MAP3K1: mitogen-activated protein kinase kinase kinase 1	pRB: Retinoblastoma protein
mg: Milligram	RAS^{V12}: RAS mutant in valine 12
ml: Milliliter	ROS: Reactive oxygen species
mm: Millimeter	ROR: Risk of recurrence
mM: Millimolar	RT: Room temperature
mm³: Cubic millimeters	RT-Q-PCR: Real time quantitative PCR
MRI: Magnetic resonance imaging	rtTA3: Reverse tetracycline-controlled transactivator 3
mRNA: Messenger RNA	SA-β-gal: Senescence-associated β -galactosidase
mTOR: mammalian target of rapamycin	SAHF: Senescence associated heterochromatin foci
NLS: Nuclear localization signal	SASP: Senescence associated secretory phenotype
nM: Nanomolar	s.e.m: Standard error of the mean
OIS: Oncogene-induced senescence	shC: Scramble shRNA
PARP: Poly (ADP-ribose) polymerase-1	shRNA: Short hairpin RNA
PBS: Phosphate buffered saline	siRNA: Small interfering RNA
PCA: principal component analysis	SOX9: SRY-box transcription factor 9
PD-1: Programmed death-1	Stp: Staurosporine
PD-L1: programmed death-ligand 1	SSC: Side scatter
PDX: Patient derived xenografts	STAT: Signal transducers and activators of transcription
PET: Positron emission tomography	TCGA: The Cancer Genome Atlas TCGA
PFA: Paraformaldehyde	
p-HP1γ: Phospho-heterochromatin protein-1 gamma	

TF: Transcription factors

TNBC: Triple negative breast cancer

TP53: Tumor protein 53

TPM: Transcripts Per Kilobase Million

TRE: Tetracycline response element

TBS-T: Tris-buffered saline solution
containing 0.01% Tween-20

VC: Vehicle

WHO: World Health Organization

Summary	19
----------------------	----

Introduction

I Cancer	23
I.1 Tumor progression and the hallmarks of cancer	23
II Breast cancer	25
II.1 Anatomy of the normal breast	25
II.2 Breast cancer epidemiology and risk factors.....	26
II.3 Breast cancer initiation and progression	27
II.4 Breast cancer classification	27
II.4.1 Histopathological classification.....	28
II.4.2 Histological grade	28
II.4.3 TNM classification.....	29
II.4.4 Receptor status classification	29
II.4.5 Molecular classification.....	30
II.5 BCa diagnosis and treatment	32
III Promyelocytic leukemia protein	33
III.1 Regulation of PML expression.....	34
III.1.1 Transcriptional regulation	34
III.1.2 Post-transcriptional regulation	34
III.1.3 Post-translational regulation	35
III.2 Biological functions of PML	35
III.2.1 Regulation of transcription.....	35
III.2.2 DNA damage response	36
III.2.3 Apoptosis	36
III.2.4 Senescence	36
III.2.5 Viral infection	37
III.3 PML in cancer.....	37
IV Senescence	38
IV.1 Types of senescence.....	39
IV.1.1 Replicative senescence	39
IV.1.2 Oncogene-induced senescence	40
IV.1.3 Stress and other inducers of senescence	40
IV.2 Hallmarks of senescence.....	41
IV.2.1 Morphological alterations.....	41
IV.2.2 Signaling pathways involved in senescence response	42
V Oncogene addiction	43
Hypothesis and Objectives	47

Materials and Methods

I	Materials	51
I.1	Cell lines and culture conditions.....	51
I.2	Drugs.....	52
II	Methods	53
II.1	Cloning	53
II.2	Stable cell line generation	56
II.2.1	Lentivirus production and target cell infection.....	57
II.3	Cellular analysis	60
II.3.1	Proliferation assay by crystal violet staining	61
II.3.2	DNA synthesis rate analysis by bromodeoxyuridine.....	61
II.3.3	Cell size analysis by flow cytometry.....	62
II.3.4	Senescence associated β -Galactosidase assay.....	63
II.3.5	Immunofluorescence	63
II.3.6	ROS production measurement.....	64
II.4	Molecular analysis.....	64
II.4.1	Gene expression analysis	64
II.4.2	Protein expression analysis	66
II.4.3	Chromatin immunoprecipitation	67
II.4.4	Senescence associated secretome analysis	68
II.5	Subcutaneous xenograft experiments in nude mice	69
II.5.1	Pathological analysis of xenograft samples	69
II.5.2	Slide processing for immunohistochemistry: antibody staining	69
II.5.3	Sample evaluation.....	70
II.6	Tumor growth analysis using chicken chorioallantoic membrane model.....	70
III	Bioinformatic analysis	71
III.1	Depmap.....	71
III.2	Patient samples.....	71
IV	Statistical analysis	71
IV.1	Secretome statistical analysis	72

Results and Discussion

I	Analysis of the pro-survival role of PML in triple negative breast cancer	75
I.1	Analysis of PML status in patient and cell line datasets	75
I.2	Generation of the working cellular systems	80
I.3	Consequences of PML silencing in cell growth.....	81
I.3.1	Effect of PML silencing on cell number.....	82
I.3.2	Effect of PML silencing on the activation of senescence <i>in vitro</i>	83
I.3.3	Effect of PML silencing in tumor growth and senescence <i>in vivo</i>	90

II Elucidation of the molecular mechanism underlying the antiproliferative effect upon PML silencing	94
II.1 Analysis of PML loss-induced molecular signaling changes	94
II.1.1 Deciphering the molecular driver of the senescence phenotype	94
II.1.2 Effect of PML loss on a large growth-sustaining signaling program	102
II.2 Deciphering PML addiction of TNBC cells vs non-TNBC cells.....	111
II.3 Arsenic trioxide as a pharmacological inhibitor of PML in TNBC	116

General discussion

I Understanding the basis of breast cancer for an improved personalized medicine ..	121
Breast cancer stratification: when is a positive truly a positive?	121
Targeted therapies: searching for the Valyrian steel against TNBC	122
II Senescence: good or evil	125

Conclusions	129
--------------------------	-----

Bibliography and Annex

I Bibliography	133
II Annex	150

Contributed publications	157
---------------------------------------	-----

Introduction

Figure I1. Representation of tumor progression.....	24
Figure I2. Revisited hallmarks of cancer	25
Figure I3. Anatomy of the human breast.....	26
Figure I4. Schematic representation of BCa progression.. ..	27
Figure I5. BCa histological grading score system.	28
Figure I6. TNM grading system used for the evaluation of BCa.. ..	29
Figure I7. Molecular classification of breast cancer.. ..	31
Figure I8. Human cells express a variety of PML isoforms.. ..	33
Figure I9. Summary of the dual functions of PML in cancer.. ..	38
Figure I10. Physiological consequences of senescence response.....	39
Figure I11. Causes of cellular senescence.. ..	40
Figure I12. Morphological and signalling pathway alterations as hallmarks of senescence.	43

Materials and Methods

Figure M1. Schematic representation of Tet-pLKO-puro inducible vector.	54
Figure M2. Schematic figure of TRIPZ™ inducible vector.	54
Figure M3. Timeline of the experimental protocol for virus production using HEK293FT cells.....	57
Figure M4. Figure showing the packaging system and lentivirus production in HEK293FT cells..	57
Figure M5. Schematic representation of experiment plating with doxycycline induction.	60

Results

Figure R1. PML mRNA expression based on ER status.....	76
Figure R2. PML mRNA expression among the molecular subtypes	77
Figure R3. PML mRNA expression in basal-like subtype and non-basal tumors	78
Figure R4. PML mRNA expression in cell lines from DepMap.....	79
Figure R5. PML protein expression in cell lines.	79
Figure R6. PML silencing in MDA-MB-231 cell line.....	80
Figure R7. Detection of PML isoforms at protein level by Bethyl antibody	80
Figure R8. Effect of inducible sh4PML in breast cancer cell lines.	81
Figure R9. PML silencing decreases growth of MDA-MB-231 cell line.....	83
Figure R10. Effect of PML silencing in the morphology of MDA-MB-231 cells	84
Figure R11. FACS analysis of the morphological changes of MDA-MB-231 cells upon PML loss	85
Figure R12. SA-β-gal staining increases after PML silencing	86
Figure R13. PML silencing affects nuclear lamina protein levels.....	87
Figure R14. PML and ROS.....	87
Figure R15. SAHF do not appear upon PML silencing	88

Figure R16. Proteomics analysis of the secretome of MDA-MB-231 cells upon PML inducible silencing	89
Figure R17. Tumor growth of MDA-MB-231 xenografts is curbed upon PML loss <i>in vivo</i>	91
Figure R18. Analysis of p-HP1 γ levels <i>in vivo</i>	91
Figure R19. Primary tumor growth of MDA-MB-231 is decreased upon PML loss in CAM model.	92
Figure R20. PML silencing increases p27 levels	95
Figure R21. p27 levels start to increase 2 days after doxycycline addition	96
Figure R22. p27 is accumulated in the nucleus upon PML loss	98
Figure R23. The increase of p27 levels deregulates cell cycle.....	99
Figure R24. Double silencing of PML and p27 rescues the senescence phenotype	101
Figure R25. Cell growth is not rescued upon PML and p27 silencing.	102
Figure R26. Correlation analysis of PML mRNA expression with MYC and PIM1 in patient datasets	104
Figure R27. Correlation analysis of PML with c-MYC and PIM1 in cell lines from DepMap	105
Figure R28. C-MYC levels are decreased when PML and p27 are silenced together	105
Figure R29. PML silencing decreases c-MYC protein and mRNA levels	106
Figure R30. PML is in the vicinity of MYC promoter.....	107
Figure R31. C-MYC silencing recapitulates the phenotype induced by PML loss.....	108
Figure R32. PML regulates PIM1 at the transcriptional level.....	109
Figure R33. PIM1 silencing further impacts in the senescence phenotype induced by PML loss	110
Figure R34. PML silencing differentially affects TNBC and non-TNBC cell growth.....	111
Figure R35. PML loss induces a senescence phenotype in high PML expressing TNBC cell lines but not in ER + cells.	112
Figure R36. PML loss induced p27 increase is limited to the MDA-MB-468 cell line.....	113
Figure R37. Growth regulatory pathways are deregulated in MDA-MB-468 cell line upon PML silencing.	113
Figure R38. C-MYC levels are only decreased in TNBC cell line.....	114
Figure R39. Secretome of Cama-1 cell line is not affected by PML silencing	115
Figure R40. Pharmacological inhibition of PML by ATO does not recapitulate the effect of genetic PML silencing.....	116

General discussion

Figure D1. The ability to stratify breast cancer patients into different subtypes implies different treatment opportunities for those patients.....	123
Figure D2. Mode of action of arsenic trioxide induced PML degradation.	124

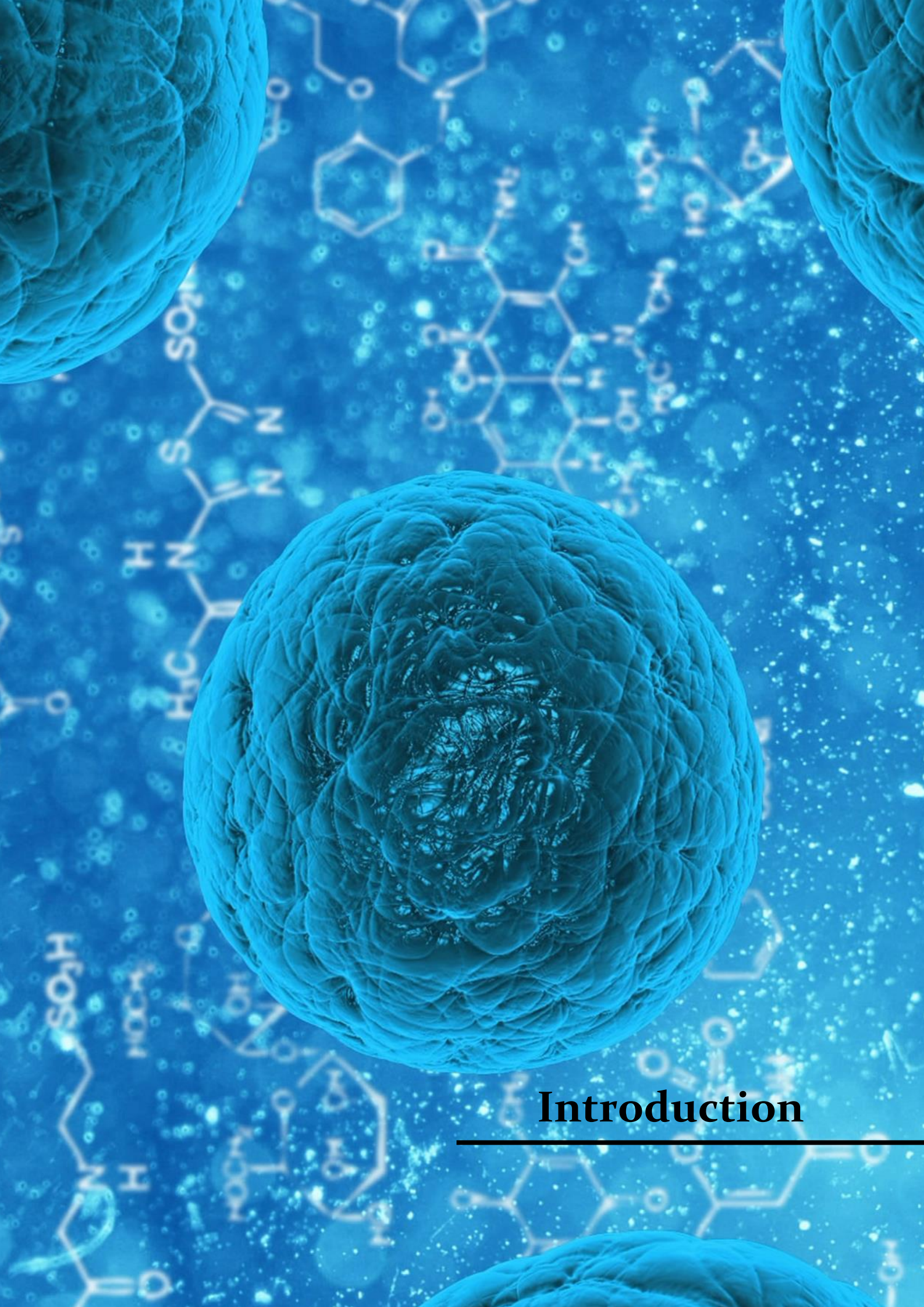
Materials and Methods

Table M1. Detailed list of the different BCa cell lines used during this work. Mutation data was taken from COSMIC database (www.sanger.ac.uk/genetics/CGP/cosmic/).....	51
Table M2. Experimental specifications for the different drugs used during the thesis work.	52
Table M3. Information about the primers used for the different cloning strategies.	55
Table M4. Specific vectors used for second generation lentivirus production (quantities for 100 mm plates).	58
Table M5. Specific vectors used for third generation lentivirus production (quantities for 100 mm plates).	59
Table M6. Approximate number of cells seeded for the different experiments with inducible silencing systems after 3 days of pre-induction in 100 mm plates.	61
Table M7. References and preparation of the antibodies used for immunofluorescence.	63
Table M8. Specifications of primer sequences and probe numbers from Universal Probe Library (Roche).	65
Table M9. References and preparation of primary and secondary antibodies employed for Western Blotting.	67
Table M10. Steps followed to process xenograft tissues in the automatic processor.	70

Annex

Table A1. DepMap cell line expression values and classification based on ER, PR and Her2 status.	150
Table A2. List of differentially secreted proteins upon silencing the PML protein in MDA-MB-231 cells.	151
Table A3. List of differentially secreted proteins upon silencing the PML protein in Cama-1 cells.	153

The hypothesis of oncogene addiction postulates that the survival and growth of certain tumor cells is dependent upon the activity of one oncogene, despite their multiple genetic and epigenetic abnormalities. This phenomenon has provided the foundation for molecular targeted therapy and a rationale for oncogene-based stratification. The promyelocytic leukemia protein (PML) is overexpressed in triple negative breast cancer (TNBC) and it regulates cancer-initiating cell function, thus suggesting that this protein can be therapeutically targeted in combination with PML-based stratification. However, the effects of PML perturbation on the bulk of tumor cells remains poorly understood. In this thesis work we demonstrated that TNBC cells are addicted to the expression of this nuclear protein. PML inhibition led to a remarkable growth arrest combined with features of senescence *in vitro* and *in vivo*. Mechanistically, we observed that growth arrest and senescence were associated to a decrease in *MYC* and *PIM1* kinase levels, with the subsequent accumulation of cyclin-dependent kinase inhibitor 1B (CDKN1B, p27), a trigger of senescence. In line with this notion, we found that PML is associated to the promoter regions of *MYC* and *PIM1*, consistent with their direct correlation in breast cancer specimens. Altogether, our results provide a feasible explanation for the functional similarities of *MYC*, *PIM1*, and PML in TNBC and encourage further study of PML-targeting strategies for the treatment of this breast cancer subtype.



Introduction

I Cancer

Cancer has been part of human life since the very beginning of their history. It encompasses a group of diseases in which an unrestrained proliferation of cells occurs leading to the formation of an abnormal cellular mass, denominated tumor. This term covers more than 100 forms of the disease, as almost every tissue can develop one or even several types of these malignancies¹. Tumors share the capability to sustain uncontrolled growth, but their heterogeneity enforces the necessity of specific molecular classifications that allow the diagnosis and treatment of tumors as unique entities². Precision medicine aims to develop prevention and treatment strategies that will benefit tumors that share specific characteristics, taking into account individual variability in genes, environment, and lifestyle for each case.

According to the World Health Organization (WHO, with data collected by the International Agency for Research in Cancer-IARC in the last Globocan 2018 report), cancer will be the leading cause of morbidity and mortality in the 21st century. In fact, 18 million new cases and 9.6 million cancer deaths were estimated for 2018. The most common cancers were those of the lung (11.6%), breast (11.6%), colorectal (10.2%), prostate (7.1%) and stomach (5.7%). All these data highlight the importance of cancer research nowadays³.

I.1 Tumor progression and the hallmarks of cancer

After decades of research the idea that cancer is a genetic disease has been extensively recognized⁴. Mutations can happen both in the germline, with inherited mutations that can shorten the time of onset of the disease, or in somatic cells, which results in sporadic tumors⁴. Different genetic and epigenetic modifications will continue accumulating in a stepwise manner during tumor progression, clonally expanding cell populations that ultimately acquire more aggressive phenotypes⁵.

The process of tumor development frequently starts with the increased proliferation of normal cells harboring oncogenic mutations, thus leading to pre-malignant lesions, such as hyperplasia and dysplasia. Subsequent mutations will make cells continue growing uncontrollably. If the tumor cells remain in the tissue of origin it will be called *in situ* cancer. Cells can accumulate more mutations becoming more aggressive, invading adjacent tissues and reaching the bloodstream or lymph nodes, ultimately establishing disseminated tumors, also known as metastases (**Fig. I1**)¹.

The differentially altered genes in each cancer at the distinct stages of the disease illustrate the complexity of tumors. This heterogeneity increases with cancer progression and it is one of the main concerns in cancer treatment.

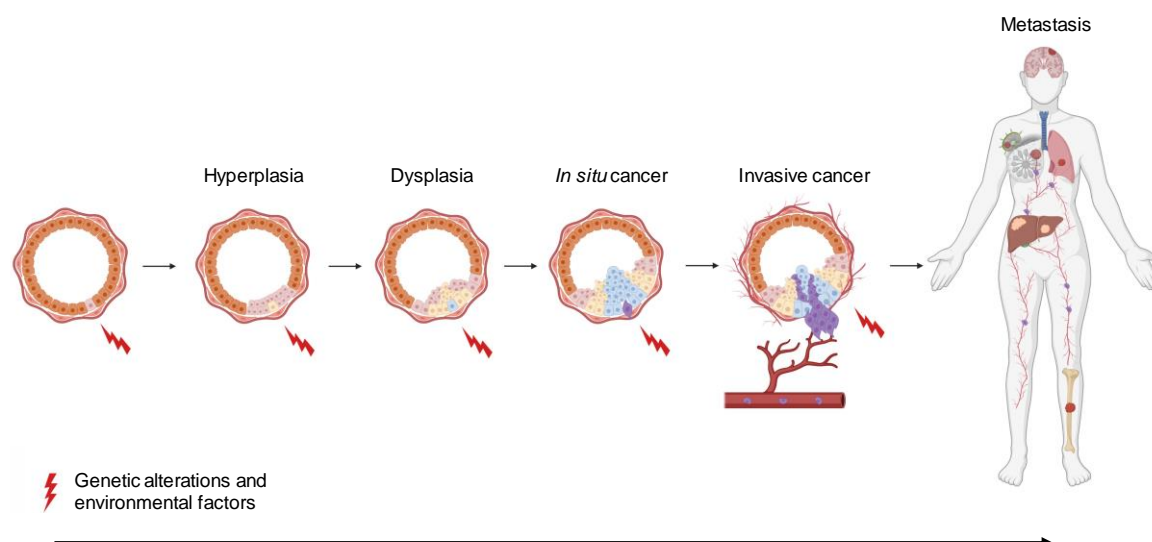


Figure I1. Representation of tumor progression.

In tumorigenesis, alterations in three types of genes have been described to be relevant: oncogenes, tumor suppressors and genome stability genes. Mutations in oncogenes and tumor suppressors lead to a constitutive activation or to a reduced activity of the gene product, respectively. Finally, stability genes are responsible of maintaining mutation rate to the minimum. Thus, their inactivation leads to higher alterations in the first two gene types affecting their correct function⁴.

Despite the complexity and the different genetic alterations involved in the multistep process of tumorigenesis, almost two decades ago Hanahan and Weinberg² identified the six capabilities any cancer cell should acquire to develop a malignant phenotype: i) self-sufficiency in growth signals, ii) insensitivity to growth-inhibitory signals, iii) evasion of programmed cell death (apoptosis), iv) limitless replicative potential, v) sustained angiogenesis and vi) tissue invasion and metastasis (**Fig. I2**).

Several mechanisms ensure the maintenance of the genome integrity, ensuring a low rate of mutations; they describe genome instability as an enabling characteristic for the acquisition of the six capabilities that allow cancer cells to survive, proliferate and disseminate. Some years later, with the gained knowledge in cancer field, the same authors proposed two emerging hallmarks⁶: evading immune destruction and reprogramming energy metabolism. In addition, tumor-promoting inflammation is described as an emerging enabling characteristic contributing to tumor growth by the secretion of growth-sustaining and cell death limiting survival factors, pro-angiogenic factors and extracellular matrix-modifying enzymes. Understanding tumor microenvironment and the role of the specialized cells that form carcinomas will open new ways of studying tumor biology.

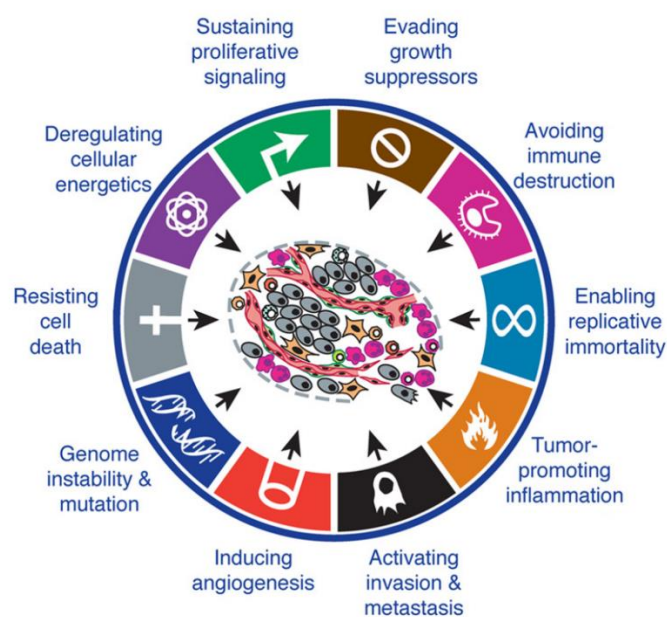


Figure I2. Revisited hallmarks of cancer (adapted from Hanahan and Weinberg, 2011⁶).

II Breast cancer

II.1 Anatomy of the normal breast

Mammary glands are unique and specialized sweat glands that differentiate mammals from other animals. Their specific function is to synthesize and secrete milk for nourishing the newborns⁷. In humans, mammary glands are present in both females and males (**Fig. I3A** and **Fig. I3B**). Female breast development occurs in different stages, from embryonic development to the complete development during adulthood, undergoing dramatic changes induced by hormones and other signaling pathways⁸. Male breast is considered a vestigial organ, as it lacks the specialized structure since there is no physiologic need for milk production.

Human mammary gland is structured into a tree-like network of branched ducts and lobes surrounded by adipose and connective tissue. The ductal system terminates in lobular units commonly known as terminal duct lobular units, the structures where milk is produced. Two types of cells comprise the mammary epithelium: an inner layer of polarized luminal epithelial cells and an outer layer of myoepithelial or basal cells, separated from the stroma by the basement membrane (**Fig. I3C**)^{9,10}.

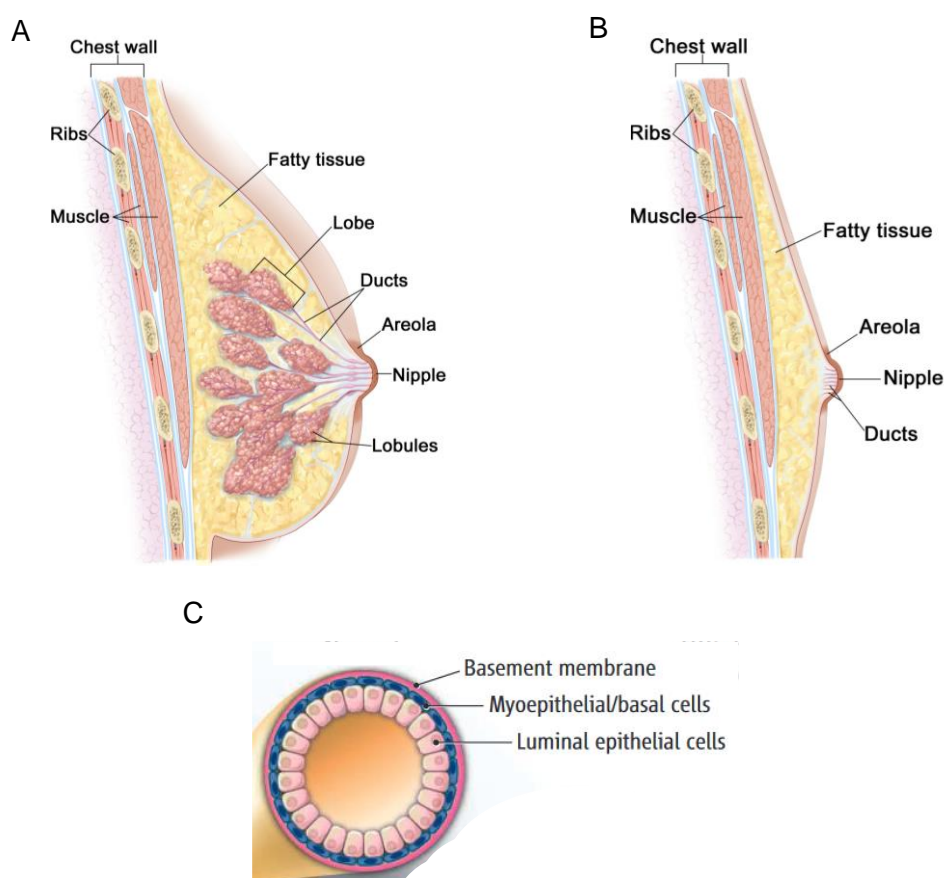


Figure 13. Anatomy of the human breast. A-B) Pictures showing the localization and structure of the different regions of the mammary gland in A) females and B) males. C) Scheme depicting the different cellular types of the mammary epithelium (adapted from Marshall, 2014¹¹).

II.2 Breast cancer epidemiology and risk factors

Breast cancer (BCa) is one of the most frequent cancers worldwide together with lung and colorectal cancer. Importantly, BCa is the most common malignancy among women. In 2018, approximately 2.1 million women were diagnosed of BCa and 626,679 died from the disease. In Spain, it was the most diagnosed neoplastic disease among women in 2018 with 32,825 cases³.

Several factors have been linked with BCa development, including gender, age (it is highly related to increasing age), ethnicity, lifestyle (diet, alcohol consumption) and reproductive factors (early menarche, late menopause, late age at first pregnancy)^{12,13}. Family history is also associated with increased BCa risk, accounting for the 5-10% of the BCa cases. Specifically, women with mutations in *BRCA1* and *BRCA2* are more likely to develop BCa by age of 70^{14,15}. BCa incidence for *BRCA* mutation carriers starts to increase with age in early adulthood¹⁶.

II.3 Breast cancer initiation and progression

Malignant tumors that originate from mammary epithelial cells are adenocarcinomas. BCa initiates due to transforming genetic and epigenetic events in a single cell. The accumulation of additional genetic changes combined with clonal expansion and selection will drive tumor progression¹⁷. The progression of BCa involves different stages, starting with pre-malignant lesions (ductal hyperproliferation and *in situ* lesions), continuing with invasive cancer and finalizing with metastatic spread. Ductal carcinoma *in situ* (DCIS) is thought to be the precursor of invasive lesions¹⁸. Progression to invasive carcinoma occurs when myoepithelial cell layer and basement membrane are lost. Upon the disruption of the normal breast tissue architecture, tumor cells can invade surrounding tissues and migrate to distant organs, leading to the formation of metastasis (**Fig. I4**). The most common sites of metastasis in BCa are lymph nodes, bone, lung, brain and liver¹⁹.

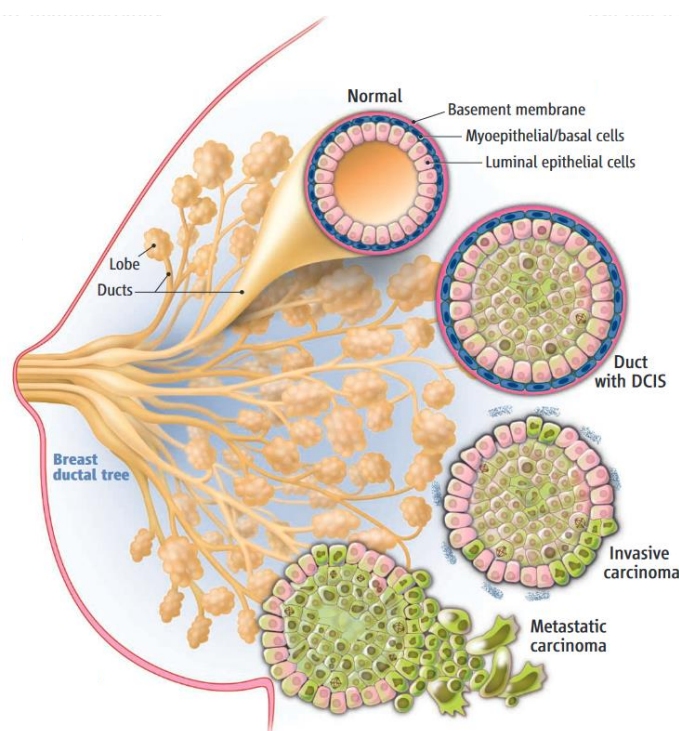


Figure I4. Schematic representation of BCa progression. Description of normal, *in situ*, invasive and metastatic lesion development (adapted from Marshall, 2014¹¹).

II.4 Breast cancer classification

BCa is genetically and clinically a very heterogeneous disease with different disease courses and treatments²⁰. Several BCa classifications have been developed based on the distinct histological, clinical and molecular phenotypes.

II.4.1 Histopathological classification

Pathology classifies tumors based on their morphological and structural characteristics observed under the microscope. BCa is classified as either non-invasive (carcinoma *in situ*) or invasive. Invasive ductal carcinoma, not otherwise specified (IDC NOS) is the most common observed BCa type, with around the 75% of the cases. This group is comprised by tumors with no special characteristics of differentiation patterns. The next most frequent histologic type is invasive lobular carcinoma (ILC) with about the 10% of the cases. Other less common carcinomas are categorized as medullary, neuroendocrine, tubular, apocrine, metaplastic, mucinous, inflammatory, comedo, adenoid cystic and micropapillary subtypes²¹. Among the *in situ* lesions, which are thought to be the precursors of invasive carcinomas, ductal and lobular (LCIS) carcinomas are the best characterized^{22,23}.

II.4.2 Histological grade

Histological grading is an important prognostic factor in BCa based on the degree of differentiation of the tumor tissue²⁴. The most used grading system is known as Nottingham (Elston-Ellis²⁴) and it is a modification of the Scarff-Bloom-Richardson grading system²⁵. In this system three parameters are evaluated: tubule formation, nuclear polymorphism and mitotic rate (**Fig. I5**). Each factor is evaluated individually and a numerical score (1-3) is given taking into account the 3 characteristics: grade 1 tumors are well differentiated, grade 2 tumors are moderately differentiated and grade 3 tumors are poorly differentiated.

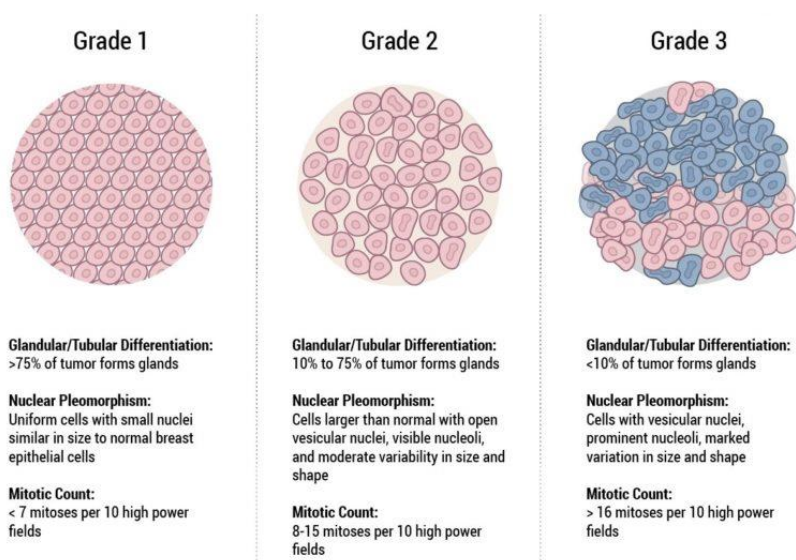


Figure I5. BCa histological grading score system. Scheme describing the characteristics and the values of tubule formation, nuclear polymorphism and mitotic rate of the Elston-Ellis grading system.

II.4.3 TNM classification

The TNM classification is a globally recognized tool in the clinical routine. This system describes the anatomic spread of the cancer: it separately classifies the tumor (T), lymph node (N), and metastatic (M) elements and then group them into stages. It provides clinicians information that helps in the evaluation of the most appropriate treatment options depending on the cancer stage. Stage I–III BCa (without distant metastasis) is considered curable, while stage IV BCa (with distant metastasis) is considered incurable^{26,27} (**Fig. I6**).

Stage	Description
Noninvasive	
0	No evidence of cancer cells or invasion of the basement membrane of the duct or neighbouring normal tissue; includes ductal carcinoma in situ
Invasive	
IA	<ul style="list-style-type: none"> • Tumour ≤ 2 cm AND • No spread outside the breast; no lymph nodes involved
IB	<ul style="list-style-type: none"> • No tumour in the breast, but microscopic metastases (> 0.2 mm but ≤ 2 mm) present in axillary lymph nodes OR • Tumour present in the breast, ≤ 2 cm, with involvement of lymph nodes
IIA	<ul style="list-style-type: none"> • No tumour in the breast, but macroscopic cancer (> 2 mm) in 1–3 axillary lymph nodes OR • Tumour ≤ 2 cm, with spread to axillary lymph nodes OR • Tumour > 2 cm but ≤ 5 cm, with no spread to axillary lymph nodes
IIB	<ul style="list-style-type: none"> • Tumour > 2 cm but ≤ 5 cm, with spread to 1–3 axillary lymph nodes OR • Tumour > 5 cm, with no spread to axillary lymph nodes
IIIA	<ul style="list-style-type: none"> • No tumour in the breast or presence of a breast tumour of any size associated with metastases in 4–9 axillary lymph nodes or in internal mammary nodes OR • Tumour > 5 cm, with spread to axillary and/or internal mammary nodes
IIIB	<ul style="list-style-type: none"> • Tumour of any size, with spread to chest wall and/or skin of the breast; may also have spread to axillary or internal mammary nodes
IIIC	<ul style="list-style-type: none"> • Tumour of any size, with spread to ≥ 10 axillary lymph nodes OR • Spread to lymph nodes above or below the collarbone (supraclavicular nodes) OR • Spread to both axillary lymph nodes and internal mammary nodes
Metastatic	
IV	Spread of cancer to other parts of the body such as liver, lung or bone

Figure I6. TNM grading system used for the evaluation of BCa. Table describing the extent of primary tumour, lymph node involvement and metastasis detection according to the TNM evaluation system (adapted from Simos *et al.*, 2015²⁸).

II.4.4 Receptor status classification

The expression of estrogen receptor (ER), progesterone receptor (PR) and human epidermal growth factor receptor 2 (HER2) are important determinants of BCa biology. Paraffin embedded BCa samples are routinely analyzed by immunohistochemical (IHC) analysis to detect ER, PR and HER2 expression. BCa tumors are classified into 3 clinically significant subtypes:

hormone receptor positive BCa and two different groups of ER negative (ER-) tumors, HER2 positive BCa and triple negative breast cancer (TNBC).

Around the 70% of human BCa express ER and may express PR, both predictive and prognostic biomarkers for this disease. ER expression is the main indicator of potential responses to hormonal therapy²⁹. ER and PR are nuclear receptors that exert their biological activity upon the binding of estrogen and progesterone, respectively. They play important roles in proliferation and cell cycle regulation of BCa cells^{30,31}. Overall survival, disease free survival and time to recurrence have been shown to be positively associated with ER expression³². Low or absent expression of PR in ER positive (ER+) breast tumors is associated with more proliferative and aggressive disease, poorer prognosis and recurrence when compared to PR positive (PR+)/ER+ tumors³³.

HER2 is a transmembrane tyrosine kinase involved in the regulation of cellular growth. HER2 is overexpressed/amplified in approximately the 15% of BCa and it is associated with a more aggressive phenotype³⁴. HER2 is an important predictive biomarker of response to HER2-targeted therapies³⁵.

Triple negative tumors are characterized by the lack of the three receptors (ER, PR and HER2). Around 15% of BCa tumors belong to this subtype. TNBC affects more frequently younger patients and it is more prevalent in African-American women³⁶. Despite its relatively small proportion among all BCa, TNBC is responsible for a relatively large proportion of BCa deaths. TNBC is significantly more aggressive and it shows poorer prognosis than tumors of the other subgroups^{37,38}. TNBC patients do not benefit from any targeted therapy and the only available systemic treatment is chemotherapy³⁹. Gene expression analysis of 21 BCa datasets identified six different TNBC subtypes: basal-like 1 and basal-like 2, immunomodulatory, mesenchymal, mesenchymal stem-like and luminal androgen receptor subgroups⁴⁰.

Ki-67 is a nuclear protein used as a proliferation marker. It is active in all cell cycle phases except G₀. Ki-67 is assessed routinely in clinical practice by IHC together with ER, PR and HER2, as proliferative activity determined by Ki-67 may reflect the aggressive behavior of BCa and provide further prognostic information^{41,42}.

BCa stratification based on receptor status is an important tool for clinicians to design a specific treatment strategy for each subtype, as ER, PR and HER2 presence or absence will be indicative of the prognosis and response to treatments.

II.4.5 Molecular classification

Microarray-based gene expression analysis of BCa tumors identified five distinct molecular subtypes, also known as BCa intrinsic subtypes: luminal A, luminal B, HER2-enriched, basal-like and normal-like (**Fig. 17**). Approximately 500 genes were described to cluster tumor

samples according to the similarities on their gene expression profiles. The five molecular subtypes are associated with different prognostic and therapeutic implications⁴³⁻⁴⁶.

Both luminal groups express ER but in a different grade. Luminal A tumors express high levels of ER and are typically low grade. They show high expression of GATA3, forkhead box A1 (FOXA1) and luminal cytokeratin 8 (KRT8) and 18 (KRT18). They show low mutation rate, with the most frequently mutated genes being phosphatidylinositol-4,5-bisphosphate 3-kinase catalytic subunit α (*PIK3CA*), *GATA3* and mitogen-activated protein kinase (MAPK) kinase kinase 1 (*MAP3K1*). Tumors of the luminal B group are characterized by a lower expression of ER. They are more proliferative, of higher grade and with worse prognosis than luminal A tumors, probably due to the similarities with the ER negative subtypes (HER2-enriched and basal-like). Luminal B tumors frequently exhibit mutations in the tumor protein *TP53* (p53, tumor protein 53) and *PIK3CA* genes, and alterations affecting the retinoblastoma and MAPK pathways. A proportion also shows overexpression of HER2.

HER2-enriched subtype is characterized by high expression of *ERBB2* and genes located closely in the same chromosome region. These tumors are commonly negative for expression of ER and luminal epithelial genes and show high expression of cell cycle associated genes. When compared with luminal tumors, HER2-enriched group shows less favorable overall and relapse-free survival.

Tumors from basal-like subtype express neither ER nor PR and are negative for HER2. They are characterized by high expression of the basal cytokeratins 5 (KRT5) and 17 (KRT17), and other genes typically expressed in mammary basal/myoepithelial cells. Basal-like tumors usually overexpress epidermal growth factor receptor (EGFR) and mutations in *TP53* are commonly described. Basal-like subtype has the worst clinical outcome among all the subtypes, with shorter overall and relapse-free survival times⁴⁷.

Finally, tumors included in the normal breast-like group show expression of genes associated with other non-epithelial cells and adipose tissue.

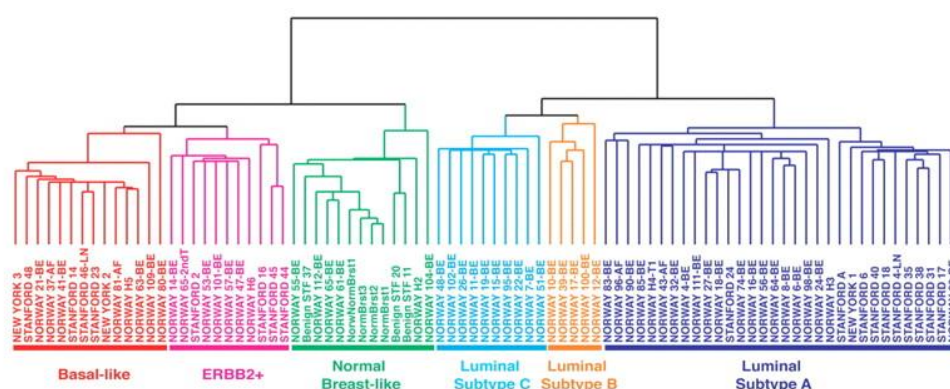


Figure 17. Molecular classification of breast cancer. Genetic expression analysis of breast carcinomas identified the five molecular subtypes that we know nowadays. Later studies failed to reproduce the luminal-C subtype and the luminal groups were divided into A and B subtypes (image of the first classification, adapted from Sørlie *et al.*, 2001⁴⁴).

II.5 BCa diagnosis and treatment

The vast majority of symptomatic BCa patients present a discrete breast lump at the time of diagnosis. A complete clinical evaluation integrates information from clinical examination (breast and lymph nodes), imaging (mammography, ultrasound, magnetic resonance imaging (MRI), positron emission tomography (PET)) and tissue biopsy (fine-needle aspiration cytology or core biopsy)⁴⁸.

Several microarray-based multigene assays have been developed and are already being used in the clinic with BCa patients. Based on different gene signatures, they give information about prognosis and treatment response:

- Prosigna™ breast cancer prognostic gene signature: this test is a PAM50-based subtype classifier, a gene signature that measures the expression of 50 different genes. The Prosigna assay reports a risk of recurrence (ROR) score (0–100), an intrinsic subtype classification (luminal A, luminal B, HER2-enriched or basal-like) and risk categorization (low, intermediate, or high) for each tumor sample. Prosigna is indicated for use in postmenopausal women with hormone receptor-positive, node-negative or node-positive early-stage (stages I, II and IIIA) BCa to be treated with endocrine therapy^{49,50}.
- MammaPrint™: this assay is focused on analyzing the risk (low or high) of relapse for newly diagnosed BCa patients. It is comprised by 70 genes associated with proliferation, invasion, metastasis, stromal integrity and angiogenesis. MammaPrint is indicated for women under the age of 55 with either ER+ or ER-, lymph node-negative BCa⁵¹.
- OncotypeDX™: the assay quantifies gene expression of 21 genes. It predicts the 10-year risk of BCa recurrence and if the patient will benefit from chemotherapy treatment in addition to hormone therapy. Oncotype DX™ is used in women with ER+, HER2-negative, early stage invasive BCa. It assigns a score between 0 and 100 that will be analyzed depending on the age of the patient⁵².

The treatment of BCa may include surgery, radiotherapy and systemic therapies (endocrine therapy, anti-HER2 therapies and chemotherapy). Nowadays, breast conservation is established as the standard of care surgical procedure for early stage BCa (without metastasis). If cancer cells are detected in lymph nodes, their surgical removal is also considered. Radiotherapy is administered after surgery to reduce the risk of relapse^{48,53}. The standard therapy for ER+ and/or PR+ tumors is endocrine therapy, with tamoxifen as the recommended hormone therapy drug. Patients with overexpression of HER2 are treated with drugs that specifically target and block its

function by inhibiting different domains. Trastuzumab (Herceptin) and Lapatinib are broadly used drugs to treat these patients. Trastuzumab is a monoclonal antibody that binds to the extracellular domain of HER2 preventing its intracellular tyrosine kinase activity⁵⁴. Lapatinib binds to the kinase domain of both HER2 and EGFR, inhibiting their signaling⁵⁵. Cytotoxic chemotherapy remains as the standard treatment for TNBC patients. HER2 tumors also benefit from preoperative chemotherapy⁵⁶.

III Promyelocytic leukemia protein

Promyelocytic leukemia (PML, also known as TRIM19, RNF71 and MYL) protein was first discovered due to its oncogenic role in acute promyelocytic leukemia (APL). *PML* gene is located in chromosome 15q22. It was identified in the t(15;17) translocation with the gene of retinoic acid receptor α (RAR α), which results in the expression of the fusion protein PML-RAR α ^{57,58}.

The PML gene consists of 9 exons that will lead to several different isoforms through alternative splicing (**Fig. I8A**). All PML isoforms share an identical N-terminal region that contains cysteine-rich zinc binding domains (RING domain and B-boxes) and a coiled coil domain. Nuclear isoforms contain a nuclear localization signal (NLS) in exon 6 that is lacking in the cytoplasmic isoform (**Fig. I8B**)^{59,60}. The C-terminal region is variable across the different isoforms and this appears to determine PML interactions^{61,62}.

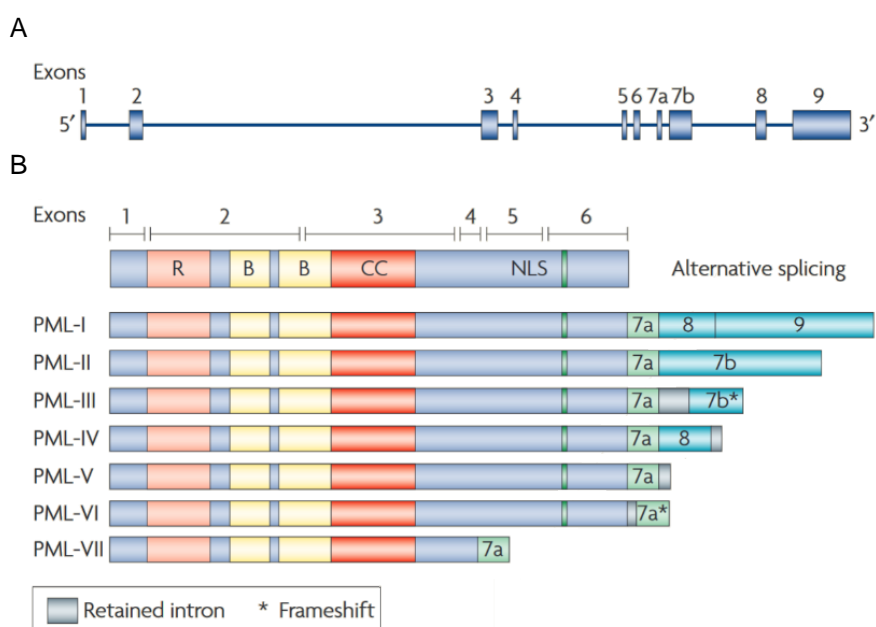


Figure I8. Human cells express a variety of PML isoforms. A) Scheme of the distribution of exons and introns of PML gene. **B)** Structure of the different PML isoforms. Nuclear PML isoforms (I-VI) share exon 1 to 6. The lack of exon 6 generates cytoplasmic PML (VI). NLS R: RING motif, B: B-box, CC: coiled-coil, NLS: nuclear localization signal. Adapted from Bernardi and Pandolfi, 2007⁶³.

PML localizes to punctuate nuclear structures known as PML nuclear bodies (PML-NB). These structures are discrete nuclear foci that range in size from 0.2 to 1 μm and in number from 1 to 30 bodies per nucleus, depending on the cell type⁶⁴. PML-NBs are dynamic and heterogeneous structures that act as scaffolds for a high number of proteins, such as p53, retinoblastoma protein (pRB), CBP/p300, histone deacetylase 7 (HDAC7) and DAXX. These proteins can localize constitutively or transiently in PML-NBs^{61,65-67}.

III.1 Regulation of PML expression

PML expression can be regulated in response to different stimuli at transcriptional, post-transcriptional and post-translational level. This regulation not only controls PML protein levels but also the nuclear body formation process and the interaction with other proteins.

III.1.1 Transcriptional regulation

Interferons (IFN) can activate PML transcription through the binding of signal transducers and activators of transcription (STAT) to IFN- α - β stimulated response element (ISRE) and an IFN- γ activation site (GAS) in the first exon of PML⁶⁸. Interferons can also induce the expression of the oncogenic fusion protein PML-RAR α ⁶⁹.

p53 can transcriptionally upregulate PML. The overexpression of RAS mutant in valine 12 (RAS^{V12}) induces a senescence response that will increase PML-NB number and size by upregulating p53^{70,71}.

III.1.2 Post-transcriptional regulation

PML expression is influenced by the cell or tissue of origin and also by the differentiation stage. One of the main contributors to these different expression patterns is alternative splicing, which results in the expression of different isoforms of PML⁶⁰. The subcellular localization of the isoforms can affect the nuclear body formation and function⁷².

III.1.3 Post-translational regulation

PML is subject to various post-translational modifications including SUMOylation, ubiquitination and phosphorylation. These modifications regulate PML protein levels, localization and activity.

The most studied PML post-translational modification is SUMOylation. PML can be modified by SUMO1, SUMO2 and SUMO3. SUMOylation is essential for the proper assembly and function of PML-NBs. It has been demonstrated that this modification is necessary for the recruitment of SP100 and DAXX, two classical nuclear body components involved in transcriptional regulation^{67,73}. In addition to PML, many proteins are SUMOylated in the PML-NBs. In fact, the RING domain of PML has been suggested to act as a SUMO E3 ligase, SUMOylating PML and other proteins⁷⁴.

PML is phosphorylated in multiple sites with each of them having a different response. Phosphorylation of PML by extracellular signal-regulated kinase 2 (ERK2) is directly linked to SUMOylation of PML in response to arsenic trioxide (ATO) treatment, inducing an apoptosis response⁷⁵. In response to DNA-damage, PML is phosphorylated by the checkpoint kinase ataxia telangiectasia Rad-3 related (ATR) kinase and checkpoint kinase-2 (CHK2). The phosphorylation by ATR mediates the translocation of PML to the nucleolus⁷⁶, while CHK2 phosphorylation triggers PML-induced apoptosis⁷⁷. Finally, casein kinase 2 (CK2), an oncogenic kinase, phosphorylates PML and induces its proteasome-dependent degradation, decreasing PML tumor suppressive activity in lung cancer⁷⁸.

PML ubiquitination, in addition to its SUMOylation, is necessary for its degradation upon ATO treatment. RNF4 is a E3 ubiquitin-protein ligase that specifically targets poly-SUMO-modified PML for degradation⁷⁹.

III.2 Biological functions of PML

PML interacts with a high number of proteins and it is able to modify their function. Therefore, PML has been described as a multi-faceted protein that plays pivotal roles in physiological and pathological conditions.

III.2.1 Regulation of transcription

PML has been described to act both as a co-activator^{80,81} and a co-repressor^{82,83} of transcription. The opposite effects in transcription by PML can be explained by several factors. The composition of the nuclear bodies by means of PML isoform will have a key role in the regulation⁸⁴.

Many transcription factors (TF) are recruited to PML-NBs or their proximity, either to take part in transcription or to be modified. PML-NBs are heterogeneous entities that can also regulate the availability of the TFs by compartmentalizing or titrating them in the nucleus⁸⁵. Interestingly, it has been proposed that PML can indirectly control transcription by remodeling chromatin structures into loop-like structures that will affect positively or negatively the transcription of the genes located there⁸⁶.

III.2.2 DNA damage response

We have previously explained how ATR is able to phosphorylate PML upon DNA damage. In addition, it has been described that PML-NB can localize to DNA repair sites and many DNA repair proteins localize to PML-NBs⁸⁷. Due to its role in targeting DNA damage pathways, PML has been linked to genomic stability. DNA helicase Bloom protein, a protein that when absent from the cell results in genomic instability and cancer predisposition, is localized into PML-NBs⁸⁸. Several proteins of the DNA damage detection and repair machinery have been observed to dynamically localize to or out of PML-NBs under stress conditions⁶⁴.

III.2.3 Apoptosis

PML is implicated in both p53-dependent and -independent apoptotic pathways. On one hand, PML activates p53 through different mechanisms: increasing its acetylation and phosphorylation^{89,90}, inhibiting the negative regulator of p53 MDM2⁹¹ or promoting p53 deubiquitination⁹². In addition, in a positive feedback loop p53 induces the expression of PML⁷¹. All these interactions regulate the stress-induced apoptosis and senescence responses. On the other hand, PML can also induce apoptosis in a p53-independent manner through IFN⁹³ and Fas⁹⁴.

III.2.4 Senescence

The role of PML in senescence was first described with its implication in RAS^{V12} induced senescence. In addition, PML is involved in the regulation of an important hallmark of senescence, the formation of senescence associated heterochromatin foci (SAHF). HIRA and ASF1a, two chromatin regulators, are essential in the process, as they drive the formation of macroH2A-containing SAHF. HIRA enters PML-NBs and transiently colocalizes with HP1 heterochromatin proteins, before the incorporation of HP1 proteins into SAHF⁹⁵.

III.2.5 Viral infection

An important role for PML has been described in anti-viral defense. PML interacts with viral proteins and inhibits their function, conferring resistance against RNA viruses or inducing apoptosis of infected cells in a p53-dependent manner. This mechanism reduces the probabilities of viral DNA integration in the genome⁹⁶.

III.3 PML in cancer

Since the discovery of its role in APL, a tumor suppressive role of PML has been observed in cancers of different origins. Many of its biological functions support this role, such as the induction of apoptosis and senescence. PML protein expression is reduced or absent in numerous cancers, such as prostate, lung, colon and lymphomas. PML loss is associated with high-grade tumors and tumor progression. Remarkably, PML gene is rarely mutated in these tumors⁹⁷.

Interestingly, in chronic myeloid leukemia (CML) PML is upregulated and its loss is predictive of favorable outcome. PML is indispensable for quiescent leukemia-initiating cell (LIC) function and its loss results in the depletion of both LIC and hematopoietic stem cells (HSC)⁹⁸. PML exerts its role through the regulation of fatty acid oxidation (FAO) under the control of the peroxisome-proliferator activated δ (PPARD)⁹⁹. In addition to CML, the analysis of BCa biopsies identified a subset of these tumors where the expression of PML was higher when compared to normal epithelium. Although PML protein expression was frequently low or absent in the majority of the samples, high PML mRNA and protein levels in TNBC were associated with high tumor grade and poor prognosis. Through the same PPARD-FAO pathway observed in CML, PML provides selective advantage under metabolic stress triggered by loss of attachment conditions¹⁰⁰. In PML high-expressing ER- breast tumors, PML regulates aggressiveness and metastatic features through the control of the stem cell gene SRY-box transcription factor 9 (SOX9)¹⁰¹ and the hypoxia-inducible factor 1 alpha (HIF1 α) signaling¹⁰². A summary of PML functions in cancer can be observed in **Fig. 19**.

These discoveries revealed PML the two faces of PML function in cancer: it can act as a classical tumor suppressor in many cancers, but in a few cases, it facilitates cancer survival¹⁰³.

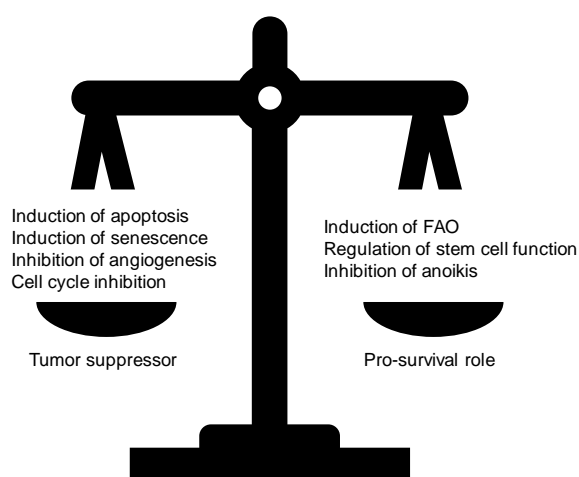


Figure I9. Summary of the dual functions of PML in cancer. PML plays opposing activities depending on the cancer setting. In one hand, it activates pathways that negatively affect tumor growth. In the other hand, it regulates the activation of pathways that sustain growth. This “friend or foe” role will be further studied to categorize different tumor types and to develop compounds against its specific function. FAO: fatty acid oxidation.

IV Senescence

The initial description of cellular senescence was made by Hayflick and Moorhead¹⁰⁴. They observed that normal cells, contrary to cancer cells, have a finite proliferative capacity characterized by cell cycle arrest. Two ideas raised from this discovery: in one hand, senescence is a beneficial mechanism because of its tumor suppressive role. It acts as a barrier in pre-malignant tumors and cancer progression^{105,106}. In the other hand, senescence has a deleterious effect, as it negatively affects regenerative capacities. In normal conditions, transient induction of senescence is beneficial because it contributes to tissue remodeling. Nevertheless, in aged tissues, inefficient clearance and regeneration leads to the accumulation of senescent cells. This contributes to the development of many age-associated diseases, such as pulmonary fibrosis, sarcopenia, diabetes and obesity¹⁰⁷. Paradoxically, the presence of senescent cells can also promote tumorigenesis through the secretion of numerous factors. These factors compose the senescence associated secretory phenotype (SASP), which will have differential effects depending on the physiological context. Inflammation, disruption of normal tissue structure and function and creation of a tumorigenic environment can be found among the deleterious effects of SASP. The beneficial effects of SASP include reinforcing the tumor suppression through the growth arrest, for facilitating tissue repair and for stimulating immune system for the clearance of senescent cells¹⁰⁸ (**Fig. I10**).

Nowadays, senescence is defined as a stress response that involves a stable cell growth arrest. It is an adaptive process to reduce energy consumption for cell division or differentiation characterized by the loss of proliferative capacity, despite continued viability and metabolic activity¹⁰⁹.

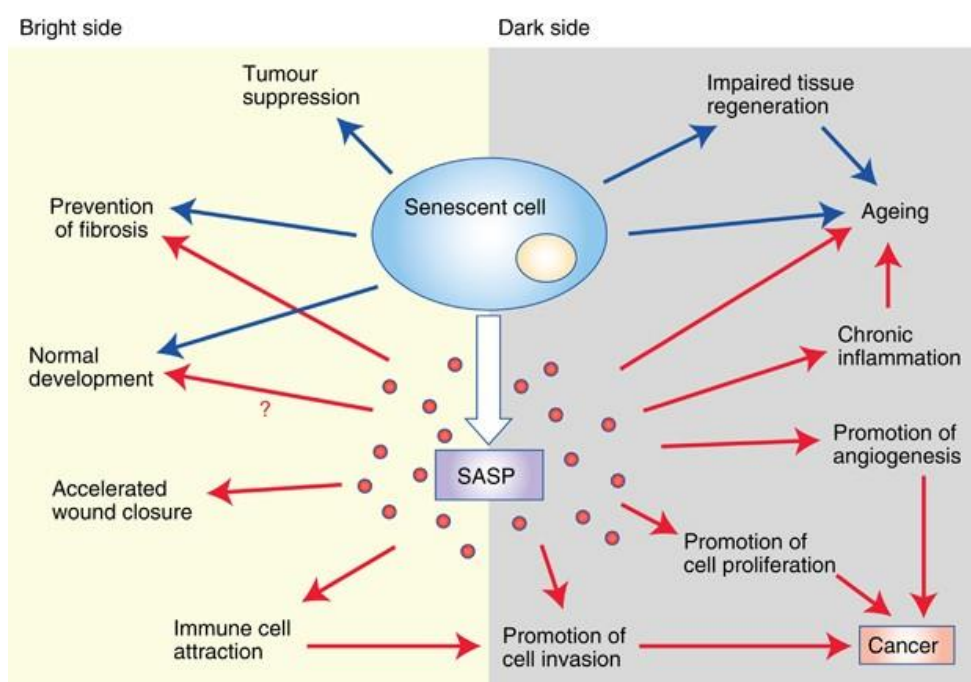


Figure I10. Physiological consequences of senescence response. Senescence can have opposed effects in cellular biology. Senescent cells secrete several factors, known as SASP, that will play a key role defining the biological outcome (adapted from Lecot *et al.*, 2016¹⁰⁸).

IV.1 Types of senescence

The senescence phenotype is highly heterogeneous and dynamic, a consequence of the different stimuli that can induce it and the effectors involved in the different signaling pathways (**Fig. I11**).

IV.1.1 Replicative senescence

Replicative senescence arises from the progressive erosion of telomeres. Cells will sense this erosion as double-strand breaks (DSB), activating a DNA damage response (DDR) that will induce senescence. Several proteins localize to DNA damage foci such as ataxia telangiectasia mutated (ATM), ATR, CHK2 and γ -H2AX¹¹⁰. The DDR triggered upon telomere loss is similar to the one induced by ionizing radiation and several chemotherapeutic agents, such as bleomycin and doxorubicin¹¹¹. Both damage- and telomere-dependent senescence responses strongly depend on p53 and p21 (also known as p21^{WAF1/Cip1}, CDKN1A) signaling^{112,113}. In addition, p16 (also known as p16^{INK4a}, CDKN2A) provides additional control to the senescence signaling pathway¹¹⁴.

IV.1.2 Oncogene-induced senescence

Oncogene-induced senescence (OIS) was first observed *in vitro* upon the expression of an oncogenic form of RAS¹¹⁵. The senescence response counteracts the cell growth stimulation induced upon oncogene activation. After that, several other oncogenes have been shown to induce OIS¹¹⁶. OIS is triggered by a mechanism independent of telomere shortening but it also induces a robust DDR¹¹⁷. The p53/p21 pathway is the main effector of OIS with the help of p16/pRB pathway. Interestingly, the loss of tumor suppressor PTEN also elicits a senescence response that opposes tumorigenesis, known as PTEN-loss induced cellular senescence (PICS)¹¹⁸.

IV.1.3 Stress and other inducers of senescence

Many different types of stress inducers, such as chemotherapeutic drugs, oncogene activation and DNA damage increase the levels of reactive oxygen species (ROS), which contribute to the induction of senescence response^{119,120}.

Chronic stimulation by β -interferon, an anti-proliferative cytokine, increases ROS levels and elicits a p53-dependent DDR and senescence response¹²¹.

Chemical inhibition of histone deacetylases, which causes perturbations in chromatin affecting gene expression, also induces senescence^{111,122,123}.

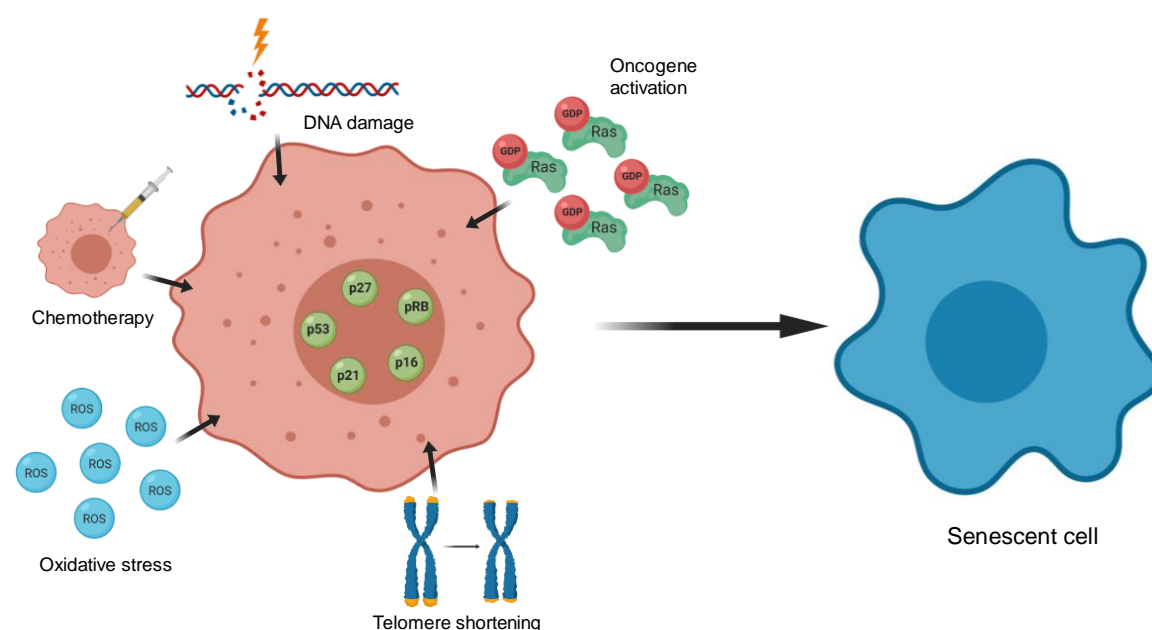


Figure I11. Causes of cellular senescence. Despite the several different stimuli that can induce senescence, p53/p21, p16/pRB and, in a lesser extent p27, are the common effectors of this response.

IV.2 Hallmarks of senescence

Senescence response is characterized by both morphological and molecular changes (**Fig. I12**) that can be detected with the help of different methodologies. These features are present in other cellular contexts, which underlines the importance of the characterization of senescence phenotype. Some of the hallmarks and the detection methods will be further discussed in Results section.

IV.2.1 Morphological alterations

IV.2.1.1 Cell size and shape

In vitro, senescent cells are characterized by an enlarged, flat and irregular cell body, with more vacuoles and sometimes multinucleated¹²⁴. These changes are easily measured with either light or fluorescence microscopy. Although it is still unclear how the majority of the morphological changes occur, several plasma membrane proteins change their expression upon activation of senescence¹²⁵.

IV.2.1.2 Increased lysosomal content

Senescence cells are characterized by the upregulation of several lysosomal proteins and increased lysosomal content¹²⁶. The measurement of the activity of senescence-associated β -galactosidase (SA- β -gal) lysosomal enzyme is one of the most commonly used markers of senescence¹²⁷. Nevertheless, its use has some technical limitations: SA- β -gal detection cannot be used in paraffin-embedded tissues nor in live cells.

IV.2.1.3 Nuclear changes

Loss of LAMIN B1 and the formation of SAHF are the most studied changes in senescence at the nuclear level. LAMIN B1 is a structural component of the nuclear lamina and its loss has been reported to be a common mark of senescence¹²⁸. SAHF are nuclear foci enriched in repressive epigenetic marks¹²⁹. However, SAHF is not a universal marker and its importance is mainly restricted to OIS¹⁰⁹.

IV.2.1.4 Mitochondria

Senescent cells show an increased number of mitochondria¹³⁰. Different mechanisms have been proposed to induce the accumulation of mitochondria: in one hand, the reduction of mitophagy leads to an increase in the number of old and dysfunctional mitochondria¹³¹. In the other hand, alterations in mitochondrial dynamics, such as fission and fusion processes, can trigger senescence¹³².

IV.2.2 Signaling pathways involved in senescence response

IV.2.2.1 Cell cycle arrest and cyclin-dependent kinase inhibitors

Cell cycle is tightly regulated by a family of protein kinases known as cyclin-dependent kinases (CDKs), which are controlled by cyclins. Among the negative regulators, CDK inhibitors (CDKIs) are especially relevant in senescence response. CDKIs are divided into two families: the INK4 family and the Cip/Kip family. In one hand, the INK4 family is composed by p16INK4a, p15INK4b, p18INK4c and p19INK4d. They specifically bind and inhibit CDK4-6 kinases, acting in the CDKs that initiate progression through cell cycle. In the other hand, the Cip/Kip family is composed by p21Cip1, p27Kip1 and p57Kip2. The members of this family associate to both CDK4-6/D and CDK2/E-A. Cip/Kip proteins activate CDK4-6/D kinases but they effectively inhibit CDK2/E-A kinases^{133,134}.

p16, p21 and p27 are commonly used as markers of senescence¹³⁵. p16/pRB pathway is often upregulated in senescence and p16 is used as a specific and unique marker for senescence both *in vitro* and *in vivo*^{136,137}. In the case of p21, it is part of p53/p21 pathway and it is preferentially upregulated by p53 in senescence^{138,139}. The role of p27 in senescence has been studied less than p16 and p21. p27 is also upregulated in senescence, preferentially when the other two pathways are not active^{106,140}.

IV.2.2.2 Secretory phenotype

Despite senescence is described as a tumor suppressive mechanism, it is known that senescent cells develop altered secretory activities that may induce changes in the tissue microenvironment. The high heterogeneity of the SASP makes it a complicated characteristic to use as an unequivocal marker for senescence¹⁴¹. Moreover, the SASP changes over time adding complexity to a state that appears to play unique effects depending on the cellular context¹⁴²

IV.2.2.3 Other molecular changes

DNA damage induces the formation of γ -H2AX-positive nuclear foci, which are used as senescence markers¹⁴³. Nevertheless, several stimuli can activate DDR and not all of them induce a senescence response.

Some senescent cells acquire resistance to apoptosis by activating several pro-survival factors, such as BCL-2 family members¹⁴⁴.

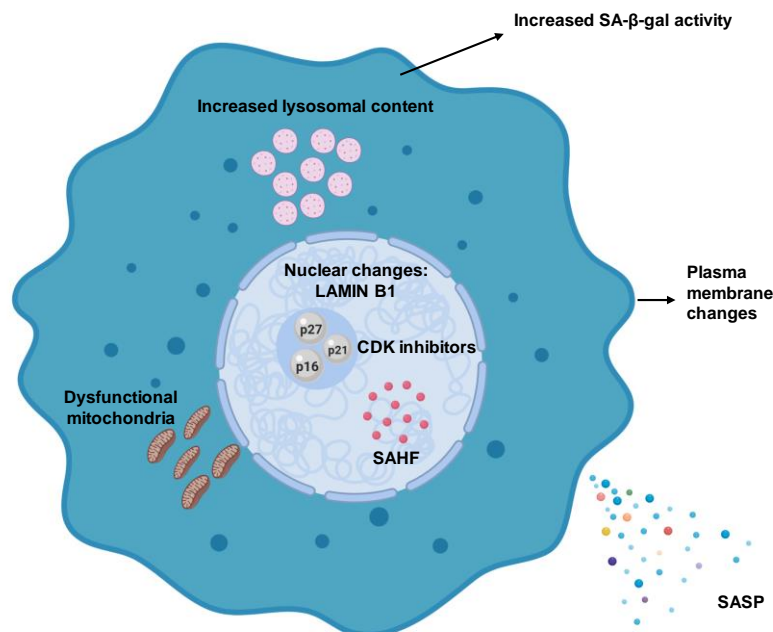


Figure I12. Morphological and signalling pathway alterations as hallmarks of senescence. SA- β -gal activity, LAMIN B1 expression, SASP composition and levels of p16, p21 and p27 are preferentially used for the identification of senescent cells. SA- β -gal: senescence-associated beta-galactosidase, SASP: senescence-associated secretory phenotype, SAHF: senescence-associated heterochromatin foci.

V Oncogene addiction

The multistage process of cancer evolution is driven by the progressive accumulation of mutations and epigenetic changes. This will affect multiple genes with diverse functions. Despite the extensive changes that are observed, targeting only one of these abnormalities can profoundly affect the growth of cancer cells. This concept is termed as “oncogene addiction”¹⁴⁵. It hypothesizes that cancer cells will be addicted to the expression of a specific gene and its targeting will have detrimental effects for the malignant phenotype, without affecting the cells that are not addicted to it.

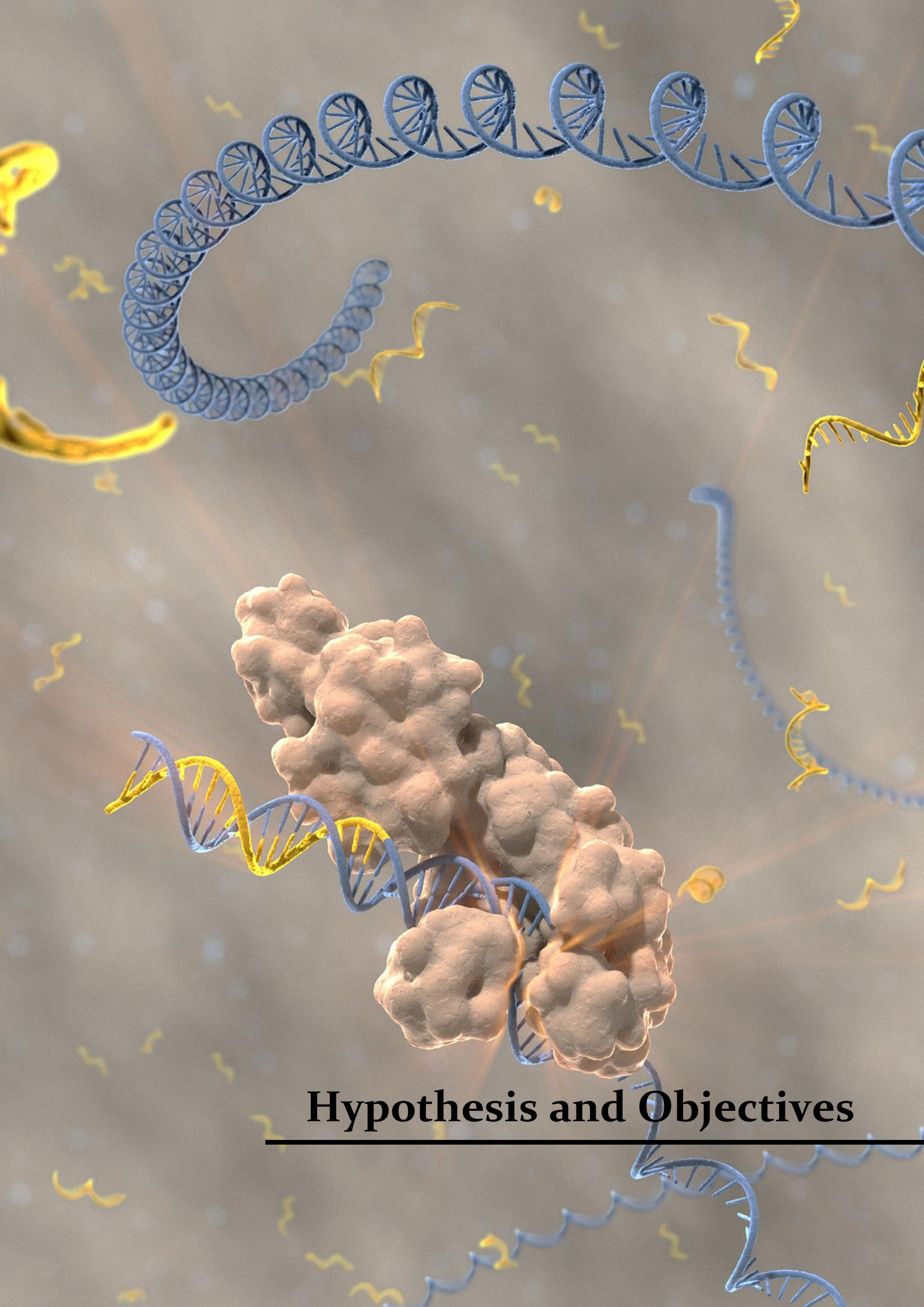
C-MYC¹⁴⁶ is a proto-oncogene that together with N-MYC and L-MYC forms the MYC family of transcription factors. It was first identified due to its homology with the viral gene v-Myc.

C-MYC is implicated in the regulation of several cellular processes, such as cell proliferation, cell cycle, metabolism, apoptosis and differentiation¹⁴⁷. To exert its functions, c-MYC dimerizes with Max and binds to DNA, regulating the expression of a large number of genes¹⁴⁸. The study of the implication of c-MYC in cancer biology has been of utmost interest since its discovery. In fact, in many cancers c-MYC has been shown to be altered mainly due to gene overexpression, gene amplification and translocations¹⁴⁹⁻¹⁵¹.

In addition to being one of the most common oncogenic events in human cancer, c-MYC is a good example of oncogene addiction. Induction of MYC in the skin results in hyperplasia but upon its downregulation all the lesions regress¹⁵². In transgenic mouse models, the inactivation of MYC results in tumor regression in different types of cancer¹⁵³⁻¹⁵⁵.

Similarly to c-MYC, switching off the BCR-ABL fusion gene results in rapid apoptosis of leukemic cells¹⁵⁶. In melanoma, upon silencing of H-RAS cells rapidly underwent apoptosis and tumor regressed¹⁵⁷.

Oncogene addiction sets the basis for targeted cancer therapies. Nevertheless, to prevent the bypass of the state of oncogene addiction, combination therapy will be of utmost importance in cancer treatment.



Hypothesis and Objectives

BCa is the most diagnosed tumor type and first cause of death by cancer worldwide among women. Early in this century, the molecular characterization of a number of breast carcinomas lead to the classification of BCa into different subtypes. TNBC remains as one of the subtypes with the worst prognosis due to the lack of specific biomarkers and effective targeted therapies for this group of patients. PML has been described as a tumor suppressor for many years, but it is overexpressed in TNBC, where it plays a pro-survival role. This thesis project focuses on the study of PML activity in TNBC and its potential as a biomarker. It is based in the following hypothesis: **PML is essential for the survival of TNBC cells and its deregulation could represent a new therapeutic opportunity.**

We based our work in the premise that TNBC cells are addicted to the expression of PML and that its inhibition will compromise their function. Our objective is to decipher the pathways sustaining PML function in TNBC taking advantage of cancer cell lines, xenograft models and *in silico* analyses.

In order to test this hypothesis, we established the following specific aims:

Aim 1: To ascertain the effect of PML silencing in the growth of TNBC cell lines.

TNBC exhibits an overexpression of PML when compared to other BCa subtypes¹⁰⁰. We have previously demonstrated that PML regulates cancer initiation and metastasis in this BCa subtype through the regulation of the stem cell factor SOX9¹⁰¹. Investigating the consequences of PML inhibition in non-cancer-initiating cells could give a more insightful perspective of its key role in BCa:

1. Analysis of PML status in different publicly available datasets and in BCa cell lines.
2. Generation of genetically modified cellular systems to study the role of PML in TNBC.
3. Evaluation of the growth-inhibitory phenotypes *in vitro* and *in vivo* upon PML targeting.

Aim 2: To decipher the molecular mechanism underlying the growth-inhibitory response in PML addicted BCa cell lines.

The lack of biomarkers in TNBC has encouraged the search for essential pathways for cancer cells that can be targeted therapeutically. The idea that cells are addicted to the expression of a single oncogene opens new opportunities:

1. Define the growth inhibitory mechanism triggered upon PML inhibition.
2. Elucidate the selective requirement of PML in TNBC vs. non-TNBC cells.
3. Study the effects of pharmacological inhibition of PML with arsenic trioxide.



Materials and methods

I Materials

I.1 Cell lines and culture conditions

Human breast carcinoma cell lines (MDA-MB-231, MCF7 and T47D) were obtained from the American Type Culture Collection (ATCC, Manassas, VA, USA) or from Leibniz-Institut-Deutsche Sammlung von Mikroorganismen und Zellkulturen GmbH (DMSZ), who provided an authentication certificate. MDA-MB-468, Cal51 and Cama-1 human breast carcinoma cell lines were generously provided by the laboratory of Dr. Maurizio Scaltriti. Virus packaging cell line HEK293FT was generously provided by the laboratory of Dr. Rosa Barrio. None of the cell lines used in this study was found in the database of commonly misidentified cell lines maintained by ICLAC and NCBI Biosample. MDA-MB-231, MCF7 and HEK293FT were cultured in Dulbecco's Modified Eagle Medium (Ref. 41966-029, Gibco), MDA-MB-468 and T47D were cultured in RPMI 1640 Medium (Ref. 61870-010, Gibco; with GlutaMAX supplement) and Cal51 and Cama-1 cell lines were cultured in DMEM/F12 Medium (Ref. 31331-028, Gibco; with GlutaMAX supplement). See **Table M1** for cell line specifications.

Table M1. Detailed list of the different BCa cell lines used during this work. Mutation data was taken from COSMIC database (www.sanger.ac.uk/genetics/CGP/cosmic/).

Cell line	Cell type	Derivation	Subtype	Mutations
MDA-MB-231 (DMSZ ACC-732)	Breast adenocarcinoma	Derived from metastatic site: pleural effusion. 50 year old Caucasian woman.	TNBC	<i>BRAF; CDKN2A; KRAS; NF2; TP53; PDGFRA</i>
MDA-MB-468	Breast adenocarcinoma	Derived from metastatic site: pleural effusion. 51 year old African-American woman.	TNBC	<i>PTEN; RB1; SMAD4; TP53</i>
Cal51	Breast adenocarcinoma	Derived from metastatic site: pleural effusion. 45 year old woman.	TNBC	<i>PIK3CA, PTEN</i>
MCF-7 (ACC115)	Breast adenocarcinoma	Derived from metastatic site: pleural effusion. 69 year old Caucasian woman.	ER+, PR+, HER2-	<i>PI3KCA; CDKN2A</i>
T47D	Breast adenocarcinoma	Derived from metastatic site: pleural effusion. 54 year old woman.	ER+, PR+, HER2-	<i>TP53; PTEN</i>
Cama-1	Breast adenocarcinoma	Derived from metastatic site: pleural effusion. 51 year old Caucasian woman.	ER+, PR+, HER2-	<i>PI3KCA; TP53</i>
HEK293FT	Human embryonic kidney cells	From human primary embryonal kidney transformed by adenovirus type 5 Negative	-	-

All culture media were supplemented with 10% inactivated Fetal Bovine Serum (FBS) (Ref. F9665, Sigma), from same lot and previously analyzed to ensure experimental reproducibility, and 1% Penicillin/Streptomycin (Ref. 15140-122, Gibco) (complete media). All the experiments were performed with complete media unless otherwise specified. HEK293FT cell line was seeded on poly-lysine (Ref. P8920, Sigma) coated plates. All cell lines were routinely monitored by PCR for mycoplasma presence and replaced in case of positive result. Cell lines were grown at 37°C in a humidified atmosphere of 5% CO₂. Cells were regularly cultured in 100 mm dishes and split every 3-4 days, maintaining them below 80-90% density, up to 30 passages maximum. To split the cells, they were incubated with trypsin-EDTA solution (Ref. 25200-056, Gibco) at 0.05% for 5 minutes at 37°C, and re-suspended in the corresponding fresh complete media. In order to do the cell counting, cells were diluted 1:1 in Trypan Blue Dye 0.4% (Ref. T8154-20ML, Sigma) and 10 µL were loaded in a Neubauer chamber to count viable cells by optical microscopy (Olympus CKX31). The Trypan Blue dye allows to determine cell viability based in the fact that dead cells show disrupted plasma membrane and allow the internalization of the dye staining their cytoplasm in blue, while alive cells remain non-stained thanks to their intact cell membrane.

I.2 Drugs

All the compounds used in this thesis were subjected to a dose response analysis in order to find the best concentration for their maximum activity without any cytotoxic effect. The information regarding the drugs is shown in **Table M2**.

Table M2. Experimental specifications for the different drugs used during the thesis work.

Drug	Supplier	Dose	Function
Puromycin	Sigma (P8833)	2 µg/mL	Cell selection after infection
Blasticidine S hydrochloride	Sigma (15205)	10 µg/mL	Cell selection after infection
Doxycycline	Sigma (D9891)	150 ng/mL	Gene-inducible system
Ampicillin sodium salt	Sigma (A0166-59)	50 µg/mL	Bacterial selection
Staurosporine	Selleckchem (S1421)	1 µM	Apoptosis induction
Arsenic (III) oxide (ATO)	Sigma (A-1010)	150 nM	PML degradation

II Methods

II.1 Cloning

Different cloning strategies were designed for *PML*, *PIM1*, *MYC* and *p27* silencing and *PML* overexpression. These strategies are explained in detail below. All the primers used are summarized in **Table M3**.

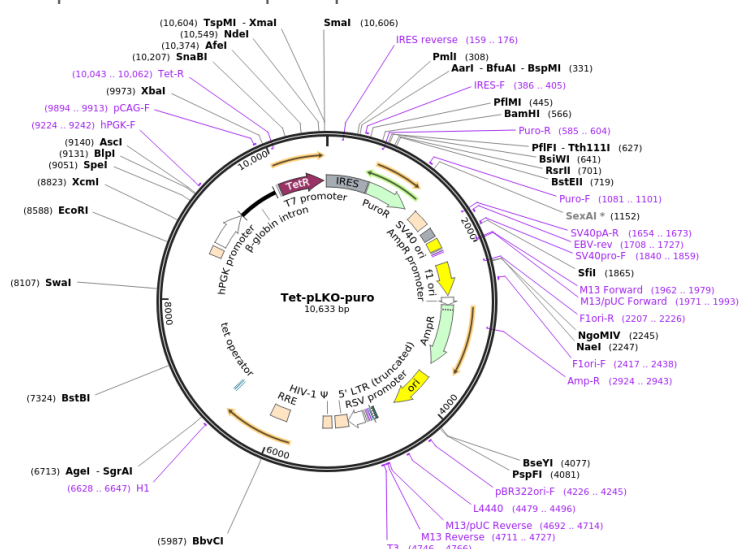
shRNA pLKO-Tet-On strategy

The strategy provided by Dr. Dmitri Wiederschain¹⁵⁸ was followed for this cloning (Addgene plasmid: 21915, **Fig. M1**) with the help of Dr. Ianire Astobiza. Validated short hairpin RNA (shRNA) sequences (for *PML*, *PIM1*, *MYC* and *p27*) were obtained from SIGMA (MISSION® shRNA). The tetracycline inducible pLKO (pLKO-Tet-On) vector is engineered to induce the shRNA expression upon doxycycline (dox) addition. Bottom or complementary primers were designed including an EcoRI restriction site at the 5' end, while top or template primers carried an AgeI restriction sequence in their 5' end. pLKO-Tet-On vector was then opened using AgeI (Ref. ER1462, Thermo Fisher) and EcoRI (Ref. ER0271, Thermo Fisher) restriction enzymes, the only cloning sites in the vector, and purified using a gel extraction kit (Ref. mi-GEL250, Metabion). Then, 11.25 μ L of each oligo (top and bottom for each shRNA at 100 μ M) were mixed with 2.5 μ L of 10X annealing buffer (1 M NaCl, 100 mM Tris-HCl, pH=7.4) in an eppendorf. This mix was placed in boiling water and left for 3-4 hours to naturally cool down. After that, 1 μ L of the oligo mixture was diluted 1:400 in 0.5X annealing buffer. For the ligation 1.5 μ L of the diluted oligo mixture, 100 ng of the digested pLKO-Tet-On vector, 2 μ L of 5X ligase buffer, 1 μ L of T4 DNA ligase (Ref. 100004917, Invitrogen) and water for a total volume of 10 μ L were used. It is important to add a vector-only negative control. After an incubation of 1 hour at room temperature (RT), ligation was transformed into ultra-competent XL-10 Gold cells (10 μ L of the ligation in 50 μ L of competent cells). The mix was kept 20 minutes in ice, then it was heat shocked for 30 seconds at 42°C and placed back into ice for 2 minutes. To ease the growth, LB Broth Lennox (Ref. 1231, Conda-Pronadisa) was added (with no antibiotic) and incubated at 37°C with shaking for 30 minutes. Finally, the transformation mix was spread into LB agar plates containing the corresponding antibiotic, 50 μ g/mL ampicillin in this case. The plates were incubated overnight at 37°C. The resulting colonies were digested with XhoI (Ref. FD0694, Thermo Fisher) enzyme to screen for positive clones, which will show a pattern of 3 different bands (2 of them below 200 base pairs due to the restriction site included in the shRNA sequence), while the negative clones will have 2 fragments. Finally, they were sequenced to confirm that the inserted fragment was correct.

Sub-cloning of scramble shRNA (shC), sh1PML, sh4PML, sh5PML and sh42MYC was done into pLKO-Tet-On-puromycin vector. Sub-cloning of shC, sh1p27, sh2p27 and sh18PIM1 into pLKO-Tet-On-blasticidin was done following the same procedure. Puromycin resistance cassette was replaced with blasticidin cassette following Gibson assembly strategy by Dr. James Sutherland (CIC bioGUNE) and Dr. Veronica Torrano (CIC bioGUNE). BamHI and SfiI were used to introduce

the selection cassette and lentiCas9-Blast (Addgene plasmid: 52962) plasmid as the source for blasticidin fragment.

Figure M1. Schematic representation of Tet-pLKO-puro inducible vector.



TRIPZ-HA-PML IV strategy

The TRIPZ™ vector from Dharmacon (**Fig. M2**) used to induce the expression of HA tagged PML is engineered to be inducible in the presence of doxycycline. This induction is enabled by 2 different components: the tetracycline response element (TRE) and the reverse tetracycline-controlled transactivator 3 (rtTA3). In the presence of doxycycline, the transactivator will bind to and activate the expression from TRE promoters. HA-PML IV cloning was performed by Dr. James Sutherland (CIC bioGUNE). Briefly, PML IV together with the HA tag was amplified using PMLIV01 and PMLIV02 from pLNCX-HA-PMLIV (from Dr. Pier Paolo Pandolfi's lab), providing AgeI and AscI restriction sites; the PCR product was then isolated and digested with the mentioned enzymes. In parallel, TRIPZ vector was digested with AgeI and MluI. PML IV sequence contained a MluI restriction site which did not allow adding the restriction sequence for that enzyme to the primers used for its amplification. The similarity between AscI and MluI restriction sequences allowed the use of different enzymes to digest the insert and the vector. Once the amplicon and the vector were digested and purified, ligation was performed using T4 ligase (Ref. 100004917, Invitrogen) and transformed into ultra-competent XL-10 Gold cells following the same protocol as in shRNA pLKO-Tet-On subcloning. Colonies were digested with AgeI and MluI for positive colony screen and sequenced to confirm the inserted sequence.

Figure M2. Schematic figure of TRIPZ™ inducible vector.

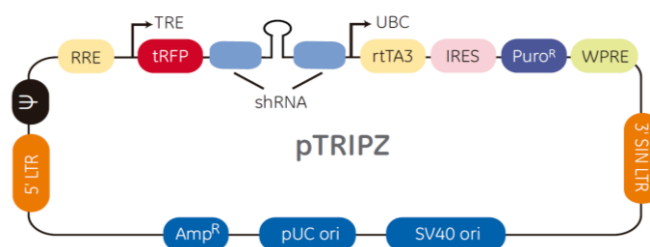


Table M3. Information about the primers used for the different cloning strategies.

Name	Primers	Purpose	Sequence
sh1PMLT01	sh1PML top	To introduce the shRNA in the pLKO-Tet-On-puro vector	CCGGCACCCGCAAGACCAACA ACATCTCGAGATGTTGTTGGTC TTGCGGGTGTTTTT
sh1PMLB01	sh1PML bottom	To introduce the shRNA in the pLKO-Tet-On-puro vector	AATTAAAAACCCCGCAAGACC AACAACATCTCGAGATGTTGTT GGTCTTGCGGGTG
sh4PMLT01	sh4PML top	To introduce the shRNA in the pLKO-Tet-On-puro vector	CCGGGCCAGTGTACGCCTTCT CCATCTCGAGATGGAGAAGGC GTACACTGGCTTTTTG
sh4PMLB01	sh4PML bottom	To introduce the shRNA in the pLKO-Tet-On-puro vector	AATTCAAAAAGCCAGTGACGC CTTCTCCATCTCGAGATGGAGA AGGCGTACACTGGCCCGG
sh5PMLT01	sh5PML top	To introduce the shRNA in the pLKO-Tet-On-puro vector	CCGGGTGTACCGGCAGATTGT GGATCTCGAGATCCACAATCTG CCGGTACACTTTTT
sh5PMLB01	sh5PML bottom	To introduce the shRNA in the pLKO-Tet-On-puro vector	AATTAAAAAGTGTACCGGCAGA TTGTGGATCTCGAGATCCACAA TCTGCCGGTACACCCGG
sh18PIM1T01	sh18PIM1 top	To introduce the shRNA in the pLKO-Tet-On-blasti vector	CCGGACATCCTTATCGACCTCA ATCCTCGAGGATTGAGGTGCA TAAGGATGTTTTTT
sh18PIM1B01	sh18PIM1 bottom	To introduce the shRNA in the pLKO-Tet-On-blasti vector	AATTAAAAACATCCTTATCGA CCTCAATCCTCGAGGATTGAG GTGCATAAGGATGT
sh42MYCT01	sh42MYC top	To introduce the shRNA in the pLKO-Tet-On-puro vector	CCGGCCTGAGACAGATCAGCA ACAACCTCGAGTTGTTGCTGATC TGCTCAGGTTTTTG
sh42MYCB01	sh42MYC bottom	To introduce the shRNA in the pLKO-Tet-On-puro vector	AATTCAAAAACCTGAGACAGAT CAGCAACAACCTCGAGTTGTTGC TGATCTGTCTCAGGCCGG
sh1p27T01	sh1p27 top	To introduce the shRNA in the pLKO-Tet-On-blasti vector	CCGGGTAGGATAAGTGAAATG GATACTCGAGTATCCATTTTAC TTATCCTACTTTTTG
sh1p27B01	sh1p27 bottom	To introduce the shRNA in the pLKO-Tet-On-blasti vector	AATTCAAAAAGTAGGATAAGTG AAATGGATACTCGAGTATCCAT TTCACCTATCCTAC
sh2p27T01	sh2p27 top	To introduce the shRNA in the pLKO-Tet-On-blasti vector	CCGGGCGCAAGTGGAATTTTCG ATTTCTCGAGAAATCGAAATTC CACTTGCGCTTTTTG
sh2p27B01	sh2p27 bottom	To introduce the shRNA in the pLKO-Tet-On-blasti vector	AATTCAAAAAGCGCAAGTGGA TTTCGATTTCTCGAGAAATCGA AATTCCAATTGCGC
PMLIV01	Age1.KozHA.P ML.for	To produce a PCR product with AgeI site in the 5' end	gatcaccgggtgccaccATGTACCCAT ACGATGTTCCAGATTACGCTGG CTCCatggagcctgcacccgcccgatc
PMLIV02	Asc1.PMLv4.r ev	To produce a PCR product with AscI site in the 3' end	gatcggcgcgcccCTAAATTAGAAAG GGGTGGGGGTAGC

II.2 Stable cell line generation

Virus generation was carried out in a BSL-2 laboratory, under the appropriate safety measurements. For the virus production HEK293FT packaging cell line was used; for the stable cell line generation, different target cell lines in which the transgene was intended to be introduced were used. In this thesis work all the cell lines were generated through lentiviral infection following this general protocol (**Fig. M3**):

Day 1

- Morning: seed HEK293FT at high density (3×10^6 cells/100 mm plate).
- Afternoon: transfect HEK293FT cells.

Day 2

- Refresh medium of the transfected HEK293FT. In the case the virus was concentrated, less volume was added.
- Seed target cell line (at least 300.000 cells per 100 mm plate, depending on the cell line used).

Day 3

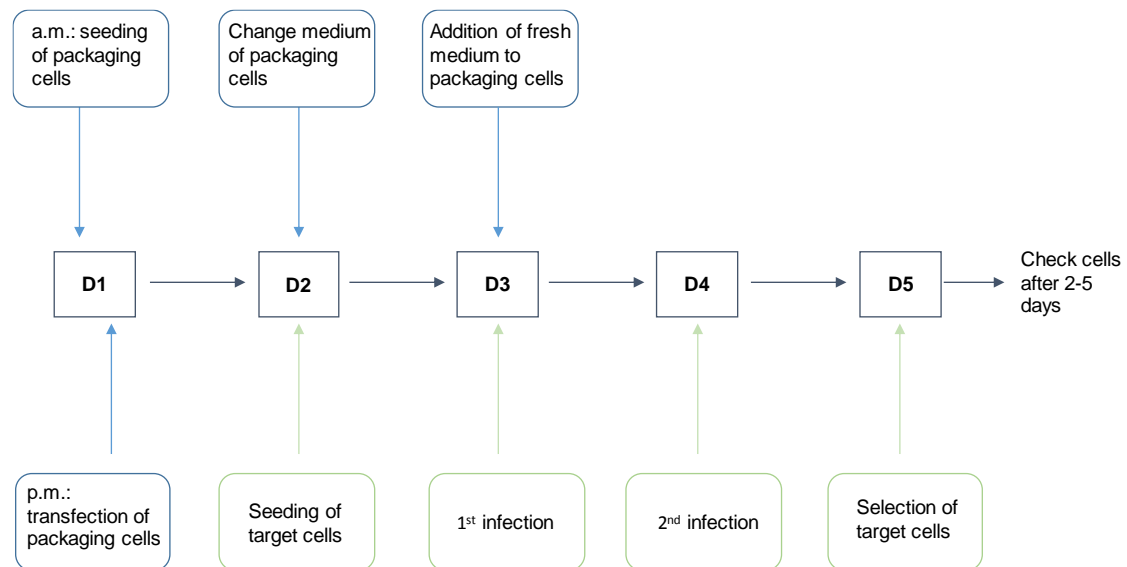
- First infection: virus-containing supernatant from HEK293FT was filtered using a 0.45 μm filter; fresh medium was added to the collected supernatant. To increase the infection efficiency, protamine sulfate (8 $\mu\text{g}/\text{mL}$) was supplemented. Fresh medium was added to packaging cells for the second infection next day.

Day 4

- Second infection: it was performed as the previous day. Packaging cells were discarded following biosafety rules.

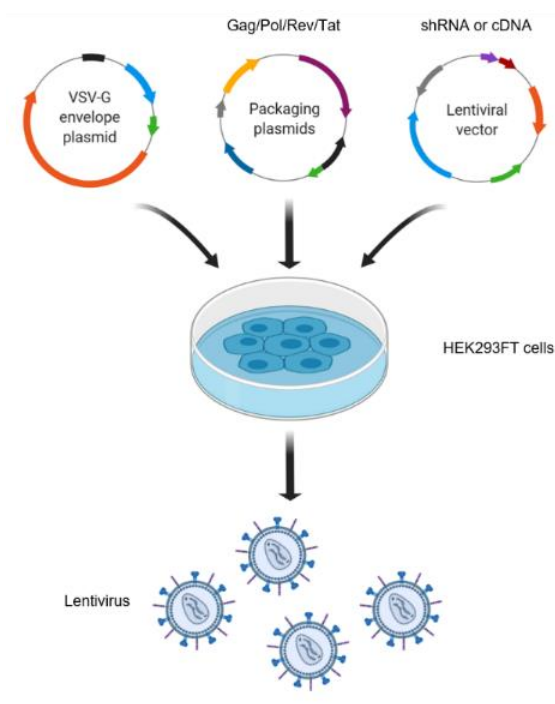
Day 5

- Selection: fresh medium was added to target cell lines supplemented with the corresponding selection antibiotic. Puromycin (2 $\mu\text{g}/\text{mL}$) selection took between 48 and 72 hours, while blasticidin (10 $\mu\text{g}/\text{mL}$) needed 5 days. A positive control (non-infected cells) was used to confirm that selection was working.

Figure M3. Timeline of the experimental protocol for virus production using HEK293FT cells.

II.2.1 Lentivirus production and target cell infection

For the lentivirus production, packaging cells were transfected with the packaging plasmids and the vector with the construct of interest (**Fig. M4**). Second generation lentivirus production was used for *PML* IV overexpression, while third generation lentivirus production was used to silence *PML*, *PIM1*, *MYC* and *p27* in BCa cell lines.

Figure M4. Figure showing the packaging system and lentivirus production in HEK293FT cells.

II.2.1.1 Second generation lentivirus production

HA-PML IV was cloned in an inducible TRIPZ vector. Second generation lentivirus production consists in 3 plasmids: the vector bearing the construct of interest and all the cis-acting sequences required, and two packaging vectors, pVSV-G and psPAX2, which provide the trans-acting factors (Gag/Pol/Rev/Tat). The separation of cis-acting and trans-acting sequences reduces the probability of recombination producing replication-competent viral particles. Due to the backbone of TRIPZ vector, another vector was needed to help in the transcription: pTAT (**Table M4**). Second generation lentivirus production was performed as described in II.2, using MDA-MB-231 as target cells, which were subjected to puromycin selection for 48-72 hours.

Table M4. Specific vectors used for second generation lentivirus production (quantities for 100 mm plates).

Vector name	Role	Encoding Sequences	Function	Origin	Amount transfected
psPAX2	Packaging vector	Gag-Pol	Integrase, reverse transcriptase, and structural proteins	Dr. James D. Sutherland	1.66 µg
		RRE	Rev-responsive element		
		Rev	Enhancer of unspliced viral genomic RNA nuclear export		
pVSV-G	Packaging vector	VSV-G	Envelope protein	Dr. James D. Sutherland	1.66 µg
pTAT	Helper vector	TAT	Enhances transcription efficiency	Dr. James D. Sutherland	1.66 µg
TRIPZ-HA-PML IV	Transfer vector	PML IV	Gene to overexpress	Dr. James D. Sutherland	5 µg

II.2.1.2 Third generation lentivirus production

Third generation virus were used for silencing of *PML*, *MYC*, *PIM1* and *p27*, using both puromycin- and blasticidin-resistance bearing pLKO vectors. For the constitutive silencing of *PML*, *MYC* and *p27* shRNA sequences were purchased from SIGMA (MISSION® shRNA Bacterial Glycerol Stock) (**Table M5**).

The different sets of shRNAs were validated and chosen for further experiments based on the silencing dynamics and knockdown levels. *PML*, *p27* and *MYC* shRNAs were also subcloned into doxycycline inducible pLKO-Tet-On vector; *PIM1* shRNA was only tested in the inducible system. Third generation lentivirus require three packaging vectors (pRRE, pREV and pVSV-G; this system decreases recombination probability and makes them more secure to handle compared to second generation) and the transfer vector (**Table M5**).

Table M5. Specific vectors used for third generation lentivirus production (quantities for 100 mm plates).

Vector name	Role	Encoding Sequences	Function Sequence	Origin	Amount transfected
pRRE	Packaging vector	Gag-Pol	Integrase, reverse transcriptase, and structural proteins	Dr. James D. Sutherland	1.66 µg
		RRE	Rev-responsive element		
pREV	Packaging vector	Rev	Enhancer of unspliced viral genomic RNA nuclear export	Dr. James D. Sutherland	1.66 µg
pVSV-G	Packaging vector	VSV-G	Envelope protein	Dr. James D. Sutherland	1.66 µg
Scramble pLKO-Tet-On	Transfer control vector	Control shRNA	CCGGCAACAAGATGAA GAGCACC AACTCGAGT TGGTGCTCTTCATCTT GTTG	-	5 µg
sh1PML pLKO-Tet-On	Transfer vector	shRNA against <i>PML</i>	CCGGCACCCGCAAGA CCAACAACATCTCGAG ATGTTGTTGGTCTTGC GGGTGTTTTT	SIGMA TRCN0000003 865	5 µg
sh4PML pLKO-Tet-On	Transfer vector	shRNA against <i>PML</i>	CCGGGCCAGTGTACG CCTTCTCCATCTCGAG ATGGAGAAGGCGTACA CTGGCTTTTTG	SIGMA TRCN0000003 867	5 µg
sh5PML pLKO-Tet-On	Transfer vector	shRNA against <i>PML</i>	CCGGGTGTACCGGCA GATTGTGGATCTCGAG ATCCACAATCTGCCGG TACACTTTTT	SIGMA TRCN0000003 868	5 µg
sh18PIM1 pLKO-Tet-On	Transfer vector	shRNA against <i>PIM1</i>	CCGGACATCCTTATCG ACCTCAATCCTCGAGG ATTGAGGTCGATAAGG ATGTTTTTT	SIGMA TRCN0000320 587	5 µg
sh42MYC pLKO-Tet-On	Transfer vector	shRNA against <i>MYC</i>	CCGGCCTGAGACAGAT CAGCAACAACCTCGAGT TGTTGCTGATCTGTCT CAGGTTTTTG	SIGMA TRCN0000039 642	5 µg
sh1p27 pLKO-Tet-On	Transfer vector	shRNA against <i>p27</i>	CCGGGCGCAAGTGGA ATTCGATTTCTCGAG AAATCGAAATCCACTT GCGCTTTTTG	SIGMA TRCN0000039 928	5 µg
sh2p27 pLKO-Tet-On	Transfer vector	shRNA against <i>p27</i>	CCGGGCGCAAGTGGA ATTCGATTTCTCGAG AAATCGAAATCCACTT GCGCTTTTTG	SIGMA TRCN0000039 930	5 µg

II.2.1.3 Lentivirus concentration

In order to optimize the infection procedure, viruses were submitted to concentration steps in some experiments. Concentrated virus aliquots were generated following the time-schedule described in **Fig. M2** until day 3. At this point, filtered supernatant from HEK293FT was combined at 3:1 proportion with Lenti-XTM Concentrator (Ref. 631232, Clontech). After mixing it by inversion carefully, it was stored at 4° overnight. The next day the procedure was repeated and after at least 30 minutes of incubation at 4°, the supernatant was mixed with the one from the previous day and centrifuged at 1,500 rcf for 45 minutes at 4°C. The pellet was resuspended in medium and distributed in 50 µL aliquots (150 µL were added per 100 mm plate). Target cell lines were infected for two consecutive days and the selection added on day 3.

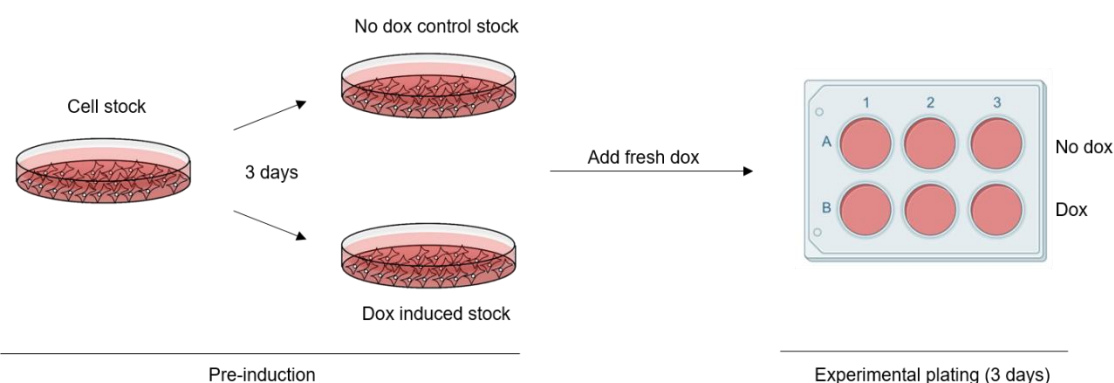
In two different situations was this procedure used to keep consistency between the different experiments performed: first, for the experiments using the *PML* and *p27* constitutive silencing. All shRNAs against *PML* showed a high silencing efficiency, and due to the dramatic decrease in their growth capacity new infections were needed for each experiment. And second, when different cell lines were going to be infected with the same construct.

II.3 Cellular analysis

All the experiments performed with cell lines carrying inducible silencing constructs, were subjected to a chronic induction with doxycycline (150 ng/mL) as explained in **Figure M5**. In the case of *PML* overexpression, doxycycline was added for 3 days (50 ng/mL).

The concentration of doxycycline used in both cases was determined in previous assays.

Figure M5. Schematic representation of experiment plating with doxycycline induction (150 ng/mL).



The number of cells used for each cell line and experiment is depicted in **Table M6**.

Table M6. Approximate number of cells seeded for the different experiments with inducible silencing systems after 3 days of pre-induction in 100 mm plates.

Assay	Cellular density per well for 3 days				Plate type
	MDA-MB-231	MDA-MB-468	MCF7	Cama-1	
Protein and RNA	1x10 ⁵ no dox 1.2x10 ⁵ dox	1x10 ⁵ no dox 1.2x10 ⁵ dox	75,000	90,000	6 well plate
FACS analysis	90,000				6 well plate
Senescence	15,000	15,000	15,000	15,000	24 well plate
Growth curves (up to 6 days)	7,500	8,500	5,000	8,500	12 well plate
Secretome	4x10 ⁶ no dox 5x10 ⁶ no dox			4x10 ⁶ no dox 5x10 ⁶ no dox	3x150 mm
BrdU/IF	20,000				24 well plate
ROS	150,000				6 well plate

II.3.1 Proliferation assay by crystal violet staining

Cells were seeded in 12-well plates for different time points. Each plate was washed with phosphate buffered saline (PBS), fixed with 10% formalin and stored at 4°C; the plate from the last day of the experiment was fixed for at least 15 minutes at RT. All plates were processed at the same time once the experiment was finished. Plates were washed again with PBS and stained with crystal violet [0.1% crystal violet (Ref. C3886, Sigma) and 20% methanol] for 1 hour. After washing with distilled water (dH₂O), plates were air dried and precipitates were dissolved in 10% acetic acid for 30 minutes. Absorbance was measured in 96-well plates in the spectrophotometer at 595 nm.

II.3.2 DNA synthesis rate analysis by bromodeoxyuridine

To analyze cell proliferation, we measured the incorporation of the pyrimidine deoxynucleoside thymidine analogue 5-bromodeoxyuridine (BrdU) into newly replicated DNA, based on the direct correlation between DNA replication and cell division.

BrdU incorporation

BrdU is a thymidine analogue that gets incorporated into DNA during its replication¹⁵⁹. Since monoclonal antibodies were developed to detect and bind to incorporated BrdU¹⁶⁰, it has been extensively used to estimate cell proliferation by immunofluorescence. In this thesis work, BrdU incorporation was performed in asynchronous cell cultures. Cells were seeded on coverslips (12 mm). BrdU (Ref. B5002, Sigma) was added to culture medium to a final concentration of 0.2 µg/mL and incubated for 6 hours at 37°C in the incubator. After incubation, cells were washed with PBS and fixed with 4% paraformaldehyde (PFA; Ref. 15710, Electron Microscopy Sciences) solution in PBS for 15 minutes. Cells were washed twice to eliminate remaining PFA and coverslips were stored in PBS at 4°C until processing.

DNA exposure and detection by immunofluorescence

For BrdU to be detected DNA must be exposed, allowing the binding of monoclonal antibodies. To this end, coverslips were incubated with HCl 2 M for 5 minutes and quickly washed twice with PBS to further neutralize the acid with Borax (sodium tetraborate 0.1 M, pH 8.5) for 5 minutes. Cells were then permeabilized with Triton X100 0.1%/Glycine 0.1 M for 5 minutes and 10% goat serum (in PBS) was employed as blocking reagent for 30 minutes at RT. Primary antibody against BrdU (Ref. B35128, Invitrogen) was incubated at 1:100 dilution in 10% goat serum overnight at 4°C in a humidification chamber. The next day, secondary anti-mouse antibody [anti-mouse Alexa594 (Ref. A11005), Invitrogen-Molecular Probes] was incubated at 1:1000 dilution in 10% goat serum for 1 hour in the dark. Finally, cells were stained with DAPI (4',6-diamidino-2-fenilindol; Ref. D1306, Thermo Fisher) (1:10,000 dilution in PBS) for nuclear staining and coverslips were mounted onto slides with ProLong Gold antifade reagent (Ref. P36930, Invitrogen). The slides were stored at 4°C in the dark until analysis with the upright fluorescent microscope AxioImager D1 (Carl Zeiss).

II.3.3 Cell size analysis by flow cytometry

To address the differences in the morphology of the cells, a BD FACSCanto™ II (BD Biosciences) flow cytometer was used for the analysis using forward scatter (FSC) and side scatter (SSC) properties. Live cells were trypsinized and resuspended in PBS and directly analyzed using the flow cytometer. Data were analyzed using the FlowJo software: cell populations of live cells were selected based on the “no dox” condition of each shRNA and differences were quantified taking this condition as control.

II.3.4 Senescence associated β -Galactosidase assay

To detect senescent cells, we analyzed the activity of senescence associated- β -galactosidase using a senescence detection kit (Ref. QIA117, Calbiochem). After fixing the cells for 10 minutes with the fixing solution, an overnight incubation with the staining mix [staining solution, X-Gal at 20 mg/ml in N,N-dimethylformamide (DMF; Ref. 227056, Sigma) and staining supplement] was performed. X-Gal is a chromogenic substrate that when added to the cells is cleaved by the lysosomal β -galactosidase enzyme giving a blue staining only to senescent cells. SA- β -Gal activity was revealed and quantified the next day. Plates were stored in glycerol 70% at 4°C. The number of senescent cells in each area was relativized to the number of total cells counted in the same area. Cells were seeded in plates or glass cover slips to acquire images with EVOS® cell imaging station (20x magnification objective).

II.3.5 Immunofluorescence

For immunofluorescence experiments, cells were seeded on 12 mm glass coverslips in 24-well plates. Cells were washed with PBS and fixed with 4% PFA solution in PBS for 15 minutes. Wells were washed twice to eliminate remaining PFA and coverslips were stored in PBS at 4°C until processing.

Cells were then permeabilized with Triton X100 0.1%/Glycine 0.1 M for 5 minutes and 10% goat serum (in PBS) was employed as blocking reagent for 30 minutes at RT. Primary antibodies were incubated in 10% goat serum overnight at 4°C in a humidification chamber (**Table M7**). The next day, secondary antibodies [anti-rabbit Alexa488 (Ref. A11034), anti-rabbit Alexa594 (Ref. A32740), anti-mouse Alexa488 (Ref. A11001) and anti-mouse Alexa594 (Ref. A11005); Invitrogen-Molecular Probes] were incubated at 1:1000 dilution in 10% goat serum for 1 hour in the dark. Finally, cells were stained with DAPI (1:10,000 dilution in PBS) for nuclear staining and coverslips were mounted onto slides with ProLong Gold antifade reagent. The slides were stored at 4°C in the dark until analysis with the upright fluorescent microscope AxioImager D1 (Carl Zeiss).

Table M7. References and preparation of the antibodies used for immunofluorescence.

Antibody	Reference	Species	Dilution
CDKN1B, p27	Ref.: 610242, BD Biosciences	Mouse	1:100
PML	Ref.: A301-167A, Bethyl laboratories	Rabbit	1:100
macroH2A1.1 (D5F6N)	Ref.: 12455, Cell Signaling	Rabbit	1:100

II.3.6 ROS production measurement

To measure the redox state of the cells 2',7'-dichlorofluorescein diacetate (DCF-DA) was used¹⁶¹. Upon cleavage by esterases and oxidation, this non-fluorescent molecule is converted into DCF, a very fluorescent product that will be measured by flow cytometry. It is excited at 495 nm and emits at 520 nm. 30 minutes before the analysis, 10 μ M of DCF-DA (Ref. 35845, Sigma) reactive was added to the cells, and 5 minutes prior to harvesting H₂O₂ (1 M) was added to the positive control well. Cells were washed twice with PBS, harvested using TrypLE™ Select Enzyme (Ref. 12563-011, Gibco) and resuspended in PBS for the analysis using BD FACSCanto™ II (BD Biosciences).

II.4 Molecular analysis

II.4.1 Gene expression analysis

II.4.1.1 RNA extraction

For *in vitro* gene expression analysis, cells were seeded in 6-well plates for a final density of around 70-80% (following the times explained in **figure M5**). Plates were washed with PBS and processed or snap-frozen in liquid-nitrogen for later RNA extraction, unless otherwise specified. RNA was extracted using NucleoSpin® RNA isolation kit from Macherey-Nagel (Ref. 740955.250) according to manufacturer's protocol. The RNA concentration was determined by using the NanoDrop ND-1000 Spectrophotometer (Thermo Fisher Scientific).

For RNA extraction from xenografts of human cancer cell lines, samples were incubated overnight at -20°C with 200 μ L of RNAlater™-ICE (Ref. AM7030, Invitrogen), which was kept at -80°C until it was used. The following day, tissues were transferred to a new tube with 800 μ L of TRI Reagent® (Ref. TR-118, MRC) with 2.8 mm ceramic beads (Ref. 13114-50, MO BIO Laboratories). Precellys® machine was used to homogenize the tissue at 6,000 rpm during 30 seconds (step repeated twice). Then, 160 μ L of chloroform (Ref. 34854, Sigma) were added and, after vortexing, the mix was centrifuged at 12,000 rcf during 15 minutes at 4°C. The aqueous phase was collected and mixed with the corresponding volume of ethanol. The same protocol used for RNA extraction from cell lines was followed after this step.

II.4.1.2 RNA retrotranscription

For RNA retrotranscription, 1 or 0.5 μ g of the obtained RNA were used for complementary DNA (cDNA) synthesis using Maxima™ H Minus cDNA Synthesis Master Mix (Ref. M1682,

Invitrogen). Resulting cDNA was diluted in fresh milli Q water and 3 μ L were used for real time quantitative PCR (RT-Q-PCR) reaction.

II.4.1.3 Real time quantitative PCR

RT-Q-PCRs were performed using either Vii7 or QS6 systems (Life Technologies). The following program was used for this approach: 2 minutes at 50 °C and 10 minutes at 95°C (hold stage) followed by 40 cycles of 15 seconds at 95°C (denaturalization) and 1 minute at 60°C (annealing and elongation). Gene expression was analyzed with primers and probes from Universal Probe Library from Roche. The Universal Probe Library Assay Design Center is available online (https://lifescience.roche.com/en_es/brands/universal-probe-library.html). This tool allows the designing of primers and also assigns the corresponding probe needed for each reaction in order to perform a TaqMan assay. For the reaction, 0.3 μ L of primer mix (20 μ M), 3 μ L of TaqMan® universal master mix II with UNG (Ref. 4440046, Applied Biosystems) and 0.05 μ L of the corresponding probe were used. For the analysis of both the house-keeping gene, GAPDH and PML gene, commercial TaqMan probes (Life technologies) were used. Comparative Ct method was selected for the quantification of gene expression changes. See **Table M8** for specific primer sequences and references.

Table M8. Specifications of primer sequences and probe numbers from Universal Probe Library (Roche).

Gene	Forward 5´-3´	Reverse 5´-3´	Probe
CDKN1B	ccctagagggcaagtacgagt	agtagaactcgggcaagctg	39
MYC	gctgcttagacgctggattt	taacgttgaggggcatcg	66
PIM1	atcaggggccaggttttc	gggccaagcaccatctaat	13
CDK2	aaagccagaaacaagttgacg	gtactgggcacaccctcagt	77
CDK4	gtgcagtcggtgtacctg	aggcagagattcgctgtgt	25
E2F3	ggttcggaatgcccttac	gatgaccgctttccttagc	40
AURKA	gcagatttgggtgtcagt	tccgacctcaatcattca	79
CDC25A	cgtcatgagaactacaaacctga	tctggtctctcaacactgacc	67
PML	Hs00971694m1		
GAPDH	Hs02758991_g1		

II.4.2 Protein expression analysis

II.4.2.1 Protein extraction

For *in vitro* protein expression analysis, cells were seeded as for gene expression analysis. All the steps were performed on ice. Cells were lysed using RIPA buffer [50 mM TrisHCl pH 7.5, 150 mM NaCl, 1 mM EDTA, 0.10% SDS, 1% Sodium Deoxycholate, 1% NP-40, 1 pill of Complete EDTA-free Protease inhibitor cocktail tablet (Ref. 04693132001, Roche) per 50 mL of buffer, and 1 mM of the phosphatase inhibitors sodium fluoride, sodium orthovanadate and β -glycerophosphate]. Lysates were maintained at 4°C with rotation for 20 minutes and then centrifuged at 13,500 rpm for 12 minutes. Protein containing supernatant was collected in new Eppendorf tubes. Protein concentration was determined with a Pierce BCA protein assay kit (Ref. 23227, Thermo Scientific).

For protein extraction from xenografts, the homogenization was performed in the presence of 400 μ L of modified RIPA lysis buffer, containing twice the concentration of inhibitors used for protein extraction from cell lines (2 mM phosphatase inhibitors and two pills of protease inhibitor cocktail).

II.4.2.2 Western blotting (WB)

Protein lysates (which were previously loaded with Laemmli buffer 5X) were boiled at 95°C for 5 minutes for protein denaturalization, and resolved either in NuPAGE® Novex® 4-12% Bis-Tris Midi Protein gels (Ref. NG1403BOX, Invitrogen) or mini protein gels (Ref. NP0322BOX, Invitrogen) at 180 V in MES SDS buffer (Ref. K856-500ML, VWR) or NuPAGE™ MOPS SDS Running Buffer (Ref. NP0001-02, Invitrogen). Pink Prestained Protein Marker (Ref. MWP02, Nippon) was used as protein weight marker (weighted in kilodalton, kDa). Proteins were transferred to nitrocellulose membranes at 100 V for 1 hour. Then, membranes were blocked with 5% non-fat milk prepared in Tris-buffered saline solution containing 0.01% Tween-20 (TBS-T). Primary antibodies were prepared in TBS-T with 0.002% sodium azide to allow long storage, and membranes were incubated with the antibodies either overnight at 4°C or for 2 hours at RT. After primary antibody incubation, membranes were washed 3 times with TBS-T for 10 minutes and incubated with the secondary antibody (1:4000 in 5% milk) for, at least, 1 hour at RT. After that, membranes were again washed three times and developed with home-made ECL [solution A: 10% Tris pH 8.5, 90% H₂O, 0.2 mM p-coumaric acid (Ref. 9008, Sigma) and 1.25 mM luminol (Ref. 09253, Sigma) and solution B: 10% H₂O₂ (3 μ L of solution B were used per 1 mL of solution A)]. Proteins were visualized using Medical X-Ray films (Konica Minolta) or iBright™ CL1000 Imaging System (Ref. A32749, Invitrogen). Densitometry-based quantification was performed using ImageJ software. See **Table M9** for references of antibodies used for Western Blotting.

Table M9. References and preparation of primary and secondary antibodies employed for Western Blotting.

Antibody	Reference	Species	Dilution
PML	A301-167A, Bethyl laboratories	Rabbit	1:1000
Cleaved PARP (Asp214) (D64E10)	Cat: 5625, Cell Signaling	Rabbit	1:1000
Cleaved caspase-3 (Asp175)	Cat: 9661, Cell Signaling	Rabbit	1:1000
CDKN1B, p27[Kip1]	Cat:610242, BD Biosciences	Mouse	1:1000
Phospho Rb (Ser780)	Cat: 9307, Cell Signaling	Rabbit	1:1000
MYC	Cat: 13987, Cell Signaling	Rabbit	1:1000
PIM1 (D8D7Y)	Cat: 54523, Cell Signaling	Rabbit	1:1000
Lamin B1	ab133741, Abcam	Rabbit	1:1000
Tubulin	T9026, Sigma	Mouse	1:1000
Hsp90	Cat: 4874, Cell Signaling	Rabbit	1:2000
β-actin	Cat: 3700, Cell Signaling	Mouse	1:2000
Secondary Rabbit Ab	111-035-144, Jackson ImmunoResearch	Rabbit	1:4000
Secondary Mouse Ab	315-035-045, Jackson ImmunoResearch	Mouse	1:4000

II.4.3 Chromatin immunoprecipitation (ChIP)

ChIP was performed using the Simple ChIP Enzymatic Chromatin IP Kit (Ref. 9003, Cell Signaling Technology). Briefly, MDA-MB-231 cells (2.5×10^7 cells) were grown in 150 mm dishes either with or without 50 ng/ml doxycycline during 3 days. To crosslink the proteins to the DNA, 35% formaldehyde (Ref. F8775-500ML, Sigma) was added to the cells for 10 min at RT. Glycine was added to dishes, and cells incubated for 5 min at RT. They were then washed twice with ice-cold PBS, and scraped into PBS plus PMSF (phenylmethylsulfonyl fluoride). Pelleted cells were lysed and nuclei were collected following manufacturer's instructions. Nuclear lysates were digested with micrococcal nuclease for 20 min at 37°C and then sonicated into 500 ml aliquots on ice for three pulses of 15 seconds using a Branson sonicator. Cells were held on ice for at least 1 minute between sonications. Lysates were clarified at 11,000 rcf for 10 min at 4°C, and chromatin was stored at 80°C. HA-Tag polyclonal antibody (Ref. C29F4, Cell Signaling Technology) and IgG antibody (Ref. 2729, Cell Signaling Technology), were incubated overnight (4°C) with rotation and then incubated 2 h (4°C) with protein G magnetic beads. Finally, chromatin was eluted from protein G magnetic beads. Washes and elution of chromatin were performed following manufacturer's instructions.

DNA quantification was carried out using a Vii7 Real-Time PCR System (Applied Biosystems) with SybrGreen reagents and primers that amplify the predicted PML binding region (based on ENCODE data) to *MYC* promoter (chr8:128748295-128748695) as follows: left primer: CCGGCTAGGGTGGAAGAG, right primer: GCTGCTATGGGCAAAGTTTC and *PIM1* promoter (chr6:37137097-37137612) as follows: left primer: ACTCCCTCCGTGACTCATGT, right primer: ACGAGGGTGGTCTTTCTGTG.

II.4.4 Senescence associated secretome analysis

The senescence associated secretome analysis was carried out by Ariane Schaub in collaboration with Josep Villanueva and Francesc Canals from the Vall d'Hebron Institute of Oncology (VHIO)¹⁶².

For this purpose, MDA-MB-231 sh4PML-Tet-On and Cama-1 sh4PML-Tet-On cells were pre-induced as described in **figure M5**. Three 150 mm plates were seeded per condition: 4×10^6 cells per plate of non-induced cells and 5×10^6 cells per plate of doxycycline induced cells. After two days, cell supernatants were removed and cells were washed 5 times: the first two washes were performed with PBS and the last three were made with serum-depleted DMEM. Cells were left to grow for 24 hours in DMEM depleted of FBS but supplemented with Penicillin/Streptomycin. Doxycycline was added to the induced cells.

After 24 hours, conditioned media (CM) was collected and one plate of each condition was trypsinized, cells were counted and stored for protein extraction. The CM was first centrifuged at 1,000 rpm for 5 minutes followed by a filtration step through 0.2 μm filtering bottles. After this, CM was concentrated using 10 kDa Amicons. First, 15 mL Amicons (Ref. UCF901024, Merck) were used, followed by 0.5 mL Amicons (Ref. UCF501069, Merck) to get final volumes close to 80 μL . The concentrated secretome was frozen at -20°C . Protein concentration was determined with a Pierce BCA protein assay kit. All samples were digested with trypsin in-solution prior to analysis by liquid chromatography–mass spectrometry (LC–MS). Tryptic digests were analyzed by shotgun proteomics using an LTQ Velos-Orbitrap mass spectrometer (Thermo Fisher Scientific, Bremen, Germany). The RAW files of each MS run were processed using Proteome Discoverer (Thermo Fisher Scientific), and MS/MS spectra were searched against the human database of Swiss-Prot using the MASCOT (Matrix Science, London, U.K) algorithm. The results files generated from MASCOT (.DAT files) were then loaded into Scaffold (Proteome Software, Portland, OR), resulting in a nonredundant list of identified proteins per sample achieving a protein false discovery rate (FDR) under 1.0%, as estimated by a search against a decoy database.

II.5 Subcutaneous xenograft experiments in nude mice

All mouse experiments were carried out following the ethical guidelines established by the Biosafety and Animal Welfare Committee at CIC bioGUNE. The procedures employed were carried out following the recommendations from AAALAC. Mice were housed under controlled environmental conditions, such as time-controlled lighting on standard 12:12 light: dark cycles, controlled temperature at $22 \pm 2^\circ\text{C}$ and 30-50% relative humidity.

MDA-MB-231 sh4PML-Tet-On cells in suspension were inoculated subcutaneously into immunocompromised 8-12-week-old female nude mice (Hsd:Athymic Nude-Foxn1 nu/nu). For this experiment 12 mice were used: 3×10^6 cells per tumor were injected, two injections per mouse, one per flank. 19 days post-injection and once tumors were established ($25\text{-}130 \text{ mm}^3$), mice were fed with chow or doxycycline diet (Ref. D12100402, Research diets) until the ethical end point of the experiment at day 31.

II.5.1 Pathological analysis of xenograft samples

At the experimental end-point of the xenograft experiment, when tumors were harvested, a third part of the tumor was fixed in 10% neutral buffered formalin, another third part was frozen and kept for molecular analysis (protein and/or RNA extraction) and the last part was embedded in OCT (Q Path®, Cat: 00411243, VWR).

The tissue processing steps were performed by Sonia Fernández (CIC bioGUNE). After 24 hours of fixation in formalin at 4°C , samples were washed with PBS, ethanol 50% and 70% (10 minutes each wash). Samples were dehydrated and infiltrated with paraffin following the steps in **Table M10** (automatic tissue processor Leica TP1020). Then, infiltrated tissues were embedded in paraffin blocks (Leica EG1150C heated embedding module and cold block). $3 \mu\text{m}$ sections were done (Leica RM2245 microtome) and adhered to slides for staining and analysis (in water bath at 60°C).

II.5.2 Slide processing for immunohistochemistry: antibody staining

Tissues were deparaffinized using the standard procedure and unmasking/antigen retrieval was performed using pH 6.0 solution for 20 min at 98°C in water bath. Tissue sections were stained for p-HP1 γ using primary antibody Phospho-HP1 γ (Ser83) (Ref. 2600, Cell Signaling technologies, 1:200) and secondary antibody Biotinylated antibody Anti-Rabbit (Ref. BP-9100, Vector Laboratories, 1:200). This was followed by Vectastain ABC solution incubation (Ref. PK-6100, Vector laboratories, 1:150) and DAB staining (Ref. SK-4105, Vector laboratories) as per the

manufacturer's protocol. Stained slides were scanned using Leica Aperio AT2 slide scanner. This procedure was performed by Dr. Ajinkya Revandkar from Dr. Andrea Alimonti's group.

Table M10. Steps followed to process xenograft tissues in the automatic processor.

Tray	Time	Reagent	Function
T1	10 min	50 % Ethanol	Dehydration
T2	1h 30 min	70 % Ethanol	Dehydration
T3	1h 30 min	80 % Ethanol	Dehydration
T4	1h 30 min	96 % Ethanol	Dehydration
T5	1h 30 min	100 % Ethanol	Dehydration
T6	1h 30 min	100 % Ethanol	Dehydration
T7	1h 30 min	100 % Ethanol	Dehydration
T8	45 min	Citrosol or Xylene substitute	Rinse, replace the ethanol with citrosol
T9	2h	Paraffin	Replace the citrosol with paraffin
T10	2h	Paraffin	Replace the citrosol with paraffin

II.5.3 Sample evaluation

The criteria for senescent staining used for quantification was a very prominent nuclear staining in which the nucleus was bigger in size and its staining was darker brown than the other cells.

II.6 Tumor growth analysis using chicken chorioallantoic membrane model

We followed the protocol published by Piero Crespo and Berta Casar¹⁶³ for the study of tumor growth of MDA-MB-231 sh4PML-Tet-On cells in the chorioallantoic membrane (CAM). Briefly, after 10 days of development, CAM is dropped by vacuuming from a small hole made in the air sack. A bigger aperture was made in the eggs near the allantoic vein, where cells were seeded carefully. The cells of the doxycycline induced group were pre-induced for 3 days before inoculation; 1×10^6 cells were inoculated per egg and doxycycline induction was maintained by adding 150 ng/mL to the inoculated pre-induced cells every day until the end of the experiment (at day 14 of development, 5 days after inoculation). Growth was measured by the weight of the primary tumor. A total number of 31 eggs was used.

III Bioinformatic analysis

III.1 Depmap

Gene expression data for *PML*, *p27*, *MYC* and *PIM1* was downloaded from Cancer Dependency Map Project at the Broad Institute (DepMap, Public 19Q3) and filtered for BCa cell lines. Cell lines with available data were classified into the different BCa subtypes based on the information available in the bibliography. Depending on the analysis different groups were made: in one hand, they were divided into ER negative and ER positive groups and in the other hand, into triple negative and rest. RNA-Seq expression data is given as Log₂ transformed TPM (Transcripts Per Kilobase Million).

Pearson correlation test was applied to analyze the relationship between paired genes.

III.2 Patient samples

Database normalization: all the datasets used for the data mining analysis were downloaded from Gene Expression Omnibus (GEO)¹⁶⁴⁻¹⁶⁸ and The Cancer Genome Atlas (TCGA) and subjected to background correction, log₂ transformation and quartile normalization. In the case of using a pre-processed dataset, this normalization was reviewed and corrected if required.

Status by ER: violin plots depicting the expression of the gene of interest between ER- and ER+ breast cancer specimens in the indicated datasets. A Student T-test is performed in order to compare the mean gene expression between two groups.

Status by subtype: violin plots depicting the expression of the gene of interest among breast cancer subtypes in the indicated datasets. An ANOVA test is performed in order to compare the mean gene expression among groups.

Correlation analysis: Pearson correlation test was applied to analyze the relationship between paired genes. From this analysis, Pearson coefficient (R) indicates the existing linear correlation (dependence) between two variables *X* and *Y*, giving a value between +1 and -1 (both included), where 1 is total positive correlation, 0 is no correlation, and -1 is total negative correlation. The p-value indicates the significance of this R coefficient.

IV Statistical analysis

All experiments were performed a minimum of three times (biological replicates) to ensure adequate statistical power, with at least two technical replicates for each independent experiment.

The xenograft, secretome and CAM experiments were done once, but with independent biological replicates.

Unless otherwise stated, data is represented by the mean \pm s.e.m. of pooled experiments. n values represent the number of independent experiments performed or the number of tumors from the different xenograft mice.

For *in vitro* experiments, normal distribution was assumed and Student's t-test was applied for two component comparisons. With fold change representations, one sample t-test with the corresponding hypothetical value (1 or 100) was used for statistical analysis. For *in vivo* experiment, a non-parametric Mann-Whitney U test was used. The confidence level used for all the statistical analyses was of 95% (alpha value = 0.05). Two-tail statistical analysis was used with experiments without a predicted result, and one-tail for the validation of hypothesis-driven experiments.

IV.1 Secretome statistical analysis

Relative spectral counting-based protein quantification analysis was performed on the different samples analyzed using Scaffold. Files containing all spectral counts for each sample and its replicates were generated and then exported to R software for normalization and statistical analysis¹⁶⁹. All statistical computations were done using the open-source statistical package R. The data were assembled in a matrix of spectral counts, where the different conditions are represented by the columns and the identified proteins are represented by the rows. An unsupervised exploratory data analysis (EDA) by means of principal components analysis and hierarchical clustering of the samples on the SpC matrix was first performed. Then, the generalized linear model (GLM) based on the Poisson distribution was used as a significance test¹⁶⁹. Finally, the Benjamini and Hochberg multitest correction was used to adjust the p values with control on the FDR.



Results and discussion

I Analysis of the pro-survival role of PML in triple negative breast cancer

The first aim of this thesis work was to decipher the contribution of PML to the growth of TNBC cells where it is overexpressed.

HYPOTHESIS

PML plays a growth sustaining role in TNBC and its targeting has an inhibitory effect in high PML expressing cells

Since the discovery of its role in the pathogenesis of acute promyelocytic leukemia^{58,170}, deciphering the role of PML in cancer has become of major interest. Although it was originally described as a tumor suppressor^{90,94,97}, PML exhibits pro-survival activity in a variety of cancers based on recent reports^{98-102,171-173}.

I.1 Analysis of PML status in patient and cell line datasets

Pandolfi's group demonstrated for the first time that PML plays a pro-survival role in BCa by providing a selective advantage through the activation of FAO to cells that undergo metabolic stress. When analyzing PML levels in normal breast epithelium and in BCa samples, they showed that a subset of BCa exhibited higher levels of PML. Interestingly, triple negative or basal like BCa was selectively enriched within this subset¹⁰⁰.

PML regulates SOX9¹⁰¹ and HIF1 α ¹⁰² signaling selectively in PML high-expressing BCa, thus controlling aggressiveness and metastatic characteristics. This function was demonstrated in the cancer-initiating cell compartment of TNBC cells, but the impact of this protein on the bulk of tumor cells is still poorly understood.

The increasing availability of OMICs data is an important source of information that can be used towards precision medicine¹⁷⁴. The problems in managing, extracting and analyzing the information that is accessible in the different datasets has encouraged the development of user friendly tools for basic cancer researchers, such as cBioportal¹⁷⁵ and Cancertool¹⁷⁶. With the help of bioinformatics, research questions can be first studied *in silico*, working with tumor derived data that would be inaccessible otherwise.

In order to further support the results described in the previous BCa studies¹⁰⁰, we took advantage of publicly available datasets in Cancertool to investigate the levels of PML mRNA in tumor samples. As different characteristics of BCa are used for their classification, we first analyzed PML gene expression in ER+ and ER- groups. We confirmed that PML expression was significantly higher in ER- tumors when compared with ER+ tumors (significant in 4 out of 5 datasets **Fig. R1**).

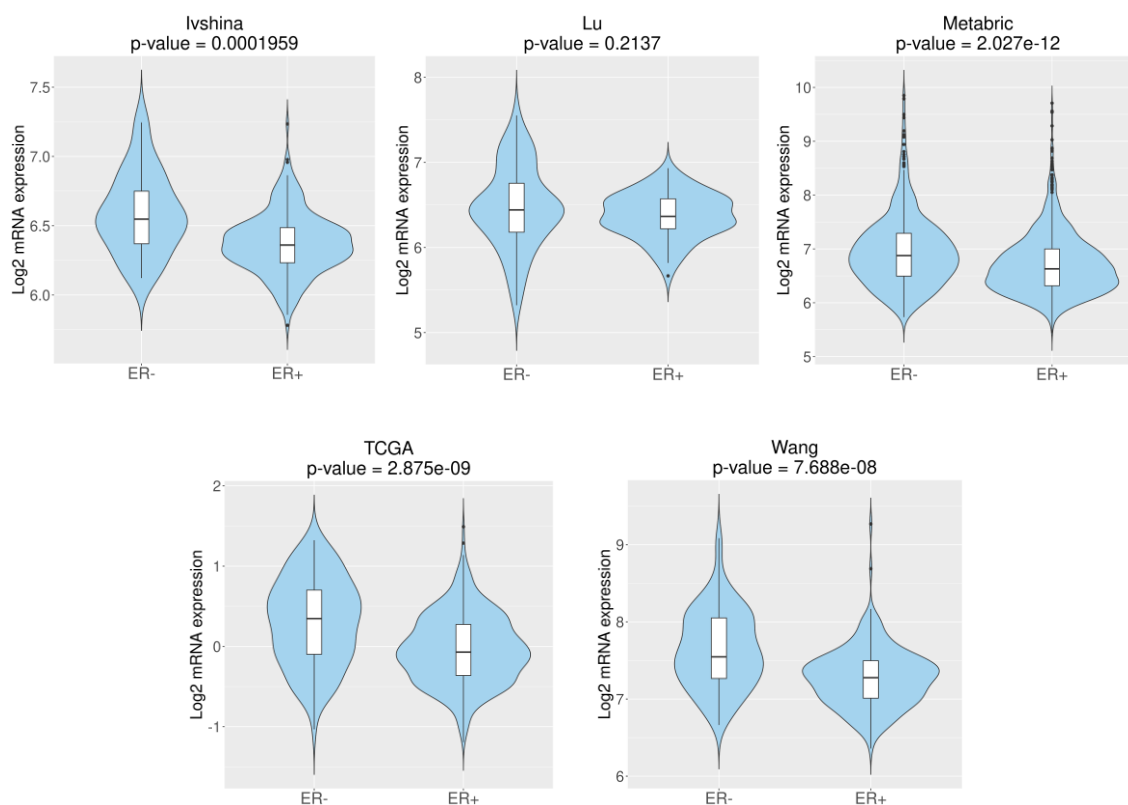


Figure R1. PML mRNA expression based on ER status. Expression levels of PML in Ivshina, Lu, Metabric, TCGA and Wang datasets. Sample size: Ivshina (n=245; ER-=34, ER+=211), Lu (n=118; ER-=49, ER+=69), Metabric (n=1973; ER-=472, ER+=1501), TCGA (n=512; ER-=114, ER+=398), Wang (n=285; ER-=77, ER+=208).

Since the information about the different molecular subtypes^{43,44} was available in these datasets, we next classified the tumors into the 5 different subtypes. Samples from the different datasets were separated into basal-like, HER2-enriched, luminal A, luminal B and normal-like BCa. In one of the datasets (Lu¹⁶⁶), all luminal tumors were grouped and there was no data available of normal-like samples. We analyzed the mRNA levels of PML across 4 datasets and found that PML expression was significantly altered among the subtypes in 3 out of 4 datasets (**Fig. R2**).

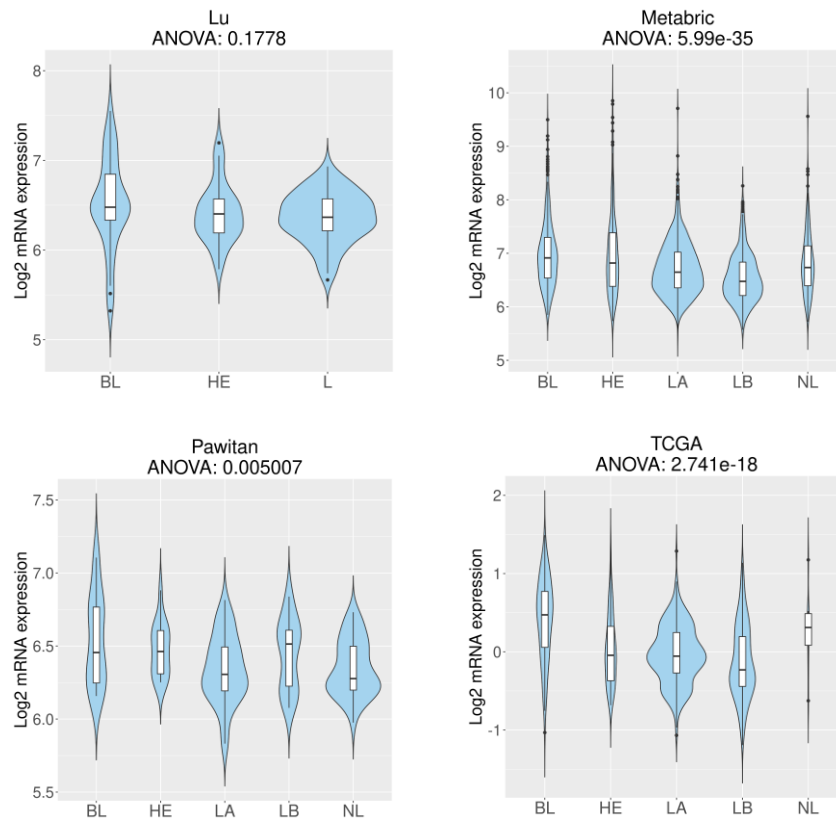


Figure R2. PML mRNA expression among the molecular subtypes. PML expression in basal-like (BL), HER2-enriched (HE), Luminal (L), Luminal A (LA), Luminal B (LB) and Normal-like (NL) subtypes. Sample size: Lu (n=124; BL=32, HE=31, L=61), Metabric (n=1974; BL=329, HE=240, LA=718, LB=488, NL=199), Pawitan (n=139; BL=25, HE=15, LA=39, LB=23, NL=37), TCGA (n=519; BL=95, HE=58, LA=231, LB=127, NL=8).

To analyze whether PML expression levels were specifically higher in basal-like tumors¹⁰⁰, we grouped the non-basal like tumors (data from the same datasets) and compared with the basal group. We confirmed that PML was significantly overexpressed in basal-like samples in 3 out of 4 datasets (**Fig. R3**).

For many years, research efforts have been focused into classifying and characterizing different cancer types with the aim of searching for biomarkers that could help in the treatment of those tumors¹⁷⁷⁻¹⁷⁹. BCa classifications have been widely used to stratify BCa patients and to treat them accordingly^{23,43,44,164,180}. Nonetheless, the lack of biomarkers is one of the main obstacles for targeted therapies in TNBC patients. These tumors lack ER expression and HER2 overexpression/amplification. In addition, several cancer genes that appear commonly mutated (BRCA1¹⁸¹, p53^{44,182}) or overexpressed (EGFR¹⁸³) have been studied as potential targets. Yet, no targeted therapies have been developed for these tumors, which are associated with poor prognosis and more aggressive phenotypes. The results obtained from the different datasets with PML mRNA expression data available further support the importance of studying the function of PML in BCa, with a particular focus in basal-like/TNBC subtypes.

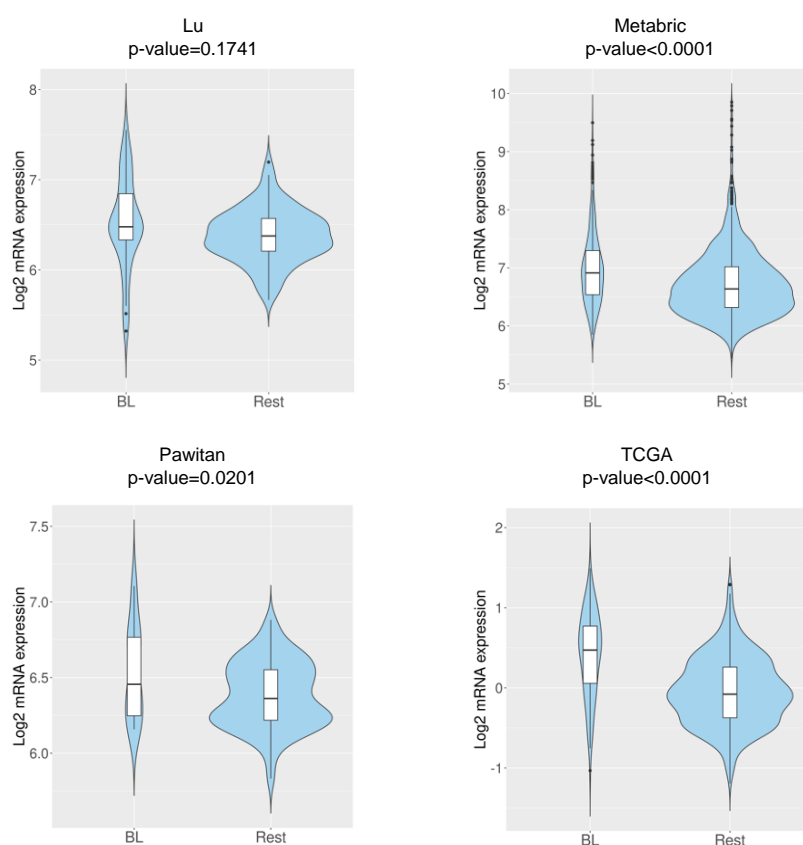


Figure R3. PML mRNA expression in basal-like subtype and non-basal tumors. Comparison of PML expression between basal-like subtype and the rest of the subtypes (HE, L, LA, LB, NL) grouped from Fig. R2.

To characterize the function of PML in BCa *in vitro*, it was important to use reliable systems capable of recapitulating the PML status observed in patient samples. For that purpose, we first took advantage of the Cancer Dependency Map project (<https://depmap.org/portal/>) to analyze PML mRNA expression across multiple available BCa cell lines (doi: 10.1038/ng.3984). The aim of DepMap is to keep updated datasets with genomic information and sensitivity to genetic or pharmacological perturbations of hundreds of cancer cell line models. BCa cell lines were classified into the different subtypes based on the information available in the bibliography (**Annex Table 1**). We performed two different comparisons based on the groups used for the analysis with patient data: ER- versus ER+ and TNBC versus Rest. We observed that PML expression was remarkably higher in ER- cell lines (**Fig. R4A**) and TNBC (**Fig. R4B**) when compared to ER+ and Rest groups, respectively. The cell lines available in our laboratory, MDA-MB-231, MDA-MB-468 and Cal51 are described as TNBC cell line models, while MCF-7, Cama-1 and T47D are derived from ER positive tumors¹⁸⁴⁻¹⁸⁶. We analyzed specifically the expression of PML in these cell lines, MDA-MB-231 and MDA-MB-468 showed the highest PML gene expression levels across the panel of cell lines (shown in **Fig. R4** in purple and green, respectively). Surprisingly, Cal51 cell line (in orange in **Fig. R4**) exhibited PML mRNA expression levels comparable to the three ER positive cell lines (shown in red, blue and pink in **Fig. R4**).

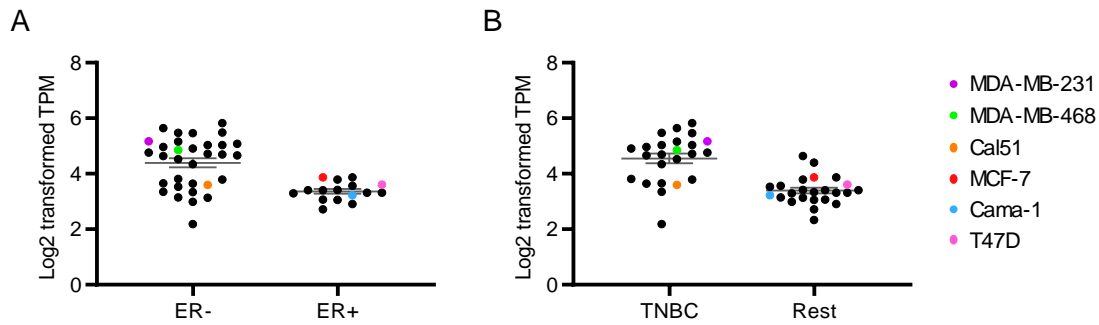


Figure R4. PML mRNA expression in cell lines from DepMap. Samples were classified by **A)** ER status (sample size: 48; ER-=32, ER+=16) or **B)** subtype (sample size: 48; TNBC=24, Rest= 24).

The second step was to validate PML expression in the 6 available cell lines by western blot (**Fig. R5**). In agreement with DepMap data, MDA-MB-231 and MDA-MB-468 were the most representative models for high-PML expressing TNBC cell lines, as PML levels were significantly higher when compared to the rest of the cell lines. Cal51 cell line did not follow the direction of the other two TNBC cell lines, with significantly lower PML protein levels. In the ER positive group, PML expression was similar in all the cell lines available.

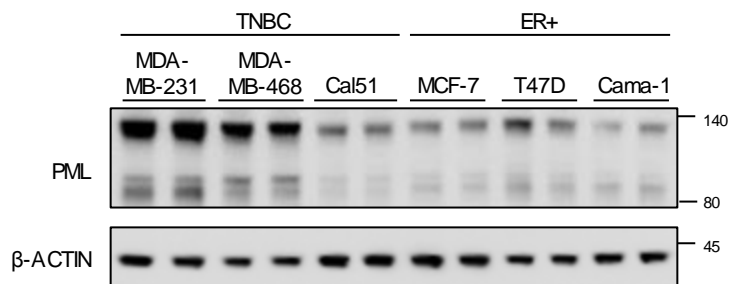


Figure R5. PML protein expression in cell lines. Western Blot showing PML protein expression in the panel of available breast cancer cell lines. Molecular weight markers (kDa) are shown to the right (n=1).

Martín-Martín *et al.*¹⁰¹ described that a subset of BCa tumors presented high PML levels and highlighted the stratification potential of PML in this cancer. In this thesis work we observe that, in both patient and cell line datasets, a subset of TNBC shows higher PML expression levels when compared to the rest of the tumors or cell lines. The evaluation of the distinct molecular alterations present in each of these tumors with different PML levels would help in their characterization and classification. Therefore, analyzing the role of PML in BCa needs further investigation for a robust patient stratification based on its expression.

Owing to the high PML expression levels in TNBC, we next aimed to silence PML in the cell lines to further characterize the role of PML in BCa.

I.2 Generation of the working cellular systems

Cell lines represent a valuable tool in cancer research. MDA-MB-231 cell line was one of the first BCa cell lines isolated¹⁸⁷ and it has been widely used in cancer research as a TNBC model.

The first approach was to silence PML with different shRNAs, using both constitutive and doxycycline-inducible lentiviral systems. Compared to other silencing methods such as siRNAs, shRNAs have demonstrated higher specificity and, therefore, less off-target effects¹⁸⁸. Two different constitutive shRNAs were used (**Fig. R6A**), while for the inducible system a third shRNA (**Fig. R6B**, induction scheme in Fig. M5) was generated together with the two used for the constitutive silencing of PML. We observed a robust silencing of PML with all the shRNAs tested, with different silencing efficacy.

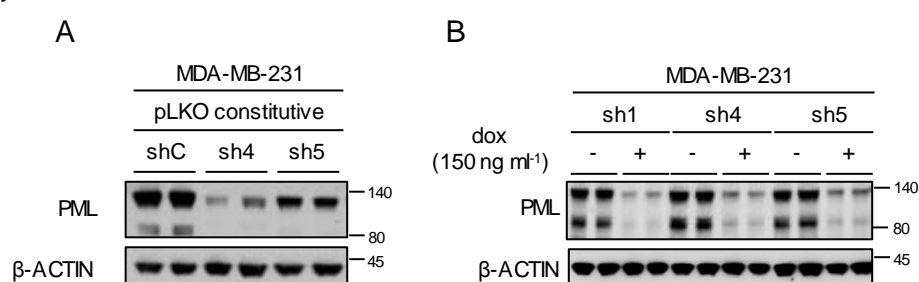


Figure R6. PML silencing in MDA-MB-231 cell line. Western Blot (representative of at least 3 experiments) showing PML protein expression after PML silencing with **A**) constitutive and **B**) inducible shRNAs. Molecular weight markers (kDa) are shown on the right.

The detection of different PML isoforms and modifications by Western Blot depends on the antibody used for the analysis. There are 6 different nuclear PML isoforms and all of them undergo post-translational modifications that will affect their function. The antibody used in this thesis work (Bethyl) detects several bands at different molecular weights. Still, it is not possible to assert if all the bands correspond to the different isoforms or are due to post-translational modifications of the protein, such as SUMOylation^{74,189}. During this thesis work we focused on the most abundant immunoreactive bands when analyzing PML protein levels, the ones with highest molecular weight. We confirmed that some of the immunoreactive bands with lower molecular weight showed an equivalent silencing degree (**Fig. R7**).

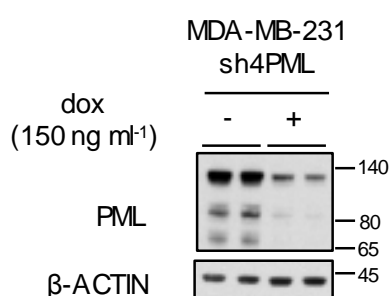


Figure R7. Detection of PML isoforms at protein level by Bethyl antibody. Western Blot showing PML protein expression after inducible PML silencing. Molecular weight markers (kDa) are shown on the right.

To further validate our results, we took advantage of different cell lines available in the laboratory: two additional TNBC and three ER+ cell lines. Surprisingly, and after several infections, it was not possible to silence PML in Cal51 cell line. In contrast, PML protein levels were significantly decreased in MDA-MB-468, equivalent to what we previously observed with MDA-MB-231 cell line (**Fig. R8A**). In the case of the ER+ cell lines, it is important to underline that their basal PML protein levels are lower than in TNBC cell lines (**Fig. R4** and **Fig.R5**). We observed a remarkable silencing in all the three ER+ cell lines, proportional to that observed in TNBC cell lines (**Fig. R8B** and **R8C**). We decided to work with MCF-7, since it is widely used as a model of hormone positive cell line, and Cama-1, as the silencing of PML in this cell line, compared to T47D, showed more consistency between experiments.

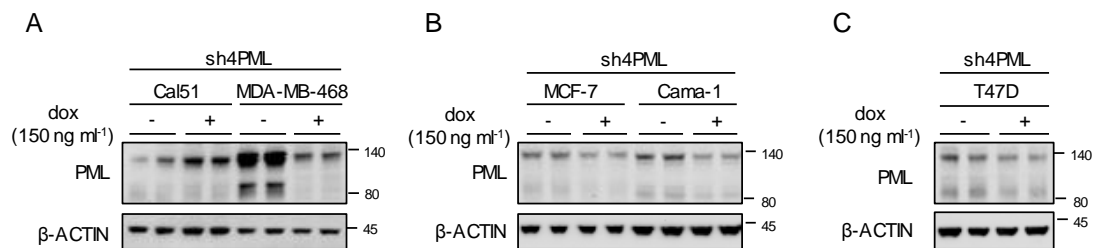


Figure R8. Effect of inducible sh4PML in breast cancer cell lines. Western Blot (representative of at least 3 experiments) showing PML protein expression after inducible PML silencing in **A**) Cal51 and MDA-MB-468, **B**) MCF-7 and Cama-1 and **C**) T47D cell lines. Molecular weight markers (kDa) are shown on the right.

Extending the analysis to different cell lines ensures the robustness of the study. Established cell lines carry different mutational background that should be taken into account when working with them. In fact, several mutations have been identified in MDA-MB-231 cell line, including *TP53*, *BRAF*, *CDKN2A* and *KRAS*. *TP53* tumor suppressor has been widely studied and mutations in this gene have been described in a broad range of different cancer types¹⁹⁰. In BCa, *TP53* mutations are associated with poor prognosis and more aggressive tumors. Interestingly, around the 80% of TNBC⁴⁵ carry mutations in this gene and aberrations in p53 are correlated with PML expression in this subgroup¹⁰⁰. Thus, it is of utmost importance a good characterization of the molecular background of the cell lines used in cancer research. This would allow to recapitulate the heterogeneity present in BCa tumors and to work with models that resemble more accurately what it is observed in patient samples.

I.3 Consequences of PML silencing in cell growth

Due to its function in APL and its loss in multiple cancers, the tumor suppressive role of PML has been deeply studied. Interestingly, PML regulates a broad range of cellular processes that are relevant in cancer, such as proliferation¹⁹¹, apoptosis^{77,192}, DNA damage response⁶⁴ and senescence^{70,90}. In contrast to its tumor suppressive role, Ito *et al.* in leukemia⁹⁸ and Carracedo *et*

al. in BCa¹⁰⁰, described a pro-survival role of PML. We have described that a subset of BCa express high levels of PML, both in patients and cell lines, with an overrepresentation of TNBC cases. We next focused on characterizing the consequences of PML silencing in the bulk of cells *in vitro*.

I.3.1 Effect of PML silencing on cell number

To tackle this question, we first aimed to study the effect of targeting PML on the cell growth in TNBC cell lines. We observed an impairment in the growth of MDA-MB-231 cells, with a significant decrease on cell number of about the 70% with constitutive PML silencing (**Fig. R9A**) and about 45% in the case of doxycycline inducible PML silencing (**Fig. R9B**). Inducible silencing provides reversible and temporal control of the shRNA expression. It allows to titrate the silencing and follow the dynamics of PML levels during the days of induction. When working with genes that challenge the survival of the cells, inducible silencing also provides the time needed for the establishment of xenografts tumors *in vivo*. We performed the first approaches with the constitutive system and confirmed the results with the inducible silencing. Since PML silencing remarkably affected cell growth, we decided to continue working with inducible system to ease the manipulation and experimental setting.

To further analyze the proliferation of the cells, we studied the incorporation of BrdU into the newly synthesized DNA of replicating cells upon PML silencing. We observed that DNA replication was reduced upon decreased levels of PML by means of BrdU positivity (**Fig. R9C**).

A feasible explanation for the reduced cell number is apoptosis, a programmed cell death process where caspases play a key role. Caspases are synthesized as inactive zymogens and can be classified into initiator and effector caspases. Caspase-3 belongs to the effector caspases group and its activation is a hallmark of apoptosis¹⁹³. Another marker is the cleavage of poly (ADP-ribose) polymerase-1 (PARP-1), a substrate of caspases in the apoptotic pathway¹⁹⁴. To study whether the cells were undergoing apoptosis, we treated the MDA-MB-231 cells with staurosporine, a well-known apoptosis inducer, for 4 hours as a positive control for cleaved caspase-3 and PARP. We collected the supernatant together with the cells that were still attached to the plate to ensure that all the cells that could have activated the apoptotic cascade were being analyzed (whether they were already dead and floating or still attached but with the signaling cascade activated). Nevertheless, no signs of apoptosis were observed upon PML silencing (**Fig. R9D**).

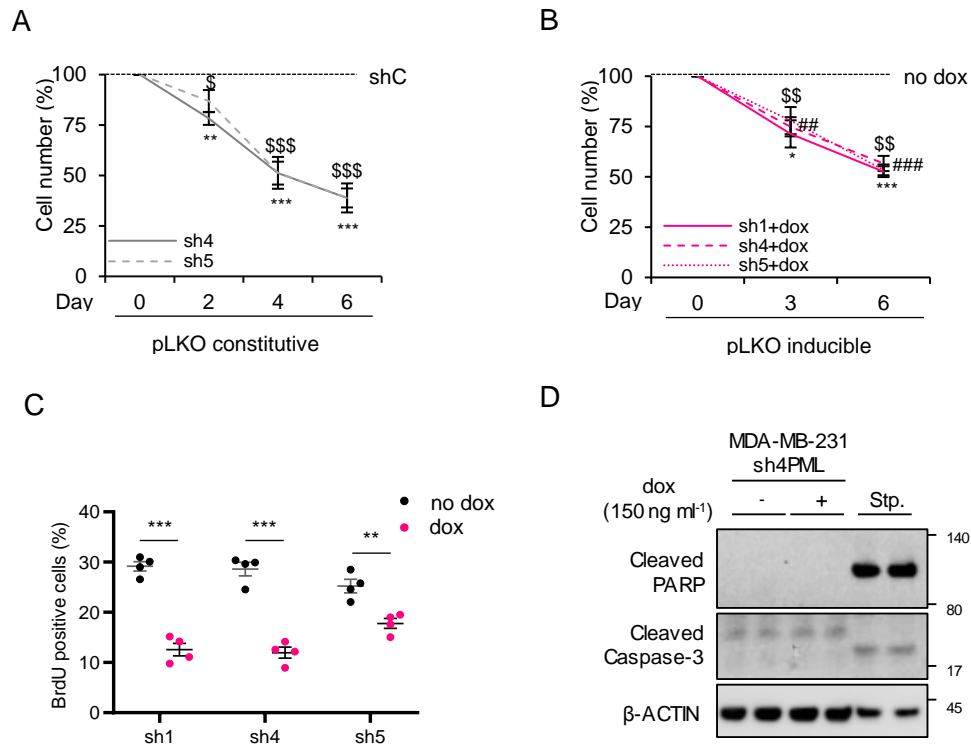


Figure R9. PML silencing decreases growth of MDA-MB-231 cell line. **A-B)** Impact of **A)** constitutive (n=12) and **B)** doxycycline-inducible (sh1 and sh5, n=4, sh4, n=7) PML silencing on cell number. **C)** Effect of inducible PML silencing in BrdU incorporation (n=4). **D)** Western Blot (representative of 3 experiments) of the effect of PML inducible silencing on apoptosis. Error bars represent s.e.m. p, p-value (*p<0.05, **p<0.01, ***p<0.001), for figure a and b (* sh4 vs shC or no dox; \$ sh5 vs shC or no dox; # sh1 vs no dox). One-tailed one sample t-test (a-b) and one-tailed Student's t-test (c) was used for cell line data analysis. shC: Scramble shRNA, sh1, sh4 and sh5: shRNA against PML, dox: doxycycline, Stp: staurosporine. Molecular weight markers (kDa) are shown on the right.

These results support our notion that PML is essential for the proliferation of TNBC cells and that its loss leads to a decrease in their ability to grow. Due to the classical definition of PML as a tumor suppressor, other functions may have been overlooked for many years in some tumors. In line with our observations, Liu *et al.*¹⁷² demonstrated that in ovarian cancers with high PML levels its silencing led to an inhibition of proliferation. These results open new questions about the anti- or pro-tumorigenic role of PML depending on the cancer context.

I.3.2 Effect of PML silencing on the activation of senescence *in vitro*

In vitro, cells that enter into senescence suffer morphological changes characterized by a larger shape, with a flatter or “fried egg-like” morphology and also appear commonly multinucleated and with more vacuoles^{195,196}. When we first observed the cells under the microscope, we could see a remarkable change in their cellular morphology. Both with the constitutive (**Fig. R10A**) and with the inducible PML silencing (**Fig. R10B**) the morphology of the cells resembled the senescence features described above.

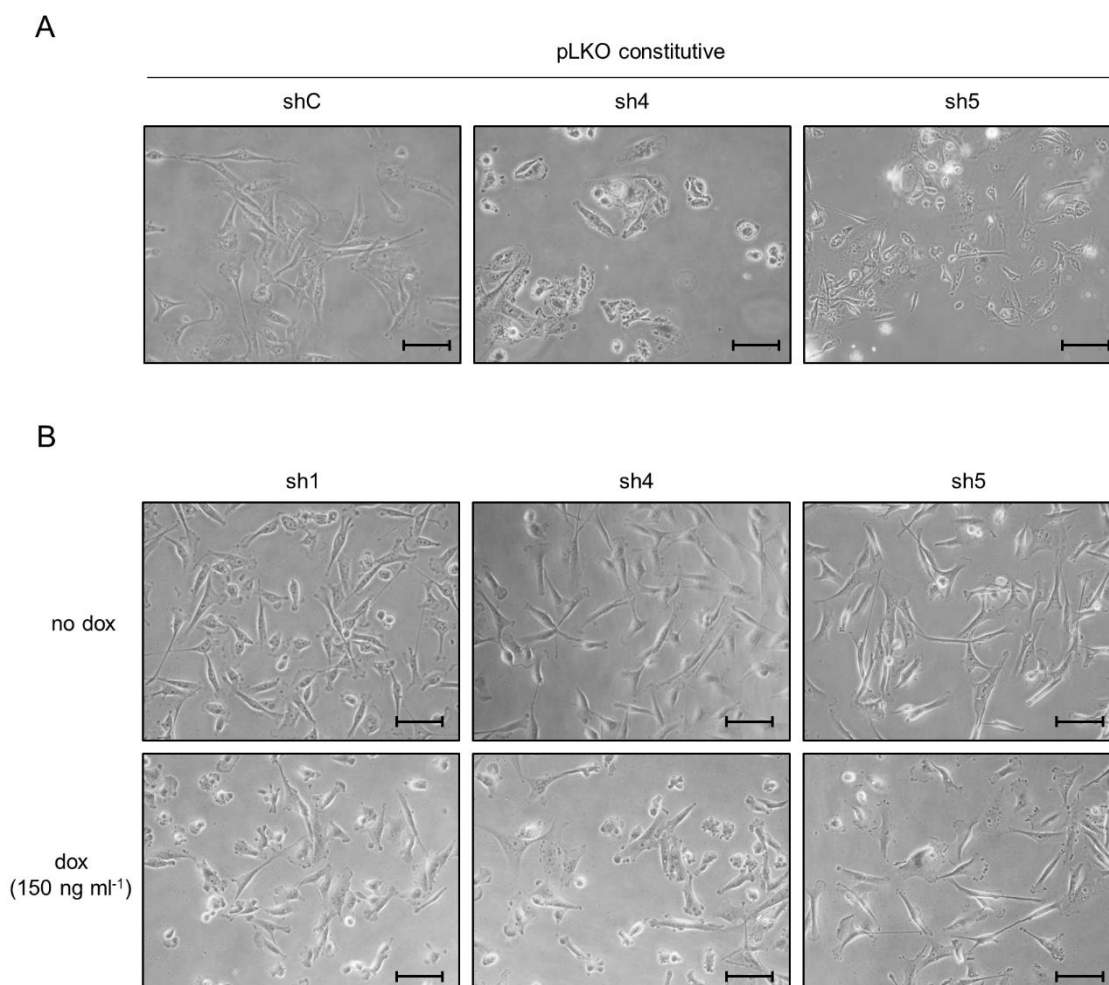


Figure R10. Effect of PML silencing in the morphology of MDA-MB-231 cells. Representative images of the morphological changes upon PML inhibition with **A)** constitutive and **B)** inducible shRNAs. Scale bar, 50 μm . sh1, sh4 and sh5: shRNA against PML, dox: doxycycline.

To further analyze these changes, we followed up by flow cytometry the alterations occurred to the cells with the inducible silencing of PML. Using the SSC and the FSC in FACS it is possible to acquire information about the complexity (i.e. granularity) and the size of the analyzed event, respectively. These are two of the main morphological features that change in senescent cells. One of the main advantages of the FACS analysis is that single cells can be analyzed separately, getting a more accurate measurement of the changes happening in the whole cell population. Cell populations were selected for each shRNA in no dox condition and compared dox conditions for increased size and granularity. Four different groups were identified as Q1, Q2, Q3 and Q4: the main population was assigned to Q4, cells with an increase in granularity were assigned to Q1, cells with an increase in both size and granularity to Q2 and cells with only an increase size to Q3. We confirmed that PML loss led to a change in the morphology of the cells characterized by an increase in the number of bigger and more complex cells (Q1+Q2+Q3) (**Fig. R11A** and **Fig. R11B**).

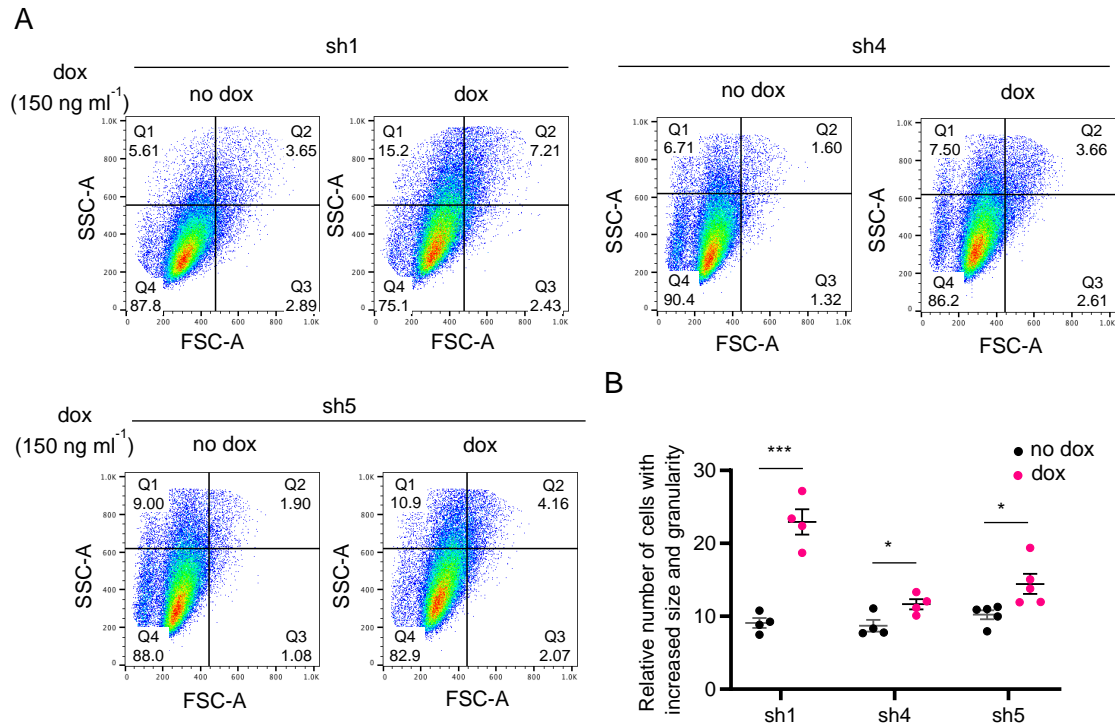


Figure R11. FACS analysis of the morphological changes of MDA-MB-231 cells upon PML loss. A) Schematic representation of one representative experiment of the defined populations represented in B upon PML inducible silencing. **B)** Effect of doxycycline-inducible PML silencing on cell size and granularity (sh1 and sh4, n=4, sh5, n=5). Error bars represent s.e.m. p, p-value (*p< 0.05, ***p< 0.001). One-tailed Student's t-test (a) was used for cell line data analysis. sh1, sh4 and sh5: shRNA against PML, Dox: doxycycline.

The detection of SA- β -gal has been used in a variety of biological situations, both *in vitro* and *in vivo*¹¹⁸, to detect senescent cells. It is considered as one of the few robust and consistent senescence markers. Nevertheless, the use of additional markers is recommended to overcome some technical limitations. On the one hand, a very confluent plate can give false positives *in vitro*, as cells will enter senescence independently of the oncogenic insult. On the other hand, the quantification of an enzymatic activity requires a correct manipulation of the samples.

β -galactosidase metabolizes X-Gal giving as a result a blue precipitate that can be detected and quantified. Interestingly, at pH 6 its activity will be specifically detected in senescent cells, but not in proliferating cells¹²⁷. As we could predict from the morphological changes observed, SA- β -gal staining levels increased upon PML silencing with all the shRNAs. The constitutive silencing of PML with the sh4 induced senescence in around the 20% of the cells (**Fig. R12A and R12B**), while with the inducible knockdown it was around the 12% (**Fig. R12C and R12D**). Nevertheless, the levels of senescence detected could not completely explain the decrease observed in growth. Thus, the implication of additional pathways that may be deregulated upon PML loss cannot be excluded.

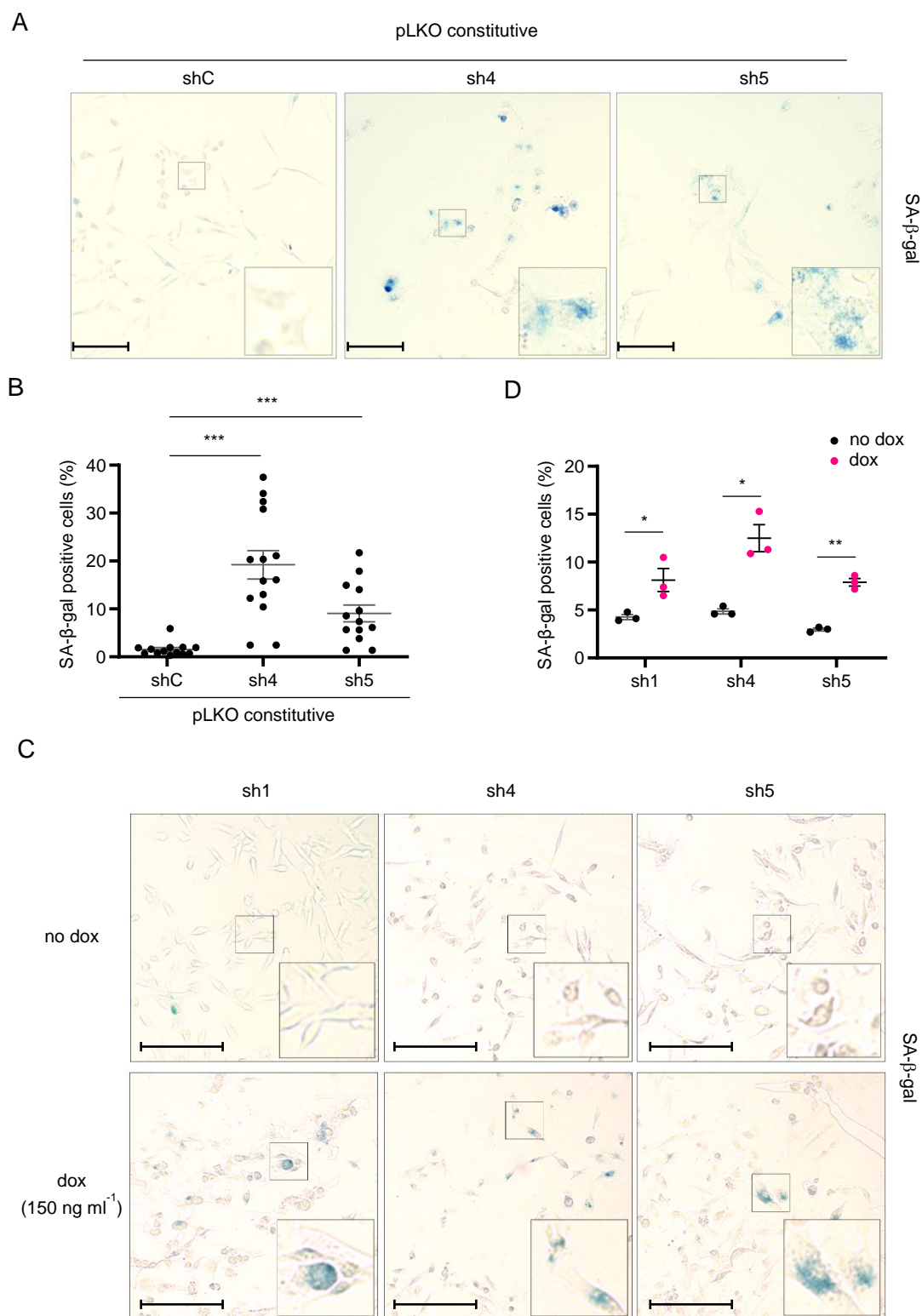


Figure R12. SA-β-gal staining increases after PML silencing. A-B) Effect of constitutive PML silencing (n=13) on the number of senescent cells (**A**, representative images of SA-β-Gal assay, scale bar 50 μm). **C-D)** Effect of inducible PML silencing (n=3) on the number of senescent cells (**C**, representative images of SA-β-Gal assay, scale bar 50 μm). Error bars represent s.e.m. p, p-value (*p< 0.05, **p< 0.01, ***p< 0.001). One tailed Student's t-test was used for cell line data analysis (b, d). sh1, sh4, and sh5: shRNA against PML, dox: doxycycline, SA-β-Gal: senescence associated beta-galactosidase.

To further characterize the senescence response, we analyzed other cellular and molecular markers that have been described as indicatives of senescence. Lamins (A, B1, B2 and C) are major structural proteins for the nuclear lamina and they help maintaining the nuclear architecture and integrity, controlling chromatin organization. It has been demonstrated that LAMIN B1 expression declines in senescence^{128,197}, in coherence with the morphological changes that occur in senescent cells. We checked the expression levels of LAMIN B1 upon PML inhibition and we observed a significant decrease in the protein levels (**Fig. R13A** and **R13B**). This data supports the results obtained with SA- β -Gal.

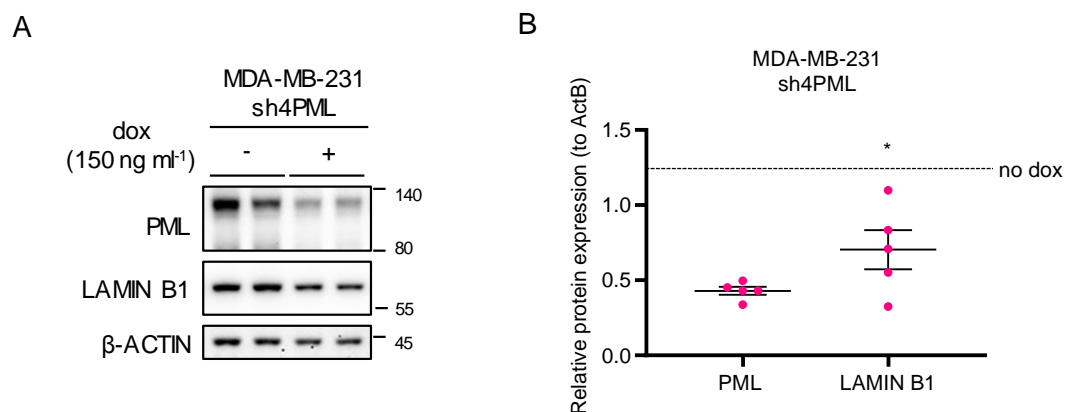


Figure R13. PML silencing affects nuclear lamina protein levels. A-B) Levels of Lamin B1 protein upon PML inducible silencing in MDA-MB-231 cells (**A**, representative of 5 experiments) and protein quantification (**B**, n=5). Error bars represent s.e.m. p, p-value (*p< 0.05). One-tailed one sample t-test (b) was used for cell line data analysis. dox: doxycycline. Molecular weight markers (kDa) are shown on the right.

PML has been depicted to act as a sensor for ROS, which act as drivers of OIS¹³⁰. PML loss has been described to both induce an increase¹⁹⁸ and a decrease¹⁹⁹ in ROS levels, depending on the context. When increased, Niwa-Kawakita et al.¹⁹⁸ described that senescence was induced. We excluded the possibility of ROS increase as a driver of senescence as PML loss did not induce its accumulation in MDA-MB-231 cells (**Fig. R14**).

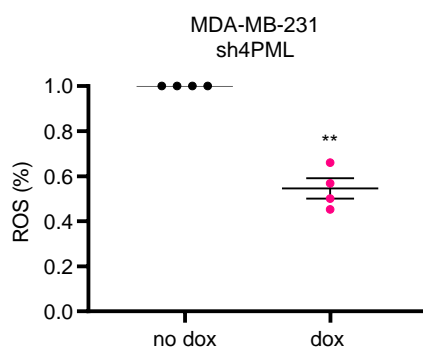


Figure R14. PML and ROS. Effect on ROS production (n=4) after inducible PML silencing in MDA-MB-231 cells. Error bars represent s.e.m. p, p-value (**p< 0.01). One-tailed one sample t-test was used for cell line data analysis. dox: doxycycline, ROS: reactive oxygen species.

SAHF are heterochromatin domains enriched in repressive marks. They contribute to the silencing of several proliferation related genes and are relatively specific of OIS²⁰⁰. They are enriched in several heterochromatin proteins that participate in SAHF formation or maintenance: lysine 9-trimethylated histone H3 (H3K9Me3), HIRA and ASF1 proteins, heterochromatin protein 1 (HP1), high-mobility group A (HMGA) proteins and pRB^{95,201}. It has also been described that SAHF are enriched in macroH2A proteins⁹⁵. Specifically, macroH2A1 variants are described to have an anti-proliferative function^{202,203}. Experimentally, SAHF can be recognized as punctate structures that can be detected by DAPI. Upon PML loss, we were not able to confirm the formation of SAHF neither by heterochromatin condensation neither with DAPI staining nor by macroH2A1.1 accumulation (**Fig. R15**), suggesting that SAHF are not essential in the senescence response upon PML loss.

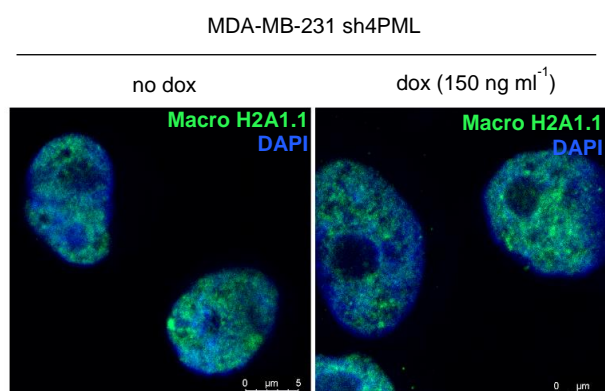


Figure R15. SAHF do not appear upon PML silencing. Immunofluorescence of macroH2A1.1 and DAPI upon inducible silencing of PML in MDA-MB-231 cells. dox: doxycycline, DAPI: 4',6-diamidino-2-phenylindole.

Upon senescence induction cells remain metabolically active^{115,204} and secrete a variety of factors that are defined as SASP. The canonical SASP has been described to be composed by soluble signaling factors (interleukins, chemokines and growth factors), secreted proteases and extracellular matrix components^{141,142}. We carried out a proteomic analysis to identify the differentially secreted factors upon PML silencing. First, protein expression was analyzed by western blot in both cells and secretome (**Fig. R16A**) to confirm the correct function of the shRNA and the absence of contamination on the secretome fraction. In the era of “omics”, principal component analysis (PCA) eases the interpretation of large data sets by capturing the most relevant information in few components. PCA analysis of the secretome confirmed the difference in the cells based on the perturbation of PML (**Fig. R16B**). The next step was to identify the proteins that were differentially expressed in the secretome of PML expressing and PML silenced cells. For this purpose, samples were clustered into “no dox” and “dox” conditions and proteins enriched upon PML silencing analyzed (**Fig. R16C** and **Annex Table 2**). Of notice, no canonical SASP could be identified but interestingly, proteins belonging to the TGF- β 1 pathway were enriched in the secretome of the cells upon PML silencing (**Fig. R16D**).

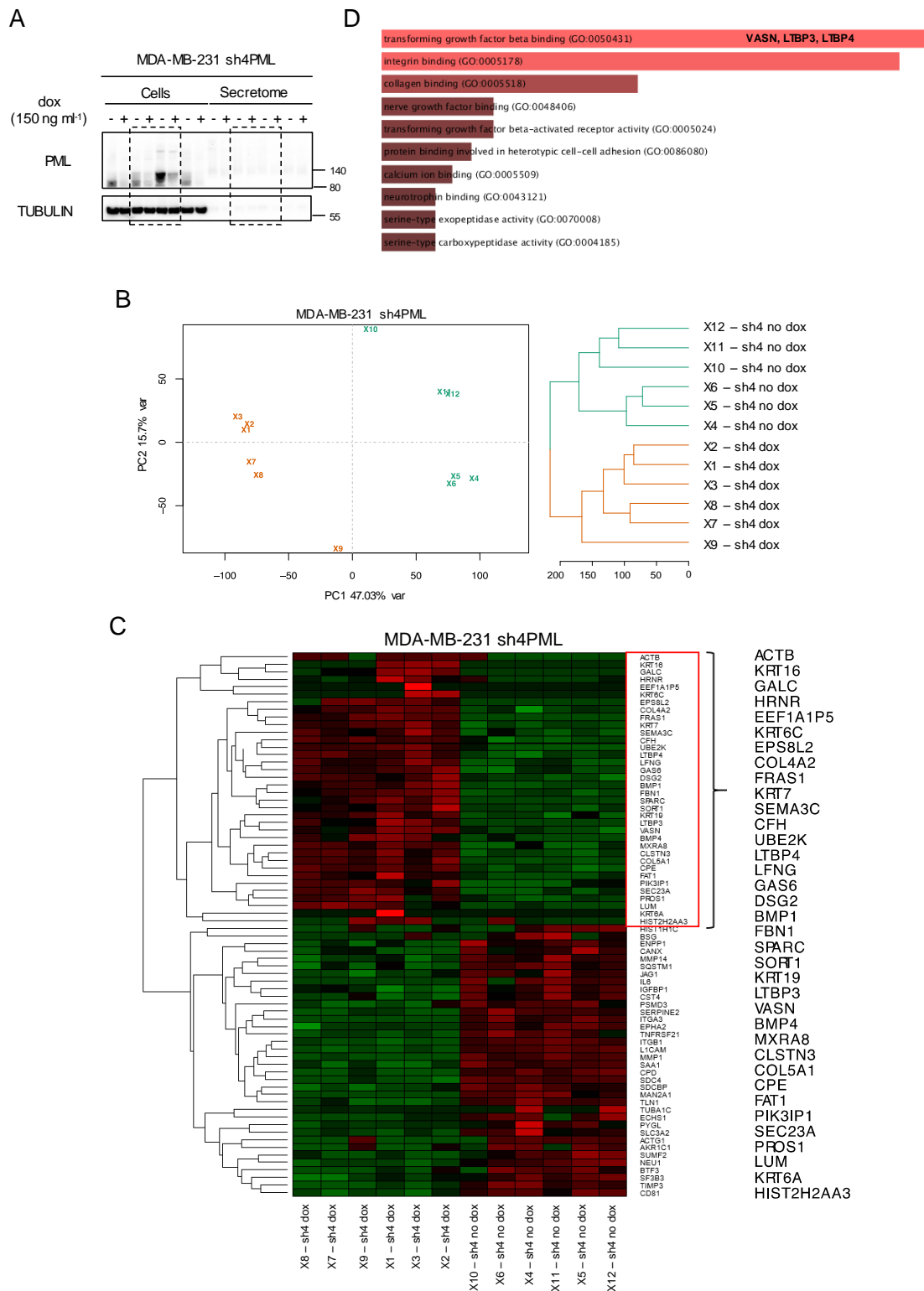


Figure R16. Proteomics analysis of the secretome of MDA-MB-231 cells upon PML inducible silencing. **A)** PML and tubulin levels in both cells extracts and secretome samples (dash lines indicate samples used in the analysis). **B)** Unsupervised exploratory data analysis by means of principal component analysis. **C)** Heat maps representing the proteins that were significantly over- and under-secreted upon PML silencing in MDA-MB-231 cells. Data analysis was based on spectral count data after exporting it from Scaffold software into R. The GLM model based on the Poisson distribution was used to test significance. Only the proteins with spectral counts of 2, Log₂FC of 0.8 and adjusted p-value of 0.05 are present in the heatmap. Columns represent samples; rows are proteins. Red represents proteins that are over-secreted and green represents proteins that are under-secreted. The data rows are centered and scaled to 1 standard deviation prior to produce the heatmap. Dox: doxycycline.

Different studies showed that PML plays a role in senescence induction through p53^{70,90}. Here we describe how the loss of PML triggers a senescence response characterized by an increase in SA- β -gal activity and the decrease of the levels of the nuclear lamina protein LAMIN B1, two well described hallmarks of senescence. In our senescence phenotype no formation of SAHF was detected. This observation is not surprising as this feature has been associated preferentially with OIS. Finally, the analysis of the secretome of the differentially expressed proteins after PML silencing described a non-canonical SASP induction, enriched with proteins of TGF- β 1 pathway. In fact, senescence without signs of inflammatory SASP has also been characterized²⁰⁵, supporting the idea that SASP may be cellular context or senescence type dependent. This should be further studied to decipher the role that these secreted factors are playing in the context of PML silencing. Altogether, we have characterized the senescence phenotype that is activated upon PML loss in TNBC.

I.3.3 Effect of PML silencing in tumor growth and senescence *in vivo*

We have previously described that PML controls the properties of cancer initiating cells, such as tumor initiation and recurrence in aggressive BCa through the modulation of SOX9¹⁰¹. To demonstrate its effect *in vivo*, two different approaches were performed: limiting dilution assays to study how PML knockdown affects breast tumor initiation and tail vein injections to show how PML loss has an impact on the establishment of the metastasis.

Here, we found that PML silencing results in the activation of senescence *in vitro*. With all the data in mind, we hypothesized that PML perturbation would have a growth suppressive activity in the bulk of the tumor cells *in vivo*. For this purpose, MDA-MB-231 cells with the inducible shRNA #4 against PML were injected in the flank of immunocompromised mice. Once tumors were established (reaching a volume of 25-130 mm³), mice were randomly separated into two different groups and doxycycline was administered in the diet in one of the groups to induce PML knockdown. In accordance with the results observed *in vitro*, PML silencing (**Fig. R17A**) led to a decrease in tumor growth by means of volume (**Fig. R17B**) and growth rate (**Fig. R17C**) measured by the slopes of each individual tumor. The rate was inferred from the linear regression calculated for the progressive change in tumor volume of each individual tumor during the period depicted in **Fig. R17B**. Tumor weight was also remarkably decreased upon PML silencing (**Fig. R17D**).

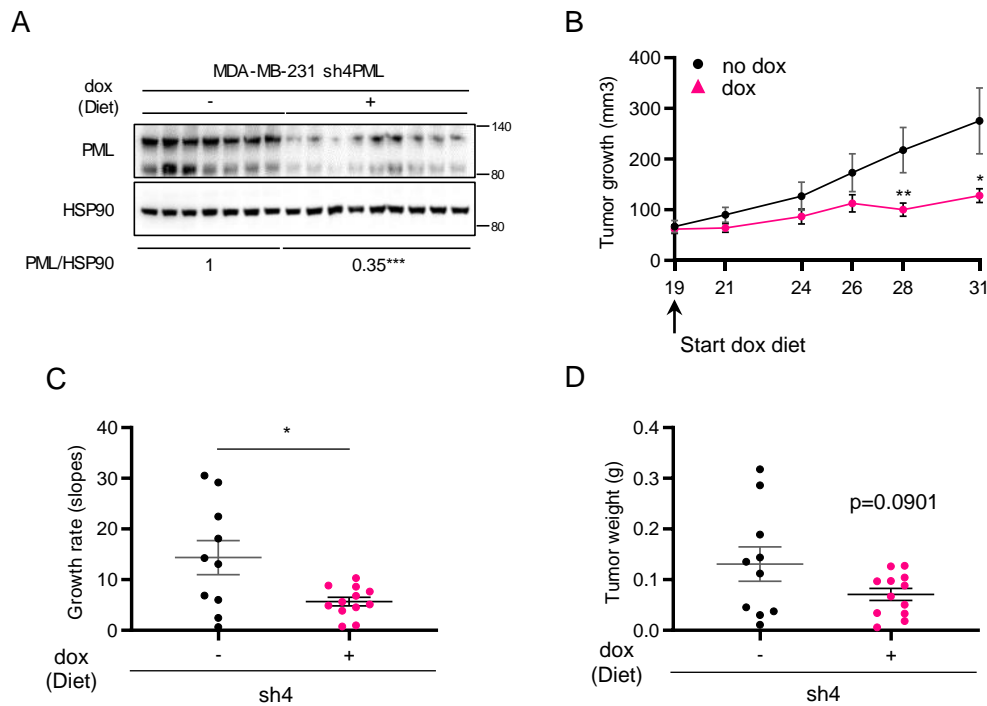


Figure R17. Tumor growth of MDA-MB-231 xenografts is curbed upon PML loss *in vivo*. **A)** PML protein expression of MDA-MB-231 xenografts with inducible sh4PML. **B-D)** Effect of PML silencing on tumor growth (sh4 no dox, n=10; sh4 dox, n=12) represented as: **B)** the volume of the tumors from doxycycline addition until day 31 of the experiment, **C)** the growth rate of each tumor and **D)** weight of the individual tumors. Error bars represent s.e.m. p, p-value (*p < 0.05, **p < 0.01). One-tailed Mann–Whitney U-test was used for xenografts (b-d). dox: doxycycline. Molecular weight markers (kDa) are shown on the right.

For the quantification of senescence *in vivo*, samples were stained against phospho-heterochromatin protein-1 gamma (p-HP1 γ), a marker that has been widely used in this context^{95,206-209}. *In vivo*, p-HP1 γ staining increased upon the activation of the shRNA against PML, indicative of the induction of senescence (**Fig. R18A** and **Fig.R18B**).

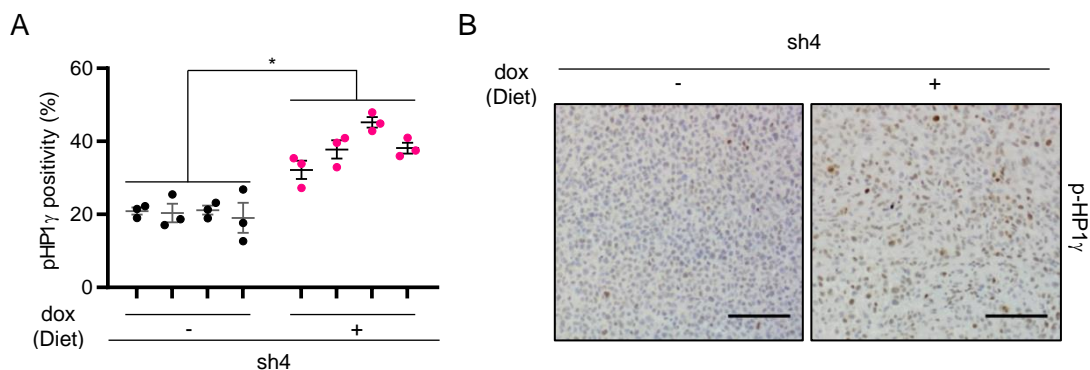


Figure R18. Analysis of p-HP1 γ levels *in vivo*. **A-B)** Analysis of senescence by means of p-HP1 γ staining in PML silenced xenografts (sh4 no dox, n=4; sh4 dox, n=4) (**B**, representative images of p-HP1 γ positive cells, scale bar 100 μ m). Error bars represent s.e.m. p, p-value (*p < 0.05). One-tailed Mann–Whitney U-test was used for xenografts (a). dox: doxycycline, p-HP1 γ : phospho-heterochromatin protein-1 gamma.

To further analyze the consequences of PML silencing in tumor growth *in vivo*, we performed a chicken CAM assay. The chick embryo model allows the study of the different stages of cancer development^{210,211}. At early stages of the development, the chick embryo is immunodeficient, sustaining the growth of grafted cells²¹². Cells are inoculated in the CAM, which allows primary tumor formation that will be surrounded by blood vessels. Cells were pre-induced for 3 days before inoculation and doxycycline added every day once the cells are inoculated. After 5 days of growth, we confirmed that cells with silenced PML grew less by means of weight of the primary tumor (**Fig. R19**).

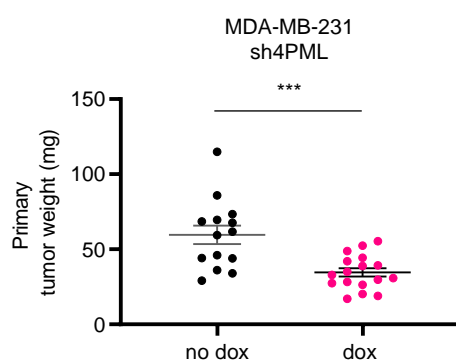


Figure R19. Primary tumor growth of MDA-MB-231 is decreased upon PML loss in CAM model. A) Primary tumor weight of MDA-MB-231 cells inoculated in the CAM upon PML inhibition (sh4 no dox, n=14; sh4 dox, n=17). Error bars represent s.e.m. p, p-value (***)p< 0.001). One-tailed Mann–Whitney U-test was used. dox: doxycycline.

SUMMARY

- PML is overexpressed in TNBC/basal tumors.
- Senescence is an antitumorigenic consequence of PML inhibition.
- PML silencing in TNBC leads to a senescence response characterized *in vitro* by an increase in SA-β-gal activity and decreased LAMIN B1 levels, without a canonical SASP or SAHF formation.
- The effect of PML silencing is recapitulated *in vivo*, with the reduction in tumor growth and the increase in senescence confirmed by an increment of p-HP1γ staining.

FUTURE PERSPECTIVES

- Develop a CRISPR/Cas9 inducible system to decipher the effect of PML knockout. This system would allow to address how the complete depletion of PML affects TNBC cells compared to the partial loss obtained with shRNAs.
- Evaluate the contribution of PML loss induced SASP to the cellular phenotype, focusing on the distinctly expressed proteins in PML silenced cells.
- The use of PDX and patient samples to further study the role of PML. Confirming the senescence phenotype in models closer to a real scenario would add clinical value to the results obtained in this study.

II Elucidation of the molecular mechanism underlying the antiproliferative effect upon PML silencing

The data obtained in the section I of the results describes how PML sustains growth in TNBC and its silencing leads to a senescence response. The second aim of this thesis was to elucidate the signaling pathways that were responsible of driving the senescence response induced after PML loss.

HYPOTHESIS

PML controls a growth-sustaining signalling program that is impaired upon its loss in PML addicted cells

II.1 Analysis of PML loss-induced molecular signaling changes

II.1.1 Deciphering the molecular driver of the senescence phenotype

Senescence can be induced by different stimuli that through common effectors will drive this response. This occurs predominantly through p53-p21 and/or p16-Rb axes²¹³, and to a lesser extent through inhibitors such as p27 that has also been described to drive senescence^{106,140,208}. The regulation of cyclins, CDKs and CDKIs is of utmost importance for the progression of cell cycle.

MDA-MB-231 cell line has p53 mutated and it is null for p16²¹⁴, two effectors on the main senescence driving pathways. Therefore, we evaluated the levels of p21 and p27 protein after PML inhibition in our TNBC cell line. We observed a significant increase of p27 with all the shRNAs generated against PML, both *in vitro* (**Fig. R20A and Fig. R20B**) and *in vivo* (**Fig. R20C**). Conversely, p21 levels were not affected upon PML silencing (**Fig. R20D**).

p27 has been described to be deregulated in different types of cancer, such as lung²¹⁵, prostate²¹⁶, ovarian²¹⁷ and breast cancer²¹⁸. In epithelial cancers, p27 has been correlated with poorly differentiated and high-grade tumors. In BCa, its prognostic potential has been widely studied with distinct results. The first studies²¹⁸⁻²²⁰ identified p27 as a prognostic marker but some discrepancies appeared with subsequent analysis. They failed to assess its prognostic significance but confirmed that low p27 levels are correlated with higher tumor grade and ER negative status^{221,222}. Regarding its status on BCa subtypes, decreased p27 immunoreactivity has been both correlated with HER2 overexpression²²³ and with TNBC²²⁴. Interestingly, it has been demonstrated that targeting different molecules involved in tumorigenesis impairs cell growth by increasing p27 levels in TNBC^{225,226}. All these studies support the notion that p27 plays an important role in BCa and it encouraged us to further study p27 function in PML loss induced senescence.

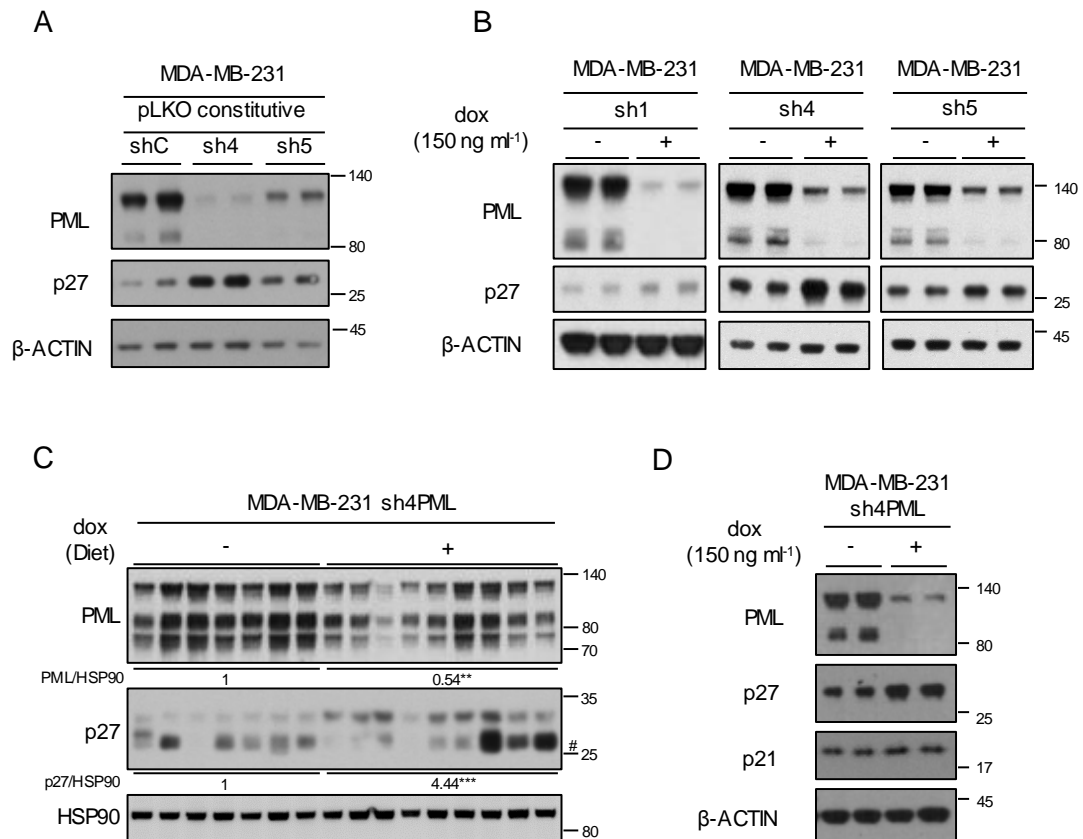


Figure R20. PML silencing increases p27 levels. **A-B)** Western Blot (representative of at least 3 experiments) showing the effect on PML and p27 expression after **A)** constitutive and **B)** doxycycline-inducible PML silencing. **C)** Impact of doxycycline-inducible PML silencing (sh4) on p27 and PML protein expression on established MDA-MB-231 xenografts. **D)** Western Blot (representative of at least 3 experiments) showing the effect on PML, p27 and p21 expression after doxycycline-inducible PML silencing. Error bars represent s.e.m. p, p-value (**p < 0.01, ***p < 0.001). shC: Scramble shRNA, sh1, sh4 and sh5: shRNA against PML, dox: doxycycline. #: Unspecific band. Molecular weight markers (kDa) are shown to the right.

A previous doxycycline titration allowed us to set the best concentration needed for a chronic silencing in which PML levels progressively decrease during the days of induction. Each shRNA targets a different sequence and they will have a different silencing efficiency. We aimed at clarifying how PML silencing dynamics affected the levels of p27 along the time to further understand the senescence response. For this purpose, PML and p27 protein levels were monitored for 6 consecutive days. Surprisingly, we observed that after 2 days of doxycycline induction, together with PML reduction, p27 levels started to increase. The sh1PML had a robust effect on PML levels at early time points (**Fig. R21A** and **R21B**) and p27 reached the highest protein levels at day 5 in sh4PML (**Fig. R21C** and **R21D**), followed by sh5PML (**Fig. R21E** and **R21F**). Despite the differences in the silencing dynamics, the phenotype was recapitulated with all the shRNAs. Working with a complex protein like PML implies that many processes and molecules work cooperatively for the correct assembly and function of the PML nuclear bodies⁶³. Understanding how the silencing dynamics can differentially affect their behavior could give insights that could be useful for the development or identification of new compounds that target PML.

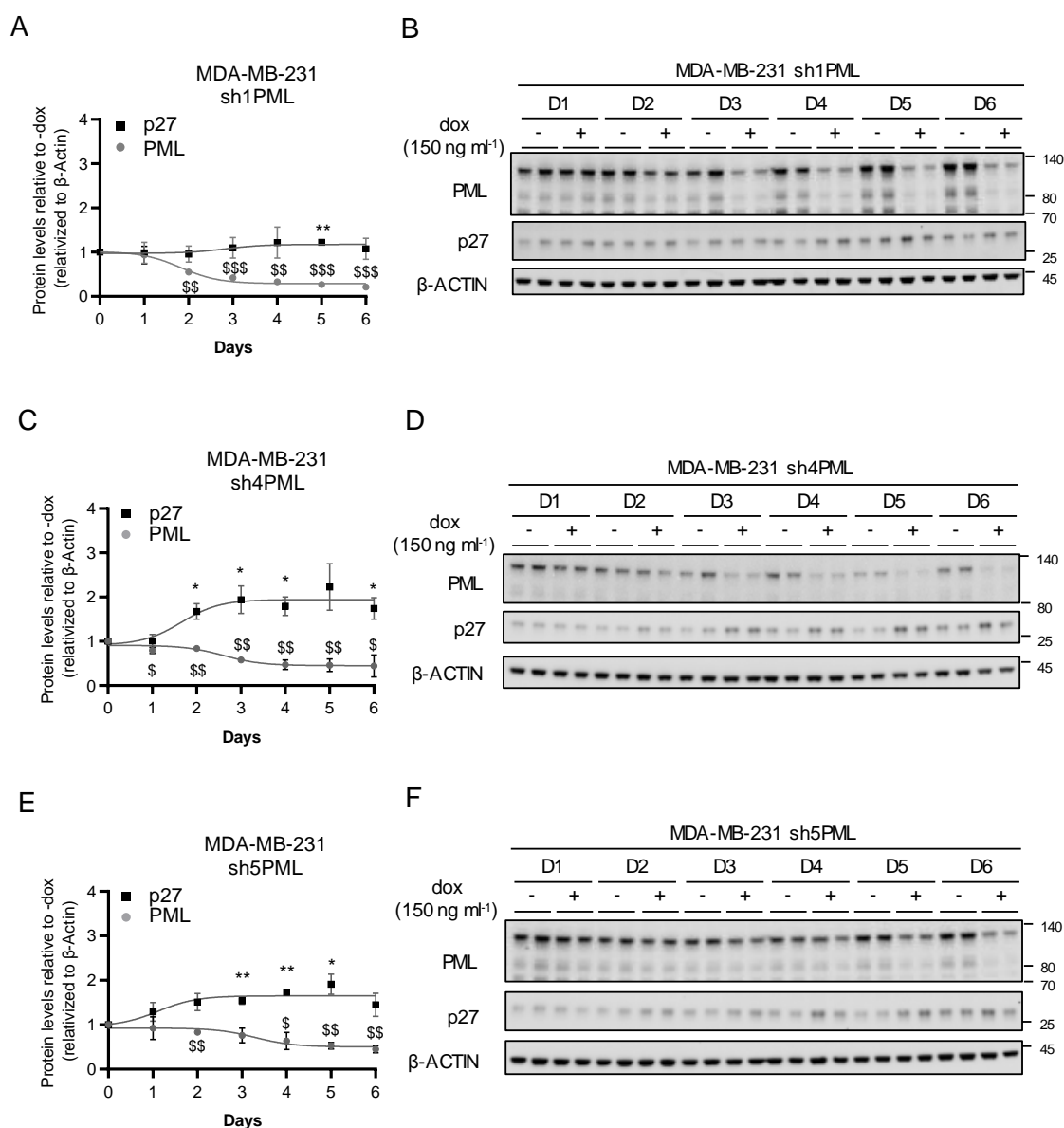


Figure R21. p27 levels start to increase 2 days after doxycycline addition. A-F) Quantification of p27 and PML protein levels along 6 days of doxycycline-inducible PML silencing on MDA-MB-231 cells with **A)** sh1 (**B**, representative western blot, n=3), **C)** sh4 (**D**, representative western blot, n=3) and **E)** sh5 (**F**, representative western blot, n=3). Error bars represent s.e.m. p, p value (*/\$p < 0.05, **/\$\$p < 0.01, ***/\$\$\$p < 0.001). One-tailed one sample t-test (a, c, e) was used for cell line data analysis. dox: doxycycline. Molecular weight markers (kDa) are shown to the right.

p27 is rarely mutated in human cancers, but rather it appears to be deregulated at transcriptional and post-translational levels, along with changes in its compartmentalization within the cell. Our data demonstrates that PML knockdown increases p27 levels so we hypothesized that p27 was being accumulated in the nucleus inhibiting cell growth upon PML inhibition. We quantified the nuclear p27 positivity and PML levels in single cells by immunofluorescence. Our first analysis was performed in a pooled culture, which does not take into account the heterogeneity of the whole

population. The analysis of single cells allows the identification of functions and patterns that would not be otherwise uncovered.

We confirmed that p27 was being accumulated in the nucleus of the cells from the PML silenced conditions (**Fig. R22A** and **Fig.R22E, bottom left**). Different phosphorylation sites have been identified to be key in the regulation of p27^{227,228}. Some of them affect the nuclear localization of the protein or its degradation in the same compartment. It was described that in some BCa, when phosphorylated by Akt/PKB in the threonine 157, p27 is excluded from the nucleus providing the tumor an advantage to grow²²⁹⁻²³¹. Another study in TNBC²³² analyzed the status of three additional phosphorylation sites to decipher the mechanism through which p27 was being accumulated in the nucleus. It would be interesting to further characterize how PML silencing affects the phosphorylation levels of p27. This would help identifying if additional molecules are responsible of this modification, thus deepening in the PML dependent p27 regulation in TNBC.

We further investigated the correlation between the nuclear p27 positive cells and PML levels. For the quantification, we established an immunofluorescence score based on previous studies^{100,101} (PML low= 0-4 dots; PML high= more than 4 dots per cell nucleus). As expected, we observed an inverse correlation between PML levels and p27 nuclear staining (**Fig. R22B, R22C** and **R22D**; representative image in **Fig. R22E**).

pRB plays critical roles in many cellular contexts, both in physiological and oncogenic situations. It is a master regulator of cell cycle, where it acts through its interaction with the E2F family of transcription factors (**Fig. R23A**). CKDIs, such as p27, inhibit cyclin-CDK complexes allowing the binding of pRB to E2F factors. This results in the blockade of E2F transcriptional program and cell cycle progression. When p27 levels decrease, p27 can no longer inhibit cyclin-CDK complexes and pRB is hyperphosphorylated by CDKs, inactivating pRb activity and promoting G1/S entry by E2F factors. To further characterize the growth inhibitory response, we studied how the increase in p27 levels affects the regulation of cell cycle. We first observed that the phosphorylation levels of pRB were decreased upon PML silencing (**Fig. R23B**). The CKDIs from Kip/Cip family, to which p27 belongs, have the capacity to bind and inhibit various CDKs, although they seem to bind to CDK2 with a higher affinity than other CDKs. The expression of several genes implicated in cell cycle regulation was validated by RT-Q-PCR upon PML silencing (**Fig. R23C**). We observed that p27 was not only being upregulated at protein level, but also at gene expression level. *E2F3* was significantly downregulated upon *PML* silencing, together with *CDK2* and to a lesser extent, *CDK4*. Aurora kinase A (*AURKA*) is a kinase important for processes involved in mitosis and has been described to be regulated by p27^{233,234}. Cell division cycle 25 homolog A (*CDC25A*) is a phosphatase that can dephosphorylate CDKs and thus control cell cycle progression²³⁵. Both *AURKA* and *CDC25A* are downregulated upon PML silencing.

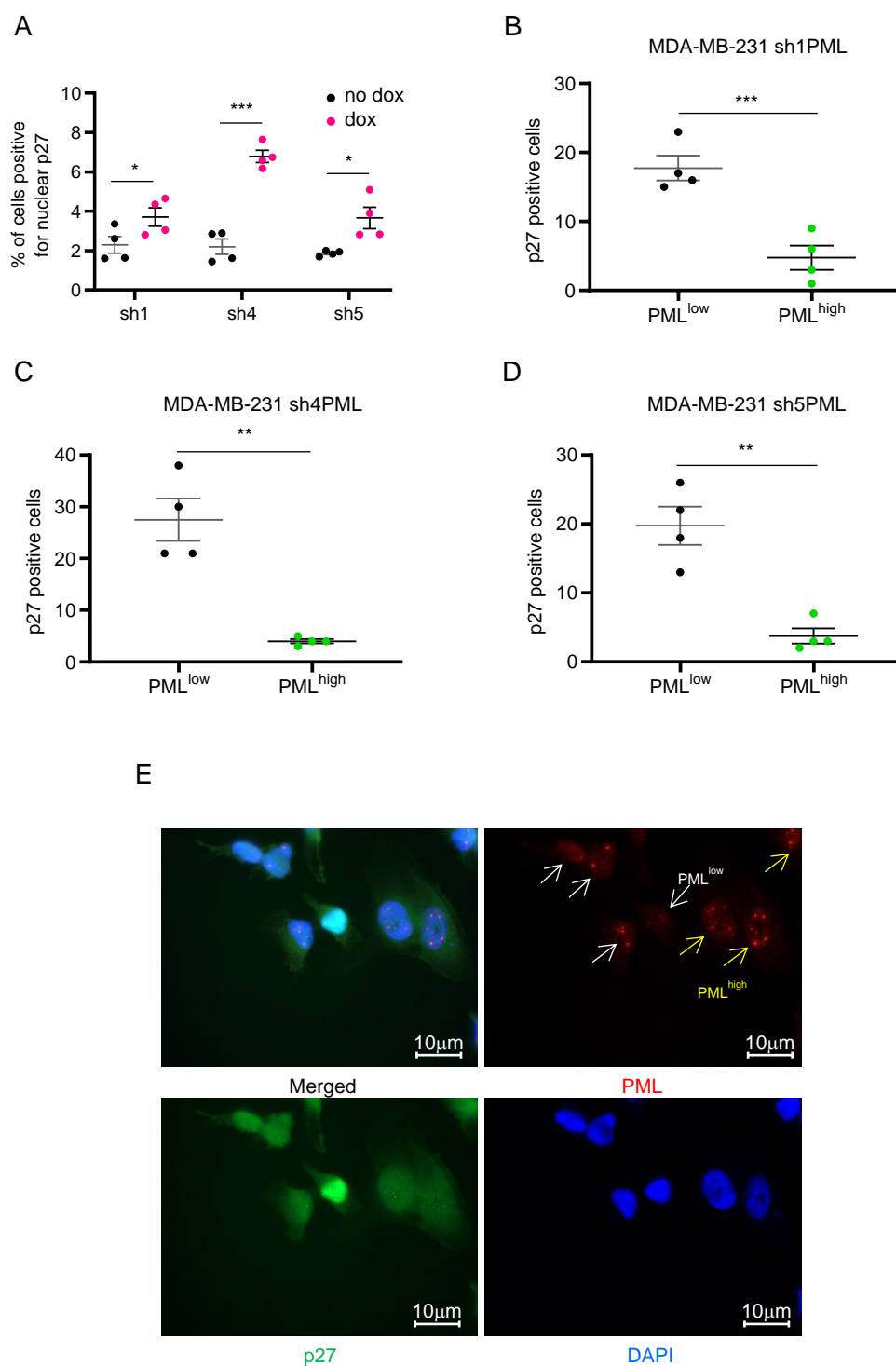


Figure R22. p27 is accumulated in the nucleus upon PML loss. **A)** Immunofluorescence quantification of nuclear p27 positive cells upon PML inducible silencing on MDA-MB-231 cells (n=4). **B-D)** Immunofluorescence quantification of the correlation of p27 positive cells and PML levels (**B**: sh1, **C**: sh4 and **D**: sh5). **E)** Representative images of p27 and PML staining upon doxycycline-inducible PML silencing in MDA-MB-231 cells. Error bars represent s.e.m. p, p value (*p < 0.05, **p < 0.01, ***p < 0.001). One-tailed Student's t-test was used for cell line data analysis (b-d). dox: doxycycline.

Altogether, our results demonstrate that PML silencing and subsequent increase in both p27 protein and mRNA levels lead to a global deregulation in cell cycle.

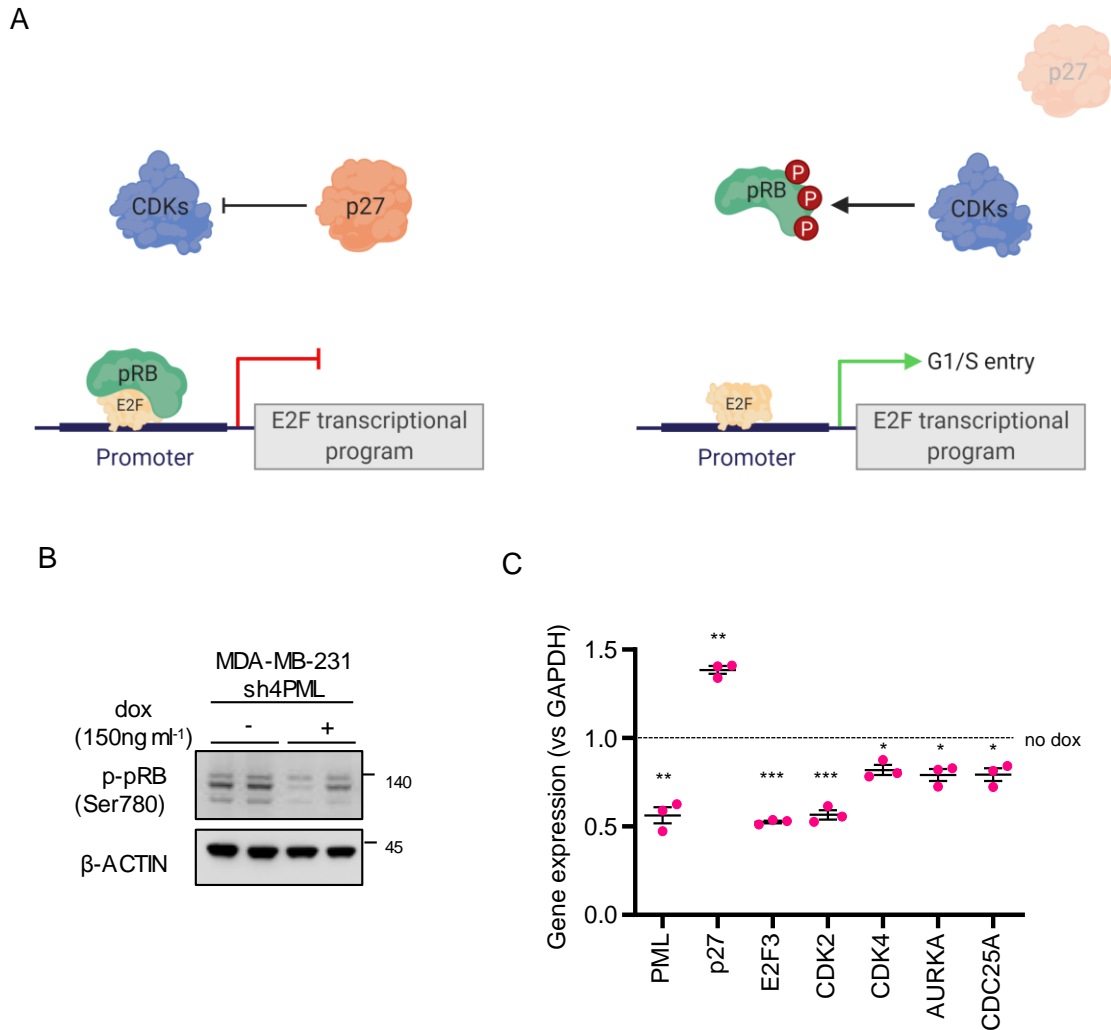


Figure R23. The increase of p27 levels deregulates cell cycle. **A)** Schematic representation of the p27-pRB protein interaction and regulation. **B)** Effect of doxycycline-inducible PML silencing on pRB phosphorylation (Ser780) (representative of 3 experiments) on MDA-MB-231 cells. **C)** Expression of p27-related cell cycle genes upon PML inducible silencing in MDA-MB-231 cells (n=3). Error bars represent s.e.m. p, p value (*p< 0.05, **p< 0.01, ***p< 0.001). One-tailed one sample t-test (c) was used for cell line data analysis. pRB: retinoblastoma protein, CDK: cyclin dependent kinases, AURKA: aurora kinase A, CDC25: cell division cycle 25 homolog A, dox: doxycycline. Molecular weight markers (kDa) are shown to the right.

The role of PML nuclear bodies in senescence has been extensively studied. Due to the function of pRB and E2F in cell proliferation their implication in senescence has also been of great interest. The classical tumor suppressor role of PML led to the study of how its overexpression induced a senescence response^{70,90,236,237}. Interestingly, many of the molecular changes associated to the senescence response are reproduced upon PML silencing in BCa as we have seen in this thesis work. Thus, it is not surprising that both PML overexpression and silencing repress the

transcription of E2F target genes^{238,239}. Vernier and colleagues²³⁹ described how during senescence pRB and E2F factors are recruited into PML-NBs to control E2F activity. We cannot discern whether the increase of p27 is the main driver of the cell cycle deregulation through the inhibition of CDK function or if PML and PML-NB biogenesis may also play a direct role in the silencing of E2F target genes, enhancing the action of p27 levels on cell cycle regulation. Therefore, deciphering the interactions of PML with different regulatory elements would help to further characterize its cellular context-dependent behavior and facilitate the design of strategies for a successful targeting of PML.

To determine the causal relationship between p27 accumulation and senescence induction upon PML silencing we performed a rescue experiment. The design of the rescue experiments is an improvement regarding specificity and reduction of off-target effects. For this purpose, we silenced p27 concomitantly with PML using both constitutive (**Fig. R24A** and **R24B**) and inducible (**Fig. R24C**, **R24D** and **R24E**) systems. We used two different p27 shRNAs, each of them with a different p27 silencing potency (**Fig. R24A**, lanes 7-9 and lanes 13-15; **Fig.R24E**, lanes 9-12), allowing us to study the rescue of the senescence phenotype with different p27 protein levels. When silencing PML and p27 together (**Fig. R24A**, lanes 10-12 and 16-18; **Fig.R24E**, lanes 21-24), we observed that decreased p27 levels prevented senescence in a dose-dependent manner (**Fig. R24B** and **R24D**). The sh1p27 slightly decreased p27 protein, while the sh2p27 totally prevented its accumulation, showing final p27 levels comparable to the expression of the control samples. This was reflected in the number of senescent cells of the double silencing samples, with senescence levels comparable between control conditions and the ones with the double silencing.

Surprisingly, when we analyzed the growth capacity of the cells in the rescue experiment, we observed that cells with the double silencing were not able to resume their growth levels to the non-silenced ones, neither with the constitutive (**Fig. R25A**) nor the inducible (**Fig. R25B**) shRNA systems. Strikingly, the silencing of p27 alone already had an effect on the growth of the cells that was firstly observed by changes in the morphology of the cells.

Altogether, these results prove that PML inhibition induces a senescence response that is mediated by an increase in p27 levels. We confirmed that p27 increase and senescence induction were a direct consequence of PML silencing by checking the lower PML expression of p27 positive individual cells. This was accompanied by a global deregulation of the cell cycle. The rescue experiment confirmed the causal contribution of PML silencing to p27 increase and to the induction of the senescence response.

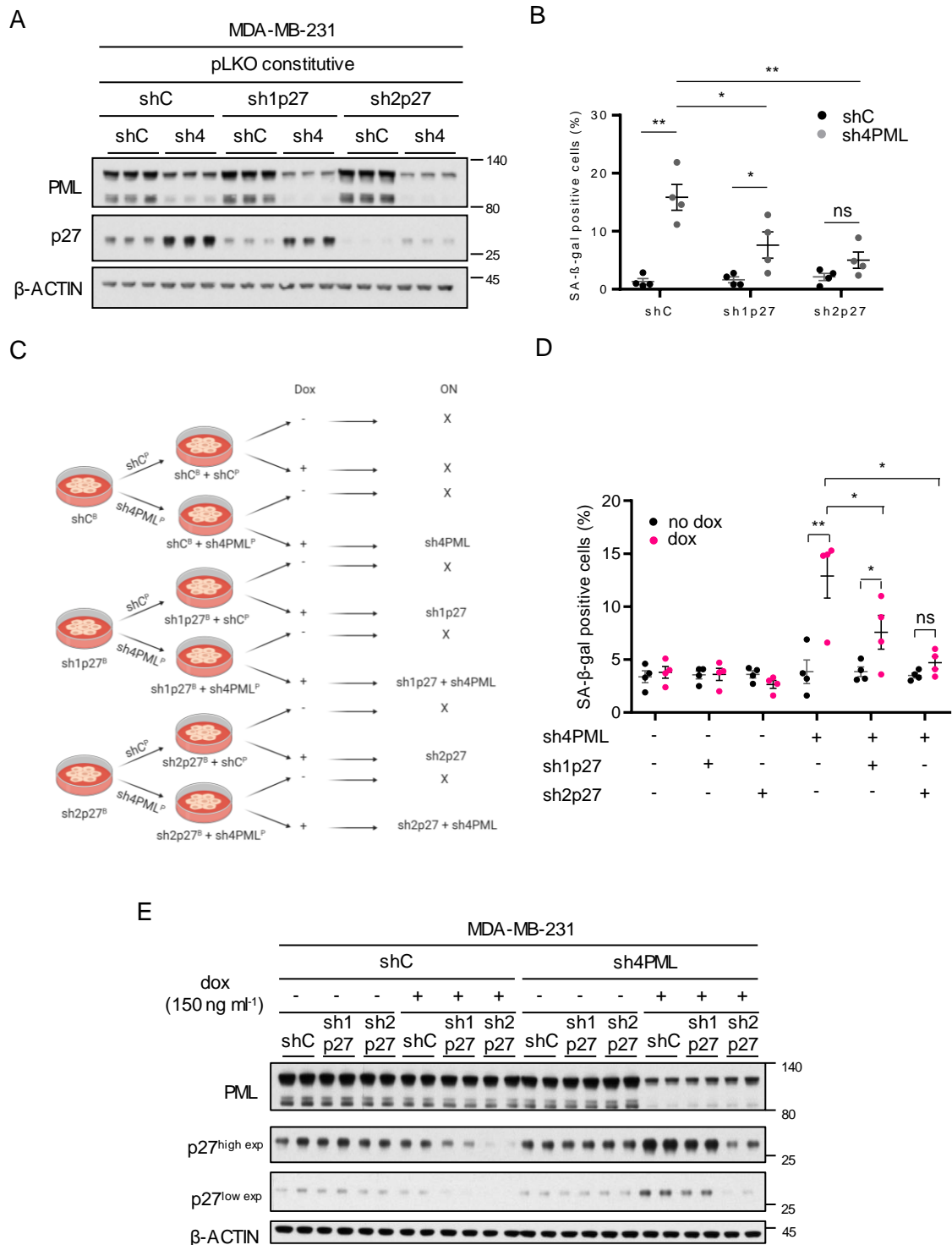


Figure R24. Double silencing of PML and p27 rescues the senescence phenotype. **A)** p27 and PML protein levels after constitutive silencing of either p27 or PML or both (representative of 4 experiments). **B)** Effect on the number of senescent cells (n=4) after constitutive p27 and/or PML silencing. **C)** Experimental design for inducible p27 silencing (sh1p27 and sh2p27, B: blasticidin selection) alone or in combination with inducible PML silencing (sh4, P: puromycin selection). **D)** Effect on the number of senescent cells (n=4) upon p27 and/or PML inducible silencing. **E)** p27 and PML protein levels upon doxycycline inducible silencing of either p27 or PML or both (representative of 3 experiments). Error bars represent s.e.m. p, p-value (*p< 0.05, **p< 0.01). One-tailed Student's t-test (b, d) was used for cell line data analysis. shC: Scramble shRNA, dox: doxycycline, SA- β -gal: Senescence-associated beta-galactosidase. Molecular weight markers (kDa) are shown to the right.

Although senescence is a major driver of the growth arrest, the levels obtained in cell number were not comparable to the amount of SA- β -Gal positivity obtained upon PML silencing (**Fig. R9A** and **Fig. R9B** compared with **Fig. R12B** and **Fig. R12D**, respectively). This is an important characteristic of the phenotype observed upon PML silencing, as it may imply that PML is regulating additional signaling pathways which deregulation leads to a defect in growth of the cancer cells.

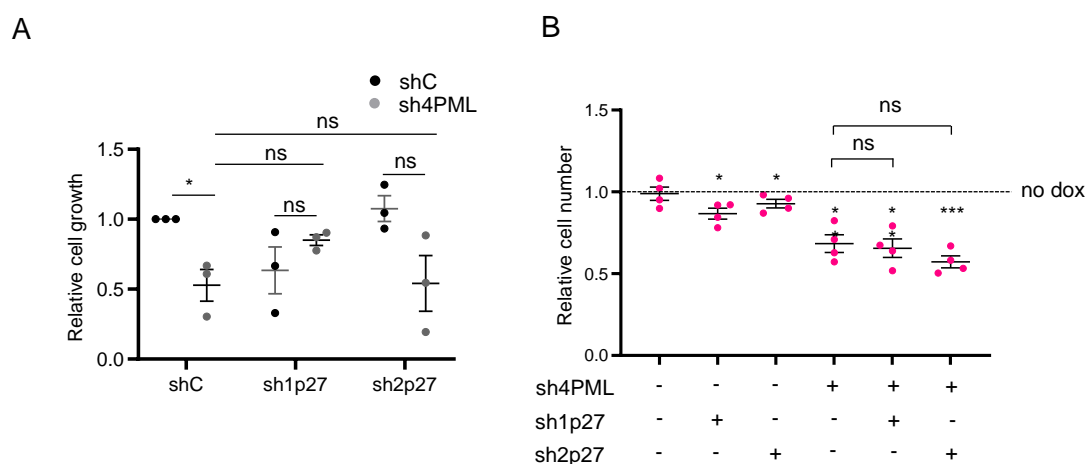


Figure R25. Cell growth is not rescued upon PML and p27 silencing. A) Effect on the relative cell number ($n = 3$) upon p27 and/or PML constitutive silencing in MDA-MB-231 cells. **B)** Effect on the relative cell number ($n = 4$) upon p27 and/or PML inducible silencing in MDA-MB-231 cells. Error bars represent s.e.m. p, p-value ($*p < 0.05$, $***p < 0.001$, ns: not significant). One-tailed one-sample t-test (a, b) was used for cell line data analysis. shC: scramble shRNA, dox: doxycycline.

II.1.2 Effect of PML loss on a large growth-sustaining signaling program

Not being able to rescue the growth arrest after blunting senescence made us wonder if additional mechanisms were involved in the PML loss induced phenotype. We hypothesized that PML should be governing a larger growth-regulatory program that induces growth arrest, p27 increase and senescence upon its loss.

In BCa, c-MYC is associated with more aggressive tumors and with a poorer prognosis. Remarkably, c-MYC is specifically overexpressed in basal-like subtype^{44,45} and confers resistance to therapies^{240,241}. Previous studies have demonstrated how PML provides an advantage to BCa cells by promoting FAO under stress conditions. Interestingly, two different studies^{242,243} have shown that targeting FAO in c-MYC-overexpressing TNBC inhibited tumor growth in a c-MYC-dependent manner. Furthermore, senescence is induced upon c-MYC downregulation¹⁵⁵ and its pharmacological inhibition depletes TNBC of cancer stem cells and also induces senescence²⁴⁴. Thus, the description of functions dependent on c-MYC that were first attributed to PML, pushed us to further study the link between them in TNBC.

PIM proteins comprise a family (PIM1, PIM2 and PIM3) of proto-oncogenic serine/threonine kinases that contribute to tumor formation and development. Proviral integration site for Moloney murine leukemia virus-1 (PIM1) was first described in hematological cancers, where a potential link with c-MYC was found for the first time²⁴⁵. PIM1 is known to be overexpressed in several solid tumors and it has been demonstrated that in prostate cancer it cooperates with c-MYC²⁴⁶⁻²⁴⁸. Interestingly, few years ago two studies described that PIM1 was overexpressed in TNBC with high c-MYC levels^{232,249}. The lack of drugs that specifically target c-MYC and the synergy demonstrated between both proteins postulated PIM1 as a promising target for this subtype of BCa.

We hypothesized that due to the similarities the axis formed by c-MYC and PIM1 has shown with the functions described for PML in TNBC, they may be collaborating in the tumor biology of high PML expressing TNBC.

In an effort to understand the relationship between PML, c-MYC and PIM1, we first evaluated their association at mRNA level in BCa patient samples. We checked if there was any correlation between PML and c-MYC or PIM1 taking all BCa subtypes into account. We found a significant direct correlation between PML and c-MYC in 2 out of 4 datasets. In the case of PIM1, the direct correlation with PML was significant in all the datasets (**Fig. R26A**).

The annotation of the characteristics of the different subtypes from patient derived samples is not always the same between the datasets. In this case, the information for the different intrinsic subtypes is not available in all the datasets analyzed in **Fig. R26A**. Therefore, we questioned if the correlation was recapitulated in the ER negative group, since PML, c-MYC and PIM1 are overexpressed specifically in TNBC. We observed a significant direct association for PML and c-MYC and PML and PIM1 in 2 out of 4 datasets (**Fig. R26B**). The presence of tumors from HER2 subtype could mask, at least in part, the results obtained with an analysis of the basal type alone.

We next aimed to corroborate the relevance of this correlation in TNBC cell lines. In this scenario, we did not find a remarkable correlation between PML and c-MYC (**Fig. R27A**). Conversely, a significant direct correlation between PML and PIM1 was observed (**Fig. R27B**). Of note, MDA-MB-231 and MDA-MB-468 cell lines showed high levels of both c-MYC and PIM1, which were correlated with high PML levels.

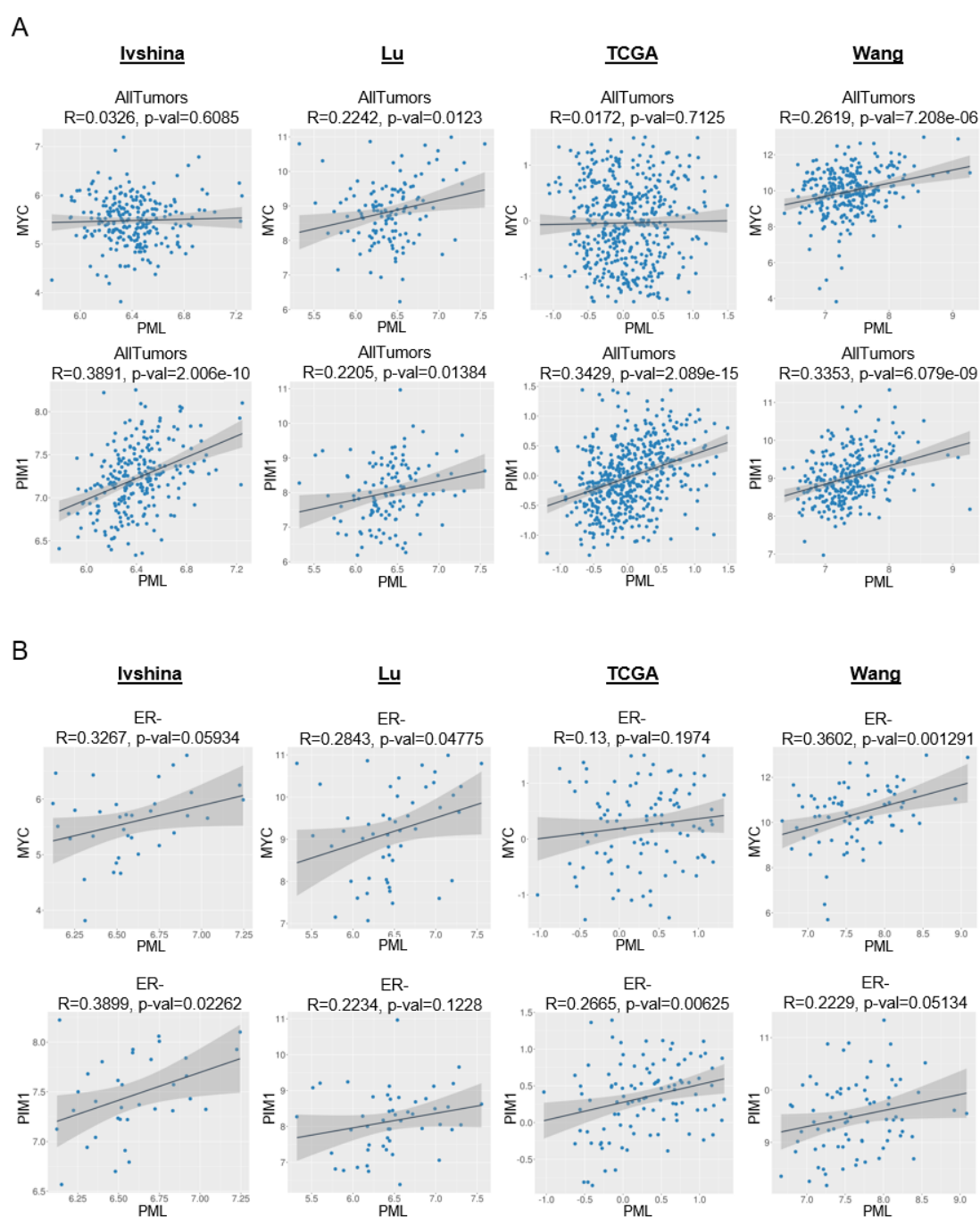


Figure R26. Correlation analysis of PML mRNA expression with MYC and PIM1 in patient datasets. A) Correlation analysis between PML and MYC (top panels) and between PML and PIM1 (bottom panels) mRNA levels in all breast cancer subtypes of tumor specimens of the indicated breast cancer datasets. Sample sizes: Ivshina (n=249), Lu (n=131), TCGA (n=522) and Wang (n=286). **B)** Correlation analysis between PML and MYC (top panels) and between PML and PIM1 (bottom panels) mRNA levels in ER negative tumor specimens of the indicated breast cancer datasets. Sample sizes: Ivshina (n = 34), Lu (n = 49), TCGA (n = 117) and Wang (n = 77).

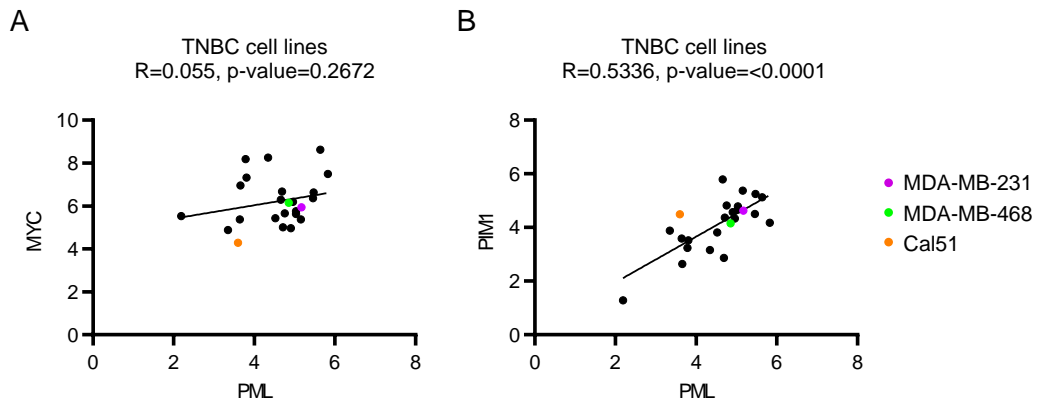


Figure R27. Correlation analysis of PML with c-MYC and PIM1 in cell lines from DepMap. A-B) Correlation analysis between **A)** PML and MYC (n=24) and **B)** PML and PIM1 (n=24).

Next, we aimed to molecularly understand the regulation of growth by PML, c-MYC and PIM1 in TNBC. Although PML and c-MYC have been described to interact under defined conditions²⁵⁰, little is known about how PML could regulate c-MYC in cancer. Interestingly, both have been described to be key in TNBC biology as promoters of tumor growth. Therefore, we decided to first evaluate c-MYC levels in PML-p27 double silenced cells. We hypothesized that c-MYC was being downregulated upon PML silencing and that could explain the impossibility to resume growth. We found that c-MYC protein levels were decreased when p27 was silenced concomitantly with PML to levels comparable to the ones observed with the silencing of PML alone (**Fig. R28**). This data also supports the notion that PML regulates a larger signaling program that could explain the decrease on growth capacity that are not reached only by meanings of senescence induction.

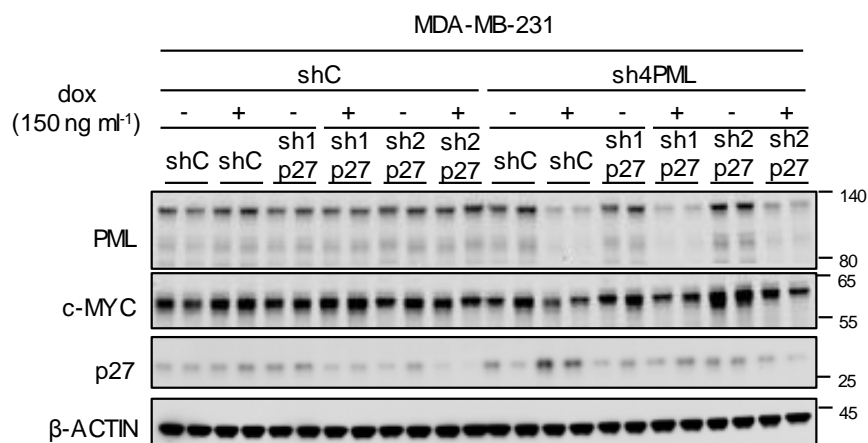


Figure R28. C-MYC levels are decreased when PML and p27 are silenced together. PML, c-MYC and p27 protein levels upon doxycycline inducible silencing of either p27 or PML or both (representative of 3 experiments). dox: doxycycline. Molecular weight markers (kDa) are shown to the right.

To deconstruct the regulation of PML and c-MYC, we studied the impact of PML silencing on c-MYC abundance at both protein and mRNA levels. We observed a significant decrease at protein level that was accompanied by the aforementioned increase in p27 (Fig. R29A and Fig. R29B). At gene expression level *in vitro*, PML targeting also induced a remarkable decrease in c-MYC gene expression (Fig. R29C). We also checked the mRNA expression in established xenografts *in vivo*, confirming not only the decrease in c-MYC levels, but also a significant increase in p27, as observed before at the *in vitro* level (Fig. R29D).

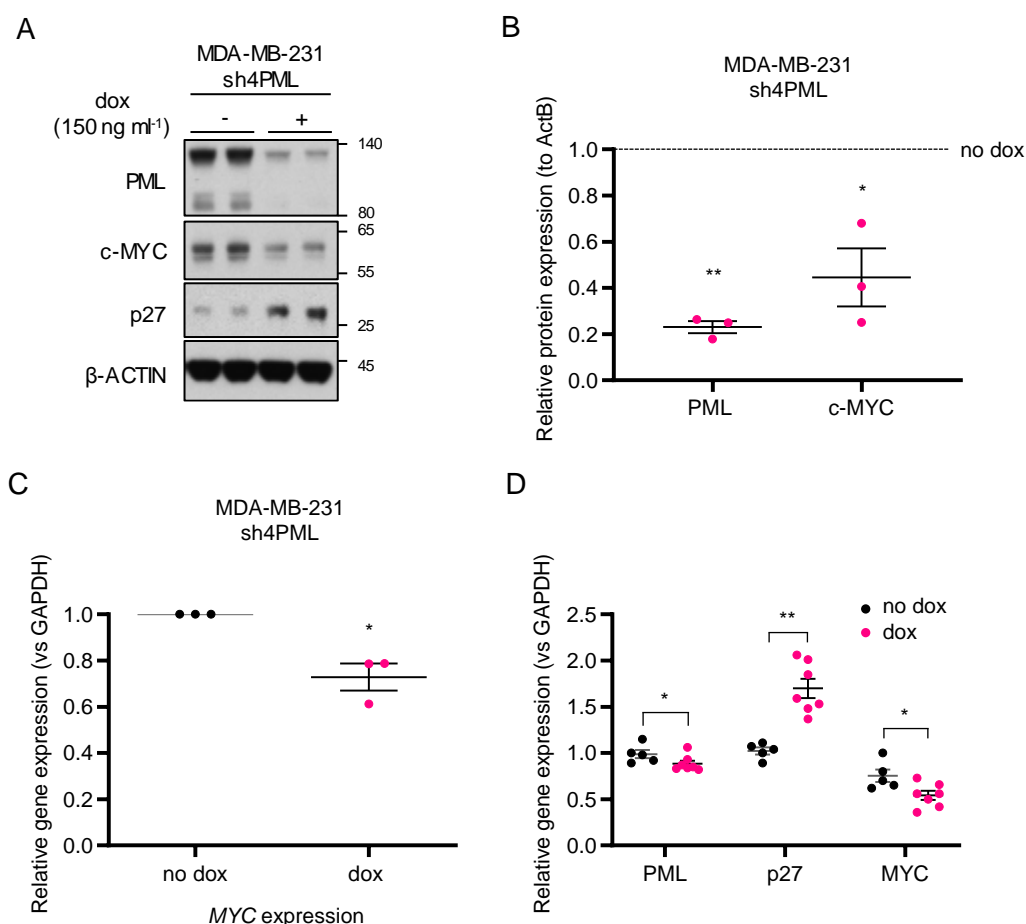
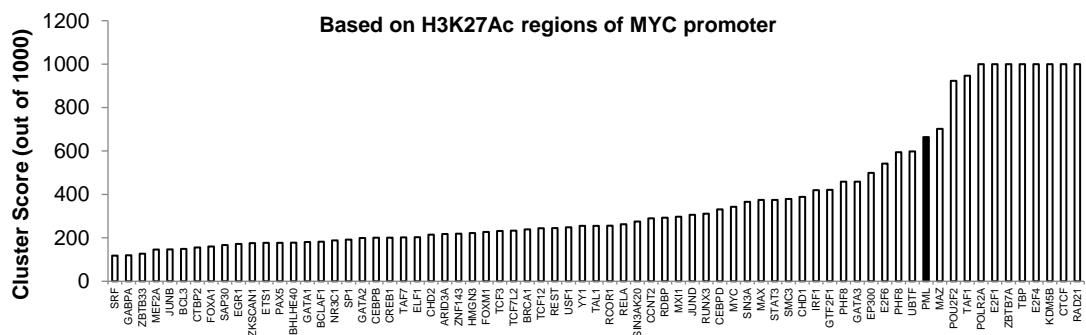


Figure R29. PML silencing decreases c-MYC protein and mRNA levels. **A-B)** Analysis of MYC, p27 and PML protein levels upon PML inducible silencing: **A)** Western Blot (representative of 3 experiments) and **B)** quantification of the protein (n=3). **C)** c-MYC gene levels after inducible silencing of PML in MDA-MB-231 cells (n=3). **D)** PML, p27 and MYC mRNA levels upon doxycycline-inducible PML silencing (sh4) of established MDA-MB-231 xenografts. Error bars represent s.e.m. p, p-value (*p< 0.05, **p< 0.01). One-tailed one sample t-test (b, c, d) was used for cell line data analysis. dox: doxycycline. Molecular weight markers (kDa) are shown to the right.

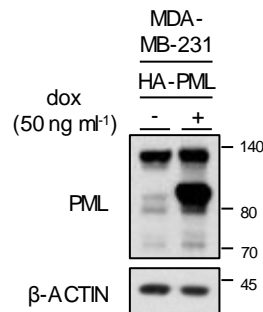
Transcriptional regulation by PML has been studied for many years but still little is known about the specific mechanism through which PML can regulate the transcription of different genes. Strikingly, PML does not have a DNA binding domain but it acts as a scaffold for many molecules⁸⁵. In fact, it has been demonstrated that PML co-activates or co-represses transcription by interacting

with other factors^{61,81,83,251}. Furthermore, we demonstrated that PML is in close proximity of SOX9 promoter and regulates its transcription in TNBC¹⁰¹. Taking this into account, we wondered if PML could regulate c-MYC transcription. We first searched in ENCODE for the ChIP-seq data of MYC promoter. We restricted the analysis with the information from H3K27 acetylated regions and classified the transcription factors based on their binding score. Surprisingly, we found that PML was among the proteins with the highest DNA-binding score (**Fig. R30A**, cluster score: 527) in MYC promoter *in silico*. To confirm this interaction, we performed a ChIP experiment with exogenously expressed PML IV protein (**Fig. R30B**) and demonstrated that PML was in the close proximity of MYC promoter (**Fig. R30C**).

A



B



C

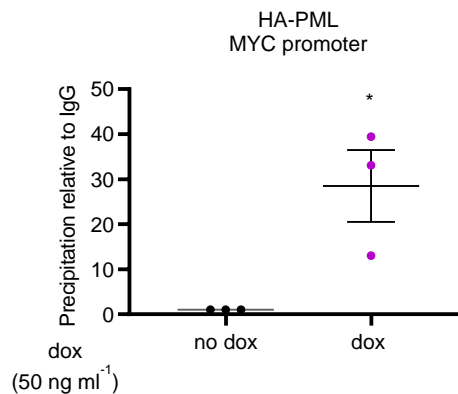


Figure R30. PML is in the vicinity of MYC promoter. **A)** Cluster score of DNA-binding proteins in MYC promoter region using ENCODE database. **B)** Western Blot (representative of at least three experiments) of exogenously expressed HA-PMLIV. **C)** MYC promoter region abundance in chromatin immunoprecipitation of exogenous HA-PMLIV using HA-tag antibody in MDA-MB-231 cells after induction with 50 ng ml⁻¹ doxycycline for 3 days (n=3). Data were normalized to IgG (negative-binding control). Error bars represent s.e.m. p, p-value (*p< 0.05). One-tailed one sample t-test (c) was used for cell line data analysis. dox: doxycycline.

We next aimed to study whether c-MYC silencing was able to recapitulate the senescence phenotype we observed upon PML loss and confirm that the effect was, at least in part, induced by c-MYC downregulation. We first confirmed the increase in p27 abundance upon c-MYC shRNA activation with no changes in PML at protein level (**Fig. R31A** and **Fig. R31B**). As expected by the

increase in p27 levels, the silencing of c-MYC induced the aforementioned senescence response (**Fig. R31C** and **Fig. R31D**). Finally, we observed that the growth capacity of the cells was also compromised when c-MYC was silenced (**Fig. R31E**).

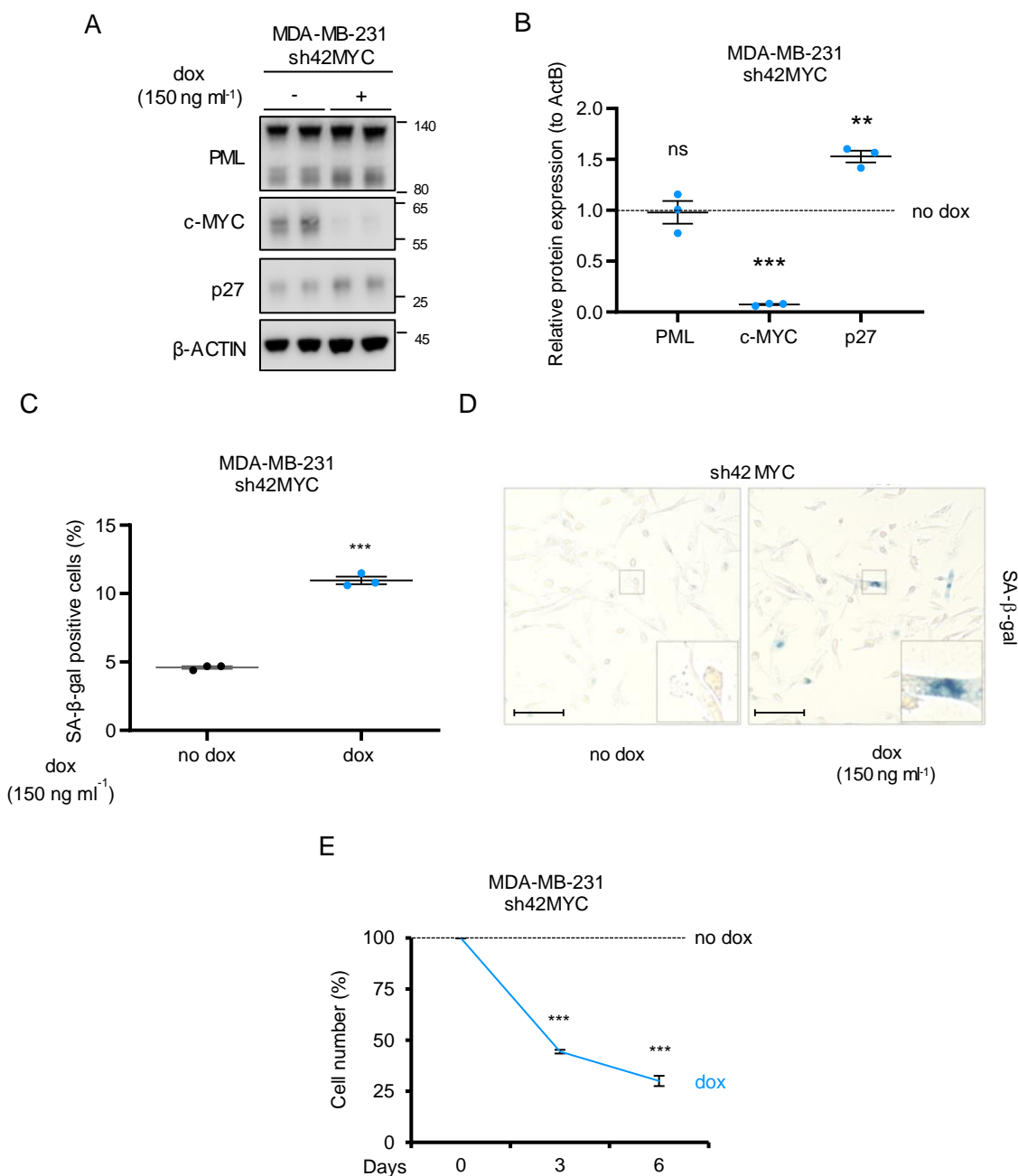


Figure R31. C-MYC silencing recapitulates the phenotype induced by PML loss. A-B) PML, c-MYC, and p27 protein levels upon doxycycline inducible silencing of MYC in MDA-MB-231 cells: **A)** Western Blot (representative of 3 experiments) and **B)** protein quantification (n=3). **C-D)** Effect on the number of senescent cells (n=3) **(D)** representative images, scale bar 50 μm) upon MYC inducible silencing in MDA-MB-231 cells. **E)** Impact on cell number (n=3) of inducible MYC silencing in MDA-MB-231 cells. Error bars represent s.e.m. p, p-value (**p< 0.01, ***p< 0.001, ns: not significant). One-tailed one sample t-test (b, e) and one-tailed Student's t-test (c) were used for cell line data analysis. sh42: shRNA against MYC, dox: doxycycline. Molecular weight markers (kDa) are shown to the right.

The increasing body of work about PIM1 has heightened the interest on this kinase. Two studies postulated PIM1 as a druggable target in TNBC due to its anti-tumorigenic role exerted by downregulating c-MYC pathway and increasing p27 levels^{232,249}. In agreement with our previous data, we hypothesized that PML loss would affect PIM1 as it did with c-MYC. We first analyzed the effect PML silencing was having in *PIM1* expression. We confirmed by ChIP analysis that PML was in the proximity of *PIM1* promoter (**Fig. R32A**, cluster score: 383 in ENCODE) and that *PIM1* mRNA expression was also significantly decreased upon PML silencing (**Fig. R32B**).

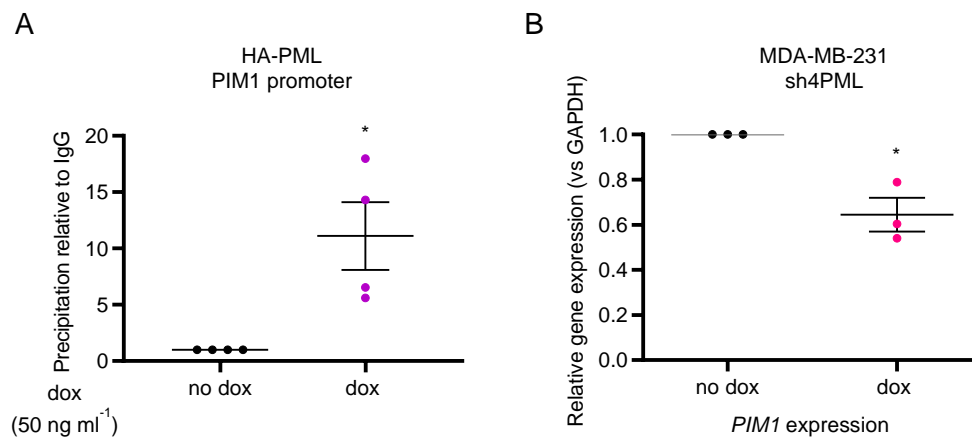


Figure R32. PML regulates PIM1 at the transcriptional level. **A)** PIM1 promoter region abundance in chromatin immunoprecipitation of exogenous HA-PML IV using HA-tag antibody in MDA-MB-231 cells after induction with 50 ng ml⁻¹ doxycycline for 3 days (n=4). Data were normalized to IgG (negative-binding control). **B)** PIM1 gene levels after PML inducible silencing in MDA-MB-231 (n=3). Error bars represent s.e.m. p, p-value (*p < 0.05). One tailed one sample t-test (a, b) was used for cell line data analysis. dox: doxycycline.

The study of transcriptional regulation by PML has been of utmost interest for researchers. Both transcriptional activation and repression have been described for PML, but mechanistically it is still unclear how this function is mediated. Here we demonstrate that PML is in the close proximity of the promoter of both c-MYC and PIM1. Due to the lack of a DNA binding domain, we hypothesize that PML should regulate the transcription through the recruitment and/or modulation of other transcriptional factors that can bind DNA regions.

Due to the function of PIM1, we speculated that its inhibition would recapitulate the previously described senescence phenotype, by further impairing c-MYC function. We silenced PIM1 and confirmed the decrease in c-MYC together with the increase in p27 at protein level (**Fig. R33A** and **Fig. R33B**). When analyzing gene expression levels, p27 was significantly increased, but no downregulation on c-MYC was observed (**Fig. R33C**). It has been described that PIM1 can phosphorylate c-MYC *in vitro*^{249,252}. Therefore, it is more likely that PIM1 regulates c-MYC post-translationally by phosphorylating different residues, without observing changes at mRNA level. We further confirmed the key role of PIM1 by a remarkable decrease on the growth capacity of the TNBC cells (**Fig. R33D**). Finally, as expected by the decrease in growth capacity and the increase in p27 abundance, the increase in the number of senescent cells was recapitulated with PIM1 silencing (**Fig. R33E** and **Fig. R33F**).

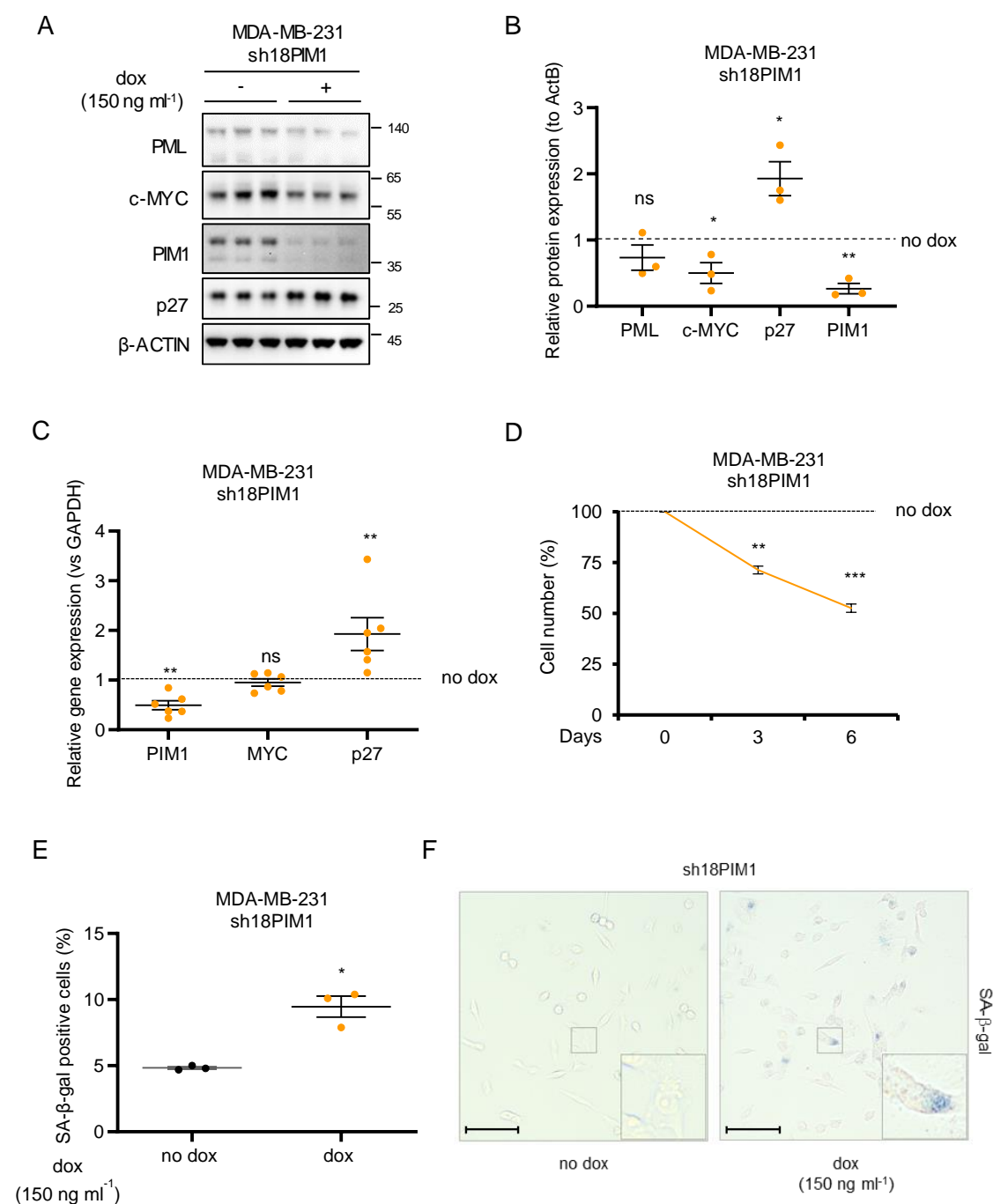


Figure R33. PIM1 silencing further impacts in the senescence phenotype induced by PML loss. A-B) p27, MYC, PIM1, and PML protein levels upon doxycycline inducible silencing of PIM1 in MDA-MB-231 cells: **A)** representative Western Blot out of three experiments and **B)** protein quantification (n=3). **C)** Gene expression levels of PIM1, MYC and p27 upon PIM1 silencing. **D)** Impact in cell number (n=3) of inducible PIM1 silencing in MDA-MB-231 cells. **E-F)** Effect on the number of senescent cells (**F)** representative images, scale bar 50 μm) upon PIM1 inducible silencing in MDA-MB-231 cells. Error bars represent s.e.m. p, p-value (*p< 0.05, **p< 0.01, ***p< 0.001). One tailed one sample t-test (b, c, d) and one-tailed student's t-test (e) were used for cell line data analysis. shC: Scramble shRNA, dox: doxycycline, SA-β-gal: senescence-associated beta-galactosidase. Molecular weight markers (kDa) are shown to the right.

C-MYC is a key regulator of cell cycle and cell proliferation and p27 is one of its most important target genes^{253,254}. Interestingly, in samples of TNBC patients a significant association between p27 loss and c-MYC overexpression has been observed²²⁴. In addition, PIM1 is a key regulator of cell cycle by downregulating p27 levels²⁵⁵. Taken together, our results strongly suggest that c-MYC and PIM1 play a key role supporting PML-elicited TNBC growth and preventing p27 accumulation and senescence response.

II.2 Deciphering PML addiction of TNBC cells vs non-TNBC cells

The concept of oncogene addiction postulates that the survival of tumor cells depends on a single oncogene regardless other genetic or epigenetic modifications, which makes it an interesting approach for targeted therapies. The data presented in this thesis supports the idea that high PML-expressing BCa cells are addicted to its elevated expression. In order to further confirm this notion, we took advantage of another TNBC cell line with high PML levels, MDA-MB-468, and two ER positive cell lines with low levels of PML, MCF-7 and Cama-1 (**Fig. R5** for protein levels). We first checked the growth capacity of the three cell lines after inducible PML silencing and we observed a remarkable growth arrest in MDA-MB-468 cell line (**Fig. R34A**), that was not due to apoptosis (**Fig. R34B**) in concordance with MDA-MB-231 cell line data. Conversely, no changes were observed in the non-TNBC cell lines (**Fig. R34C** and **Fig. R34D**).

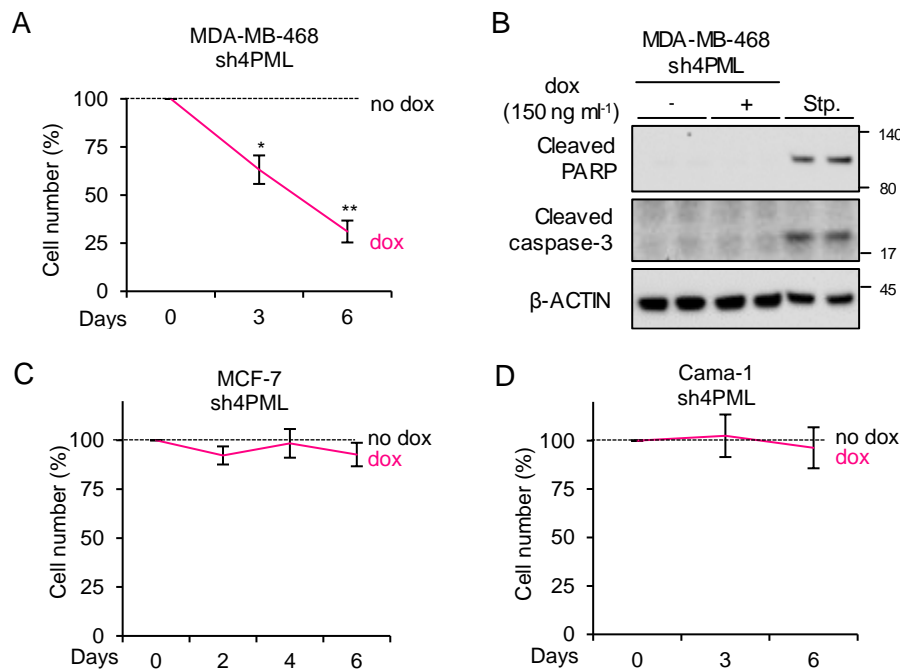


Figure R34. PML silencing differentially affects TNBC and non-TNBC cell growth. **A-B)** Impact of PML inducible silencing on **A)** cell number and in **B)** apoptosis in MDA-MB-468 cell line. **C-D)** Effect on cell number of inducible PML silencing in ER positive **C)** MCF-7 and **D)** Cama-1 cell lines. Error bars represent s.e.m. p, p-value (*p < 0.05, **p < 0.01). One tailed one sample t-test (a, c, d) was used for cell line data analysis. dox: doxycycline, Stp: staurosporine. Molecular weight markers (kDa) are shown to the right.

We next studied the senescence phenotype associated to PML loss. At the morphological level the TNBC cell line MDA-MB-468 was the only one affected by PML silencing, showing a completely disrupted cellular morphology. Conversely, no changes were observed in the morphology of non-TNBC cells (**Fig. R35A**). To confirm the presence of senescent cells we measured SA- β -gal activity. As expected, MDA-MB-468 cell line showed a significant increase in SA- β -gal positivity while ER positive cell lines did not exhibit changes in the number of senescent cells (**Fig. R35B** and **Fig. R35C**).

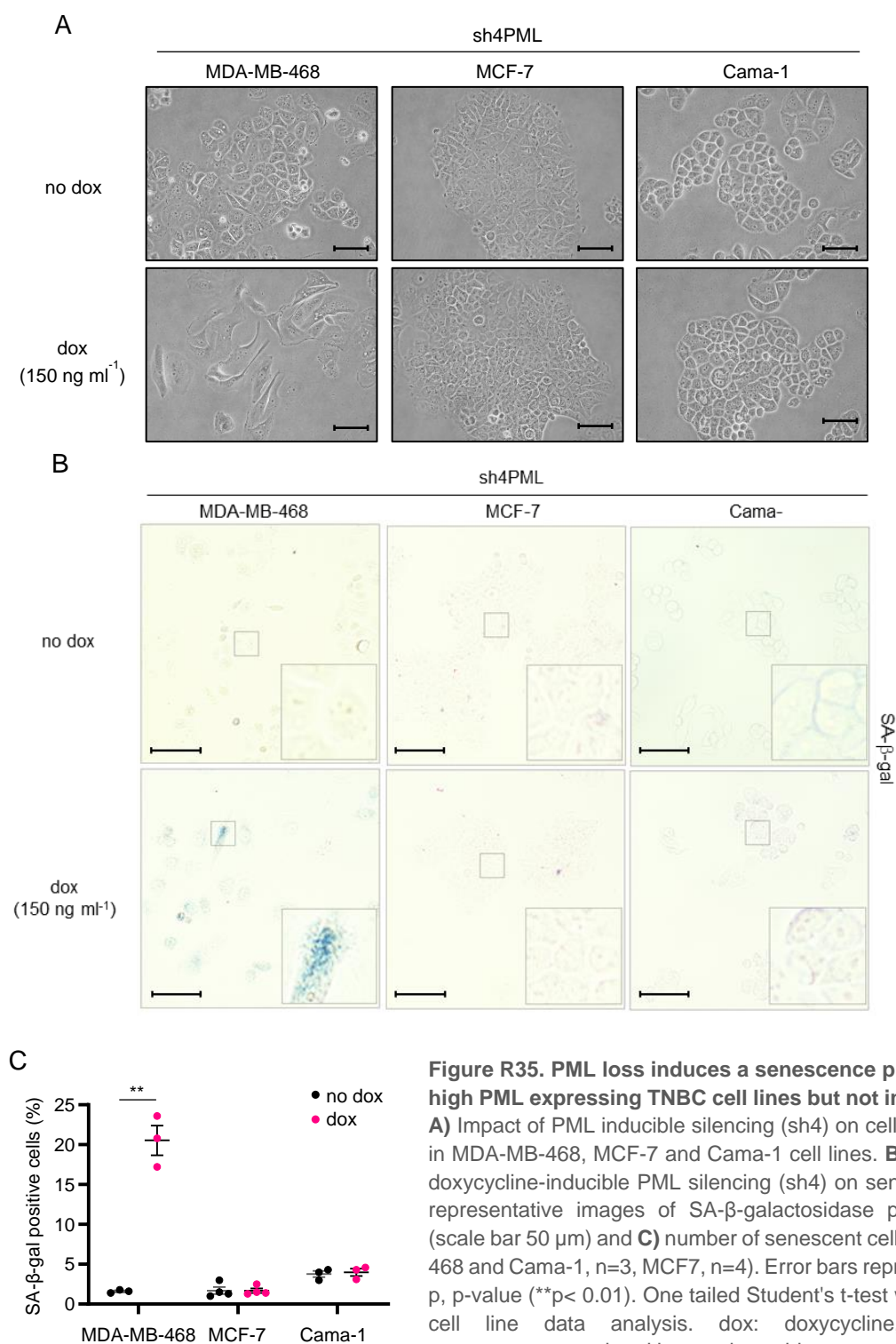


Figure R35. PML loss induces a senescence phenotype in high PML expressing TNBC cell lines but not in ER + cells. A) Impact of PML inducible silencing (sh4) on cell morphology in MDA-MB-468, MCF-7 and Cama-1 cell lines. **B-C)** Effect of doxycycline-inducible PML silencing (sh4) on senescence: **B)** representative images of SA- β -galactosidase positive cells (scale bar 50 μ m) and **C)** number of senescent cells (MDA-MB-468 and Cama-1, n=3, MCF7, n=4). Error bars represent s.e.m. p, p-value (**p < 0.01). One tailed Student's t-test was used for cell line data analysis. dox: doxycycline, SA- β -gal: senescence-associated beta-galactosidase.

At the molecular level, the senescence response induced upon PML silencing in MDA-MB-231 cell line was p27 dependent. In lane with the results obtained, a remarkable increase of p27 levels was observed in MDA-MB-468 upon PML loss. In the case of ER+ cell lines, we did not detect an induction of p27 expression (**Fig. R36**).

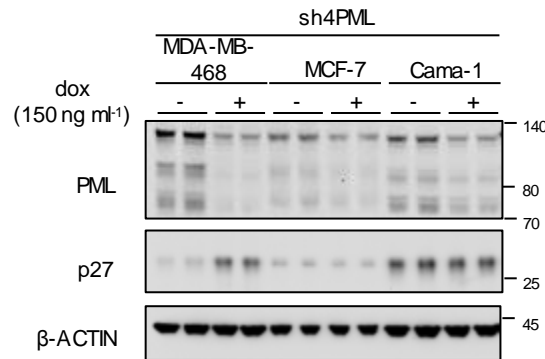


Figure R36. PML loss induced p27 increase is limited to the MDA-MB-468 cell line. A) Effect of doxycycline-inducible PML silencing on PML and p27 protein expression (representative of three experiments). dox: doxycycline. Molecular weight markers (kDa) are shown to the right.

We analyzed the effect of PML loss in the expression of several genes implicated in cell cycle regulation in MDA-MB-468 cell line. At the transcriptional level E2F3, CDK4, AURKA and CDC25A were remarkably deregulated (**Fig. R37A**). In contrast, p27 gene expression was not significantly affected by PML silencing. We have described how PML regulates PIM1 and c-MYC. We further confirmed this notion in MDA-MB-468 cell line, where both c-MYC and PIM1 gene expression levels were significantly downregulated upon PML silencing (**Fig. R37B** and **Fig. R37C**).

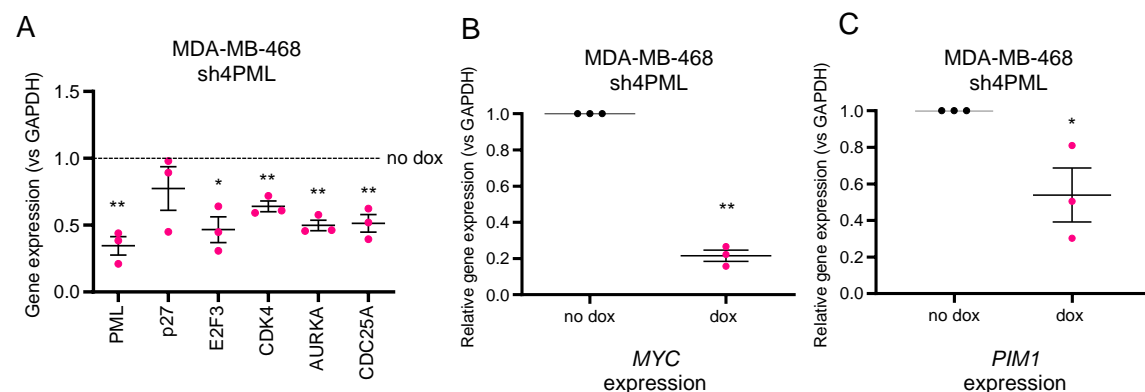


Figure R37. Growth regulatory pathways are deregulated in MDA-MB-468 cell line upon PML silencing. A) Expression of cell cycle genes upon PML inducible silencing in MDA-MB-468 cells (n=3). **B)** MYC gene levels after inducible silencing of PML in MDA-MB-468 cells (n=3). **C)** PIM1 gene levels after PML inducible silencing in MDA-MB-468 cell line (n=3). Error bars represent s.e.m. p, p value (*p < 0.05, **p < 0.01). One-tailed one sample t-test (a, b, c) was used for cell line data analysis. CDK: cyclin dependent kinases, AURKA: aurora kinase A, CDC25A: cell division cycle 25 homolog A, dox: doxycycline.

MDA-MB-468 cell line is wild-type for p16²¹⁴ and deficient for pRB^{256,257}, key effectors in some senescence responses. It would be necessary to determine if PML loss impacts p16 levels in this context. This could give a feasible explanation to the lack of upregulation of p27 at the transcriptional level at day 6 of experiment, as the implication of the p16-pRB pathway could accelerate the senescence response. It could also explain the slightly exacerbated senescence response observed in MDA-MB-468 cell line when compared to MDA-MB-231 cells.

In concordance with the previous results, at protein level in MDA-MB-468 cell line c-MYC was remarkably decreased and accompanied by the p27 increase (Fig. R38A and Fig. R38B), while no changes were observed neither in MCF-7 (Fig. R38C and Fig. R38D) nor in Cama-1 (Fig. R38E and Fig. R38F) cell lines.

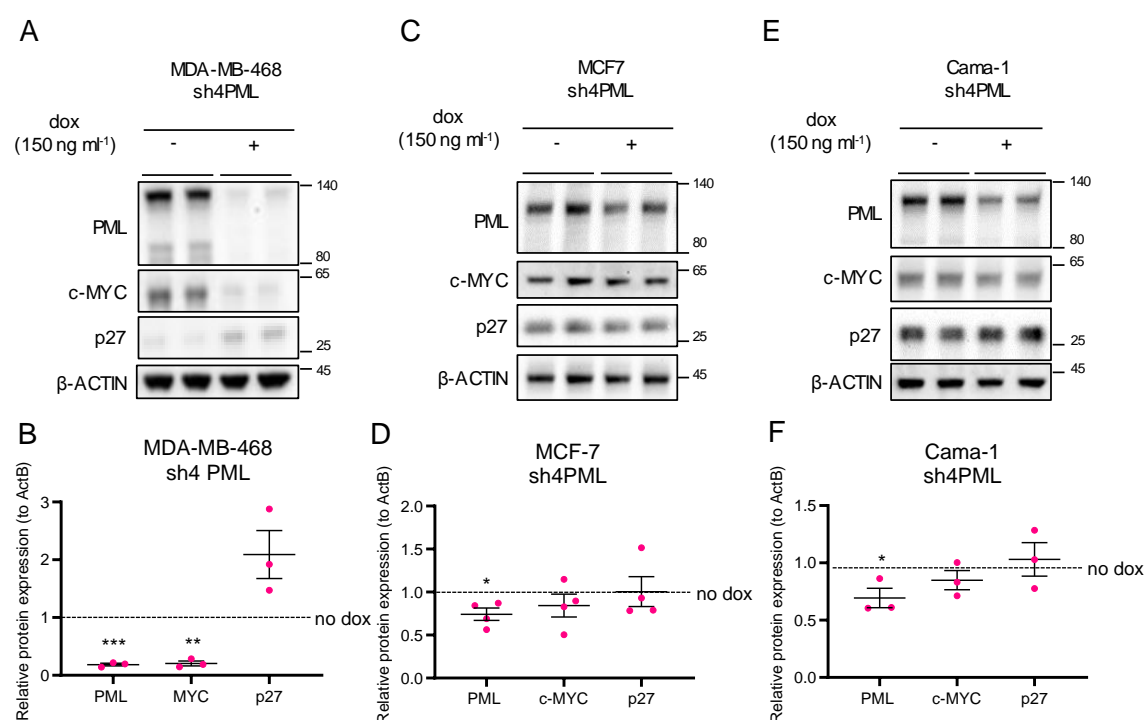


Figure R38. C MYC levels are only decreased in TNBC cell line. A-F p27, MYC and PML protein levels and protein quantification of PML inducible silencing in **A-B**) MDA-MB-468, **C-D**) MCF-7 and **E-F**) Cama-1 cell lines. Error bars represent s.e.m. p, p-value (*p < 0.05, **p < 0.01, ***p < 0.001). One tailed one sample t-test (b, d, f) was used for cell line data analysis. dox: doxycycline. Molecular weight markers (kDa) are shown to the right.

We analyzed the SASP of Cama-1 cells to further characterize the effect of PML silencing in the senescence response of an ER+ cell line (Fig.R39A). Contrary to what we observed with MDA-MB-231 cell line, PCA was not able to segregate the non-induced and induced experimental conditions (Fig. R39B) in Cama-1 cell line. When observing the differentially secreted proteins, no secretory proteins or pathways were identified to be enriched in the PML silenced group (Fig. R39C and Annex Table 3). This further confirmed the lack of a growth inhibitory effect of PML loss as a senescence response in ER+ cell lines.

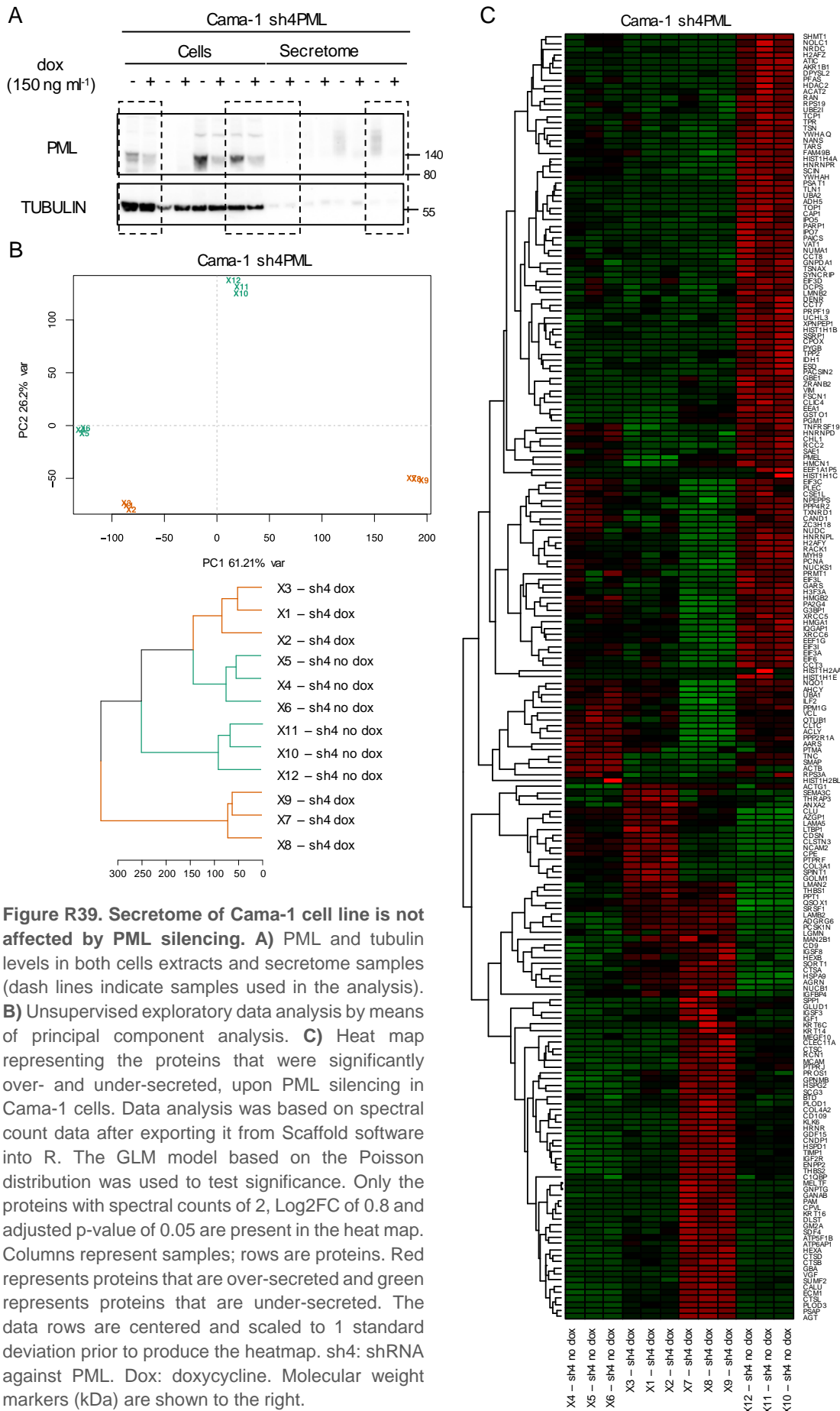


Figure R39. Secretome of Cama-1 cell line is not affected by PML silencing. **A)** PML and tubulin levels in both cells extracts and secretome samples (dash lines indicate samples used in the analysis). **B)** Unsupervised exploratory data analysis by means of principal component analysis. **C)** Heat map representing the proteins that were significantly over- and under-secreted, upon PML silencing in Cama-1 cells. Data analysis was based on spectral count data after exporting it from Scaffold software into R. The GLM model based on the Poisson distribution was used to test significance. Only the proteins with spectral counts of 2, Log2FC of 0.8 and adjusted p-value of 0.05 are present in the heat map. Columns represent samples; rows are proteins. Red represents proteins that are over-secreted and green represents proteins that are under-secreted. The data rows are centered and scaled to 1 standard deviation prior to produce the heatmap. sh4: shRNA against PML. Dox: doxycycline. Molecular weight markers (kDa) are shown to the right.

Overall, we confirmed that PML is only essential for the growth of high PML-expressing cells and that its loss does not result in a growth inhibitory response on the cells that are not addicted to its expression. The dependence on the expression of PML, specifically in the TNBC subtype, sets the rationale for the development of targeted therapies.

II.3 Arsenic trioxide as a pharmacological inhibitor of PML in TNBC

Arsenic is one of the oldest known medicines. In the 1990's, several studies reported that compounds containing high levels of arsenic trioxide (ATO, also known as Trisenox) were efficient in treating APL^{258,259}. Nowadays, it is used to cure these patients. ATO is able to induce both PML and PML/RAR α degradation. Mechanistically, E3-ubiquitin ligase RNF4 specifically targets ubiquitylated PML leading to proteasome mediated degradation^{79,260}. Until now, ATO is the only drug described to impair PML function. In addition to APL, the antitumorigenic effect of ATO has been demonstrated in glioma and TNBC, where the degradation of PML affected specifically stem cell capacity and metastatic potential^{101,102,173}. To further understand the effect in the bulk of cells, we treated MDA-MB-231 cells with a low ATO concentration. Even if the growth capacity of the cells was compromised upon treatment (**Fig. R40A**), no changes were observed neither in the number of senescent cells (**Fig. R40B**) nor in p27 or c-MYC protein levels (**Fig. R40C** and **Fig. R40D**).

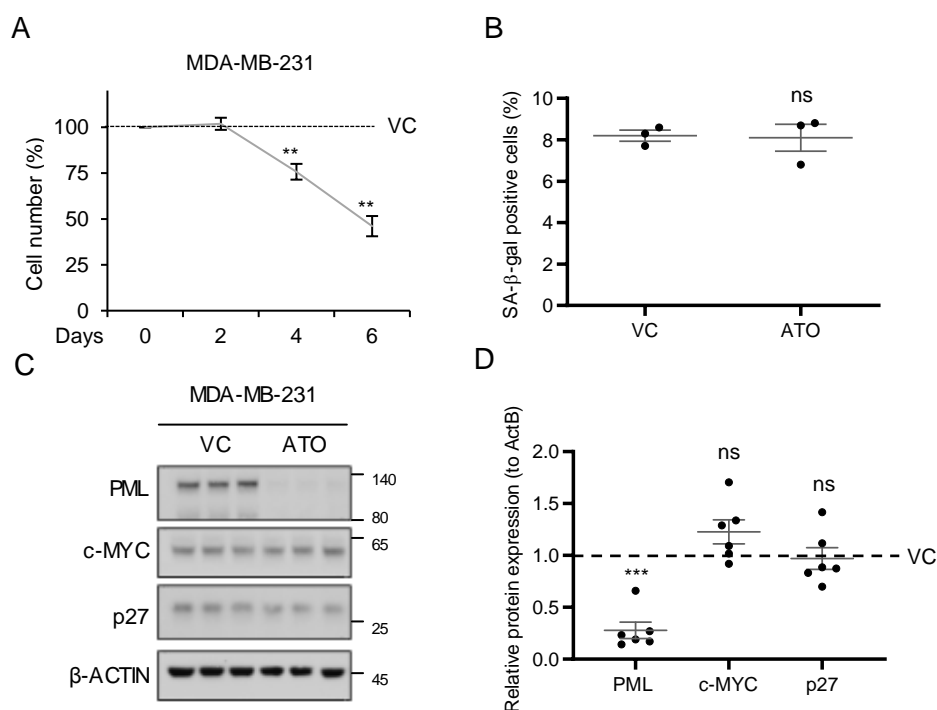


Figure R40. Pharmacological inhibition of PML by ATO does not recapitulate the effect of genetic PML silencing. **A-D**) Effect of 6 days of 150 nM arsenic trioxide treatment in MDA-MB-231 cell line: **A**) in cell number, **B**) on the number of senescent cells and **C-D**) in MYC, p27 and PML protein levels (**D**) quantification of the protein, n=5). Error bars represent s.e.m. p, p-value (**p< 0.01, ***p< 0.001, ns: not significant). One tailed one sample t-test (a, d) and one-tailed student's t-test (b) were used for cell line data analysis. VC: vehicle, ATO: arsenic trioxide. Molecular weight markers (kDa) are shown to the right.

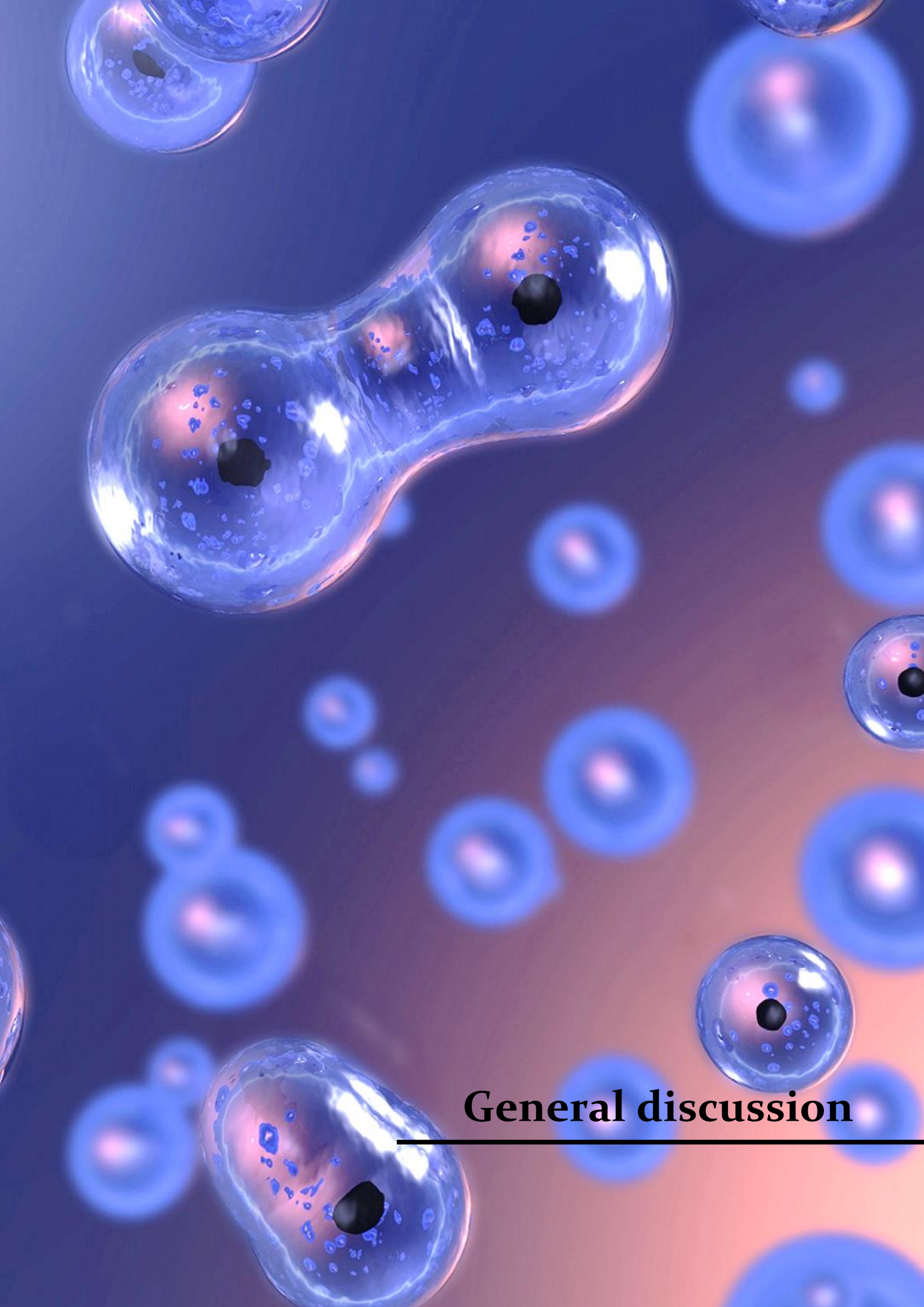
The inability of ATO to recapitulate the senescence phenotype could be explained by the dynamics of PML degradation. Some studies have reported that in very early time points after the treatment, ATO first induces the aggregation of PML molecules forming bigger PML nuclear bodies that will be subsequently degraded²⁶¹. *In vivo*, we have observed that after ATO treatment a fraction of cells showed increased nuclear body formation (data not shown). Understanding the molecular mechanism of action of ATO could shed some light for its use as a pharmacological PML inhibitor in TNBC patients. It also underlines the importance of finding additional drugs for targeted therapies against PML that could improve the treatment of high PML expressing breast cancer tumors.

SUMMARY

- p27 is the driver in PML induced senescence and it accumulates in the nucleus upon PML loss.
- PML is in the close proximity of c-MYC and PIM1 promoters and regulates their expression.
- PML governs a larger growth regulatory pathway of which c-MYC and PIM1 are essential players and senescence phenotype is recapitulated upon both c-MYC and PIM1 silencing.
- Downregulation of PML only exerts a growth inhibitory effect on high PML expressing TNBC cells that are addicted to its expression.
- Pharmacological degradation of PML with ATO does not recapitulate the phenotype.

FUTURE PERSPECTIVES

- Further confirm the causal contribution of c-MYC and PIM1 to the senescence phenotype activated upon PML loss. For this purpose, rescue experiments overexpressing c-MYC or PIM1 together with PML silencing should be performed.
- Study the prognostic value of PML, PIM1, c-MYC and p27 for BCa patients due to their key role in the biology of TNBC.
- Identification of combined therapies with ATO or new compounds that specifically target PML and its partners for their use in the clinic.



General discussion

I Understanding the basis of breast cancer for an improved personalized medicine

Breast cancer stratification: when is a positive truly a positive?

Breast cancer is the most common cancer detected among women and is characterized by a high degree of both inter- and intra-tumoral heterogeneity. Despite the differences found among the tumors, they share a number of characteristics that have allowed their classification based in different markers (both at molecular or immunohistochemical level). BCa classification has improved along the years by integrating the most recent knowledge of their biology. From a clinical perspective, it is important to classify tumors in order to adapt therapeutic strategies according to their specific characteristics. Adding molecular profiling to the clinical routine improves the limitations of immunohistochemical analysis. Nevertheless, it is still challenging to implement the genetic screening due to time consumption and costs, despite the studies that support their clinical use for a better evaluation of prognosis and treatment choice²⁶².

Several studies have conducted molecular analysis of TNBC tumors trying to decipher unique features of these tumors. Unfortunately, and regardless the efforts put on characterizing TNBC, this group of tumors remains as a challenge due to its complexity. TNBC is defined based on what it lacks rather than on what it expresses. In moving towards personalized and precision medicine, it is of utmost importance to identify factors that would help in the identification, prognosis and targeted treatment of these patients. The description of the 5 intrinsic molecular subtypes by Perou *et al.*⁴³ and Sørlie *et al.*⁴⁴ opened new opportunities on the identification of specific characteristics of BCa tumors. Both basal-like and TNBC show the poorest prognosis and highest aggressiveness when compared to other subtypes. Due to the similarities found in both groups, basal-like and TNBC have been used as synonymous in different contexts²⁶³. It is important to note that TNBC is not a surrogate of basal-like subtype. Nonetheless, a high percentage of TNBC tumors show a basal-like phenotype and the majority of the tumors classified as basal-like are triple negative (around 80% in both cases)^{47,264,265}. Thus, validating markers that specifically identify the TNBC and basal-like cancers will open new opportunities for the targeted treatment of these tumors.

The results obtained in this thesis work further support the data from Martín-Martín *et al.*¹⁰¹ and Carracedo *et al.*¹⁰⁰ and encourage us to strengthen the translational research in PML as a potential biomarker for TNBC and basal-like breast cancers. In clinical routine, the gold standard for the detection of the different markers is IHC, a technique that could be applied for the detection of PML in patient samples. For this purpose, it is important to set a threshold of positivity in order to differentiate the patients that could benefit from a future treatment. The best example of the importance of assessing correctly the positivity is the detection of ER, as it defines which patients will benefit from the endocrine therapy. Nonetheless, nowadays there is still controversy in the value

that should be used as the ER positive threshold. On one hand, the American Society of Clinical Oncology (ASCO) recommended to set the ER positivity in >1% in an effort to extend the possibility to receive hormonal therapy²⁶⁶. On the other hand, clinicians have generally used 10% as the cut-off for patients that would benefit from endocrine therapy. Tumors with low ER staining (1-9%) are less common²⁶⁷ and it has been shown that this group of patients has a lower response rate to endocrine treatment²⁶⁸. This debate in the cut-off value of a well-defined marker as ER underlines the importance of patient monitorization and tumor analysis during and after the treatment.

PML as a biomarker for BCa stratification offers a promising path that should be further explored. In this thesis work and in previous publications^{100,101}, we have proposed a score based on the staining percentage and number and size of punctate nuclear structures. This has helped in the identification and stratification of high PML expressing breast tumors, using patient samples, PDX and cell lines. We have described two different semiquantitative scoring schemes: low/high PML or a four-category classification based on PML expression. This second method was applied with patient samples, which could give a closer view of the clinical application. When PML positivity is set in 30%, around the 70% of the samples classified in this category belong to the TNBC subtype¹⁰⁰. This points the threshold of 30% as a promising value for the identification of PML positive tumors. Nevertheless, it cannot be ruled out that the group with PML staining from 10% to 30% (or lower) could contain tumors that may be dependent on the expression of this protein. This underlines the importance of defining the relationship between PML positivity and the dependence of the tumors on its expression for growth, as this would establish the rationale for PML targeted therapies. Therefore, it is a methodology that could be automatized for a rapid analysis of the samples, but still needs to increase the number of samples analyzed to set the PML positivity threshold. We have also started a collaboration with Cell Signaling Technologies for the development of an anti-PML antibody in line with our efforts to advance in PML-based research.

Targeted therapies: searching for the Valyrian steel against TNBC

Personalized and precision medicine are the ultimate objective of cancer research. The availability of highly effective therapies against ER+ and HER2+ BCa has dramatically improved the clinical outcome of these patients. However, the absence of targeted therapies for TNBC leaves chemotherapy as the only systemic treatment option nowadays (**Fig. D1**). The identification of potential drivers in TNBC would provide the opportunity to develop targeted therapies against this subset of tumors.



Figure D1. The ability to stratify breast cancer patients into different subtypes implies different treatment opportunities for those patients.

Molecular profiling has identified several promising targets with compounds that are or have been in clinical trials:

- Mutations in *BRCA1* and *BRCA2* are found in $\approx 20\%$ of TNBC²⁶⁹, which are necessary for homologous recombination and DNA repair. PARP-1 is responsible of DNA repair of single stranded DNA breaks²⁷⁰. In 2005, two different studies demonstrated the potential of PARP-1 as a synthetic lethal therapy for *BRCA* mutant TN tumors^{271,272}. Several clinical trials have tested various PARP inhibitors (Olaparib^{273,274}, Talazoparib²⁷⁵, Veliparib²⁷⁶) with promising results. Additional genetic determinants of PARP inhibitor sensitivity should be investigated.
- When compared to other types of cancer such as melanoma, BCa has not been considered as an immunogenic cancer. Nevertheless, the importance of tumor immune microenvironment in cancer progression²⁷⁷ has increased the interest on immune checkpoint elements, such as programmed death-1 (PD-1) and/or programmed death-ligand 1 (PD-L1). It has been demonstrated that a subset of TNBC patients could be benefited of an anti-PD-L1 treatment²⁷⁸⁻²⁸¹.
- EGFR overexpression correlates with basal-like breast cancer²⁸². Various agents targeting EGFR have undergone preclinical evaluation with differing results^{283,284}.
- The PI3K/AKT/mTOR pathway is more commonly activated in TNBC than in other breast cancer subtypes⁴⁵ and encouraging results have been observed in cell lines and clinical trials^{285,286}.

Despite all the promising data, the aforementioned studies highlight the limitations of these treatments. In addition to therapy resistance, the heterogeneity present in TNBC and basal-like breast cancers is likely to be the reason for therapy failure. Certainly, a single treatment is unlikely to work for all the patients, being the most effective treatment a combination of targeted therapies.

In this thesis work we have deciphered a signaling axis formed by PML, c-MYC, PIM1 and p27 that is essential for the growth of TNBC cells with high PML expression. In the case of pharmacological PML targeting, ATO is employed in the clinical routine to treat APL patients, which would ease the repurposing process for other diseases. In addition, the viability of PML knockout mice²⁸⁷ makes PML targeting a safe treatment. Nevertheless, we have not been able to recapitulate the senescence response elicited upon PML silencing with ATO treatment. Strikingly, ATO has demonstrated its antitumorigenic effect in TNBC in a stem cell and metastatic context¹⁰¹. We do not contemplate a senescence response by increasing ATO concentration, as we can observe that growth capacity is already being compromised. The mode of action of ATO involves several molecules and post-translational modifications that may be affecting the responses upon PML inhibition (**Fig. D2**). In fact, it has been demonstrated that UBC9, the SUMO-conjugating enzyme, can delay the senescence response²⁸⁸. This is a simplification of the model of ATO-induced PML degradation and its consequences, but it points out the necessity of further studying its cellular context-dependent mechanism of action. In collaboration with Kaertor Foundation (continuing the work with Innopharma) we have tried to identify new drugs able to inhibit or degrade PML.

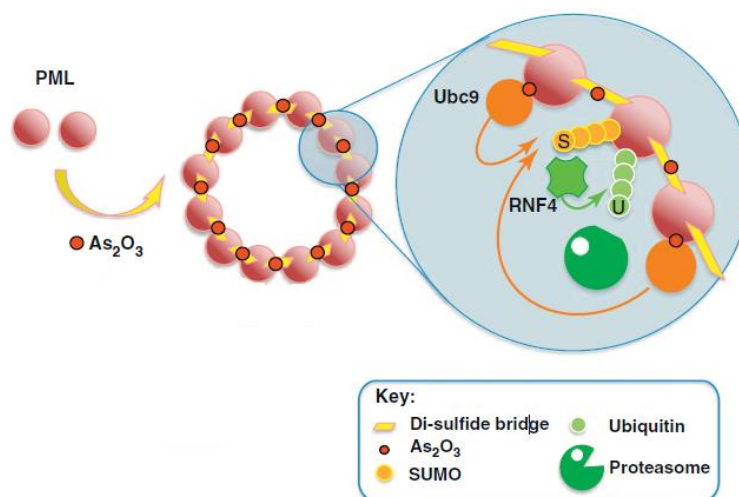


Figure D2. Mode of action of arsenic trioxide induced PML degradation (image modified from Lallemand-Breitenbach *et al.*, 2012²⁸⁹).

The key role of MYC and PIM1 in the biology of high PML expressing TNBC gives the opportunity to target them. Due to its central role in cancer biology as a master regulator of gene expression, MYC is one of the most valuable targets in cancer. Diverse strategies have been used to inhibit MYC, both direct and indirect: blockade of MYC transcription, MYC protein stability and

MYC partners or interactors. BET bromodomain inhibitors have demonstrated the highest efficacy by inhibiting MYC transcription in different malignancies²⁹⁰. In addition, the study by Beaulieu *et al.*²⁹¹ described a promising direct inhibitor that should be further studied. Nevertheless, due to difficulties in inhibiting transcription factors like MYC successfully in the clinic, efforts have been put in discovering novel targets that are synthetic lethal with MYC, such as PIM1 in TNBC^{232,249} and prostate cancer²⁹². After demonstrating the effectivity of PIM1 inhibitors both *in vitro* and *in vivo*, various compounds have entered clinical trials²⁹³. The main challenge with PIM1 inhibitors is their toxicity²⁹³. The increasing research in targeted therapies against the pathway we have described in this thesis work encourages us to further study and collaborate for the development of potential therapeutic options for a subset of TNBC patients.

Many steps have to be taken before reaching clinical application with novel drugs that arise from the discovery of druggable targets. Patient-derived organoid cultures are progressively being implemented for personalized medicine and drug screening in cancer, as they can closely recapitulate the tumor architecture and its specific molecular information²⁹⁴. Organoids may be helpful for medical applications, as it has been observed that they can model the patient response to treatment²⁹⁵. It is necessary to closely work with clinical researchers in order to increase sample availability for molecular characterization and drug testing. This would dramatically improve the research we have made and facilitate the PML, MYC and PIM directed drug screenings for a fastest application in the future.

II Senescence: good or evil

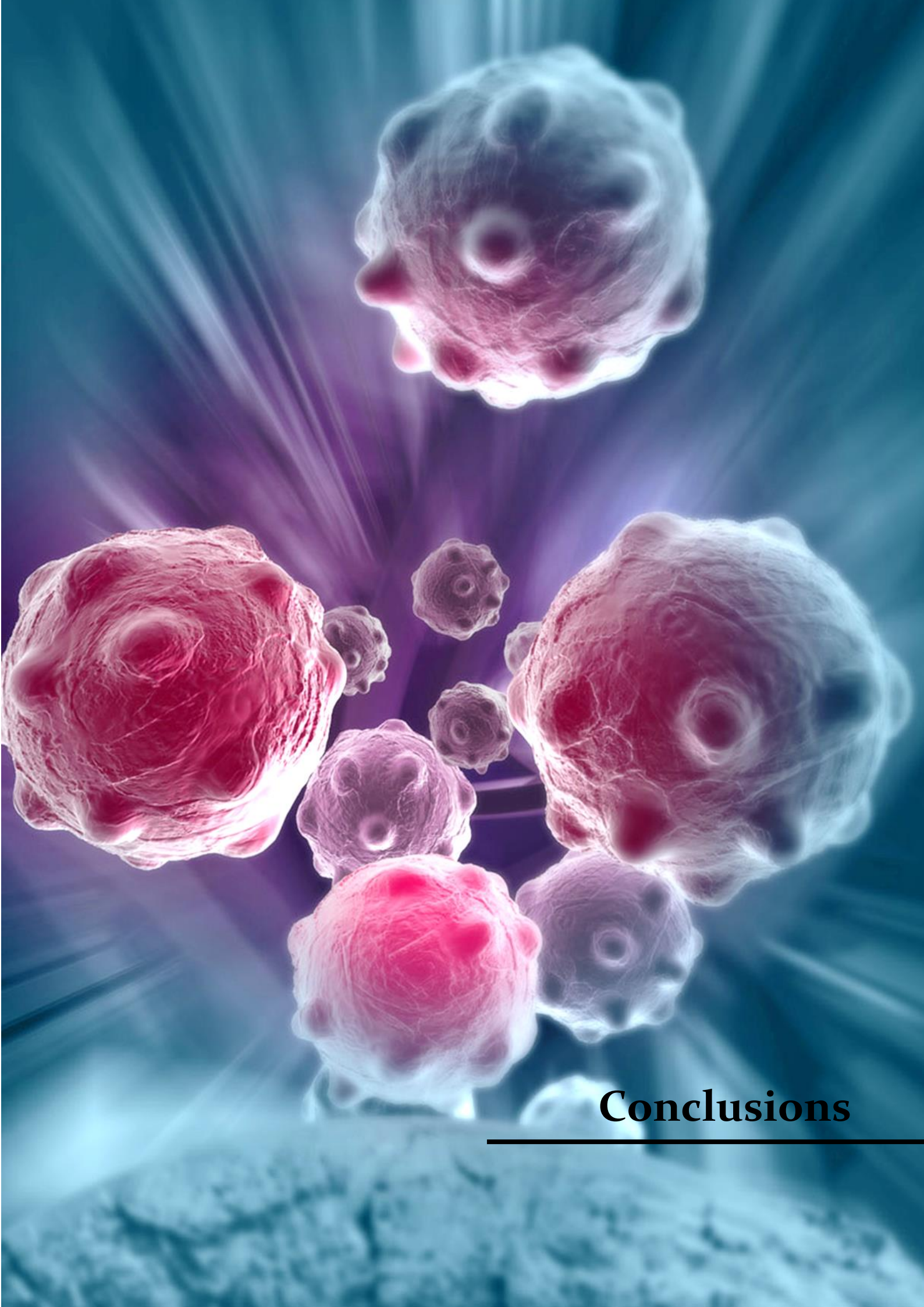
Senescence has been classically recognized as a tumor suppressive mechanism, since one of its hallmarks is irreversible cell cycle arrest. Nevertheless, the increasing information about the context dependent pro-tumorigenic role of secretory phenotype of senescent cells has turned the concept of senescence into a double-edged sword in oncology.

Depending on the cell type, the factors secreted by senescent cells will vary. It has been described that these factors can promote tumor development by inducing proliferation and invasiveness. For example, senescent human fibroblasts can stimulate the growth of premalignant and malignant mammary epithelial cells²⁹⁶. Moreover, the remodeling of the extracellular matrix by metalloproteinases might create a favorable microenvironment for tumor growth²⁹⁷. Interestingly, IL-6 and IL-8, two of the main components of the canonical SASP, have been described to promote tumorigenesis¹⁴² and to reinforce the senescence phenotype^{298,299}. The SASP also has an important effect by controlling the response of the immune system. It has been demonstrated that secreted factors can promote the clearance of the senescent cells by the immune system and therefore contribute to tumor regression^{142,300,301}.

PML was first associated with senescence by its upregulation upon mutant RAS expression in a p53-dependent manner^{70,90}. Conversely, in non-transformed fibroblasts, senescence is activated upon PML depletion, adding complexity to all the PML activities³⁰². In addition, in this thesis work we have demonstrated that in breast cancer cells with high PML expression its inhibition triggers senescence. The phenomenon is characterized by the lack of a canonical SASP and SAHF formation. Nevertheless, we have seen an enrichment in proteins belonging to TGF- β 1 pathway in secretome studies. Interestingly, TGF- β 1 shows antagonistic effects in cancer biology. On one hand, it has been described that TGF- β can induce a potent antiproliferative response in early stages of tumors³⁰³⁻³⁰⁶. On the other hand, it is also described its participation in metastasis and angiogenesis. It is widely accepted that in the later steps of tumor progression the growth inhibitory function of TGF- β is lost³⁰⁷⁻³¹⁰. In the context of senescence, it is suggested that TGF- β has a senescence promoting role³¹¹⁻³¹³. Interestingly, in a lymphoma mouse model, p53-induced apoptosis of cancer cells activates macrophages that will secrete TGF- β 1, inducing senescence in tumor cells³¹⁴.

In an effort to develop targeted therapeutics, different strategies based on senescence have been evaluated. As we have explained, despite its tumor suppressive function, senescence can exacerbate tumorigenesis through the factors that are secreted by senescent cells. In addition, the accumulation of senescent cells can be detrimental due to its contribution to organismal aging³¹⁵. Based on these characteristics of senescence, two different approaches have been proposed: senolytics, which specifically eliminate senescent cells and senostatics, therapies that are focused on modulating the SASP. Interestingly, senolytics have been proposed to improve cancer therapy as a follow up treatment after chemotherapy^{316,317}. Nevertheless, there is a need of discovering new senolytics and setting the best dosing and timing to minimize the side effects associated to some of these compounds³¹⁸⁻³²⁰.

All this data shows the need of further studying the senescence phenotype in a more complex setting. We need to take into account the effect of these molecular and cellular alterations in cancer cells and the tumor microenvironment to further exploit this pathway in TNBC after PML inhibition.



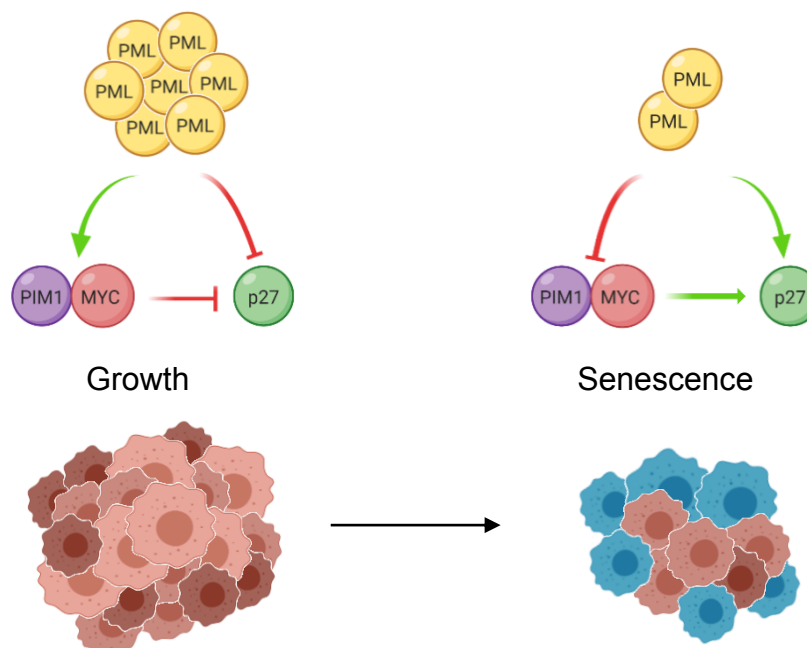
Conclusions

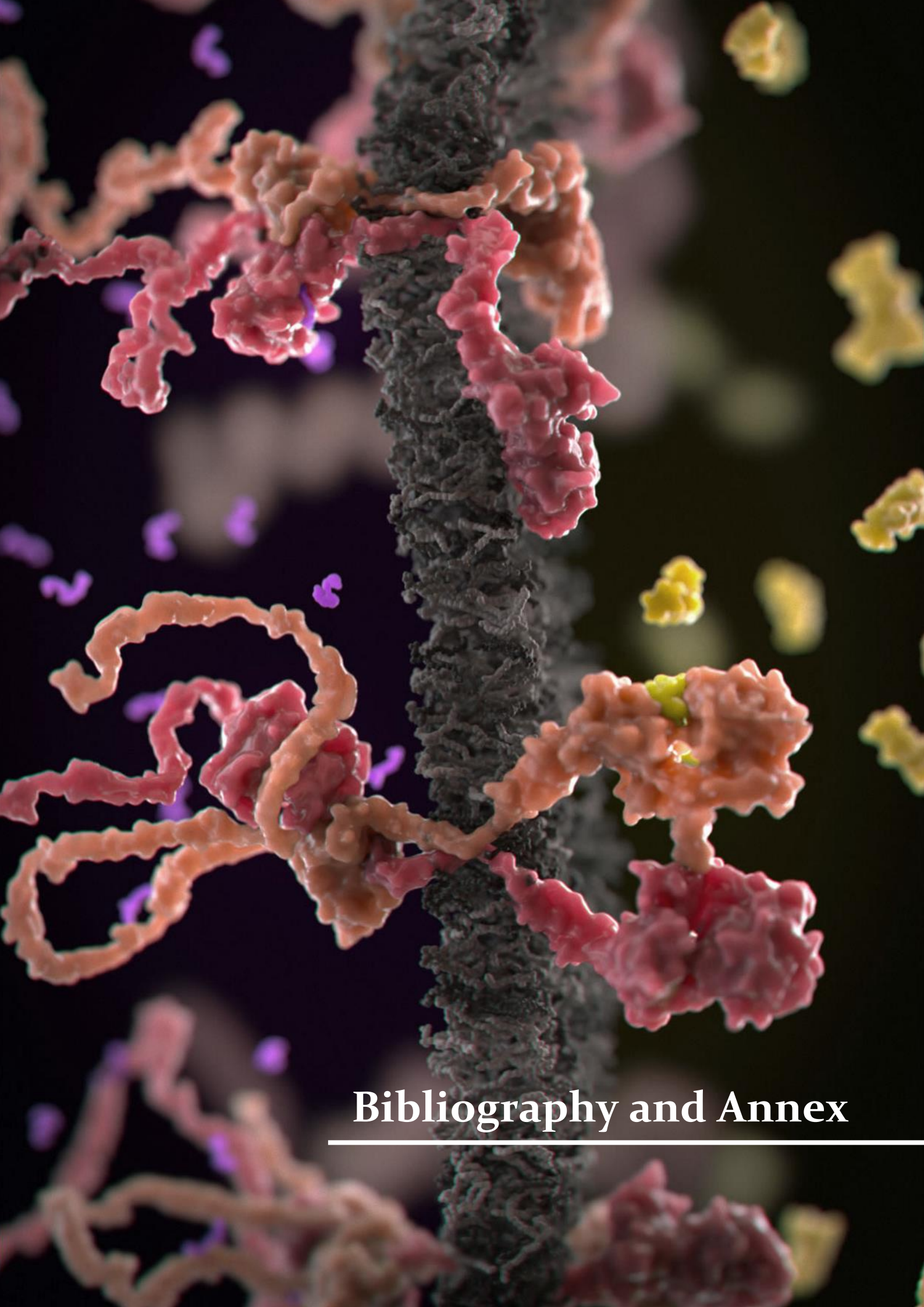
The results obtained throughout this thesis work confirm our initial hypothesis and demonstrate that PML sustains the growth of a subset of TNBC. The results are summarized as follows:

- * PML is specifically overexpressed in TNBC.
- * PML silencing in TNBC cell lines leads to a growth arrest combined with features of senescence. This senescence response is characterized by increased SA- β -galactosidase *in vitro* and intense p-HP1 γ staining in xenografts *in vivo*.
- * Mechanistically, the senescence response is triggered by an increase in p27 levels.
- * c-MYC and PIM1 support the PML-elicited TNBC growth and prevent the accumulation of p27 and the senescence response.
- * ER+ cell lines with lower levels of PML expression are not affected by its silencing.
- * The pharmacological inhibition of PML with ATO does not recapitulate the senescence response despite negatively affecting the growth capacity of the cells.

GENERAL CONCLUSION

High PML expressing TNBC are addicted to the expression of this gene and its inhibition has an antitumorigenic effect. We propose a mechanism that could be further exploited in the clinic.





Bibliography and Annex

I Bibliography

- 1 Weinberg, R. A. How cancer arises. *Sci Am* **275**, 62-70, doi:10.1038/scientificamerican0996-62 (1996).
- 2 Hanahan, D. & Weinberg, R. A. The hallmarks of cancer. *Cell* **100**, 57-70, doi:10.1016/s0092-8674(00)81683-9 (2000).
- 3 Bray, F. *et al.* Global cancer statistics 2018: GLOBOCAN estimates of incidence and mortality worldwide for 36 cancers in 185 countries. *CA Cancer J Clin* **68**, 394-424, doi:10.3322/caac.21492 (2018).
- 4 Vogelstein, B. & Kinzler, K. W. Cancer genes and the pathways they control. *Nat Med* **10**, 789-799, doi:10.1038/nm1087 (2004).
- 5 Yokota, J. Tumor progression and metastasis. *Carcinogenesis* **21**, 497-503, doi:10.1093/carcin/21.3.497 (2000).
- 6 Hanahan, D. & Weinberg, R. A. Hallmarks of cancer: the next generation. *Cell* **144**, 646-674, doi:10.1016/j.cell.2011.02.013 (2011).
- 7 Medina, D. The mammary gland: a unique organ for the study of development and tumorigenesis. *J Mammary Gland Biol Neoplasia* **1**, 5-19, doi:10.1007/bf02096299 (1996).
- 8 Macias, H. & Hinck, L. Mammary gland development. *Wiley Interdiscip Rev Dev Biol* **1**, 533-557, doi:10.1002/wdev.35 (2012).
- 9 Cristea, S. & Polyak, K. Dissecting the mammary gland one cell at a time. *Nat Commun* **9**, 2473, doi:10.1038/s41467-018-04905-2 (2018).
- 10 Gudjonsson, T., Adriance, M. C., Sternlicht, M. D., Petersen, O. W. & Bissell, M. J. Myoepithelial cells: their origin and function in breast morphogenesis and neoplasia. *J Mammary Gland Biol Neoplasia* **10**, 261-272, doi:10.1007/s10911-005-9586-4 (2005).
- 11 Marshall, E. Breast cancer. Dare to do less. *Science* **343**, 1454-1456, doi:10.1126/science.343.6178.1454 (2014).
- 12 Sun, Y. S. *et al.* Risk Factors and Preventions of Breast Cancer. *Int J Biol Sci* **13**, 1387-1397, doi:10.7150/ijbs.21635 (2017).
- 13 Trichopoulos, D., Adami, H. O., Ekblom, A., Hsieh, C. C. & Ligiou, P. Early life events and conditions and breast cancer risk: from epidemiology to etiology. *Int J Cancer* **122**, 481-485, doi:10.1002/ijc.23303 (2008).
- 14 Ellisen, L. W. & Haber, D. A. Hereditary breast cancer. *Annu Rev Med* **49**, 425-436, doi:10.1146/annurev.med.49.1.425 (1998).
- 15 Winters, S., Martin, C., Murphy, D. & Shokar, N. K. Breast Cancer Epidemiology, Prevention, and Screening. *Prog Mol Biol Transl Sci* **151**, 1-32, doi:10.1016/bs.pmbts.2017.07.002 (2017).
- 16 Kuchenbaecker, K. B. *et al.* Risks of Breast, Ovarian, and Contralateral Breast Cancer for BRCA1 and BRCA2 Mutation Carriers. *JAMA* **317**, 2402-2416, doi:10.1001/jama.2017.7112 (2017).
- 17 Polyak, K. Breast cancer: origins and evolution. *J Clin Invest* **117**, 3155-3163, doi:10.1172/JCI33295 (2007).
- 18 Burstein, H. J., Polyak, K., Wong, J. S., Lester, S. C. & Kaelin, C. M. Ductal carcinoma in situ of the breast. *N Engl J Med* **350**, 1430-1441, doi:10.1056/NEJMra031301 (2004).
- 19 Patanaphan, V., Salazar, O. M. & Risco, R. Breast cancer: metastatic patterns and their prognosis. *South Med J* **81**, 1109-1112 (1988).
- 20 Stingl, J. & Caldas, C. Molecular heterogeneity of breast carcinomas and the cancer stem cell hypothesis. *Nat Rev Cancer* **7**, 791-799, doi:10.1038/nrc2212 (2007).
- 21 Li, C. I., Uribe, D. J. & Daling, J. R. Clinical characteristics of different histologic types of breast cancer. *Br J Cancer* **93**, 1046-1052, doi:10.1038/sj.bjc.6602787 (2005).

- 22 Malhotra, G. K., Zhao, X., Band, H. & Band, V. Histological, molecular and functional subtypes of breast cancers. *Cancer Biol Ther* **10**, 955-960, doi:10.4161/cbt.10.10.13879 (2010).
- 23 Weigelt, B. & Reis-Filho, J. S. Histological and molecular types of breast cancer: is there a unifying taxonomy? *Nat Rev Clin Oncol* **6**, 718-730, doi:10.1038/nrclinonc.2009.166 (2009).
- 24 Elston, C. W. & Ellis, I. O. Pathological prognostic factors in breast cancer. I. The value of histological grade in breast cancer: experience from a large study with long-term follow-up. *Histopathology* **19**, 403-410, doi:10.1111/j.1365-2559.1991.tb00229.x (1991).
- 25 Bloom, H. J. & Richardson, W. W. Histological grading and prognosis in breast cancer; a study of 1409 cases of which 359 have been followed for 15 years. *Br J Cancer* **11**, 359-377, doi:10.1038/bjc.1957.43 (1957).
- 26 Carter, C. L., Allen, C. & Henson, D. E. Relation of tumor size, lymph node status, and survival in 24,740 breast cancer cases. *Cancer* **63**, 181-187, doi:10.1002/1097-0142(19890101)63:1<181::aid-cnrcr2820630129>3.0.co;2-h (1989).
- 27 Sobin, L. H. TNM: principles, history, and relation to other prognostic factors. *Cancer* **91**, 1589-1592, doi:10.1002/1097-0142(20010415)91:8+<1589::aid-cnrcr1170>3.0.co;2-k (2001).
- 28 Simos, D. *et al.* Imaging for distant metastases in women with early-stage breast cancer: a population-based cohort study. *CMAJ* **187**, E387-397, doi:10.1503/cmaj.150003 (2015).
- 29 Early Breast Cancer Trialists' Collaborative, G. Effects of chemotherapy and hormonal therapy for early breast cancer on recurrence and 15-year survival: an overview of the randomised trials. *Lancet* **365**, 1687-1717, doi:10.1016/S0140-6736(05)66544-0 (2005).
- 30 Ciocca, D. R. & Fanelli, M. A. Estrogen receptors and cell proliferation in breast cancer. *Trends Endocrinol Metab* **8**, 313-321, doi:10.1016/s1043-2760(97)00122-7 (1997).
- 31 Fanelli, M. A. *et al.* Estrogen receptors, progesterone receptors, and cell proliferation in human breast cancer. *Breast Cancer Res Treat* **37**, 217-228, doi:10.1007/BF01806503 (1996).
- 32 Hammond, M. E. *et al.* American Society of Clinical Oncology/College Of American Pathologists guideline recommendations for immunohistochemical testing of estrogen and progesterone receptors in breast cancer. *J Clin Oncol* **28**, 2784-2795, doi:10.1200/JCO.2009.25.6529 (2010).
- 33 Patani, N., Martin, L. A. & Dowsett, M. Biomarkers for the clinical management of breast cancer: international perspective. *Int J Cancer* **133**, 1-13, doi:10.1002/ijc.27997 (2013).
- 34 Slamon, D. J. *et al.* Human breast cancer: correlation of relapse and survival with amplification of the HER-2/neu oncogene. *Science* **235**, 177-182, doi:10.1126/science.3798106 (1987).
- 35 Oh, D. Y. & Bang, Y. J. HER2-targeted therapies - a role beyond breast cancer. *Nat Rev Clin Oncol* **17**, 33-48, doi:10.1038/s41571-019-0268-3 (2020).
- 36 Morris, G. J. *et al.* Differences in breast carcinoma characteristics in newly diagnosed African-American and Caucasian patients: a single-institution compilation compared with the National Cancer Institute's Surveillance, Epidemiology, and End Results database. *Cancer* **110**, 876-884, doi:10.1002/cncr.22836 (2007).
- 37 Dent, R. *et al.* Triple-negative breast cancer: clinical features and patterns of recurrence. *Clin Cancer Res* **13**, 4429-4434, doi:10.1158/1078-0432.CCR-06-3045 (2007).
- 38 Mersin, H., Yildirim, E., Berberoglu, U. & Gulben, K. The prognostic importance of triple negative breast carcinoma. *Breast* **17**, 341-346, doi:10.1016/j.breast.2007.11.031 (2008).
- 39 Tan, A. R. & Swain, S. M. Therapeutic strategies for triple-negative breast cancer. *Cancer J* **14**, 343-351, doi:10.1097/PPO.0b013e31818d839b (2008).

- 40 Lehmann, B. D. *et al.* Identification of human triple-negative breast cancer subtypes and preclinical models for selection of targeted therapies. *J Clin Invest* **121**, 2750-2767, doi:10.1172/JCI45014 (2011).
- 41 Nishimura, R. *et al.* Ki-67 as a prognostic marker according to breast cancer subtype and a predictor of recurrence time in primary breast cancer. *Exp Ther Med* **1**, 747-754, doi:10.3892/etm.2010.133 (2010).
- 42 Soliman, N. A. & Yussif, S. M. Ki-67 as a prognostic marker according to breast cancer molecular subtype. *Cancer Biol Med* **13**, 496-504, doi:10.20892/j.issn.2095-3941.2016.0066 (2016).
- 43 Perou, C. M. *et al.* Molecular portraits of human breast tumours. *Nature* **406**, 747-752, doi:10.1038/35021093 (2000).
- 44 Sorlie, T. *et al.* Gene expression patterns of breast carcinomas distinguish tumor subclasses with clinical implications. *Proc Natl Acad Sci U S A* **98**, 10869-10874, doi:10.1073/pnas.191367098 (2001).
- 45 Cancer Genome Atlas, N. Comprehensive molecular portraits of human breast tumours. *Nature* **490**, 61-70, doi:10.1038/nature11412 (2012).
- 46 Norum, J. H., Andersen, K. & Sorlie, T. Lessons learned from the intrinsic subtypes of breast cancer in the quest for precision therapy. *Br J Surg* **101**, 925-938, doi:10.1002/bjs.9562 (2014).
- 47 Banerjee, S. *et al.* Basal-like breast carcinomas: clinical outcome and response to chemotherapy. *J Clin Pathol* **59**, 729-735, doi:10.1136/jcp.2005.033043 (2006).
- 48 Benson, J. R. *et al.* Early breast cancer. *Lancet* **373**, 1463-1479, doi:10.1016/S0140-6736(09)60316-0 (2009).
- 49 Gnant, M. *et al.* Predicting distant recurrence in receptor-positive breast cancer patients with limited clinicopathological risk: using the PAM50 Risk of Recurrence score in 1478 postmenopausal patients of the ABCSG-8 trial treated with adjuvant endocrine therapy alone. *Ann Oncol* **25**, 339-345, doi:10.1093/annonc/mdt494 (2014).
- 50 Nielsen, T. *et al.* Analytical validation of the PAM50-based Prosigna Breast Cancer Prognostic Gene Signature Assay and nCounter Analysis System using formalin-fixed paraffin-embedded breast tumor specimens. *BMC Cancer* **14**, 177, doi:10.1186/1471-2407-14-177 (2014).
- 51 van 't Veer, L. J. *et al.* Gene expression profiling predicts clinical outcome of breast cancer. *Nature* **415**, 530-536, doi:10.1038/415530a (2002).
- 52 Sparano, J. A. *et al.* Prospective Validation of a 21-Gene Expression Assay in Breast Cancer. *N Engl J Med* **373**, 2005-2014, doi:10.1056/NEJMoa1510764 (2015).
- 53 Harbeck, N. & Gnant, M. Breast cancer. *Lancet* **389**, 1134-1150, doi:10.1016/S0140-6736(16)31891-8 (2017).
- 54 Hudis, C. A. Trastuzumab--mechanism of action and use in clinical practice. *N Engl J Med* **357**, 39-51, doi:10.1056/NEJMra043186 (2007).
- 55 Segovia-Mendoza, M., Gonzalez-Gonzalez, M. E., Barrera, D., Diaz, L. & Garcia-Becerra, R. Efficacy and mechanism of action of the tyrosine kinase inhibitors gefitinib, lapatinib and neratinib in the treatment of HER2-positive breast cancer: preclinical and clinical evidence. *Am J Cancer Res* **5**, 2531-2561 (2015).
- 56 Rouzier, R. *et al.* Breast cancer molecular subtypes respond differently to preoperative chemotherapy. *Clin Cancer Res* **11**, 5678-5685, doi:10.1158/1078-0432.CCR-04-2421 (2005).
- 57 de The, H. *et al.* The PML-RAR alpha fusion mRNA generated by the t(15;17) translocation in acute promyelocytic leukemia encodes a functionally altered RAR. *Cell* **66**, 675-684, doi:10.1016/0092-8674(91)90113-d (1991).

- 58 de The, H., Chomienne, C., Lanotte, M., Degos, L. & Dejean, A. The t(15;17) translocation of acute promyelocytic leukaemia fuses the retinoic acid receptor alpha gene to a novel transcribed locus. *Nature* **347**, 558-561, doi:10.1038/347558a0 (1990).
- 59 Fagioli, M. *et al.* Alternative splicing of PML transcripts predicts coexpression of several carboxy-terminally different protein isoforms. *Oncogene* **7**, 1083-1091 (1992).
- 60 Jensen, K., Shiels, C. & Freemont, P. S. PML protein isoforms and the RBCC/TRIM motif. *Oncogene* **20**, 7223-7233, doi:10.1038/sj.onc.1204765 (2001).
- 61 Alcalay, M. *et al.* The promyelocytic leukemia gene product (PML) forms stable complexes with the retinoblastoma protein. *Mol Cell Biol* **18**, 1084-1093, doi:10.1128/mcb.18.2.1084 (1998).
- 62 Fogal, V. *et al.* Regulation of p53 activity in nuclear bodies by a specific PML isoform. *EMBO J* **19**, 6185-6195, doi:10.1093/emboj/19.22.6185 (2000).
- 63 Bernardi, R. & Pandolfi, P. P. Structure, dynamics and functions of promyelocytic leukaemia nuclear bodies. *Nat Rev Mol Cell Biol* **8**, 1006-1016, doi:10.1038/nrm2277 (2007).
- 64 Dellaire, G. & Bazett-Jones, D. P. PML nuclear bodies: dynamic sensors of DNA damage and cellular stress. *Bioessays* **26**, 963-977, doi:10.1002/bies.20089 (2004).
- 65 Gao, C. *et al.* Histone deacetylase 7 promotes PML sumoylation and is essential for PML nuclear body formation. *Mol Cell Biol* **28**, 5658-5667, doi:10.1128/MCB.00874-08 (2008).
- 66 Lallemand-Breitenbach, V. & de The, H. PML nuclear bodies. *Cold Spring Harb Perspect Biol* **2**, a000661, doi:10.1101/cshperspect.a000661 (2010).
- 67 Zhong, S. *et al.* Role of SUMO-1-modified PML in nuclear body formation. *Blood* **95**, 2748-2752 (2000).
- 68 Stadler, M. *et al.* Transcriptional induction of the PML growth suppressor gene by interferons is mediated through an ISRE and a GAS element. *Oncogene* **11**, 2565-2573 (1995).
- 69 Nason-Burchenal, K. *et al.* Interferon augments PML and PML/RAR alpha expression in normal myeloid and acute promyelocytic cells and cooperates with all-trans retinoic acid to induce maturation of a retinoid-resistant promyelocytic cell line. *Blood* **88**, 3926-3936 (1996).
- 70 Ferbeyre, G. *et al.* PML is induced by oncogenic ras and promotes premature senescence. *Genes Dev* **14**, 2015-2027 (2000).
- 71 de Stanchina, E. *et al.* PML is a direct p53 target that modulates p53 effector functions. *Mol Cell* **13**, 523-535, doi:10.1016/s1097-2765(04)00062-0 (2004).
- 72 Bellodi, C. *et al.* A cytoplasmic PML mutant inhibits p53 function. *Cell Cycle* **5**, 2688-2692, doi:10.4161/cc.5.22.3504 (2006).
- 73 Ishov, A. M. *et al.* PML is critical for ND10 formation and recruits the PML-interacting protein daxx to this nuclear structure when modified by SUMO-1. *J Cell Biol* **147**, 221-234, doi:10.1083/jcb.147.2.221 (1999).
- 74 Shen, T. H., Lin, H. K., Scaglioni, P. P., Yung, T. M. & Pandolfi, P. P. The mechanisms of PML-nuclear body formation. *Mol Cell* **24**, 331-339, doi:10.1016/j.molcel.2006.09.013 (2006).
- 75 Hayakawa, F. & Privalsky, M. L. Phosphorylation of PML by mitogen-activated protein kinases plays a key role in arsenic trioxide-mediated apoptosis. *Cancer Cell* **5**, 389-401, doi:10.1016/s1535-6108(04)00082-0 (2004).
- 76 Bernardi, R. *et al.* PML regulates p53 stability by sequestering Mdm2 to the nucleolus. *Nat Cell Biol* **6**, 665-672, doi:10.1038/ncb1147 (2004).
- 77 Yang, S., Kuo, C., Bisi, J. E. & Kim, M. K. PML-dependent apoptosis after DNA damage is regulated by the checkpoint kinase hCds1/Chk2. *Nat Cell Biol* **4**, 865-870, doi:10.1038/ncb869 (2002).
- 78 Scaglioni, P. P. *et al.* A CK2-dependent mechanism for degradation of the PML tumor suppressor. *Cell* **126**, 269-283, doi:10.1016/j.cell.2006.05.041 (2006).

- 79 Tatham, M. H. *et al.* RNF4 is a poly-SUMO-specific E3 ubiquitin ligase required for arsenic-induced PML degradation. *Nat Cell Biol* **10**, 538-546, doi:10.1038/ncb1716 (2008).
- 80 Vallian, S. *et al.* Modulation of Fos-mediated AP-1 transcription by the promyelocytic leukemia protein. *Oncogene* **16**, 2843-2853, doi:10.1038/sj.onc.1201837 (1998).
- 81 Shima, Y. *et al.* PML activates transcription by protecting HIPK2 and p300 from SCFFbx3-mediated degradation. *Mol Cell Biol* **28**, 7126-7138, doi:10.1128/MCB.00897-08 (2008).
- 82 Vallian, S., Chin, K. V. & Chang, K. S. The promyelocytic leukemia protein interacts with Sp1 and inhibits its transactivation of the epidermal growth factor receptor promoter. *Mol Cell Biol* **18**, 7147-7156, doi:10.1128/mcb.18.12.7147 (1998).
- 83 Vallian, S. *et al.* Transcriptional repression by the promyelocytic leukemia protein, PML. *Exp Cell Res* **237**, 371-382, doi:10.1006/excr.1997.3801 (1997).
- 84 Condemine, W. *et al.* Characterization of endogenous human promyelocytic leukemia isoforms. *Cancer Res* **66**, 6192-6198, doi:10.1158/0008-5472.CAN-05-3792 (2006).
- 85 Zhong, S., Salomoni, P. & Pandolfi, P. P. The transcriptional role of PML and the nuclear body. *Nat Cell Biol* **2**, E85-90, doi:10.1038/35010583 (2000).
- 86 Kumar, P. P. *et al.* Functional interaction between PML and SATB1 regulates chromatin-loop architecture and transcription of the MHC class I locus. *Nat Cell Biol* **9**, 45-56, doi:10.1038/ncb1516 (2007).
- 87 Boe, S. O. *et al.* Promyelocytic leukemia nuclear bodies are predetermined processing sites for damaged DNA. *J Cell Sci* **119**, 3284-3295, doi:10.1242/jcs.03068 (2006).
- 88 Eladad, S. *et al.* Intra-nuclear trafficking of the BLM helicase to DNA damage-induced foci is regulated by SUMO modification. *Hum Mol Genet* **14**, 1351-1365, doi:10.1093/hmg/ddi145 (2005).
- 89 Moller, A. *et al.* PML is required for homeodomain-interacting protein kinase 2 (HIPK2)-mediated p53 phosphorylation and cell cycle arrest but is dispensable for the formation of HIPK domains. *Cancer Res* **63**, 4310-4314 (2003).
- 90 Pearson, M. *et al.* PML regulates p53 acetylation and premature senescence induced by oncogenic Ras. *Nature* **406**, 207-210, doi:10.1038/35018127 (2000).
- 91 Kurki, S., Latonen, L. & Laiho, M. Cellular stress and DNA damage invoke temporally distinct Mdm2, p53 and PML complexes and damage-specific nuclear relocalization. *J Cell Sci* **116**, 3917-3925, doi:10.1242/jcs.00714 (2003).
- 92 Takahashi, Y., Lallemand-Breitenbach, V., Zhu, J. & de The, H. PML nuclear bodies and apoptosis. *Oncogene* **23**, 2819-2824, doi:10.1038/sj.onc.1207533 (2004).
- 93 Crowder, C., Dahle, O., Davis, R. E., Gabrielsen, O. S. & Rudikoff, S. PML mediates IFN-alpha-induced apoptosis in myeloma by regulating TRAIL induction. *Blood* **105**, 1280-1287, doi:10.1182/blood-2004-04-1614 (2005).
- 94 Wang, Z. G. *et al.* PML is essential for multiple apoptotic pathways. *Nat Genet* **20**, 266-272, doi:10.1038/3073 (1998).
- 95 Zhang, R. *et al.* Formation of MacroH2A-containing senescence-associated heterochromatin foci and senescence driven by ASF1a and HIRA. *Dev Cell* **8**, 19-30, doi:10.1016/j.devcel.2004.10.019 (2005).
- 96 McNally, B. A., Trgovcich, J., Maul, G. G., Liu, Y. & Zheng, P. A role for cytoplasmic PML in cellular resistance to viral infection. *PLoS One* **3**, e2277, doi:10.1371/journal.pone.0002277 (2008).
- 97 Gurrieri, C. *et al.* Loss of the tumor suppressor PML in human cancers of multiple histologic origins. *J Natl Cancer Inst* **96**, 269-279, doi:10.1093/jnci/djh043 (2004).
- 98 Ito, K. *et al.* PML targeting eradicates quiescent leukaemia-initiating cells. *Nature* **453**, 1072-1078, doi:10.1038/nature07016 (2008).
- 99 Ito, K. *et al.* A PML-PPAR-delta pathway for fatty acid oxidation regulates hematopoietic stem cell maintenance. *Nat Med* **18**, 1350-1358, doi:10.1038/nm.2882 (2012).

- 100 Carracedo, A. *et al.* A metabolic prosurvival role for PML in breast cancer. *J Clin Invest* **122**, 3088-3100, doi:10.1172/JCI62129 (2012).
- 101 Martin-Martin, N. *et al.* Stratification and therapeutic potential of PML in metastatic breast cancer. *Nat Commun* **7**, 12595, doi:10.1038/ncomms12595 (2016).
- 102 Ponente, M. *et al.* PML promotes metastasis of triple-negative breast cancer through transcriptional regulation of HIF1A target genes. *JCI Insight* **2**, e87380, doi:10.1172/jci.insight.87380 (2017).
- 103 Martin-Martin, N., Sutherland, J. D. & Carracedo, A. PML: Not all about Tumor Suppression. *Front Oncol* **3**, 200, doi:10.3389/fonc.2013.00200 (2013).
- 104 Hayflick, L. & Moorhead, P. S. The serial cultivation of human diploid cell strains. *Exp Cell Res* **25**, 585-621, doi:10.1016/0014-4827(61)90192-6 (1961).
- 105 Chen, Z. *et al.* Crucial role of p53-dependent cellular senescence in suppression of Pten-deficient tumorigenesis. *Nature* **436**, 725-730, doi:10.1038/nature03918 (2005).
- 106 Majumder, P. K. *et al.* A prostatic intraepithelial neoplasia-dependent p27 Kip1 checkpoint induces senescence and inhibits cell proliferation and cancer progression. *Cancer Cell* **14**, 146-155, doi:10.1016/j.ccr.2008.06.002 (2008).
- 107 Childs, B. G., Durik, M., Baker, D. J. & van Deursen, J. M. Cellular senescence in aging and age-related disease: from mechanisms to therapy. *Nat Med* **21**, 1424-1435, doi:10.1038/nm.4000 (2015).
- 108 Lecot, P., Alimirah, F., Desprez, P. Y., Campisi, J. & Wiley, C. Context-dependent effects of cellular senescence in cancer development. *Br J Cancer* **114**, 1180-1184, doi:10.1038/bjc.2016.115 (2016).
- 109 Sharpless, N. E. & Sherr, C. J. Forging a signature of in vivo senescence. *Nat Rev Cancer* **15**, 397-408, doi:10.1038/nrc3960 (2015).
- 110 d'Adda di Fagagna, F. *et al.* A DNA damage checkpoint response in telomere-initiated senescence. *Nature* **426**, 194-198, doi:10.1038/nature02118 (2003).
- 111 Petrova, N. V., Velichko, A. K., Razin, S. V. & Kantidze, O. L. Small molecule compounds that induce cellular senescence. *Aging Cell* **15**, 999-1017, doi:10.1111/accel.12518 (2016).
- 112 Herbig, U., Jobling, W. A., Chen, B. P., Chen, D. J. & Sedivy, J. M. Telomere shortening triggers senescence of human cells through a pathway involving ATM, p53, and p21(CIP1), but not p16(INK4a). *Mol Cell* **14**, 501-513, doi:10.1016/s1097-2765(04)00256-4 (2004).
- 113 Di Leonardo, A., Linke, S. P., Clarkin, K. & Wahl, G. M. DNA damage triggers a prolonged p53-dependent G1 arrest and long-term induction of Cip1 in normal human fibroblasts. *Genes Dev* **8**, 2540-2551, doi:10.1101/gad.8.21.2540 (1994).
- 114 Jacobs, J. J. & de Lange, T. Significant role for p16INK4a in p53-independent telomere-directed senescence. *Curr Biol* **14**, 2302-2308, doi:10.1016/j.cub.2004.12.025 (2004).
- 115 Serrano, M., Lin, A. W., McCurrach, M. E., Beach, D. & Lowe, S. W. Oncogenic ras provokes premature cell senescence associated with accumulation of p53 and p16INK4a. *Cell* **88**, 593-602, doi:10.1016/s0092-8674(00)81902-9 (1997).
- 116 Zhu, J., Woods, D., McMahon, M. & Bishop, J. M. Senescence of human fibroblasts induced by oncogenic Raf. *Genes Dev* **12**, 2997-3007, doi:10.1101/gad.12.19.2997 (1998).
- 117 Di Micco, R. *et al.* Oncogene-induced senescence is a DNA damage response triggered by DNA hyper-replication. *Nature* **444**, 638-642, doi:10.1038/nature05327 (2006).
- 118 Alimonti, A. *et al.* A novel type of cellular senescence that can be enhanced in mouse models and human tumor xenografts to suppress prostate tumorigenesis. *J Clin Invest* **120**, 681-693, doi:10.1172/JCI40535 (2010).
- 119 Lee, A. C. *et al.* Ras proteins induce senescence by altering the intracellular levels of reactive oxygen species. *J Biol Chem* **274**, 7936-7940, doi:10.1074/jbc.274.12.7936 (1999).
- 120 Macip, S. *et al.* Inhibition of p21-mediated ROS accumulation can rescue p21-induced senescence. *EMBO J* **21**, 2180-2188, doi:10.1093/emboj/21.9.2180 (2002).

- 121 Moiseeva, O., Mallette, F. A., Mukhopadhyay, U. K., Moores, A. & Ferbeyre, G. DNA damage signaling and p53-dependent senescence after prolonged beta-interferon stimulation. *Mol Biol Cell* **17**, 1583-1592, doi:10.1091/mbc.e05-09-0858 (2006).
- 122 Munro, J., Barr, N. I., Ireland, H., Morrison, V. & Parkinson, E. K. Histone deacetylase inhibitors induce a senescence-like state in human cells by a p16-dependent mechanism that is independent of a mitotic clock. *Exp Cell Res* **295**, 525-538, doi:10.1016/j.yexcr.2004.01.017 (2004).
- 123 Ogryzko, V. V., Hirai, T. H., Russanova, V. R., Barbie, D. A. & Howard, B. H. Human fibroblast commitment to a senescence-like state in response to histone deacetylase inhibitors is cell cycle dependent. *Mol Cell Biol* **16**, 5210-5218, doi:10.1128/mcb.16.9.5210 (1996).
- 124 Herranz, N. & Gil, J. Mechanisms and functions of cellular senescence. *J Clin Invest* **128**, 1238-1246, doi:10.1172/JCI95148 (2018).
- 125 Althubiti, M. *et al.* Characterization of novel markers of senescence and their prognostic potential in cancer. *Cell Death Dis* **5**, e1528, doi:10.1038/cddis.2014.489 (2014).
- 126 Cho, S. & Hwang, E. S. Status of mTOR activity may phenotypically differentiate senescence and quiescence. *Mol Cells* **33**, 597-604, doi:10.1007/s10059-012-0042-1 (2012).
- 127 Dimri, G. P. *et al.* A biomarker that identifies senescent human cells in culture and in aging skin in vivo. *Proc Natl Acad Sci U S A* **92**, 9363-9367, doi:10.1073/pnas.92.20.9363 (1995).
- 128 Freund, A., Laberge, R. M., Demaria, M. & Campisi, J. Lamin B1 loss is a senescence-associated biomarker. *Mol Biol Cell* **23**, 2066-2075, doi:10.1091/mbc.E11-10-0884 (2012).
- 129 Chandra, T. *et al.* Independence of repressive histone marks and chromatin compaction during senescent heterochromatic layer formation. *Mol Cell* **47**, 203-214, doi:10.1016/j.molcel.2012.06.010 (2012).
- 130 Moiseeva, O., Bourdeau, V., Roux, A., Deschenes-Simard, X. & Ferbeyre, G. Mitochondrial dysfunction contributes to oncogene-induced senescence. *Mol Cell Biol* **29**, 4495-4507, doi:10.1128/MCB.01868-08 (2009).
- 131 Tai, H. *et al.* Autophagy impairment with lysosomal and mitochondrial dysfunction is an important characteristic of oxidative stress-induced senescence. *Autophagy* **13**, 99-113, doi:10.1080/15548627.2016.1247143 (2017).
- 132 Lee, S. *et al.* Mitochondrial fission and fusion mediators, hFis1 and OPA1, modulate cellular senescence. *J Biol Chem* **282**, 22977-22983, doi:10.1074/jbc.M700679200 (2007).
- 133 Besson, A., Dowdy, S. F. & Roberts, J. M. CDK inhibitors: cell cycle regulators and beyond. *Dev Cell* **14**, 159-169, doi:10.1016/j.devcel.2008.01.013 (2008).
- 134 Sherr, C. J. & Roberts, J. M. CDK inhibitors: positive and negative regulators of G1-phase progression. *Genes Dev* **13**, 1501-1512, doi:10.1101/gad.13.12.1501 (1999).
- 135 Nardella, C., Clohessy, J. G., Alimonti, A. & Pandolfi, P. P. Pro-senescence therapy for cancer treatment. *Nat Rev Cancer* **11**, 503-511, doi:10.1038/nrc3057 (2011).
- 136 Baker, D. J. *et al.* Clearance of p16Ink4a-positive senescent cells delays ageing-associated disorders. *Nature* **479**, 232-236, doi:10.1038/nature10600 (2011).
- 137 Burd, C. E. *et al.* Monitoring tumorigenesis and senescence in vivo with a p16(INK4a)-luciferase model. *Cell* **152**, 340-351, doi:10.1016/j.cell.2012.12.010 (2013).
- 138 Campisi, J. & d'Adda di Fagagna, F. Cellular senescence: when bad things happen to good cells. *Nat Rev Mol Cell Biol* **8**, 729-740, doi:10.1038/nrm2233 (2007).
- 139 Jackson, J. G. & Pereira-Smith, O. M. p53 is preferentially recruited to the promoters of growth arrest genes p21 and GADD45 during replicative senescence of normal human fibroblasts. *Cancer Res* **66**, 8356-8360, doi:10.1158/0008-5472.CAN-06-1752 (2006).
- 140 Lin, H. K. *et al.* Skp2 targeting suppresses tumorigenesis by Arf-p53-independent cellular senescence. *Nature* **464**, 374-379, doi:10.1038/nature08815 (2010).

- 141 Coppe, J. P., Desprez, P. Y., Krtolica, A. & Campisi, J. The senescence-associated secretory phenotype: the dark side of tumor suppression. *Annu Rev Pathol* **5**, 99-118, doi:10.1146/annurev-pathol-121808-102144 (2010).
- 142 Coppe, J. P. *et al.* Senescence-associated secretory phenotypes reveal cell-nonautonomous functions of oncogenic RAS and the p53 tumor suppressor. *PLoS Biol* **6**, 2853-2868, doi:10.1371/journal.pbio.0060301 (2008).
- 143 Lou, Z. & Chen, J. Cellular senescence and DNA repair. *Exp Cell Res* **312**, 2641-2646, doi:10.1016/j.yexcr.2006.06.009 (2006).
- 144 Yosef, R. *et al.* Directed elimination of senescent cells by inhibition of BCL-W and BCL-XL. *Nat Commun* **7**, 11190, doi:10.1038/ncomms11190 (2016).
- 145 Weinstein, I. B. Cancer. Addiction to oncogenes--the Achilles heel of cancer. *Science* **297**, 63-64, doi:10.1126/science.1073096 (2002).
- 146 Vennstrom, B., Sheiness, D., Zabielski, J. & Bishop, J. M. Isolation and characterization of c-myc, a cellular homolog of the oncogene (v-myc) of avian myelocytomatosis virus strain 29. *J Virol* **42**, 773-779 (1982).
- 147 Dang, C. V. *et al.* The c-Myc target gene network. *Semin Cancer Biol* **16**, 253-264, doi:10.1016/j.semcan.2006.07.014 (2006).
- 148 Blackwood, E. M., Kretzner, L. & Eisenman, R. N. Myc and Max function as a nucleoprotein complex. *Curr Opin Genet Dev* **2**, 227-235, doi:10.1016/s0959-437x(05)80278-3 (1992).
- 149 Nesbit, C. E., Tersak, J. M. & Prochownik, E. V. MYC oncogenes and human neoplastic disease. *Oncogene* **18**, 3004-3016, doi:10.1038/sj.onc.1202746 (1999).
- 150 Beroukhim, R. *et al.* The landscape of somatic copy-number alteration across human cancers. *Nature* **463**, 899-905, doi:10.1038/nature08822 (2010).
- 151 Boxer, L. M. & Dang, C. V. Translocations involving c-myc and c-myc function. *Oncogene* **20**, 5595-5610, doi:10.1038/sj.onc.1204595 (2001).
- 152 Pelengaris, S., Littlewood, T., Khan, M., Elia, G. & Evan, G. Reversible activation of c-Myc in skin: induction of a complex neoplastic phenotype by a single oncogenic lesion. *Mol Cell* **3**, 565-577, doi:10.1016/s1097-2765(00)80350-0 (1999).
- 153 Felsher, D. W. & Bishop, J. M. Reversible tumorigenesis by MYC in hematopoietic lineages. *Mol Cell* **4**, 199-207, doi:10.1016/s1097-2765(00)80367-6 (1999).
- 154 Pelengaris, S., Khan, M. & Evan, G. I. Suppression of Myc-induced apoptosis in beta cells exposes multiple oncogenic properties of Myc and triggers carcinogenic progression. *Cell* **109**, 321-334, doi:10.1016/s0092-8674(02)00738-9 (2002).
- 155 Wu, C. H. *et al.* Cellular senescence is an important mechanism of tumor regression upon c-Myc inactivation. *Proc Natl Acad Sci U S A* **104**, 13028-13033, doi:10.1073/pnas.0701953104 (2007).
- 156 Huettner, C. S., Zhang, P., Van Etten, R. A. & Tenen, D. G. Reversibility of acute B-cell leukaemia induced by BCR-ABL1. *Nat Genet* **24**, 57-60, doi:10.1038/71691 (2000).
- 157 Chin, L. *et al.* Essential role for oncogenic Ras in tumour maintenance. *Nature* **400**, 468-472, doi:10.1038/22788 (1999).
- 158 Wiederschain, D. *et al.* Single-vector inducible lentiviral RNAi system for oncology target validation. *Cell Cycle* **8**, 498-504, doi:10.4161/cc.8.3.7701 (2009).
- 159 Darzynkiewicz, Z. & Juan, G. Analysis of DNA content and BrdU incorporation. *Curr Protoc Cytom* **Chapter 7**, Unit 7 7, doi:10.1002/0471142956.cy0707s02 (2001).
- 160 Gratzner, H. G. Monoclonal antibody to 5-bromo- and 5-iododeoxyuridine: A new reagent for detection of DNA replication. *Science* **218**, 474-475, doi:10.1126/science.7123245 (1982).
- 161 Diaz, G., Liu, S., Isola, R., Diana, A. & Falchi, A. M. Mitochondrial localization of reactive oxygen species by dihydrofluorescein probes. *Histochem Cell Biol* **120**, 319-325, doi:10.1007/s00418-003-0566-8 (2003).

- 162 Gregori, J., Villarreal, L., Sanchez, A., Baselga, J. & Villanueva, J. An effect size filter improves the reproducibility in spectral counting-based comparative proteomics. *J Proteomics* **95**, 55-65, doi:10.1016/j.jprot.2013.05.030 (2013).
- 163 Crespo, P. & Casar, B. The Chick Embryo Chorioallantoic Membrane as an in vivo Model to Study Metastasis. *Bio-protocol* **6**, e1962, doi:10.21769/BioProtoc.1962 (2016).
- 164 Curtis, C. *et al.* The genomic and transcriptomic architecture of 2,000 breast tumours reveals novel subgroups. *Nature* **486**, 346-352, doi:10.1038/nature10983 (2012).
- 165 Ivshina, A. V. *et al.* Genetic reclassification of histologic grade delineates new clinical subtypes of breast cancer. *Cancer Res* **66**, 10292-10301, doi:10.1158/0008-5472.CAN-05-4414 (2006).
- 166 Lu, X. *et al.* Predicting features of breast cancer with gene expression patterns. *Breast Cancer Res Treat* **108**, 191-201, doi:10.1007/s10549-007-9596-6 (2008).
- 167 Pawitan, Y. *et al.* Gene expression profiling spares early breast cancer patients from adjuvant therapy: derived and validated in two population-based cohorts. *Breast Cancer Res* **7**, R953-964, doi:10.1186/bcr1325 (2005).
- 168 Wang, Y. *et al.* Gene-expression profiles to predict distant metastasis of lymph-node-negative primary breast cancer. *Lancet* **365**, 671-679, doi:10.1016/S0140-6736(05)17947-1 (2005).
- 169 Villarreal, L. *et al.* Unconventional secretion is a major contributor of cancer cell line secretomes. *Mol Cell Proteomics* **12**, 1046-1060, doi:10.1074/mcp.M112.021618 (2013).
- 170 Kakizuka, A. *et al.* Chromosomal translocation t(15;17) in human acute promyelocytic leukemia fuses RAR alpha with a novel putative transcription factor, PML. *Cell* **66**, 663-674, doi:10.1016/0092-8674(91)90112-c (1991).
- 171 Chung, Y. L. & Wu, M. L. Dual oncogenic and tumor suppressor roles of the promyelocytic leukemia gene in hepatocarcinogenesis associated with hepatitis B virus surface antigen. *Oncotarget* **7**, 28393-28407, doi:10.18632/oncotarget.8613 (2016).
- 172 Liu, S. B., Shen, Z. F., Guo, Y. J., Cao, L. X. & Xu, Y. PML silencing inhibits cell proliferation and induces DNA damage in cultured ovarian cancer cells. *Biomed Rep* **7**, 29-35, doi:10.3892/br.2017.919 (2017).
- 173 Zhou, W. *et al.* Arsenic trioxide disrupts glioma stem cells via promoting PML degradation to inhibit tumor growth. *Oncotarget* **6**, 37300-37315, doi:10.18632/oncotarget.5836 (2015).
- 174 Simon, R. Bioinformatics in cancer therapeutics--hype or hope? *Nat Clin Pract Oncol* **2**, 223, doi:10.1038/ncponc0176 (2005).
- 175 Cerami, E. *et al.* The cBio cancer genomics portal: an open platform for exploring multidimensional cancer genomics data. *Cancer Discov* **2**, 401-404, doi:10.1158/2159-8290.CD-12-0095 (2012).
- 176 Cortazar, A. R. *et al.* CANCERTOOL: A Visualization and Representation Interface to Exploit Cancer Datasets. *Cancer Res* **78**, 6320-6328, doi:10.1158/0008-5472.CAN-18-1669 (2018).
- 177 Perez-Moreno, P., Brambilla, E., Thomas, R. & Soria, J. C. Squamous cell carcinoma of the lung: molecular subtypes and therapeutic opportunities. *Clin Cancer Res* **18**, 2443-2451, doi:10.1158/1078-0432.CCR-11-2370 (2012).
- 178 Guinney, J. *et al.* The consensus molecular subtypes of colorectal cancer. *Nat Med* **21**, 1350-1356, doi:10.1038/nm.3967 (2015).
- 179 Bailey, P. *et al.* Genomic analyses identify molecular subtypes of pancreatic cancer. *Nature* **531**, 47-52, doi:10.1038/nature16965 (2016).
- 180 Viale, G. The current state of breast cancer classification. *Ann Oncol* **23 Suppl 10**, x207-210, doi:10.1093/annonc/mds326 (2012).
- 181 Lakhani, S. R. *et al.* The pathology of familial breast cancer: predictive value of immunohistochemical markers estrogen receptor, progesterone receptor, HER-2, and p53

- in patients with mutations in BRCA1 and BRCA2. *J Clin Oncol* **20**, 2310-2318, doi:10.1200/JCO.2002.09.023 (2002).
- 182 Bergh, J., Norberg, T., Sjogren, S., Lindgren, A. & Holmberg, L. Complete sequencing of the p53 gene provides prognostic information in breast cancer patients, particularly in relation to adjuvant systemic therapy and radiotherapy. *Nat Med* **1**, 1029-1034, doi:10.1038/nm1095-1029 (1995).
- 183 Nogi, H. *et al.* EGFR as paradoxical predictor of chemosensitivity and outcome among triple-negative breast cancer. *Oncol Rep* **21**, 413-417 (2009).
- 184 Giovanni, J. *et al.* Establishment and characterisation of a new tumorigenic cell line with a normal karyotype derived from a human breast adenocarcinoma. *Br J Cancer* **62**, 8-13, doi:10.1038/bjc.1990.219 (1990).
- 185 Neve, R. M. *et al.* A collection of breast cancer cell lines for the study of functionally distinct cancer subtypes. *Cancer Cell* **10**, 515-527, doi:10.1016/j.ccr.2006.10.008 (2006).
- 186 Grigoriadis, A. *et al.* Molecular characterisation of cell line models for triple-negative breast cancers. *BMC Genomics* **13**, 619, doi:10.1186/1471-2164-13-619 (2012).
- 187 Cailleau, R., Young, R., Olive, M. & Reeves, W. J., Jr. Breast tumor cell lines from pleural effusions. *J Natl Cancer Inst* **53**, 661-674, doi:10.1093/jnci/53.3.661 (1974).
- 188 Rao, D. D., Senzer, N., Cleary, M. A. & Nemunaitis, J. Comparative assessment of siRNA and shRNA off target effects: what is slowing clinical development. *Cancer Gene Ther* **16**, 807-809, doi:10.1038/cgt.2009.53 (2009).
- 189 Duprez, E. *et al.* SUMO-1 modification of the acute promyelocytic leukaemia protein PML: implications for nuclear localisation. *J Cell Sci* **112 (Pt 3)**, 381-393 (1999).
- 190 Hollstein, M., Sidransky, D., Vogelstein, B. & Harris, C. C. p53 mutations in human cancers. *Science* **253**, 49-53, doi:10.1126/science.1905840 (1991).
- 191 Yang, Q. *et al.* Pharmacological inhibition of BMK1 suppresses tumor growth through promyelocytic leukemia protein. *Cancer Cell* **18**, 258-267, doi:10.1016/j.ccr.2010.08.008 (2010).
- 192 Giorgi, C. *et al.* PML regulates apoptosis at endoplasmic reticulum by modulating calcium release. *Science* **330**, 1247-1251, doi:10.1126/science.1189157 (2010).
- 193 Jin, Z. & El-Deiry, W. S. Overview of cell death signaling pathways. *Cancer Biol Ther* **4**, 139-163, doi:10.4161/cbt.4.2.1508 (2005).
- 194 Kaufmann, S. H., Desnoyers, S., Ottaviano, Y., Davidson, N. E. & Poirier, G. G. Specific proteolytic cleavage of poly(ADP-ribose) polymerase: an early marker of chemotherapy-induced apoptosis. *Cancer Res* **53**, 3976-3985 (1993).
- 195 Kuilman, T., Michaloglou, C., Mooi, W. J. & Peeper, D. S. The essence of senescence. *Genes Dev* **24**, 2463-2479, doi:10.1101/gad.1971610 (2010).
- 196 Hernandez-Segura, A., Nehme, J. & Demaria, M. Hallmarks of Cellular Senescence. *Trends Cell Biol* **28**, 436-453, doi:10.1016/j.tcb.2018.02.001 (2018).
- 197 Shimi, T. *et al.* The role of nuclear lamin B1 in cell proliferation and senescence. *Genes Dev* **25**, 2579-2593, doi:10.1101/gad.179515.111 (2011).
- 198 Niwa-Kawakita, M. *et al.* PML is a ROS sensor activating p53 upon oxidative stress. *J Exp Med* **214**, 3197-3206, doi:10.1084/jem.20160301 (2017).
- 199 Gentric, G. *et al.* PML-Regulated Mitochondrial Metabolism Enhances Chemosensitivity in Human Ovarian Cancers. *Cell Metab* **29**, 156-173 e110, doi:10.1016/j.cmet.2018.09.002 (2019).
- 200 Kosar, M. *et al.* Senescence-associated heterochromatin foci are dispensable for cellular senescence, occur in a cell type- and insult-dependent manner and follow expression of p16(ink4a). *Cell Cycle* **10**, 457-468, doi:10.4161/cc.10.3.14707 (2011).
- 201 Narita, M. *et al.* Rb-mediated heterochromatin formation and silencing of E2F target genes during cellular senescence. *Cell* **113**, 703-716, doi:10.1016/s0092-8674(03)00401-x (2003).

- 202 Kapoor, A. *et al.* The histone variant macroH2A suppresses melanoma progression through regulation of CDK8. *Nature* **468**, 1105-1109, doi:10.1038/nature09590 (2010).
- 203 Novikov, L. *et al.* QKI-mediated alternative splicing of the histone variant MacroH2A1 regulates cancer cell proliferation. *Mol Cell Biol* **31**, 4244-4255, doi:10.1128/MCB.05244-11 (2011).
- 204 Dorr, J. R. *et al.* Synthetic lethal metabolic targeting of cellular senescence in cancer therapy. *Nature* **501**, 421-425, doi:10.1038/nature12437 (2013).
- 205 Coppe, J. P. *et al.* Tumor suppressor and aging biomarker p16(INK4a) induces cellular senescence without the associated inflammatory secretory phenotype. *J Biol Chem* **286**, 36396-36403, doi:10.1074/jbc.M111.257071 (2011).
- 206 Di Mitri, D. *et al.* Re-education of Tumor-Associated Macrophages by CXCR2 Blockade Drives Senescence and Tumor Inhibition in Advanced Prostate Cancer. *Cell Rep* **28**, 2156-2168 e2155, doi:10.1016/j.celrep.2019.07.068 (2019).
- 207 Di Mitri, D. *et al.* Tumour-infiltrating Gr-1+ myeloid cells antagonize senescence in cancer. *Nature* **515**, 134-137, doi:10.1038/nature13638 (2014).
- 208 Revandkar, A. *et al.* Inhibition of Notch pathway arrests PTEN-deficient advanced prostate cancer by triggering p27-driven cellular senescence. *Nat Commun* **7**, 13719, doi:10.1038/ncomms13719 (2016).
- 209 Toso, A. *et al.* Enhancing chemotherapy efficacy in Pten-deficient prostate tumors by activating the senescence-associated antitumor immunity. *Cell Rep* **9**, 75-89, doi:10.1016/j.celrep.2014.08.044 (2014).
- 210 Deryugina, E. I. & Quigley, J. P. Chick embryo chorioallantoic membrane model systems to study and visualize human tumor cell metastasis. *Histochem Cell Biol* **130**, 1119-1130, doi:10.1007/s00418-008-0536-2 (2008).
- 211 Herrmann, A., Moss, D. & See, V. The Chorioallantoic Membrane of the Chick Embryo to Assess Tumor Formation and Metastasis. *Methods Mol Biol* **1464**, 97-105, doi:10.1007/978-1-4939-3999-2_9 (2016).
- 212 Ribatti, D. The chick embryo chorioallantoic membrane (CAM) assay. *Reprod Toxicol* **70**, 97-101, doi:10.1016/j.reprotox.2016.11.004 (2017).
- 213 Schmitt, C. A. *et al.* A senescence program controlled by p53 and p16INK4a contributes to the outcome of cancer therapy. *Cell* **109**, 335-346, doi:10.1016/s0092-8674(02)00734-1 (2002).
- 214 Hollestelle, A. *et al.* Distinct gene mutation profiles among luminal-type and basal-type breast cancer cell lines. *Breast Cancer Res Treat* **121**, 53-64, doi:10.1007/s10549-009-0460-8 (2010).
- 215 Esposito, V. *et al.* Prognostic role of the cyclin-dependent kinase inhibitor p27 in non-small cell lung cancer. *Cancer Res* **57**, 3381-3385 (1997).
- 216 Tsihlias, J. *et al.* Loss of cyclin-dependent kinase inhibitor p27Kip1 is a novel prognostic factor in localized human prostate adenocarcinoma. *Cancer Res* **58**, 542-548 (1998).
- 217 Masciullo, V. *et al.* Frequent loss of expression of the cyclin-dependent kinase inhibitor p27 in epithelial ovarian cancer. *Cancer Res* **59**, 3790-3794 (1999).
- 218 Catzavelos, C. *et al.* Decreased levels of the cell-cycle inhibitor p27Kip1 protein: prognostic implications in primary breast cancer. *Nat Med* **3**, 227-230, doi:10.1038/nm0297-227 (1997).
- 219 Porter, P. L. *et al.* Expression of cell-cycle regulators p27Kip1 and cyclin E, alone and in combination, correlate with survival in young breast cancer patients. *Nat Med* **3**, 222-225, doi:10.1038/nm0297-222 (1997).
- 220 Tan, P. *et al.* The cell cycle inhibitor p27 is an independent prognostic marker in small (T1a,b) invasive breast carcinomas. *Cancer Res* **57**, 1259-1263 (1997).

- 221 Barbareschi, M. *et al.* p27(kip1) expression in breast carcinomas: an immunohistochemical study on 512 patients with long-term follow-up. *Int J Cancer* **89**, 236-241 (2000).
- 222 Leivonen, M., Nordling, S., Lundin, J., von Boguslawski, K. & Haglund, C. p27 expression correlates with short-term, but not with long-term prognosis in breast cancer. *Breast Cancer Res Treat* **67**, 15-22, doi:10.1023/a:1010623326118 (2001).
- 223 Spataro, V. J. *et al.* Decreased immunoreactivity for p27 protein in patients with early-stage breast carcinoma is correlated with HER-2/neu overexpression and with benefit from one course of perioperative chemotherapy in patients with negative lymph node status: results from International Breast Cancer Study Group Trial V. *Cancer* **97**, 1591-1600, doi:10.1002/cncr.11224 (2003).
- 224 Khan, F., Ricks-Santi, L. J., Zafar, R., Kanaan, Y. & Naab, T. Expression of p27 and c-Myc by immunohistochemistry in breast ductal cancers in African American women. *Ann Diagn Pathol* **34**, 170-174, doi:10.1016/j.anndiagpath.2018.03.013 (2018).
- 225 Chin, Y. R. *et al.* Targeting Akt3 signaling in triple-negative breast cancer. *Cancer Res* **74**, 964-973, doi:10.1158/0008-5472.CAN-13-2175 (2014).
- 226 Song, W. *et al.* Targeting EphA2 impairs cell cycle progression and growth of basal-like/triple-negative breast cancers. *Oncogene* **36**, 5620-5630, doi:10.1038/onc.2017.170 (2017).
- 227 Hnit, S. S. *et al.* p27(Kip1) signaling: Transcriptional and post-translational regulation. *Int J Biochem Cell Biol* **68**, 9-14, doi:10.1016/j.biocel.2015.08.005 (2015).
- 228 Viglietto, G., Motti, M. L. & Fusco, A. Understanding p27(kip1) deregulation in cancer: down-regulation or mislocalization. *Cell Cycle* **1**, 394-400, doi:10.4161/cc.1.6.263 (2002).
- 229 Liang, J. *et al.* PKB/Akt phosphorylates p27, impairs nuclear import of p27 and opposes p27-mediated G1 arrest. *Nat Med* **8**, 1153-1160, doi:10.1038/nm761 (2002).
- 230 Shin, I. *et al.* PKB/Akt mediates cell-cycle progression by phosphorylation of p27(Kip1) at threonine 157 and modulation of its cellular localization. *Nat Med* **8**, 1145-1152, doi:10.1038/nm759 (2002).
- 231 Viglietto, G. *et al.* Cytoplasmic relocation and inhibition of the cyclin-dependent kinase inhibitor p27(Kip1) by PKB/Akt-mediated phosphorylation in breast cancer. *Nat Med* **8**, 1136-1144, doi:10.1038/nm762 (2002).
- 232 Horiuchi, D. *et al.* PIM1 kinase inhibition as a targeted therapy against triple-negative breast tumors with elevated MYC expression. *Nat Med* **22**, 1321-1329, doi:10.1038/nm.4213 (2016).
- 233 Orlando, S. *et al.* p27Kip1 and p21Cip1 collaborate in the regulation of transcription by recruiting cyclin-Cdk complexes on the promoters of target genes. *Nucleic Acids Res* **43**, 6860-6873, doi:10.1093/nar/gkv593 (2015).
- 234 Pippa, R. *et al.* p27Kip1 represses transcription by direct interaction with p130/E2F4 at the promoters of target genes. *Oncogene* **31**, 4207-4220, doi:10.1038/onc.2011.582 (2012).
- 235 Jinno, S. *et al.* Cdc25A is a novel phosphatase functioning early in the cell cycle. *EMBO J* **13**, 1549-1556 (1994).
- 236 Ablain, J. *et al.* Activation of a promyelocytic leukemia-tumor protein 53 axis underlies acute promyelocytic leukemia cure. *Nat Med* **20**, 167-174, doi:10.1038/nm.3441 (2014).
- 237 Acevedo, M. *et al.* A CDK4/6-Dependent Epigenetic Mechanism Protects Cancer Cells from PML-induced Senescence. *Cancer Res* **76**, 3252-3264, doi:10.1158/0008-5472.CAN-15-2347 (2016).
- 238 Talluri, S. & Dick, F. A. The retinoblastoma protein and PML collaborate to organize heterochromatin and silence E2F-responsive genes during senescence. *Cell Cycle* **13**, 641-651, doi:10.4161/cc.27527 (2014).
- 239 Vernier, M. *et al.* Regulation of E2Fs and senescence by PML nuclear bodies. *Genes Dev* **25**, 41-50, doi:10.1101/gad.1975111 (2011).

- 240 Carey, J. P. W. *et al.* Synthetic Lethality of PARP Inhibitors in Combination with MYC Blockade Is Independent of BRCA Status in Triple-Negative Breast Cancer. *Cancer Res* **78**, 742-757, doi:10.1158/0008-5472.CAN-17-1494 (2018).
- 241 Lee, K. M. *et al.* MYC and MCL1 Cooperatively Promote Chemotherapy-Resistant Breast Cancer Stem Cells via Regulation of Mitochondrial Oxidative Phosphorylation. *Cell Metab* **26**, 633-647 e637, doi:10.1016/j.cmet.2017.09.009 (2017).
- 242 Camarda, R. *et al.* Inhibition of fatty acid oxidation as a therapy for MYC-overexpressing triple-negative breast cancer. *Nat Med* **22**, 427-432, doi:10.1038/nm.4055 (2016).
- 243 Casciano, J. C. *et al.* MYC regulates fatty acid metabolism through a multigenic program in claudin-low triple negative breast cancer. *Br J Cancer*, doi:10.1038/s41416-019-0711-3 (2020).
- 244 Yang, A. *et al.* MYC Inhibition Depletes Cancer Stem-like Cells in Triple-Negative Breast Cancer. *Cancer Res* **77**, 6641-6650, doi:10.1158/0008-5472.CAN-16-3452 (2017).
- 245 van Lohuizen, M. *et al.* Predisposition to lymphomagenesis in pim-1 transgenic mice: cooperation with c-myc and N-myc in murine leukemia virus-induced tumors. *Cell* **56**, 673-682, doi:10.1016/0092-8674(89)90589-8 (1989).
- 246 Dhanasekaran, S. M. *et al.* Delineation of prognostic biomarkers in prostate cancer. *Nature* **412**, 822-826, doi:10.1038/35090585 (2001).
- 247 Wang, J. *et al.* Pim1 kinase is required to maintain tumorigenicity in MYC-expressing prostate cancer cells. *Oncogene* **31**, 1794-1803, doi:10.1038/onc.2011.371 (2012).
- 248 Wang, J. *et al.* Pim1 kinase synergizes with c-MYC to induce advanced prostate carcinoma. *Oncogene* **29**, 2477-2487, doi:10.1038/onc.2010.10 (2010).
- 249 Braso-Maristany, F. *et al.* PIM1 kinase regulates cell death, tumor growth and chemotherapy response in triple-negative breast cancer. *Nat Med* **22**, 1303-1313, doi:10.1038/nm.4198 (2016).
- 250 Cairo, S. *et al.* PML interacts with Myc, and Myc target gene expression is altered in PML-null fibroblasts. *Oncogene* **24**, 2195-2203, doi:10.1038/sj.onc.1208338 (2005).
- 251 Wu, W. S. *et al.* The growth suppressor PML represses transcription by functionally and physically interacting with histone deacetylases. *Mol Cell Biol* **21**, 2259-2268, doi:10.1128/MCB.21.7.2259-2268.2001 (2001).
- 252 Zhang, Y., Wang, Z., Li, X. & Magnuson, N. S. Pim kinase-dependent inhibition of c-Myc degradation. *Oncogene* **27**, 4809-4819, doi:10.1038/onc.2008.123 (2008).
- 253 Yang, W. *et al.* Repression of transcription of the p27(Kip1) cyclin-dependent kinase inhibitor gene by c-Myc. *Oncogene* **20**, 1688-1702, doi:10.1038/sj.onc.1204245 (2001).
- 254 Mateyak, M. K., Obaya, A. J. & Sedivy, J. M. c-Myc regulates cyclin D-Cdk4 and -Cdk6 activity but affects cell cycle progression at multiple independent points. *Mol Cell Biol* **19**, 4672-4683, doi:10.1128/mcb.19.7.4672 (1999).
- 255 Morishita, D., Katayama, R., Sekimizu, K., Tsuruo, T. & Fujita, N. Pim kinases promote cell cycle progression by phosphorylating and down-regulating p27Kip1 at the transcriptional and posttranscriptional levels. *Cancer Res* **68**, 5076-5085, doi:10.1158/0008-5472.CAN-08-0634 (2008).
- 256 Jones, R. A. *et al.* RB1 deficiency in triple-negative breast cancer induces mitochondrial protein translation. *J Clin Invest* **126**, 3739-3757, doi:10.1172/JCI81568 (2016).
- 257 Robinson, T. J. *et al.* RB1 status in triple negative breast cancer cells dictates response to radiation treatment and selective therapeutic drugs. *PLoS One* **8**, e78641, doi:10.1371/journal.pone.0078641 (2013).
- 258 Soignet, S. L. *et al.* Complete remission after treatment of acute promyelocytic leukemia with arsenic trioxide. *N Engl J Med* **339**, 1341-1348, doi:10.1056/NEJM199811053391901 (1998).
- 259 Wang, Z. Y. & Chen, Z. Acute promyelocytic leukemia: from highly fatal to highly curable. *Blood* **111**, 2505-2515, doi:10.1182/blood-2007-07-102798 (2008).

- 260 Lallemand-Breitenbach, V. *et al.* Arsenic degrades PML or PML-RARalpha through a SUMO-triggered RNF4/ubiquitin-mediated pathway. *Nat Cell Biol* **10**, 547-555, doi:10.1038/ncb1717 (2008).
- 261 Lallemand-Breitenbach, V. *et al.* Role of promyelocytic leukemia (PML) sumolation in nuclear body formation, 11S proteasome recruitment, and As2O3-induced PML or PML/retinoic acid receptor alpha degradation. *J Exp Med* **193**, 1361-1371, doi:10.1084/jem.193.12.1361 (2001).
- 262 Cejalvo, J. M. *et al.* Intrinsic Subtypes and Gene Expression Profiles in Primary and Metastatic Breast Cancer. *Cancer Res* **77**, 2213-2221, doi:10.1158/0008-5472.CAN-16-2717 (2017).
- 263 Kreike, B. *et al.* Gene expression profiling and histopathological characterization of triple-negative/basal-like breast carcinomas. *Breast Cancer Res* **9**, R65, doi:10.1186/bcr1771 (2007).
- 264 Rakha, E. A. *et al.* Prognostic markers in triple-negative breast cancer. *Cancer* **109**, 25-32, doi:10.1002/cncr.22381 (2007).
- 265 Bertucci, F. *et al.* How basal are triple-negative breast cancers? *Int J Cancer* **123**, 236-240, doi:10.1002/ijc.23518 (2008).
- 266 Hammond, M. E. *et al.* American Society of Clinical Oncology/College of American Pathologists guideline recommendations for immunohistochemical testing of estrogen and progesterone receptors in breast cancer. *Arch Pathol Lab Med* **134**, 907-922, doi:10.1043/1543-2165-134.6.907 (2010).
- 267 Collins, L. C., Botero, M. L. & Schnitt, S. J. Bimodal frequency distribution of estrogen receptor immunohistochemical staining results in breast cancer: an analysis of 825 cases. *Am J Clin Pathol* **123**, 16-20, doi:10.1309/hcf035n9wk40etj0 (2005).
- 268 Yi, M. *et al.* Which threshold for ER positivity? a retrospective study based on 9639 patients. *Ann Oncol* **25**, 1004-1011, doi:10.1093/annonc/mdu053 (2014).
- 269 Gonzalez-Angulo, A. M. *et al.* Incidence and outcome of BRCA mutations in unselected patients with triple receptor-negative breast cancer. *Clin Cancer Res* **17**, 1082-1089, doi:10.1158/1078-0432.CCR-10-2560 (2011).
- 270 Ray Chaudhuri, A. & Nussenzweig, A. The multifaceted roles of PARP1 in DNA repair and chromatin remodelling. *Nat Rev Mol Cell Biol* **18**, 610-621, doi:10.1038/nrm.2017.53 (2017).
- 271 Bryant, H. E. *et al.* Specific killing of BRCA2-deficient tumours with inhibitors of poly(ADP-ribose) polymerase. *Nature* **434**, 913-917, doi:10.1038/nature03443 (2005).
- 272 Farmer, H. *et al.* Targeting the DNA repair defect in BRCA mutant cells as a therapeutic strategy. *Nature* **434**, 917-921, doi:10.1038/nature03445 (2005).
- 273 Robson, M. *et al.* Olaparib for Metastatic Breast Cancer in Patients with a Germline BRCA Mutation. *N Engl J Med* **377**, 523-533, doi:10.1056/NEJMoa1706450 (2017).
- 274 Tutt, A. *et al.* Oral poly(ADP-ribose) polymerase inhibitor olaparib in patients with BRCA1 or BRCA2 mutations and advanced breast cancer: a proof-of-concept trial. *Lancet* **376**, 235-244, doi:10.1016/S0140-6736(10)60892-6 (2010).
- 275 Litton, J. K. *et al.* Talazoparib in Patients with Advanced Breast Cancer and a Germline BRCA Mutation. *N Engl J Med* **379**, 753-763, doi:10.1056/NEJMoa1802905 (2018).
- 276 Rugo, H. S. *et al.* Adaptive Randomization of Veliparib-Carboplatin Treatment in Breast Cancer. *N Engl J Med* **375**, 23-34, doi:10.1056/NEJMoa1513749 (2016).
- 277 Pardoll, D. M. The blockade of immune checkpoints in cancer immunotherapy. *Nat Rev Cancer* **12**, 252-264, doi:10.1038/nrc3239 (2012).
- 278 Mittendorf, E. A. *et al.* PD-L1 expression in triple-negative breast cancer. *Cancer Immunol Res* **2**, 361-370, doi:10.1158/2326-6066.CIR-13-0127 (2014).
- 279 Sabatier, R. *et al.* Prognostic and predictive value of PDL1 expression in breast cancer. *Oncotarget* **6**, 5449-5464, doi:10.18632/oncotarget.3216 (2015).

- 280 Schmid, P. *et al.* Atezolizumab and Nab-Paclitaxel in Advanced Triple-Negative Breast Cancer. *N Engl J Med* **379**, 2108-2121, doi:10.1056/NEJMoa1809615 (2018).
- 281 Schmid, P. *et al.* Atezolizumab plus nab-paclitaxel as first-line treatment for unresectable, locally advanced or metastatic triple-negative breast cancer (IMpassion130): updated efficacy results from a randomised, double-blind, placebo-controlled, phase 3 trial. *Lancet Oncol* **21**, 44-59, doi:10.1016/S1470-2045(19)30689-8 (2020).
- 282 Corkery, B., Crown, J., Clynes, M. & O'Donovan, N. Epidermal growth factor receptor as a potential therapeutic target in triple-negative breast cancer. *Ann Oncol* **20**, 862-867, doi:10.1093/annonc/mdn710 (2009).
- 283 Carey, L. A. *et al.* TBCRC 001: randomized phase II study of cetuximab in combination with carboplatin in stage IV triple-negative breast cancer. *J Clin Oncol* **30**, 2615-2623, doi:10.1200/JCO.2010.34.5579 (2012).
- 284 Hoadley, K. A. *et al.* EGFR associated expression profiles vary with breast tumor subtype. *BMC Genomics* **8**, 258, doi:10.1186/1471-2164-8-258 (2007).
- 285 Kim, S. B. *et al.* Ipatasertib plus paclitaxel versus placebo plus paclitaxel as first-line therapy for metastatic triple-negative breast cancer (LOTUS): a multicentre, randomised, double-blind, placebo-controlled, phase 2 trial. *Lancet Oncol* **18**, 1360-1372, doi:10.1016/S1470-2045(17)30450-3 (2017).
- 286 Yunokawa, M. *et al.* Efficacy of everolimus, a novel mTOR inhibitor, against basal-like triple-negative breast cancer cells. *Cancer Sci* **103**, 1665-1671, doi:10.1111/j.1349-7006.2012.02359.x (2012).
- 287 Rego, E. M. *et al.* Role of promyelocytic leukemia (PML) protein in tumor suppression. *J Exp Med* **193**, 521-529, doi:10.1084/jem.193.4.521 (2001).
- 288 McManus, F. P. *et al.* Quantitative SUMO proteomics reveals the modulation of several PML nuclear body associated proteins and an anti-senescence function of UBC9. *Sci Rep* **8**, 7754, doi:10.1038/s41598-018-25150-z (2018).
- 289 Lallemand-Breitenbach, V., Zhu, J., Chen, Z. & de The, H. Curing APL through PML/RARA degradation by As2O3. *Trends Mol Med* **18**, 36-42, doi:10.1016/j.molmed.2011.10.001 (2012).
- 290 Delmore, J. E. *et al.* BET bromodomain inhibition as a therapeutic strategy to target c-Myc. *Cell* **146**, 904-917, doi:10.1016/j.cell.2011.08.017 (2011).
- 291 Beaulieu, M. E. *et al.* Intrinsic cell-penetrating activity propels Omomyc from proof of concept to viable anti-MYC therapy. *Sci Transl Med* **11**, doi:10.1126/scitranslmed.aar5012 (2019).
- 292 Kirschner, A. N. *et al.* PIM kinase inhibitor AZD1208 for treatment of MYC-driven prostate cancer. *J Natl Cancer Inst* **107**, doi:10.1093/jnci/dju407 (2015).
- 293 Luszczak, S. *et al.* PIM kinase inhibition: co-targeted therapeutic approaches in prostate cancer. *Signal Transduct Target Ther* **5**, 7, doi:10.1038/s41392-020-0109-y (2020).
- 294 Sachs, N. *et al.* A Living Biobank of Breast Cancer Organoids Captures Disease Heterogeneity. *Cell* **172**, 373-386 e310, doi:10.1016/j.cell.2017.11.010 (2018).
- 295 Vlachogiannis, G. *et al.* Patient-derived organoids model treatment response of metastatic gastrointestinal cancers. *Science* **359**, 920-926, doi:10.1126/science.aao2774 (2018).
- 296 Krtolica, A., Parrinello, S., Lockett, S., Desprez, P. Y. & Campisi, J. Senescent fibroblasts promote epithelial cell growth and tumorigenesis: a link between cancer and aging. *Proc Natl Acad Sci U S A* **98**, 12072-12077, doi:10.1073/pnas.211053698 (2001).
- 297 Liu, D. & Hornsby, P. J. Senescent human fibroblasts increase the early growth of xenograft tumors via matrix metalloproteinase secretion. *Cancer Res* **67**, 3117-3126, doi:10.1158/0008-5472.CAN-06-3452 (2007).
- 298 Acosta, J. C. *et al.* Chemokine signaling via the CXCR2 receptor reinforces senescence. *Cell* **133**, 1006-1018, doi:10.1016/j.cell.2008.03.038 (2008).

- 299 Kuilman, T. *et al.* Oncogene-induced senescence relayed by an interleukin-dependent inflammatory network. *Cell* **133**, 1019-1031, doi:10.1016/j.cell.2008.03.039 (2008).
- 300 Xue, W. *et al.* Senescence and tumour clearance is triggered by p53 restoration in murine liver carcinomas. *Nature* **445**, 656-660, doi:10.1038/nature05529 (2007).
- 301 Rakhra, K. *et al.* CD4(+) T cells contribute to the remodeling of the microenvironment required for sustained tumor regression upon oncogene inactivation. *Cancer Cell* **18**, 485-498, doi:10.1016/j.ccr.2010.10.002 (2010).
- 302 Marchesini, M. *et al.* PML is required for telomere stability in non-neoplastic human cells. *Oncogene* **35**, 1811-1821, doi:10.1038/onc.2015.246 (2016).
- 303 Seoane, J. *et al.* TGFbeta influences Myc, Miz-1 and Smad to control the CDK inhibitor p15INK4b. *Nat Cell Biol* **3**, 400-408, doi:10.1038/35070086 (2001).
- 304 Yang, J., Song, K., Krebs, T. L., Jackson, M. W. & Danielpour, D. Rb/E2F4 and Smad2/3 link survivin to TGF-beta-induced apoptosis and tumor progression. *Oncogene* **27**, 5326-5338, doi:10.1038/onc.2008.165 (2008).
- 305 Pierce, D. F., Jr. *et al.* Mammary tumor suppression by transforming growth factor beta 1 transgene expression. *Proc Natl Acad Sci U S A* **92**, 4254-4258, doi:10.1073/pnas.92.10.4254 (1995).
- 306 Polyak, K. *et al.* p27Kip1, a cyclin-Cdk inhibitor, links transforming growth factor-beta and contact inhibition to cell cycle arrest. *Genes Dev* **8**, 9-22, doi:10.1101/gad.8.1.9 (1994).
- 307 Gomis, R. R., Alarcon, C., Nadal, C., Van Poznak, C. & Massague, J. C/EBPbeta at the core of the TGFbeta cytostatic response and its evasion in metastatic breast cancer cells. *Cancer Cell* **10**, 203-214, doi:10.1016/j.ccr.2006.07.019 (2006).
- 308 Parvani, J. G., Galliher-Beckley, A. J., Schiemann, B. J. & Schiemann, W. P. Targeted inactivation of beta1 integrin induces beta3 integrin switching, which drives breast cancer metastasis by TGF-beta. *Mol Biol Cell* **24**, 3449-3459, doi:10.1091/mbc.E12-10-0776 (2013).
- 309 Micalizzi, D. S., Wang, C. A., Farabaugh, S. M., Schiemann, W. P. & Ford, H. L. Homeoprotein Six1 increases TGF-beta type I receptor and converts TGF-beta signaling from suppressive to supportive for tumor growth. *Cancer Res* **70**, 10371-10380, doi:10.1158/0008-5472.CAN-10-1354 (2010).
- 310 Dalal, B. I., Keown, P. A. & Greenberg, A. H. Immunocytochemical localization of secreted transforming growth factor-beta 1 to the advancing edges of primary tumors and to lymph node metastases of human mammary carcinoma. *Am J Pathol* **143**, 381-389 (1993).
- 311 Debacq-Chainiaux, F. *et al.* Repeated exposure of human skin fibroblasts to UVB at subcytotoxic level triggers premature senescence through the TGF-beta1 signaling pathway. *J Cell Sci* **118**, 743-758, doi:10.1242/jcs.01651 (2005).
- 312 Senturk, S. *et al.* Transforming growth factor-beta induces senescence in hepatocellular carcinoma cells and inhibits tumor growth. *Hepatology* **52**, 966-974, doi:10.1002/hep.23769 (2010).
- 313 Rapisarda, V. *et al.* Integrin Beta 3 Regulates Cellular Senescence by Activating the TGF-beta Pathway. *Cell Rep* **18**, 2480-2493, doi:10.1016/j.celrep.2017.02.012 (2017).
- 314 Reimann, M. *et al.* Tumor stroma-derived TGF-beta limits myc-driven lymphomagenesis via Suv39h1-dependent senescence. *Cancer Cell* **17**, 262-272, doi:10.1016/j.ccr.2009.12.043 (2010).
- 315 van Deursen, J. M. The role of senescent cells in ageing. *Nature* **509**, 439-446, doi:10.1038/nature13193 (2014).
- 316 Demaria, M. *et al.* Cellular Senescence Promotes Adverse Effects of Chemotherapy and Cancer Relapse. *Cancer Discov* **7**, 165-176, doi:10.1158/2159-8290.CD-16-0241 (2017).
- 317 Guerrero, A. *et al.* Cardiac glycosides are broad-spectrum senolytics. *Nat Metab* **1**, 1074-1088, doi:10.1038/s42255-019-0122-z (2019).

- 318 Hickson, L. J. *et al.* Senolytics decrease senescent cells in humans: Preliminary report from a clinical trial of Dasatinib plus Quercetin in individuals with diabetic kidney disease. *EBioMedicine* **47**, 446-456, doi:10.1016/j.ebiom.2019.08.069 (2019).
- 319 Montani, D. *et al.* Pulmonary arterial hypertension in patients treated by dasatinib. *Circulation* **125**, 2128-2137, doi:10.1161/CIRCULATIONAHA.111.079921 (2012).
- 320 Tse, C. *et al.* ABT-263: a potent and orally bioavailable Bcl-2 family inhibitor. *Cancer Res* **68**, 3421-3428, doi:10.1158/0008-5472.CAN-07-5836 (2008).

Images Sources (Backgrounds)

- Biorender
- www.wallpapercave.com
- <https://angstrom3d.com/neb-catalog-images>
- www.wallpapersafari.com/

II Annex

Table A1. DepMap cell line expression values and classification based on ER, PR and Her2 status.

Cell line	TPM (log2)	ER	PR	Her2
BT20_BREAST	5,033863	-	-	-
BT549_BREAST	4,960697	-	-	-
CAL120_BREAST	3,808385	-	-	-
CAL148_BREAST	3,654206	-	-	-
CAL51_BREAST	3,600508	-	N/A	-
CAL851_BREAST	4,519793	-	-	-
DU4475_BREAST	3,349082	-	-	-
HCC1143_BREAST	5,829088	-	-	-
HCC1187_BREAST	5,475409	-	-	-
HCC1395_BREAST	5,46107	-	-	-
HCC1599_BREAST	5,640679	-	-	-
HCC1806_BREAST	3,64039	-	-	-
HCC1937_BREAST	4,759688	-	-	-
HCC2157_BREAST	4,341274	-	-	-
HCC38_BREAST	5,154211	-	-	-
HCC70_BREAST	5,032101	-	-	-
HDQP1_BREAST	4,910733	-	-	-
HMC18_BREAST	3,785551	-	-	-
HS578T_BREAST	4,655924	-	-	-
MDAMB157_BREAST	4,715344	-	-	-
MDAMB231_BREAST	5,16792	-	-	-
MDAMB436_BREAST	4,689299	-	-	-
MDAMB453_BREAST	2,185867	-	-	-
MDAMB468_BREAST	4,851999	-	-	-
AU565_BREAST	3,343408	-	-	+
HCC1419_BREAST	2,990955	-	-	+
HCC1569_BREAST	5,082362	-	-	+
HCC1954_BREAST	4,643279	-	-	+
HCC202_BREAST	3,532317	-	-	+
HCC2218_BREAST	3,145677	-	-	+
JIMT1_BREAST	5,482203	-	-	+
SKBR3_BREAST	3,139142	-	-	+
UACC893_BREAST	2,330558	-	-	+
BT474_BREAST	2,722466	+	+	+
BT483_BREAST	3,320485	+	+	-
CAMA1_BREAST	3,221877	+		-
EFM19	3,314697	+	+	-
EFM192A	3,294253	+	+	-
HCC1428_BREAST	2,914565	+	+	-
HCC1500_BREAST	3,068671	+	+	-
KPL1_BREAST	3,874797	+		-
MCF7_BREAST	3,873813	+	+	-
MDAMB134VI_BREAST	3,061776	+	-	-
MDAMB175VII_BREAST	3,560715	+	-	-
MDAMB361_BREAST	3,795975	+	+	+
MDAMB415_BREAST	4,401221	+		-
T47D_BREAST	3,612352	+	+	-
UACC812_BREAST	3,415488	+	-	+
ZR751_BREAST	3,41007	+	-	-
ZR7530_BREAST	3,404631	+	-	+

Table A2. List of differentially secreted proteins upon silencing the PML protein in MDA-MB-231 cells.

Gene Name	Positive ^a	Negative ^b	Log ₂ FC	adj p-value ^c
ACTB	65,3	15	2,168	2,65E-45
ACTG1	13,3	63,2	-2,199	3,79E-43
KRT16	9	0	37,7	8,28E-16
TUBA1C	2,2	16	-2,84	2,54E-14
KRT6C	7,3	0	30,09	7,02E-13
EEF1A1P5	6,8	0	28,27	5,16E-12
MMP1	0,2	7,7	-5,477	3,08E-11
BMP1	8	0,7	3,629	2,41E-09
MAN2A1	0	4	-32,68	1,34E-06
CLSTN3	7,5	1,2	2,729	1,45E-06
ITGB1	4	13,5	-1,71	2,59E-06
TNFRSF21	0,5	5,8	-3,5	2,66E-06
COL5A1	14,2	4,8	1,596	2,74E-06
FBN1	22,8	10,5	1,165	2,74E-06
TLN1	23,2	42,2	-0,8189	2,74E-06
SPARC	3,2	0	32,36	1,41E-05
KRT6A	3	0	28,98	2,93E-05
LTBP4	10	3	1,783	3,01E-05
SQSTM1	2,7	9,8	-1,837	3,43E-05
L1CAM	4	12,2	-1,56	4,20E-05
FRAS1	2,8	0	33,7	4,77E-05
SERPINE2	0,3	4,3	-3,656	5,65E-05
KRT7	8,5	2,3	1,909	5,90E-05
CPD	0,2	3,7	-4,414	7,44E-05
LUM	3,3	0,2	4,371	0,0001401
CPE	10,7	3,8	1,522	0,0001518
FAT1	3,8	0,3	3,568	0,0001518
TIMP3	0,3	4	-3,543	0,000152
NEU1	0,7	4,8	-2,813	0,0002139
ENPP1	1,7	7	-2,024	0,0002601
EPS8L2	2,3	0	30,54	0,0002992
ITGA3	0	2,3	-33,33	0,000455
PROS1	9	3,2	1,553	0,0005347
AKR1C1	3,5	10	-1,473	0,0005644
LTBP3	2,2	0	33,24	0,0005681
GALC	2,2	0	31,58	0,0005681
CD81	0,8	4,8	-2,492	0,0006621
IL6	0	2,2	-30,34	0,000793
ECHS1	0,3	3,3	-3,28	0,001325
SEC23A	3,2	0,3	3,295	0,001366
CFH	7,8	2,8	1,513	0,002035
SUMF2	0,3	3,2	-3,204	0,002174
EPHA2	2,7	7,8	-1,51	0,002632
KRT19	11,8	5,7	1,106	0,003352
GAS6	12,7	6,3	1,045	0,003882
LFNG	2,8	0,3	3,131	0,00403
SDCBP	0,8	4,2	-2,278	0,004093
UBE2K	2,3	0,2	3,852	0,004193
BMP4	2,3	0,2	3,851	0,004193
PYGL	3,5	8,8	-1,293	0,005184
IGFBP1	4,5	10,3	-1,151	0,006241
SAA1	0,5	3,2	-2,616	0,007954
MXRA8	3	0,5	2,629	0,008305
JAG1	3,2	8	-1,291	0,009363
CST4	2	6	-1,537	0,01085

HIST1H1C	1,5	5	-1,69	0,01406
SDC4	6,2	12,2	-0,9348	0,0169
BTF3	0,5	2,8	-2,463	0,0203
DSG2	8,2	3,8	1,136	0,0203
VASN	4	1,2	1,82	0,0205
SEMA3C	4,8	1,7	1,579	0,02166
MMP14	0,8	3,5	-2,024	0,02305
CANX	0,3	2,3	-2,76	0,02583
BSG	0,5	2,7	-2,371	0,03072
HIST2H2AA3	4,3	1,5	1,57	0,03543
HRNR	2,8	0,7	2,128	0,03625
SORT1	4,8	1,8	1,442	0,03753
COL4A2	9,3	5	0,9451	0,04005
PSMD3	1,8	5	-1,403	0,04453
SLC3A2	3,3	7,3	-1,093	0,04517
SF3B3	1	3,5	-1,765	0,04646
PIK3IP1	2	0,3	2,631	0,0493
THBS1	194,7	129	0,6395	1,69E-19
MYH9	96,3	66	0,591	2,89E-08
FLNB	138,8	107,5	0,4142	2,74E-06
KRT9	51,7	35,3	0,5922	0,0001426
HSPA5	71,3	96,3	-0,3876	0,0006753
GSN	32,2	21,2	0,6494	0,001826
AP1G1	1,8	0	30,19	0,002035
AHNAK	38	26,2	0,5821	0,002174
MATN2	0	1,8	-32,96	0,00267
CNN2	1,7	0	32,94	0,003784
PDIA4	19	30,3	-0,6292	0,004491
CTSC	12,3	21,3	-0,7452	0,006266
HYOU1	13,2	22,3	-0,7174	0,007086
HSP90AA1	71,5	92,3	-0,3232	0,008745
NAMPT	18,8	28,8	-0,5686	0,01708
KRT1	73,2	59,8	0,3355	0,01783
EFEMP1	23,2	15,5	0,625	0,01818
HSPG2	56,8	45,2	0,3767	0,0205
KRT8	21,3	14,2	0,6362	0,02239
ACBD3	1,2	0	30,92	0,02398
SEMA3B	1,2	0	32,42	0,02398
ASPH	1,2	0	28,09	0,02398
ALDH9A1	1,2	0	30,92	0,02414
KRT13	1,2	0	32,73	0,02431
HSP90B1	30,7	42,5	-0,425	0,03072
KRT2	32,5	44,3	-0,3999	0,04114
LOXL4	1	0	30,73	0,04517
SEMA7A	12,3	19,5	-0,6165	0,04517
F3	1	0	35,49	0,04517
KRT4	1	0	32,57	0,04517
GGH	12	19	-0,6172	0,04882

Notes: a: Average normalized spectral counts from cells where PML is silenced. b: Average normalized spectral counts from cells where PML is expressed. c: the adjusted p-values have been corrected for multiple hypothesis testing according to Benjamini and Hochberg.

Table A3. List of differentially secreted proteins upon silencing the PML protein in Cama-1 cells.

Gene Name	Positive ^a	Negative ^b	Log ₂ FC	adj p-value ^c
KRT16	7,5	0,2	5,853	4,92E-14
CPVL	3,5	0,2	4,754	3,52E-06
CTSB	8,3	0,5	4,343	8,77E-13
KRT6C	4,7	0,3	4,169	2,01E-07
GNPTG	2	0	34,96	0,0001193
MELTF	2	0	34,96	0,0001193
ADGRG6	3,5	0	34,14	5,65E-07
PAM	3,5	0	34,07	1,44E-07
IGF1	2	0	31,67	0,00018
DLST	2,2	0	31,57	6,54E-05
MAN2B1	2	0	30,46	0,0002208
ATP6AP1	3,8	0,3	3,795	1,23E-05
AGT	5,2	0,5	3,665	3,20E-07
IGSF8	3,2	0,3	3,464	0,0002133
PCSK1N	5	0,5	3,458	2,89E-06
GM2A	3,5	0,5	3,09	0,0001814
PPT1	5,2	0,8	2,752	2,70E-05
LAMB2	23,7	4	2,736	9,95E-23
ANXA2	2	0,3	2,691	0,01643
CTSA	6	1,2	2,552	9,97E-06
PROS1	2,2	0,5	2,381	0,01638
KLK6	2	0,5	2,361	0,01909
LGMN	3	0,7	2,335	0,00539
CD109	4,8	1,3	2,219	0,0002133
CTSL	28,7	7,3	2,217	2,94E-22
SEMA3C	4,2	1	2,108	0,002333
GBA	5,3	1,5	2,107	0,0002133
CD9	3,7	1	2,068	0,004037
THRAP3	2	0,5	2,066	0,04868
SUMF2	4,5	1,3	2,05	0,001021
SCG3	2,2	0,7	2,017	0,03138
PLOD1	15,2	4,5	2,006	2,10E-10
ATP5F1B	8,3	2,5	1,954	9,74E-06
HSPG2	3,2	1	1,947	0,009834
SPP1	2	0,7	1,946	0,04365
CTSC	2,5	0,8	1,927	0,02292
HEXA	12,2	3,8	1,906	7,51E-08
IGSF3	4	1,3	1,861	0,004482
PTPRF	4,8	1,3	1,832	0,003419
MEGF10	2,8	1	1,83	0,01909
HSPA9	6,3	2	1,81	0,0004584
SPINT1	6	1,7	1,798	0,001198
RCN1	2,7	1	1,776	0,02639
LTBP1	5,8	1,8	1,686	0,002117
GLUD1	3,8	1,5	1,679	0,009834
LAMA5	19	6,2	1,674	2,21E-09
COL3A1	3,8	1,2	1,666	0,01794
GANAB	9,5	3,7	1,641	2,57E-05
IGFBP4	2,8	1	1,638	0,04167
NUCB1	5,5	2	1,636	0,002646
GDF15	7,8	3,2	1,609	0,0001871
ACTG1	43,3	16,2	1,6	6,02E-21
ECM1	51,7	21,2	1,534	7,62E-24
HRNR	4,8	2,2	1,482	0,00792
CTSD	15,3	6,5	1,467	7,27E-07

SDF4	11,3	4,8	1,452	3,21E-05
HEXB	6,8	2,8	1,446	0,002174
ENPP2	40,8	18,2	1,441	1,75E-17
CALU	19,7	8,8	1,398	4,65E-08
CLEC11A	5	2,3	1,398	0,01062
PLOD3	33,2	15	1,358	1,05E-12
HSPD1	14	6,7	1,323	1,40E-05
THBS1	35	15,3	1,307	3,41E-12
MCAM	4,8	2,5	1,268	0,0204
SORT1	6,2	3	1,234	0,01181
LMAN2	20,7	9,8	1,202	1,39E-06
CDSN	7	3,2	1,144	0,01516
GPNMB	6,7	3,7	1,108	0,01568
C1QBP	6,8	3,7	1,107	0,01516
PSAP	56,5	30,5	1,101	1,77E-15
NCAM2	6,3	3	1,081	0,02957
PTPRJ	6,5	3,8	1,078	0,01799
QSOX1	22,3	11,5	1,072	5,86E-06
AGRN	97	52	1,043	1,42E-23
AZGP1	23	11,8	1,04	8,44E-06
IGF2R	29	16,8	1,036	1,70E-07
GOLM1	7,7	4	0,9976	0,02236
CPE	11,7	6	0,9855	0,004482
CLSTN3	7,5	3,8	0,9683	0,03092
TIMP1	13,3	8,2	0,9474	0,002032
BTD	9	5,5	0,9192	0,01694
VGFB	42,2	26	0,9144	1,42E-08
COL4A2	11,7	7,3	0,9044	0,006328
THBS2	80,3	50,8	0,896	9,74E-16
KRT14	8	5,5	0,8674	0,03104
CLU	20,3	11,8	0,8597	0,0005396
SRSF1	16,3	10,2	0,8183	0,003198
CNDP1	31	20,8	0,8156	1,48E-05
ACTB	0,5	33,2	-6,02	6,27E-52
PYGB	0,2	6,3	-4,887	7,52E-08
PARP1	0,2	5,8	-4,857	1,49E-07
CHL1	0,2	4,5	-4,523	7,05E-06
UBA2	0,2	4,7	-4,51	6,86E-06
VAT1	0,2	4	-4,261	5,99E-05
SSRP1	0,2	3,5	-4,094	0,0002133
ATIC	0,5	10	-4,033	3,55E-11
PSAT1	0	4,5	-36,74	7,31E-07
AKR1B1	0	3,7	-33,64	9,89E-06
HIST1H1B	0	7	-32,8	1,44E-10
TLN1	0	5,2	-31,98	7,81E-08
TOP1	0	2,8	-31,6	0,0001068
ADH5	0	3	-31,46	7,01E-05
SHMT1	0	2,2	-31,35	0,0008571
NOLC1	0	2	-31,26	0,001397
IPO7	0	2,2	-31,14	0,000962
PFAS	0	3,3	-30,64	1,66E-05
DPYSL2	0,2	3,2	-3,933	0,0006571
CCT7	0,2	2,7	-3,719	0,002311
TSNAX	0,2	2,5	-3,603	0,004076
CAND1	0,3	4	-3,442	0,0001235
NANS	0,3	4,2	-3,383	0,0001604
PRPF19	0,2	2,2	-3,372	0,01097
ZRANB2	0,2	2	-3,224	0,01799

SMAP	0,3	3,2	-3,152	0,001197
HDAC2	0,3	3,3	-3,043	0,001811
EEF1A1P5	0	5,5	-29,57	3,63E-08
HIST1H1E	0	4,8	-29,43	2,50E-07
HIST1H1C	0	2,7	-28,73	0,0002133
HIST1H2BL	0	2,3	-28,58	0,0001179
HIST1H2AA	0	2,7	-28,57	0,0002133
FSCN1	0,8	7,7	-2,84	2,44E-06
ESD	0,3	2,8	-2,797	0,006854
CLIC4	0,3	2,7	-2,639	0,0132
NUMA1	0,5	3,7	-2,637	0,002174
PACSIN2	0,5	3,8	-2,629	0,002095
NRDC	0,3	2,5	-2,625	0,01517
SAE1	0,3	2,3	-2,557	0,0203
PPP4R2	0,3	2,2	-2,542	0,02364
EIF3D	0,3	2,2	-2,457	0,0309
LMNB2	0,3	2,2	-2,457	0,0309
PAICS	0,7	4,3	-2,399	0,001846
TPP2	0,7	4,5	-2,393	0,001765
GBE1	0,3	2,2	-2,339	0,04252
EIF3L	0,7	3,8	-2,324	0,003465
HNRNPR	1,2	6,7	-2,312	6,75E-05
ZC3H18	0,5	2,7	-2,28	0,01704
H2AFZ	1,3	7,7	-2,269	2,55E-05
CSE1L	0,7	3,5	-2,238	0,006362
SCIN	1,7	9	-2,216	5,22E-06
EIF3C	0,8	4,2	-2,19	0,002799
EIF3A	1	5	-2,153	0,001198
H2AFY	1	5	-2,13	0,001397
TNFRSF19	0,7	3,3	-2,124	0,01156
PRMT1	0,8	4	-2,096	0,005129
CAP1	2	10	-2,083	4,13E-06
DENR	0,7	3,3	-2,071	0,01433
EIF3I	0,8	4	-2,067	0,006012
IDH1	1	5	-2,059	0,002165
DCPS	0,5	2,3	-2,015	0,04841
VIM	3,8	19	-1,997	3,06E-10
OTUB1	0,8	3,5	-1,986	0,01097
TPR	1	4,3	-1,877	0,00792
TSN	1	4,2	-1,852	0,009796
XPNPEP1	0,7	2,8	-1,789	0,04868
G3BP1	1,5	5,7	-1,756	0,002762
HMGA1	1,3	4,8	-1,694	0,00792
TNC	16,3	58	-1,692	2,38E-26
RPS3A	0,8	3	-1,692	0,04379
HNRNPL	2,3	8,5	-1,689	0,0002561
TCP1	1,5	5,7	-1,678	0,004677
CCT3	1,2	4,2	-1,663	0,01643
RPS19	1	3,7	-1,653	0,0287
ACAT2	1,2	4,2	-1,598	0,02225
XRCC6	5,5	18,7	-1,591	6,95E-08
PLEC	1,3	4,3	-1,589	0,01643
PPM1G	1,3	4,3	-1,589	0,01643
UCHL3	1,2	4,2	-1,571	0,02521
EIF6	1,3	4,5	-1,566	0,01736
SYNCRIP	1	3,5	-1,543	0,04675
RCC2	4,3	14,3	-1,541	5,86E-06
AARS	2	6	-1,53	0,004646

NUCKS1	4	12,5	-1,485	4,02E-05
H3F3A	1,5	4,8	-1,485	0,01799
TARS	4,8	15,5	-1,475	5,64E-06
MYH9	2,5	7,8	-1,466	0,002039
FAM49B	2	6,2	-1,447	0,007708
PGM1	3,7	12,3	-1,425	0,0001585
IPO5	4,8	15,2	-1,418	1,48E-05
YWHAH	1,8	5,5	-1,39	0,01637
PCNA	2,3	6,7	-1,374	0,007232
HMGB2	5,3	15,2	-1,371	1,67E-05
GNPDA1	1,8	5,5	-1,351	0,01965
NQO1	2,2	6	-1,35	0,01232
PPP2R1A	2,2	5,8	-1,331	0,01433
HNRNPD	4	11,2	-1,321	0,0005241
EEA1	1,8	5,7	-1,306	0,02458
CLTC	7,5	18,7	-1,222	9,97E-06
GSTO1	3,2	9,2	-1,196	0,00643
AHCY	5,3	13	-1,162	0,0006619
TXNRD1	2,7	6,5	-1,14	0,025
IQGAP1	5,8	14,3	-1,129	0,0005241
GARS	3,8	9,3	-1,095	0,008559
PA2G4	6,3	14,8	-1,083	0,0006207
EEF1G	4,8	11,2	-1,063	0,004244
NUDC	3,2	7,3	-1,058	0,02508
PMEL	4,5	10,8	-1,05	0,006328
ILF2	3	6,7	-1,037	0,03557
CCT8	5,8	13,3	-0,9941	0,003239
RACK1	7,3	16,5	-0,9925	0,0008948
YWHAQ	11	24,8	-0,9853	2,97E-05
HIST1H4A	11,3	25,7	-0,9827	2,32E-05
PTMA	10	20,5	-0,9753	0,0001375
RAN	3,8	8,7	-0,9632	0,02611
ACLY	8,8	18,2	-0,9353	0,0007296
HMCN1	5,2	11,5	-0,9167	0,01312
UBE2I	4	8,7	-0,9107	0,03503
VCL	6,3	12,5	-0,9043	0,00775
NPEPPS	4,8	9,7	-0,8469	0,03442
UBA1	7,8	15	-0,8357	0,006505
XRCC5	9,5	18,8	-0,8244	0,002539
CPOX	0	2,2	-36	0,001081

Notes: a: Average normalized spectral counts from cells where PML is silenced. b: Average normalized spectral counts from cells where PML is expressed. c: the adjusted p-values have been corrected for multiple hypothesis testing according to Benjamini and Hochberg.

CONTRIBUTED PUBLICATIONS



Targeting PML in triple negative breast cancer elicits growth suppression and senescence

Leire Arreal¹ · Marco Piva¹ · Sonia Fernández^{1,2} · Ajinkya Revandkar^{3,4} · Ariane Schaub- Clerigué¹ · Josep Villanueva^{2,5} · Amaia Zabala-Letona^{1,2} · Mikel Pujana¹ · Ianire Astobiza^{1,2} · Ana Rosa Cortazar^{1,2} · Ivana Hermanova¹ · Laura Bozal-Basterra¹ · Amaia Arruabarrena-Aristorena¹ · Jana R. Crespo¹ · Lorea Valcarcel-Jimenez¹ · Patricia Zúñiga-García¹ · Francesc Canals⁵ · Veronica Torrano^{1,2,6} · Rosa Barrio¹ · James D. Sutherland¹ · Andrea Alimonti^{3,4} · Natalia Martin-Martin^{1,2} · Arkaitz Carracedo^{1,2,6,7}

Received: 24 November 2018 / Revised: 18 July 2019 / Accepted: 23 July 2019 / Published online: 1 October 2019
© The Author(s) 2019. This article is published with open access

Abstract

Oncogene addiction postulates that the survival and growth of certain tumor cells is dependent upon the activity of one oncogene, despite their multiple genetic and epigenetic abnormalities. This phenomenon provides a foundation for molecular targeted therapy and a rationale for oncogene-based stratification. We have previously reported that the Promyelocytic Leukemia protein (PML) is upregulated in triple negative breast cancer (TNBC) and it regulates cancer-initiating cell function, thus suggesting that this protein can be therapeutically targeted in combination with PML-based stratification. However, the effects of PML perturbation on the bulk of tumor cells remained poorly understood. Here we demonstrate that TNBC cells are addicted to the expression of this nuclear protein. PML inhibition led to a remarkable growth arrest combined with features of senescence *in vitro* and *in vivo*. Mechanistically, the growth arrest and senescence were associated to a decrease in MYC and PIM1 kinase levels, with the subsequent accumulation of CDKN1B (p27), a trigger of senescence. In line with this notion, we found that PML is associated to the promoter regions of MYC and PIM1, consistent with their direct correlation in breast cancer specimens. Altogether, our results provide a feasible explanation for the functional similarities of MYC, PIM1, and PML in TNBC and encourage further study of PML targeting strategies for the treatment of this breast cancer subtype.

These author contributed equally: Natalia Martin-Martin, Arkaitz Carracedo

Edited by M Deshmukh

Supplementary information The online version of this article (<https://doi.org/10.1038/s41418-019-0407-5>) contains supplementary material, which is available to authorized users.

✉ Arkaitz Carracedo
acarracedo@cicbiogune.es

¹ CIC bioGUNE, Derio, Spain

² CIBERONC, Derio, Spain

³ Institute of Oncology Research (IOR) and Oncology Institute of Southern Switzerland (IOSI), Bellinzona, CH 6500, Switzerland

⁴ Faculty of Biology and Medicine, University of Lausanne (UNIL), Lausanne, CH 1011, Switzerland

⁵ Vall d'Hebron Institute of Oncology (VHIO), Barcelona, Spain

⁶ Biochemistry and Molecular Biology Department, University of the Basque Country (UPV/EHU), Bilbao, Spain

⁷ IKERBASQUE, Basque Foundation for Science, Bilbao, Spain

Introduction

Breast cancer exemplifies the potential of gene expression profiling to classify the disease into molecular subtypes [1–3]. However, these classifications do not inform about the molecular mediators of tumor progression and metastasis in each subtype of breast cancer. To address this question, we and others have defined genes and pathways that are relevant to breast cancer progression, metastasis, and resistance to therapy [4–6]. The Promyelocytic Leukemia protein (PML), the essential component of the PML nuclear bodies (PML-NBs), induces apoptosis and inhibits angiogenesis and cell cycle progression in cancer, thus complying with the definition of a tumor suppressor [7, 8]. Paradoxically, PML exerts a prosurvival role conferring a selective advantage in chronic myeloid leukemia and specific solid tumors [6, 9–15]. In breast cancer, PML regulates aggressiveness and metastatic features through the control of the stem cell gene, *SOX9*, and the Hypoxia-inducible factor 1 alpha (HIF1 α) signaling [13, 15]. Moreover, the

regulation of cancer-initiating cell (CIC) and metastatic potential is restricted to PML high-expressing estrogen receptor-negative breast tumors, predominantly triple negative breast cancer (TNBC).

The concept that the perturbation of a driver cancer gene can exert an exacerbated tumor suppressive response in tumor cells is defined as “oncogene addiction” and provides a rationale for molecular targeted therapy [16]. Senescence is a stress response that involves a stable cell growth arrest as well as an adaptive process to reduce energy consumption for cell division or differentiation and therefore assure the survival and viability of the cell [17, 18]. Senescence is induced *in vitro* by different stimuli including DNA damage, oxidative stress, oncogene activation, mitochondrial dysfunction, or chemotherapy [17, 18]. Cyclin-dependent kinase inhibitor family (CDKi) is a key regulator of the senescence response, predominantly through p53-p21 and/or p16-RB axes [17, 18]. To a lesser extent, CDKN1B (p27) has been reported to participate in the activation of the senescence response, in conditions where p21 and/or p16 are not active [19, 20]. Of note, PML is required for a fully functional senescence response upon oncogene activation in tumors where it functions as a tumor suppressor. In addition, the PML-NBs coordinate the activation of p53 and the formation of the senescence-associated heterochromatin foci (SAHF) [21–23].

TNBC exhibits increased levels and activity of various oncogenes, including MYC and PIM1 [24–27]. Importantly, these genes regulate metabolic and signaling activities in this breast tumor subtype, and they represent an attractive therapeutic vulnerability [24, 26–28]. Whereas similarities exist among the reported activities of MYC, PIM1, and PML, their functional association remains obscure. In this study, we demonstrate that TNBC cells that express high PML levels are addicted to the nuclear protein, and its targeting elicits a growth suppressive response that encompasses MYC and PIM1 downregulation and the activation of p27-dependent senescence.

Results

PML silencing induces senescence and prevents tumor growth *in vivo*

The identification of PML as a novel target in aggressive breast cancer tumors [13, 15] prompted us to investigate the molecular consequences of its inhibition in an established cell culture. To this end, we generated and validated three PML-targeting doxycycline-inducible and two constitutive short hairpin RNAs (shRNAs) (Fig. 1a and Supplementary Fig. 1a) [15]. PML silencing triggered a robust morphological change in PML-high expressing cells, MDA-MB-231

(Fig. 1b and Supplementary Fig. 1b), characterized by a significant increase in size (FSC-A) and granularity (SSC-A) analyzed by FACS (Fig. 1c and Supplementary Fig. 1c). These changes in morphology were indicative of a senescence response. Indeed, the evaluation of senescence-associated β -galactosidase (SA- β -gal) activity in both inducible and constitutive systems confirmed this notion (Fig. 1d, e and Supplementary Fig. 1d, e) in MDA-MB-231 cells. Senescence is defined as an irreversible cell cycle arrest. Indeed, we could confirm the cell cycle arrest upon PML genetic inhibition, by means of BrdU analysis (Fig. 1f) and crystal violet cell number assay (Supplementary Fig. 1f, g) and that it was not due to an increase in apoptosis (Supplementary Fig. 1h). Of note, arsenic trioxide (ATO) did not elicit a senescence phenotype (Supplementary Fig. 1i). This compound exerts a biphasic effect on PML; first favors the formation of the PML NBs and then the degradation of PML. Therefore, the inability of ATO to recapitulate PML silencing could be due to its molecular mode of action.

We monitored additional features that were reported for certain types of oncogene-induced senescence [29]. On the one hand, proteomics analysis of the supernatant of these cells indicated that PML silencing resulted in a distinct secretome, without signs of a canonical SASP (senescence-associated secretory phenotype) (Supplementary Fig. 1j–l and Supplementary Table 1). On the other hand, we ascertained the formation of SAHF. We could not confirm the existence of SAHF neither at the level of chromatin condensation nor the formation of macroH2A1.1 foci (Supplementary Fig. 1m). Lamin B1 loss is a senescence-associated biomarker [30, 31]. We demonstrated that in our system PML loss induced a decrease in Lamin B1 protein levels (Supplementary Fig. 1n–o).

Of note, PML regulates oxidative stress responses [7, 32]. We ruled out that reactive oxygen species (ROS) elevation drives senescence in our system since PML loss does not induce its accumulation (Supplementary Fig. 1p).

Breast CIC capacity is reduced upon PML knockdown in TNBC cells (with high PML expression), as we demonstrated in limiting dilution assays with MDA-MB-231 cells [15]. Here, we hypothesized that the activation of senescence would result in a tumor suppressive response in established tumors, where the contribution of CIC is negligible. To test this notion, MDA-MB-231 cells were injected in the flank of immunocompromised mice, and once the tumors were established (reaching a volume of 25–130 mm³) doxycycline was administered in the food pellets to induce PML silencing. In agreement with the response observed *in vitro*, xenograft growth was curbed upon PML knockdown (Fig. 1g, h and Supplementary Fig. 1q–r) and senescence increase was confirmed by means of p-HP1 γ staining (Fig. 1i, j) [33]. Our data suggest that

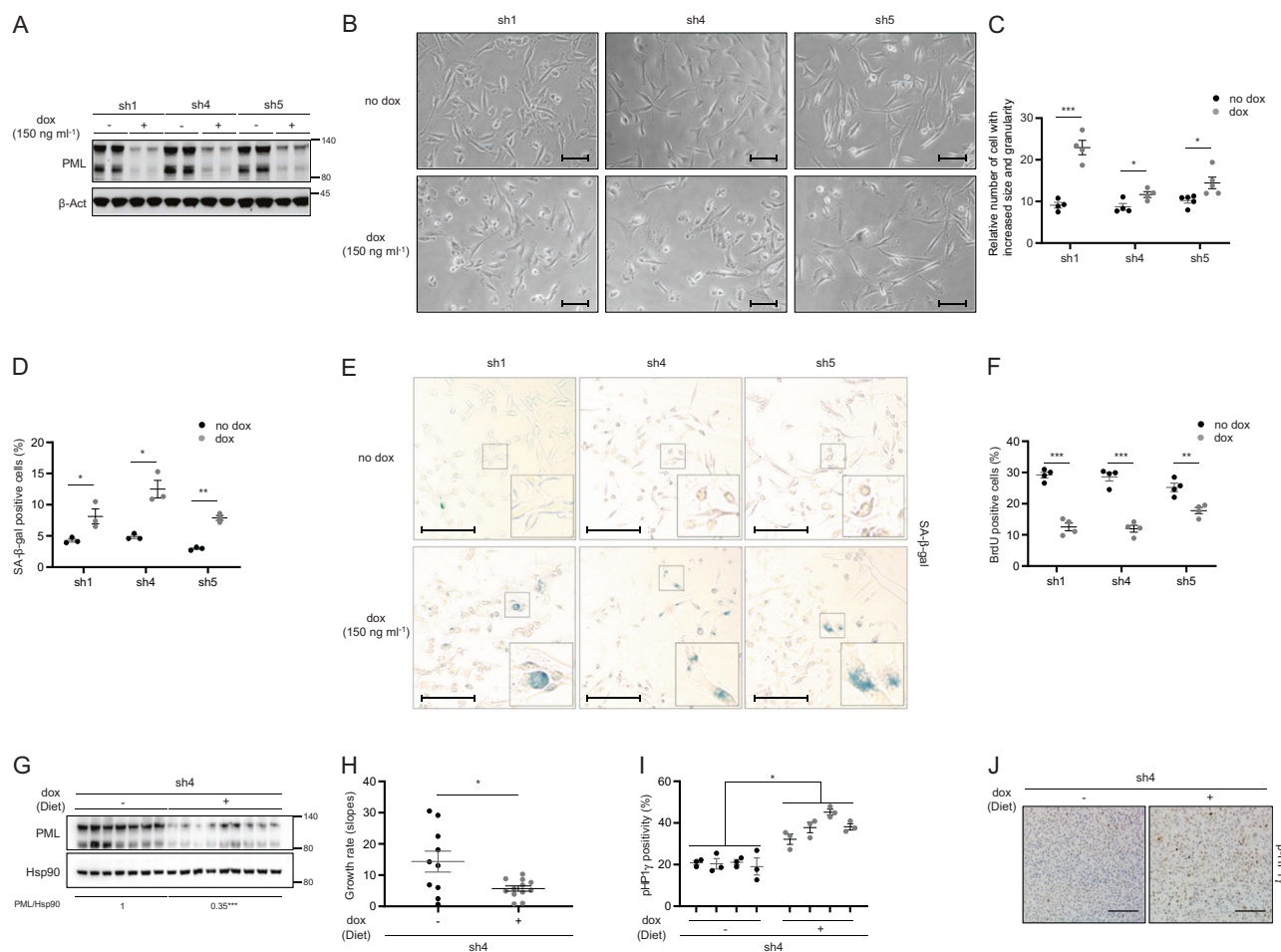


Fig. 1 PML silencing induces senescence. Effect of doxycycline-inducible (150 ng ml^{-1} ; 3 + 3 days) PML silencing (sh1, sh4, and sh5) on PML protein expression (a, representative of at least three experiments), on the morphology (b, representative images, scale bar, $50 \mu\text{m}$), on cell size and granularity (c, FACS analysis, sh1 and sh4, $n = 4$, sh5, $n = 5$), on the number of senescent cells (d; $n = 3$, representative images of SA- β -Galactosidase assay, scale bar $50 \mu\text{m}$) (e) and on the number of BrdU positive cells (f, $n = 4$) in MDA-MB-231 cells. Impact of doxycycline-inducible PML silencing (sh4) of established MDA-MB-231 xenografts on PML protein expression (g), on tumor growth rate represented as the growth rate of each tumor (h, sh4 no dox, $n = 10$; sh4 dox, $n = 12$; growth rate was inferred from the linear

regression calculated for the progressive change in tumor volume of each individual tumor during the period depicted in Supplementary Fig. 1p) and on number of senescent cells measured by p-HP1 γ staining (i, sh4 no dox, $n = 4$; sh4 dox, $n = 4$); representative images of p-HP1 γ positive cells, scale bar $100 \mu\text{m}$ (j) of the tumors. Error bars represent s.e.m. p, p -value ($*p < 0.05$, $**p < 0.01$, $***p < 0.001$). One-tailed Student's t -test was used for cell line data analysis (c, d, f) and one-tailed Mann–Whitney U -test for xenografts (h, i). sh1, sh4, and sh5: shRNA against *PML*, dox: doxycycline, SA- β -gal: senescence-associated beta-galactosidase, BrdU: bromodeoxyuridine, p-HP1 γ : phospho-heterochromatin protein-1 gamma, molecular weight markers (kDa) are shown to the right

PML silencing in a PML-high expressing TNBC cell line triggers a senescence response with a partial presence of classical markers of this process.

p27 is the driver in PML loss-induced senescence

Senescence is executed and sustained at the molecular level through the activation of growth suppressors, including p53 and the cyclin-dependent kinase (CDKs) inhibitors p21, p16, and p27 [17, 20, 29]. Since MDA-MB-231 cells harbor loss of p16 and p53 mutation [34, 35], we proposed p27 as a candidate to drive PML silencing-induced senescence in our cell system. Importantly, p27 protein levels were increased

upon both inducible (Fig. 2a and Supplementary Fig. 2a) and constitutive (Supplementary Fig. 2b) PML silencing with all the shRNA tested in MDA-MB-231 cells. Moreover, we observed that the induction of p27 protein levels occurred as soon as 2 days following PML inactivation and it was maintained up to 6 days of PML silencing (Fig. 2b, c and Supplementary Fig. 2c–f).

The function of p27 is controlled by changes in its levels along with its compartmentalization within the cell [36]. To confirm the functionality of accumulated p27 in PML-silenced cells, we quantified p27 nuclear localization by immunofluorescence. As predicted, PML silencing elicited an increase of nuclear p27 in cells with the three inducible

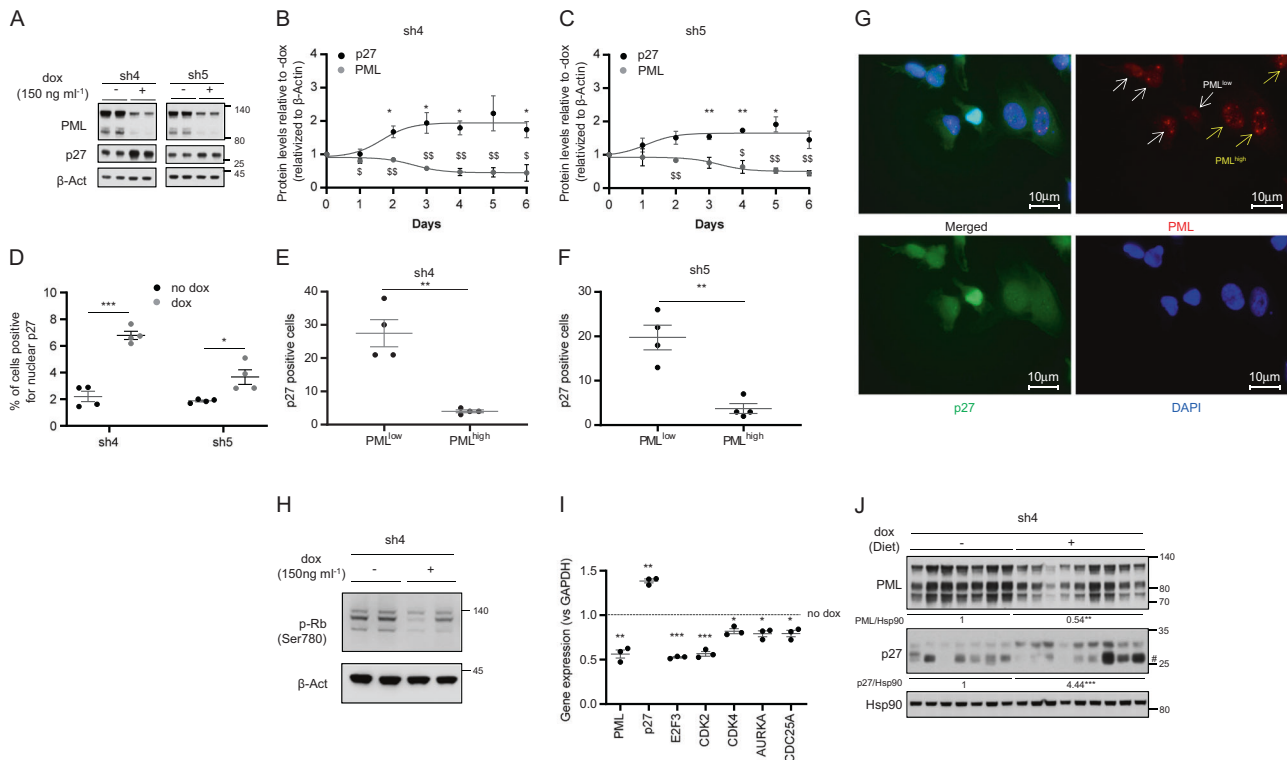


Fig. 2 p27 is induced after PML silencing. **a** Effect of doxycycline-inducible (150 ng ml^{-1} ; 3 + 3 days) PML silencing (sh4, sh5) on p27 and PML protein expression (representative of at least three experiments) on MDA-MB-231 cells. **b, c** Quantification of p27 and PML protein levels along 6 days of doxycycline-inducible PML silencing on MDA-MB-231 cells ($n = 3$) with two different shRNAs. **d** Immunofluorescence quantification of nuclear p27 positive cells upon PML inducible silencing on MDA-MB-231 cells ($n = 4$). **e–g** Immunofluorescence quantification of the correlation of p27 positive cells and PML levels in these cells (**e–f**) and representative images of p27 and PML staining (**g**) upon doxycycline-inducible PML silencing in MDA-MB-231 cells ($n = 4$). **h** Effect of doxycycline-inducible (150 ng ml^{-1} ;

3 + 3 days) PML silencing (sh4) on RB phosphorylation (Ser780) (representative of three experiments) on MDA-MB-231 cells. **i** Expression of p27-related cell cycle genes upon PML inducible silencing in MDA-MB-231 cells ($n = 3$). **j** Impact of doxycycline-inducible PML silencing (sh4) on p27 and PML protein expression on established MDA-MB-231 xenografts. Error bars represent s.e.m. p , p -value ($*/\$/p < 0.05$, $**/\$/p < 0.01$, $***/\$/p < 0.001$). One-tailed one-sample t -test (**b, c, i**) and one-tailed Student's t -test were used for cell line data analysis (**d–f**). sh4 and sh5: shRNA against *PML*, dox: doxycycline. #Unspecific band. Molecular weight markers (kDa) are shown to the right

shRNA tested (Fig. 2d and Supplementary Fig. 2g). Since the effect of shRNAs was analyzed in a pooled culture, it is plausible that there would be heterogeneity in PML levels across cells within the culture dish. We therefore evaluated whether the increase in nuclear p27 was ascribed to cells with a profound decrease in PML immunoreactivity. We established an immunofluorescence score based on previous studies [6, 15] (PML low = 0–4 dots; PML high = more than 4 dots per cell nuclei). In line with our previous results, we observed a significant inverse association between PML immunoreactivity and p27 nuclear staining (Fig. 2e–g and Supplementary Fig. 2h). Moreover, the elevated activity of p27 upon PML silencing was consistent with the increase in its mRNA levels, the blockade of Retinoblastoma protein (Rb) phosphorylation and the reduced transcription of downstream regulated cell cycle-related genes (Fig. 2h, i and Supplementary Fig. 2i). In agreement with the results observed in vitro, p27 accumulation was recapitulated upon PML knockdown in vivo (Fig. 2j).

Our results reveal that PML silencing in TNBC cells with high expression of the nuclear protein triggers a senescence response associated to p27 accumulation. To ascertain the causal contribution of p27 to the execution of the senescence response, we silenced p27 in MDA-MB-231 cells concomitantly with PML silencing, using inducible (Fig. 3a, b) or constitutive (Supplementary Fig. 3a) shRNA systems. Preventing p27 accumulation upon PML loss hampered the induction of senescence in a dose-dependent manner according to the potency of the shRNA against p27 (Fig. 3c and Supplementary Fig. 3b). Our results demonstrate that PML loss elicits a senescence response mediated by the upregulation of p27 in PML high expressing TNBC cells.

Although senescence is a major driver of growth arrest, we noticed that the amount of SA- β -Gal positivity upon PML silencing was not comparable to the extent of growth arrest detected (Fig. 1 and Supplementary Fig. 1). Taking advantage of our capacity to ablate senescence by silencing p27, we ascertained the contribution of this response to the

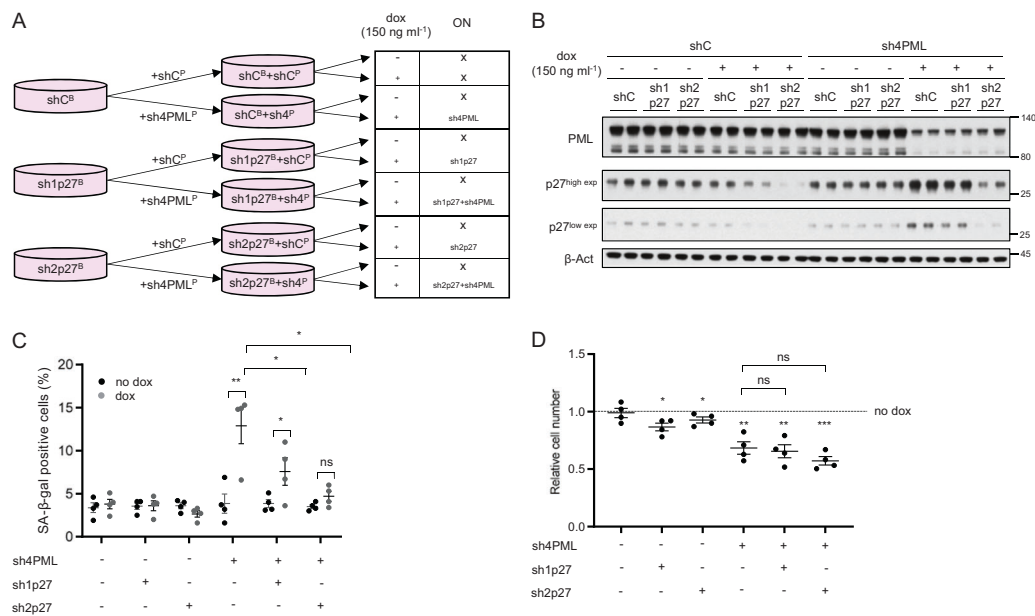


Fig. 3 p27 is the driver in PML loss-induced senescence. **a** Experimental design for inducible p27 silencing (sh1p27 and sh2p27, B: blasticidin selection) alone or in combination with inducible PML silencing (sh4, P: puromycin selection) in MDA-MB-231 cells. **b** p27 and PML protein levels upon doxycycline inducible silencing of either p27 or PML or both in MDA-MB-231 cells (representative of three experiments). **c** Effect on the number of senescent cells ($n = 4$) upon p27 and/or PML inducible silencing in MDA-MB-231 cells. **d** Effect

on the relative cell number ($n = 4$) upon p27 and/or PML inducible silencing in MDA-MB-231 cells. Error bars represent s.e.m. p , p -value ($*p < 0.05$, $**p < 0.01$, $***p < 0.001$). One-tailed Student's t -test (**c**) and one-tailed one-sample t -test (**d**) were used for cell line data analysis. shC: scramble shRNA, Dox: doxycycline, SA- β -gal: senescence-associated beta-galactosidase. Molecular weight markers (kDa) are shown to the right

cell number reduction. Importantly, the growth arrest caused by PML silencing was not recovered by blunting senescence (Fig. 3d and Supplementary Fig. 3c), thus suggesting that an additional mechanism may be involved.

MYC and PIM1 are regulated by PML in TNBC

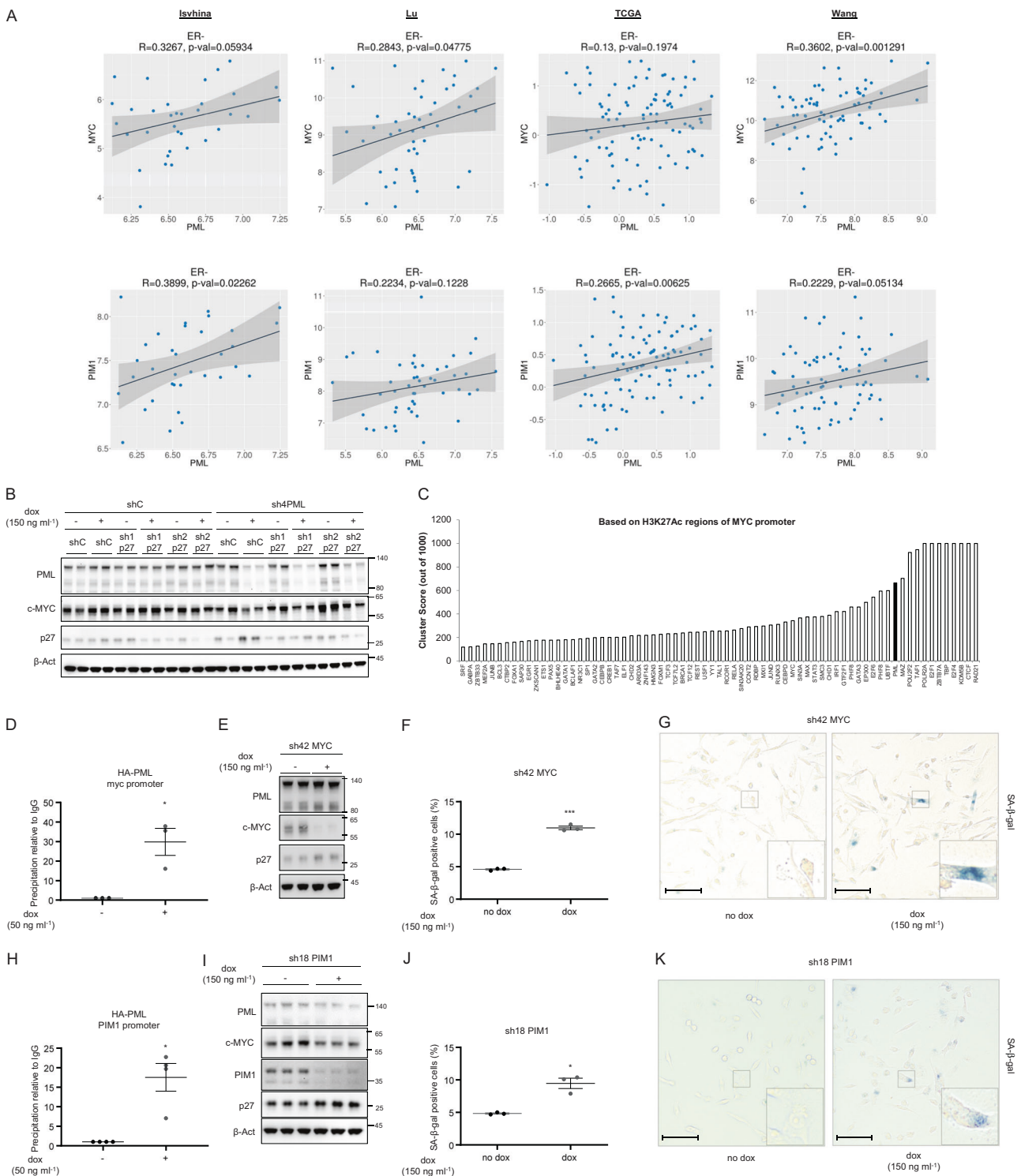
Our data demonstrate that preventing p27 accumulation is not sufficient to rescue the growth arrest caused by PML loss. We reasoned that the mechanism through which PML was regulating growth arrest, p27 accumulation and senescence might depend on a larger growth-regulatory program. Interestingly, the oncogenic axis comprised with MYC and PIM1 kinase shares many similarities with PML concerning its activity in TNBC. MYC and PIM1 are upregulated in TNBC [24, 26, 27] and inhibit p27 accumulation and function [37]. In addition, MYC regulates metabolic functions attributed to PML, including fatty acid β oxidation [6, 10, 38, 39] and its inhibition induces cellular senescence in lymphoma, osteosarcoma, and hepatocellular carcinoma [40]. With this data in mind, we first evaluated the association of PML, MYC, and PIM1 in breast cancer. We found a significant direct correlation in various breast cancer transcriptomics datasets. This association was evident in two out of four datasets for MYC-PML and four out of four for

PIM1-PML, when accounting all breast cancer subtypes (Supplementary Fig. 4a). Since the effect of these genes is restricted to tumors that lack hormone receptors, we refined the analysis by focusing on estrogen receptor (ER) negative tumors. In this scenario, the correlation was recapitulated in various datasets (Fig. 4a).

We next aimed at deconstructing the molecular regulation of PML, MYC, and PIM1. First, we monitored the impact of PML silencing on MYC abundance. As predicted, inducible PML shRNA activation resulted in a remarkable decrease in MYC protein and mRNA levels in vitro and in vivo (Supplementary Fig. 4b–h) in two PML high expressing cells, MDA-MB-231 and MDA-MB-468. Of note, in line with our senescence results (Supplementary Fig. 1i), ATO did not alter the abundance of p27 and MYC (Supplementary Fig. 4i–j).

We next asked to which extent MYC downregulation was retained in cells devoid of p27-dependent senescence response. To address this question, we checked MYC expression upon PML/p27 double silencing in MDA-MB-231 cells. The decrease in MYC expression upon PML loss was not recovered with p27 silencing (Fig. 4b), thus providing a feasible explanation for the lack of rescue in growth capacity.

We have previously shown that PML can regulate gene expression in line with its association with discreet



promoter regions [15]. Since PML silencing resulted in reduced MYC mRNA levels (Supplementary Fig. 4d, h), we interrogated MYC promoter in silico using ENCODE [41]. We found PML among the proteins with highest confidence DNA-binding score in MYC promoter region (Fig. 4c, cluster score: 527). We performed chromatin immunoprecipitation (ChIP) analysis of ectopically expressed PML and

confirmed that PML is in the vicinity of MYC promoter (Fig. 4d). To ascertain if MYC silencing recapitulated the effect of PML inhibition, we used a validated shRNA targeting this oncogene (sh42) [42, 43] and confirmed that MYC silencing resulted in increased p27 levels (Fig. 4e and Supplementary Fig. 4k), senescence (Fig. 4f, g) and growth arrest (Supplementary Fig. 4l).

◀ **Fig. 4** PML regulates MYC and PIM1 expression in TNBC. **a** Correlation analysis between PML and MYC (top panels) and between PML and PIM1 (bottom panels) mRNA levels in ER negative tumor specimens of the indicated breast cancer datasets. Sample sizes: Ivshina ($n = 34$), Lu ($n = 49$), TCGA ($n = 117$) and Wang ($n = 77$). **b** p27, MYC, and PML protein levels upon doxycycline inducible silencing of either p27 or PML or both in MDA-MB-231 cells (representative of three experiments). **c** Cluster score of DNA-binding proteins in MYC promoter region using ENCODE database. **d** MYC promoter region abundance in chromatin immunoprecipitation (ChIP) of exogenous HA-PMLIV using HA-tag antibody in MDA-MB-231 cells after induction with 50 ng ml⁻¹ doxycycline for 3 days ($n = 3$). Data were normalized to IgG (negative-binding control). **e** p27, MYC, and PML protein levels upon doxycycline inducible silencing of MYC (sh42) in MDA-MB-231 cells (representative of three experiments). Effect on the number of senescent cells ($n = 3$) (**f**) and representative images, scale bar 50 μ m, (**g**) upon MYC inducible silencing in MDA-MB-231 cells. **h** PIM1 promoter region abundance in chromatin immunoprecipitation (ChIP) of exogenous HA-PMLIV using HA-tag antibody in MDA-MB-231 cells after induction with 50 ng ml⁻¹ doxycycline for 3 days ($n = 4$). Data were normalized to IgG (negative-binding control). **i** p27, MYC, PIM1, and PML protein levels upon doxycycline inducible silencing of PIM1 (sh18) in MDA-MB-231 cells (representative of three experiments). **j–k** Effect on the number of senescent cells ($n = 3$) and representative images, scale bar 50 μ m, (**k**) upon PIM1 inducible silencing in MDA-MB-231 cells. Error bars represent s.e.m. p , p -value ($*p < 0.05$, $***p < 0.001$). One-tailed one sample t -test (**d**, **h**) and one-tailed student's t -test (**f**, **j**) were used for cell line data analysis. shC: Scramble shRNA, Dox: doxycycline, SA- β -gal: senescence-associated beta-galactosidase. Molecular weight markers (kDa) are shown to the right

In the last few years, an important body of work has demonstrated that PIM1 is an important partner of MYC function in prostate cancer and TNBC [24, 26]. Moreover, PIM1 can regulate MYC transcriptional signature and p27 [24, 26]. We monitored the impact of PML on PIM1 expression and function. PML loss resulted in a decrease in PIM1 gene expression in two PML high expressing cells, MDA-MB-231, and MDA-MB-468 (Supplementary Fig. 4m–n). Importantly, we confirmed that PML is in close proximity to PIM1 promoter by ChIP analysis (Fig. 4h, cluster score: 383 in ENCODE). We hypothesized that loss of PIM1 would further impact on MYC function and recapitulate the aforementioned PML and MYC phenotype. We silenced PIM1 using a validated shRNA (sh18) [24] and corroborated that the targeting of PIM1 led to decrease in MYC abundance, increase in p27 levels, senescence, and growth arrest in MDA-MB-231 cells (Fig. 4i–k and Supplementary Fig. 4o–q). Altogether, our results provide strong support for the role of MYC-PIM1 axis supporting PML-elicited TNBC growth and preventing the accumulation of p27 and senescence.

PML loss-elicited growth suppression in breast cancer is selective of high PML expressing TNBC

The inactivation of a single oncogene can compromise the development and survival of tumor cells despite their

genetic or epigenetic abnormalities [16]. We have previously reported that high PML levels in TNBC are required for adequate CIC function [15]. Here, the data presented support the notion that the bulk of tumor cells in a TNBC with elevated PML is “addicted” to the expression of the protein. In turn, acute depletion of the nuclear protein results in growth arrest and senescence. To ascertain whether the “addiction” was restricted to TNBC cells, we took advantage of various breast cancer cell lines belonging to distinct subtypes with differing levels of PML. A second TNBC cell line (MDA-MB-468) that presented high levels of PML protein was compared with ER+ cells [15] (Fig. 5a). Silencing of PML in MDA-MB-468 cells elicited a remarkable growth arrest, which was not detected in the ER+ cells Cama-1 and MCF7 (Fig. 5b and Supplementary Fig. 5a–c). In line with this notion, Cama-1 and MCF7 cells did not exhibit neither the reduction in MYC expression nor the induction of p27-dependent senescence, as compared with MDA-MB-468 cells (Fig. 5c, d and Supplementary Fig. 5d–g). Moreover, the morphological changes induced by the loss of PML were only present in TNBC cells (Supplementary Fig. 5h). Since PML silencing resulted in a distinct secretory phenotype (albeit not a canonical SASP), we monitored the secretome of the ER+ cell line Cama-1. In agreement with our prior data, unsupervised clustering based on the secretome was ineffective in segregating experimental conditions according to PML status. Similarly, principal component analysis and hierarchical clustering reinforced the notion that Cama-1 are refractory to PML level perturbation (Supplementary Fig. 5i–k and Supplementary Table 2).

Discussion

PML has been a paradigmatic tumor suppressor since its discovery [7, 8, 44]. A variety of molecular activities directly support its reported capacity to prevent many of the hallmarks of cancer, including the induction of apoptosis and the inhibition of proliferation or angiogenesis [7]. Molecular partners such as p53 have reinforced this notion. However, the discovery of tumoral contexts, where the presence of PML is required has broadened the picture of the roles of this nuclear protein in disease. Depletion of PML impairs the self-renewal activity in the leukemic stem cell from chronic myeloid leukemia [9, 10]. This phenotype is the consequence of both cell autonomous (the hyper-activation of mTOR complex1 and the reduction in PPAR δ -fatty acid oxidation activity [9, 10]) and non-cell autonomous activities (regulation of the mesenchymal stem cell in the leukemic niche [45]), which trigger symmetric commitment and the loss of the CIC compartment.

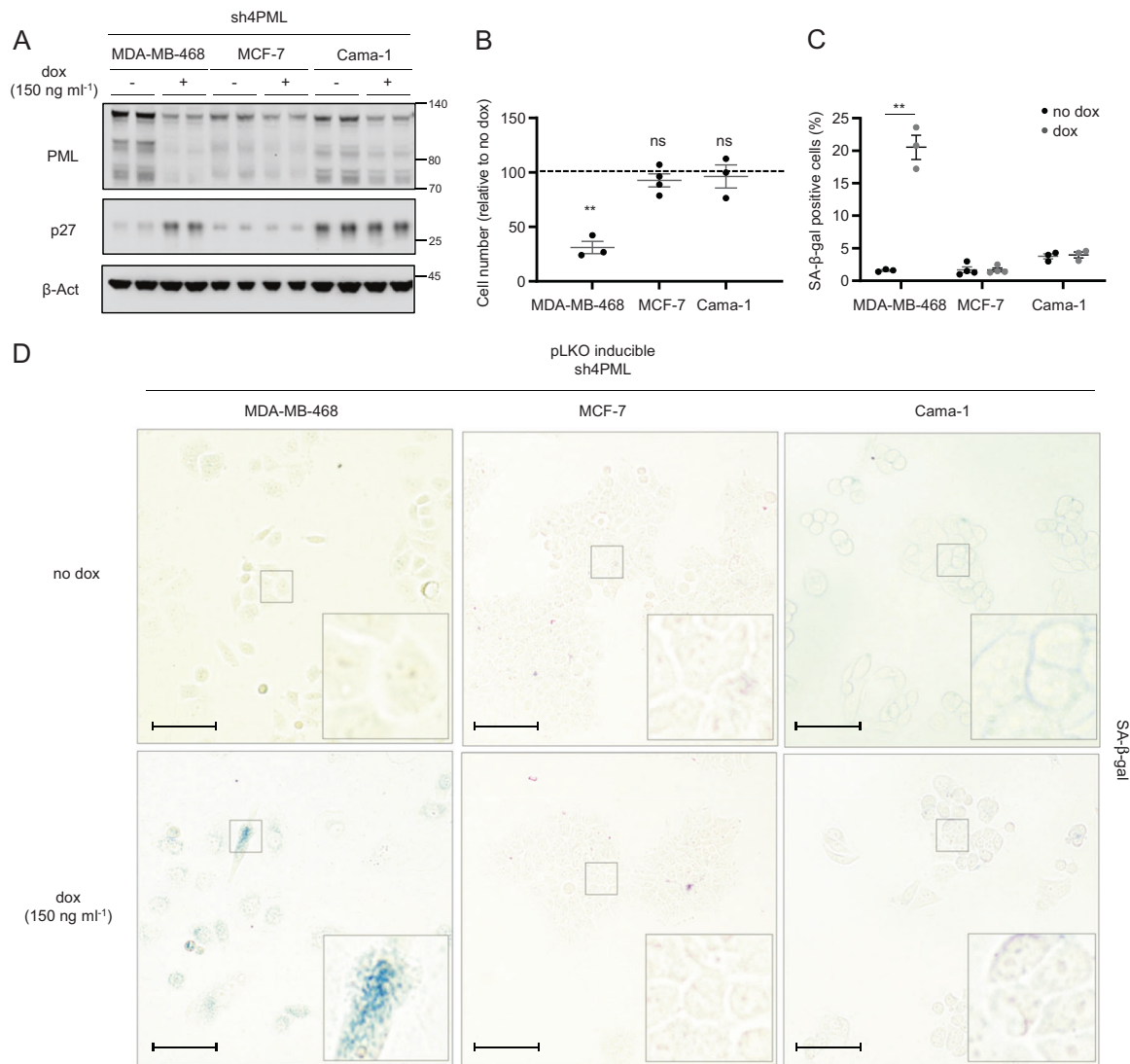


Fig. 5 The antiproliferative program elicited by PML loss is restricted to PML-high expressing TNBC cells. Effect of doxycycline-inducible (150 ng ml⁻¹; 3 + 3 days) PML silencing (sh4) on PML and p27 protein expression (**a**, representative of three experiments), on cell number (**b**, MDA-MB-468 and Cama-1, $n = 3$, MCF7, $n = 4$) and on the number of senescent cells (**c**, MDA-MB-468 and Cama-1, $n = 3$, MCF7, $n = 4$; representative images of SA-β-galactosidase positive

cells (**d**) in MDA-MB-468, MCF-7, and Cama-1 cells, scale bar 50 μm. Error bars represent s.e.m. p , p -value ($*p < 0.05$, $**p < 0.01$, $***p < 0.001$, ns: not significant). One-tailed one sample t -test (**b**) and one-tailed Student's t -test were used for cell line data analysis (**c**). Dox: doxycycline, SA-β-gal: senescence-associated beta-galactosidase. Molecular weight markers (kDa) are shown to the right

The regulation of CIC activity was recently translated to solid tumors. To date, glioma and a subset of breast cancers exhibit PML-dependent self-renewal activity [14, 15], whereas other tumors, such as ovarian cancers or some experimental models of hepatocarcinoma development, exhibit a broad tumor suppressive response upon PML inhibition [11, 12]. PML expression is selectively exacerbated in a subset of breast tumors (TNBC) [6, 13, 15]. Yet, we lack basic understanding around the impact of PML on the function of this cell subtype. In this study, we demonstrate that PML depletion in the bulk of TNBC cells in culture and in vivo triggers a tumor suppressive response

consisting on growth arrest and the activation of senescence.

PML has been previously related to the regulation of the senescence response [21]. However, the majority of studies associate PML expression to the execution of this growth suppressive response upon the activation of oncogenes or replicative stress [11]. Experimentally, ectopic PML expression triggers senescence, and, conversely, PML deletion bypasses the senescence response elicited by the oncogenic form of RAS, thus enabling transformation [46–48]. Mechanistically, PML supports p53 activity and participates in the formation of SAHF [21]. In turn, PML loss

bypasses the senescence response. Paradoxically, our results indicate that, in cancer cells with high dependence on PML expression, its inhibition also triggers a senescence response that lacks canonical SASP and SAHF. This phenomenon might have been overlooked in prior studies due to the lack of data at the time on the role of PML favoring cancer cell function in specific tumor subsets. Of note, the activation of senescence in non-transformed fibroblasts upon PML depletion adds complexity to already extensive portfolio of PML activities [49].

Oncogene addiction [16] is perceived as an attractive opportunity in the era of targeted therapies. Our results are consistent with PML addiction in TNBC cells, even if this protein cannot be formally considered an oncogene. The data produced by us and others [6, 13, 15] argue in favor of a molecular make up in this subtype of breast cancer that requires the presence of PML in high doses, as opposed to estrogen receptor-positive tumor cells. In this regard, the control of MYC and PIM1 expression by PML provides a feasible explanation for the accumulation of p27 and the induction of senescence when PML is silenced. To which extent the relationship between PML, MYC, and PIM1 is operative in other tumor types becomes now an exciting question to address. Since PML lacks a dedicated domain to recognize and bind discreet DNA sequences, the existence of yet unidentified PML-interacting transcription factors that enable this regulatory mode warrants further research.

The results obtained in this study represent a conceptual leap in how we perceive the role of PML in TNBC, and suggest that targeting this nuclear protein can be beneficial at multiple levels, including impairing the CIC function [15], blunting hypoxia signaling [13], and triggering a senescence response. The quantification of the relative relevance of each PML effector pathway in the overall activity of PML could open new opportunities to apply the biology of PML-regulated TNBC function for breast cancer treatment.

Materials and methods

Cell culture

MDA-MB-231, MDA-MB-468, MCF-7, and Cama-1 cell lines were obtained from the American Type Culture Collection (ATCC, Manassas, VA, USA) or from Leibniz-Institut—Deutsche Sammlung von Mikroorganismen und Zellkulturen GmbH (DMSZ) who provided an authentication certificate. None of the cell lines used in this study was found in the database of commonly misidentified cell lines maintained by ICLAC and NCBI Biosample. Cell lines were routinely monitored for mycoplasma contamination and quarantined while treated if positive. MDA-MB-231

and MCF-7 cells were maintained in DMEM media, MDA-MB-468 were maintained in RPMI media, and Cama-1 were maintained in DMEM-F12 media, all supplemented with 10% (v/v) foetal bovine serum and 1% (v/v) penicillin-streptomycin.

Generation of stable cell lines

293FT cells were used for lentiviral production. Lentiviral vectors expressing shRNAs against human *PML* and *p27* from the Mission® shRNA Library were purchased from Sigma-Aldrich. Cells were transfected with lentiviral vectors following standard procedures, and viral supernatant was used to infect cells. Selection was done using puromycin (2 µg ml⁻¹; P8833, Sigma) for 48 h or blasticidin (10 µg ml⁻¹; Cat. 15205, Sigma) for 5 days. As a control, a lentivirus with scrambled shRNA (shC) was used. Short hairpins sequence: shC: CCGCAACAAGATGAAGAG CACCAACTCGAGTTGGTGTCTTTCATCTTGTGTTT TT; sh1PML (TRCN000003865): CCGCAATAACAAC GACAGCCCAGAACTCGAGTTCTGGGCTGTCGTTGT ATTGTTTTT; sh4PML (TRCN 000003867): CCGGG CCAGTGTACGCCTTCTCCATCTCGAGATGGAGAAG GCGTACACTGGCTTTTTT; sh5PML (TRCN 000003868): CCGGGTGTACCGGCAGATTGTGGATCTCGAGATCC-ACAATCTGCCGGTACACTTTTT; sh1p27 (TRCN 0000039928): CCGGGTAGGATAAGTGAAATGGATA CTCGAGTATCCATTTCACCTTATCCTACTTTTTTG; sh2p27 (TRCN 0000039930): CCGGGCGCAAGTGGAA TTTTCGATTTCTCGAGAAATCGAAATTCACCTGCGC TTTTTG. sh42MYC (TRCN0000039642): CCGGCCTGA GACAGATCAGCAACAACACTCGAGTTGTTGCTGATCT GTCTCAGGTTTTT. sh18PIM1 (TRCN0000010118): CCGGACATCCTTATCGACCTCAATCCTCGAGGATT GAGGTGATAAGGATGTTTTTTT.

Sub-cloning of shC, sh1PML, sh4PML, sh5PML, and sh42myc into pLKO-Tet-On-Puromycin vector was done introducing *AgeI* and *EcoRI* in the 5' end of top and bottom shRNA oligos respectively (following the strategy provided by Dr. Dmitri Wiederschain [50], Addgene plasmid: 21915). Sub-cloning of shC, sh1p27, sh2p27, and sh18PIM1 into pLKO-Tet-On-Blasticidin was done following the same procedure. Puromycin resistance cassette was replaced by Blasticidin cassette following Gibson assembly strategy.

Reagents

Doxycycline (Cat. D9891, Sigma) was used at 150 ng ml⁻¹ to induce the expression of shRNA from pLKO-Tet-On vectors. Doxycycline-mediated inducible shRNA expression was performed by treating cell cultures for 72 h with the antibiotic (150 ng ml⁻¹) and then seeding for cellular or

molecular assays in the presence of doxycycline for three more days (unless otherwise specified). ATO (Cat. A1010, Sigma-Aldrich) was prepared at a concentration of 100 mM in NaOH 1 N and subsequently diluted to 0.1 mM in PBS for a working solution. ATO was used at 150 nM for 6 days as indicated in figure legends.

Cell growth analysis and size measurement by FACS

Cell number quantification was done with crystal violet as reported [5]. For FACS analysis MDA-MB-231 cells were trypsinized and resuspended in PBS to be analysed based on their size (FSC) and granularity (SSC) using a BD FACS-Canto™ II (BD Biosciences) flow cytometer upon PML doxycycline-inducible silencing. Data represented in Fig. 1c correspond to the sum of Q1 + Q2 + Q3 populations selected as in Supplementary Fig. 1c. Data were analysed using the FlowJo software; cell populations were selected for each shRNA (no dox condition) and differences quantified for increasing size and granularity.

Senescence associated-β-galactosidase detection

To quantify the number of senescent cells, constitutive or inducible PML/MYC/PIM1/p27 silencing cells was performed as described previously and cells were seeded in 24-well plates in duplicate. An overnight incubation with the senescence detection kit (QIA117, Calbiochem) was performed and SA-β-Gal activity was revealed and quantified (three areas per well, more than 200 cells per condition). The number of senescent cells in each area was relativized to the number of total cells counted per area. Cells were seeded in plates or glass cover slips to acquire images with EVOS® cell imaging station (×20 magnification objective).

Western blotting, immunofluorescence and BrdU

Western blot analysis was carried out as previously described [5]. Briefly, cells were seeded on six-well plates. Cell lysates were prepared with RIPA buffer (50 mM TrisHCl pH 7.5, 150 mM NaCl, 1 mM EDTA, 0.1% SDS, 1% Nonidet P40, 1% sodium deoxycholate, 1 mM Sodium Fluoride, 1 mM sodium orthovanadate, 1 mM beta-glycerophosphate and protease inhibitor cocktail; Roche). The following antibodies were used for Western blotting: rabbit polyclonal anti-PML, 1:1000 dilution (Cat: A301-167A, Bethyl laboratories), mouse monoclonal anti-p27[Kip1], 1:1000 dilution (Cat: 610242, BD Biosciences), mouse monoclonal anti-beta-ACTIN, 1:2000 dilution (Cat: 3700, Cell Signaling), rabbit polyclonal Hsp90, 1:2000 dilution (Cat: 4874, Cell Signaling), rabbit polyclonal c-Myc, 1:1000 dilution (Cat: 13987, Cell Signaling), rabbit

polyclonal PIM1, 1:1000 dilution (ab75776, Abcam), rabbit polyclonal Lamin B1 (ab133741, Abcam), rabbit monoclonal anti-cleaved PARP (Asp214), 1:1000 dilution (Cat: 5625, Cell Signaling), rabbit polyclonal anti-cleaved caspase 3 (Asp175), 1:1000 dilution (Cat: 9661, Cell Signaling), mouse monoclonal anti-α-Tubulin (66031-1-Ig, Proteintech), 1:2500 dilution, rabbit monoclonal anti-phospho-Rb (Ser780) 1:1000 dilution (Cat: 9307, Cell Signaling). After standard SDS-PAGE and Western blotting techniques, proteins were visualized using the ECL on iBright™ CL1000 Imaging System (Cat: A32749, Invitrogen). Densitometry-based quantification was performed using ImageJ software. Uncropped scans are provided in Supplementary Fig. 6.

For immunofluorescence, cells were seeded on glass cover slips in 24-well plates, cells were fixed with 4% para-formaldehyde (15 min), PBS (three times wash), 1% Triton X-100 (5 min), PBS (three times wash), 10% goat serum (1 h) and anti-PML antibody 1:100 dilution (catalog A301-167A; Bethyl laboratories), anti-p27[Kip1] antibody 1:100 dilution (Cat: 610242, BD Biosciences) and anti-macroH2A1.1 antibody 1:100 (Cat: 12455, Cell Signaling) were added ON (4 °C) in goat serum. Cover slips were washed with PBS three times and incubated with secondary antibodies (anti-rabbit Alexa488, anti-rabbit Alexa594, anti-mouse Alexa488, and anti-mouse Alexa594; Invitrogen-Molecular Probes) for 1 h (room temperature). Cover slips were washed with PBS three times, and DAPI added to stain nuclei (10 min), followed by mounting with ProLong™ Gold Antifade Mountant (Cat: P36930, Invitrogen). Immunofluorescence images were obtained with AxioImager D1 microscope (Zeiss) or with a confocal microscopy (Leica SP8) with ×63 objectives. At least three different areas per cover slip were quantified.

For BrdU analysis cells were seeded as for immunofluorescence. Prior to fixing, cells were incubated in the presence of BrdU (3 ug ml⁻¹). Cells were fixed with 4% para-formaldehyde (15 min), PBS (three times wash) and DNA exposed with 2 M HCl (5 min), PBS (3 times wash) and 0.1 M sodium borate. After that, PBS (three times wash), 1% Triton X-100 (5 min), PBS (three times wash), 10% goat serum (1 h), and monoclonal anti-BrdU (MoBU-1) antibody 1:100 dilution (Cat: B35128, Invitrogen) was added ON (4 °C) in goat serum. Cover slips were washed three times with PBS and incubated with secondary antibodies (anti-mouse Alexa594; Invitrogen-Molecular Probes) for 1 h (room temperature). Cover slips were washed three times with PBS and DAPI added to stain nuclei (10 min), followed by mounting with ProLong™ Gold Antifade Mountant (Cat: P36930, Invitrogen). Images were obtained with an AxioImager D1 microscope (Zeiss). At least three different areas per cover slip were quantified.

Quantitative real-time PCR

Cells were seeded as for western blot. Total RNA was extracted from cells using NucleoSpin RNA isolation kit from Macherey-Nagel (ref: 740955.250). Complementary DNA was produced from 1 µg of RNA using Maxima™ H Minus cDNA Synthesis Master Mix (Cat# M1682, Invitrogen). Taqman probes were obtained from Applied Biosystems. Amplifications were run in a Viia7 or QS6 Real-Time PCR Systems (Applied Biosystems) using the following probes: PML (Hs00971694_m1, cat: 4331182). For p27 (CDKN1B), MYC, PIM1, CDK2, CDK4, E2F3, AURKA, and CDC25A amplification, Universal Probe Library (Roche) primers and probes were employed (p27, For: ccctagagggcaagtacgagt, Rev: agtagaactcgggcaagctg, probe: 39; MYC, For: gctgcttagacgctggattt, Rev: taacttgaggggcactcg, probe: 66; PIM1, For: atcaggggccaggttttc, Rev: gggccaagcaccatctaat, probe: 13; CDK2, For: aaagcagaacaagttagc, Rev: gtactgggcacaccctcagt, probe 77; CDK4, For: gtgcagtcggtgtacctg, Rev: aggcagagatcctgtgt, probe 25; E2F3, For: ggttctggaaatgcccttac, Rev: gatgaccgctttctcctagc, probe 40; AURKA, For: gca-gattttgggtgtcagt, Rev: tccgacctcaatcattca, probe 79; CDC25A, For: cgtcatgagaactcaaacctga, Rev: tctgtctctcaactgacc, probe 67). All quantitative PCR with reverse transcription data presented were normalized using GAPDH (Hs02758991_g1, cat: 4331182) from Applied Biosystems as housekeeping.

Mice

Xenograft experiments were carried out following the ethical guidelines established by the Biosafety and Welfare Committee at CIC bioGUNE. The procedures employed were carried out following the recommendations from AAALAC. Xenograft experiments were performed as previously described [5], injecting 3×10^6 cells per tumor, two injections per mouse, one per flank. All mice (female Hsd: Athymic Nude-Foxn1 nu/nu) were inoculated at 8–12 weeks of age. Nineteen days post injection, once tumors were established ($25\text{--}130\text{ mm}^3$), mice were fed with chow or doxycycline diet (Research diets, D12100402) until the experimental endpoint.

p-HP1γ immunohistochemistry

After sacrifice, formalin-fixed paraffin embedded xenograft tissues were stained for p-HP1γ. Tissues were deparaffinized using the standard procedure and unmasking/antigen retrieval was performed using pH 6.0 solution for 20 min at 98 °C in water bath. Tissue sections were stained for p-HP1γ using primary antibody Phospho-HP1γ (Ser83) (Cat. No: 2600, Cell Signaling technologies, 1:200) and

secondary antibody Biotinylated antibody Anti-Rabbit (BP-9100, Vector Laboratories, 1:200). This was followed by Vectastain ABC solution incubation (PK-6100, Vector laboratories, 1:150) and DAB staining (SK-4105, Vector laboratories) as per the manufacturer's protocol. Stained slides were scanned using Leica Aperio AT2 slide scanner. The criteria for senescent staining used for quantification was a very prominent nuclear staining in which the nucleus was bigger in size and its staining was darker brown than the other cells.

ChIP

ChIP was performed using the SimpleChIP® Enzymatic Chromatin IP Kit (Cat #9003, Cell Signaling Technology, Inc) as reported [15]. DNA quantification was carried out using a Viia7 Real-Time PCR System (Applied Biosystems) with SybrGreen reagents and primers that amplify the predicted PML binding region to MYC promoter (chr8:128748295–128748695) as follows: left primer: CCGGCTAGGGTGAAGAG, right primer: GCTGCTA TGGGCAAAGTTTC and PIM1 promoter (chr6: 37137097–37137612) as follows: left primer: ACTCCCTC CGTGACTCATGT, right primer: ACGAGGGTGG TCTTTCTGTG.

Secretome analysis

Secretomes were prepared as previously described [51]. MDA-MB-231 sh4 PML tet on and Cama-1 sh4 PML tet on cells were pre-induced with doxycycline (150 ng ml^{-1}) for 3 days. Three 150 cm^2 plates were seeded per condition: 4×10^6 cells per plate of non-induced cells and 5×10^6 cells per plate of doxycycline induced cells. After two days, cell supernatants were removed and cells were washed five times: the first two washes were performed with PBS and the last three were made with serum-depleted DMEM. Cells were left to grow for 24 h in serum-depleted DMEM. Doxycycline was maintained (150 ng ml^{-1}). Two biological replicates, each with three technical replicates were processed.

After 24 h supernatant was collected and one dish per condition was trypsinized and counted to check cell number and PML expression. The supernatant was first spun at 1000 rpm for 5 min followed by filtration through $0.2\text{ }\mu\text{m}$ filtering bottles. After this, it was concentrated using 10 kDa Amicons; first, 15 mL Amicons (Ref. UCF901024, Merck) were used, followed by 0.5 mL Amicons (Ref. UCF501069, Merck) to get final volumes close to $80\text{ }\mu\text{L}$. The concentrated secretome was frozen at $-20\text{ }^\circ\text{C}$ until proteomics analysis. Protein concentration was determined with a Pierce BCA protein assay kit (Thermo Scientific). All samples were digested with trypsin in-solution prior to

analysis by liquid chromatography–mass spectrometry (LC–MS). Tryptic digests were analysed by shotgun proteomics using an LTQ Velos-Orbitrap mass spectrometer (Thermo Fisher Scientific, Bremen, Germany). The RAW files of each MS run were processed using Proteome Discoverer (Thermo Fisher Scientific), and MS/MS spectra were searched against the human database of Swiss-Prot using the MASCOT (Matrix Science, London, U.K) algorithm. The results files generated from MASCOT (.DAT files) were then loaded into Scaffold (Proteome Software, Portland, OR), resulting in a nonredundant list of identified proteins per sample achieving a protein false discovery rate (FDR) under 1.0%, as estimated by a search against a decoy database.

Secretome statistical analysis

Relative spectral counting-based protein quantification analysis was performed on the different samples analyzed using Scaffold. Files containing all spectral counts for each sample and its replicates were generated and then exported to R software for normalization and statistical analysis [52]. All statistical computations were done using the open-source statistical package R. The data were assembled in a matrix of spectral counts, where the different conditions are represented by the columns and the identified proteins are represented by the rows. An unsupervised exploratory data analysis by means of principal components analysis and hierarchical clustering of the samples on the SpC matrix was first performed. Then, the GLM model based on the Poisson distribution was used as a significance test [52]. Finally the Benjamini and Hochberg multitest correction was used to adjust the *p*-values with control on the FDR.

Full information regarding the proteins detected in the secretome analysis can be found in Supplementary Tables 1 and 2.

ROS analysis

MDA-MB-231 cells with inducible shRNA against PML (sh4) were pre-induced with doxycycline (150 ng ml⁻¹) for 3 days. Then, cells were seeded in a six-well plate in triplicate (1.5 × 10⁵ cells/well) maintaining the doxycycline concentration. Two additional wells with non-induced cells were used for positive and negative ROS controls respectively.

After 72 h, 10 μM of 2', 7'-Dichlorofluorescein diacetate (DCF-DA) (Sigma-Aldrich Ref: 35845) reactive was added to each well and cells were incubated for 30 min. In the last 5 min of the incubation time, 1 M hydrogen peroxide (H₂O₂) was added to the positive control well.

Subsequently, cells were washed with PBS and raised from plates employing 500 μL of trypLE reactive (Gibco™

ref: 12563–011). After that, cells were washed twice with abundant PBS to eliminate the excess of DCF-DA reactive and pellets were re-suspended in 500 μL PBS for FACS analysis. Samples were analyzed in FACS CANTO II for green fluorescence.

Datasets

Database normalization

All the datasets used for the data mining analysis were downloaded from GEO and TCGA, and subjected to background correction, log₂ transformation, and quartile normalization. In the case of using a pre-processed dataset, this normalization was reviewed and corrected if required.

Correlation analysis

Pearson correlation test was applied to analyse the relationship between paired genes. From this analysis, Pearson coefficient (R) indicates the existing linear correlation (dependence) between two variables *X* and *Y*, giving a value between +1 and -1 (both included), where 1 is total positive correlation, 0 is no correlation, and -1 is total negative correlation. The *p*-value indicates the significance of this R coefficient.

Statistical analysis

No statistical method was used to predetermine sample size. The experiments were not randomized. The investigators were not blinded to allocation during experiments and outcome assessment. Data analysed by parametric tests are represented by the mean ± s.e.m. of pooled experiments unless otherwise stated. *n* values represent the number of independent experiments performed or the number of individual mice. For each in vitro independent experiment, technical replicates were used and a minimum number of three experiments were performed to ensure adequate statistical power. In the in vitro experiments, normal distribution was assumed and one sample *t*-test was applied for one component comparisons with control and Student's *t*-test for two component comparisons. For in vivo experiments, a non-parametric Mann–Whitney *U*-test was used. Two-tailed statistical analysis was applied for experimental design without predicted result, and one-tail for validation or hypothesis-driven experiments. The confidence level used for all the statistical analyses was of 0.95 (alpha value = 0.05).

Acknowledgements Apologies to those whose related publications were not cited due to space limitations. LA, AS, MPu, AA-A, and LV-J were supported by the Basque Government of education. IH was

supported by the Program “Juan de la Cierva” from MINECO. FC acknowledges the Proteomics Unit at VHIO is a member ProteoRed, PRB3 (Grant IPT17/0019—ISCIII-SGEFI/ERDF. RB acknowledges projects BFU2017–84653-P, Consolider BFU2014–57703-REDC, and SAF2017–90900-REDT (MINECO/FEDER, EU). The work of VT is founded by Fundación Vasca de Innovación e Investigación Sanitarias, BIOEF (BIO15/CA/052), the AECC J.P. Bizkaia, the Basque Department of Health (2016111109) and the MINECO (RTI2018–097267-B-I00 (MCIU/AEI/FEDER, UE)). AA was supported by ERC consolidator (683136) and Swiss Cancer League (KFS4267–08–2017) grant, Dr. Josef Steiner Foundation, Swiss Card-Onco-Grant of Alfred and Annemarie von Sick grant, Helmut Horten Foundation, SNSF (310030_176045) and PCUK (RIA15-ST2–018). NM-M was supported by the Spanish Association Against Cancer (AECC), AECC JP Vizcaya and CIBERONC. The work of A. Carracedo is supported by the Basque Department of Industry, Tourism and Trade (Elkartek) and the department of education (IKERTALDE IT1106–16), the BBVA foundation, the MINECO (SAF2016–79381-R (FEDER/EU); Severo Ochoa Excellence Accreditation SEV-2016–0644; Excellence Networks SAF2016–81975-REDT), European Training Networks Project (H2020-MSCA-ITN-308 2016 721532), the AECC (IDEAS175CARR, GCTRA18006CARR), La Caixa Foundation (HR17–00094), FERO foundation, the AstraZeneca Oncology prize and the European Research Council (Starting Grant 336343, PoC 754627). CIBERONC was co-funded with FEDER funds and funded by ISCIII.

Authors contributions LA, NM-M, and MP performed the majority of the in vitro and in vivo experiments, unless specified otherwise. SF-R, JRC, AA-A, LV-J, PZ-G, and IH contributed to specific in vitro analyses. MPu and AZ-L performed ROS analyses. AS and VT coordinated or performed secretome preparation. AR performed the histochemical staining and quantification of p-HP1 γ staining. IA contributed to the sub-cloning of shC, sh1p27, and sh2p27 into pLKO-Tet-On- Blastocidin. ARC performed the bioinformatic and biostatistical analysis. JV and FC performed or coordinated the secretome analysis. LB-B provided support with imaging analyses. RB and JDS provided technical advice. AA supervised the histochemical staining and quantification of p-HP1 γ staining. AC and NM-M directed the project, contributed to data analysis and wrote the manuscript.

Compliance with ethical standards

Conflict of interest The authors declare that they have no conflict of interest.

Publisher’s note Springer Nature remains neutral with regard to jurisdictional claims in published maps and institutional affiliations.

Open Access This article is licensed under a Creative Commons Attribution 4.0 International License, which permits use, sharing, adaptation, distribution and reproduction in any medium or format, as long as you give appropriate credit to the original author(s) and the source, provide a link to the Creative Commons license, and indicate if changes were made. The images or other third party material in this article are included in the article’s Creative Commons license, unless indicated otherwise in a credit line to the material. If material is not included in the article’s Creative Commons license and your intended use is not permitted by statutory regulation or exceeds the permitted use, you will need to obtain permission directly from the copyright holder. To view a copy of this license, visit <http://creativecommons.org/licenses/by/4.0/>.

References

- Sorlie T, Perou CM, Tibshirani R, Aas T, Geisler S, Johnsen H, et al. Gene expression patterns of breast carcinomas distinguish tumor subclasses with clinical implications. *Proc Natl Acad Sci USA*. 2001;98:10869–74.
- van de Vijver MJ, He YD, van’t Veer LJ, Dai H, Hart AA, Voskuil DW, et al. A gene-expression signature as a predictor of survival in breast cancer. *N Engl J Med*. 2002;347:1999–2009.
- Curtis C, Shah SP, Chin SF, Turashvili G, Rueda OM, Dunning MJ, et al. The genomic and transcriptomic architecture of 2000 breast tumours reveals novel subgroups. *Nature*. 2012;486:346–52.
- Bos PD, Zhang XH, Nadal C, Shu W, Gomis RR, Nguyen DX, et al. Genes that mediate breast cancer metastasis to the brain. *Nature*. 2009;459:1005–9.
- Carracedo A, Ma L, Teruya-Feldstein J, Rojo F, Salmena L, Alimonti A, et al. Inhibition of mTORC1 leads to MAPK pathway activation through a PI3K-dependent feedback loop in human cancer. *J Clin Invest*. 2008;118:3065–74.
- Carracedo A, Weiss D, Leliaert AK, Bhasin M, de Boer VC, Laurent G, et al. A metabolic prosurvival role for PML in breast cancer. *J Clin Investig*. 2012;122:3088–100.
- Tessier S, Martin-Martin N, de The H, Carracedo A, Lallemand-Breitenbach V. Promyelocytic leukemia protein, a protein at the crossroad of oxidative stress and metabolism. *Antioxid Redox Signal*. 2017;26:432–44.
- Bernardi R, Pandolfi PP. Structure, dynamics and functions of promyelocytic leukaemia nuclear bodies. *Nat Rev Mol Cell Biol*. 2007;8:1006–16.
- Ito K, Bernardi R, Morotti A, Matsuoka S, Saglio G, Ikeda Y, et al. PML targeting eradicates quiescent leukaemia-initiating cells. *Nature*. 2008;453:1072–8.
- Ito K, Carracedo A, Weiss D, Arai F, Ala U, Avigan DE, et al. A PML–PPAR- δ pathway for fatty acid oxidation regulates hematopoietic stem cell maintenance. *Nat Med*. 2012;18:1350–8.
- Chung YL, Wu ML. Dual oncogenic and tumor suppressor roles of the promyelocytic leukemia gene in hepatocarcinogenesis associated with hepatitis B virus surface antigen. *Oncotarget*. 2016;7:28393–407.
- Liu SB, Shen ZF, Guo YJ, Cao LX, Xu Y. PML silencing inhibits cell proliferation and induces DNA damage in cultured ovarian cancer cells. *Biomed Rep*. 2017;7:29–35.
- Ponente M, Campanini L, Cuttano R, Piunti A, Delledonne GA, Coltella N, et al. PML promotes metastasis of triple-negative breast cancer through transcriptional regulation of HIF1A target genes. *JCI Insight*. 2017;2:e87380.
- Zhou W, Cheng L, Shi Y, Ke SQ, Huang Z, Fang X, et al. Arsenic trioxide disrupts glioma stem cells via promoting PML degradation to inhibit tumor growth. *Oncotarget*. 2015;6:37300–15.
- Martin-Martin N, Piva M, Urosecvic J, Aldaz P, Sutherland JD, Fernandez-Ruiz S, et al. Stratification and therapeutic potential of PML in metastatic breast cancer. *Nat Commun*. 2016;7:12595.
- Weinstein IB, Joe A. Oncogene addiction. *Cancer Res*. 2008;68:3077–80. discussion 3080.
- Childs BG, Durik M, Baker DJ, van Deursen JM. Cellular senescence in aging and age-related disease: from mechanisms to therapy. *Nat Med*. 2015;21:1424–35.
- Nardella C, Clohessy JG, Alimonti A, Pandolfi PP. Pro-senescence therapy for cancer treatment. *Nat Rev Cancer*. 2011;11:503–11.
- Lin HK, Chen Z, Wang G, Nardella C, Lee SW, Chan CH, et al. Skp2 targeting suppresses tumorigenesis by Arf-p53-independent cellular senescence. *Nature*. 2010;464:374–9.

20. Majumder PK, Grisanzio C, O'Connell F, Barry M, Brito JM, Xu Q, et al. A prostatic intraepithelial neoplasia-dependent p27 Kip1 checkpoint induces senescence and inhibits cell proliferation and cancer progression. *Cancer Cell*. 2008;14:146–55.
21. Ivanschitz L, De The H, Le Bras MPML. SUMOylation, and Senescence. *Front Oncol*. 2013;3:171.
22. Zhang R, Poustovoitov MV, Ye X, Santos HA, Chen W, Daganzo SM, et al. Formation of MacroH2A-containing senescence-associated heterochromatin foci and senescence driven by ASF1a and HIRA. *Dev Cell*. 2005;8:19–30.
23. Lo Re O, Vinciguerra M. Histone MacroH2A1: a chromatin point of intersection between fasting, senescence and cellular regeneration. *Genes (Basel)*. 2017;8.
24. Braso-Maristany F, Filosto S, Catchpole S, Marlow R, Quist J, Francesch-Domenech E, et al. PIM1 kinase regulates cell death, tumor growth and chemotherapy response in triple-negative breast cancer. *Nat Med*. 2016;22:1303–13.
25. Cancer Genome Atlas N. Comprehensive molecular portraits of human breast tumours. *Nature*. 2012;490:61–70.
26. Horiuchi D, Camarda R, Zhou AY, Yau C, Momcilovic O, Balakrishnan S, et al. PIM1 kinase inhibition as a targeted therapy against triple-negative breast tumors with elevated MYC expression. *Nat Med*. 2016;22:1321–9.
27. Horiuchi D, Kusdra L, Huskey NE, Chandriani S, Lenburg ME, Gonzalez-Angulo AM, et al. MYC pathway activation in triple-negative breast cancer is synthetic lethal with CDK inhibition. *J Exp Med*. 2012;209:679–96.
28. Zhao W, Qiu R, Li P, Yang J. PIM1: a promising target in patients with triple-negative breast cancer. *Med Oncol*. 2017;34:142.
29. Hernandez-Segura A, Nehme J, Demaria M. Hallmarks of cellular senescence. *Trends Cell Biol*. 2018;28:436–53.
30. Dreesen O, Chojnowski A, Ong PF, Zhao TY, Common JE, Lunny D, et al. Lamin B1 fluctuations have differential effects on cellular proliferation and senescence. *J Cell Biol*. 2013;200:605–17.
31. Freund A, Laberge RM, Demaria M, Campisi J. Lamin B1 loss is a senescence-associated biomarker. *Mol Biol Cell*. 2012;23:2066–75.
32. Niwa-Kawakita M, Ferhi O, Soilihi H, Bras le M, Lallemand-Breitenbach V, Huges de H. PML is a ROS sensor activating p53 upon oxidative stress. *J Exp Med*. 2017;214:3197–206.
33. Di Mitri D, Toso A, Chen JJ, Sarti M, Pinton S, Jost TR, et al. Tumour-infiltrating Gr-1+ myeloid cells antagonize senescence in cancer. *Nature*. 2014;515:134–7.
34. Bazarov AV, Van Sluis M, Hines WC, Bassett E, Beliveau A, Campeau E, et al. p16(INK4a)-mediated suppression of telomerase in normal and malignant human breast cells. *Aging Cell*. 2010;9:736–46.
35. Bykov VJ, Issaeva N, Shilov A, Hultcrantz M, Pugacheva E, Chumakov P, et al. Restoration of the tumor suppressor function to mutant p53 by a low-molecular-weight compound. *Nat Med*. 2002;8:282–8.
36. Rodier G, Montagnoli A, Di Marcotullio L, Coulombe P, Draetta GF, Pagano M, et al. p27 cytoplasmic localization is regulated by phosphorylation on Ser10 and is not a prerequisite for its proteolysis. *EMBO J*. 2001;20:6672–82.
37. Morishita D, Katayama R, Sekimizu K, Tsuruo T, Fujita N. Pim kinases promote cell cycle progression by phosphorylating and down-regulating p27Kip1 at the transcriptional and post-transcriptional levels. *Cancer Res*. 2008;68:5076–85.
38. Carracedo A, Cantley LC, Pandolfi PP. Cancer metabolism: fatty acid oxidation in the limelight. *Nat Rev Cancer*. 2013;13:227–32.
39. Camarda R, Zhou AY, Kohnz RA, Balakrishnan S, Mahieu C, Anderton B, et al. Inhibition of fatty acid oxidation as a therapy for MYC-overexpressing triple-negative breast cancer. *Nat Med*. 2016;22:427–32.
40. Wu CH, van Riggelen J, Yetil A, Fan AC, Bachireddy P, Felsher DW. Cellular senescence is an important mechanism of tumor regression upon c-Myc inactivation. *Proc Natl Acad Sci USA*. 2007;104:13028–33.
41. Consortium EP. The ENCODE (ENCyclopedia Of DNA Elements) Project. *Science*. 2004;306:636–40.
42. Liu R, Zhang T, Zhu G, Xing M. Regulation of mutant TERT by BRAF V600E/MAP kinase pathway through FOS/GABP in human cancer. *Nat Commun*. 2018;9:579.
43. Nakano T, Kanai Y, Amano Y, Yoshimoto T, Matsubara D, Shibano T, et al. Establishment of highly metastatic KRAS mutant lung cancer cell sublines in long-term three-dimensional low attachment cultures. *PLoS One*. 2017;12:e0181342.
44. Martin-Martin N, Sutherland JD, Carracedo A. PML: not all about tumor suppression. *Front Oncol*. 2013;3:200.
45. Guarnerio J, Mendez LM, Asada N, Menon AV, Fung J, Berry K, et al. A non-cell-autonomous role for Pml in the maintenance of leukemia from the niche. *Nat Commun*. 2018;9:66.
46. Bischof O, Kirsh O, Pearson M, Itahana K, Pelicci PG, Dejean A. Deconstructing PML-induced premature senescence. *EMBO J*. 2002;21:3358–69.
47. Ferbeyre G, de Stanchina E, Querido E, Baptiste N, Prives C, Lowe SW. PML is induced by oncogenic ras and promotes premature senescence. *Genes Dev*. 2000;14:2015–27.
48. Pearson M, Carbone R, Sebastiani C, Ciocco M, Fagioli M, Saito S, et al. PML regulates p53 acetylation and premature senescence induced by oncogenic Ras. *Nature*. 2000;406:207–10.
49. Marchesini M, Matocci R, Tasselli L, Cambiaghi V, Orleth A, Furia L, et al. PML is required for telomere stability in non-neoplastic human cells. *Oncogene*. 2016;35:1811–21.
50. Wiederschain D, Wee S, Chen L, Loo A, Yang G, Huang A, et al. Single-vector inducible lentiviral RNAi system for oncology target validation. *Cell Cycle*. 2009;8:498–504.
51. Gregori J, Villarreal L, Sanchez A, Baselga J, Villanueva J. An effect size filter improves the reproducibility in spectral counting-based comparative proteomics. *J Proteom*. 2013;95:55–65.
52. Villarreal L, Mendez O, Salvans C, Gregori J, Baselga J, Villanueva J. Unconventional secretion is a major contributor of cancer cell line secretomes. *Mol Cell Proteom*. 2013;12:1046–60.

Supplementary Figure legends

Supplementary Figure 1. (a-b) Effect of PML constitutive silencing (sh4, sh5) on PML protein expression (**a**, representative of at least 3 experiments) and on the morphology (**b**, representative images, scale bar 50 μ m). (**c**) Schematic representation of one representative experiment of the defined populations represented in main Fig.1c upon inducible PML silencing on MDA-MB-231 cells. (**d-e**) Effect on the number of senescent cells upon constitutive PML silencing (**d**; n=13) and representative images of SA- β -Galactosidase assay in MDA-MB-231 cells, scale bar 50 μ m (**e**). (**f-g**) Impact on cell number upon either constitutive (**f**, n=12) or inducible (**g**, sh1 and sh5, n=4, sh4, n=7) PML silencing in MDA-MB-231 cells. (**h**) Effect of PML inducible silencing (sh4) on apoptosis using staurosporine (Stp) as a positive control. (**i**) Effect on the number of senescent cells after 150 nM arsenic trioxide treatment during 6 days in MDA-MB-231 cells. (**j-l**) Proteomics analysis of the secretome of MDA-MB-231 cells upon PML inducible silencing: (**j**) PML and tubulin levels in both cells extracts and secretome samples (dash lines indicate samples used in the analysis), (**k**) unsupervised exploratory data analysis by means of principal component analysis and (**l**) heat maps representing the proteins that were significantly over- and under-secreted upon PML silencing in MDA-MB-231 cells. Data analysis was based on spectral count data after exporting it from Scaffold software into R. The GLM model based on the Poisson distribution was used to test significance. Only the proteins with spectral counts of 2, Log2FC of 0.8 and adjusted p-value of 0.05 are present in the heatmap. Columns represent samples; rows are proteins. Red represents proteins that are over-secreted and green represents proteins that are under-secreted. The data rows are centred and scaled to 1 standard deviation prior to produce the heat map. (**m**) Immunofluorescence of macroH2A1.1 and DAPI upon inducible silencing of PML in MDA-MB-231 cells. (**n-o**) Levels of Lamin B1 protein upon PML inducible silencing in MDA-MB-231 cells (**n**, representative of 5 experiments) and (**o**) protein quantification (n=5). (**p**) Effect on ROS production (n=4) after inducible PML silencing in MDA-MB-231 cells. (**q-r**) Impact of inducible PML silencing

on tumour growth (**q**) and tumour weight (**r**) of established MDA-MB-231 xenografts (sh4 no dox, n=10; sh4 dox, n=12). Error bars represent s.e.m. p, p-value (*p< 0.05, **p< 0.01, ***p< 0.001) for figure f and g (* sh4 vs shC or dox; \$ sh5 vs shC; # sh1 vs shC). One-tailed Student's t-test (d, i) and one-tailed one sample t-test (f-g, o-p) were used for cell line data analysis, and one-tailed Mann-Whitney U-test for xenografts (q-r). shC: Scramble shRNA, sh1, sh4 and sh5: shRNA against *PML*, Dox: doxycycline, SA-β-gal: Senescence-associated beta-galactosidase, VC: vehicle control, ATO: arsenic trioxide, ROS: reactive oxygen species. Molecular weight markers (kDa) are shown to the right.

Supplementary Figure 2. (a-b) Protein levels of p27 and PML after either inducible (sh1) (**a**) or constitutive (**b**) PML silencing in MDA-MB-231 cells (representative of 3 experiments). (**c**) Quantification of p27 and PML protein levels along 6 days of doxycycline-inducible PML silencing on MDA-MB-231 cells (n=3) with sh1. (**d-f**) Representative western blots of inducible PML silencing with the 3 different short hairpins during 6 days of induction graphed on main Fig. 2b-c and Suppl. Fig. 2c. (**g-h**) Immunofluorescence quantification of nuclear p27 positive cells (**g**) and correlation of p27 positive cells and PML levels (**h**) (upon PML inducible silencing on MDA-MB-231 cells with sh1). (**i**) Schematic representation of the p27-Rb protein interaction and regulation. Error bars represent s.e.m. p, p-value (*p< 0.05, **p< 0.01, ***p< 0.001). One-tailed Student's t-test (g-h) and one-sample t-test (c) were used for cell line data analysis. shC: Scramble shRNA, sh1, sh4 and sh5: shRNA against *PML*, Dox: doxycycline, D: day, RB: retinoblastoma protein. CDK: cyclin dependent kinases. Molecular weight markers (kDa) are shown to the right.

Supplementary Figure 3. (a) p27 and PML protein levels after constitutive silencing of either p27 or PML or both in MDA-MB-231 cells (representative of 4 experiments). (**b-c**) Effect on the number of senescent cells (n=4) (**b**) and cell growth (n=3) (**c**) after constitutive p27 and/or PML silencing. Error bars represent s.e.m. p, p-value (*p< 0.05, **p< 0.01, ***p< 0.001 compared with shC or as indicated, ns: not significant). One-tailed Student's t-test (b) and one-tailed one-sample t-test (c)

were used for cell line data analysis. shC: Scramble shRNA, SA- β -gal: Senescence-associated beta-galactosidase. Molecular weight markers (kDa) are shown to the right.

Supplementary Figure 4. **(a)** Correlation analysis between PML and MYC (top panels) and between PML and PIM1 (bottom panels) mRNA levels in all breast cancer subtypes of tumor specimens of the indicated breast cancer datasets. Sample sizes: Ivshina (n=249), Lu (n=131), TCGA (n=522) and Wang (n=286). **(b-d)** MYC, p27 and PML protein levels (representative of 3 experiments) **(b)**, quantification of the protein (n=3) **(c)** and MYC gene levels **(d)** after inducible silencing of PML (sh4) in MDA-MB-231 cells (n=3). **(e)** PML, p27 and MYC mRNA levels upon doxycycline-inducible PML silencing (sh4) of established MDA-MB-231 xenografts. **(f-h)** MYC, p27 and PML protein levels (representative of 3 experiments) **(f)**, quantification of the protein (n=3) **(g)** and MYC gene levels **(h)** after inducible silencing of PML (sh4) in MDA-MB-468 cells (n=3). **(i-j)** MYC, p27 and PML protein levels (representative of 5 experiments) **(i)** and quantification of the protein (n=5) **(j)** after 150 nM arsenic trioxide treatment during 6 days in MDA-MB-231 cells. **(k-l)** Protein quantification from Fig. 4e **(k)** and impact in cell number (n=3) **(l)** of inducible MYC silencing (sh42) in MDA-MB-231 cells. **(m-n)** PIM1 gene levels after PML inducible silencing in MDA-MB-231 (n=3) **(m)** and MDA-MB-468 (n=3) **(n)** cells. **(o-q)** Protein quantification from Fig. 4i **(o)**, gene expression levels of PIM1, MYC and p27 **(p)** and impact in cell number (n=3) **(q)** of inducible PIM1 silencing (sh18) in MDA-MB-231 cells. Error bars represent s.e.m. p, p-value (*p< 0.05, **p< 0.01, ***p< 0.001, ns: not significant). One-tailed one sample t-test (c-d, g-h, j-q) was used for cell line data analysis and one-tailed Mann-Whitney U-test for xenografts (e). sh4: shRNA against *PML*, sh42: shRNA against *MYC*, sh18: shRNA against *PIM1*. Dox: doxycycline. VC: vehicle control. ATO: arsenic trioxide. Molecular weight markers (kDa) are shown to the right.

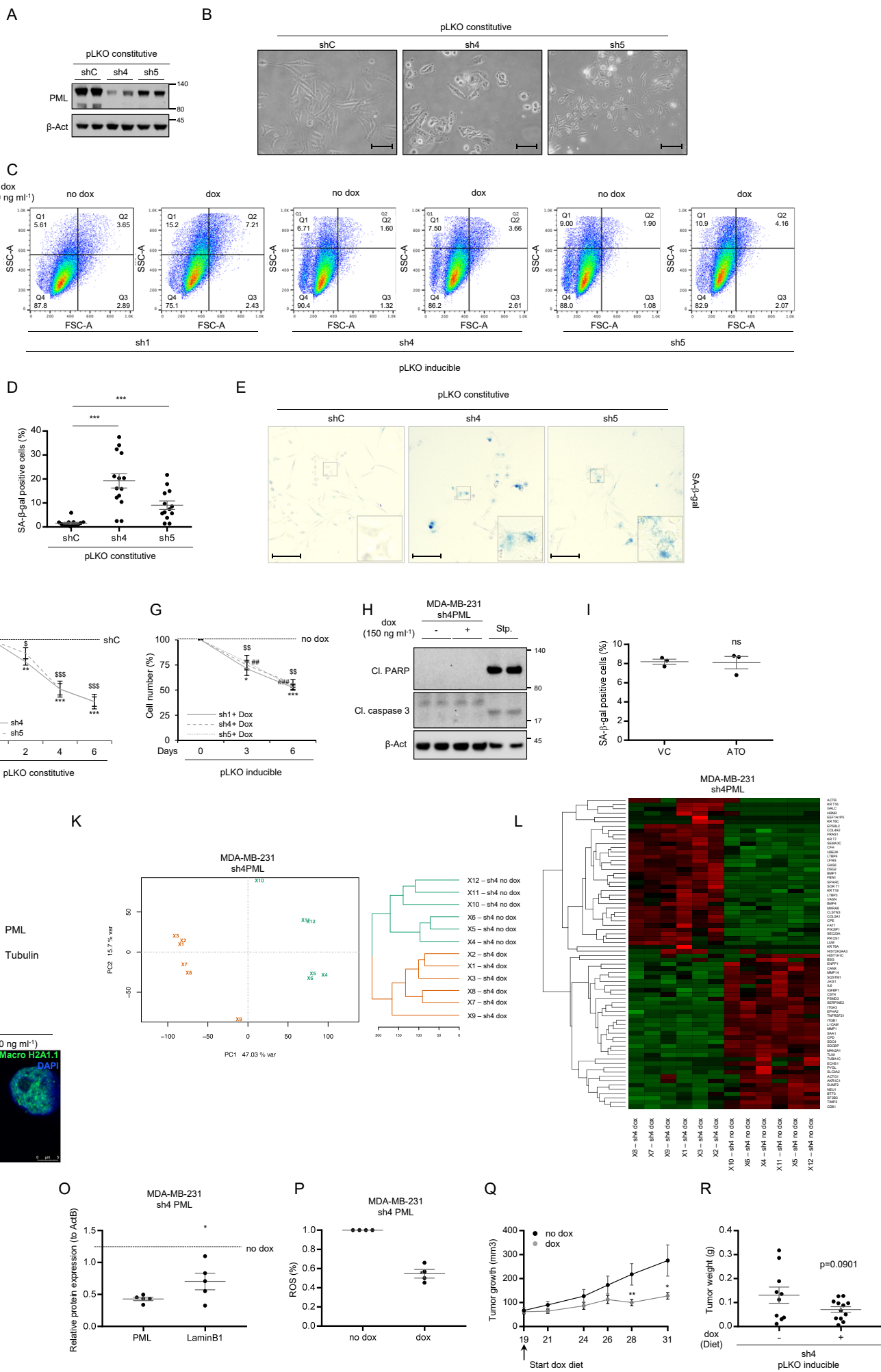
Supplementary Figure 5. **(a-c)** Impact of PML inducible silencing (sh4) on cell number in MDA-MB-468 **(a)**, MCF-7 **(b)** and Cama-1 **(c)** cell lines. **(d-e)** p27, MYC and PML protein levels **(d)** and

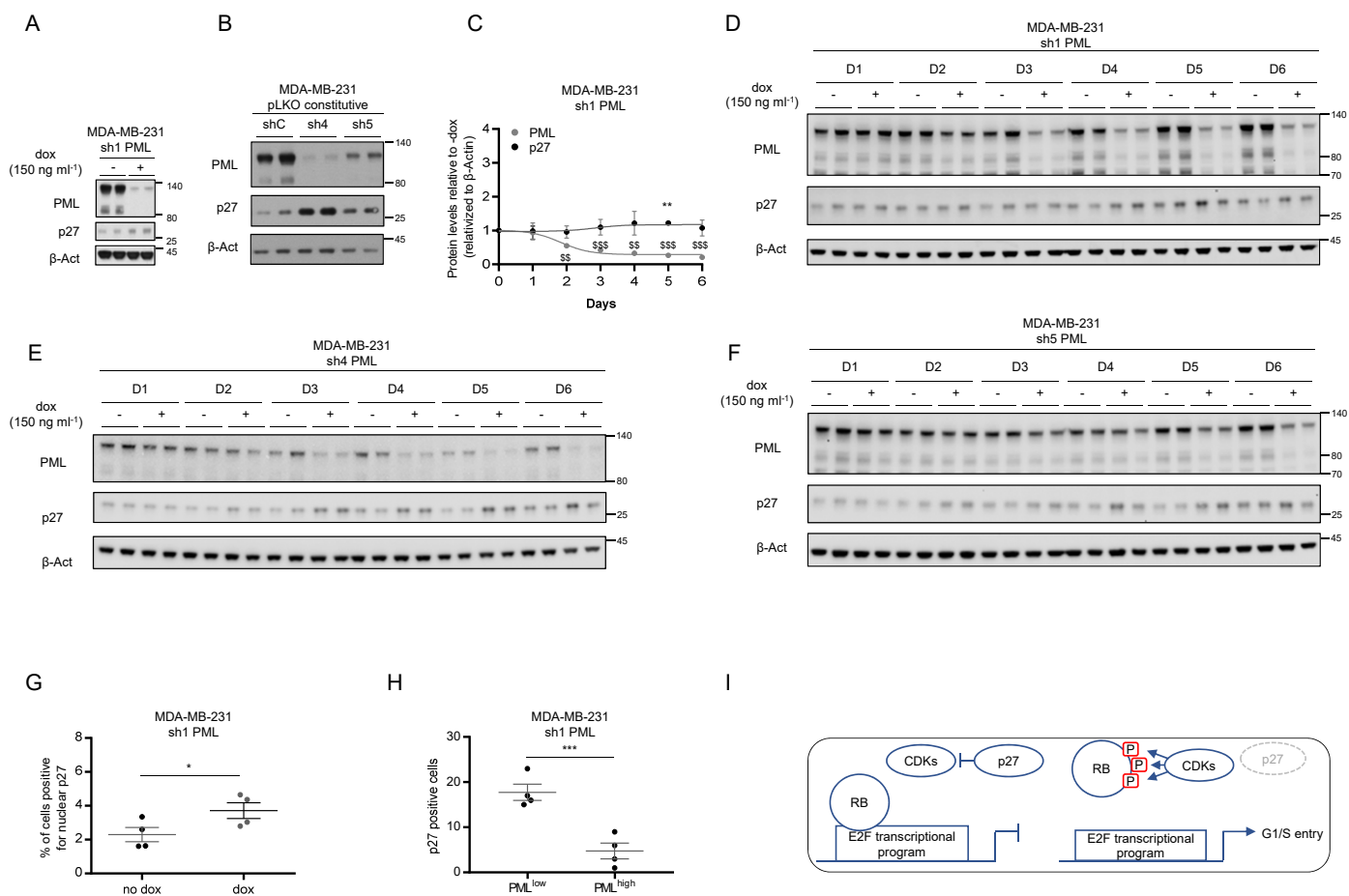
protein quantification **(e)** of PML inducible silencing in MCF-7 cells. **(f-g)** p27, MYC and PML protein levels **(f)** and protein quantification **(g)** of PML inducible silencing in Cama-1 cells. **(h)** Impact of PML inducible silencing (sh4) on cell morphology in MDA-MB-468, MCF-7 and Cama-1 cell lines, scale bar 50 μ m. **(i-k)** Proteomics analysis of the secretome of Cama-1 cells upon PML inducible silencing: **(i)** PML and tubulin levels in both cells extracts and secretome samples (dash lines indicate samples used in the analysis), **(j)** unsupervised exploratory data analysis by means of principal component analysis and **(k)** heat maps representing the proteins that were significantly over- and under-secreted, upon PML silencing in Cama-1 cells. Data analysis was based on spectral count data after exporting it from Scaffold software into R. The GLM model based on the Poisson distribution was used to test significance. Only the proteins with spectral counts of 2, Log₂FC of 0.8 and adjusted p-value of 0.05 are present in the heat map. Columns represent samples; rows are proteins. Red represents proteins that are over-secreted and green represents proteins that are under-secreted. The data rows are centered and scaled to 1 standard deviation prior to produce the heatmap. Error bars represent s.e.m. p, p-value (*p< 0.05, **p< 0.01, ***p< 0.001). One-tailed one sample t-test was used for cell line data analysis (a-c, e, g). sh4: shRNA against *PML*. Dox: doxycycline. Molecular weight markers (kDa) are shown to the right.

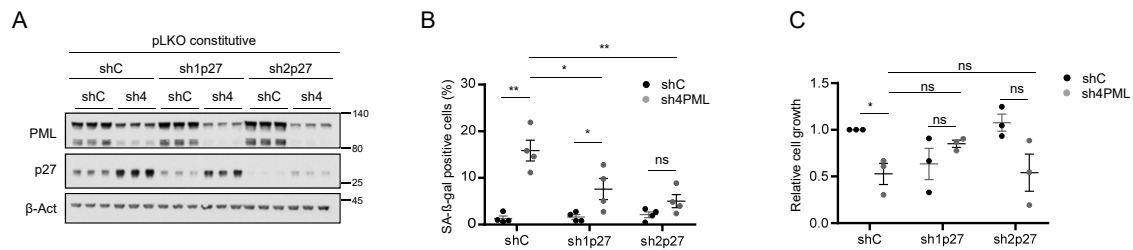
Supplementary Figure 6. Uncropped scans.

Supplemental Table 1. List of differentially secreted proteins upon silencing the PML protein in MDA-MB-231 cells.

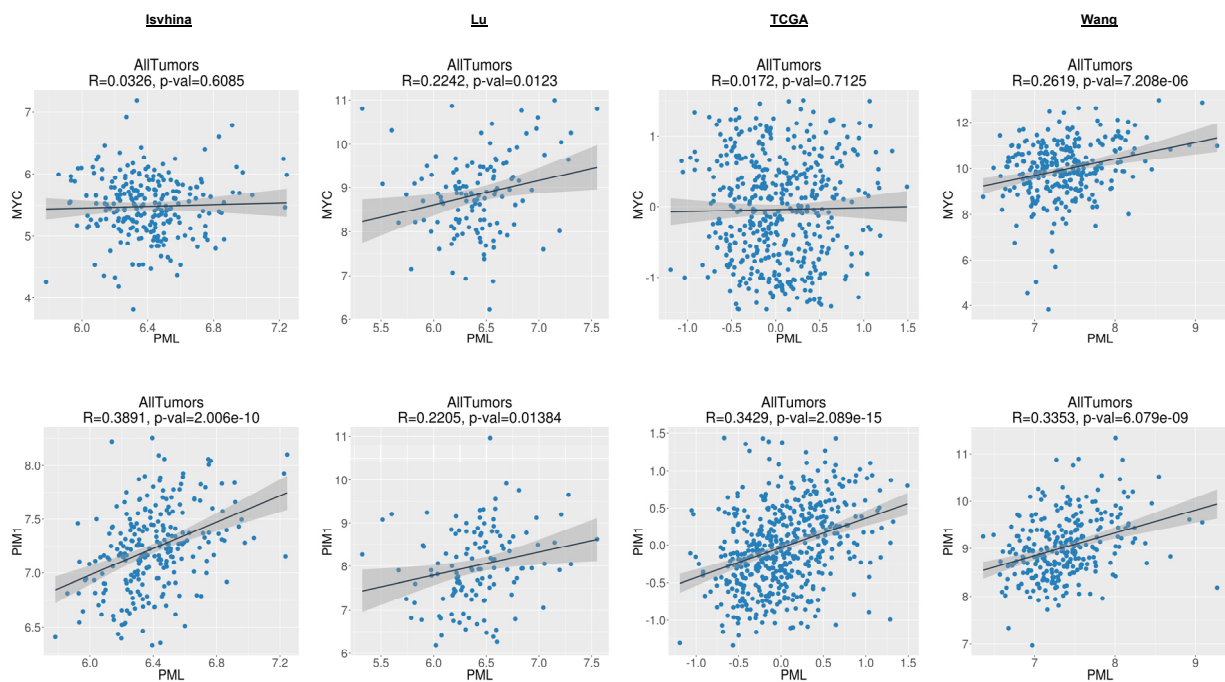
Supplemental Table 2. List of differentially secreted proteins upon silencing the PML protein in Cama-1 cells.



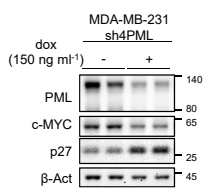




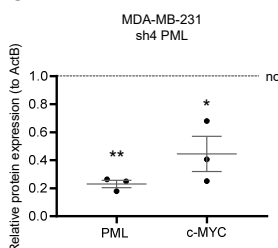
A



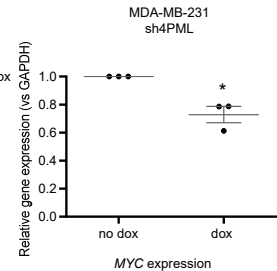
B



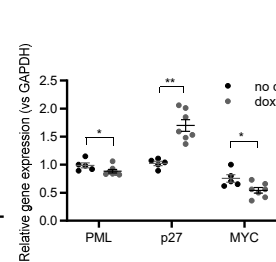
C



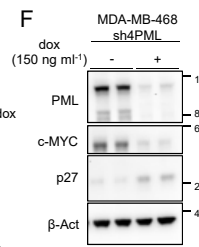
D



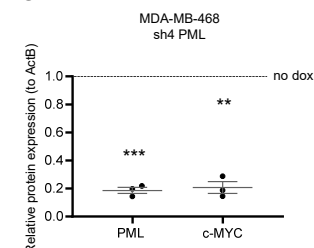
E



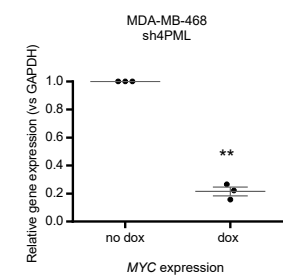
F



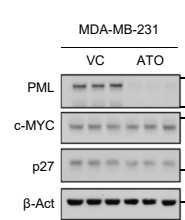
G



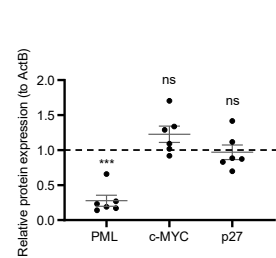
H



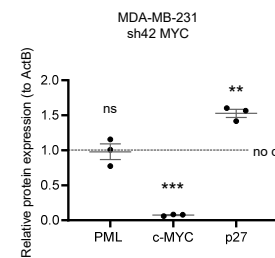
I



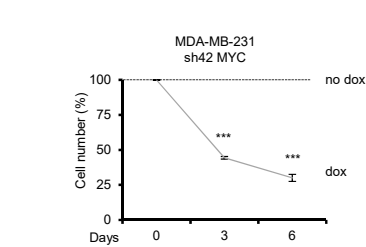
J



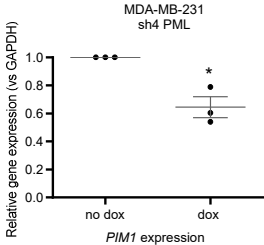
K



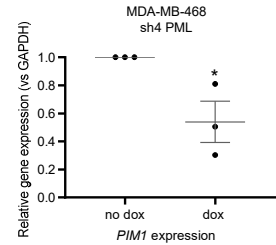
L



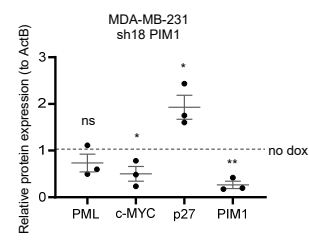
M



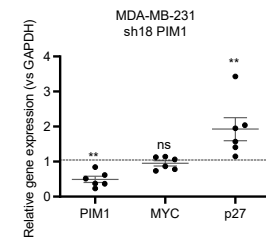
N



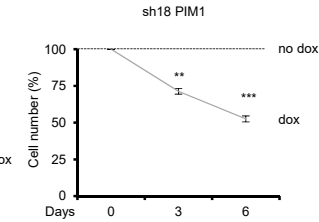
O



P



Q



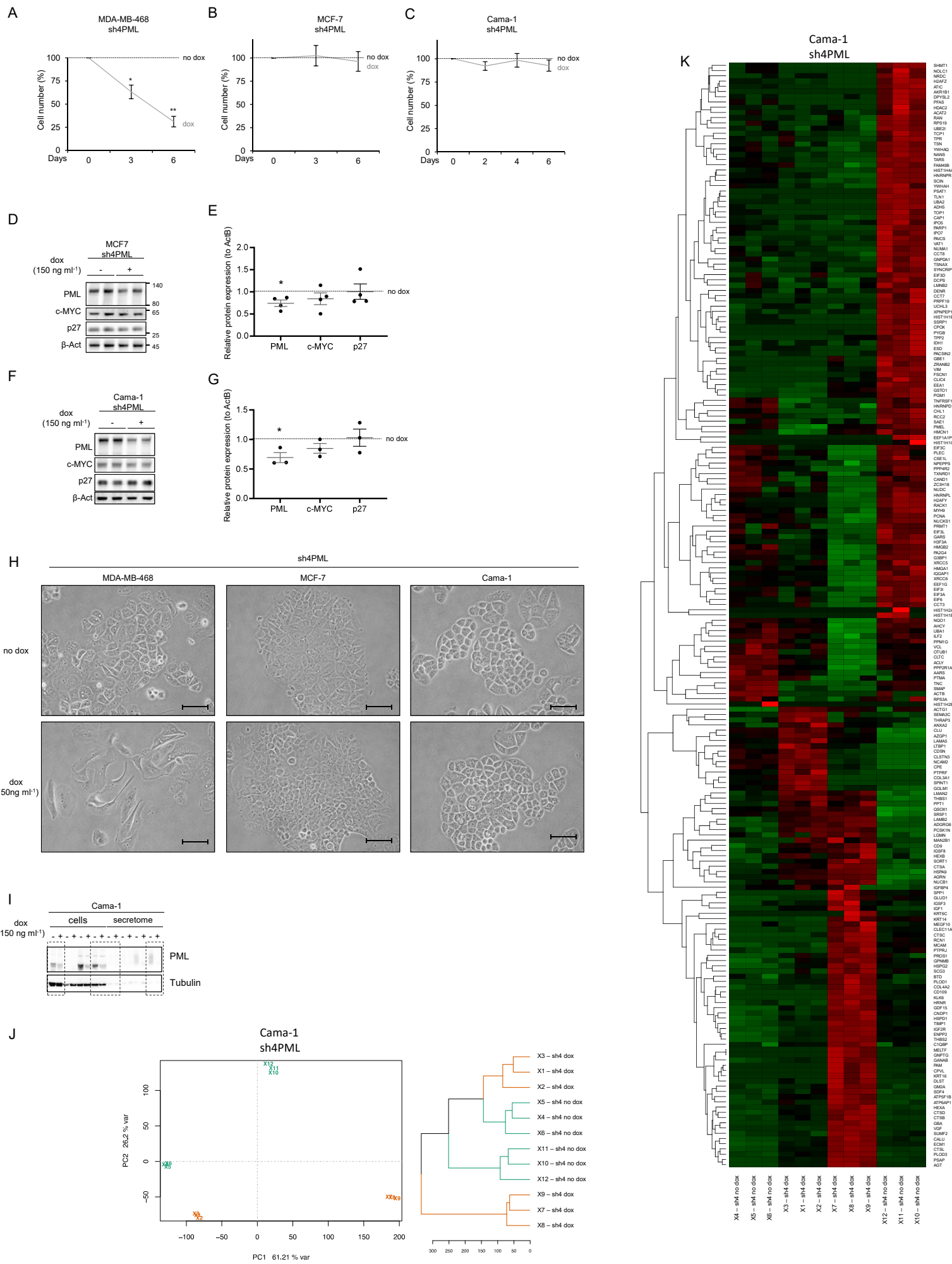


Figure 1A

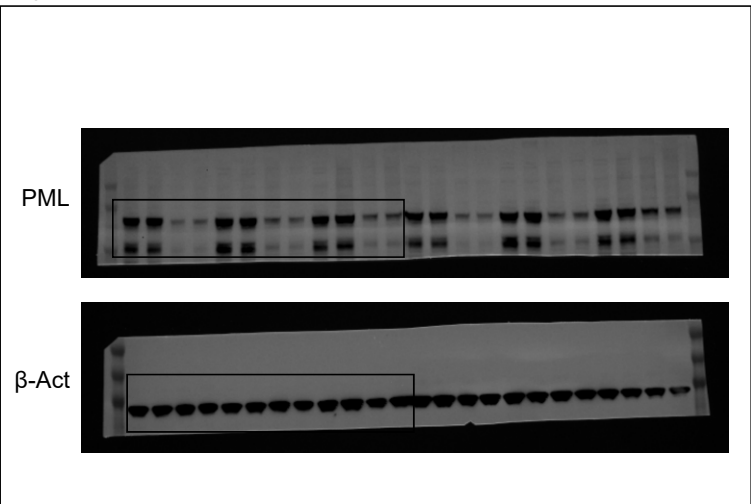


Figure 1G

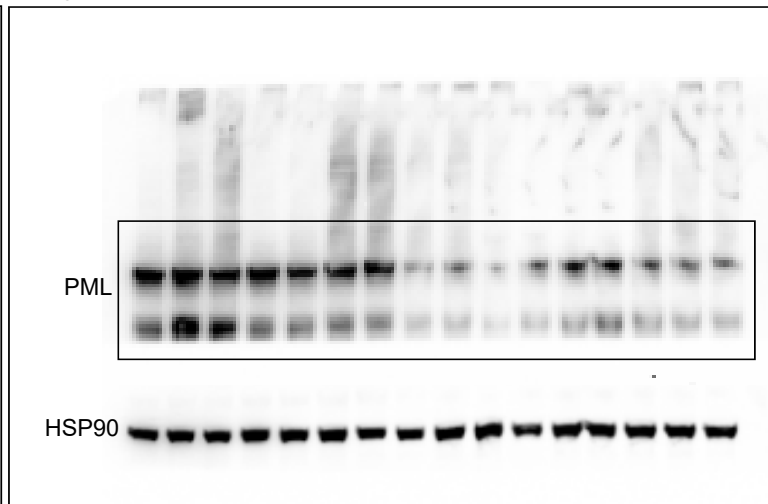


Figure S1A

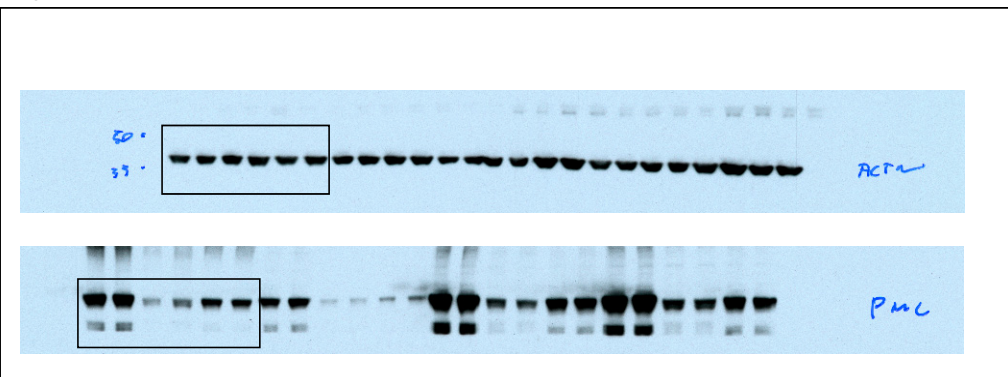


Figure S1H

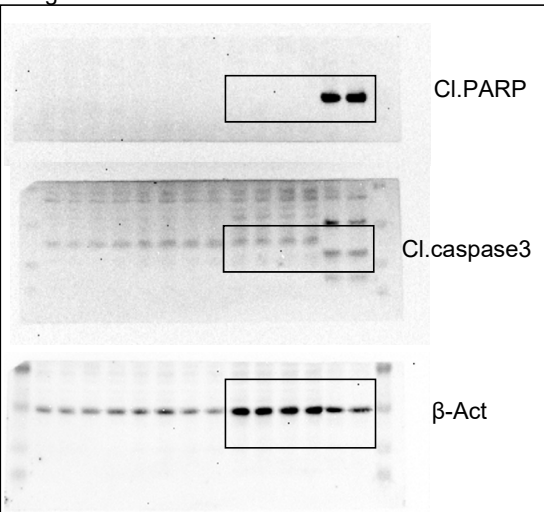


Figure S1I

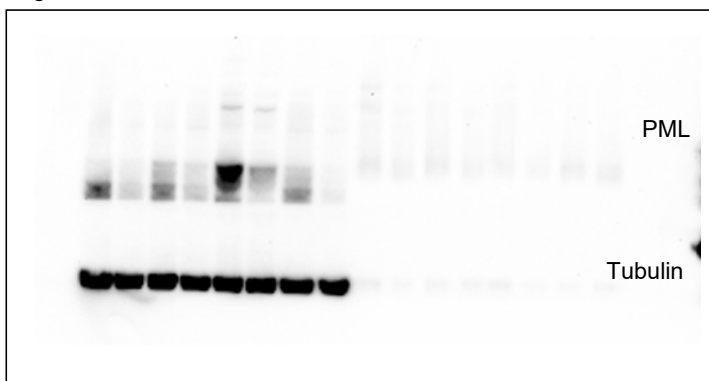


Figure S1m

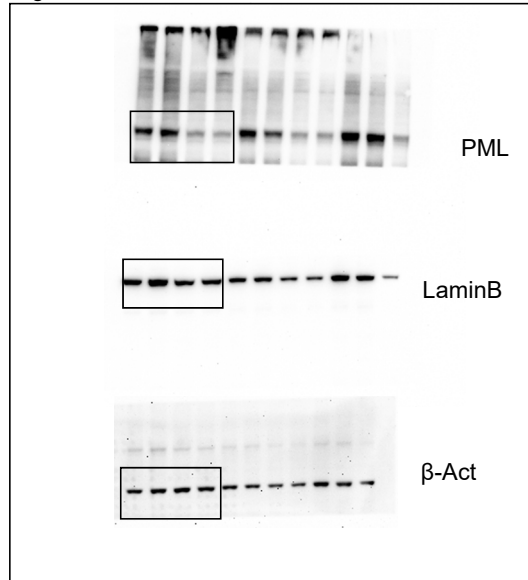


Figure 2A

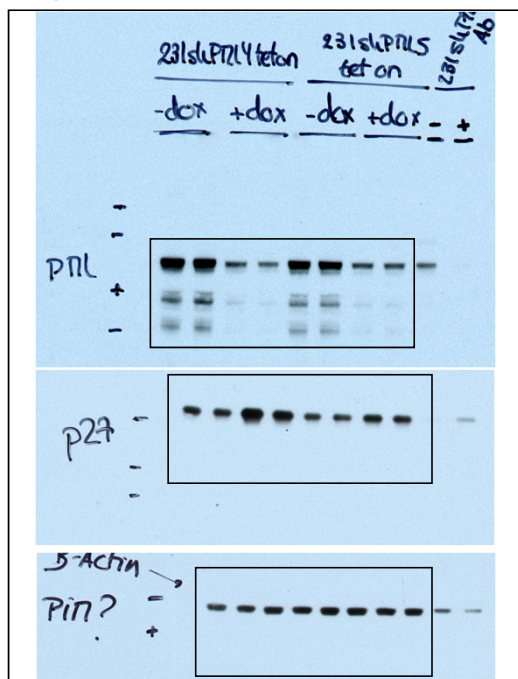


Figure 2H

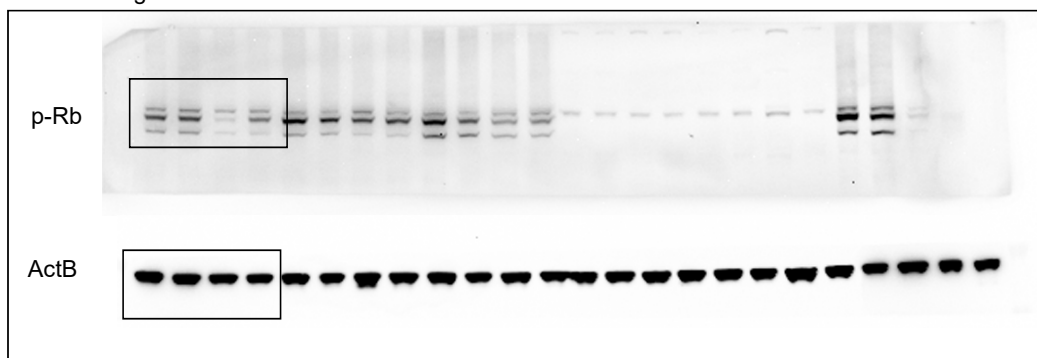


Figure 2J

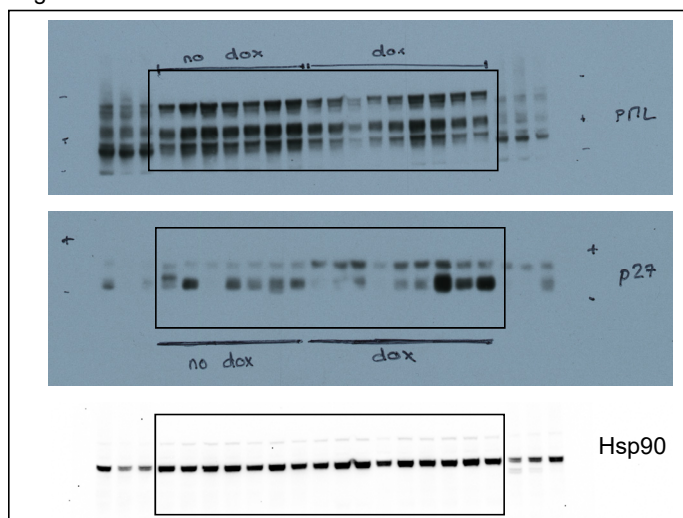


Figure S2A

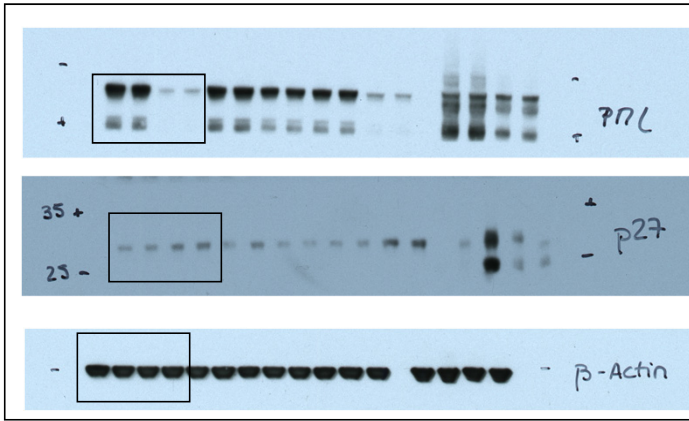


Figure S2B

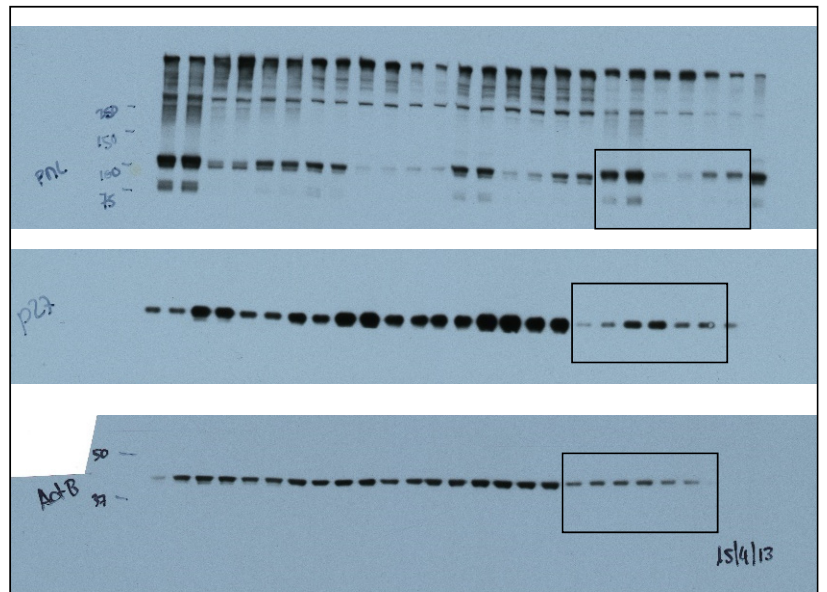


Figure S2D

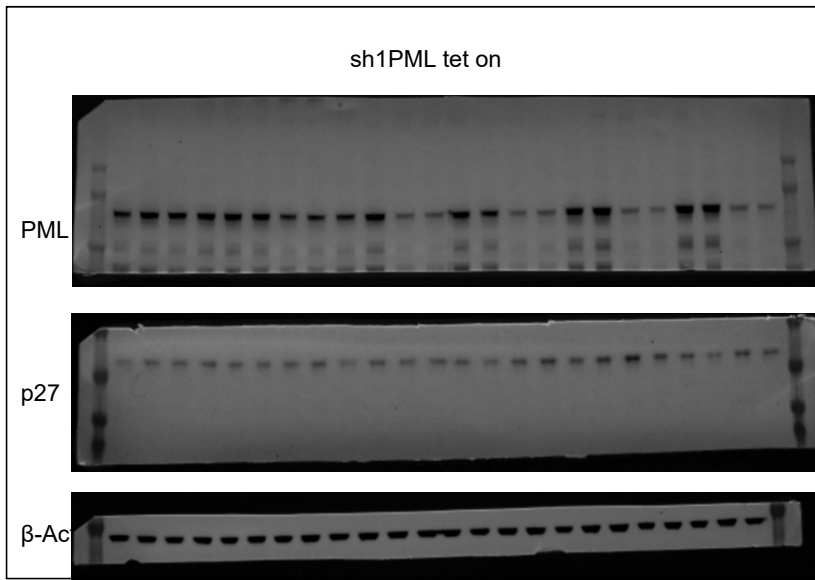


Figure S2E

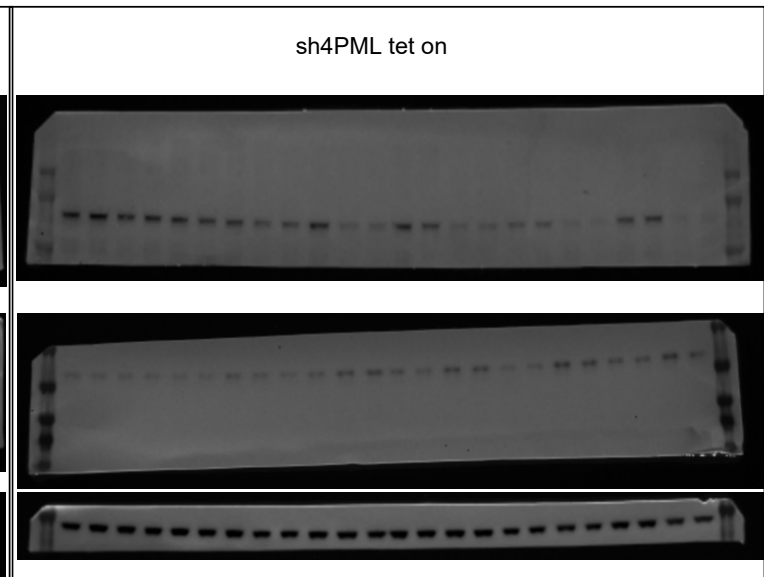


Figure S2F

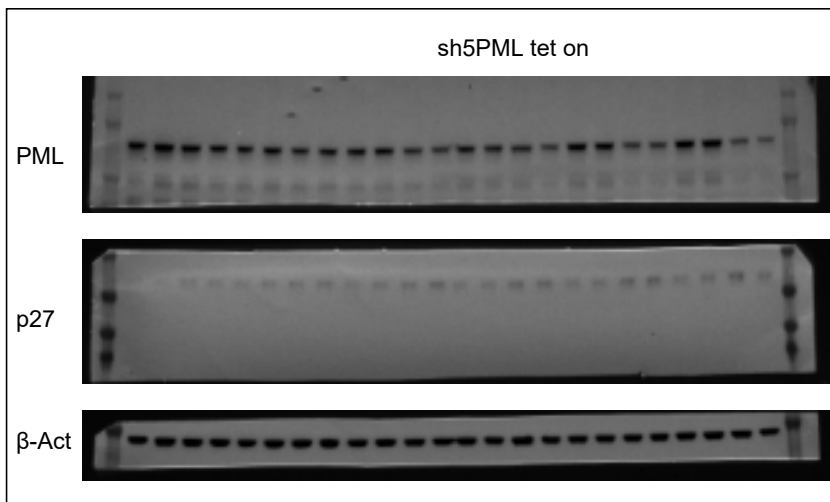


Figure 3B

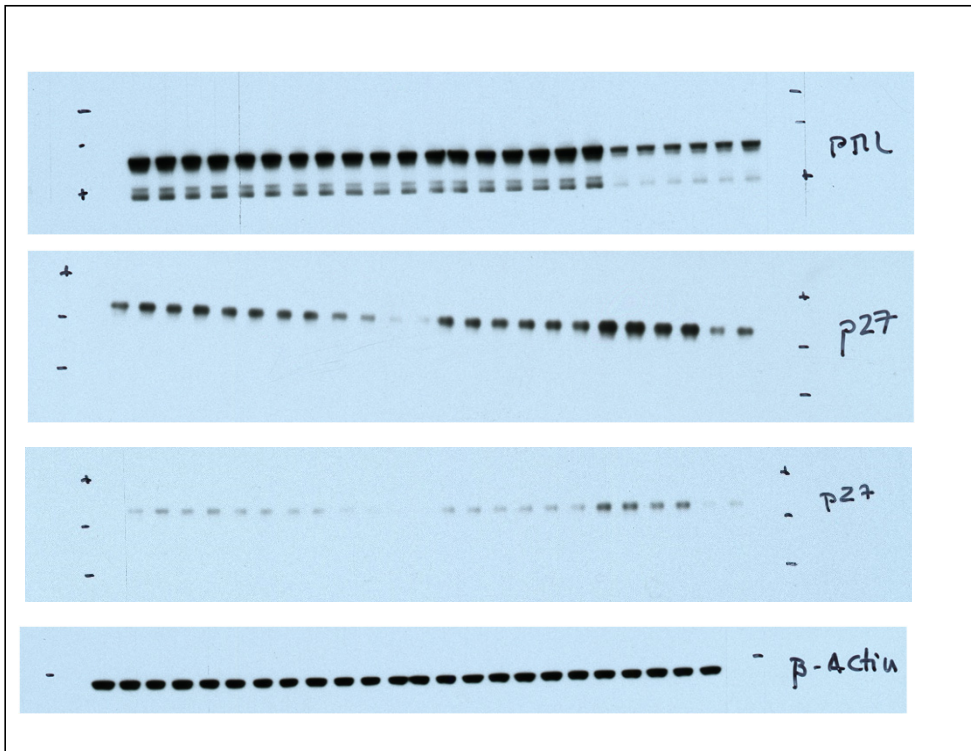


Figure S3A

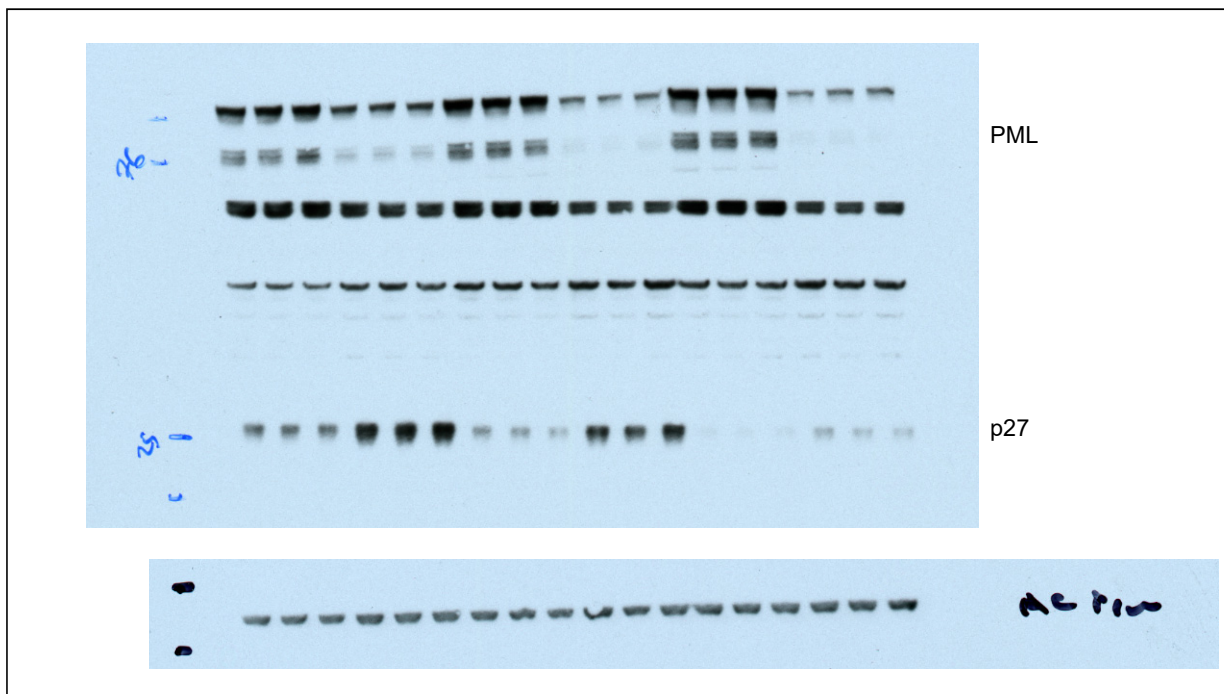


Figure 4B

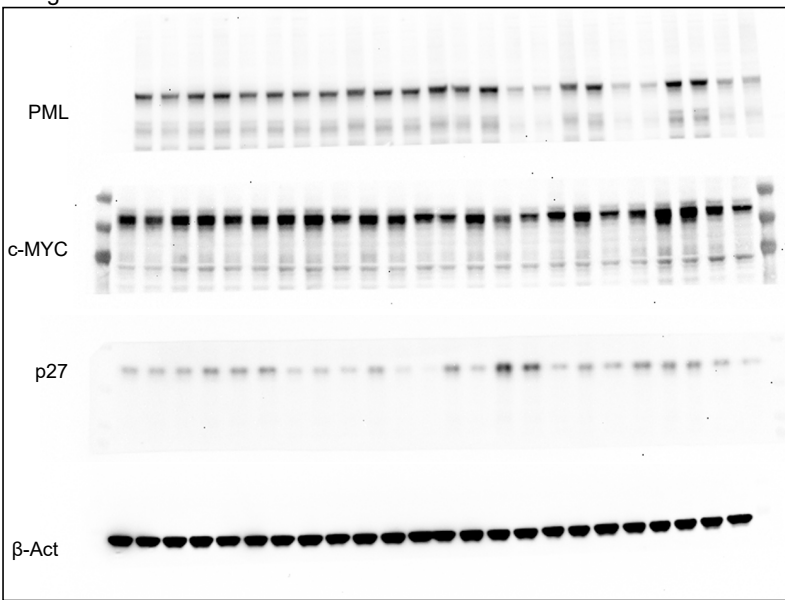


Figure 4E

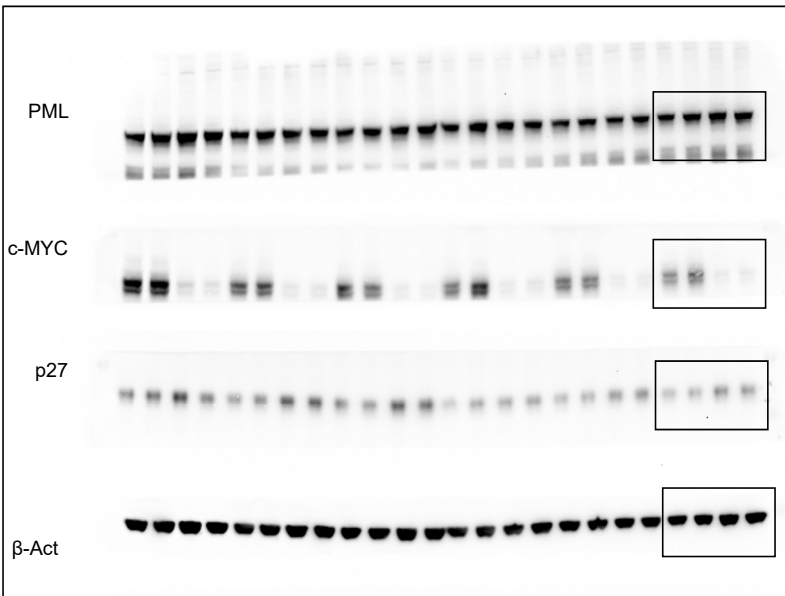


Figure 4I

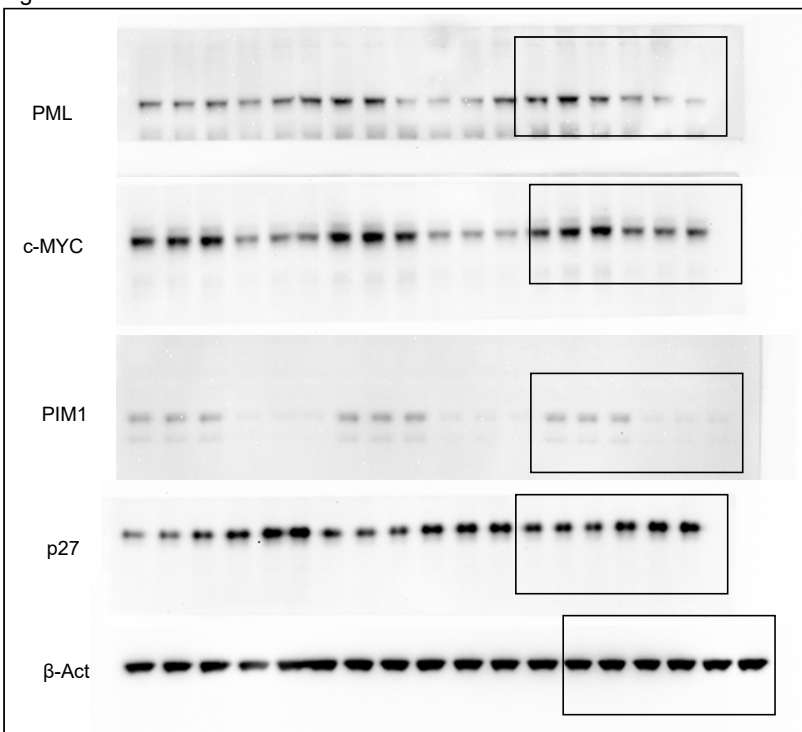


Figure S4B

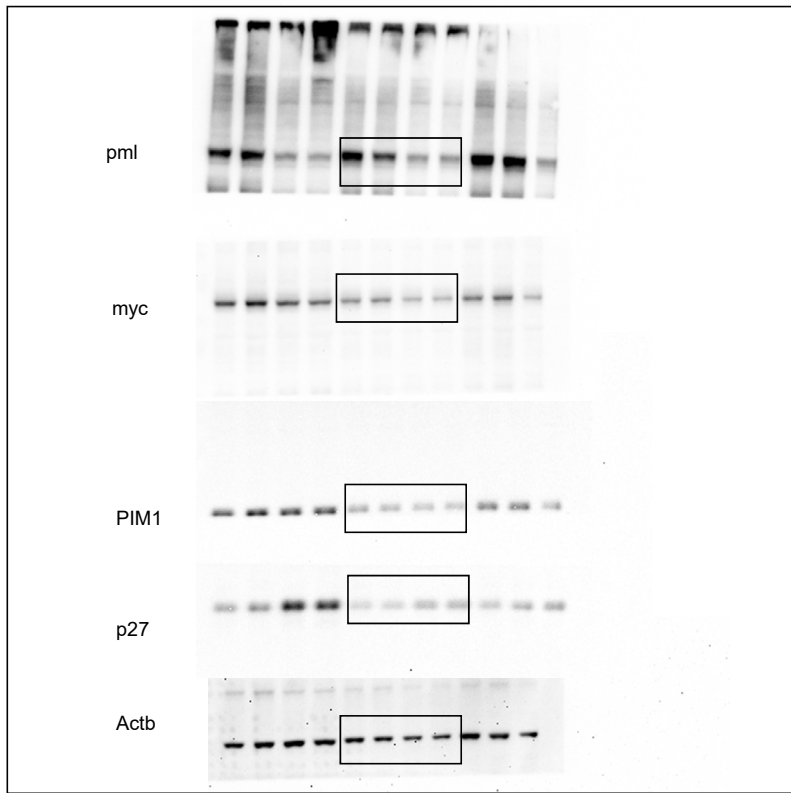
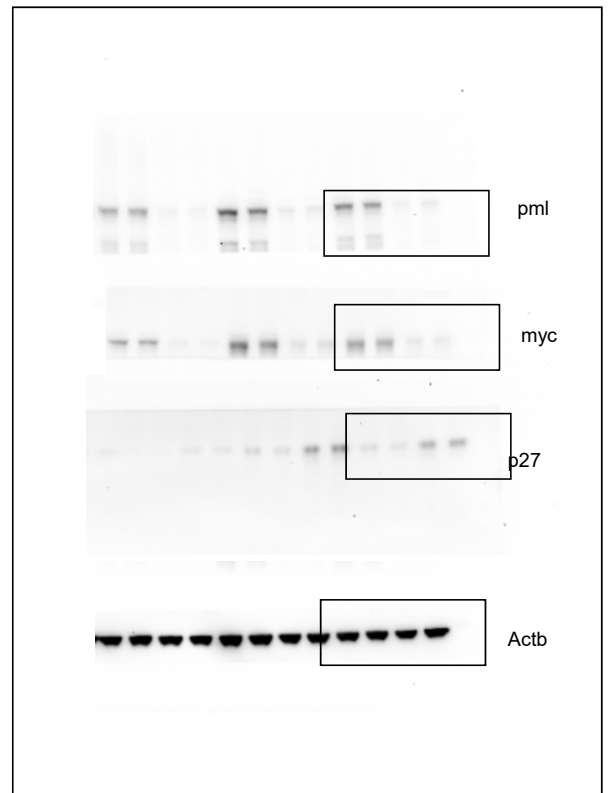


Figure S4F



Supp. Figure 6 (cont)

Figure S4I

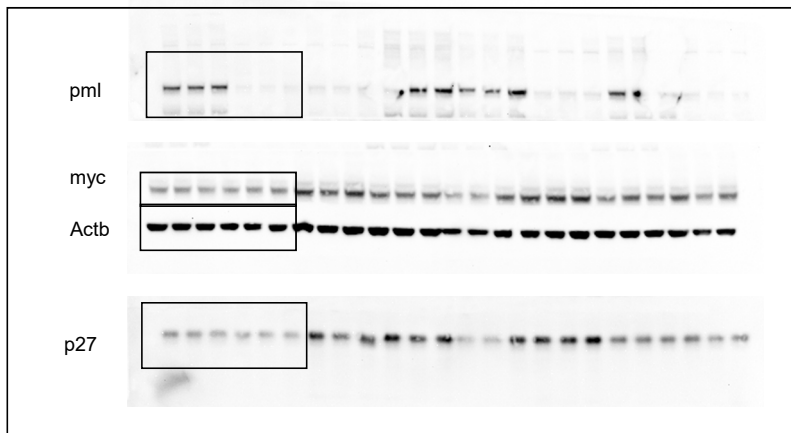


Figure 5A

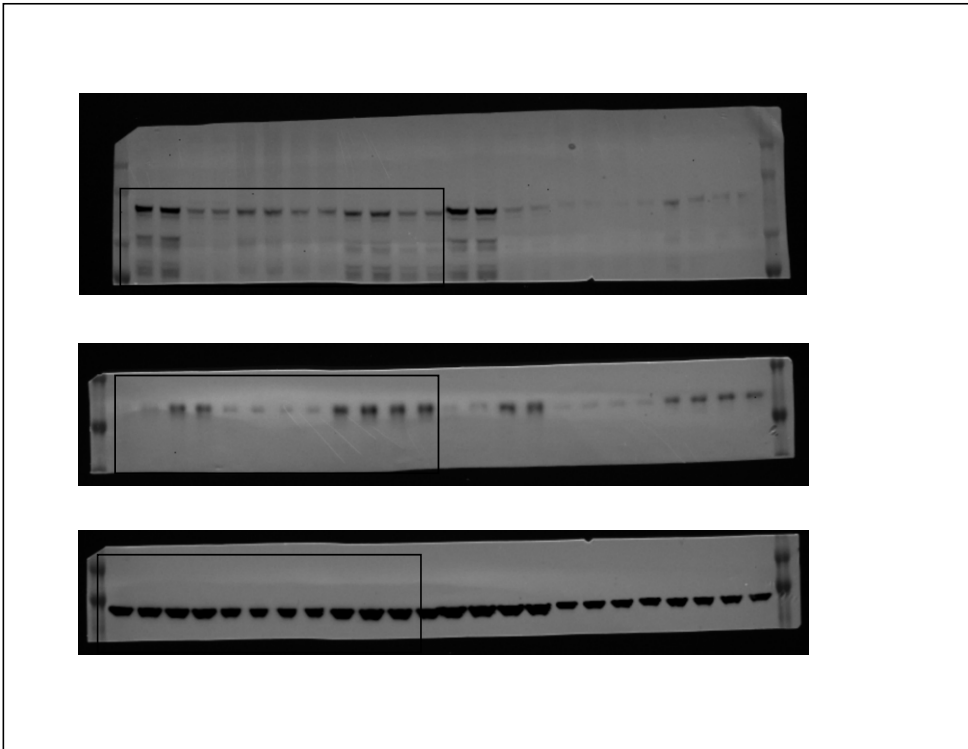


Figure S5D and S5F

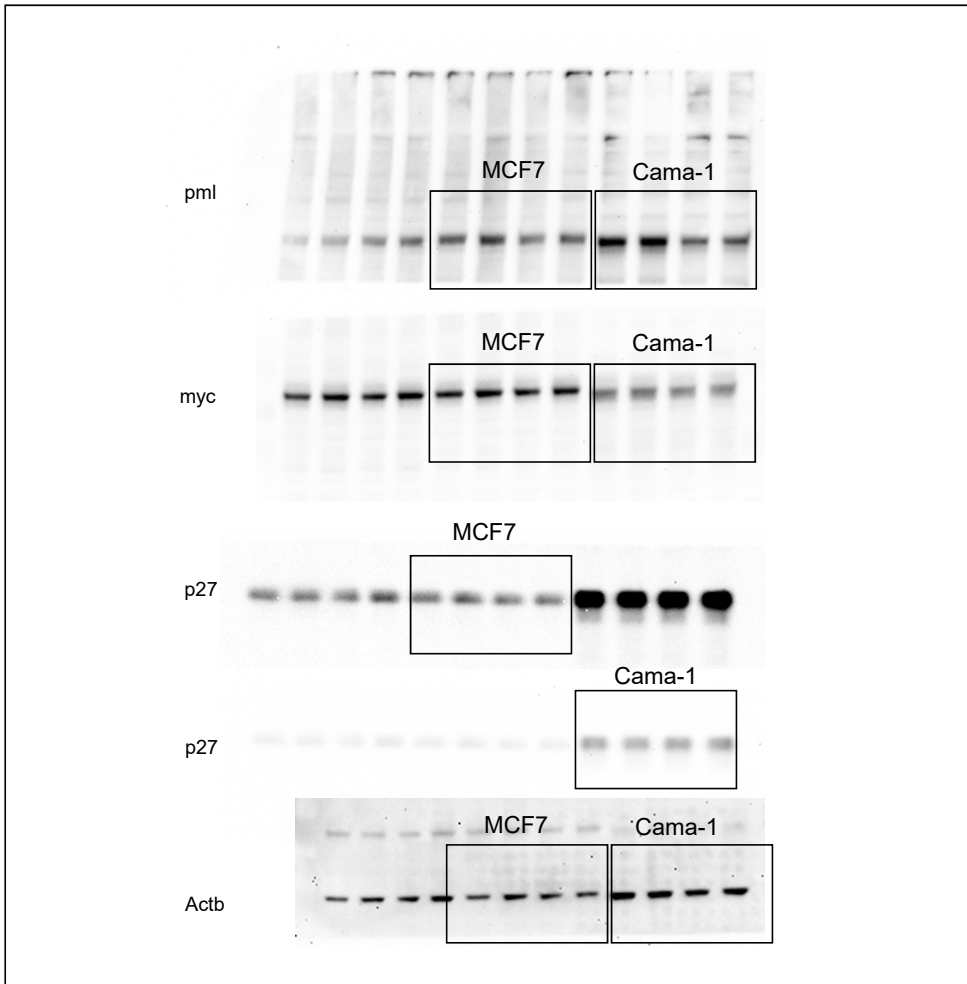
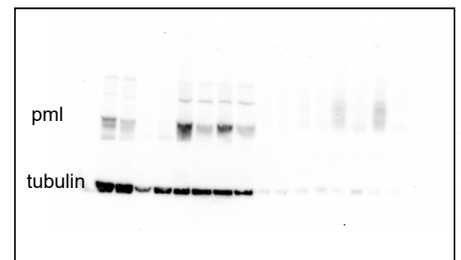


Figure S5I



Supplemental Table 1. List of differentially secreted proteins upon silencing the PML protein in MDA-MB-231 cells.

Gene Name	Positive ^a	Negative ^b	Log ₂ FC	adj p-value ^c
ACTB	65,3	15	2,168	2,65E-45
ACTG1	13,3	63,2	-2,199	3,79E-43
KRT16	9	0	37,7	8,28E-16
TUBA1C	2,2	16	-2,84	2,54E-14
KRT6C	7,3	0	30,09	7,02E-13
EEF1A1P5	6,8	0	28,27	5,16E-12
MMP1	0,2	7,7	-5,477	3,08E-11
BMP1	8	0,7	3,629	2,41E-09
MAN2A1	0	4	-32,68	1,34E-06
CLSTN3	7,5	1,2	2,729	1,45E-06
ITGB1	4	13,5	-1,71	2,59E-06
TNFRSF21	0,5	5,8	-3,5	2,66E-06
COL5A1	14,2	4,8	1,596	2,74E-06
FBN1	22,8	10,5	1,165	2,74E-06
TLN1	23,2	42,2	-0,8189	2,74E-06
SPARC	3,2	0	32,36	1,41E-05
KRT6A	3	0	28,98	2,93E-05
LTBP4	10	3	1,783	3,01E-05
SQSTM1	2,7	9,8	-1,837	3,43E-05
L1CAM	4	12,2	-1,56	4,20E-05
FRAS1	2,8	0	33,7	4,77E-05
SERPINE2	0,3	4,3	-3,656	5,65E-05
KRT7	8,5	2,3	1,909	5,90E-05
CPD	0,2	3,7	-4,414	7,44E-05
LUM	3,3	0,2	4,371	0,0001401
CPE	10,7	3,8	1,522	0,0001518
FAT1	3,8	0,3	3,568	0,0001518
TIMP3	0,3	4	-3,543	0,000152
NEU1	0,7	4,8	-2,813	0,0002139
ENPP1	1,7	7	-2,024	0,0002601
EPS8L2	2,3	0	30,54	0,0002992
ITGA3	0	2,3	-33,33	0,000455
PROS1	9	3,2	1,553	0,0005347
AKR1C1	3,5	10	-1,473	0,0005644
LTBP3	2,2	0	33,24	0,0005681
GALC	2,2	0	31,58	0,0005681
CD81	0,8	4,8	-2,492	0,0006621
IL6	0	2,2	-30,34	0,000793
ECHS1	0,3	3,3	-3,28	0,001325
SEC23A	3,2	0,3	3,295	0,001366
CFH	7,8	2,8	1,513	0,002035
SUMF2	0,3	3,2	-3,204	0,002174
EPHA2	2,7	7,8	-1,51	0,002632
KRT19	11,8	5,7	1,106	0,003352
GAS6	12,7	6,3	1,045	0,003882
LFNG	2,8	0,3	3,131	0,00403
SDCBP	0,8	4,2	-2,278	0,004093
UBE2K	2,3	0,2	3,852	0,004193
BMP4	2,3	0,2	3,851	0,004193
PYGL	3,5	8,8	-1,293	0,005184
IGFBP1	4,5	10,3	-1,151	0,006241
SAA1	0,5	3,2	-2,616	0,007954
MXRA8	3	0,5	2,629	0,008305
JAG1	3,2	8	-1,291	0,009363
CST4	2	6	-1,537	0,01085

HIST1H1C	1,5	5	-1,69	0,01406
SDC4	6,2	12,2	-0,9348	0,0169
BTF3	0,5	2,8	-2,463	0,0203
DSG2	8,2	3,8	1,136	0,0203
VASN	4	1,2	1,82	0,0205
SEMA3C	4,8	1,7	1,579	0,02166
MMP14	0,8	3,5	-2,024	0,02305
CANX	0,3	2,3	-2,76	0,02583
BSG	0,5	2,7	-2,371	0,03072
HIST2H2AA3	4,3	1,5	1,57	0,03543
HRNR	2,8	0,7	2,128	0,03625
SORT1	4,8	1,8	1,442	0,03753
COL4A2	9,3	5	0,9451	0,04005
PSMD3	1,8	5	-1,403	0,04453
SLC3A2	3,3	7,3	-1,093	0,04517
SF3B3	1	3,5	-1,765	0,04646
PIK3IP1	2	0,3	2,631	0,0493
THBS1	194,7	129	0,6395	1,69E-19
MYH9	96,3	66	0,591	2,89E-08
FLNB	138,8	107,5	0,4142	2,74E-06
KRT9	51,7	35,3	0,5922	0,0001426
HSPA5	71,3	96,3	-0,3876	0,0006753
GSN	32,2	21,2	0,6494	0,001826
AP1G1	1,8	0	30,19	0,002035
AHNAK	38	26,2	0,5821	0,002174
MATN2	0	1,8	-32,96	0,00267
CNN2	1,7	0	32,94	0,003784
PDIA4	19	30,3	-0,6292	0,004491
CTSC	12,3	21,3	-0,7452	0,006266
HYOU1	13,2	22,3	-0,7174	0,007086
HSP90AA1	71,5	92,3	-0,3232	0,008745
NAMPT	18,8	28,8	-0,5686	0,01708
KRT1	73,2	59,8	0,3355	0,01783
EFEMP1	23,2	15,5	0,625	0,01818
HSPG2	56,8	45,2	0,3767	0,0205
KRT8	21,3	14,2	0,6362	0,02239
ACBD3	1,2	0	30,92	0,02398
SEMA3B	1,2	0	32,42	0,02398
ASPH	1,2	0	28,09	0,02398
ALDH9A1	1,2	0	30,92	0,02414
KRT13	1,2	0	32,73	0,02431
HSP90B1	30,7	42,5	-0,425	0,03072
KRT2	32,5	44,3	-0,3999	0,04114
LOXL4	1	0	30,73	0,04517
SEMA7A	12,3	19,5	-0,6165	0,04517
F3	1	0	35,49	0,04517
KRT4	1	0	32,57	0,04517
GGH	12	19	-0,6172	0,04882

Notes:

a: Average normalized spectral counts from cells where PML is silenced

b: Average normalized spectral counts from cells where PML is expressed

c: the adjusted p-values have been corrected for multiple hypothesis testing according to Benjamini and Hochberg

Supplemental Table 2. List of differentially secreted proteins upon silencing the PML protein in CAMA1 cells.

Gene Name	Positive ^a	Negative ^b	Log ₂ FC	adj p-value ^c
KRT16	7,5	0,2	5,853	4,92E-14
CPVL	3,5	0,2	4,754	3,52E-06
CTSB	8,3	0,5	4,343	8,77E-13
KRT6C	4,7	0,3	4,169	2,01E-07
GNPTG	2	0	34,96	0,0001193
MELTF	2	0	34,96	0,0001193
ADGRG6	3,5	0	34,14	5,65E-07
PAM	3,5	0	34,07	1,44E-07
IGF1	2	0	31,67	0,00018
DLST	2,2	0	31,57	6,54E-05
MAN2B1	2	0	30,46	0,0002208
ATP6AP1	3,8	0,3	3,795	1,23E-05
AGT	5,2	0,5	3,665	3,20E-07
IGSF8	3,2	0,3	3,464	0,0002133
PCSK1N	5	0,5	3,458	2,89E-06
GM2A	3,5	0,5	3,09	0,0001814
PPT1	5,2	0,8	2,752	2,70E-05
LAMB2	23,7	4	2,736	9,95E-23
ANXA2	2	0,3	2,691	0,01643
CTSA	6	1,2	2,552	9,97E-06
PROS1	2,2	0,5	2,381	0,01638
KLK6	2	0,5	2,361	0,01909
LGMN	3	0,7	2,335	0,00539
CD109	4,8	1,3	2,219	0,0002133
CTSL	28,7	7,3	2,217	2,94E-22
SEMA3C	4,2	1	2,108	0,002333
GBA	5,3	1,5	2,107	0,0002133
CD9	3,7	1	2,068	0,004037
THRAP3	2	0,5	2,066	0,04868
SUMF2	4,5	1,3	2,05	0,001021
SCG3	2,2	0,7	2,017	0,03138
PLOD1	15,2	4,5	2,006	2,10E-10
ATP5F1B	8,3	2,5	1,954	9,74E-06
HSPG2	3,2	1	1,947	0,009834
SPP1	2	0,7	1,946	0,04365
CTSC	2,5	0,8	1,927	0,02292
HEXA	12,2	3,8	1,906	7,51E-08
IGSF3	4	1,3	1,861	0,004482
PTPRF	4,8	1,3	1,832	0,003419
MEGF10	2,8	1	1,83	0,01909
HSPA9	6,3	2	1,81	0,0004584
SPINT1	6	1,7	1,798	0,001198
RCN1	2,7	1	1,776	0,02639
LTBP1	5,8	1,8	1,686	0,002117
GLUD1	3,8	1,5	1,679	0,009834
LAMA5	19	6,2	1,674	2,21E-09
COL3A1	3,8	1,2	1,666	0,01794
GANAB	9,5	3,7	1,641	2,57E-05
IGFBP4	2,8	1	1,638	0,04167
NUCB1	5,5	2	1,636	0,002646
GDF15	7,8	3,2	1,609	0,0001871
ACTG1	43,3	16,2	1,6	6,02E-21
ECM1	51,7	21,2	1,534	7,62E-24
HRNR	4,8	2,2	1,482	0,00792
CTSD	15,3	6,5	1,467	7,27E-07
SDF4	11,3	4,8	1,452	3,21E-05

HEXB	6,8	2,8	1,446	0,002174
ENPP2	40,8	18,2	1,441	1,75E-17
CALU	19,7	8,8	1,398	4,65E-08
CLEC11A	5	2,3	1,398	0,01062
PLOD3	33,2	15	1,358	1,05E-12
HSPD1	14	6,7	1,323	1,40E-05
THBS1	35	15,3	1,307	3,41E-12
MCAM	4,8	2,5	1,268	0,0204
SORT1	6,2	3	1,234	0,01181
LMAN2	20,7	9,8	1,202	1,39E-06
CDSN	7	3,2	1,144	0,01516
GNPMB	6,7	3,7	1,108	0,01568
C1QBP	6,8	3,7	1,107	0,01516
PSAP	56,5	30,5	1,101	1,77E-15
NCAM2	6,3	3	1,081	0,02957
PTPRJ	6,5	3,8	1,078	0,01799
QSOX1	22,3	11,5	1,072	5,86E-06
AGRN	97	52	1,043	1,42E-23
AZGP1	23	11,8	1,04	8,44E-06
IGF2R	29	16,8	1,036	1,70E-07
GOLM1	7,7	4	0,9976	0,02236
CPE	11,7	6	0,9855	0,004482
CLSTN3	7,5	3,8	0,9683	0,03092
TIMP1	13,3	8,2	0,9474	0,002032
BTD	9	5,5	0,9192	0,01694
VGF	42,2	26	0,9144	1,42E-08
COL4A2	11,7	7,3	0,9044	0,006328
THBS2	80,3	50,8	0,896	9,74E-16
KRT14	8	5,5	0,8674	0,03104
CLU	20,3	11,8	0,8597	0,0005396
SRSF1	16,3	10,2	0,8183	0,003198
CNDP1	31	20,8	0,8156	1,48E-05
ACTB	0,5	33,2	-6,02	6,27E-52
PYGB	0,2	6,3	-4,887	7,52E-08
PARP1	0,2	5,8	-4,857	1,49E-07
CHL1	0,2	4,5	-4,523	7,05E-06
UBA2	0,2	4,7	-4,51	6,86E-06
VAT1	0,2	4	-4,261	5,99E-05
SSRP1	0,2	3,5	-4,094	0,0002133
ATIC	0,5	10	-4,033	3,55E-11
PSAT1	0	4,5	-36,74	7,31E-07
AKR1B1	0	3,7	-33,64	9,89E-06
HIST1H1B	0	7	-32,8	1,44E-10
TLN1	0	5,2	-31,98	7,81E-08
TOP1	0	2,8	-31,6	0,0001068
ADH5	0	3	-31,46	7,01E-05
SHMT1	0	2,2	-31,35	0,0008571
NOLC1	0	2	-31,26	0,001397
IPO7	0	2,2	-31,14	0,000962
PFAS	0	3,3	-30,64	1,66E-05
DPYSL2	0,2	3,2	-3,933	0,0006571
CCT7	0,2	2,7	-3,719	0,002311
TSNAX	0,2	2,5	-3,603	0,004076
CAND1	0,3	4	-3,442	0,0001235
NANS	0,3	4,2	-3,383	0,0001604
PRPF19	0,2	2,2	-3,372	0,01097
ZRANB2	0,2	2	-3,224	0,01799
SMAP	0,3	3,2	-3,152	0,001197
HDAC2	0,3	3,3	-3,043	0,001811
EEF1A1P5	0	5,5	-29,57	3,63E-08
HIST1H1E	0	4,8	-29,43	2,50E-07

HIST1H1C	0	2,7	-28,73	0,0002133
HIST1H2BL	0	2,3	-28,58	0,0001179
HIST1H2AA	0	2,7	-28,57	0,0002133
FSCN1	0,8	7,7	-2,84	2,44E-06
ESD	0,3	2,8	-2,797	0,006854
CLIC4	0,3	2,7	-2,639	0,0132
NUMA1	0,5	3,7	-2,637	0,002174
PACSIN2	0,5	3,8	-2,629	0,002095
NRDC	0,3	2,5	-2,625	0,01517
SAE1	0,3	2,3	-2,557	0,0203
PPP4R2	0,3	2,2	-2,542	0,02364
EIF3D	0,3	2,2	-2,457	0,0309
LMNB2	0,3	2,2	-2,457	0,0309
PAICS	0,7	4,3	-2,399	0,001846
TPP2	0,7	4,5	-2,393	0,001765
GBE1	0,3	2,2	-2,339	0,04252
EIF3L	0,7	3,8	-2,324	0,003465
HNRNPR	1,2	6,7	-2,312	6,75E-05
ZC3H18	0,5	2,7	-2,28	0,01704
H2AFZ	1,3	7,7	-2,269	2,55E-05
CSE1L	0,7	3,5	-2,238	0,006362
SCIN	1,7	9	-2,216	5,22E-06
EIF3C	0,8	4,2	-2,19	0,002799
EIF3A	1	5	-2,153	0,001198
H2AFY	1	5	-2,13	0,001397
TNFRSF19	0,7	3,3	-2,124	0,01156
PRMT1	0,8	4	-2,096	0,005129
CAP1	2	10	-2,083	4,13E-06
DENR	0,7	3,3	-2,071	0,01433
EIF3I	0,8	4	-2,067	0,006012
IDH1	1	5	-2,059	0,002165
DCPS	0,5	2,3	-2,015	0,04841
VIM	3,8	19	-1,997	3,06E-10
OTUB1	0,8	3,5	-1,986	0,01097
TPR	1	4,3	-1,877	0,00792
TSN	1	4,2	-1,852	0,009796
XPNPEP1	0,7	2,8	-1,789	0,04868
G3BP1	1,5	5,7	-1,756	0,002762
HMGGA1	1,3	4,8	-1,694	0,00792
TNC	16,3	58	-1,692	2,38E-26
RPS3A	0,8	3	-1,692	0,04379
HNRNPL	2,3	8,5	-1,689	0,0002561
TCP1	1,5	5,7	-1,678	0,004677
CCT3	1,2	4,2	-1,663	0,01643
RPS19	1	3,7	-1,653	0,0287
ACAT2	1,2	4,2	-1,598	0,02225
XRCC6	5,5	18,7	-1,591	6,95E-08
PLEC	1,3	4,3	-1,589	0,01643
PPM1G	1,3	4,3	-1,589	0,01643
UCHL3	1,2	4,2	-1,571	0,02521
EIF6	1,3	4,5	-1,566	0,01736
SYNCRIP	1	3,5	-1,543	0,04675
RCC2	4,3	14,3	-1,541	5,86E-06
AARS	2	6	-1,53	0,004646
NUCKS1	4	12,5	-1,485	4,02E-05
H3F3A	1,5	4,8	-1,485	0,01799
TARS	4,8	15,5	-1,475	5,64E-06
MYH9	2,5	7,8	-1,466	0,002039
FAM49B	2	6,2	-1,447	0,007708
PGM1	3,7	12,3	-1,425	0,0001585
IPO5	4,8	15,2	-1,418	1,48E-05

YWHAH	1,8	5,5	-1,39	0,01637
PCNA	2,3	6,7	-1,374	0,007232
HMGB2	5,3	15,2	-1,371	1,67E-05
GNPDA1	1,8	5,5	-1,351	0,01965
NQO1	2,2	6	-1,35	0,01232
PPP2R1A	2,2	5,8	-1,331	0,01433
HNRNP	4	11,2	-1,321	0,0005241
EEA1	1,8	5,7	-1,306	0,02458
CLTC	7,5	18,7	-1,222	9,97E-06
GSTO1	3,2	9,2	-1,196	0,00643
AHCY	5,3	13	-1,162	0,0006619
TXNRD1	2,7	6,5	-1,14	0,025
IQGAP1	5,8	14,3	-1,129	0,0005241
GARS	3,8	9,3	-1,095	0,008559
PA2G4	6,3	14,8	-1,083	0,0006207
EEF1G	4,8	11,2	-1,063	0,004244
NUDC	3,2	7,3	-1,058	0,02508
PMEL	4,5	10,8	-1,05	0,006328
ILF2	3	6,7	-1,037	0,03557
CCT8	5,8	13,3	-0,9941	0,003239
RACK1	7,3	16,5	-0,9925	0,0008948
YWHAQ	11	24,8	-0,9853	2,97E-05
HIST1H4A	11,3	25,7	-0,9827	2,32E-05
PTMA	10	20,5	-0,9753	0,0001375
RAN	3,8	8,7	-0,9632	0,02611
ACLY	8,8	18,2	-0,9353	0,0007296
HMCN1	5,2	11,5	-0,9167	0,01312
UBE2I	4	8,7	-0,9107	0,03503
VCL	6,3	12,5	-0,9043	0,00775
NPEPPS	4,8	9,7	-0,8469	0,03442
UBA1	7,8	15	-0,8357	0,006505
XRCC5	9,5	18,8	-0,8244	0,002539
CPOX	0	2,2	-36	0,001081

Notes:

a: Average normalized spectral counts from cells where PML is silenced

b: Average normalized spectral counts from cells where PML is expressed

c: the adjusted p-values have been corrected for multiple hypothesis testing according to Benjamini and Hochberg

ARTICLE

Received 27 Oct 2015 | Accepted 12 Jul 2016 | Published 24 Aug 2016

DOI: 10.1038/ncomms12595

OPEN

Stratification and therapeutic potential of PML in metastatic breast cancer

Natalia Martín-Martín^{1,*}, Marco Piva^{1,*}, Jelena Urosevic², Paula Aldaz³, James D. Sutherland¹, Sonia Fernández-Ruiz¹, Leire Arreal¹, Verónica Torrano¹, Ana R. Cortazar¹, Evarist Planet^{4,5}, Marc Guiu², Nina Radosevic-Robin^{6,7}, Stephane Garcia⁸, Iratxe Macías¹, Fernando Salvador², Giacomo Domenici¹, Oscar M. Rueda⁹, Amaia Zabala-Letona¹, Amaia Arruabarrena-Aristorena¹, Patricia Zúñiga-García¹, Alfredo Caro-Maldonado¹, Lorea Valcárcel-Jiménez¹, Pilar Sánchez-Mosquera¹, Marta Varela-Rey^{1,10}, Maria Luz Martínez-Chantar^{1,10}, Juan Anguita^{1,11}, Yasir H. Ibrahim^{12,13}, Maurizio Scaltriti¹⁴, Charles H. Lawrie^{3,11}, Ana M. Aransay^{1,10}, Juan L. Iovanna⁸, Jose Baselga¹⁵, Carlos Caldas⁹, Rosa Barrio¹, Violeta Serra¹², Maria dM Vivanco¹, Ander Matheu^{3,11,**}, Roger R. Gomis^{2,16,**} & Arkaitz Carracedo^{1,11,17}

Patient stratification has been instrumental for the success of targeted therapies in breast cancer. However, the molecular basis of metastatic breast cancer and its therapeutic vulnerabilities remain poorly understood. Here we show that PML is a novel target in aggressive breast cancer. The acquisition of aggressiveness and metastatic features in breast tumours is accompanied by the elevated PML expression and enhanced sensitivity to its inhibition. Interestingly, we find that STAT3 is responsible, at least in part, for the transcriptional upregulation of PML in breast cancer. Moreover, PML targeting hampers breast cancer initiation and metastatic seeding. Mechanistically, this biological activity relies on the regulation of the stem cell gene *SOX9* through interaction of PML with its promoter region. Altogether, we identify a novel pathway sustaining breast cancer aggressiveness that can be therapeutically exploited in combination with PML-based stratification.

¹CIC bioGUNE, Bizkaia Technology Park, Bulding 801a, 48160 Derio, Spain. ²Oncology Programme, Institute for Research in Biomedicine (IRB-Barcelona), 08028 Barcelona, Spain. ³Oncology Area, Biodonostia Institute, 20014 San Sebastian, Spain. ⁴Biostatistics and Bioinformatics Unit, Institute for Research in Biomedicine (IRB-Barcelona), 08028 Barcelona, Spain. ⁵School of Life Sciences, Ecole Polytechnique Fédérale de Lausanne (EPFL), 1015 Lausanne, Switzerland. ⁶ERTICa Research Group, University of Auvergne EA4677, Clermont-Ferrand, France. ⁷Biodiagnostics Laboratory OncoGenAuvergne, Pathology Unit, Jean Perrin Comprehensive Cancer Center, 63000 Clermont-Ferrand, France. ⁸Centre de Recherche en Cancérologie de Marseille (CRCM), INSERM UMR 1068, CNRS UMR 7258, Aix-Marseille University and Institut Paoli-Calmettes, Parc Scientifique et Technologique de Luminy, 13288 Marseille, France. ⁹Cancer Research UK Cambridge Institute, University of Cambridge, Li Ka Shing Centre, Robinson Way, Cambridge CB2 0RE, UK. ¹⁰Centro de Investigación Biomédica en Red de Enfermedades Hepáticas y Digestivas (CIBERehd). ¹¹IKERBASQUE, Basque foundation for science, 48013 Bilbao, Spain. ¹²Experimental Therapeutics Group, Vall d'Hebron University Hospital, 08035 Barcelona, Spain. ¹³Weill Cornell Medicine, New York 10021, USA. ¹⁴Human Oncology and Pathogenesis Program, Department of Pathology, Memorial Sloan-Kettering Cancer Center, 10065 New York, USA. ¹⁵Human Oncology and Pathogenesis Program, Department of Medicine, Memorial Sloan-Kettering Cancer Center, 10065 New York, USA. ¹⁶Institució Catalana de Recerca i Estudis Avançats (ICREA), 08010 Barcelona, Spain. ¹⁷Biochemistry and Molecular Biology Department, University of the Basque Country (UPV/EHU), 48949 Leioa, Spain. * These authors contributed equally to this work. ** These authors jointly supervised this work. Correspondence and requests for materials should be addressed to A.C. (email: acarracedo@cicbiogune.es).

Patient stratification for cancer therapy is an excellent illustration of precision medicine, and biomarker-based treatment selection has tremendously aided in the success of current cancer therapies¹. In this sense, the current ability to molecularly define and differentiate breast cancer (BCa) into molecular subtypes^{2,3} has allowed the identification of patients at risk of relapse⁴ and has led to biomarker signatures used to spare low-risk patients from aggressive chemotherapy⁵.

Tumours are heterogeneous entities and most cancers retain a differential fraction of cells with increased self-renewal capability (cancer stem or initiating cells)⁶. Cancer-initiating cells (CICs) exhibit a unique spectrum of biological, biochemical and molecular features that have granted them an important role in disease recurrence and metastatic dissemination in BCa^{7,8}. Despite the accepted relevance of CICs in cancer progression, the molecular cues governing their activity and function remain largely unknown. The sex determining region Y Box 9 (SOX9) is a recently described regulator of cell differentiation and self-renewal^{9–11} and is found upregulated in BCa^{12–14}.

The promyelocytic leukaemia (PML) protein negatively regulates survival and proliferation pathways in cancer, functions that have established it as a classical pro-apoptotic and growth inhibitory tumour suppressor^{15,16}. PML is the essential component of multi-protein sub-nuclear structures commonly referred to as the PML nuclear bodies. PML multimerizes to function as a scaffold critical for the composition and assembly of the entire complex, a process that is regulated by Small Ubiquitin-like Modifier (SUMO)-mediated modifications and interactions^{15,16}. Despite the general perception of being PML a bona fide tumour suppressor in cancer, a series of recent studies have demonstrated that PML exhibits activities in cancer that go far and beyond tumour suppression¹⁷. The work in chronic myeloid leukaemia has evidenced that PML expression can be promoted in certain cancers, providing a selective advantage to tumour cells^{18,19}. Moreover, PML is found upregulated in a subset of BCa²⁰. However, to which extent PML targeting could be a valuable therapeutic approach in solid cancers remains obscure.

In this study, we reveal the therapeutic and stratification potential of PML in BCa and the molecular cues, underlying the therapeutic response unleashed by PML inhibition.

Results

PML silencing hampers BCa-initiating cell capacity. The elevated expression of PML in a subset of BCa^{17,20} strongly suggests that it could represent an attractive target for therapy. To ascertain the molecular and biological processes controlled by PML in BCa, we carried out short hairpin RNA (shRNA) lentiviral delivery-mediated PML silencing in different cellular systems. Four constitutively expressed shRNAs exhibited activity against PML (Fig. 1a; Supplementary Fig. 1a–d). PML knockdown elicited a potent reduction in the number of ALDH1-positive cells and in oncosphere formation (OS, readout of self-renewal potential^{7,21}), in up to three PML-high-expressing basal-like BCa (BT549 and MDA-MB-231) or immortalized (HBL100) cell lines tested (Fig. 1b–d; Supplementary Fig. 1e–g). This phenotype was recapitulated with a doxycycline-inducible lentiviral shRNA system targeting PML (sh4; Fig. 1e,f; Supplementary Fig. 1h).

Self-renewal capacity is a core feature of CICs⁷. On the basis of this notion, we hypothesized that PML could regulate tumour initiation in BCa. We performed tumour formation assays in immunocompromised mice, using MDA-MB-231 cells (PML-high-expressing triple-negative breast cancer (TNBC)) transduced with non-targeting (shRNA Scramble: shC) or PML-targeting shRNAs. PML silencing exhibited a profound

defect in tumour formation capacity, resulting in a decrease in the frequency of tumour-initiating cells from 1/218 (shC) to 1/825 (sh5) and completely abolished (1/infinite) in sh4 (Fig. 1g; Supplementary Fig. 1i).

To extrapolate these observations to the complexity of human BCa, we characterized a series of patient-derived xenografts (PDXs; Table 1; Supplementary Fig. 1j). The distribution of PML expression in the different subtypes of engrafted tumours was reminiscent of patient data, with a higher proportion of PML-high-expressing tumours in basal-like/triple-negative subtype²⁰. Taking advantage of the establishment of a PML-high-expressing PDX-derived cell line (PDX44), we sought to corroborate the results obtained in the PML-high-expressing cell lines. As with MDA-MB-231 cells, PML silencing was effective in the PDX44-derived cell line (Fig. 1h) and resulted in a significant decrease in OS formation (Fig. 1i). *In vivo*, PML silencing decreased tumour-forming capacity of PDX44 cells (tumour-initiating cell frequency was estimated of 1/39.6 in shC, 1/100 in sh5 and 1/185 in sh4; Fig. 1j; Supplementary Fig. 1k).

These data demonstrate that PML expression is required for BCa-initiating cell function in TNBC cells.

PML sustains metastatic potential in BCa. CIC activity is associated with tumour initiation and recurrence^{7,22}. We have previously shown that PML expression is associated to early recurrence²⁰, which we validated in an independent data set²³ (Supplementary Fig. 2a). The development of metastatic lesions is based on the acquisition of novel features by cancer cells²⁴. On the basis of our data, we surmised that the activity of PML on CICs could impact on the survival and growth in distant organs. To test this hypothesis, we measured metastasis-free survival (MFS) in two well-annotated large messenger RNA (mRNA) data sets^{3,25,26}. First, we evaluated the impact of high PML expression in MFS in the MSK/EMC (Memorial Sloan Kettering Cancer Center-Erasmus Medical Center) data set^{25,26}. As predicted, PML expression above the mean was associated with reduced MFS (Fig. 2a). Second, we validated this observation in the METABRIC data set, focusing on early metastasis (up to 5 years)³. On the one hand, we confirmed the MSK/EMC data (Fig. 2b; hazard ratio (HR) = 1.31, log-rank test $P = 0.006$). On the other hand, a Cox continuous model demonstrated an association of PML expression with the increased risk of metastasis (HR = 2.305, $P = 0.002$). Of note, we tested the expression of PML in patients with complete pathological response or residual disease after therapy²⁷, but could not find a significant association of these parameters in two data sets (Supplementary Fig. 2b).

The molecular alterations associated to metastatic capacity can be studied using BCa cell lines, in which metastatic cell sub-clones have been selected through the sequential enrichment in immunocompromised mice²⁸. If PML is a causal event in the acquisition of metastatic capacity, then changes in its expression should be observed in this cellular system. As predicted, PML mRNA and protein expression were elevated in three distinct metastatic sub-clones compared with their parental counterparts^{25,26} (Fig. 2c; Supplementary Fig. 2c).

Metastasis surrogate assays provide valuable information about the capacity of cancer cells to home and colonize secondary organs²⁹. TNBC cells exhibit metastatic tropism to the lung³⁰, and the molecular requirements of this process have begun to be clarified through the generation of highly metastatic sub-clones³¹. Our patient analysis suggests that PML expression is favoured in primary tumours, with higher capacity to disseminate. Moreover, cell sub-clone analysis further reveals that PML expression is selected for in the process of metastatic selection. With this data

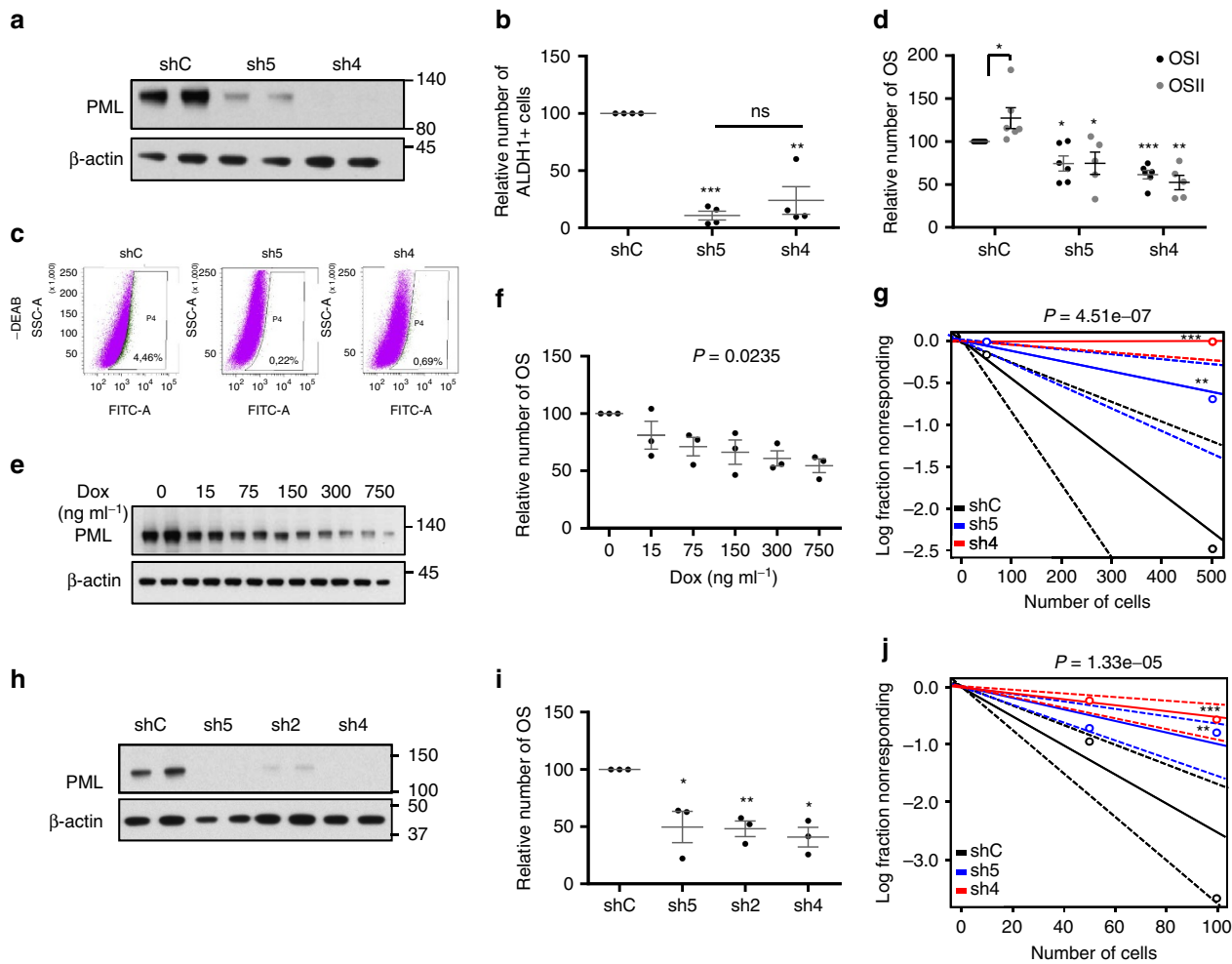


Figure 1 | Genetic targeting of *PML* hampers breast cancer initiation potential. (a) *PML* levels (representative western blot out of four independent experiments) upon *PML* silencing with two shRNAs (sh) in MDA-MB-231 cells. (b) Percentage of ALDH1+ cells upon *PML* silencing with two shRNAs in MDA-MB-231 cells ($n = 4$). (c) Representative flow cytometry analysis out of three independent experiments of the ALDH1+ population in shC or shPML-transduced MDA-MB-231 cells (FITC: fluorescein-isothiocyanate, SSC-A: side-scatter). (d) Effect of *PML* silencing on primary (OSI) and secondary (OSII) OS formation in MDA-MB-231 cells ($n = 5$ for OSI in shPML cells and $n = 6$ for shC and OSI in shPML cells). (e,f) *PML* levels (representative western blot out of three independent experiments) (e) and OS formation ($n = 3$) (f) upon *PML* inducible silencing (shPML#4) with the indicated doses of doxycycline in MDA-MB-231 cells. (g) Limiting dilution experiment after xenotransplantation. Nude mice were inoculated with 500,000 or 50,000 MDA-MB-231 cells ($n = 12$ injections per experimental condition). Tumour-initiating cell number was calculated using the ELDA platform. A log-fraction plot of the limiting dilution model fitted to the data is presented. The slope of the line is the log-active cell fraction (solid lines: mean; dotted lines: 95% confidence interval; circles: values obtained in each cell dilution). (h) *PML* levels (representative western blot out of four independent experiments) upon *PML* silencing in the PDX44-derived cell line. (i) OSI formation upon *PML* silencing in PDX44 cells ($n = 3$). (j) Limiting dilution experiment after xenotransplantation. Nude mice were inoculated either with 100,000 or 10,000 PDX44 cells ($n = 20$ injections per experimental condition). Tumour-initiating cell number was calculated using the ELDA platform as in (g). Error bars represent s.e.m., P value ($*P < 0.05$; $**P < 0.01$; $***P < 0.001$ compared with shC or as indicated). Statistics test: one-tail unpaired t -test (b,d,i), analysis of variance (f) and χ^2 -test (g,j). dox, doxycycline; OS, oncospheres; shC, Scramble shRNA; sh2, sh4 and sh5, shRNA against *PML*.

in mind, we asked to which extent *PML* would be responsible for the enhanced metastatic capacity. To address this question, we silenced *PML* in a highly metastatic sub-clone derived from MDA-MB-231 and injected these cells in the tail vein of nude mice. We chose tail vein injection due to the fact that other metastasis models based on the orthotopic implantation of cells in the mammary fat pad²⁵ are influenced by primary tumour formation, which we reported to be altered by *PML* (Fig. 1). The reduction of *PML* was confirmed in the injected cells (Fig. 2d). Strikingly, *PML* silencing led to a significant reduction in lung metastatic foci formation (Fig. 2e). When evaluating the immunoreactivity of *PML* in the metastatic lesions (Fig. 2e–g), we observed a direct association between *PML* silencing at the time of injection (Fig. 2d) and the immunoreactivity of *PML* in

metastatic foci (Fig. 2g). We evaluated whether the lack of *PML* could be limiting metastatic growth capacity by eliciting an apoptotic response, rather than CIC capacity. However, no differential apoptosis was detected by the means of cleaved caspase-3 staining (Supplementary Fig. 2d–e).

These data demonstrate that the genetic targeting of *PML* results in a tumour-suppressive response, characterized by decreased BCa-initiating cell function and consequently, reduced tumour initiation and metastasis.

STAT3 participates in the regulation of *PML* expression. Our data demonstrate that *PML* is transcriptionally regulated in BCa. *PML* gene expression is regulated upon various external stimuli,

Table 1 | PDX characterization based on BCa subtype (intrinsic subtype is presented in brackets).

PDX	Subtype	PML
31	TNBC (HER2 enriched)	—
102	ER + (basal like)	—
131	ER + (luminal B)	—
156	ER + (basal like)	—
197	TNBC (basal like)	—
4	ER + (luminal B)	+
6	ER + (luminal A)	+
10	HER2 + (HER2 enriched)	+
39	ER + (luminal B)	+
60	ER + (basal like)	+
98	ER + (basal like)	+
136	TNBC (basal like)	+
137	TNBC (basal like)	+
161	ER + (luminal B)	+
93	TNBC (NA)	++
179	TNBC (NA)	++
44	TNBC (basal like)	+++
88	TNBC (basal like)	+++
89	TNBC (NA)	+++
94	TNBC (basal like)	+++
124	TNBC (basal like)	+++
127	TNBC (basal like)	+++
167	TNBC (basal like)	+++

ER, oestrogen receptor; NA, not applicable; TNBC, triple-negative breast cancer.

including type I and II interferons and interleukin 6, which are mediated by interferon regulatory factors and signal transducers and activators of transcription (STATs), respectively^{32–35}. Specifically, it has been reported that activated STAT3 but not STAT1 correlates with *PML* mRNA and protein levels in fibroblasts, HeLa and U2OS cell lines³⁴. Since, STAT3 is activated in oestrogen receptor (ER)-negative BCa³⁶, we hypothesized that this transcription factor may be responsible for the transcriptional activation of *PML* in this tumour type. We silenced *STAT3* with two different short hairpins (sh41 and sh43), and showed that this approach led to the decrease in *PML* protein and gene expression in the different cell lines tested (Fig. 3a; Supplementary Fig. 3a–b). Moreover, pharmacological inhibition of the Janus kinase/signal transducers and activators of transcription (JAK/STAT) pathway at two different levels (SI3-201, an inhibitor of STAT3 phosphorylation and activation; TG1013148, a potent and highly selective ATP-competitive inhibitor of JAK2) decreased *PML* levels (Fig. 3b,c). In coherence with the activity of *PML*, genetic and pharmacological inhibition of STAT3 in MDA-MB-231 cells reduced the primary OS formation capacity (Fig. 3d–f). Importantly, *PML* gene expression levels in a cohort of 448 patients (MSK/EMC) correlated with the activity of STAT3, as confirmed with two different STAT3 signatures (Fig. 3g; ref. 37; [http://software.broadinstitute.org/gsea/msigdb/cards/V\\$STAT3_01](http://software.broadinstitute.org/gsea/msigdb/cards/V$STAT3_01)). In addition, immunohistochemical analysis confirmed an association between the *PML* immunoreactivity and phosphorylated STAT3 levels in the Marseille cohort (Fig. 3h). Our results provide strong support for the role of STAT3 as an upstream regulator of *PML* in BCa.

Elevated *PML* expression predicts response to arsenic trioxide.

PML can be pharmacologically inhibited with arsenic trioxide (Trisenox, ATO), which induces SUMO-dependent ubiquitylation and proteasome-mediated degradation of the protein^{38,39}. Similar to our results obtained by knocking down *PML* via

shRNA, low doses of ATO decreased *PML* levels and exerted a negative effect on the OS formation capacity both in MDA-MB-231 and PDX44 cells (Fig. 4a,b). Moreover, ATO reduced the tumour formation capacity in a xenograft model derived from MDA-MB-231 cells in full coherence with the genetic approach (tumour-initiating cell frequency was estimated of 1/279 in vehicle and 1/703 in ATO; Fig. 4c; Supplementary Fig. 4a).

We hypothesized that cells with elevated *PML* would be ‘addicted’⁴⁰ to the expression of the protein and hence be more sensitive to the action of *PML* inhibitors. To prove this notion, we studied additional cell lines with high (BT549, HBL100) or low (MCF7, T47D) *PML* expression. With this approach, we could demonstrate that the effect of *PML* silencing on the OS formation was exquisitely restricted to *PML*-high-expressing cells (Fig. 4d). This effect was recapitulated with ATO (Fig. 4e), where *PML*-low cells remained refractory to the drug in terms of the OS formation capacity.

Our results open a new avenue for the treatment of tumours that exhibit elevation in *PML* expression. *PML* elevation is predominant in ER-negative tumours (Supplementary Fig. 4b), which also present worse prognosis than ER-positive BCa^{2,41}. Whereas luminal subtypes present better overall prognosis, there is a subset of patients within this subtype that exhibits aggressive disease⁴². We hypothesized that within this *PML*-low-expressing subtypes, the worse prognosis subgroup would exhibit increased *PML* levels. Indeed, MFS analysis within each intrinsic subtype confirmed that ER-positive BCa (luminal A and luminal B) contained a subset of patients with higher *PML* and worse prognosis (Supplementary Fig. 4c–g).

Our results in ER-positive tumours indicate that the *PML* expression is enriched in patients harbouring tumours of poor prognosis^{2,3}. These results are coherent with our data in metastatic clone selection (Fig. 2c), suggesting that the acquisition of aggressive features is accompanied by the elevation of *PML* expression and ‘addiction’ to the protein. We therefore sought to study whether metastatic ER-positive cell sub-clones, which present elevated *PML* expression, would exhibit sensitivity to *PML* inhibition, in contrast to the parental cells. Indeed, ATO reduced the OS formation selectively in *PML*-high-expressing metastatic cells derived from MCF7, whereas the parental cells remained refractory to the drug (Fig. 4f,g). Our results strongly suggest that *PML* elevation in BCa is associated to a dependence on its expression and hence enforces the need for patient stratification based on *PML* levels before the establishment of *PML*-directed therapies.

PML regulates BCa-initiating cell function through SOX9.

To ascertain the molecular mechanism by which *PML* regulates BCa-initiating cell function, we first evaluated the expression levels of this gene in a sorted population of ALDH1-positive versus -negative MDA-MB-231 cells (Fig. 5a,b), and in adherent cultures versus OS (CIC-enriched cultures) (Fig. 5c). Strikingly, *PML* expression increased in both experimental approaches (Fig. 5b,c), together with the levels of well-established stem cell regulators (Fig. 5c). On this basis, we hypothesized that *PML* might control the expression of stem cell factors, as a mean to regulate BCa-initiating cell function. SOX9 is a recently described regulator of cell differentiation and self-renewal^{9,10,11} and is upregulated in BCa^{12–14}. Constitutive (Fig. 5d; Supplementary Fig. 5a–b) and inducible (Fig. 5e) *PML* silencing exerted an inhibitory effect on SOX9 expression that correlated with the OS formation capacity (Fig. 5f). *PML* pharmacological inhibition also induced a decrease on SOX9 expression (Fig. 5g; Supplementary Fig. 5c–d). This regulatory activity was corroborated in the PDX44 cell line (Fig. 5h,i; Supplementary Fig. 5e), and in a

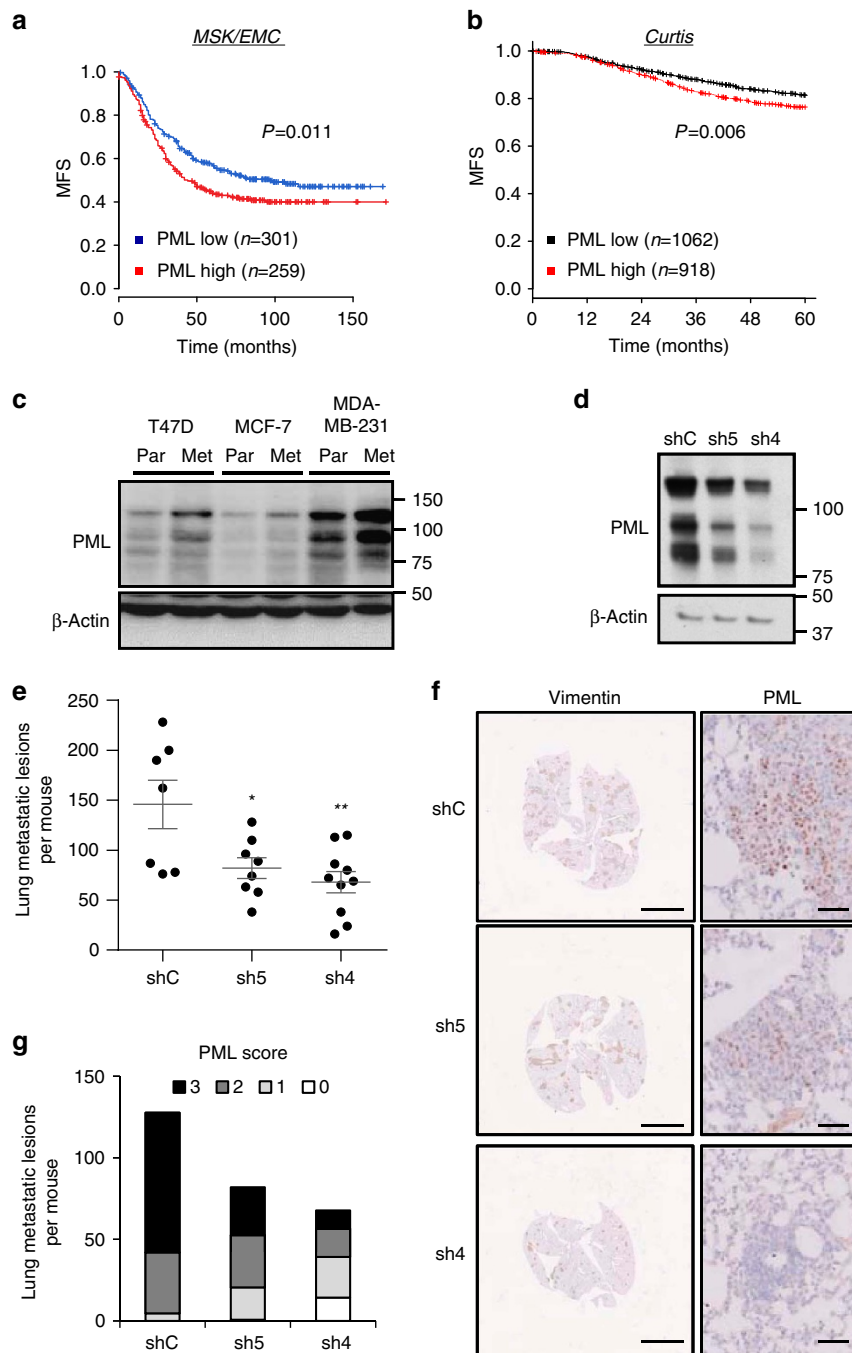


Figure 2 | PML is associated to breast cancer metastatic dissemination. (a,b) Kaplan-Meier representations of MFS based on *PML* RNA expression. (a) MSK/EMC data set, $n = 560$. (b) Curtis data set (MFS before 60 months), $n = 1980$. PML high: above the mean expression; PML low: below the mean expression. (c) Representative western blot out of three independent experiments, showing *PML* protein expression in cell line sub-clones selected for high metastatic potential (Par = parental and Met = metastatic). (d-g) Effect of *PML* silencing on metastatic capacity of intravenously injected metastatic MDA-MB-231 sub-clones ($n = 10$ mice per condition): Western blot showing *PML* silencing in cells at the time of injection (d), number of metastatic lesions (e), representative immunostaining of Vimentin (scale bar, 3 mm) and *PML* (scale bar, 50 μm) as indicator of metastatic lesions (f), and number of metastatic lesions for each *PML* immunoreactivity score (22 metastatic foci were scored and extrapolated to the number of total metastatic foci in each lung) (g). Error bars represent s.e.m., P value (* $P < 0.05$; ** $P < 0.01$ compared with shC). Statistical test: Gehan-Breslow-Wilcoxon test (a,b) and one-tail unpaired t-test (e). MFS, metastasis-free survival; shC: Scramble shRNA; sh4 and sh5, shRNA against *PML*.

correlative manner in the PDX data set (Fig. 5j), as well as in the aforementioned Marseille data set (Fig. 5k).

We next ascertained the molecular cues regulating *SOX9* expression downstream *PML*. Since the regulation was observed at the mRNA level, we interrogated *SOX9* promoter *in silico* and in public datasets. The ENCODE project has provided a vast

amount of information about regulators and binding sites⁴³. *SOX9* promoter exhibited a 2 kb region of acetylated H3K27 (H3K27Ac), which would indicate the proximal regulatory region. To our surprise, we found *PML* among the 10 proteins with highest confidence DNA-binding score in *SOX9* promoter region (Fig. 5l; cluster score = 527 (refs 44–46)). There is limited

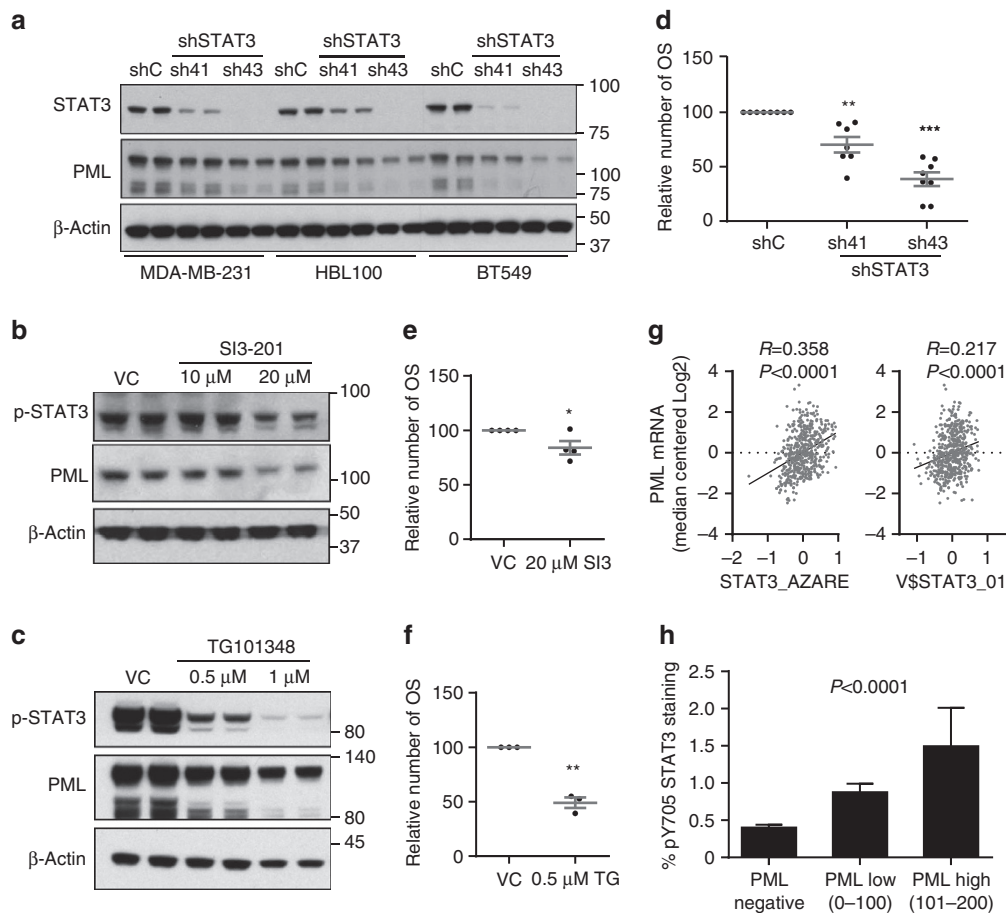


Figure 3 | STAT3 regulates PML expression in breast cancer. (a) Representative western blot out of three independent experiments showing STAT3 and PML protein expression upon *STAT3* silencing with two different shRNA (sh41 and sh43). (b,c) Representative western blot out of three independent experiments, showing STAT3 and PML protein expression upon *STAT3* inhibition using SI3-201 (b) and TG101314 (c) in MDA-MB-231 cells. (d-f) Effect of *STAT3* inhibition on primary OS formation using sh41 and sh43 against *STAT3* ($n = 7$) (d), SI3-201 (SI3; $n = 4$) (e) and TG101314 (TG; $n = 3$) (f) in MDA-MB-231 cells. (g) Correlation of two different *STAT3* gene signatures with *PML* gene expression in the MSK/EMC data set. (h) Immunoreactivity of pY705 *STAT3* protein in patient biopsies with varying expression of *PML* in the Marseille cohort ($n = 737$). Error bars represent s.e.m., P value ($*P < 0.05$; $**P < 0.01$; $***P < 0.001$ compared with shC or VC as indicated). Statistics test: one-tail unpaired t -test (d,e,f), Pearson correlation (g) and analysis of variance (h). OSI, primary oncospheres; shC, Scramble shRNA; sh41 and sh43, shRNA against *STAT3*; VC, vehicle control.

evidence of the capacity of PML to regulate gene expression in concordance with transcription factors through association with DNA^{47–49}. We performed chromatin immunoprecipitation (ChIP) analysis of ectopically expressed and endogenous PML, as well as SOX9 expression analysis in these conditions. We confirmed that PML is in close proximity to *SOX9* promoter region and that its ectopic expression upregulates *SOX9* transcript and protein levels (Fig. 5m; Supplementary Fig. 5f–j). It is worth noting that PML does not present a canonical DNA-binding domain, and it is therefore plausible that it lies in close proximity to *SOX9* promoter through the interaction with intermediary DNA-binding proteins.

The regulation of *SOX9* led us to hypothesize that this transcription factor mediated the effects of PML on the regulation of CIC function. On the one hand, we ascertained whether *SOX9* silencing would recapitulate the effects of PML inhibition. We set up two shRNAs targeting *SOX9* (Fig. 6a) that exhibited a potent effect on primary (Fig. 6b) and secondary (Supplementary Fig. 6a) OS formation. Moreover, *SOX9* silencing in MDA-MB-231 cells reduced the tumour formation capacity *in vivo* (tumour-initiating cell frequency was estimated of 1/71.7 in shC, completely abolished (1/infinite) in sh9.1 and 1/4145.5 in sh9.2; Fig. 6c; Supplementary Fig. 6b–c), in agreement with other reports¹².

On the other hand, we evaluated the capacity of ectopically expressed *SOX9* to bypass the effects of PML silencing on CIC function. Ectopic *SOX9*-expressing BCa cells were refractory to *PML* genetic inhibition in terms of the OS formation (Fig. 6d,e) and tumour formation (tumour-initiating cell frequency was estimated of 1/139.8 in shC/Mock, 1/57.5 in shC/*SOX9*, 1/1506 in sh4/Mock and 1/270.8 in sh4/*SOX9*; Fig. 6f; Supplementary Fig. 6d). Importantly, the *in vitro* observation was recapitulated in ATO-treated cells (Fig. 6g).

These data reveal a novel molecular mechanism by which PML controls the expression of the stem cell factor *SOX9* to regulate BCa-initiating cell function (Fig. 6h). It is worth noting that we found PML at the promoter region of other stem cell genes, such as *LGR5* (Supplementary Fig. 6e–g), indicating that the capacity of this protein to regulate CIC function could involve a larger and more complex transcriptional program.

Discussion

Finding successful targeted treatment strategies for women at risk of metastatic BCa is of outstanding clinical interest. Our data unveil the therapeutic potential of targeting PML in combination

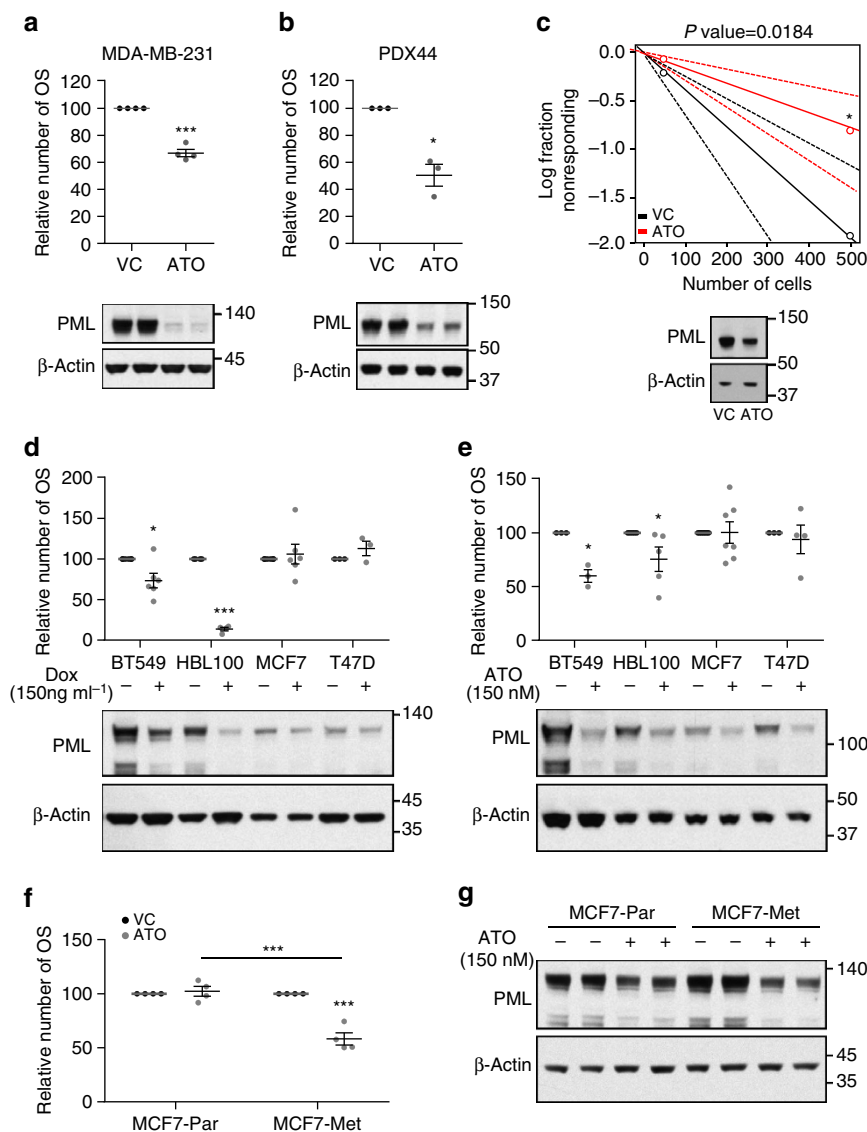


Figure 4 | PML inhibition selectively targets PML-high-expressing breast cancer cells. (a,b) Effect of 150 nM ATO treatment on OSI formation (top panels) in MDA-MB-231 ($n = 4$) (a) and PDX44 cells ($n = 3$) (b) and PML protein expression (3-day treatment, lower panels, representative western blot out of four—MDA-MB-231—or three—PDX44-independent experiments). (c) Limiting dilution experiment after xenotransplantation. Nude mice were inoculated with 500,000 or 50,000 MDA-MB-231 cells ($n = 20$ injections per experimental condition). ATO cells were pre-treated with 150 nM ATO 2 days before injection. Tumour-initiating cell number was calculated using the ELDA platform. A log-fraction plot of the limiting dilution model fitted to the data is presented. The slope of the line is the log-active cell fraction (solid lines: mean; dotted lines: 95% confidence interval; circles: values obtained in each cell dilution). A PML western blot from cells at the time of injection is presented in lower panel. (d,e) OSI formation in cell lines with high (BT549 and HBL100) and low (MCF7 and T47D) PML expression upon PML genetic silencing (MCF7 and T47D $n = 3$, and BT549 and HBL100 $n = 6$) (d) and 150 nM ATO (BT549 $n = 3$, HBL100 $n = 5$, MCF7 $n = 7$ and T47D $n = 4$) (e). A representative PML western blot out of three independent experiments is presented in lower panels. (f,g) Effect of 150 nM ATO on OSI formation ($n = 4$) (f) and on PML levels (a representative western blot is presented out of four independent experiments) (g) in MCF7 parental cells and MCF7 metastatic sub-clone. Error bars represent s.e.m., P value ($*P < 0.05$; $***P < 0.001$ compared with each control). Statistics test: one-tail unpaired t -test (a,b,d,e,f), χ^2 -test (c). ATO, arsenic trioxide; Met, metastatic; OSI, primary oncospheres; Par, parental; VC, vehicle control.

with a stratification companion that identifies patients harbouring PML-high-expressing BCa.

We demonstrate that PML targeting impacts on BCa-initiating cell function, and hence on cancer initiation and dissemination. In addition, we observed that PML expression is increased in BCa-initiating cells, highly metastatic sub-clones and in BCa patients at risk of metastasis. These data suggest that, in a subset of BCas, PML sustains the function of BCa-initiating cells and in turn supports the metastatic dissemination capacity⁶.

We show that PML-directed therapies are efficient in BCa cells with elevated expression of the protein. Such phenomenon has been defined as ‘addiction’^{40,50,51}, and it represents an exciting avenue in the establishment of novel therapeutic initiatives. Importantly, targeted therapies have been particularly successful when combined with a predictive biomarker. The availability of a clinically validated protocol to detect PML immunoreactivity⁵² offers a unique opportunity to define the patients that would benefit from therapies based on PML inhibition. In addition, our

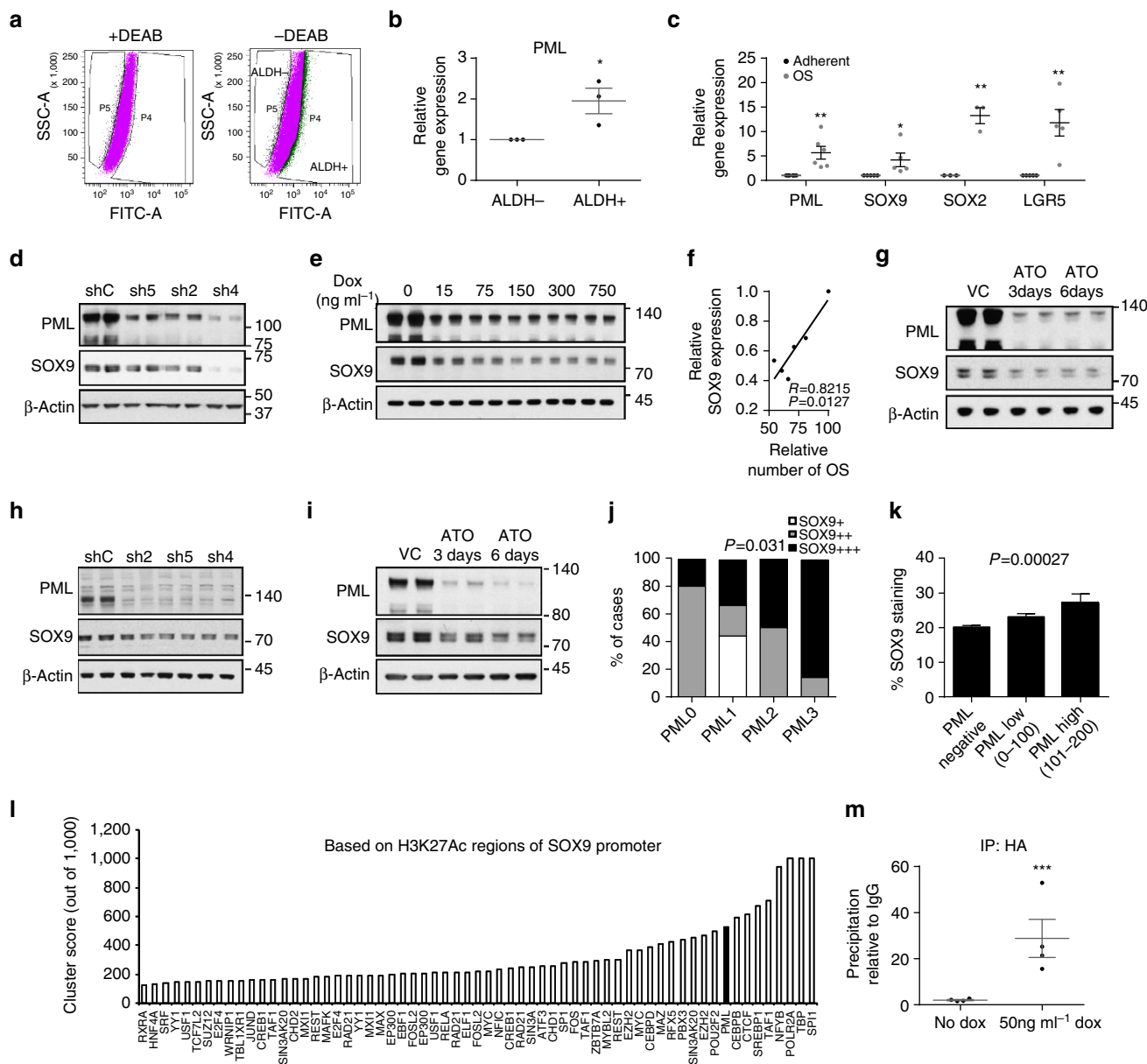


Figure 5 | PML regulates SOX9 expression in breast cancer. (a) Flow cytometry analysis of MDA-MB-231 cells based on ALDH1 activity. (b) PML gene expression in the two populations sorted in a ($n = 3$). (c) Expression of self-renewal-associated genes in OSI compared with adherent MDA-MB-231 cells (PML $n = 6$, SOX9 and LGR5 $n = 5$ and SOX2 $n = 3$). (d,e) Representative western blot out of four independent experiments depicting the downregulation of SOX9 protein upon constitutive (d) and inducible (e) PML silencing in MDA-MB-231 cells. (f) Correlation analysis of SOX9 protein densitometry from (e) and OSI formation in MDA-MB-231 cells ($n = 3$). (g) Representative western blot out of four independent experiments depicting the downregulation of SOX9 protein upon 150 nM ATO treatment in MDA-MB-231 cells. (h,i) Representative western blot out of three independent experiments depicting the downregulation of SOX9 protein upon PML silencing (h) and 150 nM ATO treatment (i) in PDX44 cells. (j) PML and SOX9 immunoreactivity assayed by immunohistochemistry in a panel of PDX samples (Table 1). (k) SOX9 immunoreactivity in patient biopsies with varying expression of PML in the Marseille cohort ($n = 737$). (l) Cluster score of DNA-binding proteins in SOX9 promoter region using ENCODE database. (m) SOX9 promoter region abundance in chromatin immunoprecipitation (ChIP) of exogenous HA-PMLIV using HA-tag antibody in MDA-MB-231 cells after induction with 50 ng ml⁻¹ doxycycline for 3 days ($n = 4$). Data were normalized to IgG (negative-binding control). Error bars represent s.e.m., P value ($*P < 0.05$, $**P < 0.01$, $***P < 0.001$ compared with control). Statistic test: one-tail unpaired t -test (b,c,m), Pearson correlation (f), χ^2 -test (j) and analysis of variance (k). ATO, arsenic trioxide; DEAB, diethylaminobenzaldehyde; dox, doxycycline; OSI, primary oncospheres; shC, Scramble shRNA; sh2, sh4 and sh5, shRNA against PML; VC, vehicle control.

proof-of-concept demonstration of the therapeutic efficacy of PML pharmacological inhibition with ATO indicates that (1) repositioning of ATO (that is currently used in the treatment of acute PML) for BCa therapy is a viable approach, (2) there is strong support for the development of novel and more effective PML inhibitors and (3) the identification of combined

therapies with PML inhibitors in BCa is a novel and exciting area of investigation.

Mechanistically, our data demonstrate that PML is in close proximity to the promoter region of SOX9, and positively regulates the expression of the gene. SOX9 has been recently established as a central regulator of normal and cancer stem

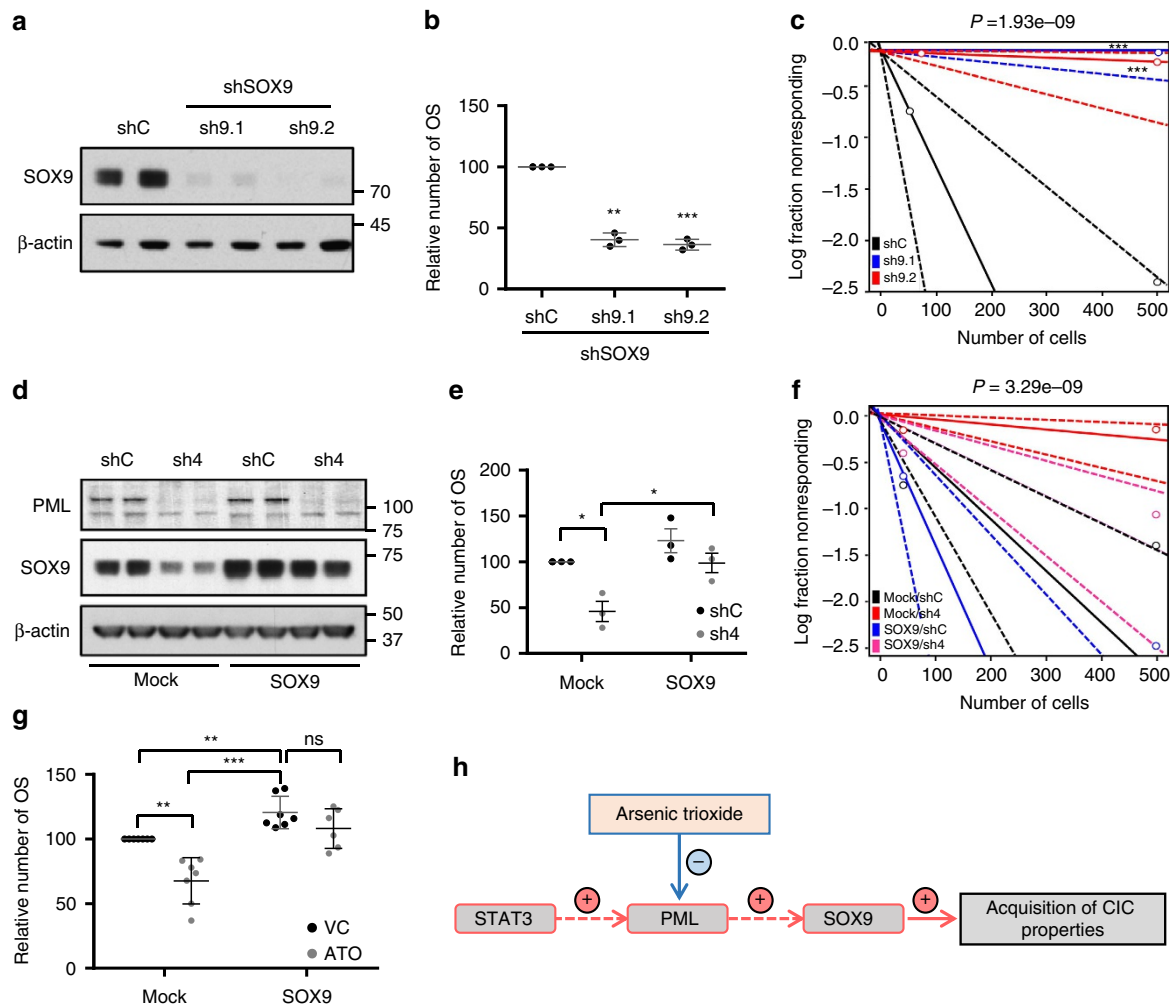


Figure 6 | SOX9 is critical for the regulation of breast cancer-initiating capacity downstream PML. (a,b) Effect of SOX9 silencing with two shRNA (sh9.1 and sh9.2) on SOX9 protein expression (representative western blot out of three independent experiments) (a) and on OSI formation ($n=3$) (b) in MDA-MB-231 cells. (c) Limiting dilution experiment after xenotransplantation. Nude mice were inoculated with 500,000 or 50,000 MDA-MB-231 cells ($n=8$ injections per experimental condition). Tumour-initiating cell number was calculated using the ELDA platform. A log-fraction plot of the limiting dilution model fitted to the data is presented. The slope of the line is the log-active cell fraction (solid lines: mean; dotted lines: 95% confidence interval; circles: values obtained in each cell dilution). (d,e) Effect of ectopic SOX9 expression on the consequences of PML silencing. Representative western blot (out of three independent experiments) depicting expression of PML and SOX9 (endogenous and ectopic protein are detected) (d) and OSI formation ($n=3$) (e) in the different experimental conditions in MDA-MB-231 cells. (f) Limiting dilution experiment to assess frequency of tumour-initiating cells after xenotransplantation. Nude mice were inoculated either with 500,000 or 50,000 MDA-MB-231 cells ($n=12$ per experimental condition, except in shC/Mock and sh4/SOX9, $n=16$). Tumour-initiating cell number was calculated using the ELDA platform as in c. (g) OSI formation in MDA-MB-231 cells transduced with the indicated constructs (mock, SOX9) and treated with vehicle or 150 nM ATO ($n=6$). (h) Diagram of the molecular mechanism by which PML controls the expression of the stem cell factor SOX9 to regulate BCa-initiating cell function. Error bars represent s.e.m., P value ($*P<0.05$; $**P<0.01$; $***P<0.001$ compared with its control or as indicated). Statistic test: one-tail unpaired t -test (b,e,g) and χ^2 -test (c,f). ATO, arsenic trioxide; OSI, primary oncospheres; shC, Scramble shRNA; sh9.1 and sh9.2, shRNA against SOX9; sh4, shRNA against PML; VC, vehicle control.

cells^{9–13,53–61}. This activity is executed in part through the functional interplay with epithelial-to-mesenchymal transition regulators such as SLUG^{12,53,56}. In BCa, SOX9 is found overexpressed in the TNBC subtype, and regulates the WNT/beta-catenin pathway¹⁴. In addition, this transcription factor is a main driver of the transcriptional signature of this subtype of BCa⁶². All these features make SOX9 an ideal target for BCa therapy. However, development of small molecules targeting transcription factors has been an outstanding challenge with limited success⁶³. Our data demonstrating that PML sustains SOX9 expression in aggressive BCa opens the possibility to bypass this limitation and inhibit the function of the transcription factor through upstream PML targeting.

In summary, our data provide proof-of-concept demonstration of the fact that PML-inhibiting compounds could exhibit strong potential for BCa therapy upon PML-based stratification.

Methods

Cell culture. MDA-MB-231, BT594, HBL100, MCF7 and T47D cell lines were obtained from the American Type Culture Collection (Manassas, VA, USA) or from Leibniz-Institut—Deutsche Sammlung von Mikroorganismen und Zellkulturen GmbH (DMSZ, Germany), who provided an authentication certificate. None of the cell lines used in this study was found in the database of commonly misidentified cell lines maintained by ICLAC and NCBI biosample. PDX44-derived cell line was generated by Dr Ibrahim and Dr Serra starting from xenograft tumours. Cell lines were routinely monitored for mycoplasma contamination and quarantined, while treated if positive. All cell lines were

maintained in DMEM media supplemented with 10% (v/v) foetal bovine serum and 1% (v/v) penicillin–streptomycin. OS formation assays were carried out as previously described⁶⁴. In brief, single-cell suspensions were plated in six-well tissue culture plates covered with poly-2-hydroxyethyl-methacrylate (Sigma, St Louis, MO) to prevent cell attachment, at a density of 3,000 cells per ml in serum-free DMEM supplemented with 1% penicillin/streptomycin, 1% B27 (Invitrogen, Carlsbad, CA, USA), 10 ng ml⁻¹ epidermal growth factor (EGF) (Sigma, St. Louis, MO) and 2 ng ml⁻¹ fibroblast Growth Factor, basic (FGFb) (Invitrogen, Carlsbad, CA, USA). After 6 days in culture, OS were counted using a light microscope. For secondary OS formation, following the same protocol, 100,000 cells were plated in 100 mm dishes and collected by gentle centrifugation (200g) and dissociated enzymatically (5 min in 1:1 TrypLE solution at 37 °C, Life Technologies, cat: 12604013) and single cells were re-plated at a density of 3,000 cells per ml in six-well tissue culture plates for 6 days.

Generation of stable cell lines. 293FT cells were used for lentiviral production. Lentiviral vectors expressing shRNAs against human *PML*, *STAT3* and *SOX9* from the Mission shRNA Library were purchased from Sigma-Aldrich or Addgene. Cells were transfected with lentiviral vectors following standard procedures, and viral supernatant was used to infect cells. Selection was done using puromycin (2 µg ml⁻¹) for 48 h. As a control, a lentivirus with scrambled shRNA (shC) was used. Short hairpins sequence: sh1PML (TRCN0000003865): CCGCAATACAA CGACAGCCGAGAATCGAGTCTGGGCTGTCGTTGATTGTTTTT, sh2PML (TRCN0000003865): CCGCAATACAACGACAGCCGAGAATCGAGTCTGGGCTGTCGTTGATTGTTTTT; sh4PML (TRCN 0000003867): CCGGCCAGTGTACGCCCTCTCCATCTCGAGATGGAGAAGCGGTACACT GGGTTTTT; sh5PML (TRCN 0000003867): CCGGGTGACCGGCAGATTGT GGATCTCGAGATCCACAATCTGCCGGTACACTTTTT; shC: CCGGCAACAA GATGAAGAGCACCACCTCGAGTGGTGTCTTCTCATCTTGTGTTG. sh4STAT3 (TRCN0000020841): CCGGGCTGAAATCATCATGCGGCTATCTCGAGATAGC CCATGATGATTTTCACTTTTT; sh43STAT3 (TRCN0000020843): CCGGGCAA AGAATCACATGCCACTTCTCGAGAAGTGGCATGTGATTCTTTGCTTTTT. sh1SOX9 (Addgene, GenBank ID: RHS3979-9587792; GCATCCTCAATTTCTG TATA); sh2SOX9 (TRCN0000342824): CCGGCTCCACCTTACCTACATGAAC TCGAGTTCATGTAGGTGAAGGTGGAGTTTTG. Sub-cloning of shC and sh4PML into pLKO-Tet-On vector was done introducing AgeI and EcoRI in the 5'-end of top and bottom shRNA oligos, respectively (following the strategy provided by Dr Dmitri Wiederschain⁶⁵, Addgene plasmid: 21915). HA-PMLIV was sub-cloned into a TRIPZ vector using Age1–Mlu1 sites.

Immunoassays. Western blot analysis was carried out as previously described²⁰. Uncropped scans are provided as part of the Supplementary Information (Supplementary Fig. 7). In brief, cells were seeded on six-well plates and 4 days (unless otherwise specified) after seeding cell lysates were prepared with RIPA buffer (50 mM TrisHCl pH 7.5, 150 mM NaCl, 1 mM EDTA, 0.1% SDS, 1% Nonidet P40, 1% sodium deoxycholate, 1 mM sodium fluoride, 1 mM sodium orthovanadate, 1 mM beta-glycerophosphate and protease inhibitor cocktail; Roche). The following antibodies were used for western blotting: rabbit polyclonal anti-PML, 1:1,000 dilution (cat: A301-167A; Bethyl laboratories), rabbit polyclonal anti-phospho-STAT3 (Tyr705) 1:1,000 dilution and total STAT3 1:1,000 dilution (cat: 9145, 9132 respectively; Cell Signaling), rabbit polyclonal anti-SOX9 1:2,000 dilution (cat: AB5535; CHEMICON International), HA-Tag polyclonal antibody 1:2,000 dilution (cat: C29F4, Cell Signaling Technology, Inc) and mouse monoclonal anti-beta-ACTIN 1:2,000 dilution (clone: AC-74, catalogue: A5316, Sigma-Aldrich). After standard SDS–polyacrylamide gel electrophoresis and western blotting techniques, proteins were visualized using the enhanced chemiluminescence (ECL) system.

For immunofluorescence, cells were seeded on glass cover slips in 24-well plates and 4 days after seeding, cells were fixed with 4% paraformaldehyde (15 min), PBS (three times wash), 1% Triton X-100 (5 min), PBS (three times wash), 10% goat serum (1 h) and anti-PML antibody 1:100 dilution (catalogue A301-167A; Bethyl laboratories) was added overnight (4 °C) in goat serum. Cover slips were washed with PBS three times and incubated with secondary antibody (anti-rabbit Alexa488; Invitrogen-Molecular Probes) for 1 h (room temperature). Cover slips were washed with PBS three times, and 4,6-diamidino-2-phenylindole added to stain nuclei (10 min), followed by mounting with Mowiol. Immunofluorescence images were obtained with an AxioImager D1 microscope.

For immunohistochemistry, tissues were fixed in 10% neutral-buffered formalin and embedded in paraffin according to standard procedures. Three to four µm-thick sections were stained for PML (clone PG-M3 Santa Cruz Biotechnology Inc, sc-966, 1:200 dilution), and vimentin (1:1,000, NCL-L-VIM-V9, Novocastra). Antigen retrieval was performed with citrate buffer (pH 6). Detection was performed with the ABC Kit from Vector Laboratories and 3,3'-diaminobenzidine (DAB)-based development. Sections were counterstained with haematoxylin. The PML general immunoreactivity scoring system (used in Fig. 1h) is described in ref. 20. For the Marseille data set, PML (1:200), SOX9 (1:400, Millipore) and phospho-STAT3 (Tyr705) (1:100, Cell Signalling; M9C6) immunostaining was performed as reported^{11,20}. The percentage of PML-high (Ph) and -low (Pl) immunoreactive tumour cells in the Marseille data set was quantified separately and the *h*-score was calculated, attributing a relative value of 1 × to Pl and 2 × to Ph intensity nuclear

signal ($h = (1 \times \text{Pl}) + (2 \times \text{Ph})$). For SOX9 automated quantification and construction of tissue microarrays (TMAs) in the Marseille data set was carried out as reported²³. In brief, cores were punched from the selected paraffin blocks, and distributed in new blocks including two cores of 0.6 mm diameter for each tumour. All the TMA blocks were stored at 4 °C. TMA serial tissue sections were prepared 24 h before immunohistochemistry processing and stored at 4 °C. The immunoperoxidase procedures were performed using an automated Ventana Benchmark XT auto-stainer. This device allowed identical well-controlled procedures for antigen retrieval and Ventana kits.

Quantitative real-time PCR. Cells were seeded as for western blot. Total RNA was extracted from cells using NucleoSpin RNA isolation kit from Macherey-Nagel (ref: 740955.240C). Complementary DNA was produced from 1 µg of RNA using qScript cDNA SuperMix (Quanta Bioscience, ref: 95048). Taqman probes were obtained from Applied Biosystems. Amplifications were run in a Viiia7 Real-Time PCR System (Applied Biosystems) using the following probes: *PML* (Hs00971694_m1, cat: 4331182) and *SOX9* (Hs01001343_g1, cat: 4331182). For *STAT3*, *SOX2* and *LGR5* amplification, Universal Probe Library (Roche) primers and probes were employed (*STAT3*, For: cccttgaggatgagatcaaga, Rev: aagcgcctatc tgctggct; probe: 14; *SOX2*, For: gggggaatggacctgtatag, Rev: gcaagctctaccgtacca; probe: 65; *LGR5*, For: accagactatgctcttggaaac, Rev: ttccacaggagtggtacct; probe: 78). *β-actin* (Hs99999903_m1, cat: 4331182) and *GAPDH* (Hs02758991_g1, cat: 4331182) housekeeping assays from Applied Biosystems showed similar results (all quantitative PCR with reverse transcription data presented were normalized using *GAPDH*).

ALDH1 activity by FACS. To measure the ALDH1 activity present in the cells, the ALDEFLUOR assay was carried out according to manufacturer's (Stemcell Technologies) guidelines. In brief, dissociated MDA-MB-231 cells were resuspended in ALDEFLUOR assay buffer at a final concentration of 1.10⁶ ml⁻¹. ALDH substrate, bodipyaminoacetaldehyde was added to the cells at a final concentration of 1.5 mM. Immediately, half of the cells were transferred to an Eppendorf tube containing a two fold molar excess of the ALDH inhibitor, diethylaminobenzaldehyde. Both tubes were incubated for 45 min at 37 °C, and after this incubation cells were centrifuged at 250g for 5 min at 4 °C and resuspended in ice-cold ALDEFLUOR assay buffer. Cells were analysed using a FACSAria1 (Becton Dickinson) flow cytometer. DRAQ7 (BiosituS) was added prior analysis to each tube for dead cell exclusion. FACSAria1 was also used for sorting cells. Data were analysed using the FACSDiva software.

Reagents. For *in vitro* experiments, SI3-201 (Sigma-Aldrich, SML0330) was prepared at 10 mg ml⁻¹ in dimethylsulfoxide and used at the indicated concentrations. TG101348 (Santa Cruz, sc-364740) was prepared 100 mg ml⁻¹ in dimethylsulfoxide and used at the indicated concentrations. ATO (Sigma-Aldrich) was prepared at a concentration of 100 mM in NaOH 1 N and subsequently diluted to 0.1 mM in PBS for a 1,000 × working solution. ATO was used at 150 nM either 3 or 6 days as indicated in figure legends. For *in vivo* experiments a dose of 5 mg kg⁻¹ per day was intraperitoneally administered.

Mice. Xenograft experiments were carried out following the ethical guidelines established by the Biosafety and Welfare Committee at CIC bioGUNE and Biodonostia Institute. The procedures employed were carried out following the recommendations from AAALAC. Xenograft experiments were performed as previously described⁶⁶, injecting either 5.10⁵ or 5.10⁴ cells per condition (unless otherwise specified), four injections per mouse. Metastasis experiment was approved by the institutional animal care and use committee of IRB-Barcelona. For tail vein injections, cells were resuspended in PBS and injected into tail vein of mice using a 26 G needle (1.2 × 10⁵ cells per mouse), as previously described²⁵. Cell lung colonization capacity was scored 21 days post inoculation by human vimentin. PML expression was scored as undetectable (PML 0) and detectable (PML 1 +, 2 + and 3 +). All mice (female Hsd:ATHymic Nude-Foxn1 nu/nu) were inoculated at 8–12 weeks of age.

ChIP. ChIP was performed using the SimpleChIP Enzymatic Chromatin IP Kit (cat: 9003, Cell Signaling Technology, Inc). MDA-MB-231 cells were grown in 150 mm dishes either with or without 50 ng ml⁻¹ doxycycline during 3 days. Cells from three 150 mm dishes (2.5 × 10⁷ cells) were cross-linked with 35% formaldehyde for 10 min at room temperature. Glycine was added to dishes, and cells incubated for 5 min at room temperature. Cells were then washed twice with ice-cold PBS, and scraped into PBS + PMSF. Pelleted cells were lysed and nuclei were collected following manufacturer's instructions. Nuclear lysates were digested with micrococcal nuclease for 20 min at 37 °C and then sonicated in 500 µl aliquots on ice for three pulses of 15 s using a Branson sonicator. Cells were held on ice for at least 1 min between sonifications. Lysates were clarified at 11,000g for 10 min at 4 °C, and chromatin was stored at –80 °C. HA-Tag polyclonal antibody (cat: C29F4, Cell Signaling Technology), rabbit polyclonal anti-PML (cat: A301-167A; Bethyl laboratories) and IgG antibody (cat: 2729, Cell Signaling Technology, Inc), were incubated overnight (4 °C) with rotation and protein G magnetic beads were

incubated 2 h (4 °C). Washes and elution of chromatin were performed following manufacturer's instructions. DNA quantification was carried out using a ViiA7 Real-Time PCR System (Applied Biosystems) with SybrGreen reagents and primers that amplify the predicted PML binding region to SOX9 promoter (chr17:70117013-70117409) as follows: left primer: ccggaactttcttgcag and right primer: cggcgagcacttaggaag.

Patient data sets, bioinformatics and statistical analysis. All studies involving human subjects were approved by the corresponding committees with informed consent as stated in the original publications^{3,23,25}. The use of MSK/EMC and Marseille cohorts were previously described^{23,25}. For MSK/EMC, MFS curves were plotted using Kaplan–Meier estimates and compared using the Gehan–Breslow–Wilcoxon test. Two groups were compared using mean PML expression values as the cutoff between PML high and low. Kaplan–Meier survival and correlation analysis in patient samples: publicly available and clinically annotated BCa cohorts with gene expression profiles (GSE2603, GSE2034, GSE5327 and GSE12276) were pooled as described above. To remove systematic biases, before merging the expression measurements were converted to z scores for all genes. For intrinsic subtype classification, we carried out the following analysis: for luminal genes, *ESR1* and *PGR1* presented a bimodal distribution. We used package *mlcut* to fit a mixture of normal distributions with two components and obtain the posterior probability that each patient belongs to the luminal low and luminal high components. A patient was considered luminal low if the posterior probability of belonging to this group was > 80%. The same criterion was used for luminal high. When a patient was neither luminal high nor luminal low, it was considered luminal intermediate. Proliferation status (Prol) and *ERBB2* expression did not present a bimodal distribution. Therefore, half of the patients with lowest mean values were considered proliferation low. The rest were considered proliferation high. After defining high and low populations for each parameter, the subtypes were constructed as follows: luminal A: Prol low, *ESR1* intermediate or high, luminal intermediate or high; luminal B: Prol high, *ESR1* intermediate or high, luminal intermediate or high; *HER2* enriched: Prol high, *ESR1* intermediate or low, luminal intermediate or low; *ERBB2* high; basal like: Prol high, *ESR1* low, luminal low; *ERBB2* low, *PGR1* low. Sixty-four patients could not be assigned to any subtype according to PAM50's classification. A Cox proportional hazards model was fitted to compute HR. Likelihood ratio tests were performed to compute P values. The HR was checked for constancy over time, fulfilling Cox model assumptions.

For Curtis data set patients, RNA was extracted from 1,980 tumours as described³. RNA hybridizations were performed using Illumina HT-12 v3 platform and analysed using the bioconductor bead array package⁶⁷. The BASH algorithm⁶⁸ was applied to correct for spatial artefacts in the arrays. Bead-level data were summarized and re-annotated as described in ref. 3. Log-intensity values for PML expression were scaled to z scores. Probe selection was performed on the basis of probe quality, 3'-position, no other genomic matches and no single-nucleotide polymorphisms in the region. On the basis of these criteria, PML probe ILMN_1731299 was selected for analysis. Survival analysis was done using as endpoints MFS at 5 years (distant metastasis as event). Two groups were compared using mean PML expression values as the cutoff between PML high and low. We used the log-rank test as implemented in the survival R package⁶⁹.

For therapy response analysis, publicly available data sets (GSE22093 and GSE23988) were downloaded from Gene Expression Omnibus (GEO), and subjected to background correction, log₂ transformation and quartile normalization.

For correlation analysis with *STAT3* signatures, gene sets were extracted (ref. 37, and [http://software.broadinstitute.org/gsea/msigdb/cards/V\\$STAT3_01](http://software.broadinstitute.org/gsea/msigdb/cards/V$STAT3_01)) and average signal value in the MSK/EMC data set was calculated. These values were used to perform the correlation analysis with PML signal values (Pearson correlation).

No statistics were applied to determine sample size. The experiments were not randomized. The investigators were not blinded to allocation during experiments and outcome assessment. Data analysed by parametric tests are represented by the mean ± s.e.m. of pooled experiments unless otherwise stated. *n* values represent the number of independent experiments performed or the number of individual mice or patient specimens. For each independent *in vitro* experiment, at least three technical replicates were used and a minimum number of three experiments were performed to ensure adequate statistical power. Analysis of variance test was used for multi-component comparisons and Student's *t*-test for two-component comparisons. In the *in vitro* experiments, normal distribution was confirmed or assumed (for *n* < 5) and Student's *t*-test was applied for two-component comparisons. Two-tailed statistical analysis was applied for experimental design without predicted result, and one tail for validation or hypothesis-driven experiments. The confidence level used for all the statistical analyses was of 0.95 (alpha value = 0.05). Tumour-initiating cell frequency was estimated using ELDA software as previously described⁷⁰.

Data availability. Data from public repositories analysed throughout this manuscript (see the 'Patient data sets, bioinformatics and statistical analysis' section) is available as indicated in the referenced publications.

References

- Haber, D. A., Gray, N. S. & Baselga, J. The evolving war on cancer. *Cell* **145**, 19–24 (2011).
- Sorlie, T. *et al.* Gene expression patterns of breast carcinomas distinguish tumor subclasses with clinical implications. *Proc. Natl Acad. Sci. USA* **98**, 10869–10874 (2001).
- Curtis, C. *et al.* The genomic and transcriptomic architecture of 2,000 breast tumours reveals novel subgroups. *Nature* **486**, 346–352 (2012).
- Normanno, N. *et al.* Prognostic applications of gene expression signatures in breast cancer. *Oncology (Williston Park)* **77**(Suppl 1): 2–8 (2009).
- van de Vijver, M. J. *et al.* A gene-expression signature as a predictor of survival in breast cancer. *N. Engl. J. Med.* **347**, 1999–2009 (2002).
- Stingl, J. & Caldas, C. Molecular heterogeneity of breast carcinomas and the cancer stem cell hypothesis. *Nat. Rev. Cancer* **7**, 791–799 (2007).
- Valent, P. *et al.* Cancer stem cell definitions and terminology: the devil is in the details. *Nat. Rev. Cancer* **12**, 767–775 (2012).
- Li, F., Tiede, B., Massague, J. & Kang, Y. Beyond tumorigenesis: cancer stem cells in metastasis. *Cell Res.* **17**, 3–14 (2007).
- Jo, A. *et al.* The versatile functions of Sox9 in development, stem cells, and human diseases. *Genes Dis.* **1**, 149–161 (2014).
- Larsimont, J. C. *et al.* Sox9 controls self-renewal of oncogene targeted cells and links tumor initiation and invasion. *Cell Stem Cell* **17**, 60–73 (2015).
- Matheu, A. *et al.* Oncogenicity of the developmental transcription factor Sox9. *Cancer Res.* **72**, 1301–1315 (2012).
- Guo, W. *et al.* Slug and Sox9 cooperatively determine the mammary stem cell state. *Cell* **148**, 1015–1028 (2012).
- Malhotra, G. K. *et al.* The role of Sox9 in mouse mammary gland development and maintenance of mammary stem and luminal progenitor cells. *BMC Dev. Biol.* **14**, 47 (2014).
- Wang, H. *et al.* SOX9 regulates low density lipoprotein receptor-related protein 6 (LRP6) and T-cell factor 4 (TCF4) expression and Wnt/beta-catenin activation in breast cancer. *J. Biol. Chem.* **288**, 6478–6487 (2013).
- Bernardi, R. & Pandolfi, P. P. Structure, dynamics and functions of promyelocytic leukaemia nuclear bodies. *Nat. Rev. Mol. Cell. Biol.* **8**, 1006–1016 (2007).
- Carracedo, A., Ito, K. & Pandolfi, P. P. The nuclear bodies inside out: PML conquers the cytoplasm. *Curr. Opin. Cell. Biol.* **23**, 360–366 (2011).
- Martin-Martin, N., Sutherland, J. D. & Carracedo, A. PML: not all about tumor suppression. *Front. Oncol.* **3**, 200 (2013).
- Ito, K. *et al.* PML targeting eradicates quiescent leukaemia-initiating cells. *Nature* **453**, 1072–1078 (2008).
- Ito, K. *et al.* A PML–PPAR- δ pathway for fatty acid oxidation regulates hematopoietic stem cell maintenance. *Nat. Med.* **18**, 1350–1358 (2012).
- Carracedo, A. *et al.* A metabolic prosurvival role for PML in breast cancer. *J. Clin. Invest.* **122**, 3088–3100 (2012).
- Li, H. *et al.* Stem cell marker aldehyde dehydrogenase 1 (ALDH1)-expressing cells are enriched in triple-negative breast cancer. *Int. J. Biol. Markers* **28**, e357–e364 (2013).
- Baccelli, I. & Trumpp, A. The evolving concept of cancer and metastasis stem cells. *J. Cell Biol.* **198**, 281–293 (2012).
- Charpin, C. *et al.* Validation of an immunohistochemical signature predictive of 8-year outcome for patients with breast carcinoma. *Int. J. Cancer* **131**, E236–E243 (2012).
- Chiang, A. C. & Massague, J. Molecular basis of metastasis. *N. Engl. J. Med.* **359**, 2814–2823 (2008).
- Morales, M. *et al.* RARRES3 suppresses breast cancer lung metastasis by regulating adhesion and differentiation. *EMBO Mol. Med.* **6**, 865–881 (2014).
- Pavlovic, M. *et al.* Enhanced MAF Oncogene Expression and Breast Cancer Bone Metastasis. *J. Natl Cancer Inst.* **107**, djv256 (2015).
- Iwamoto, T. *et al.* Gene pathways associated with prognosis and chemotherapy sensitivity in molecular subtypes of breast cancer. *J. Natl Cancer Inst.* **103**, 264–272 (2011).
- Minn, A. J. *et al.* Genes that mediate breast cancer metastasis to lung. *Nature* **436**, 518–524 (2005).
- Bos, P. D., Nguyen, D. X. & Massague, J. Modeling metastasis in the mouse. *Curr. Opin. Pharmacol.* **10**, 571–577 (2010).
- Gupta, G. P. *et al.* ID genes mediate tumor reinitiation during breast cancer lung metastasis. *Proc. Natl Acad. Sci. USA* **104**, 19506–19511 (2007).
- Bos, P. D. *et al.* Genes that mediate breast cancer metastasis to the brain. *Nature* **459**, 1005–1009 (2009).
- Dror, N. *et al.* Interferon regulatory factor-8 is indispensable for the expression of promyelocytic leukemia and the formation of nuclear bodies in myeloid cells. *J. Biol. Chem.* **282**, 5633–5640 (2007).

33. Stadler, M. *et al.* Transcriptional induction of the PML growth suppressor gene by interferons is mediated through an ISRE and a GAS element. *Oncogene* **11**, 2565–2573 (1995).
34. Hubackova, S., Krejčíková, K., Bartek, J. & Hodny, Z. Interleukin 6 signaling regulates promyelocytic leukemia protein gene expression in human normal and cancer cells. *J. Biol. Chem.* **287**, 26702–26714 (2012).
35. Lavau, C. *et al.* The acute promyelocytic leukaemia-associated PML gene is induced by interferon. *Oncogene* **11**, 871–876 (1995).
36. Yeh, Y. T. *et al.* STAT3 ser727 phosphorylation and its association with negative estrogen receptor status in breast infiltrating ductal carcinoma. *Int. J. Cancer* **118**, 2943–2947 (2006).
37. Azare, J. *et al.* Constitutively activated Stat3 induces tumorigenesis and enhances cell motility of prostate epithelial cells through integrin beta 6. *Mol. Cell. Biol.* **27**, 4444–4453 (2007).
38. Tatham, M. H. *et al.* RNF4 is a poly-SUMO-specific E3 ubiquitin ligase required for arsenic-induced PML degradation. *Nat. Cell. Biol.* **10**, 538–546 (2008).
39. Lallemand-Breitenbach, V. *et al.* Arsenic degrades PML or PML-RARalpha through a SUMO-triggered RNF4/ubiquitin-mediated pathway. *Nat. Cell. Biol.* **10**, 547–555 (2008).
40. Weinstein, I. B. Cancer. Addiction to oncogenes—the Achilles heel of cancer. *Science* **297**, 63–64 (2002).
41. Perou, C. M., Parker, J. S., Prat, A., Ellis, M. J. & Bernard, P. S. Clinical implementation of the intrinsic subtypes of breast cancer. *Lancet Oncol.* **11**, 718–719 (2010).
42. Perou, C. M. *et al.* Molecular portraits of human breast tumours. *Nature* **406**, 747–752 (2000).
43. Consortium EP. The ENCODE (ENCyclopedia Of DNA Elements) Project. *Science* **306**, 636–640 (2004).
44. Gerstein, M. B. *et al.* Architecture of the human regulatory network derived from ENCODE data. *Nature* **489**, 91–100 (2012).
45. Wang, J. *et al.* Sequence features and chromatin structure around the genomic regions bound by 119 human transcription factors. *Genome Res.* **22**, 1798–1812 (2012).
46. Wang, J. *et al.* Factorbook.org: a Wiki-based database for transcription factor-binding data generated by the ENCODE consortium. *Nucleic Acids Res.* **41**, D171–D176 (2013).
47. Vernier, M. *et al.* Regulation of E2Fs and senescence by PML nuclear bodies. *Genes Dev.* **25**, 41–50 (2011).
48. von Mikecz, A., Zhang, S., Montminy, M., Tan, E. M. & Hemmerich, P. CREB-binding protein (CBP)/p300 and RNA polymerase II colocalize in transcriptionally active domains in the nucleus. *J. Cell Biol.* **150**, 265–273 (2000).
49. Kuo, H. Y. *et al.* PML represses lung cancer metastasis by suppressing the nuclear EGFR-mediated transcriptional activation of MMP2. *Cell Cycle* **13**, 3132–3142 (2014).
50. Weinstein, B. Relevance of the concept of oncogene addiction to hormonal carcinogenesis and molecular targeting in cancer prevention and therapy. *Adv. Exp. Med. Biol.* **617**, 3–13 (2008).
51. Weinstein, I. B. & Joe, A. Oncogene addiction. *Cancer Res.* **68**, 3077–3080 discussion 3080 (2008).
52. Lo-Coco, F. & Ammatuna, E. The biology of acute promyelocytic leukemia and its impact on diagnosis and treatment. *Hematology. Am. Soc. Hematol. Educ. Program* **156-161**, 514 (2006).
53. Fazilaty, H., Gardaneh, M., Akbari, P., Zekri, A. & SLUG, Behnam B. and SOX9 Cooperatively Regulate Tumor Initiating Niche Factors in Breast Cancer. *Cancer Microenviron.* **9**, 71–74 (2016).
54. Hiraoka, K. *et al.* SOX9-mediated upregulation of LGR5 is important for glioblastoma tumorigenicity. *Biochem. Biophys. Res. Commun.* **460**, 216–221 (2015).
55. Hong, Y. *et al.* Upregulation of sex-determining region Y-box 9 (SOX9) promotes cell proliferation and tumorigenicity in esophageal squamous cell carcinoma. *Oncotarget* **6**, 31241–31254 (2015).
56. Luanpitpong, S. *et al.* SLUG is required for SOX9 stabilization and functions to promote cancer stem cells and metastasis in human lung carcinoma. *Oncogene* **35**, 2824–2833 (2016).
57. Roche, K. C. *et al.* SOX9 maintains reserve stem cells and preserves radioresistance in mouse small intestine. *Gastroenterology* **149**, 1553–1563 e1510 (2015).
58. Scott, C. E. *et al.* SOX9 induces and maintains neural stem cells. *Nat. Neurosci.* **13**, 1181–1189 (2010).
59. Furuyama, K. *et al.* Continuous cell supply from a Sox9-expressing progenitor zone in adult liver, exocrine pancreas and intestine. *Nat. Genet.* **43**, 34–41 (2011).
60. Adam, R. C. *et al.* Pioneer factors govern super-enhancer dynamics in stem cell plasticity and lineage choice. *Nature* **521**, 366–370 (2015).
61. Garros-Regulez, L. *et al.* mTOR inhibition decreases SOX2-SOX9 mediated glioma stem cell activity and temozolomide resistance. *Expert. Opin. Ther. Targets* **20**, 393–405 (2016).
62. Willis, S. *et al.* Enriched transcription factor signatures in triple negative breast cancer indicates possible targeted therapies with existing drugs. *Meta Gene* **4**, 129–141 (2015).
63. Johnston, S. J. & Carroll, J. S. Transcription factors and chromatin proteins as therapeutic targets in cancer. *Biochim. Biophys. Acta.* **1855**, 183–192 (2015).
64. Piva, M. *et al.* Sox2 promotes tamoxifen resistance in breast cancer cells. *EMBO Mol. Med.* **6**, 66–79 (2014).
65. Wiederschain, D. *et al.* Single-vector inducible lentiviral RNAi system for oncology target validation. *Cell Cycle* **8**, 498–504 (2009).
66. Carracedo, A. *et al.* Inhibition of mTORC1 leads to MAPK pathway activation through a PI3K-dependent feedback loop in human cancer. *J. Clin. Invest.* **118**, 3065–3074 (2008).
67. Dunning, M. J., Smith, M. L., Ritchie, M. E. & Tavare, S. beadarray: R classes and methods for Illumina bead-based data. *Bioinformatics* **23**, 2183–2184 (2007).
68. Cairns, J. M., Dunning, M. J., Ritchie, M. E., Russell, R. & Lynch, A. G. BASH: a tool for managing BeadArray spatial artefacts. *Bioinformatics* **24**, 2921–2922 (2008).
69. Therneau, T. M. & Grambsch, P. M. *Statistics for Biology and Health* (Springer, 2000).
70. Hu, Y. & Smyth, G. K. ELDA: extreme limiting dilution analysis for comparing depleted and enriched populations in stem cell and other assays. *J. Immunol. Methods* **347**, 70–78 (2009).

Acknowledgements

Apologies to those whose related publications were not cited due to space limitations. We thank Dr Miquel Angel Pujana for insightful discussions, Dr Monika González for technical help, Dr Miriam Rábano for technical help with flow cytometry cell sorting and Dr Aleix Prat for the evaluation of the intrinsic subtypes in PDX. The work of A.C. is supported by the Ramón y Cajal award, the Basque Department of Industry, Tourism and Trade (Etorrek), Health (2012111086) and Education (PI2012-03), Marie Curie (277043), Movember Foundation (GAP1), ISCIII (PI10/01484, PI13/00031), FERO (VIII Fellowship) and ERC (336343). N.M.-M. and P.A. are supported by the Spanish Association Against Cancer (AECC), AECC JP Vizcaya and Guipuzcoa, respectively. J.U. and F.S. are Juan de la Cierva Researchers (MINECO). L.A., A.A.-A. and L.V.-J. are supported by the Basque Government of education. M.L.-M.C. acknowledges SAF2014-54658-R and Asociación Española contra el Cancer. R.B. acknowledges Spanish MINECO (BFU2014-52282-P, Consolider BFU2014-57703-REDC), the Departments of Education and Industry of the Basque Government (PI2012/42) and the Bizkaia County. M.S., V.S. and J.B. acknowledge Banco Bilbao Vizcaya Argentaria (BBVA) Foundation (Tumour Biomarker Research Program). M.S. and J.B. are supported by NIH grant P30 CA008748. M.d.M.V. is supported by the Institute of Health Carlos III (PI11/02251, PI14/01328) and Basque Government, Health Department (2014111145). A.M. is supported by ISCIII (CP10/00539, PI13/02277) and Marie Curie CIG 2012/712404. V.S. is supported by the SCIII (PI13/01714, CP14/00228), the FERO Foundation and the Catalan Agency AGAUR (2014 SGR 1331). R.R.G. research support is provided by the Spanish Ministry of Science and Innovation grant SAF2013-46196, BBVA Foundation, the Generalitat de Catalunya (2014 SGR 535), Institució Catalana de Recerca i Estudis Avançats, the Spanish Ministerio de Economía y Competitividad (MINECO) and FEDER funds (SAF2013-46196).

Authors contributions

N.M.-M. and M.P. performed all the *in vitro* and *in vivo* experiments, unless specified otherwise. P.A., J.U., M.G., F.S., A.M. and R.R.G. performed or coordinated (A.M. and R.R.G.) *in vivo* tumour formation and metastasis assays. J.D.S. and R.B. generated PML inducible overexpressing and silencing lentiviral vectors. S.F.-R. performed the histochemical stainings and contributed to *in vitro* analyses. L.A. and I.M. contributed to *in vitro* analyses. V.T. contributed to the SOX9 promoter analysis. N.R.-R., S.G. and J.L.I. performed or coordinated (J.L.I.) the immunohistochemical scoring in patient specimens. A.R.C., E.P., O.M.R., A.M.A. and C.C. performed or coordinated (A.M.A. and C.C.) the bioinformatic and biostatistical analysis. G.D. performed ALDH1 analysis. Y.I., M.S., J.B. and V.S. generated the PDX. A.Z.-L., A.A.-A., P.Z., A.C.-M., L.V.-J., P.S.-M., M.V.-R., M.L.-M.C., J.A. and C.H.L. contributed to the experimental design and discussion. M.d.M.V., A.M. and R.R.G. contributed to the experimental design, data analysis and discussion. A.C. directed the project, contributed to data analysis and wrote the manuscript.

Additional information

Supplementary Information accompanies this paper at <http://www.nature.com/naturecommunications>

Competing financial interests: The authors declare no competing financial interests.

Reprints and permission information is available online at <http://npg.nature.com/reprintsandpermissions/>

How to cite this article: Martín-Martín, N. *et al.* Stratification and therapeutic potential of PML in metastatic breast cancer. *Nat. Commun.* 7:12595 doi: 10.1038/ncomms12595 (2016).



This work is licensed under a Creative Commons Attribution 4.0 International License. The images or other third party material in this article are included in the article's Creative Commons license, unless indicated otherwise in the credit line; if the material is not included under the Creative Commons license, users will need to obtain permission from the license holder to reproduce the material. To view a copy of this license, visit <http://creativecommons.org/licenses/by/4.0/>

© The Author(s) 2016

mTORC1-dependent AMD1 regulation sustains polyamine metabolism in prostate cancer

Amaia Zabala-Letona^{1,2*}, Amaia Arruabarrena-Aristorena^{1*}, Natalia Martín-Martín^{1,2}, Sonia Fernandez-Ruiz^{1,2}, James D. Sutherland¹, Michelle Clasquin³, Julen Tomas-Cortazar¹, Jose Jimenez⁴, Ines Torres⁵, Phong Quang³, Pilar Ximenez-Embun⁶, Ruzica Bago⁷, Aitziber Ugalde-Olano⁸, Ana Loizaga-Iriarte⁹, Isabel Lacasa-Viscasillas⁹, Miguel Unda⁹, Verónica Torrano^{1,2}, Diana Cabrera¹, Sebastiaan M. van Liempd¹, Ylenia Cendon^{6,10}, Elena Castro⁶, Stuart Murray³, Ajinkya Revandkar^{11,12}, Andrea Alimonti^{11,12}, Yinan Zhang¹³, Amelia Barnett³, Gina Lein³, David Pirman³, Ana R. Cortazar¹, Leire Arreal¹, Ludmila Prudkin⁴, Ianire Astobiza¹, Lorea Valcarcel-Jimenez¹, Patricia Zuñiga-García¹, Itziar Fernandez-Dominguez¹, Marco Piva¹, Alfredo Caro-Maldonado¹, Pilar Sánchez-Mosquera¹, Mireia Castillo-Martín^{14,15}, Violeta Serra⁴, Naiara Beraza^{1,†}, Antonio Gentilella^{16,17}, George Thomas¹⁶, Mikel Azkargorta^{1,18}, Felix Elortza^{1,18,19}, Rosa Farràs²⁰, David Olmos^{6,21}, Alejo Efeyan⁶, Juan Anguita^{1,22}, Javier Muñoz^{6,18}, Juan M. Falcón-Pérez^{1,19,22}, Rosa Barrio¹, Teresa Macarulla^{2,4}, Jose M. Mato^{1,19}, Maria L. Martinez-Chantar^{1,19}, Carlos Cordon-Cardo¹⁴, Ana M. Aransay^{1,19}, Kevin Marks³, José Baselga²³, Josep Taberner^{2,4}, Paolo Nuciforo⁴, Brendan D. Manning¹³, Katya Marjon³ & Arkaitz Carracedo^{1,2,22,24}

Activation of the PTEN-PI3K-mTORC1 pathway consolidates metabolic programs that sustain cancer cell growth and proliferation^{1,2}. Here we show that mechanistic target of rapamycin complex 1 (mTORC1) regulates polyamine dynamics, a metabolic route that is essential for oncogenicity. By using integrative metabolomics in a mouse model³ and human biopsies⁴ of prostate cancer, we identify alterations in tumours affecting the production of decarboxylated S-adenosylmethionine (dcSAM) and polyamine synthesis. Mechanistically, this metabolic rewiring stems from mTORC1-dependent regulation of S-adenosylmethionine decarboxylase 1 (AMD1) stability. This novel molecular regulation is validated in mouse and human cancer specimens. AMD1 is upregulated in human prostate cancer with activated mTORC1. Conversely, samples from a clinical trial with the mTORC1 inhibitor everolimus⁵ exhibit a predominant decrease in AMD1 immunoreactivity that is associated with a decrease in proliferation, in line with the requirement of dcSAM production for oncogenicity. These findings provide fundamental information about the complex regulatory landscape controlled by mTORC1 to integrate and translate growth signals into an oncogenic metabolic program.

Alterations in the phosphoinositide 3-kinase (PI3K) pathway have been reported in a high percentage of human cancers^{6,7}. We sought to identify metabolic requirements of prostate cancer taking advantage of a faithful genetically engineered mouse model of this disease driven by loss of *Pten*³, a negative regulator of the PI3K pathway that is frequently downregulated in this tumour type^{6,8}. First, we performed high-throughput quadrupole time-of-flight mass spectrometry (q-TOF-MS) to examine metabolic alterations at two time points (3 and 6 months, onset of prostate intraepithelial neoplasia (PIN) and invasive prostate carcinoma, respectively) (Extended Data Fig. 1a, b) in two different prostate lobes (Extended Data Fig. 1c).

From 7,722 ions, we assigned metabolite identification (Human Metabolome Database score ≥ 40) to 632 (Supplementary Table 1). We did not observe significant influence of the prostate lobe or the time point of analysis, and after precluding significant alterations in candidate metabolic pathways, we focused on metabolites consistently and significantly altered in all conditions (Extended Data Fig. 1d, e and Supplementary Table 2). We identified 72 unique metabolites (73 assigned ions) fulfilling the criteria (Fig. 1a and Supplementary Table 1). Pathway enrichment analysis in this set did not show significantly altered pathways including a considerable number of metabolites (Supplementary Table 3). Strikingly, representation in waterfall plot revealed an increase in polyamine-synthesis-related metabolites in *Pten*^{pc-/-} mice (Fig. 1b). These results were validated in this genetically engineered mouse model and human prostate cancer tissues by quantitative liquid chromatography (LC)/MS (Extended Data Fig. 1f, g and Supplementary Table 4).

To determine how metabolic rewiring affects polyamine dynamics, we set up ¹³C-labelling metabolic analysis to trace the fate of L-methionine-derived carbons *in vivo* (Extended Data Fig. 2a). Next, we injected [¹³C₅]L-methionine intravenously in *Pten*^{pc+/+} and *Pten*^{pc-/-} mice (Extended Data Fig. 2b). Prostate tissue analysis revealed an elevation in ¹³C-labelled decarboxylated S-adenosylmethionine (dcSAM), together with increased synthesis and fractional labelling of polyamines (Fig. 1c, Extended Data Fig. 2c, d and Supplementary Table 5). Importantly, the increase of SAM decarboxylation (elevated dcSAM/SAM ratio) in both mouse and human pathological tissues strongly suggested that the enzyme that catalyses this reaction (S-adenosylmethionine decarboxylase 1, AMD1) is potentially responsible for the metabolic changes observed in prostate cancer (Fig. 1d-f).

To address the contribution of dcSAM production to cell oncogenicity in prostate cancer, we ectopically expressed AMD1 in cell lines from

¹CIC bioGUNE, Bizkaia Technology Park, 801 Building, 48160 Derio, Spain. ²CIBERONC, Instituto de Salud Carlos III, C/ Monforte de Lemos 3-5, Pabellón 11, Planta 0, 28029 Madrid, Spain.

³AGIOS Pharmaceuticals, Cambridge, Massachusetts, 02139, USA. ⁴Vall d'Hebron Institute of Oncology (VHIO), Universidad Autónoma de Barcelona, 08035 Barcelona, Spain. ⁵Department of Pathology, Vall d'Hebron Hospital, Universitat Autònoma de Barcelona, 08035 Barcelona, Spain. ⁶Spanish National Cancer Research Centre (CNIO), 28029 Madrid, Spain. ⁷MRC Protein Phosphorylation and Ubiquitylation Unit, College of Life Sciences, University of Dundee, Dow Street, Dundee DD1 5EH, UK. ⁸Department of Pathology, Basurto University Hospital, 48013 Bilbao, Spain. ⁹Department of Urology, Basurto University Hospital, 48013 Bilbao, Spain. ¹⁰School of Medicine, Universidad Autónoma de Madrid, 28049 Madrid, Spain. ¹¹Institute of Oncology Research (IOR) and Oncology Institute of Southern Switzerland (IOSI), Bellinzona CH 6500, Switzerland. ¹²Faculty of Biology and Medicine, University of Lausanne (UNIL), Lausanne CH 1011, Switzerland. ¹³Department of Genetics and Complex Diseases, Harvard School of Public Health, Boston, Massachusetts 02115, USA. ¹⁴Department of Pathology, Icahn School of Medicine at Mount Sinai, New York 10029-5674, USA. ¹⁵Department of Pathology, Fundação Champalimaud, 1400-038 Lisboa, Portugal. ¹⁶Laboratory of Metabolism and Cancer, Catalan Institute of Oncology, ICO, Bellvitge Biomedical Research Institute, IDIBELL, 08908 Barcelona, Spain. ¹⁷Department of Biochemistry and Physiology, Faculty of Pharmacy, Universitat de Barcelona, 08028 Barcelona, Catalunya, Spain. ¹⁸Carlos III Networked Proteomics Platform (ProteoRed-ISCI), Instituto de Salud Carlos III, C/ Monforte de Lemos 3-5, Pabellón 11, Planta 0, 28029 Madrid, Spain. ¹⁹Centro de Investigación Biomédica en Red de Enfermedades Hepáticas y Digestivas (CIBERehd), Instituto de Salud Carlos III, C/ Monforte de Lemos 3-5, Pabellón 11, Planta 0, 28029 Madrid, Spain. ²⁰Centro de Investigación Príncipe Felipe, Eduardo Primo Yúfera 3, 46012 Valencia, Spain. ²¹CNIO-IBIMA Genitourinary Cancer Unit, Medical Oncology Department, Hospitales Universitarios Virgen de la Victoria y Regional de Málaga, 29010 Málaga, Spain. ²²Ikerbasque, Basque foundation for science, 48011 Bilbao, Spain. ²³Human Oncology & Pathogenesis Program, Memorial Sloan-Kettering Cancer Center, New York 10065, USA. ²⁴Biochemistry and Molecular Biology Department, University of the Basque Country (UPV/EHU), 48940 Bilbao, Spain. †Present address: Gut Health and Food Safety Programme, Institute of Food Research, Norwich Research Park, Norwich NR4 7UA, UK.

*These authors contributed equally to this work.

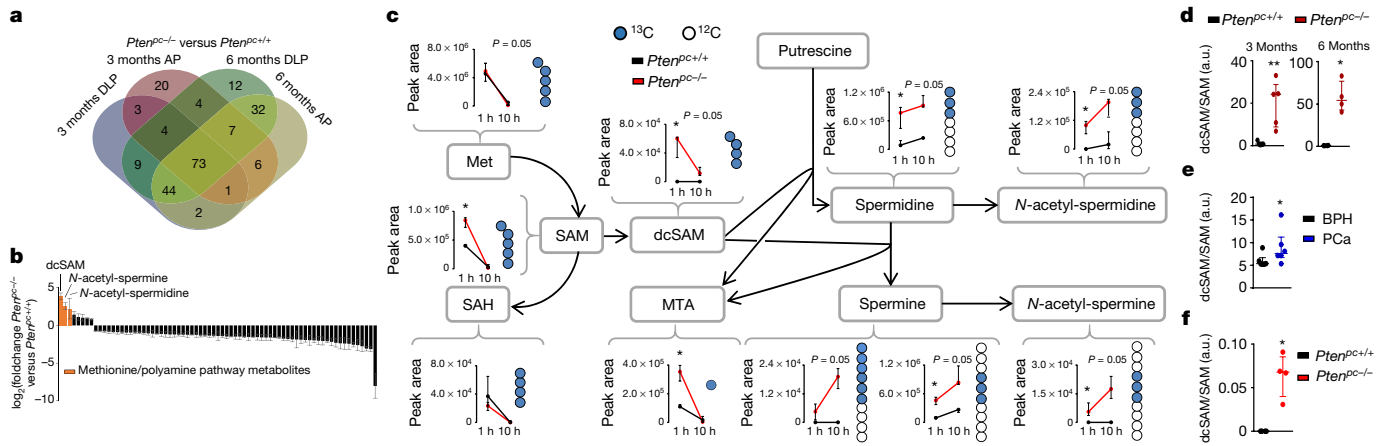


Figure 1 | Integrative metabolomics in prostate cancer reveals a rewiring from methionine metabolism towards polyamine synthesis. **a, b**, Venn diagram (anterior prostate (AP) and dorsolateral prostate (DLP)) (**a**) and waterfall plot (**b**) of altered metabolites from q-TOF-MS metabolomic analysis performed in *Pten^{pc-/-}* and *Pten^{pc+/+}* (6 months *Pten^{pc+/+}* anterior prostate, *n* = 4 mice; remainder of conditions, *n* = 5 mice) mouse prostate samples at the indicated age. Values in **b** represent the average of the log₂(fold change) with the s.e.m. of the two lobes and two time points (3 and 6 months of age) per metabolite. **c**, Incorporation of carbon-13 (¹³C) from intravenously injected [¹³C₅]L-methionine (100 mg kg⁻¹) into the indicated metabolites at 3 months of age (anterior prostate). Peak

area refers to natural abundance-corrected values (*n* = 4 mice at 1 h; *n* = 3 mice at 10 h). Median ± interquartile range. Blue dots: ¹³C; white dots: ¹²C; 1 h/10 h: prostate samples extracted after 1-h/10-h pulse with [¹³C₅]L-methionine. SAH, S-adenosylhomocysteine; Met, methionine. **d**, dcSAM/SAM ratios from Extended Data Fig. 1f (*n* = 4 as indicated by dots); a.u., arbitrary units. **e**, dcSAM/SAM ratio from Extended Data Fig. 1g (*n* = 6 as indicated by dots). BPH, benign prostate hyperplasia; PCa, prostate cancer. **f**, dcSAM/SAM ratio from Fig. 1c at 1 h (*n* = 4 as indicated by dots). **P* < 0.05; ***P* < 0.01. One-tailed (*c*–*f*) Mann–Whitney *U*-test was used for data analysis.

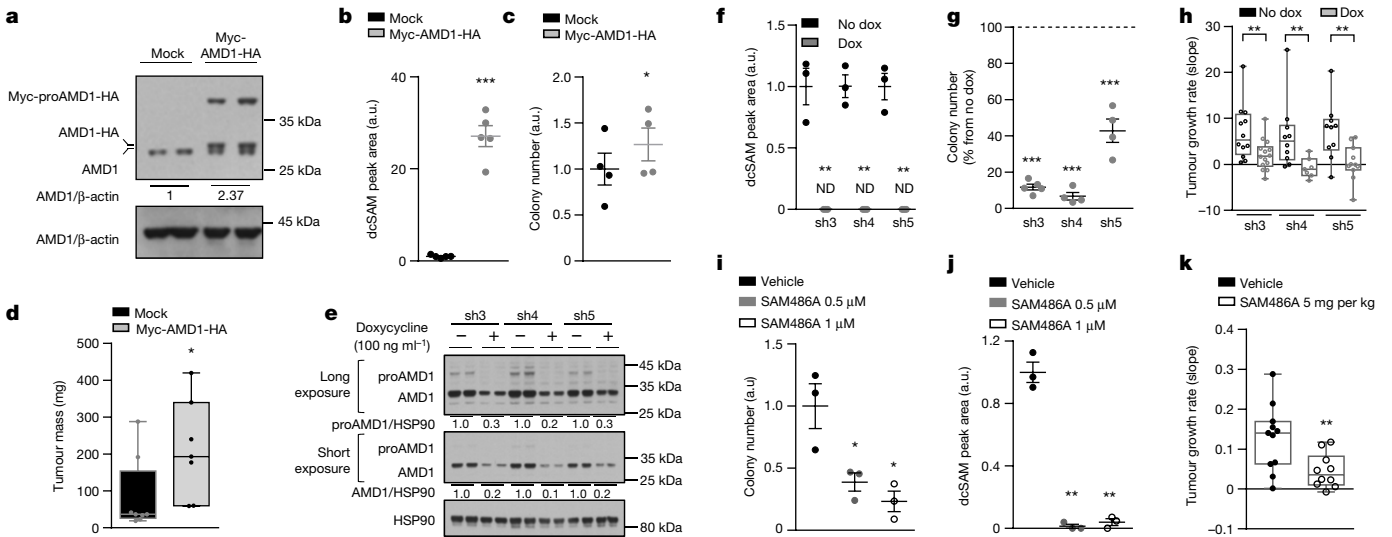


Figure 2 | Genetic and pharmacological AMD1 modulation affects prostate cancer oncogenicity. **a–c**, Impact of ectopic Myc-AMD1–HA expression (**a**, representative of three independent experiments) on dcSAM abundance (**b**, *n* = 5 independent experiments) and anchorage-independent growth (**c**, *n* = 4 independent experiments) in DU145 cells *in vitro*. Mock, empty vector. Myc-AMD1–HA, Myc and haemagglutinin (HA)-tagged AMD1 ectopic expression. Mean ± s.e.m. **d**, Impact of ectopic Myc-AMD1–HA expression on tumour mass in DU145 xenografts grown for 43 days (mock, *n* = 8 tumours; Myc-AMD1–HA, *n* = 7 tumours). Box-and-whisker plot. **e–g**, Effect of doxycycline (dox)-inducible (100 ng ml⁻¹; a minimum of 72 h) AMD1 silencing (sh3–sh5) on AMD1 protein expression (**e**, representative of three independent experiments), dcSAM abundance (**f**, *n* = 3 independent experiments), and anchorage-independent growth (**g**, *n* = 4 independent experiments) in DU145 cells. Dashed line in **g** indicates relative cell number of non-induced cells. No dox, without doxycycline treatment; Dox, doxycycline-induced (100 ng ml⁻¹) condition; sh, short hairpin RNA. Mean ± s.e.m. **h**, Impact of inducible AMD1 silencing on tumour growth rate of

established DU145 xenografts (tumour numbers: sh3 no dox, *n* = 12; sh3 dox, *n* = 14; sh4 no dox, *n* = 10; sh4 dox, *n* = 7; sh5 no dox, *n* = 10; sh5 dox, *n* = 11). Growth rate was inferred from the linear regression calculated for the progressive change in tumour volume of each individual tumour during the period depicted in Extended Data Fig. 3q–s. Box-and-whisker plot. **i, j**, Effect of pharmacological AMD1 inhibition with SAM486A on anchorage-independent growth (**i**, *n* = 3 independent experiments) and dcSAM abundance (**j**, *n* = 3 independent experiments) in DU145 cells. Mean ± s.e.m. **k**, Impact of SAM486A treatment for 14 days (5 mg per kg (body weight) per day, 5 days per week) on tumour growth rate of established DU145 xenografts (vehicle, *n* = 11 tumours; SAM486A, *n* = 10 tumours). Growth rate was inferred from the linear regression calculated for the progressive change in tumour volume of each individual tumour during the period depicted in Extended Data Fig. 4i. Box-and-whisker plot. **P* < 0.05; ***P* < 0.01; ****P* < 0.001. One-tailed Student's *t*-test was used for cell line data analysis (**b, c, f, g, i, j**) and one-tailed Mann–Whitney *U*-test for xenografts (**d, h, k**).

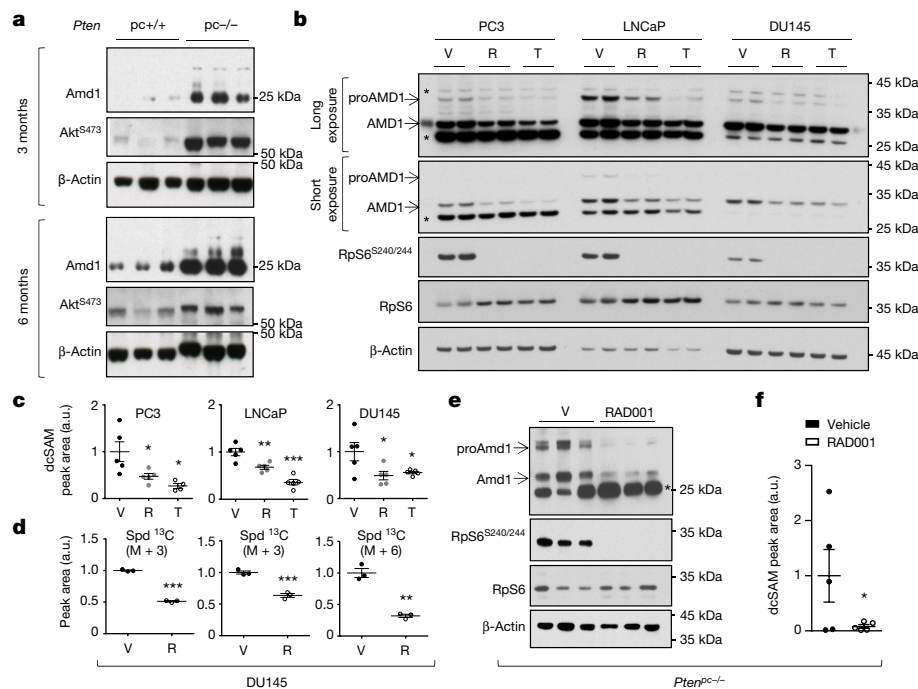


Figure 3 | mTORC1 regulates AMD1 expression, dcSAM production, and polyamine dynamics. **a**, Amd1 protein abundance in *Pten*^{pc-/-} and *Pten*^{pc+/+} prostate tissue from mice of the indicated age ($n = 3$ mice). AKT^{S473} is shown as control of PI3K pathway over-activation. 3 months, 3-month-old mouse prostate analysis; 6 months, 6-month-old prostate analysis. **b**, Representative western blot (out of three) depicting the changes in expression of the indicated proteins upon 24 h treatment of PC3, DU145, and LNCaP cells with vehicle (V, dimethylsulfoxide (DMSO)), rapamycin (R, 20 nM), and Torin-1 (T, 250 nM for PC3 and DU145, 125 nM for LNCaP). **c**, dcSAM abundance in PC3, LNCaP, and DU145 ($n = 4$ or 5 independent experiments as indicated by dots), upon 24 h treatment with vehicle (DMSO), rapamycin (20 nM), and Torin-1

(250 nM for PC3 and DU145, 125 nM for LNCaP). Mean \pm s.e.m. **d**, Incorporation of carbon-13 (¹³C) from [¹³C₅]L-methionine (2 h pulse) into the indicated metabolites after 30 h treatment with vehicle (DMSO) or rapamycin (20 nM) in DU145 cells ($n = 3$ independent experiments). Spd¹³C (M + 3): spermidine labelled in three carbons; Spm¹³C (M + 3): spermine labelled in three carbons; Spm¹³C (M + 6): spermine labelled in six carbons. Mean \pm s.e.m. **e**, **f**, Effect of 4-week RAD001 treatment on mTORC1 activity (RpS6^{S240/244}) and Amd1 protein expression (**e**, $n = 3$ mice), and dcSAM abundance (**f**, $n = 5$ mice), in prostate tissue extracts from *Pten*^{pc-/-} mice. Data in **f** are mean \pm s.e.m. * $P < 0.05$; ** $P < 0.01$; *** $P < 0.001$. Asterisks in western blots indicate non-specific bands; arrows indicate specific bands. One-tailed Student's *t*-test (**c**, **d**, **f**) was used.

this tumour type. AMD1 is produced as a pro-enzyme (proAMD1), which is subject to self-cleavage and heterotetramerization, resulting in the active enzyme⁹. After validation of a polyclonal antibody for the detection of proAMD1 and AMD1 (Extended Data Fig. 3a, b), we generated prostate cancer cells over-expressing AMD1, which resulted in increased dcSAM abundance (Fig. 2a, b). Interestingly, this perturbation increased foci formation, anchorage-independent growth, and *in vivo* tumour growth (Fig. 2c, d and Extended Data Fig. 3c–f).

If AMD1 activity is essential for prostate cancer cell function, targeting this enzyme would represent an attractive therapeutic strategy. To test this notion, we generated and validated three AMD1-targeting doxycycline-inducible and two constitutive short hairpin RNAs (shRNAs) (Fig. 2e and Extended Data Fig. 3g–j), which resulted in a profound reduction in dcSAM levels, the inhibition of two-dimensional and anchorage-independent growth, and tumour growth *in vivo* (Fig. 2f–h and Extended Data Fig. 3k–t). We excluded doxycycline-dependent (Extended Data Fig. 3u, v) and off-target effects of the shRNA (by ectopic expression of shRNA-resistant wild type and non-processable (S229A¹⁰) AMD1 mutants) (Extended Data Fig. 4a–c). Of note, we did not observe a contribution of *MTAP*^{11–14} or 5'-methylthioadenosine (MTA, a product of dcSAM metabolism to produce polyamines) to the effect of AMD1 inhibition (Extended Data Fig. 4d–f).

A pharmacological inhibitor of AMD1, SAM486A, has been designed and evaluated in pre-clinical and clinical settings^{15–18}. Pharmacological AMD1 inhibition recapitulated the biological consequences of genetic silencing, in the absence of overt toxicity *in vivo* (Fig. 2i–k, Extended Data Fig. 4g–k and Supplementary Table 6). Our results collectively demonstrate that AMD1 activity is required for prostate cancer oncogenicity.

We next sought to elucidate the mechanism underlying the production of dcSAM. Interestingly, AMD1 protein levels were increased in prostate tissue from *Pten*^{pc-/-} mice in the absence of transcriptional modulation, consistent with messenger RNA (mRNA) analysis in human prostate cancer data sets (Fig. 3a and Extended Data Fig. 5a–c). To ascertain whether this phenotype was a direct consequence of the loss of *PTEN*, we analysed *PTEN*-deficient prostate cancer cells (LNCaP). Re-expression of yellow fluorescent protein (YFP)–PTEN^{WT}, but not catalytically inactive YFP–PTEN^{C124S}, in these cells resulted in the reduction in AMD1 protein levels (Extended Data Fig. 5d)¹⁹. Further dissection of the PI3K–mTORC1 pathway revealed that only mTORC1 blockers among various signalling inhibitors decreased proAMD1 and AMD1 protein abundance (without consistent effects on mRNA expression; Fig. 3b and Extended Data Fig. 5e–h). The regulation of this enzyme by mTORC1 was validated upon genetic modulation of positive and negative regulators of the complex, RAPTOR and TSC2, respectively (Extended Data Fig. 5e, i, j). Importantly, mTORC1 inhibitor-elicited AMD1 down-regulation was accompanied by a decrease in dcSAM production and polyamine synthesis (Fig. 3c, d). Of interest, spermidine supplementation in rapamycin-treated PC3 cells (*PTEN*-deficient) elicited a significant (albeit small) increase in cell number (Extended Data Fig. 6a).

To ascertain the requirement of mTORC1 activation for dcSAM accumulation *in vivo*, we treated *Pten*^{pc-/-} mice with the rapamycin-derivative RAD001 and found that Amd1 and dcSAM abundance was reduced in line with the inhibition of mTORC1 in prostate tissue (Fig. 3e, f and Extended Data Fig. 6b, c). Of note, a second genetically engineered mouse model of prostate cancer based on the expression of the *TRAMP* transgene²⁰, which presented low

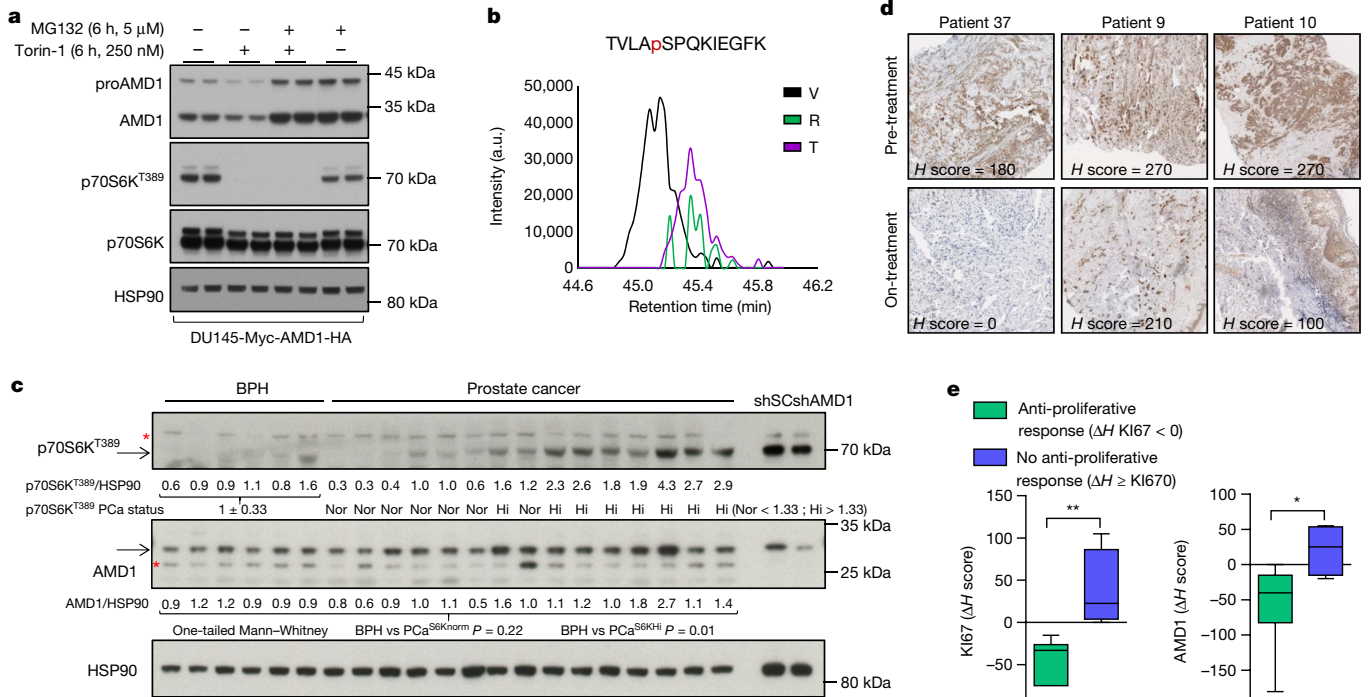


Figure 4 | mTORC1 regulates AMD1 stability and this molecular regulation is recapitulated *in vivo*. **a**, Representative western blot (out of three) of DU145 cells expressing Myc-AMD1-HA treated with vehicle or Torin-1 (250 nM, 6 h) in the presence or absence of MG132 (5 μ M, 6 h). **b**, Extracted ion chromatogram of the TVLASPQKIEGFK phosphorylated proAMD1 peptide upon 6 h treatment with vehicle (V, DMSO), rapamycin (R, 20 nM), and Torin-1 (T, 250 nM) in DU145 cells. **c**, Western blot analysis (individual tissue specimens are presented) of AMD1 and p70S6K^{T389} in prostate tissue samples of BPH and prostate cancer. Densitometry values of AMD1 and p70S6K^{T389} are provided below the scans (corrected by HSP90 immunoreactivity). p70S6K^{T389} prostate cancer status was defined as normal (Nor; PCa^{S6K^{norm}}) when the densitometry values of the prostate cancer sample were lower

mTORC1 activation, did not exhibit an increase in Amd1 or dcSAM abundance, in support of our postulated mTORC1-AMD1 regulation (Extended Data Fig. 6d, e and Supplementary Table 7).

Mechanistically, we excluded the contribution of ornithine decarboxylase 1 (ref. 21) (ODC1; Extended Data Fig. 7a–e) and canonical mTORC1 downstream effectors and pathways^{1,22,23}, including translation initiation, p70S6K, 4EBP, and macro-autophagy (since DU145 cells lack functional ATG5 (ref. 24) but retain the mTORC1-dependent regulation of AMD1) (Extended Data Fig. 7f–i). Interestingly, we found that mTORC1 inhibition-dependent decrease in AMD1 (wild type and S229A) protein levels was rescued by the proteasome inhibitor MG132 (Fig. 4a and Extended Data Fig. 8a, b). To elucidate the molecular link between mTORC1 activity and proAMD1 stability, we performed a phosphoproteomic analysis on ectopic proAMD1/AMD1 and identified a single phosphorylated residue (S298) on the pro-enzyme and enzyme (TVLAPSPQKIEGFK) (Extended Data Fig. 8c) that was compatible with a consensus mTORC1 site²⁵. Importantly, treatment for 6 h with rapamycin or Torin-1 reduced the phosphorylation of S298 in the pro-enzyme (and the ratio phospho-proAMD1/total proAMD1) but not the enzyme, leading us to hypothesize that S298 phosphorylation could be controlled by mTORC1 and promote proAMD1 stability (Fig. 4b and Extended Data Fig. 8d–f). We evaluated the stability of proAMD1 after treatment for 2 h with Torin-1 (before the detection of any effect on pro-enzyme abundance) and found reduced half-life upon mTORC1 inhibition (Extended Data Fig. 8g–k). To establish the contribution of S298 phosphorylation in the regulation of proAMD1 stability, we inactivated this

than (mean \pm s.d.) of the BPH specimens, and high (Hi, PCa^{S6K^{Hi}}) when greater. The statistical analysis related to differential AMD1 immunoreactivity was done by analysing PCa^{S6K^{Nor}} ($n = 7$) and PCa^{S6K^{Hi}} ($n = 8$) versus the BPH specimens ($n = 6$) separately. **d**, Representative AMD1 immunoreactivity images of three specimens from patients before (Pre-treatment) or after (On-treatment) therapy with everolimus ($n = 14$ specimen pairs). **e**, Box-and-whisker plot of the immunoreactivity of KI67 and AMD1 in cancer patients with (ΔH score for KI67 < 0) or without (ΔH score for KI67 \geq 0) anti-proliferative tumour response upon treatment with everolimus. * $P < 0.05$; ** $P < 0.01$. Arrows indicate specific immunoreactive bands. Red asterisk in western blot indicates non-specific band. Mann-Whitney U -test (c, e).

phosphorylation site (S298A). As predicted, non-phosphorylated proAMD1^{S298A} exhibited decreased half-life, and this parameter was augmented upon inhibition of the proteasome (Extended Data Fig. 9a–c). These results support the notion that mTORC1 activity promotes proAMD1 stability, at least in part, through the regulation of its phosphorylation in S298, hence allowing enzyme processing and activity. *In vitro* mTORC1 kinase assay with glutathione S -transferase (GST)-proAMD1^{S229A} did not show significant activity towards proAMD1 phosphorylation in these conditions, suggesting either that mTORC1 does not directly phosphorylate S298, or that additional cellular conditions (for example, biochemical conditions, adaptor or intermediary proteins, subcellular compartments) are required for mTORC1 to phosphorylate proAMD1 (Extended Data Fig. 9d). It is worth noting that our data do not rule out additional mechanisms downstream of mTORC1 regulating proteasome-mediated protein degradation^{23,26}. To extend this mechanistic link to human prostate cancer, we extracted protein from well-diagnosed benign prostate hyperplasia (BPH) and prostate cancer specimens⁴ (Supplementary Table 4). The results revealed that AMD1 was selectively more abundant in prostate cancer specimens exhibiting high mTORC1 activity, and that the phosphorylation of p70S6K significantly correlated with the levels of AMD1 (correlation coefficient $R = 0.81$; Fig. 4c and Extended Data Fig. 9e).

mTORC1 inhibitors are currently used to treat certain tumours (despite the unpredicted inefficacy in many others)²⁷, and previous work by us has contributed to defining the pharmacodynamic properties of everolimus in individuals with advanced cancers of different

origin^{5,28,29}. Strikingly, we observed a predominant decrease (64% of cases) in AMD1 immunoreactivity in 14 biopsies obtained from patients treated with this drug relative to a biopsy of the same lesion before treatment (Fig. 4d, Extended Data Fig. 9f and Supplementary Table 8). When we stratified patients on the basis of the anti-proliferative response achieved after everolimus therapy (responders: differential KI67 *H* score, $\Delta H < 0$, $n = 6$ specimen pairs; non-responders: differential KI67 *H* score, $\Delta H \geq 0$, $n = 4$ specimen pairs; where $\Delta H = (H \text{ score on therapy}) - (H \text{ score pre-therapy})$), we found that only AMD1 (among all targets analysed) presented significantly decreased immunoreactivity in responders (Fig. 4e and Extended Data Fig. 9g).

Polyamine production is a hallmark of highly proliferating cells³⁰, but their regulation by oncogenic signals remains largely unknown. Our results demonstrate that increased polyamine synthesis is associated with oncogenic signalling in prostate cancer. The regulation of AMD1 production and dcSAM synthesis downstream of mTORC1 described herein provides a mechanistic explanation for the control of this metabolic program (Extended Data Fig. 9h). AMD1 is an unprecedented metabolic target of this protein complex and supports its role in cancer cell proliferation. Importantly, the control of dcSAM and polyamine synthesis is relevant beyond the cancer scenario, and suggests that physiological and developmental processes that require active cell proliferation might be tightly associated with the regulation of AMD1 and polyamine synthesis downstream of mTORC1.

Online Content Methods, along with any additional Extended Data display items and Source Data, are available in the online version of the paper; references unique to these sections appear only in the online paper.

Received 12 September 2016; accepted 4 May 2017.

Published online 28 June 2017.

- Efeyan, A., Comb, W. C. & Sabatini, D. M. Nutrient-sensing mechanisms and pathways. *Nature* **517**, 302–310 (2015).
- Ben-Sahra, I. & Manning, B. D. mTORC1 signaling and the metabolic control of cell growth. *Curr. Opin. Cell Biol.* **12**, 72–82 (2017).
- Chen, Z. *et al.* Crucial role of p53-dependent cellular senescence in suppression of Pten-deficient tumorigenesis. *Nature* **436**, 725–730 (2005).
- Ugalde-Olano, A. *et al.* Methodological aspects of the molecular and histological study of prostate cancer: focus on PTEN. *Methods* **77–78**, 25–30 (2015).
- Taberero, J. *et al.* Dose- and schedule-dependent inhibition of the mammalian target of rapamycin pathway with everolimus: a phase I tumor pharmacodynamic study in patients with advanced solid tumors. *J. Clin. Oncol.* **26**, 1603–1610 (2008).
- Carracedo, A. & Pandolfi, P. P. The PTEN-PI3K pathway: of feedbacks and cross-talks. *Oncogene* **27**, 5527–5541 (2008).
- Engelman, J. A., Luo, J. & Cantley, L. C. The evolution of phosphatidylinositol 3-kinases as regulators of growth and metabolism. *Nat. Rev. Genet.* **7**, 606–619 (2006).
- Song, M. S., Salmena, L. & Pandolfi, P. P. The functions and regulation of the PTEN tumour suppressor. *Nat. Rev. Mol. Cell Biol.* **13**, 283–296 (2012).
- Pegg, A. E. S-Adenosylmethionine decarboxylase. *Essays Biochem.* **46**, 25–45 (2009).
- Xiong, H. & Pegg, A. E. Mechanistic studies of the processing of human S-adenosylmethionine decarboxylase proenzyme. Isolation of an ester intermediate. *J. Biol. Chem.* **274**, 35059–35066 (1999).
- Kryukov, G. V. *et al.* MTAP deletion confers enhanced dependency on the PRMT5 arginine methyltransferase in cancer cells. *Science* **351**, 1214–1218 (2016).
- Marjon, K. *et al.* MTAP deletions in cancer create vulnerability to targeting of the MAT2A/PRMT5/RIOK1 axis. *Cell Reports* **15**, 574–587 (2016).
- Mavrakis, K. J. *et al.* Disordered methionine metabolism in MTAP/CDKN2A-deleted cancers leads to dependence on PRMT5. *Science* **351**, 1208–1213 (2016).
- Shlomi, T., Fan, J., Tang, B., Kruger, W. D. & Rabinowitz, J. D. Quantitation of cellular metabolic fluxes of methionine. *Anal. Chem.* **86**, 1583–1591 (2014).
- Esken, F. A. *et al.*; European Organization for Research and Treatment of Cancer Early Clinical Studies Group. Phase I and pharmacological study of weekly administration of the polyamine synthesis inhibitor SAM 486A (CGP 48 664) in patients with solid tumors. *Clin. Cancer Res.* **6**, 1736–1743 (2000).
- Paridaens, R. *et al.* A phase I study of a new polyamine biosynthesis inhibitor, SAM486A, in cancer patients with solid tumours. *Br. J. Cancer* **83**, 594–601 (2000).
- Regenass, U. *et al.* CGP 48664, a new S-adenosylmethionine decarboxylase inhibitor with broad spectrum antiproliferative and antitumor activity. *Cancer Res.* **54**, 3210–3217 (1994).
- Siu, L. L. *et al.* A phase I and pharmacokinetic study of SAM486A, a novel polyamine biosynthesis inhibitor, administered on a daily-times-five every-three-week schedule in patients with advanced solid malignancies. *Clin. Cancer Res.* **8**, 2157–2166 (2002).

- Serra, H. *et al.* PTEN mediates Notch-dependent stalk cell arrest in angiogenesis. *Nat. Commun.* **6**, 7935 (2015).
- Greenberg, N. M. *et al.* Prostate cancer in a transgenic mouse. *Proc. Natl Acad. Sci. USA* **92**, 3439–3443 (1995).
- Origanti, S. *et al.* Ornithine decarboxylase mRNA is stabilized in an mTORC1-dependent manner in Ras-transformed cells. *Biochem. J.* **442**, 199–207 (2012).
- Bale, S. & Ealick, S. E. Structural biology of S-adenosylmethionine decarboxylase. *Amino Acids* **38**, 451–460 (2010).
- Zhang, Y. *et al.* Coordinated regulation of protein synthesis and degradation by mTORC1. *Nature* **513**, 440–443 (2014).
- Ouyang, D. Y. *et al.* Autophagy is differentially induced in prostate cancer LNCaP, DU145 and PC-3 cells via distinct splicing profiles of ATG5. *Autophagy* **9**, 20–32 (2013).
- Hsu, P. P. *et al.* The mTOR-regulated phosphoproteome reveals a mechanism of mTORC1-mediated inhibition of growth factor signaling. *Science* **332**, 1317–1322 (2011).
- Zhao, J., Zhai, B., Gygi, S. P. & Goldberg, A. L. mTOR inhibition activates overall protein degradation by the ubiquitin proteasome system as well as by autophagy. *Proc. Natl Acad. Sci. USA* **112**, 15790–15797 (2015).
- Huang, Z. *et al.* Clinical efficacy of mTOR inhibitors in solid tumors: a systematic review. *Future Oncol.* **11**, 1687–1699 (2015).
- O'Reilly, K. E. *et al.* mTOR inhibition induces upstream receptor tyrosine kinase signaling and activates Akt. *Cancer Res.* **66**, 1500–1508 (2006).
- Carracedo, A. *et al.* Inhibition of mTORC1 leads to MAPK pathway activation through a PI3K-dependent feedback loop in human cancer. *J. Clin. Invest.* **118**, 3065–3074 (2008).
- Gerner, E. W. & Meyskens, F. L., Jr. Polyamines and cancer: old molecules, new understanding. *Nat. Rev. Cancer* **4**, 781–792 (2004).

Supplementary Information is available in the online version of the paper.

Acknowledgements We thank N. Sonenberg for providing 4EBP1- and 4EBP2-targeting shRNAs, D. Alessi for discussions and technical advice, A.M. Cuervo and E. Arias-Perez for technical advice, the Basque biobank for research (BIOEF) for critical support with human specimens and Novartis for providing SAM486A. Funding: Ramón y Cajal award (to A.C., A.E., J.M., D.O.), Juan de la Cierva (to E.C., A.C.-M.), BFU grant (to R.B.: BFU2014-52282-P and BFU2011-25986), SAF grant (to A.C.: SAF2016-79381-R, FEDER/EU; M.L.M.-C.: SAF2014-54658-R; to J.M.F.-P.: SAF2015-66312; to J.M.M.: SAF 2014-52097R; to A.E.: SAF2015-67538-R; to J.A.: SAF2015-65327R; to G.T.: SAF2011-24967) from the Spanish Ministry of Economy, Industry and Competitiveness (MINECO); European Union (to A.C.: ERC-StG-336343, PoC754627; to A.C.-M.: CIG 660191; to J.A.: 602272; to A.E.: ERC-2014-STG-638891); Basque Government Department of Health (to V.T.: 2016111109; to J.M.F.-P.: 2015111149), Department of Education (to A.C.: PI2012/03 and IKERTALDE I.T.1106-16; to R.B.: PI2012/42; to M.L.M.-C.: 2013) and PhD grants (to A.A.-A. and L.V.-J.): AECC (to V.T.: 2016 JP Bizkaia; to N.M.-M.: 2011 JP Bizkaia; to M.L.M.-C.); ISCIII (to A.C.: PI10/01484, PI13/00031; to J.M.: Proteored PR.B.2 and grant PT13/0001; to R.F.: PI15/209; to V.S.: PI13/01714, CP14/00228); Ramón Areces foundation (to J.M.F.-P.); Basque Department of Industry, Tourism and Trade (Etorlek) (to A.C.); FERRO Foundation (to A.C., V.S.); Fundación Vasca de Innovación e Investigación Sanitarias, BIOEF (to V.T.: BIO15/CA/052); BBVA Foundation (to A.C.; P.N. team); National Institutes of Health (to C.C.-C. and M.C.: P01CA087497; to J.M.M.: R01AT001576); Fundación CRIS contra el Cáncer (to D.O. team); 2014 Stewart Rahr Young Investigator Award from the Prostate Cancer Foundation (to D.O.); FPU predoctoral fellowship (to Y.C.: 15/05126); Catalan Agency AGAUR (to V.S.: 2014 SGR 1331); Medical Research Council (to R. Bago, D. Alessi laboratory: grant number MC_UU_12016/2). The activity of CIBERONC was co-funded with FEDER funds.

Author Contributions *In vitro* studies: A.Z.-L. and A.A.-A. with support from N.M.-M., S.F.-R., and L.A. *In vivo* studies: A.Z.-L., A.A.-A. and N.M.-M. with support for tail vein from N.B. Genotyping: P.S.-M. Metabolomics analysis: M.Clas., P.Q., S.M., A.B., G.L., and D.P., K. Marks and K. Marjon at AGIOS and D.C., S.M.V.L., and J.M.F.-P. at CIC bioGUNE. Everolimus trial samples and staining: V.S., J.J., L.P., P.N., I.T., J.T., T.M., and J.B. Human prostate specimens: A.U.-O., A.L.-I., I.L.-V., and M.U. Histochemical analysis in mice: S.F.-R., A. Rev., and A. Alim. Generation of molecular AMD1 tools: J.D.S. and R.B. Immune cell analysis and GST-AMD1 purification: J.T.-C., I.F.-D., and J.A. Phosphoproteomics: P.X.-E., A.E., and J.M. Kinase assay: R. Bago. TRAMP mice material: statistical supervision and bioinformatics, A.R.-C.; polysome profiling, A.G. and G.T. Genetically engineered mouse model pathology: M.C.-M. and C.C.-C. Technical support and discussions: B.D.M., J.M.M., M.L.M.-C., M.A., F.E., I.A., A.M.A., V.T., L.V.-J., P.Z.-G., M.P., A.C.-M., R.F., and Y.Z. K. Marjon directed the metabolomics strategy, analysed the results, and contributed to discussions and manuscript preparation and revision. A.C. directed the project, supervised data analysis, and wrote the manuscript.

Author Information Reprints and permissions information is available at www.nature.com/reprints. The authors declare no competing financial interests. Readers are welcome to comment on the online version of the paper. Publisher's note: Springer Nature remains neutral with regard to jurisdictional claims in published maps and institutional affiliations. Correspondence and requests for materials should be addressed to A.C. (acarracedo@cicbiogune.es).

METHODS

Patient samples. All prostate specimens were obtained upon informed consent and with evaluation and approval from the corresponding ethics committee (Comité de Ética en Investigación Clínica (CEIC) codes OHEUN11-12 and OHEUN14-14)⁴. Clinico-pathological information is included as Supplementary Table 4. The details of the clinical trial with everolimus are described in ref. 5 and in Supplementary Table 8.

Animals. All mouse experiments were performed following the ethical guidelines established by the Biosafety and Animal Welfare Committee at CIC bioGUNE, Derio, Spain (under protocol P-CBG-CBBA-0715). The procedures used followed the recommendations from the Association for Assessment and Accreditation of Laboratory Animal Care International (AAALAC). Xenograft experiments were performed as previously described (maximum total tumour volume per mouse 1.5 cm^3)³¹, injecting 4×10^6 (AMD1 silencing) or 4×10^6 (AMD1 ectopic expression) cells with Matrigel (BD Biosciences) per condition in two flanks per mouse. Doxycycline was administered *in vivo* in the food pellets (Research diets, D12100402). Genetically engineered mouse model experiments were performed in a mixed background as reported³². The *Pten*^{lox} conditional knockout allele has been described elsewhere⁷. Prostate epithelium-specific deletion was effected by the Pb-Cre4 (ref. 3). Mice were fasted for 6 h before tissue harvest (9:00–15:00) to prevent metabolic alterations due to immediate food intake. The TRAMP mice strain was originally obtained from The Jackson Laboratory repository. Animals were maintained at the Animal Facility (awarded with AAALAC accreditation) of the Spanish National Cancer Research Centre (CNIO) in accordance with the guidelines stated in the International Guiding Principles for Biomedical Research Involving Animals, developed by the Council for International Organizations of Medical Sciences. All animal experiments were approved by the Competent Authority of the Comunidad de Madrid. The generation and characterization of TRAMP mice have been previously described²⁰. At CNIO, TRAMP mice originally provided in FVB/NJ genetic background were backcrossed to a C57BL/6 background by successive mating of (T/+) male-mice to (+/+) C57BL/6 female-mice and then maintained in a C57BL/6 background.

To address the potential undesirable effects of systemic AMD1 inhibition, we administered SAM486A intraperitoneally (5 mg per kg (body weight) per day, 5 days per week) for 17 days in immunocompetent C57BL/6 mice. We measured body and organ weight, blood biochemistry, haematocrit, and white blood cell count (information provided in Supplementary Table 6). Terminal blood harvest was performed intracardially after CO₂inhalation-based euthanasia. For non-terminal harvest, a facial vein blood sample was obtained by puncture with a sterile 4 mm lancet (MEDIpoint, USA). For plasma preparation, blood was deposited in tubes with dipotassium EDTA (Microtainer, Becton Dickinson, Franklin, New Jersey, USA) (for haematocrit and FACS analysis) or heparinized tubes (10 μl , 1 U μl^{-1}) (for plasma metabolomics). For haematocrit analysis, blood samples were analysed using an Abacus Junior Vet analyser (Diatron, Hungary) according to the manufacturer's guidelines. For blood biochemistry, a Selectra Junior Spinlab 100 analyser (Vital Scientific, Dieren, The Netherlands) was used. A calibrated control was run before each use and was within established ranges before analysing samples. For white blood cell analysis, the spleen of SAM486A or saline-treated mice was grinded by using a syringe plunger and passing the cells through a 70 μm cell strainer; cellular composition was evaluated by flow cytometry, using the following antibodies: CD4, CD8, B220, Ly6C, F4/80, GR-1, CD25, CD11b, CD44, CD73, FR4, Nrp-1 (Miltenyi Biotec).

Purification and activation of mouse splenic CD4⁺ T cells. To address the toxicity of SAM486A, we purified CD4 T cells from the spleen of C57BL/6 mice by negative selection using a CD4 purification kit following the manufacturer's instructions (Miltenyi Biotec, Auburn, California, USA). Five hundred thousand CD4 T cells were activated in TexMACS Medium (Miltenyi Biotec) with plate-bound anti-CD3 (5 $\mu\text{g ml}^{-1}$) and soluble anti-CD28 (1 $\mu\text{g ml}^{-1}$) in the presence of vehicle or SAM486A (1 μM) for 16 and 96 h and assessed for interleukin(IL)-2 production by capture enzyme-linked immunosorbent assay (ELISA) (R&D Systems, MAB702). To analyse the effect of SAM486A on T-cell proliferation, purified CD4 T cells were recovered 4 days after activation and treatment and counted in a haemocytometer chamber.

Immunization with ovalbumin. To address the effect of SAM486A on immune cell proliferation *in vivo*, we administered SAM486A intraperitoneally (5 mg per kg (body weight) per day, 5 days per week) for 17 days in immunocompetent C57BL/6 mice, and then immunized them subcutaneously with 50 μg ovalbumin in complete Freund's adjuvant and kept on treatment. After 2 weeks, the mice were analysed for ovalbumin-specific serum immunoglobulin-G(IgG) and immunoglobulin-M(IgM) levels by ELISA³³.

Reagents. Cell lines were purchased from Leibniz-Institut Deutsche Sammlung von Mikroorganismen und Zellkulturen (DSMZ) and tested negative for mycoplasma. An authentication certificate was provided by DSMZ for cell lines. Rapamycin (prepared in DMSO, final concentration 20 nM), Torin-1 (prepared

in DMSO, final concentration 125–250 nM), dimethylfluorornithine (DFMO, prepared in water, final concentration 50 μM), PF-4708671 (PF47, prepared in DMSO, final concentration 10 μM), hydroxychloroquine (HCQ, prepared in water, final concentration 30 ng ml^{-1}), MG132 (5 μM , prepared in DMSO), PD0325901 (100 nM, prepared in DMSO), SB203580 (5 μM , prepared in DMSO), SP600125 (10 μM , prepared in DMSO), spermidine (0.5–1 μM , prepared in water), 5'-deoxy-5'-(methylthio)adenosine (MTA, final concentration 25 μM), and cycloheximide (CHX, prepared in ethanol, final concentration 5 $\mu\text{g ml}^{-1}$) were purchased from LC Laboratories (rapamycin, PD0325901), Sigma (CHX, PF47, HCQ, spermidine, MTA), Calbiochem (SB203580), and Tocris (Torin-1, DFMO, SP600125). RAD001 was purchased from Selleckchem and administered 6 days per week by oral gavage (prepared in 1.5% NMP/98.5% PEG) at 10 mg per kg (body weight). SAM486A was provided by Novartis and prepared in water (*in vitro*) or saline solution (*in vivo*, 5 mg per kg (body weight) per day intraperitoneally Monday–Friday). [¹³C₃] L-methionine was purchased from Cambridge Isotope Laboratories and administered intravenously at a final concentration of 100 mg kg^{-1} *in vivo* and at 30 $\mu\text{g ml}^{-1}$ *in vitro* (with dialysed FBS). Doxycycline was purchased from Sigma and used at 500 ng ml^{-1} for overexpression of *YFP-PTEN*, 100 ng ml^{-1} for silencing of *AMD1*, and 250 ng ml^{-1} for silencing of *RAPTOR* and *TSC2*. shRNAs against *AMD1* were purchased from Sigma (TRCN0000078462: sh3; TRCN0000078460: sh4; TRCN0000078461: sh5) and the control shRNA sequence included (CCGGC AACAAGATGAAGAGCACCACACTCGAGTTGGTGTCTTTCATCTTGTG)³⁴. shRNAs against *4EBP1* and *4EBP2* were provided by N. Sonenberg³⁵. Sub-cloning of shRNA *AMD1* into pLKO-Tet-On vector was done by introducing AgeI and EcoRI in the 5' end of top and bottom shRNA oligonucleotides respectively (TET-pLKO puro was a gift from D. Wiederschain³⁶, Addgene plasmid 21915). *Myc-AMD1-HA*-expressing vector was generated starting from the open reading frame obtained from PlasmID Harvard (<https://plasmid.med.harvard.edu/PLASMID/Home.xhtml>) and cloned into a modified retroviral pLNCX vector harbouring BglII-Sall sites (cloned with BamHI-Sall). RNA interference (RNAi)-resistant versions of *AMD1* were generated using overlap extension PCR and cloned into a lentiviral backbone derived from vector pLenti-Cas9-blast (Cas9 removed; lentiCas9-Blast was a gift from F. Zhang, Addgene 52962; ref. 37) using a HiFi Assembly Kit (NEB). The resulting vectors expressed *AMD1-HA-2A-blast* (wild type or S229A) with the *AMD1-HA* portion being excisable using BshT1-BamHI. The target of *AMD1* shRNA3 (5'-gtctccaagagacgtttcattc-3') was changed to an RNAi-resistant version (5'-gtGAGcaacCGTAGAtTatCtt-3'). Cloning details are available upon request. All clones were sequence-validated. Site-directed mutagenesis for generation of *AMD1*^{S229A} and *AMD1*^{S298A} was performed using an Agilent QuikChange II Site-Directed Mutagenesis Kit. *YFP-PTEN*-expressing lentiviral constructs were described in ref. 19.

Cellular and molecular assays. Cell number quantification was done with crystal violet²⁹. Doxycycline-mediated inducible shRNA expression was performed by treating cell cultures for 72–96 h with the antibiotic (100–250 ng ml^{-1}) and then seeding for cellular or molecular assays in the presence of doxycycline. Western blot was performed as previously described³⁸ and run in Nupage gradient precast gels (Life Technologies) in MOPS or MES buffer (depending on the proteins analysed; note that the migration pattern of molecular mass markers varies in these two buffers). Anti-AMD1 was from Proteintech (11052-1-AP). Anti-RpS6^{S240/244}, anti-RpS6, anti-p70S6K^{T389}, anti-p70S6K, anti-LC3B, anti-HSP90, anti-PTEN, anti-AKT^{S473}, anti-AKT, anti-4EBP1, and anti-RAPTOR antibodies were from Cell Signalling Technologies. Anti- β -actin antibody was from Sigma and anti-TSC2 from Thermo Scientific (MA5-15004). Densitometry-based quantification was performed using ImageJ software. For half-life assays, DU145 cells stably expressing the indicated constructs were challenged with CHX (5 $\mu\text{g ml}^{-1}$) and protein was extracted at the indicated time points (cells were treated with vehicle (DMSO), MG132 (5 μM), or Torin-1 (250 nM) 120 min before CHX challenges when indicated). Anchorage-independent growth assays were performed as previously described³⁹, seeding 3000 (PC3) or 5000 (DU145) cells per well. RNA was extracted using a NucleoSpin RNA isolation kit from Macherey-Nagel (740955.240C). One microgram of total RNA was used for complementary DNA (cDNA) synthesis using qScript cDNA Supermix from Quanta (95048). Quantitative PCR (qPCR) was performed as previously described³⁸. Applied Biosystems TaqMan probes were as follows: *Amd1/AMD1* (Mm04207265, Hs00750876s1), β -ACTIN/ β -Actin (Hs99999903_m1/Mm00607939_s1), and *GAPDH/Gapdh* (Hs02758991_g1/Mm99999915_g1). Universal Probe Library (UPL, Roche) probes were as follows: *AMD1* (probe 72, primer F: CAGACCTCTATGATGACCTGA; primer R: TCAGGTACGAAATCCACTCT), *Odc1* (probe 80, primer F: GCTAAGTCG ACCTTGTGAGGA; primer R: AGCTGCTCATGGTTCTCGAT), *ODC1* (probe 34, primer F: AAAACATGGGCGCTTACTACT; primer R: TGGAATTGC TGCATGAGTTG), and *Mtap* (probe 12, primer F: CCATGGCAACCGACT ATGAT; primer R: AAACCCCATCCACTGACACT). Foci assays were performed seeding 500 cells per well (six-well plate) and staining and counting them by crystal

violet after 10 days. Lentiviral and retroviral transductions were performed as previously described^{34,38}.

Kinase assay. Human AMD1 variants (carboxy-terminal HA tag, non-processing mutant S229A; S298 (wild type) or S298A; details available upon request) were prepared by overlapping PCR and cloned as BamHI–NotI into pGEX-6P-1 (GE Healthcare). Sequence-confirmed clones were induced with 1 mM IPTG (isopropyl- β -D-thiogalactoside) for 16 h at 20 °C in C41 (DE3) pLysS (Lucigen). GST fusion proteins were purified first by glutathione affinity chromatography (eluted in 40 mM reduced glutathione; 25 mM HEPES pH 8; 50 mM KCl; 0.1% BME buffer) and then separated by gel filtration chromatography. Proteins were concentrated by ultrafiltration (Vivaspin 5K MWCO cut-off; Sartorius) and used for kinase assays.

Endogenous mTORC1 complex was immunoprecipitated from HEK293 cells using anti-Raptor antibody (S682B, fourth bleed, <https://mrcppureagents.dundee.ac.uk/>) coupled to Protein G Sepharose beads (Amersham). The cells were stimulated with IGF (50 ng ml⁻¹) for 20 min before lysis in mTORC1 lysis buffer (40 mM HEPES pH 7.4, 120 mM NaCl, 1 mM EDTA, 0.3% (w/v), CHAPS, 10 mM Na-pyrophosphate, 10 mM Na-glycerophosphate, 1 mM Na-orthovanadate, protease inhibitor cocktail (Roche)). The immunoprecipitate was washed twice with mTORC1 lysis buffer, containing 0.5 M NaCl, twice with mTORC1 lysis buffer, and twice with mTORC1 kinase assay buffer (25 mM HEPES pH 7.4, 50 mM KCl). The substrates were added to immunoprecipitate in kinase assay buffer (15 μ l) before adding the 10 μ l of the ATP mixture (10 mM MnCl₂, 100 μ M ATP, 1 μ Ci [γ -³²P]ATP in kinase buffer). The reaction was performed in a thermomixer at 30 °C for 30 min and was terminated by adding the 4 \times sample buffer (NuPAGE LDS sample buffer, Life Technologies). The reaction mixture was loaded on gel. Dried gel was exposed to X-ray films (Amersham). One microlitre of reaction mixture was loaded on gel for immunoblot analysis. GST-S6K^{D236A} (DU32609, <https://mrcppureagents.dundee.ac.uk/>) was purified from HEK293 cells pretreated with 0.1 μ M AZD-8055. The protein was purified using GST–Sepharose beads (Amersham) according to the manufacturer's instructions. Anti-Raptor (S682B, fourth bleed, <https://mrcppureagents.dundee.ac.uk/>), anti-phospho-S6K1 T389 (9205, Cell Signaling Technology), anti-GST (S902A, third bleed, <https://mrcppureagents.dundee.ac.uk/>).

Immunohistochemical analysis. Histochemical analysis by haematoxylin and eosin, anti-RpS6^{S235/6}, anti-Akt^{S473} (Cell Signaling Technology), and Pten (51-2400) immunostaining was performed as previously described^{40,41}. Immunohistochemical analysis of AMD1 (Proteintech, dilution 1/100) was performed using DAKO EnVision FLEX High pH (DAKO). The scoring system was based on the quantification of the percentage of cells' negative, low (1+), medium (2+), or high (3+) immunoreactivity. Subsequently, the *H* score was calculated as follows: $H = (\text{percentage of cells } 1+) + (2 \times (\text{percentage of cells } 2+)) + [3 \times (\text{percentage of cells } 3+)]$. Differential *H* score was calculated as $\Delta H = H_{\text{on treatment}} - H_{\text{pre-treatment}}$.

Metabolomic analysis. For *in vitro* metabolomic analysis, growing cells were washed with ammonium carbonate pH 7.4 and snap-frozen in liquid nitrogen. Metabolites were extracted from cells or tissues with cold 80/20 (v/v) methanol/water. Samples were then dried and stored at -80 °C until MS analysis. High-throughput time-of-flight analysis was conducted using flow injection analysis as previously described⁴². In short, samples were re-suspended and injected on an Agilent 1100 coupled with an Agilent 6520 QToF mass spectrometer with an electrospray ionization source. The mobile phase consisted of 60/40 methanol/water with 0.1% formic acid and was used to deliver 2 μ l of each sample to the MS, flowing at 150 μ l min⁻¹. Data were collected in positive mode with 4 GHz HiRes resolving power with internal lock masses. Data processing was conducted with Matlab R2010b. Relative cell number or protein amount was used for normalization.

Quantitative LC/MS was conducted as previously described⁴³. A ThermoAccela 1250 pump delivered a gradient of 0.025% heptafluorobutyric acid, 0.1% formic acid in water and acetonitrile at 400 μ l min⁻¹. The stationary phase was an Atlantis T3, 3 μ m, 2.1 mm \times 150 mm column. A QExactive mass spectrometer was used at 70,000 resolving power to acquire data in full-scan mode. Data analysis was conducted in MAVEN⁴⁴ and Spotfire. Peak areas derived from stable isotope labelling experiments were corrected for naturally occurring isotope abundance.

For plasma [¹³C]methionine analysis, blood samples from mice were extracted at the indicated times, transferred at room temperature to heparinized collection tubes, and centrifuged at 13,000 r.p.m. and 4 °C for 10 min. Plasma was transferred to fresh tubes and processed for ultra-high-performance LC coupled to mass spectrometry (UPLC–MS) analysis. Briefly, to 40 μ l aliquots of mouse plasma, 40 μ l of water/0.15% formic acid was added. Subsequently, proteins were precipitated by addition of 120 μ l of acetonitrile. To optimize extraction, after addition of acetonitrile, the samples were sonicated for 10 min at 4 °C and agitated at 1,400 r.p.m. for 30 min at 4 °C. Next, the samples were centrifuged at 14,000 r.p.m. for 30 min at 4 °C. The supernatant was transferred to a fresh vial and measured

with a UPLC system (Acquity, Waters, Manchester, UK) coupled to a time-of-flight mass spectrometer (SYNAPT G2, Waters). A 2.1 mm \times 100 mm, 1.7 μ m BEH AMIDE column (Waters), thermostated at 40 °C was used for the assay. Solvent A (aqueous phase) consisted of 99.5% water, 0.5% formic acid, and 20 mM ammonium formate, while solvent B (organic phase) consisted of 29.5% water, 70% MeCN, 0.5% formic acid, and 1 mM ammonium formate. To obtain a good separation of the analytes, the following gradient was used: from 5% A to 50% A in 2.4 min in curved gradient (number 8, as defined by Waters), from 50% A to 99.9% A in 0.2 min constant at 99.9% A for 1.2 min, back to 5% A in 0.2 min. The flow rate was 0.250 ml min⁻¹ and the injection volume was 2 μ l. All samples were injected randomly and analytes were measured in enhanced duty cycle mode, optimized for the mass of the analyte in question. Methionine and [¹³C₅]L-methionine were measured in scan function 1 (enhanced duty cycle at 152), SAH and [¹³C₄]SAH were measured in scan function 2 (enhanced duty cycle at 387), and SAM and [¹³C₅]SAM were measured in scan function 3 (enhanced duty cycle at 402). Extracted ion traces were obtained for methionine ($m/z = 150.0589$), [¹³C₅]L-methionine ($m/z = 155.0756$), SAH ($m/z = 385.1294$), [¹³C₄]SAH ($m/z = 389.1428$), SAM ($m/z = 399.145$), and [¹³C₅]SAM ($m/z = 404.1618$) in a 20 mDa window and subsequently smoothed (two points, two iterations) and integrated with QuanLynx software (Waters). For quantitation, stock solutions of 10 mM in water for each of the analytes were prepared. Stock solutions were pooled and diluted to obtain a mixture including all analytes. The mixture was further diluted in water to obtain the concentrations as used in the calibration curve. The calibration range for all analytes included the following concentrations: 100, 50, 25, 10, 5, 2.5, 1, 0.5, 0.25, 0.1, 0.05, and 0.025 μ M.

Targeted metabolomics. Levels of dcSAM in cell cultures and tissues were analysed by UPLC–MS. Briefly, extraction and homogenization were done in methanol/acetic acid (80/20% v/v). Speed-vacuum-dried metabolites were solubilized in 100 μ l of a mixture of water/acetonitrile (40/60% v/v) and injected onto the UPLC–MS system (Acquity and SYNAPT G2, Waters). The extracted ion traces were obtained for dcSAM (retention time = 3.0 minutes, $m/z = 355.16$). Corrected signals were normalized to relative cell number.

Polysome profiling. Distribution of mRNAs across sucrose gradients was performed as described earlier⁴⁵, except for minor modifications.

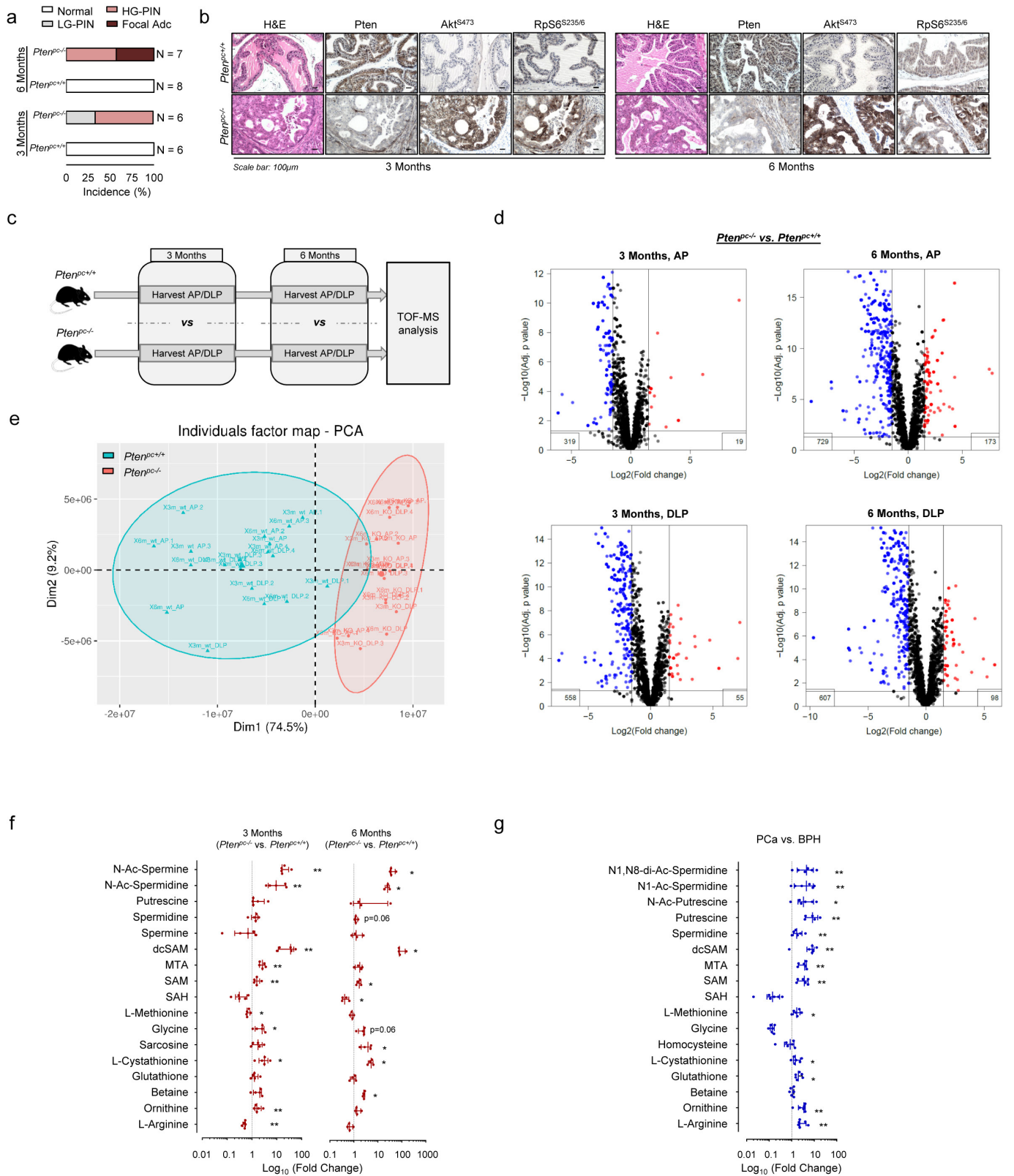
Phosphoproteomic analysis of AMD1. DU145 cells stably expressing Myc-AMD1–HA were plated in two or three 150 mm plates per condition to ensure a final density no higher than 50–60% and sufficient protein amounts to immunoprecipitate ectopic AMD1 (using agarose HA-beads, Sigma, according to the manufacturer's instructions). Cells were treated for 6 h with rapamycin (20 nM) and Torin-1 (250 nM) before immunoprecipitation. Protein eluates from the immunoprecipitated samples were separated by SDS–PAGE. The bands corresponding to AMD1 and the pro-enzyme were visualized using Sypro-Ruby (Invitrogen), excised, and in-gel digested with trypsin. The resulting peptides were analysed by LC–MS/MS using an LTQ Orbitrap Velos mass spectrometer (Thermo Scientific). Raw files were searched against a Uniprot *Homo sapiens* database (20,187 sequences) using Sequest-HT as the search engine through the Proteome Discoverer 1.4 (Thermo Scientific) software. Peptide identifications were filtered by Percolator at a false discovery rate of 1% using the target-decoy strategy. Label-free quantification was performed with MaxQuant, and extracted ion chromatograms for AMD1 phosphopeptides were manually validated in Xcalibur 2.2 (Thermo).

Bioinformatic analysis. All the data sets used for the data mining analysis^{46–49} were downloaded from the Gene Expression Omnibus, and subjected to background correction, log₂ transformation, and quartile normalization. In the case of using a pre-processed data set, this normalization was reviewed and corrected if required.

Statistical analysis. No statistics were applied to determine sample size. The experiments were not randomized. The investigators were not blinded to allocation during experiments and outcome assessment. Data analysed by parametric tests are represented by the mean \pm s.e.m. of pooled experiments; for non-parametric tests, the median with interquartile range is depicted, unless otherwise stated. Values of *n* represent the number of independent experiments performed or the number of individual mice or patient specimens. For each independent *in vitro* experiment, at least three technical replicates were used and a minimum number of three experiments were performed to ensure adequate statistical power. Analysis of variance was used for multi-component comparisons and Student's *t*-test for two-component comparisons. In the *in vitro* experiments, normal distribution was confirmed or assumed (for $n < 5$). Two-tailed statistical analysis was applied for experimental design without predicted result, and one-tailed analysis for validation or hypothesis-driven experiments. The confidence level used for all the statistical analyses was 0.95 ($\alpha = 0.05$).

Data availability. The authors declare that data supporting the findings of this study are available within the paper and its supplementary information files. Source data for unprocessed scans and Fig. 2d and Extended Data Figs 3d, q–s and 4i are provided with the paper.

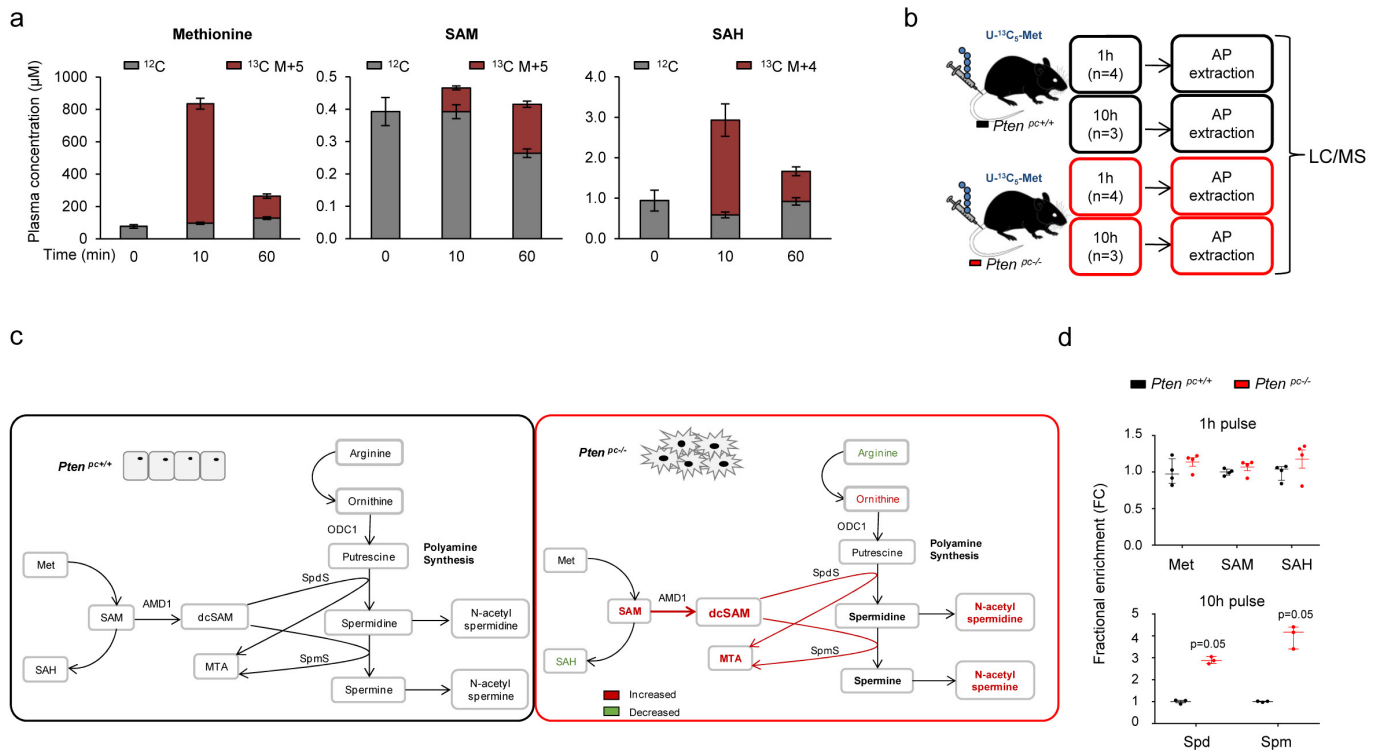
31. Song, M. S. *et al.* Nuclear PTEN regulates the APC-CDH1 tumor-suppressive complex in a phosphatase-independent manner. *Cell* **144**, 187–199 (2011).
32. Chen, Z. *et al.* Differential p53-independent outcomes of p19(Arf) loss in oncogenesis. *Sci. Signal.* **2**, ra44 (2009).
33. Motameni, A. R. *et al.* Delivery of the immunosuppressive antigen Salp15 to antigen-presenting cells by *Salmonella enterica* serovar Typhimurium *aroA* mutants. *Infect. Immun.* **72**, 3638–3642 (2004).
34. Torrano, V. *et al.* The metabolic co-regulator PGC1 α suppresses prostate cancer metastasis. *Nat. Cell Biol.* **18**, 645–656 (2016).
35. Dowling, R. J. *et al.* mTORC1-mediated cell proliferation, but not cell growth, controlled by the 4E-BPs. *Science* **328**, 1172–1176 (2010).
36. Wiederschain, D. *et al.* Single-vector inducible lentiviral RNAi system for oncology target validation. *Cell Cycle* **8**, 498–504 (2009).
37. Sanjana, N. E., Shalem, O. & Zhang, F. Improved vectors and genome-wide libraries for CRISPR screening. *Nat. Methods* **11**, 783–784 (2014).
38. Carracedo, A. *et al.* A metabolic prosurvival role for PML in breast cancer. *J. Clin. Investigation* **122**, 3088–3100 (2012).
39. Salazar, M. *et al.* Loss of Tribbles pseudokinase-3 promotes Akt-driven tumorigenesis via FOXO inactivation. *Cell Death Differ.* **22**, 131–144 (2015).
40. Alimonti, A. *et al.* A novel type of cellular senescence that can be enhanced in mouse models and human tumor xenografts to suppress prostate tumorigenesis. *J. Clin. Invest.* **120**, 681–693 (2010).
41. Revandkar, A. *et al.* Inhibition of Notch pathway arrests PTEN-deficient advanced prostate cancer by triggering p27-driven cellular senescence. *Nat. Commun.* **7**, 13719 (2016).
42. Fuhrer, T., Heer, D., Begemann, B. & Zamboni, N. High-throughput, accurate mass metabolome profiling of cellular extracts by flow injection-time-of-flight mass spectrometry. *Anal. Chem.* **83**, 7074–7080 (2011).
43. Jha, A. K. *et al.* Network integration of parallel metabolic and transcriptional data reveals metabolic modules that regulate macrophage polarization. *Immunity* **42**, 419–430 (2015).
44. Melamud, E., Vastag, L. & Rabinowitz, J. D. Metabolomic analysis and visualization engine for LC-MS data. *Anal. Chem.* **82**, 9818–9826 (2010).
45. Fumagalli, S., Ivanenkov, V. V., Teng, T. & Thomas, G. Suprainduction of p53 by disruption of 40S and 60S ribosome biogenesis leads to the activation of a novel G2/M checkpoint. *Genes Dev.* **26**, 1028–1040 (2012).
46. Grasso, C. S. *et al.* The mutational landscape of lethal castration-resistant prostate cancer. *Nature* **487**, 239–243 (2012).
47. Lapointe, J. *et al.* Gene expression profiling identifies clinically relevant subtypes of prostate cancer. *Proc. Natl Acad. Sci. USA* **101**, 811–816 (2004).
48. Taylor, B. S. *et al.* Integrative genomic profiling of human prostate cancer. *Cancer Cell* **18**, 11–22 (2010).
49. Tomlins, S. A. *et al.* Integrative molecular concept modeling of prostate cancer progression. *Nat. Genet.* **39**, 41–51 (2007).



Extended Data Figure 1 | See next page for caption.

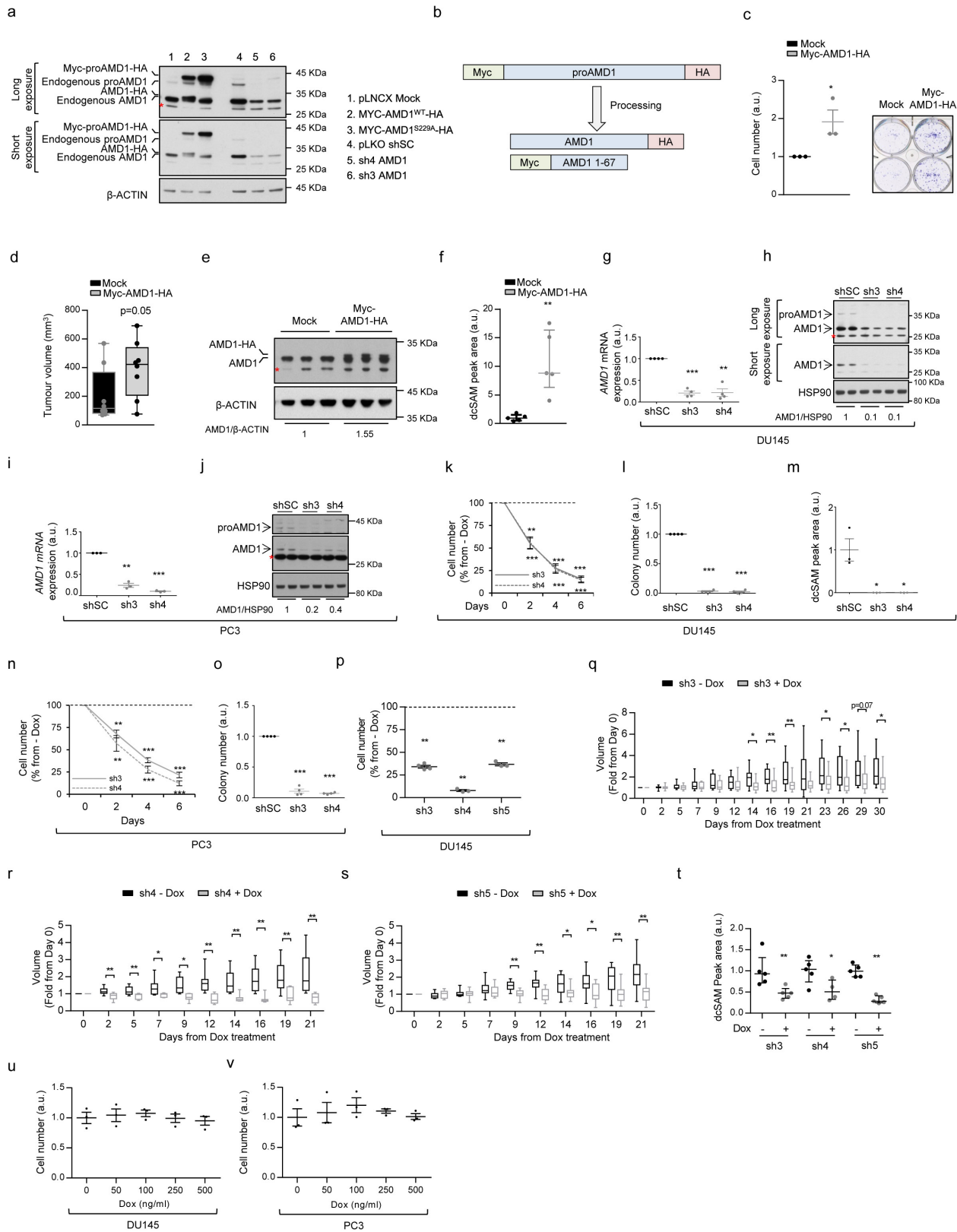
Extended Data Figure 1 | Metabolomics characterization of mouse and human prostate cancer. **a**, Incidence of pathological alterations observed in $Pten^{pc+/+}$ and $Pten^{pc-/-}$ mice. Number of mice as indicated. LG-PIN, low-grade prostatic intraepithelial neoplasia; HG-PIN: high-grade prostatic intraepithelial neoplasia; Focal Adc, focal adenocarcinoma. **b**, Representative immunohistochemical images of prostate tissue stained with haematoxylin and eosin (H&E), Pten, Akt^{S473}, and RpS6^{S235/6} from mice at 3 and 6 months of age (representative of three mice per condition). **c**, Experimental design of the TOF-MS metabolomics analysis. AP, anterior prostate; DLP, dorsolateral prostate. **d**, **e**, Volcano plot (**d**) and principal component analysis (PCA, **e**) from altered metabolites in TOF-MS metabolomic analysis performed in $Pten^{pc-/-}$ and $Pten^{pc+/+}$

mouse prostate samples at the indicated age (6 months $Pten^{pc+/+}$ anterior prostate, $n = 4$ mice; remainder of conditions, $n = 5$ mice). Grey dots: not significantly altered; red dots: significantly increased in $Pten^{pc-/-}$ prostate extracts; blue dots: significantly decreased in $Pten^{pc-/-}$ prostate extracts. **f**, LC/MS analysis of methionine cycle and polyamine pathway metabolites from $Pten^{pc-/-}$ versus $Pten^{pc+/+}$ mouse prostate samples at the indicated age (anterior prostate 3 months, $n = 5$ mice; 6 months, $n = 4$ mice). Median \pm interquartile range. **g**, LC/MS analysis of methionine cycle and polyamine pathway metabolites from prostate cancer versus BPH human specimens (six prostate specimens per condition). Median \pm interquartile range. * $P < 0.05$; ** $P < 0.01$; *** $P < 0.001$. One-tailed Mann–Whitney U -test (**f**, **g**) was used for data analysis.



Extended Data Figure 2 | Metabolic tracing of ^{13}C L-methionine in *Pten*-prostate specific knockout mice. a, Plasma LC/MS analysis of the indicated metabolite concentration after intravenous injection of $[\text{U-}^{13}\text{C}_5]$ L-methionine (100 mg kg^{-1}) in C57BL/6 mice at 3 months of age (time 0 min, $n = 7$ mice; time 10 min/60 min, $n = 6$ mice). The unlabelled (M + 0, ^{12}C) and major labelled (^{13}C , M + 4 or M + 5) metabolite concentration is presented in the histogram. Error bars, s.e.m. **b**, Experimental design of the $[\text{U-}^{13}\text{C}_5]$ L-methionine (100 mg kg^{-1}) *in vivo*. $\text{U-}^{13}\text{C}_5\text{-Met}$, L-methionine labelled with ^{13}C in five carbons; 1 h, prostate samples

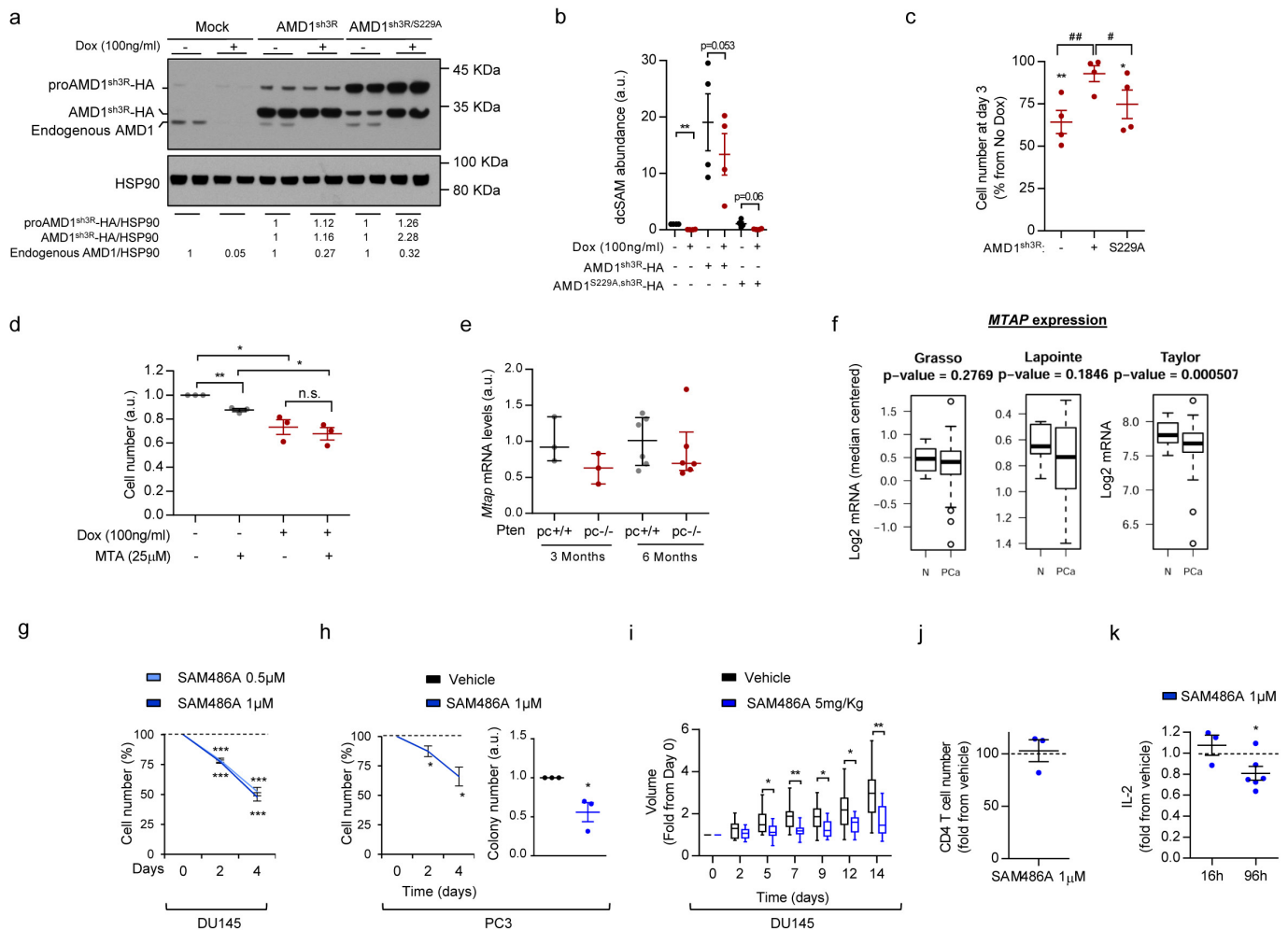
extracted after 1 h pulse with $[\text{U-}^{13}\text{C}_5]$ L-methionine; 10 h, prostate samples extracted after 10 h pulse with $[\text{U-}^{13}\text{C}_5]$ L-methionine; **c**, Summary schematic of the alterations observed in the metabolomic analysis in $Pten^{pc-/-}$ versus $Pten^{pc+/+}$. Spm, spermine; spd, spermidine; ODC1, ornithine decarboxylase 1; SpdS, spermidine synthase; SpmS, spermine synthase. **d**, Fractional labelling of the indicated metabolites from Fig. 1c. Median \pm interquartile range (1 h (top), $n = 4$; 10 h (bottom), $n = 3$). FC, fold change. One-tailed Mann-Whitney *U*-test (**d**) was used for data analysis.



Extended Data Figure 3 | See next page for caption.

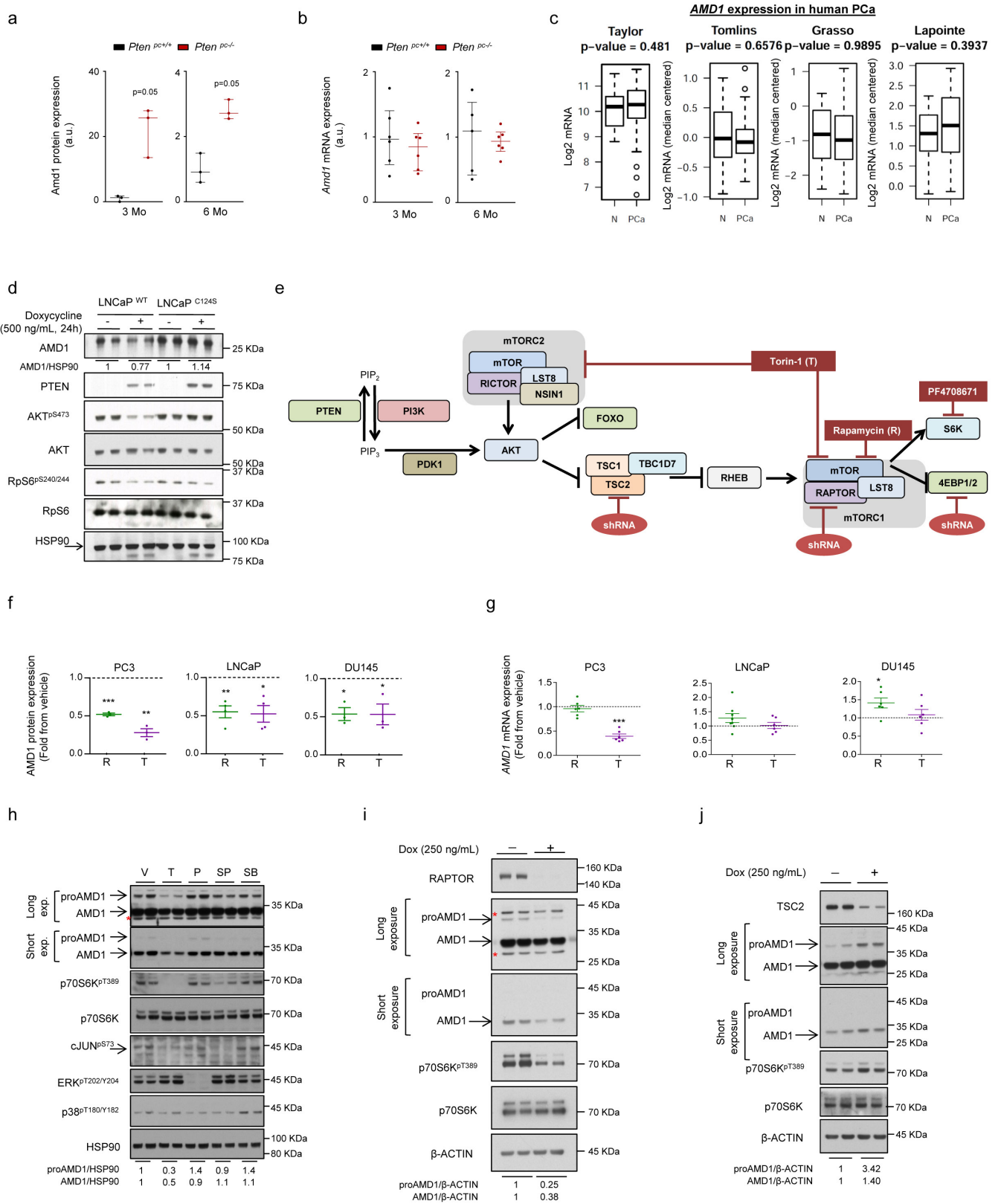
Extended Data Figure 3 | Genetic modulation of AMD1 in prostate cancer cells. **a**, Technical setup of anti-AMD1 antibody using the indicated constructs or shRNAs in DU145 cells. AMD1^{S229A} mutant lacks processing ability and is expressed exclusively as a pro-enzyme (representative western blot out of three independent experiments). **b**, Schematic representation of tagged ectopic AMD1 processing. **c**, Impact of ectopic Myc-AMD1-HA expression on foci number in DU145 cells *in vitro* ($n = 3$ independent experiments). **d–f**, Impact of ectopic Myc-AMD1-HA expression on tumour volume (**d**, $n = 8$ tumours per condition), AMD1 protein levels (**e**, $n = 3$ tumours per condition), and dcSAM abundance (**f**, $n = 5$ tumours per condition) in DU145 xenografts grown for 43 days. Data in **d** are represented as box-and-whisker plot. **f**, Dot plot with the median and the interquartile range. **g–o**, Effect of constitutive silencing of AMD1 (**g**, **i**, mRNA levels; **h–j**, protein expression) on cell number (**k**, **n**), anchorage-independent growth (**l**, **o**), and dcSAM abundance (**m**) with two different hairpins in DU145 (**g**, **h**, **k**, **l**, **m**) and PC3 (**i**, **j**, **n**, **o**) cells ($n = 3$ or 4 independent experiments as indicated by dots). shSC, scramble

short hairpin; sh3 and sh4, two different short-hairpins targeting AMD1. Mean \pm s.e.m. **p**, Effect of doxycycline-inducible (100 ng ml^{-1}) AMD1 silencing on cell number in DU145 cells (sh3, $n = 4$; sh4 and sh5, $n = 3$ independent experiments as indicated by dots). **q–s**, Impact of AMD1-inducible silencing in tumour volume from DU145 xenografts (tumours analysed: sh3 no doxycycline, $n = 12$; sh3 doxycycline, $n = 14$; sh4 no doxycycline, $n = 10$; sh4 doxycycline, $n = 7$; sh5 no doxycycline, $n = 10$; sh5 doxycycline, $n = 11$). Box-and-whisker plot. **t**, Impact of AMD1-inducible silencing in dcSAM abundance in DU145 xenografts from **q** to **s** ($n = 5$ tumours). Median \pm interquartile range. **u**, **v**, Dose-dependent effect of doxycycline on cell number in DU145 (**u**) and PC3 (**v**) cells (cell number measured at day 6) ($n = 3$ independent experiments as indicated by dots). * $P < 0.05$; ** $P < 0.01$; *** $P < 0.001$. Error bars, mean \pm s.e.m. Red asterisk in western blots indicates non-specific band. Dashed lines indicate cell numbers in scramble short-hairpin-transduced cells. One-tailed *t*-test (**c**, **g**, **i**, **k–p**, **u**, **v**), and one-tailed Mann-Whitney *U*-test (**d**, **f**, **q–t**).



Extended Data Figure 4 | Genetic and pharmacological manipulation of AMD1 in prostate cancer cells. **a–c**, DU145 cells carrying doxycycline-inducible shRNA against AMD1 (sh3) were transduced with empty (Mock), sh3-resistant wild type (AMD1^{sh3R}), or processing-deficient (AMD1^{sh3R/S229A}) AMD1 constructs. AMD1 protein (**a**, representative experiment out of four), dcSAM abundance (**b**), and cell number expression (**c**) in the aforementioned cells ($n = 4$ independent experiments as indicated by dots). Asterisks indicate significant differences compared with the corresponding DU145 cells in the absence of doxycycline, and hash symbol indicates significant differences in the indicated comparison. Mean \pm s.e.m. **d**, Effect of MTA (25 μ M) on AMD1 silencing (sh3)-elicited anti-proliferative activity. MTA was administered at day 0 and cells were analysed at day 3 ($n = 3$ independent experiments as indicated by dots). **e**, *Mtap* gene expression levels in *Pten*^{pc+/+} and *Pten*^{pc-/-} mice at the indicated time points (see Extended Data Fig. 1a) (3 months, $n = 3$ mice; 6 months, $n = 6$ mice). Median \pm interquartile range. **f**, *MTAP* gene expression analysis in publicly available data sets (see Methods);

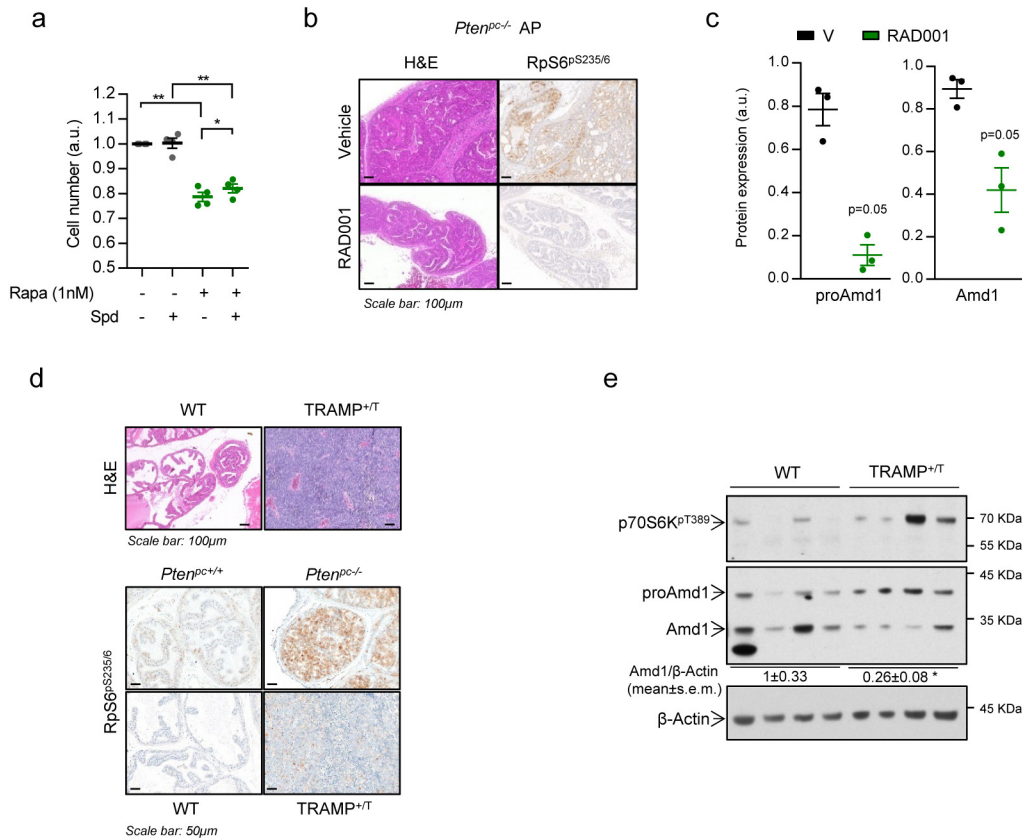
N, normal; number of patients analysed: ref. 48, normal $n = 29$, prostate cancer $n = 150$; ref. 46, normal $n = 12$, prostate cancer $n = 76$; ref. 47, normal, $n = 9$, prostate cancer, $n = 17$). **g, h**, Effect of pharmacological AMD1 inhibition with SAM486A on cell number (**g** and left **h**; DU145, $n = 5$; PC3, $n = 4$ independent experiments as indicated by dots), and anchorage-independent growth (right **h**, $n = 3$ independent experiments as indicated by dots) in PC3 or DU145 cells as indicated. Mean \pm s.e.m. **i**, Effect of pharmacological AMD1 inhibition with SAM486A in established DU145 xenograft tumour volume (vehicle, $n = 11$ tumours; SAM486A, $n = 10$ tumours). Box-and-whisker plot. **j, k**, Effect of pharmacological AMD1 inhibition with SAM486A in activated T CD4 cell number (96 h (**j**), $n = 3$ independent experiments as indicated by dots) or IL-2 production (**k**, $n = 3–6$ independent experiments as indicated by dots). $*/\#P < 0.05$; $**/\#\#P < 0.01$; $***P < 0.001$. Dashed line indicates cell number (**g, h** left) or IL-2 abundance (**j, k**) in vehicle-treated cells. Student's *t*-test (**b–d, f–h, j, k**) and one-tailed Mann–Whitney test (**e, i**).



Extended Data Figure 5 | See next page for caption.

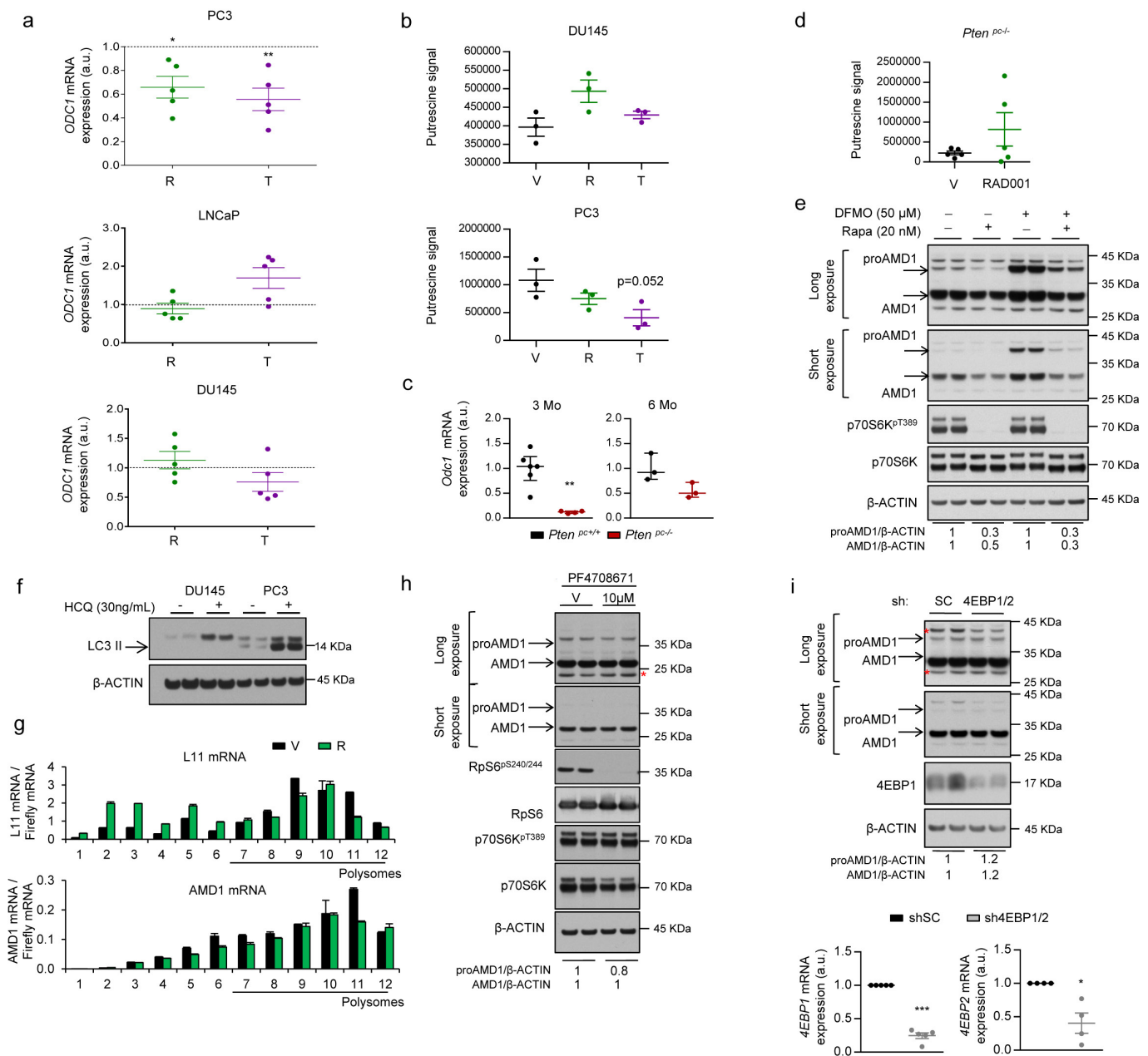
Extended Data Figure 5 | PTEN–PI3K–mTORC1-dependent regulation of AMD1 in prostate cancer. **a, b**, Amd1 protein quantification from Fig. 3a (a, $n = 3$ mice) and mRNA expression (b, $n = 5$ or 6 mice as indicated by dots) in *Pten*^{bc-/-} and *Pten*^{bc+/+} mice of the indicated age. Median \pm interquartile range. **c**, *AMD1* gene expression analysis in publicly available data sets (see Methods; number of patients analysed: ref. 48, normal $n = 29$, prostate cancer $n = 150$; ref. 46, normal $n = 12$, prostate cancer $n = 76$; ref. 47, normal $n = 9$, prostate cancer $n = 17$). **d**, Representative western blot showing the expression of the indicated proteins upon doxycycline-inducible expression (24 h) of YFP–PTEN^{WT} or catalytically inactive YFP–PTEN^{C124S} in *PTEN*-deficient LNCaP prostate cancer cells ($n = 3$ independent experiments). **e**, Schematic representation of the PI3K signalling pathway and the pharmacological/genetic tools used in this study. **f**, ProAMD1 and AMD1 protein quantification from Fig. 3b (sample number as indicated by dots). **g**, *AMD1* gene expression upon treatment (24 h) with vehicle (V, DMSO), rapamycin (R, 20nM) and

Torin-1 (T, 250 nM for PC3 and DU145, 125 nM for LNCaP) (LNCaP, $n = 8$ for Torin-1 and $n = 6$ for rapamycin; PC3 and DU145, $n = 6$ independent experiments as indicated by dots). Mean \pm s.e.m. **h**, Representative western blot analysis of AMD1 levels upon 24-h treatment of DU145 cells with vehicle, Torin-1 (mTORC1/2 inhibitor; 250 nM), PD032901 (ERK-MAPK inhibitor, PD; 100 nM), SP600125 (JNK-SAPK inhibitor, SP; 10 μ M), and SB203580 (p38-MAPK inhibitor, SB; 5 μ M) ($n = 3$ independent experiments). **i**, Impact of inducible *RAPTOR* silencing in DU145 cells on proAMD1 protein levels (doxycycline-induced, 250 ng ml⁻¹) (representative experiment out of $n = 6$). **j**, Impact of inducible *TSC2* silencing in DU145 cells on proAMD1 protein levels (doxycycline-induced, 250 ng ml⁻¹) (representative experiment out of $n = 6$). * $P < 0.05$; ** $P < 0.01$; *** $P < 0.001$. Red asterisk in western blots indicates non-specific band. Arrows indicate specific immunoreactive bands. Student's *t*-test (c, f, g) and Mann–Whitney test (a, b).



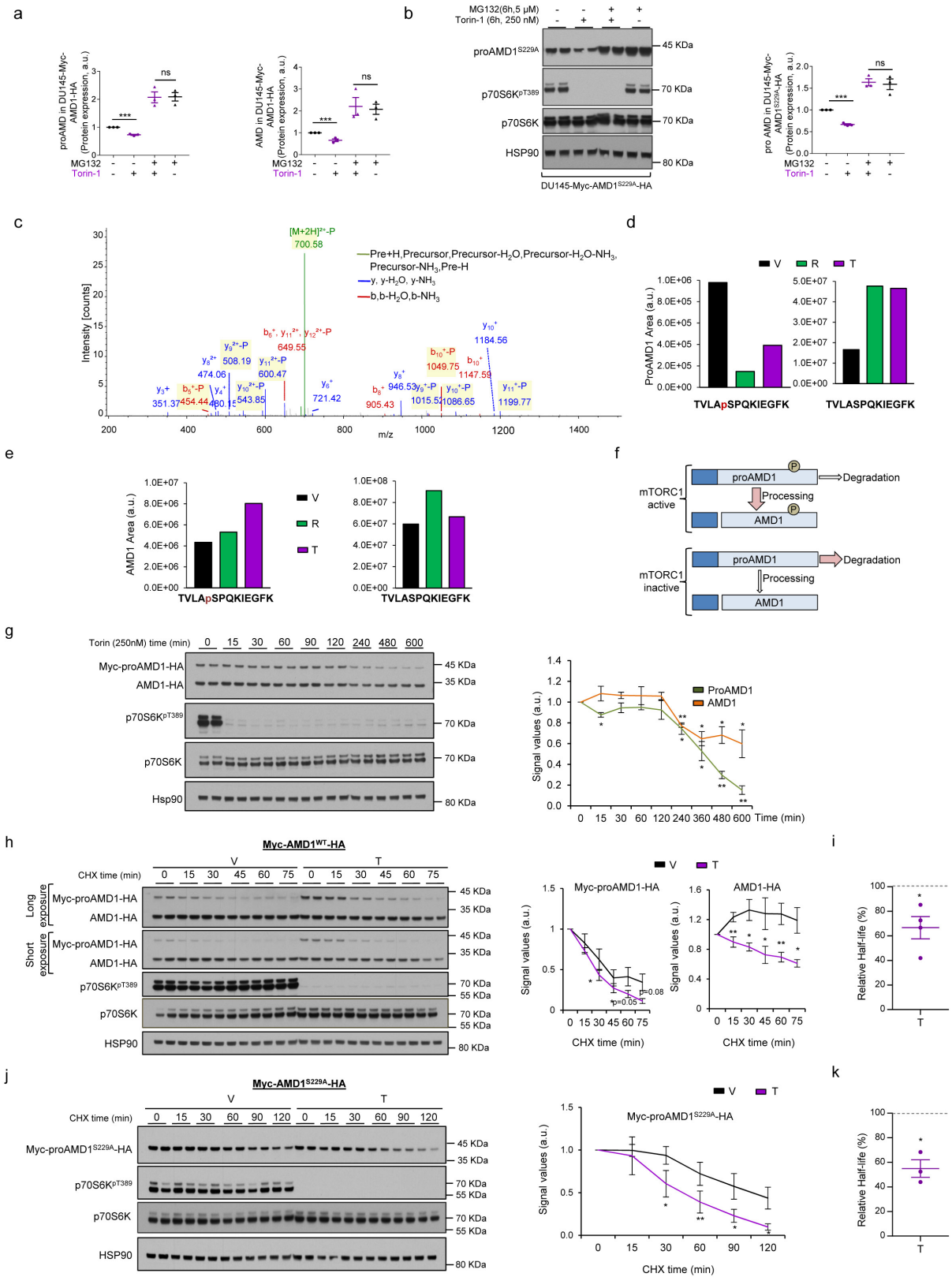
Extended Data Figure 6 | mTORC1-dependent AMD1 regulation *in vivo*. **a**, Effect of spermidine (Spd, 0.75 µM) on PC3 cell number upon rapamycin treatment (1 nM, outcome measured 72 h after treatment). Drugs were administered at day 0 and only spermidine was additionally administered at day 1 ($n = 4$ independent experiments as indicated by dots). **b**, Effect of RAD001 treatment on prostate pathological features and mTORC1 activity (haematoxylin and eosin and RpS6^{S235/6} staining by immunohistochemistry) ($n = 3$ mice). **c**, ProAmd1 and Amd1 protein abundance quantification from Fig. 3e (left; number of mice as indicated

by dots). **d**, Representative immunohistochemical images of prostate tissue from wild-type or TRAMP mice (+/T, 28–32 weeks old) stained with haematoxylin and eosin (top) and RpS6^{S235/6} (bottom, *Pten^{pc+/+}* and *Pten^{pc-/-}* prostate tissues are presented as a comparison of the RpS6 phosphorylation levels) ($n = 3$ mice). **e**, Evaluation of AMD1 expression by western blot in prostate tissues from wild-type or TRAMP mice (+/T, 28–32 weeks old) ($n = 4$ mice). * $P < 0.05$; ** $P < 0.01$. Error bars, mean ± s.e.m. Arrows indicate specific immunoreactive bands. Student's *t*-test (**a**) and Mann–Whitney test (**c**, **e**).



Extended Data Figure 7 | Contribution of mTORC1 effector pathways and targets on the regulation of AMD1. **a**, *ODC1* gene expression upon treatment (24 h) of vehicle (DMSO), rapamycin (20 nM) and Torin-1 (250 nM for PC3 and DU145, 125 nM for LNCaP) in PC3, LNCaP, and DU145 cells ($n = 5$ independent experiments as indicated by dots). Mean \pm s.e.m. **b**, Putrescine abundance upon treatment (24 h) of vehicle (DMSO), rapamycin (20 nM), and Torin-1 (250 nM) in DU145 and PC3 cells ($n = 3$ independent experiments as indicated by dots). Mean \pm s.e.m. **c**, *Odc1* gene expression in 3- and 6-month-old *Pten*^{pc+/+} and *Pten*^{pc-/-} mice ($n = 3-6$ as indicated by dots). Median \pm interquartile range. **d**, Putrescine abundance in 12-week-old *Pten*^{pc-/-} mice upon treatment with vehicle or RAD001 (10 mg per kg (body weight), 6 days per week) for 4 weeks ($n = 5$ mice). Mean \pm s.e.m. **e**, Representative western blot ($n = 3$ independent experiments) depicting the changes in expression of the indicated proteins upon 24 h treatment of DU145 cells with rapamycin (20 nM) and/or DFMO (an inhibitor of ODC1, 50 μ M) with

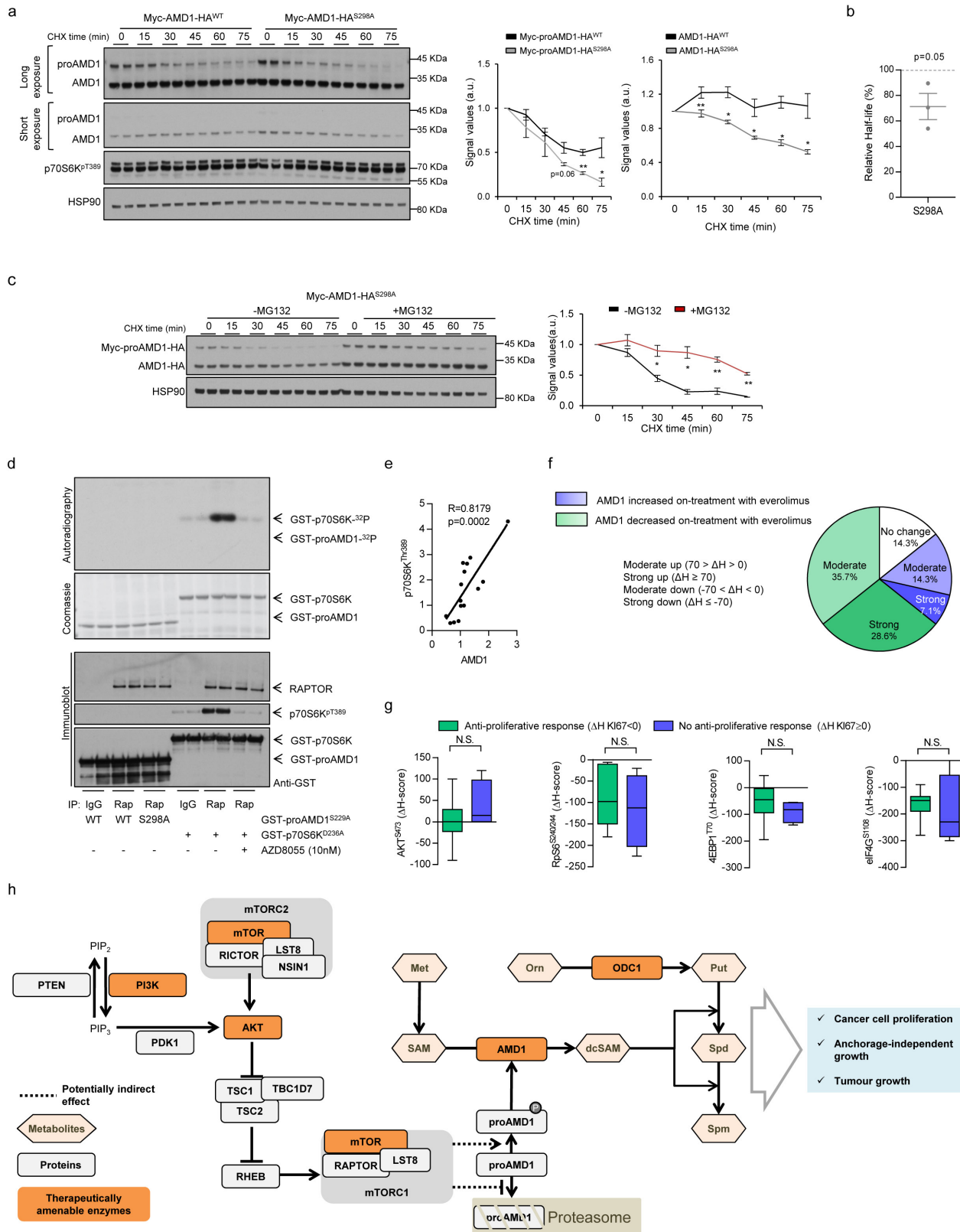
the corresponding vehicles. **f**, Representative western blot showing LC3 lipidation in HCQ-treated (6 h) DU145 and PC3 cells, as a readout of macro-autophagy ($n = 3$ independent experiments). Arrow indicates LC3-II. **g**, For the analysis of translation initiation, polysome profiling analysis of AMD1 and L11 as positive control in DU145 cells treated with vehicle or rapamycin (20 nM, 8 h) is shown. Error bars, s.d. from technical replicates. **h**, Effect of pharmacological p70S6K inhibition with PF4708671 (10 μ M) on AMD1 protein expression in DU145 cells (representative experiment out of five). **i**, Effect of 4EBP1/2 silencing on proAMD1 and AMD1 protein expression (upper panels) (representative experiment out of three). Lower panels show 4EBP1 ($n = 5$ independent experiments) and 4EBP2 ($n = 4$ independent experiments) gene expression in shRNA-transduced DU145 cells. * $P < 0.05$; ** $P < 0.01$; *** $P < 0.001$. Red asterisks in western blots indicate non-specific band. Arrows indicate specific immunoreactive bands. Student's *t*-test (**a**, **b**, **d**, **i**) and Mann-Whitney *U*-test (**c**).



Extended Data Figure 8 | See next page for caption.

Extended Data Figure 8 | Regulation of proAMD1 stability by mTORC1. **a**, ProAmd1 (left) and Amd1 (right) protein abundance quantification from Fig. 4a ($n = 3$ independent experiments as indicated by dots). Error bars, mean \pm s.e.m. **b**, Representative western blot of DU145 cells expressing Ser-229-Ala (S229A) mutant Myc-AMD1-HA treated with vehicle or Torin-1 (250 nM, 6 h) in the presence or absence of MG132 (5 μ M, 6 h) ($n = 3$ independent experiments). Quantification is provided in the right panel. **c**, Representative MS/MS spectrum of the TVLASPKIEGFK peptide in proAMD1 and AMD1, in which phosphorylation was unambiguously assigned to the S298 residue. **d**, Calculated areas under the curves from extracted ion chromatogram in Fig. 4b of the TVLASPKIEGFK peptide for phosphorylated (highlighted in red in the sequence, left) and total (right) proAMD1. **e**, Calculated areas under the curves from extracted ion chromatogram of the TVLASPKIEGFK peptide for phosphorylated (highlighted in brown in the sequence, left) and total (right) AMD1. **f**, Schematic representation

of the working hypothesis of proAMD1 regulation by mTORC1-dependent phosphorylation. **g**, Effect of Torin (250 nM) on proAMD1 and AMD1 protein at different time points in Myc-AMD1-HA-expressing DU145 cells (representative western blot out of three independent experiments; right, densitometric quantification). Error bars, s.e.m. **h**, **i**, Representative western blot depicting the stability of ectopic proAMD1 and AMD1 in DU145 cells challenged with vehicle or Torin-1 (250 nM, 2 h) upon CHX treatment (densitometry of proAMD1 and AMD1 levels is represented in right panels (**h**) and half-life reduction in proAMD1 (**i**) ($n = 4$ independent experiments). **j**, **k**, Representative western blot depicting the stability of S229A mutant Myc-AMD1-HA construct in DU145 cells challenged with vehicle or Torin-1 (250 nM, 2 h) upon CHX treatment (densitometry of proAMD1 is represented in the right panel (**j**) and half-life reduction in proAMD1 (**k**) ($n = 3$ independent experiments). Mean \pm s.e.m. NS, not significant. * $P < 0.05$; ** $P < 0.01$; *** $P < 0.001$. Student's t -test.



Extended Data Figure 9 | See next page for caption.

Extended Data Figure 9 | Contribution of proAMD1 phosphorylation downstream mTORC1 to the stability of the enzyme. **a, b**, Representative western blot depicting the stability of wild type and S298A phospho-mutant Myc-AMD1-HA constructs in DU145 cells upon cycloheximide treatment (densitometry of proAMD1 and AMD1 is represented in right panels **(a)** and half-life reduction in proAMD1 **(b)**) ($n = 3$ independent experiments). Mean \pm s.e.m. **c**, Representative western blot depicting the stability of S298A phospho-mutant Myc-AMD1-HA construct in DU145 cells challenged with vehicle (V) or MG132 (5 μ M) upon CHX treatment (densitometry of proAMD1 is represented in right panel, $n = 3$ independent experiments). Mean \pm s.e.m. **d**, mTORC1 kinase activity (by means of RAPTOR immunoprecipitation from HEK293 cells) on GST-proAMD1^{S229A} or GST-proAMD1^{S229A/S298A}, using bacteria-purified proteins. GST-p70S6K is presented as positive control. AZD8055 is used as control of mTORC1 inhibition. **e**, Correlation analysis between

p70S6K^{T389} and AMD1 densitometry values in prostate cancer specimens from Fig. 4c ($n = 15$ patient specimens). **f**, Quantification of AMD1 immunoreactivity in response to everolimus in tumour biopsies, on the basis of the ΔH score ($n = 14$ specimen pairs). **g**, Box-and-whisker plot of the immunoreactivity of mTOR downstream effectors (AKT^{S473}, RpS6^{PS240/244}, 4EBP1/2^{pT70}, eIF4G^{PS1108}) in cancer patients with (ΔH score for KI67 < 0; $n = 6$ specimen pairs) or without (ΔH score for KI67 \geq 0; $n = 4$ specimen pairs) anti-proliferative tumour response upon treatment with everolimus. **h**, Schematic representation of the main findings of this study. Orn, ornithine; Put, putrescine; Spm, spermine; ODC1, ornithine decarboxylase 1; PIP₂, phosphatidyl inositol bisphosphate; PIP₃, phosphatidyl inositol triphosphate; * $P < 0.05$; ** $P < 0.01$; NS, not significant. Arrows indicate specific immunoreactive/autoradiographic bands. One-tailed Student's t -test (**a-c**), two-tailed Mann-Whitney test (**g**), and Spearman's correlation analysis (**e**).

PPAR δ Elicits Ligand-Independent Repression of Trefoil Factor Family to Limit Prostate Cancer Growth



Natalia Martín-Martín^{1,2}, Amaia Zabala-Letona^{1,2}, Sonia Fernández-Ruiz^{1,2}, Leire Arreal¹, Laura Camacho^{1,3}, Mireia Castillo-Martin⁴, Ana R. Cortazar^{1,2}, Verónica Torrano^{1,2}, Ianire Astobiza¹, Patricia Zúñiga-García¹, Aitziber Ugalde-Olano^{2,5}, Ana Loizaga-Iriarte^{2,6}, Miguel Unda^{2,6}, Lorea Valcárcel-Jiménez¹, Amaia Arruabarrena-Aristorena¹, Marco Piva¹, Pilar Sánchez-Mosquera¹, Ana M. Aransay^{1,7}, Antonio Gomez-Muñoz³, Rosa Barrio¹, James D. Sutherland¹, and Arkaitz Carracedo^{1,2,3,8}

Abstract

The nuclear receptor PPAR- β/δ (PPAR δ) has essential roles in fatty acid catabolism and energy homeostasis as well as cell differentiation, inflammation, and metabolism. However, its contributions to tumorigenesis are uncertain and have been disputed. Here, we provide evidence of tumor suppressive activity of PPAR δ in prostate cancer through a noncanonical and ligand-independent pathway. PPAR δ was downregulated in prostate cancer specimens. In murine prostate epithelium, PPAR δ gene deletion resulted in increased cellularity. Genetic modulation of PPAR δ in human prostate cancer cell lines validated the tumor suppressive activity of this gene *in vitro* and *in vivo*. Mechanistically, PPAR δ exerted its activity in a DNA binding-dependent and ligand-independent

manner. We identified a novel set of genes repressed by PPAR δ that failed to respond to ligand-mediated activation. Among these genes, we observed robust regulation of the secretory trefoil factor family (TFF) members, including a causal and correlative association of TFF1 with prostate cancer biology *in vitro* and in patient specimens. Overall, our results illuminate the oncosuppressive function of PPAR δ and understanding of the pathogenic molecular pathways elicited by this nuclear receptor.

Significance: These findings challenge the presumption that the function of the nuclear receptor PPAR β/δ in cancer is dictated by ligand-mediated activation. *Cancer Res*; 78(2): 399–409. ©2017 AACR.

Introduction

In the process of cellular transformation, cancer cells exhibit profound changes in nutrient uptake and utilization as a way to generate substrates for the production of biomass. This metabolic switch in cancer cells involves rewiring of cellular signaling and reprogramming of metabolic pathways. One of the main triggers for metabolic reprogramming is the alteration in cancer genes that remodel the signaling landscape (1). Seminal investigations have demonstrated that most cancer cells reprogram their metabolism to increase glucose uptake for glycolysis and decrease the

flux toward TCA cycle and oxidative phosphorylation, using additional nutrients for anabolism. We have recently demonstrated that the regulation of metabolism downstream nuclear receptors affects prostate cancer progression and metastasis (2). More importantly, this study demonstrates for the first time that genetic events such as PGC1 α alteration can trigger metabolic reprogramming in prostate cancer. Prostate cancer is the fifth leading cause of death by cancer worldwide (3), second in the male population, and it has been related to changes in glucose metabolism and lipid biosynthesis. However, the contribution of fatty acid oxidation (FAO) pathways to the pathogenesis and progression of prostate cancer remained obscure.

The family of peroxisome proliferator-activated receptors (PPAR) plays a central role in metabolic regulation, but their role in cancer is yet to be clarified (4, 5). In particular, PPAR β/δ (PPAR δ , PPAR δ) is a transcription factor that belongs to this family of nuclear receptors that control target gene expression in response to endogenous and exogenous ligands (6, 7). PPAR δ is constitutively expressed in tissues (7), and its canonical transcriptional activity relies on heterodimeric binding to PPAR response elements (PPRE) with a retinoid X receptor (RXR) moiety (8, 9). This activity is relevant for cell differentiation, macrophage activation, and cancer (10). The contribution of PPAR δ in tumor biology through the regulation of multiple pathways (i.e., proliferation, apoptosis, wound healing, invasion, or migration) remains controversial and has been summarized in recent reviews (10, 11). Three primary modes

¹CIC bioGUNE, Bizkaia Technology Park, Derio, Spain. ²CIBERONC, Madrid, Spain. ³Biochemistry and Molecular Biology Department, University of the Basque Country (UPV/EHU), Bilbao, Spain. ⁴Champalimaud Centre for the Unknown, Portugal. ⁵Department of Pathology, Basurto University Hospital, Bilbao, Spain. ⁶Department of Urology, Basurto University Hospital, Bilbao, Spain. ⁷Centro de Investigación Biomédica en Red de Enfermedades Hepáticas y Digestivas (CIBEREHD), Madrid, Spain. ⁸IKERBASQUE, Basque Foundation for Science, Bilbao, Spain.

Note: Supplementary data for this article are available at Cancer Research Online (<http://cancerres.aacrjournals.org/>).

Corresponding Author: Arkaitz Carracedo, CIC bioGUNE, Bizkaia Technology Park 801A bld., 48160, Derio, Spain. Phone: 34-94-406-13-08; Fax: 34-94-406-13-01; E-mail: acarracedo@bicbiogune.es

doi: 10.1158/0008-5472.CAN-17-0908

©2017 American Association for Cancer Research.

of regulation by PPAR δ have been described (12, 13): (i) canonical ligand-induced activation and/or derepression by PPAR δ , (ii) ligand-independent repression by PPAR δ , and (iii) ligand-independent activation by PPAR δ .

In the current study, we ascertained the biological activity of PPAR δ in prostate cancer. Our results reveal that PPAR δ exerts a tumor suppressive activity that is independent of ligand-mediated activation. Furthermore, we show that repression of trefoil factor family (TFF) member 1 (TFF1) is causal to the biological function of PPAR δ . This study opens a new avenue in the biological activity of PPAR δ that might lead to the identification of novel pathophysiological functions of this nuclear receptor.

Materials and Methods

Reagents

Doxycycline (Sigma) was used at different doses to induce the expression of cDNA or shRNA from TRIPZ. GW501516 (Enzo Life Sciences; ALX-420-032-M001) was dissolved in DMSO and used at 0.1 μ mol/L concentration. GW0742 and L165,041 (Tocris, refs. 2229 and 1856, respectively) were dissolved in DMSO and used at 1 μ mol/L concentration. Etomoxir (Sigma) dissolved in water and used at 200 μ mol/L concentration. Recombinant human TFF1 protein (R and D systems) was dissolved in PBS at 100 μ mol/L and used at 1 μ mol/L final concentration.

Patient samples

All samples were obtained from the Basque Biobank for research (BIOEF, Basurto University Hospital) upon informed consent and with evaluation and approval from the corresponding ethics committee (CEIC-E code OHEUN11-12 and OHEUN14-14). The patient studies were conducted in accordance with the ethical guidelines from the Declaration of Helsinki.

Cell culture

DU145, PC3, LNCAP, PWR1E, VCAP, C4-2, and 22RV1 cell lines were obtained from the ATCC or from Leibniz-Institut—Deutsche Sammlung von Mikroorganismen und Zellkulturen GmbH (DSMZ), who provided an authentication certificate, and the identity was validated by microsatellite analysis. None of the cell lines used in this study was found in the database of commonly misidentified cell lines maintained by ICLAC and NCBI Biosample. All cell lines were routinely monitored for *Mycoplasma* contamination and quarantined while treated if positive. DU145, PC3, and VCAP cell lines were maintained in DMEM media supplemented with 10% (v/v) fetal bovine serum (FBS) and 1% (v/v) penicillin–streptomycin. The 22RV1, LNCAP, and C4-2 cell lines were maintained in RPMI media supplemented with 10% (v/v) FBS and 1% (v/v) penicillin–streptomycin.

Generation of stable cell lines

293FT cells were used for lentiviral production. Lentiviral vectors expressing shRNAs against human *PPARD* and human *TFF1* from the Mission shRNA Library were purchased from SigmaAldrich. Cells were transfected with lentiviral vectors following standard procedures, and viral supernatant was used to infect cells. Selection was done using puromycin (2 μ g/mL) for 48 hours. As a control, a lentivirus expressing scrambled shRNA (shC) was used. Short hairpins sequence: shC: CCGCAACAA-GATGAAGAGCACCAACTCGAGTTGGTGTCTTTCATCTTGTTC;

sh#64 against *PPARD*: CCGGCCGCAAACCCCTTCAGTGA-TATCTCGAGATATCACTGAAGGGTTTTCGGTTTTT and sh#50 against *TFF1*: CCGGTATCCTAATACCATCGACGCTCTCGAGG-ACGTCGATGGTATTAGGATATTTTTG. pBabe-puro was a gift from Hartmut Land & Jay Morgenstern & Bob Weinberg; Addgene plasmid #1764 (14), pBabe puro PPAR delta was a gift from Bruce Spiegelman; Addgene plasmid #8891 (15). Point mutations of *PPARD* DNA binding motif (two conserved cysteine residues, Cys-90 and Cys-93, were mutated to alanines) were created by site-directed mutagenesis by using a Quick change site-directed mutagenesis kit (Stratagene) as reported (16). HA-PPARD inducible system was constructed by cloning *PPARD* into TRIPZ vector as reported (2). Briefly, HA-PPARD was subcloned using Age1 and Mlu1 sites into a TOPO cloning vector and then transferred to TRIPZ vector. *PPARD* targeting shRNA was subcloned from pSM2c (Open Biosystems, #5467) using Xho1 and Mlu1 sites into a TRIPZ vector. *TFF1* was amplified from human cDNA pool (heart/thyroid mix) using primers TZ.Age.TFF1.for and TZ.Mlu.pA.TFF1.rev, and inserted into TRIPZ (Age1-Mlu1) using Gibson cloning. Final clone was confirmed by Sanger sequencing. Sequences are available by request.

Western blotting

Western blot analysis was carried out as previously described (17). Briefly, cells were seeded on 6-well plates and 4 days (unless otherwise specified) after seeding cell lysates were prepared with RIPA buffer (50 mmol/L TrisHCl pH 7.5, 150 mmol/L NaCl, 1 mmol/L EDTA, 0.1% SDS, 1% Nonidet P40, 1% sodium deoxycholate, 1 mmol/L sodium fluoride, 1 mmol/L sodium orthovanadate, and 1 mmol/L beta-glycerophosphate and protease inhibitor cocktail; Roche). The following antibodies were used for Western blotting: mouse monoclonal anti-PPAR δ , 1:500 dilution (Santa Cruz Biotechnology, F7, sc-74440) for detection of endogenous PPAR δ , rabbit polyclonal anti-PPAR δ , 1:1,000 dilution (Santa Cruz Biotechnology, K20: sc-1987) for exogenous protein, rabbit polyclonal anti-caveolin-1, 1:2,000 (BD Biosciences, Cat. No. 610059), rabbit monoclonal anti-TFF1, 1:1,000 (Cell Signaling Technology, 15571), rabbit polyclonal anti-HSP-90, 1:1,000 (Santa Cruz Biotechnology, sc-4874), rabbit polyclonal anti-GAPDH, 1:1,000 (Santa Cruz Biotechnology, sc-2118) and mouse monoclonal anti-beta-Actin 1:2,000 dilution (clone: AC-74, catalog: A5316, Sigma-Aldrich). After standard SDS-PAGE and Western blotting techniques, proteins were visualized using the ECL system.

Histopathologic analysis

After euthanasia, histologic evaluation of a hematoxylin and eosin (H&E)-stained section from formalin-fixed paraffin-embedded prostate tissues was performed. After histopathologic evaluation, quantitative assessment of the prostate glandular structures by counting the number of epithelial cells in 5 high power fields (total area of 0.431 mm²) of representative zones of the prostate was performed. Mean number of cells per mm² was compared between wild-type and *PPARD*^{pc-/-} mice at different ages (9 *PPARD*^{pc-/-} mice with ages: 9–12 months; 10 *PPARD*^{pc-/-} mice with ages: 18–20 months; 16 wild-type mice with ages: 9–12 months; 11 wild-type mice with ages: 18–20 months).

Quantitative real-time PCR

Cells were seeded as for Western blot. Total RNA was extracted from cells using a NucleoSpin RNA isolation kit from Macherey-

Nagel (ref: 740955.240C). cDNA was produced from 1 μ g of RNA using qScript cDNA SuperMix (Quanta Bioscience, ref: 95048). Taqman probes were obtained from Applied Biosystems. Amplifications were run in a Vii7 or QS6 Real-Time PCR System (Applied Biosystems) using the following probes: *PPARD* (Hs04187066_g1, cat: 4331182). For *ADFP*, *PDK4*, *ANGPTL4*, *Caveolin-1*, *TFF1*, *TFF2* and *TFF3* amplification, Universal Probe Library (Roche) primers and probes were used (*ADFP*, For: tcagctcattctactgttcacc, Rev: cctgaatttctgattggcact; probe: 72; *PDK4*, For: cagtgaattgtttaaagctg, Rev: ggtcatctgggcttttctca; probe: 31; *ANGPTL4*, For: gttgaccggctcacaat, Rev: ggaacagctcctgcaatc; probe: 44; *CAV-1* For: aacacgtagctgcccttcag, Rev: ggatgggaacgggtgtagat, probe: 24; *TFF1*, For: gatccctgcagaagtgtctaaaa, Rev: ccctggtgcttctactca, probe: 35; *TFF2*, For: ccagatgatcctctggaac, Rev: ggaagtgtccttccaac, probe: 37; *TFF3*, For: tggagtgctcagaaggt, Rev: gctgctgttgactccag, probe: 4). β -Actin (Hs99999903_m1, cat: 4331182) and *GAPDH* (Hs02758991_g1, cat: 4331182) housekeeping assays from Applied Biosystems showed similar results (all qRT-PCR data presented were normalized using *GAPDH*).

Cellular assays

FAO and soft-agar colony formation were performed as previously described (2). Relative invasive growth experiments were carried out plating 700 cells upside down in suspension in 20% methylcellulose medium drops. A sphere was formed in every individual drop, and thus was considered a biological replicate. After 3 days, when the spheres were formed, they were embedded in a collagen based medium (55% collagen I, 20% DMEM 5 \times , 21.3% H₂O and 3% 0.1 N NaOH), and photos were taken after collagen polymerization (0-hour time point). After 16 hours, photos were taken again and the relative invasive growth was calculated with the relative area increase.

Mice

Xenograft experiments were carried out following the ethical guidelines established by the Biosafety and Welfare Committee at CIC bioGUNE and in accordance with an Institutional Animal Care and Use Committee. The procedures used were carried out following the recommendations from AAALAC. Xenograft experiments were performed as previously described (2), injecting either 3 \times 10⁶ (*PPARD* silencing and *TFF1* ectopic expression) or 3 \times 10⁵ (*PPARD* ectopic expression) cells per condition (unless otherwise specified), two to four injections per mouse. All mice (male Hsd:Athymic Nude-Foxn1 nu/nu) were inoculated at 8 to 12 weeks of age. The *Ppard*^{Floxed} conditional knockout allele has been described elsewhere (18). Prostate epithelium-specific deletion was effected by the Pb-Cre4 (19). Mice were fasted for 6 hours prior to tissue harvest (9 am–3 pm) in order to prevent metabolic alterations due to immediate food intake.

Chromatin immunoprecipitation

Chromatin immunoprecipitation (ChIP) was performed using the SimpleChIP Enzymatic Chromatin IP Kit (Cat: 9003, Cell Signaling Technology, Inc.). PC3 cells were grown in 150-mm dishes either with or without 500 ng/mL doxycycline during 3 days. Cells from three 150 mm dishes (2.5 \times 10⁷ cells) were cross-linked with 35% formaldehyde for 10 minutes at room temperature. Glycine was added to dishes, and cells incubated for 5 minutes at room temperature. Cells were then washed twice

with ice-cold PBS and scraped into PBS + PMSF. Pelleted cells were lysed and nuclei were harvested following the manufacturer's instructions. Nuclear lysates were digested with micrococcal nuclease for 20 minutes at 37°C and then sonicated in 500 μ L aliquots on ice for 3 pulses of 15 seconds using a Branson sonicator. Cells were held on ice for at least 1 minute between sonications. Lysates were clarified at 11,000 \times g for 10 minutes at 4°C, and chromatin was stored at –80°C. HA-Tag polyclonal antibody (Cat: C29F4, Cell Signaling Technology) and IgG antibody (Cat: 2729, Cell Signaling Technology) were incubated overnight (4°C) with rotation and protein G magnetic beads were incubated 2 hours (4°C). Washes and elution of chromatin were performed following the manufacturer's instructions. DNA quantification was carried out using a Vii7 Real-Time PCR System (Applied Biosystems) with SybrGreen reagents and primers that amplify the predicted PPAR δ binding region to *TFF1* or *TFF3* promoter or to region of the promoter of PPAR δ canonical target genes containing the canonical PPAR δ DNA binding domain (as shown in Supplementary Table S1).

Transcriptomic analysis

For transcriptomic analysis in empty-vector-transduced PC3 cells and *PPARD*-expressing counterparts, the Illumina whole-genome -HumanHT-12_V4.0 (DirHyb, nt) method was used as reported previously (2). Probes not detected in at least one sample ($P > 0.01$) were excluded for subsequent analyses as they are considered to represent transcripts that are not expressed. For the detection of differentially expressed genes, a linear model was fitted to the data, and empirical Bayes moderated t -statistics were calculated using the limma package from Bioconductor. Adjustment of P values was done by the determination of false discovery rates (FDR) using Benjamini-Hochberg procedure. Establishment of differentially expressed genes was based on fold change (fc) ≥ 1.5 or ≤ -1.5 and adjusted P value ≤ 0.05 .

Data availability

Transcriptomics data are available at GEO (GSE95054). The link for the reviewers is provided At <https://www.ncbi.nlm.nih.gov/geo/query/acc.cgi?token=glcvicamrtelngd&acc=GSE95054>.

Statistics and reproducibility

No statistical method was used to predetermine sample size. The experiments were not randomized. The investigators were not blinded to allocation during experiments and outcome assessment. Unless otherwise stated, data analyzed by parametric tests are represented by the mean \pm SEM of pooled experiments and median \pm interquartile range for experiments analyzed by non-parametric tests. N values represent the number of independent experiments performed, the number of individual mice or patient specimens. For each independent *in vitro* experiment, at least three technical replicates were used and a minimum number of three experiments were performed to ensure adequate statistical power. In the *in vitro* experiments, normal distribution was assumed and one sample t test was applied for one-component comparisons with control and Student t test for two-component comparisons. For *in vivo* experiments as well as for experimental analysis of human biopsies (from Basurto University Hospital), a nonparametric Mann-Whitney exact test was used. Spearman rank correlation coefficient was applied for correlation analysis for samples not following a normal distribution. The confidence level

used for all the statistical analyses was of 95% (alpha value = 0.05). Two-tailed statistical analysis was applied for experimental design without predicted result, and one-tail for validation or hypothesis-driven experiments.

Results

PPAR δ inhibits prostate cancer aggressiveness

In order to elucidate the contribution of PPAR δ to prostate cancer biology, we first undertook an *in vivo* approach. We evaluated *PPARD* mRNA (11 benign prostate hyperplasia and 16 primary prostate cancer tissue extracts harvested following the guidelines reported; ref. 20) in human specimens. The results revealed a significant downregulation of *PPARD* in cancerous tissues compared with benign disease (Fig. 1A). Importantly, these results were corroborated in publicly available datasets using Oncomine (21; Supplementary Table S2). Next, we deleted *Ppard* conditionally in the mouse prostate epithelium using Probasin-Cre4 promoter (19), which led to increased cellularity

both in adult (9–12 months old) and aged (18–20 months old) mice (Fig. 1B–D).

These results are supportive of an oncosuppressive role of PPAR δ in prostate cancer and prompted us to characterize the biological and molecular consequences of *PPARD* manipulation in experimental systems. Using benign immortalized prostate cells (PWR1E) as a baseline, we identified prostate cell lines with elevated (DU145) or reduced (PC3, LNCAP) expression of PPAR δ , so we chose these to genetically manipulate PPAR δ levels (Supplementary Fig. S1A–S1C). DU145 cells were subject to *PPARD* silencing by means of constitutive (pLKO, sh64; Supplementary Fig. S1D–S1F) or inducible (TRIPZ-shPPARD) expression of short hairpin (sh) RNAs against *PPARD* gene (different hairpin sequences were used to exclude off-target effects; Supplementary Fig. S1G). In coherence with the *in vivo* data, *PPARD* silencing resulted in increased aggressiveness features of DU145 cells, namely soft-agar colony formation and invasive growth (Fig. 1E and F; Supplementary Fig. S1H). Importantly, *PPARD* silencing-induced prostate cancer aggressiveness was confirmed *in*

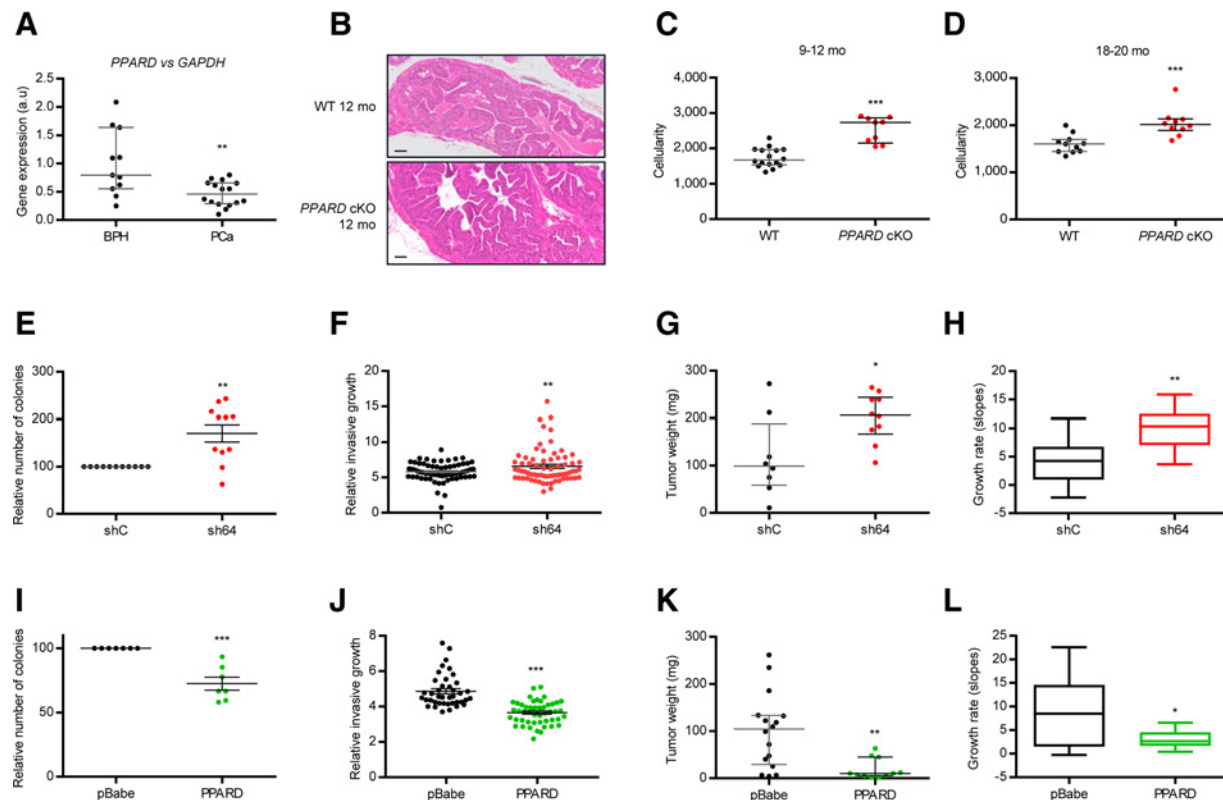


Figure 1.

PPAR δ exhibits tumor suppressor activity. **A**, *PPARD* expression in prostate cancer (PCa; $n = 16$) and benign prostate hyperplasia (BPH; $n = 11$) patients. **B**, Representative images of H&E-stained tissues of wild-type (WT) and *PPARD* knock out (*PPARD* cKO) of 12-month-old mice. **C** and **D**, Quantitative assessment of the prostate glandular structures by counting the number of epithelial cells. Mean number of cells per mm² is represented as 9- to 12- and 18- to 20-month-old mice (9 months, $n = 16$; 12 months, $n = 9$; 18 months, $n = 11$; 20 months, $n = 10$). **E** and **F**, Effect of *PPARD* silencing with a short hairpin (sh64) in DU145 cells on anchorage independent growth ($n = 11$; **E**) and on the invasive growth capacity after 16 hours ($n = 3$; in each individual experiment, a mean of 20 colonies was counted and is represented in **F**). **G** and **H**, Impact of *PPARD* silencing in DU145 cells on tumor weight (**G**) and tumor growth rate ($n = 5$ mice; two injections per mouse; **H**). **I** and **J**, Effect of *PPARD* ectopic expression in PC3 cells on anchorage-independent growth ($n = 7$; **I**) and on the invasive growth capacity after 16 hours ($n = 3$; in each individual experiment, a mean of 20 colonies was counted and is represented in **J**). **K** and **L**, Impact of *PPARD* ectopic expression in PC3 cells on tumor weight (**K**) and tumor growth rate ($n = 5$ mice; four injections per mouse; **L**). Scale bar, 50 μ m. Error bars, SEM. *, $P < 0.05$; **, $P < 0.01$; ***, $P < 0.001$ compared with control. Statistics test: two-tailed Student *t* test (**A**), one-tailed Mann-Whitney *U* test (**C**, **D**, **F**–**H**, **J**–**L**), one-sample *t* test (**E** and **I**). a.u., arbitrary units; shC, scramble shRNA.

in vivo. Using subcutaneous xenografts, we observed that *PPARD* silencing in DU145 cells led to elevated tumor growth rate and tumor mass (Fig. 1G and H). Conversely, we overexpressed this gene with constitutive (pBabe-*PPARD*; Supplementary Fig. S1I–S1K) or inducible (TRIPZ-HA-*PPARD*) viral vectors (Supplementary Fig. S1L) and we evaluated the biological consequences. *PPARD* ectopic expression in PC3 cells resulted in reduced soft-agar colony formation and invasive growth (Fig. 1I and J; Supplementary Fig. S1M). Moreover, inoculation of PPAR δ -expressing PC3 cells in the flank of immunocompromised mice resulted in reduced tumor growth rate and mass (Fig. 1K and L). It is worth noting a recent report that presented evidence of positive regulation of caveolin-1 (CAV1) downstream PPAR δ leading to prostate cancer growth (22). However, we could not corroborate the biological nor the molecular results reported (Fig. 1; Supplementary Fig. S1N–S1P). Taken together, our results reveal that PPAR δ expression decreased the aggressiveness of prostate cancer cells *in vitro* and *in vivo*, in line with the decrease in *PPARD* expression observed in human prostate cancer specimens.

The prostate tumor suppressive activity of PPAR δ is ligand independent

PPARs exist in ligand-free and ligand-bound states. Unliganded PPARs have been reported to operate as a transcriptional repressor through the interaction with histone deacetylase complexes (HDAC), whereas ligand binding favors the release of HDACs and the interaction with histone acetyltransferases (HAT), leading to transcriptional activation (9, 23). One of the biochemical routes regulated by the transcriptional program downstream PPAR δ is FAO (24, 25). We evaluated the expression of canonical PPAR δ target genes (*ADFP*, *ANGPTL4*, *PKD4*; ref. 26) and FAO. Interestingly, endogenous *PPARD* silencing increased both readouts (Fig. 2A and B, Supplementary Fig. S2A). Conversely, PPAR δ overexpression in PC3 and LNCaP cells reduced the expression of these targets (Fig. 2C; Supplementary Fig. S2B–S2F) and inhibited FAO (Fig. 2D). We sought to validate these results in human specimens. Taking advantage of the previously presented sample set (Fig. 1A), we evaluated the mRNA levels of the aforementioned PPAR δ targets and observed a significant upregulation (Fig. 2E–G). Furthermore, the negative correlation of PPAR δ with these targets and the strong correlation among themselves supported the repressive activity reported *in vitro* (Fig. 2H–J; Supplementary Table S3). These results indicate that PPAR δ functions as a transcriptional repressor in prostate cancer probably owing to the lack of endogenous ligands in sufficient concentration, in agreement with other reports (27).

To ascertain whether ligand-bound PPAR δ would switch to a transcriptional activator mode in prostate cancer, we treated control or *PPARD*-expressing PC3 cells with the synthetic agonist GW501516 (GW; ref. 24). GW treatment did not alter *PPARD* levels (Supplementary Fig. S2G) but switched the activity on its canonical targets from transcriptional repression to activation (Fig. 2K), which was accompanied by elevation of FAO (Fig. 2L). These results were validated with structurally unrelated synthetic PPAR δ ligands (Supplementary Fig. S2H–S2J). Of note, the direct regulation of these target genes by PPAR δ was confirmed by ChIP analysis (Supplementary Fig. S2K–S2M).

Our results show that canonical PPAR δ target regulation switches from transcriptional repression to activation based on

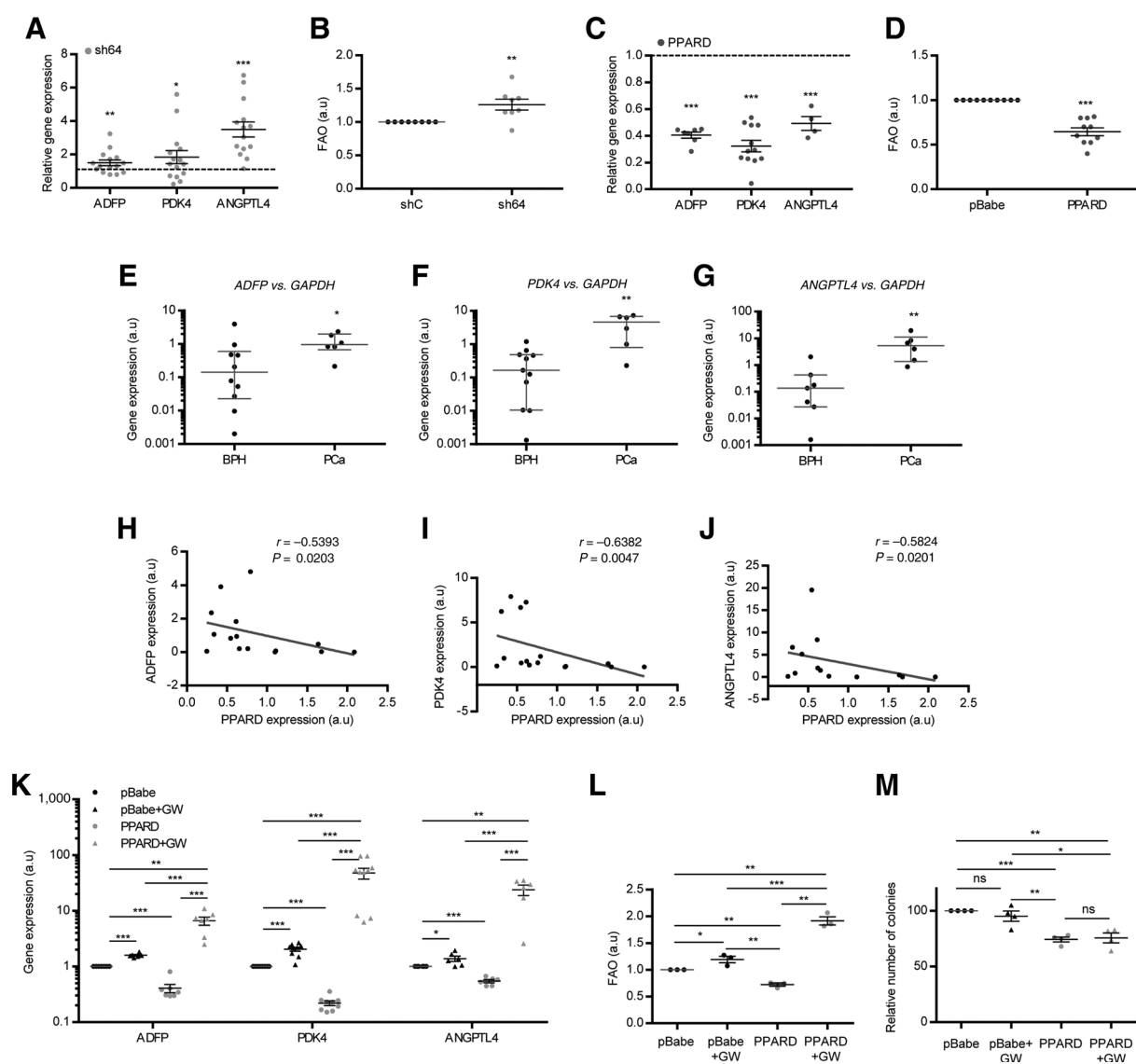
ligand availability. Because we have shown that PPAR δ opposes prostate cancer growth, we asked whether PPAR δ agonists would also revert this tumor suppressive activity. Strikingly, PPAR δ -expressing PC3 cells treated with GW did not recover their ability to grow in anchorage-independent conditions (Fig. 2M). Overall, our results strongly suggest that the tumor suppressive activity of PPAR δ in prostate cancer relies on an unprecedented ligand-independent function of the nuclear receptor.

The prostate tumor suppressive activity of PPAR δ is DNA binding dependent

Because PPAR δ regulates the vast majority of its biological activities through binding to DNA, we next studied to which extent the DNA binding capacity of this nuclear receptor was required for its biological activity. We generated a DNA binding mutant (DNA^{mut}) PPAR δ (16), which we transduced into PC3 cells. As predicted, PPAR δ -DNA^{mut} failed to mimic the activity of its WT counterpart on the regulation of canonical targets and FAO (Supplementary Fig. S3A–S3E). With regard to the biological activity, PPAR δ -DNA^{mut} did not reduce soft-agar colony formation nor invasive growth (Fig. 3A and B). *In vivo*, PPAR δ -DNA^{mut} expressing PC3 cells did not exhibit reduced tumor growth rate and mass compared with empty-vector transduced cells, and showed a significant recovery in these parameters compared with WT PPAR δ -expressing counterparts (Fig. 3C and D). These data show that the tumor suppressive activity of PPAR δ , which we report to be ligand independent, requires binding of the nuclear receptor to DNA.

PPAR δ represses trefoil factor family gene expression to inhibit prostate cancer aggressiveness

Our results reveal that PPAR δ exerts a tumor suppressive activity that is ligand-independent and DNA-binding dependent. Thus, we developed an experimental design to identify the transcriptional targets of this nuclear factor that would be potentially associated with this biological activity (Fig. 4A), based on two premises: (i) that their expression is regulated in PPAR δ overexpressing cells; (ii) that the type of regulation elicited by PPAR δ is not reverted in the presence of an agonist (thus ligand independent). On the one hand, we performed transcriptomics analysis with empty-vector transduced PC3 cells and *PPARD*-expressing counterparts. From this comparison, we focused on PPAR δ -regulated genes. On the other hand, this approach was carried out with *PPARD*-expressing cells in the absence or presence of GW, which would allow us to rule out those genes regulated upon ligand binding. We therefore selected genes that presented a significant difference in expression upon PPAR δ expression (PC3-*PPARD* vs. PC3-pBabe, $P < 0.05$; $-1.5 > \text{fold change} > 1.5$) that was retained also upon ligand treatment (PC3-*PPARD* + GW vs. PC3-pBabe, $P < 0.05$; $-1.5 > \text{fold change} > 1.5$) as illustrated in Fig. 4A. This analysis led to the identification of candidate genes to mediate the ligand-independent activity of PPAR δ . Surprisingly, the TFF stood among the top 10 genes downregulated by PPAR δ , which expression was not reverted by ligand treatment (Fig. 4B and Supplementary Table S4). We validated the repression of *TFF1* and 3 upon *PPARD* expression by real-time quantitative PCR, whereas *TFF2* expression was at the limit of detection (Fig. 4C; Supplementary Fig. S4A). As predicted from the experimental design, the repression of *TFF1* and 3 elicited by PPAR δ expression was not reverted by the treatment with structurally unrelated ligands of the nuclear receptor (Fig. 4C;

**Figure 2.**

PPARδ tumor suppressive activity is ligand independent. **A**, Expression of *PPARδ* canonical target genes ($n = 15$) upon *PPARδ* silencing with a short hairpin (sh64) in DU145 cells. **B**, Effect of *PPARδ* silencing on FAO ($n = 8$) in DU145 cells. **C**, Expression of *PPARδ* canonical target genes ($n = 15$) upon *PPARδ* ectopic expression in PC3 cells. **D**, Effect of *PPARδ* ectopic expression cells on FAO ($n = 10$) in PC3 cells. **E-G**, *PPARδ* target gene expression, *ADFP* (**E**), *PDK4* (**F**), and *ANGPTL4* (**G**) in prostate cancer (PCa; $n = 16$) and benign prostate hyperplasia (BPH; $n = 11$) patients. **H-J**, Correlation analysis of *PPARδ* expression with *ADFP* ($n = 15$; **H**), *PDK4* ($n = 16$; **I**), and *ANGPTL4* ($n = 13$; **J**) in prostate tissue used in **E-G** and Fig. 1A. **K-M**, Effect of *PPARδ* synthetic ligand GW506015 (GW, 0.1 $\mu\text{mol/L}$, 48 hours) on *PPARδ* canonical target genes expression (*ADFP*, $n = 7$; *PDK4*, $n = 10$; *ANGPTL4*, $n = 6$; **K**), on FAO ($n = 3$; **L**), and on anchorage-independent growth ($n = 4$; **M**) upon *PPARδ* ectopic expression in PC3 cells. Error bars, SEM. *, $P < 0.05$; **, $P < 0.01$; ***, $P < 0.001$ compared with control. Statistics test: one sample t test when compared with control (**A-D** and **K-M**) and Student t test in two-component comparisons (**K-M**), one-tailed Mann-Whitney U test (**E-G**), and Spearman correlation (**H-J**). shC, scramble shRNA; a.u., arbitrary units.

Supplementary Fig. S4A–S4C). Conversely, *PPARδ* silencing in DU145 cells resulted in increased *TFF1* expression (Fig. 4D). Importantly, *TFF1* and 3 were significantly upregulated in our cohort of prostate cancer specimens compared with benign prostate hyperplasia (Fig. 4E; Supplementary Fig. S4D). Deeper analysis of *PPARδ* and *TFF* expression in patient-derived specimens revealed a significant inverse correlation between the expression of the nuclear factor and *TFF1*, but not *TFF3* (Fig. 4F; Supplementary Fig. S4E).

Our data show that *PPARδ* regulates the expression of *TFFs* in a ligand-independent manner. To elucidate whether this effect was direct on the promoter of the candidate genes, we performed ChIP with HA-tagged *PPARδ* (Supplementary Fig. S4F and S4G). The analysis showed that this nuclear factor binds to the proximal region of *TFF1* and also to a large region of the *TFF3* promoter (Fig. 4G; Supplementary Fig. S4H). It is worth noting that the distal R6 region of *TFF1* promoter did not exhibit any significant *PPARδ* binding, thus acting as an internal negative control of the assay.

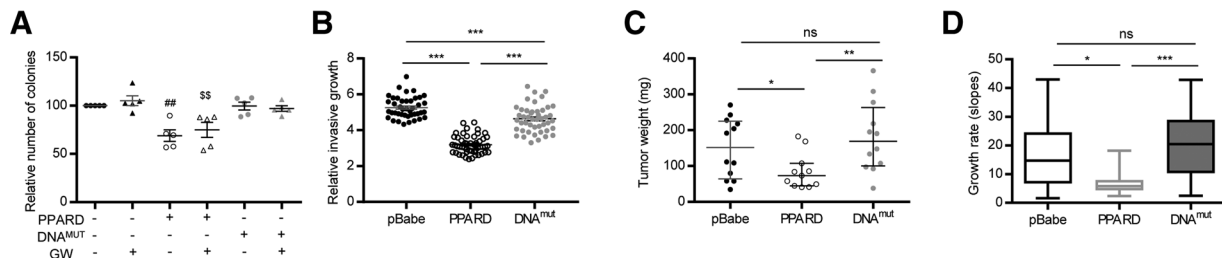


Figure 3. PPAR δ acts as a *cis* transcriptional repressor. **A**, Effect of PPAR δ synthetic ligand GW506015 (GW, 0.1 μ mol/L, 48 hours) on anchorage independent growth ($n = 5$) upon *PPAR* and *PPAR* DNA^{mut} (DNA^{mut}) ectopic expression in PC3 cells. **B–D**, Effect of *PPAR* DNA^{mut} on the invasive growth capacity ($n = 3$, in which in each individual experiment, a mean of 20 colonies was counted and is represented in **B**), on tumor weight (**C**), and tumor growth rate ($n = 3$ mice; four injections per mouse; **D**) upon *PPAR* and *PPAR* DNA^{mut} (DNA^{mut}) ectopic expression in PC3 cells. Error bars, SEM. *, $P < 0.05$; **, $P < 0.01$; ***, $P < 0.001$ as indicated; #, compared with pBabe; \$, compared with pBabe + GW. Statistics test: one sample *t* test when compared with control (**A**) and Student *t* test in two-component comparisons (**A**) and one-tailed Mann-Whitney *U* test (**B–D**). ns, not significant.

TFFs are secreted proteins that act on cellular signaling through poorly defined mechanisms (28). In order to elucidate the contribution of *TFF1* to prostate cancer, we overexpressed *TFF1* in DU145 cells using an inducible (TRIPZ-TFF1) viral vector (Supplementary Fig. S5A and S5B) and observed increased soft-agar

colony formation *in vitro* (Fig. 5A) and tumor growth rate and mass *in vivo* (Fig. 5B and C).

Next, we ascertained the requirements of TFF1 regulation for the tumor suppressive activity of PPAR δ . On the one hand, we treated *PPAR*-expressing cells with recombinant human TFF1

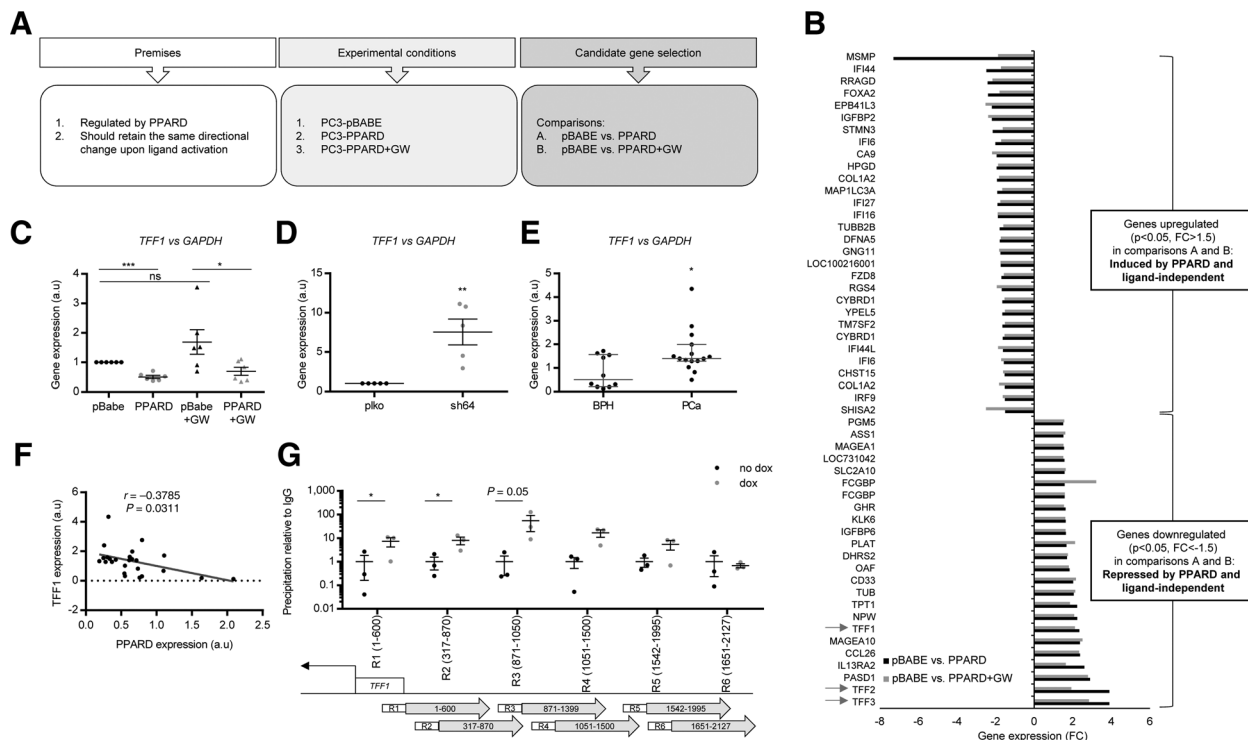


Figure 4. PPAR δ represses TFF1 independently of ligand. **A**, Data processing diagram from the microarray analysis carried out in pBabe, *PPAR*, and *PPAR* + GW (0.1 μ mol/L, 48 hours) PC3 cells ($n = 3$ per group). **B**, Fold change (FC) expression of PPAR δ upregulated and downregulated genes independently of ligand obtained in **A**. Arrows, members of the *TFF*. **C**, Effect of PPAR δ synthetic ligand GW506015 (GW, 0.1 μ mol/L, 48 hours) on *TFF1* gene expression ($n = 6$) in PC3 cells upon *PPAR* ectopic expression. **D**, *TFF1* gene expression ($n = 5$) upon *PPAR* silencing with a short hairpin (sh64) in DU145 cells. **E**, *TFF1* gene expression in prostate cancer (PCa; $n = 15$) and benign prostate hyperplasia (BPH; $n = 10$) patients. **F**, Correlation analysis of *TFF1* and *PPAR* gene expression in cancer and benign prostate hyperplasia patients ($n = 25$). **G**, ChIP of exogenous HA-PPAR on *TFF1* promoter using HA-tag antibody in PC3 cells after induction with 0.5 μ g/mL doxycycline for 3 days ($n = 3$). Data were normalized to IgG (negative-binding control). Bottom, the different regions (R1–R6) chosen for the analysis of PPAR occupancy. R6, negative binding control. Error bars, SEM. *, $P < 0.05$; ***, $P < 0.001$ compared with control. Statistics test: one sample *t* test when compared with control (**C** and **D**) and Student *t* test in two-component comparisons (**C**), one-tailed Mann-Whitney *U* test (**E**), Spearman correlation (**F**), and one-tailed Student *t* test (**G**). ns, not significant; a.u., arbitrary units; dox, doxycycline.

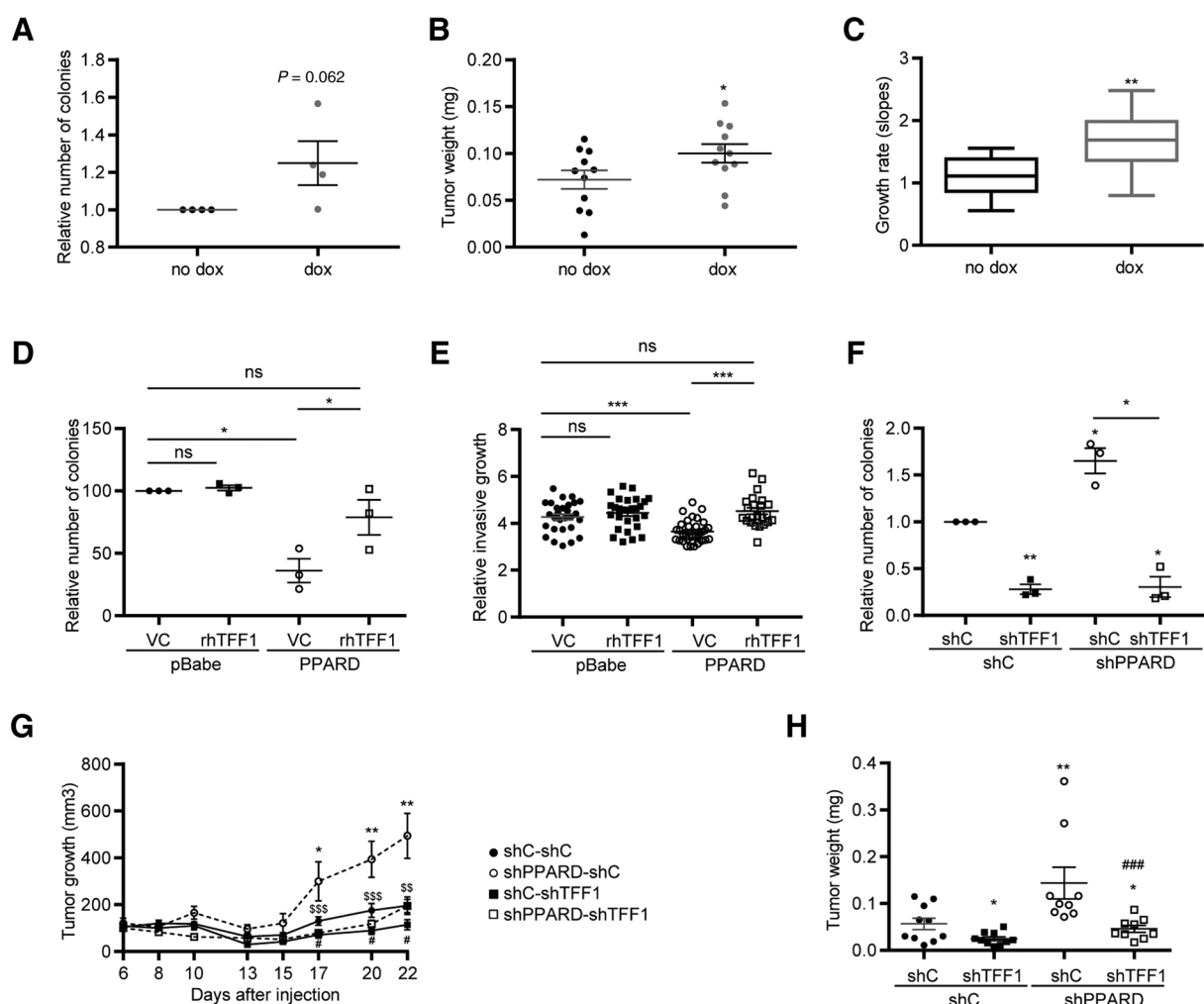


Figure 5.

TFF1 downregulation contributes to the tumor suppressive activity of PPAR δ in prostate cancer. **A**, Effect of *TFF1* ectopic expression (induction with 0.5 μ g/mL doxycyclin) in DU145 cells on anchorage-independent growth ($n = 4$). **B** and **C**, Effect of *TFF1* conditional overexpression in established prostate tumors of DU145 cells on tumor weight (**B**) and tumor growth rate ($n = 6$ mice; two injections per mouse; **C**). Doxycycline diet was given to the treatment group on day 12 after xenograft injection when tumors reached 100 mm 3 . **D** and **E**, Effect of recombinant human TFF1 protein (rhTFF1) on anchorage-independent growth ($n = 3$; **D**) and on the invasive growth capacity ($n = 3$; in each individual experiment, a mean of 10 colonies was counted and is represented in **E**) upon *PPAR Δ* ectopic expression in PC3 cells. **F–H**, Effect of *TFF1* silencing with a short hairpin (shTFF1) upon *PPAR Δ* silencing with a short hairpin (shPPAR Δ , previously identified as sh64) in DU145 cells *in vitro* on anchorage-independent growth ($n = 3$; **F**) and *in vivo* in tumor growth and mass ($n = 5$ mice; two flanks per mouse; **G** and **H**). shC, pLKO lentiviral vector expressing scramble shRNA; VC, vehicle control. Error bars, SEM; */#/\$, $P < 0.05$; **/###/\$\$, $P < 0.01$; ***/###/\$\$\$, $P < 0.001$. For **G**: *, shPPAR Δ -shC vs. shC-shC; #, shTFF1-shC vs. shC-shC; \$, shPPAR Δ -shC vs. shC-shC; for **H**: *, indicated condition vs. shC-shC; #, indicated condition vs. shPPAR Δ -shC. Statistics test: one-sample t test when compared with control (**A**, **D**, **F**) and Student t test in two-component comparisons (**D** and **F**), one-tailed Mann-Whitney U test (**B**, **C**, **E**, **G**, **H**); ns, not significant; a.u., arbitrary units; dox, doxycycline.

(rhTFF1) protein. As predicted, rhTFF1 partially rescued the defect of *PPAR Δ* -expressing cells in anchorage-independent growth (Fig. 5D) and invasive growth (Fig. 5E). On the other hand, we transduced DU145 cells carrying constitutive scramble or *PPAR Δ* shRNAs with *TFF1* shRNA-expressing lentivirus (or scramble shRNA expressing controls; the efficacy of *TFF1* silencing was tested in the TFF1 high-expressing PC3 cell line; Supplementary Fig. S5C and S5D). The results confirmed that *TFF1*-silenced cells exhibited reduced colony forming ability and tumor growth, and, importantly, failed to show the elevation in this parameter elicited by *PPAR Δ* shRNA (Fig. 5F–H). Overall, our data provide evidence of a tumor suppressive

activity of PPAR δ stemming from the ligand-independent regulation of TFF1 in prostate cancer.

Discussion

The physiological activity of PPAR δ has been described in great detail (9–11). However, its role in cancer remains controversial. In addition, conclusions of PPAR δ activity based on the use of synthetic agonists have added complexity to its biological activity. It has been reported that activation of PPAR δ by synthetic ligands such as GW501516 or GW0742 promotes oncogenesis in prostate, thyroid, breast cancer, or liposarcoma cells, whereas

antagonizing PPAR δ inhibits tumorigenesis in lung, liver, breast, or prostate cell lines (29–31). Conversely, various studies have demonstrated that the activation of PPAR δ by agonists reverts or inhibits tumorigenesis in colorectal, liver, skin, breast, testicular, pancreatic cancer, or neuroblastoma cells (32–39), in line with the notion that the deregulation of this nuclear receptor promotes oncogenesis in *Ppard*-deficient mice and colorectal cancer cells (40, 41). The expression status of PPAR δ in cancer has been evaluated by different groups with contrasting results, which may be related to the tissue of origin and the method for quantification of *PPARD* levels (42–44). Importantly, the publication of the Human Protein Atlas portal (44) allowed a comprehensive analysis of PPAR δ protein expression in different tissues and demonstrated a lower expression of this nuclear receptor in prostate, colorectal, urethral, liver, breast or ovarian cancer, among others. Our results provide evidence for a decrease of PPAR δ expression in prostate cancer that has consequences on the biology of the disease, suggesting that tumor suppression could be a major role for this nuclear receptor in the prostate epithelium.

The vast majority of effects elicited by PPAR δ depend on specific ligands binding to the ligand binding domain (LBD) of the nuclear factor (9). However, recent studies report transcriptional activity of PPAR δ that does not require ligand challenge. First, PPAR δ -regulated transcriptional repression of *ANGPTL4* mediates tumor suppression in breast cancer (27). Interestingly, the authors identify in this study 105 genes that are sensitive to *PPARD* silencing but not to the effect of agonists or inverse agonists. Second, an extensive study on the transcriptional regulation by PPAR δ in keratinocytes identified different modes of action of this nuclear receptor (13). Importantly, a significant number of genes in this study presented a regulation by PPAR δ that was constitutive and ligand independent, suggesting that this factor could cross-talk with other transcriptional regulators (13). Our results provide evidence for a repressive and ligand-independent activity of PPAR δ in prostate cancer that drives tumor suppression.

The TFF comprises three members that were identified as secreted factors produced by cells in mucosa. Interestingly, the function of TFFs has been related to inflammation, proliferation, and invasiveness, and these factors have been categorized as growth factor-like molecules. The alteration of TFF expression has been widely studied and reviewed (28, 45), and there is an overall consensus that these proteins are overexpressed in tumors, with a few exceptions. In prostate cancer TFF1 and 3 are upregulated and have been proposed as tissue and body fluid cancer biomarkers (46–52). Moreover, experimental evidence demonstrate that expression of TFF1 and 3 in prostate cancer increases oncogenicity by means of proliferation, survival, anchorage-independent growth, and invasiveness (53, 54), which we validate in our experimental systems *in vitro* and *in vivo*. Yet, little is known about their regulation. The upregulation has been addressed at different levels, and hypomethylation of the promoter has been postulated as a mechanism in prostate cancer (45, 55). Our results show that PPAR δ is a negative regulator of TFF expression, which could contribute the upregulation of TFFs observed in prostate cancer.

TFF regulation by PPAR δ in a ligand-independent manner would allow the uncoupling of its ligand-dependent physiological activities from tumor-suppressive constitutive functions of the nuclear factor. This new perspective opens new and exciting opportunities to elucidate the dualities of this family of nuclear receptors in cancer.

Disclosure of Potential Conflicts of Interest

No potential conflicts of interest were disclosed.

Authors' Contributions

Conception and design: N. Martín-Martín, A. Carracedo

Development of methodology: N. Martín-Martín, A. Zabala-Letona, V. Torrano, M. Unda, A.M. Aransay, R. Barrio, J.D. Sutherland, A. Carracedo

Acquisition of data (provided animals, acquired and managed patients, provided facilities, etc.): M. Castillo-Martín, A. Loizaga-Iriarte, M. Unda, A.M. Aransay

Analysis and interpretation of data (e.g., statistical analysis, biostatistics, computational analysis): N. Martín-Martín, A.R. Cortazar, V. Torrano, A.M. Aransay, A. Carracedo

Writing, review, and/or revision of the manuscript: N. Martín-Martín, A. Carracedo

Administrative, technical, or material support (i.e., reporting or organizing data, constructing databases): A.R. Cortazar, P. Sanchez-Mosquera, A.M. Aransay

Study supervision: A. Carracedo

Other (contributed to *in vitro* and/or *in vivo* analysis): A. Zabala-Letona, L. Arreal, L. Camacho, P. Zuñiga-García, L. Valcarcel-Jimenez, A. Arruabarrena-Aristorena, M. Piva

Other (performed the histochemical staining and *in vitro* analyses): S. Fernandez-Ruiz

Other (mouse uropathology): M. Castillo

Other (human uropathology): A. Ugalde-Olano

Other (development of TFF1-related molecular tools): I. Astobiza

Other (co-supervision of L. Camacho): A. Gomez-Muñoz

Acknowledgments

Apologies to those whose related publications were not cited due to space limitations. N. Martín-Martín is supported by the Spanish Association Against Cancer (AECC), AECC JP Vizcaya. L. Arreal, A. Arruabarrena-Aristorena, and L. Valcarcel-Jimenez are supported by the Basque Government of Education. R. Barrio acknowledges Spanish MINECO (BFU2014-52282-P, Consolider BFU2014-57703-REDC), the Departments of Education and Industry of the Basque Government (PI2012/42) and the Bizkaia County. The work of A. Carracedo is supported by the Basque Department of Industry, Tourism and Trade (Etorrek) and the Department of Education (IKERTALDE IT1106-16, also participated by A. Gomez-Muñoz), the BBVA Foundation, the MINECO (SAF2016-79381-R (FEDER/EU); Severo Ochoa Excellence Accreditation (SEV-2016-0644) and the European Research Council (Starting Grant 336343, PoC 754627). CIBERONC was co-funded with FEDER funds. We are thankful to the Basque Biobank for Research (BIOEF) for the support in the acquisition and management of human specimens.

The costs of publication of this article were defrayed in part by the payment of page charges. This article must therefore be hereby marked *advertisement* in accordance with 18 U.S.C. Section 1734 solely to indicate this fact.

Received March 30, 2017; revised September 18, 2017; accepted November 14, 2017; published OnlineFirst November 29, 2017.

References

1. Vander Heiden MG, Cantley LC, Thompson CB. Understanding the Warburg effect: the metabolic requirements of cell proliferation. *Science* 2009;324:1029–33.
2. Torrano V, Valcarcel-Jimenez L, Cortazar AR, Liu X, Urošević J, Castillo-Martín M, et al. The metabolic co-regulator PGC1 α suppresses prostate cancer metastasis. *Nat Cell Biol* 2016;18:645–56.

3. Kypka R, Unda M, Carracedo A. Is the bench getting closer to the bedside in the war on cancer? A quick look at prostate cancer. *Front Endocrinol* 2012;3:53.
4. Braissant O, Foufelle F, Scotto C, Dauca M, Wahli W. Differential expression of peroxisome proliferator-activated receptors (PPARs): tissue distribution of PPAR- α , - β , and - γ in the adult rat. *Endocrinology* 1996;137:354–66.
5. Takahashi S, Tanaka T, Sakai J. New therapeutic target for metabolic syndrome: PPAR δ . *Endocr J* 2007;54:347–57.
6. Feige JN, Gelman L, Michalik L, Desvergne B, Wahli W. From molecular action to physiological outputs: peroxisome proliferator-activated receptors are nuclear receptors at the crossroads of key cellular functions. *Prog Lipid Res* 2006;45:120–59.
7. Varga T, Czimmerer Z, Nagy L. PPARs are a unique set of fatty acid regulated transcription factors controlling both lipid metabolism and inflammation. *Biochim Biophys Acta* 2011;1812:1007–22.
8. Glass CK, Ogawa S. Combinatorial roles of nuclear receptors in inflammation and immunity. *Nat Rev Immunol* 2006;6:44–55.
9. Peters JM, Shah YM, Gonzalez FJ. The role of peroxisome proliferator-activated receptors in carcinogenesis and chemoprevention. *Nat Rev Cancer* 2012;12:181–95.
10. Peters JM, Gonzalez FJ, Muller R. Establishing the role of PPAR β /delta in carcinogenesis. *Trends Endocrinol Metab* 2015;26:595–607.
11. Peters JM, Yao PL, Gonzalez FJ. Targeting peroxisome proliferator-activated receptor-beta/delta (PPAR β /delta) for cancer chemoprevention. *Curr Pharmacol Rep* 2015;1:121–8.
12. Adhikary T, Kaddatz K, Finkernagel F, Schonbauer A, Meissner W, Scharfe M, et al. Genome-wide analyses define different modes of transcriptional regulation by peroxisome proliferator-activated receptor-beta/delta (PPAR β /delta). *PLoS One* 2011;6:e16344.
13. Khozoe C, Borland MG, Zhu B, Baek S, John S, Hager GL, et al. Analysis of the peroxisome proliferator-activated receptor-beta/delta (PPAR β /delta) cistrome reveals novel co-regulatory role of ATF4. *BMC Genomics* 2012;13:665.
14. Morgenstern JP, Land H. Advanced mammalian gene transfer: high titre retroviral vectors with multiple drug selection markers and a complementary helper-free packaging cell line. *Nucleic Acids Res* 1990;18:3587–96.
15. Brun RP, Tontonoz P, Forman BM, Ellis R, Chen J, Evans RM, et al. Differential activation of adipogenesis by multiple PPAR isoforms. *Genes Dev* 1996;10:974–84.
16. Shi Y, Hon M, Evans RM. The peroxisome proliferator-activated receptor delta, an integrator of transcriptional repression and nuclear receptor signaling. *Proc Natl Acad Sci U S A* 2002;99:2613–8.
17. Carracedo A, Weiss D, Leliart AK, Bhasin M, de Boer VC, Laurent G, et al. A metabolic prosurvival role for PML in breast cancer. *J Clin Invest* 2012;122:3088–100.
18. Barak Y, Liao D, He W, Ong ES, Nelson MC, Olefsky JM, et al. Effects of peroxisome proliferator-activated receptor delta on placentation, adiposity, and colorectal cancer. *Proc Natl Acad Sci U S A* 2002;99:303–8.
19. Chen Z, Trotman LC, Shaffer D, Lin HK, Dotan ZA, Niki M, et al. Crucial role of p53-dependent cellular senescence in suppression of Pten-deficient tumorigenesis. *Nature* 2005;436:725–30.
20. Ugalde-Olano A, Egia A, Fernandez-Ruiz S, Loizaga-Iriarte A, Zuniga-Garcia P, Garcia S, et al. Methodological aspects of the molecular and histological study of prostate cancer: focus on PTEN. *Methods* 2015;77–78:25–30.
21. Rhodes DR, Yu J, Shanker K, Deshpande N, Varambally R, Ghosh D, et al. ONCOMINE: a cancer microarray database and integrated data-mining platform. *Neoplasia* 2004;6:1–6.
22. Her NG, Jeong SI, Cho K, Ha TK, Han J, Ko KP, et al. PPAR δ promotes oncogenic redirection of TGF- β 1 signaling through the activation of the ABCA1-Cav1 pathway. *Cell Cycle* 2013;12:1521–35.
23. Evans RM, Barish GD, Wang YX. PPARs and the complex journey to obesity. *Nat Med* 2004;10:355–61.
24. Ito K, Carracedo A, Weiss D, Arai F, Ala U, Avigan DE, et al. A PML–PPAR δ pathway for fatty acid oxidation regulates hematopoietic stem cell maintenance. *Nat Med* 2012;18:1350–8.
25. Carracedo A, Cantley LC, Pandolfi PP. Cancer metabolism: fatty acid oxidation in the limelight. *Nat Rev Cancer* 2013;13:227–32.
26. Peters JM, Foreman JE, Gonzalez FJ. Dissecting the role of peroxisome proliferator-activated receptor-beta/delta (PPAR β /delta) in colon, breast, and lung carcinogenesis. *Cancer Metastasis Rev* 2011;30:619–40.
27. Adhikary T, Brandt DT, Kaddatz K, Stockert J, Naruhn S, Meissner W, et al. Inverse PPAR β /delta agonists suppress oncogenic signaling to the ANGPTL4 gene and inhibit cancer cell invasion. *Oncogene* 2013;32:5241–52.
28. Kjellev S. The trefoil factor family - small peptides with multiple functionalities. *Cell Mol Life Sci* 2009;66:1350–69.
29. Stephen RL, Gustafsson MC, Jarvis M, Tatoud R, Marshall BR, Knight D, et al. Activation of peroxisome proliferator-activated receptor delta stimulates the proliferation of human breast and prostate cancer cell lines. *Cancer Res* 2004;64:3162–70.
30. Wagner KD, Benchetrit M, Bianchini L, Michiels JF, Wagner N. Peroxisome proliferator-activated receptor beta/delta (PPAR β /delta) is highly expressed in liposarcoma and promotes migration and proliferation. *J Pathol* 2011;224:575–88.
31. Zeng L, Geng Y, Tretiakova M, Yu X, Sicinski P, Kroll TG. Peroxisome proliferator-activated receptor-delta induces cell proliferation by a cyclin E1-dependent mechanism and is up-regulated in thyroid tumors. *Cancer Res* 2008;68:6578–86.
32. Bility MT, Devlin-Durante MK, Blazantin N, Glick AB, Ward JM, Kang BH, et al. Ligand activation of peroxisome proliferator-activated receptor beta/delta (PPAR beta/delta) inhibits chemically induced skin tumorigenesis. *Carcinogenesis* 2008;29:2406–14.
33. Coleman JD, Thompson JT, Smith RW 3rd, Prokopczyk B, Vanden Heuvel JP. Role of peroxisome proliferator-activated receptor beta/delta and B-cell lymphoma-6 in regulation of genes involved in metastasis and migration in pancreatic cancer cells. *PPAR Res* 2013;2013:121956.
34. Foreman JE, Sharma AK, Amin S, Gonzalez FJ, Peters JM. Ligand activation of peroxisome proliferator-activated receptor-beta/delta (PPAR β /delta) inhibits cell growth in a mouse mammary gland cancer cell line. *Cancer Lett* 2010;288:219–25.
35. Harman FS, Nicol CJ, Marin HE, Ward JM, Gonzalez FJ, Peters JM. Peroxisome proliferator-activated receptor-delta attenuates colon carcinogenesis. *Nat Med* 2004;10:481–3.
36. Hollingshead HE, Killins RL, Borland MG, Cirroir EE, Billin AN, Willson TM, et al. Peroxisome proliferator-activated receptor-beta/delta (PPAR-beta/delta) ligands do not potentiate growth of human cancer cell lines. *Carcinogenesis* 2007;28:2641–9.
37. Yao PL, Chen L, Dobrzanski TP, Zhu B, Kang BH, Muller R, et al. Peroxisome proliferator-activated receptor-beta/delta inhibits human neuroblastoma cell tumorigenesis by inducing p53- and SOX2-mediated cell differentiation. *Mol Carcinog* 2017;56:1472–83.
38. Yao PL, Chen LP, Dobrzanski TP, Phillips DA, Zhu B, Kang BH, et al. Inhibition of testicular embryonal carcinoma cell tumorigenicity by peroxisome proliferator-activated receptor-beta/delta- and retinoic acid receptor-dependent mechanisms. *Oncotarget* 2015;6:36319–37.
39. Yao PL, Morales JL, Zhu B, Kang BH, Gonzalez FJ, Peters JM. Activation of peroxisome proliferator-activated receptor-beta/delta (PPAR-beta/delta) inhibits human breast cancer cell line tumorigenicity. *Mol Cancer Ther* 2014;13:1008–17.
40. Muller-Brusselbach S, Ebrahimsade S, Jakes J, Eckhardt J, Rapp UR, Peters JM, et al. Growth of transgenic RAF-induced lung adenomas is increased in mice with a disrupted PPAR β /delta gene. *Int J Oncol* 2007;31:607–11.
41. Yang L, Olsson B, Pfeifer D, Jonsson JI, Zhou ZC, Jiang X, et al. Knockdown of peroxisome proliferator-activated receptor-beta induces less differentiation and enhances cell-fibronectin adhesion of colon cancer cells. *Oncogene* 2010;29:516–26.
42. He TC, Chan TA, Vogelstein B, Kinzler KW. PPAR δ is an APC-regulated target of nonsteroidal anti-inflammatory drugs. *Cell* 1999;99:335–45.
43. Modica S, Gofflot F, Murzilli S, D'Orazio A, Salvatore L, Pellegrini F, et al. The intestinal nuclear receptor signature with epithelial localization patterns and expression modulation in tumors. *Gastroenterology* 2010;138:636–48, 48 e1–12.
44. Uhlen M, Fagerberg L, Hallstrom BM, Lindskog C, Oksvold P, Mardinoglu A, et al. Proteomics. Tissue-based map of the human proteome. *Science* 2015;347:1260419.
45. Busch M, Dunker N. Trefoil factor family peptides—friends or foes? *Biomol Concepts* 2015;6:343–59.

46. Abdou AG, Aiad HA, Sultan SM. pS2 (TFF1) expression in prostate carcinoma: correlation with steroid receptor status. *APMIS* 2008;116:961–71.
47. Faith DA, Isaacs WB, Morgan JD, Fedor HL, Hicks JL, Mangold IA, et al. Trefoil factor 3 overexpression in prostatic carcinoma: prognostic importance using tissue microarrays. *Prostate* 2004;61:215–27.
48. Garraway IP, Seligson D, Said J, Horvath S, Reiter RE. Trefoil factor 3 is overexpressed in human prostate cancer. *Prostate* 2004;61:209–14.
49. Liu M, Jin RS. [Expressions of TFF1 and TFF3 in prostate cancer and prostatic intraepithelial neoplasia and their clinical significance]. *Zhonghua Nan Ke Xue* 2015;21:315–9.
50. Park K, Chiu YL, Rubin MA, Demichelis F, Mosquera JM. V-ets erythroblastosis virus E26 oncogene homolog (avian)/Trefoil factor 3/high-molecular-weight cytokeratin triple immunostain: a novel tissue-based biomarker in prostate cancer with potential clinical application. *Hum Pathol* 2013;44:2282–92.
51. Terry S, Nicolaiew N, Basset V, Semprez F, Soyeux P, Maille P, et al. Clinical value of ERG, TFF3, and SPINK1 for molecular subtyping of prostate cancer. *Cancer* 2015;121:1422–30.
52. Vestergaard EM, Borre M, Poulsen SS, Nexø E, Tørring N. Plasma levels of trefoil factors are increased in patients with advanced prostate cancer. *Clin Cancer Res* 2006;12:807–12.
53. Bougen NM, Amiry N, Yuan Y, Kong XJ, Pandey V, Vidal LJ, et al. Trefoil factor 1 suppression of E-CADHERIN enhances prostate carcinoma cell invasiveness and metastasis. *Cancer Lett* 2013;332:19–29.
54. Perera O, Evans A, Pertziger M, MacDonald C, Chen H, Liu DX, et al. Trefoil factor 3 (TFF3) enhances the oncogenic characteristics of prostate carcinoma cells and reduces sensitivity to ionising radiation. *Cancer Lett* 2015;361:104–11.
55. Vestergaard EM, Nexø E, Tørring N, Borre M, Orntoft TF, Sørensen KD. Promoter hypomethylation and upregulation of trefoil factors in prostate cancer. *Int J Cancer* 2010;127:1857–65.

Low-dose statin treatment increases prostate cancer aggressiveness

Alfredo Caro-Maldonado¹, Laura Camacho^{1,2,*}, Amaia Zabala-Letona^{1,3,*}, Verónica Torrano^{1,3}, Sonia Fernández-Ruiz^{1,3}, Kepa Zamacola-Bascaran¹, Leire Arreal¹, Lorea Valcárcel-Jiménez¹, Natalia Martín-Martín^{1,3}, Juana M. Flores⁴, Ana R. Cortazar¹, Patricia Zúñiga-García¹, Amaia Arruabarrena-Aristorena¹, Fabienne Guillaumond^{5,6,7,8}, Diana Cabrera¹, Juan M. Falcón-Perez^{1,9,10}, Ana M. Aransay^{1,9}, Antonio Gomez-Muñoz², Mireia Olivan¹¹, Juan Morote¹¹ and Arkaitz Carracedo^{1,2,3,10}

¹ CIC bioGUNE, Bizkaia Technology Park, Derio, Spain

² Biochemistry and Molecular Biology Department, University of the Basque Country, Bilbao, Spain

³ CIBERONC, Madrid, Spain

⁴ Department of Animal Medicine and Surgery, School of Veterinary Medicine, Complutense University of Madrid, Madrid, Spain

⁵ Centre de Recherche en Cancérologie de Marseille, U1068, Institut National de la Santé et de la Recherche Médicale, Paris, France

⁶ Institut Paoli-Calmettes, Marseille, France

⁷ UMR 7258, Centre National de la Recherche Scientifique, Paris, France

⁸ Université Aix-Marseille, Marseille, France

⁹ Centro de Investigación Biomédica en Red de Enfermedades Hepáticas y Digestivas, Madrid, Spain

¹⁰ IKERBASQUE, Basque foundation for science, Bilbao, Spain

¹¹ Department of Urology and Research Group in Urology, Vall d'Hebron Hospital, Vall d'Hebron Research Institute, and Universitat Autònoma de Barcelona, Barcelona, Spain

* These authors have contributed equally to this work

Correspondence to: Arkaitz Carracedo, **email:** acaracedo@cicbiogune.es

Keywords: prostate cancer; statins; cholesterol; obesity; mouse models

Received: July 13, 2017

Accepted: October 13, 2017

Published: October 31, 2017

Copyright: Caro-Maldonado et al. This is an open-access article distributed under the terms of the Creative Commons Attribution License 3.0 (CC BY 3.0), which permits unrestricted use, distribution, and reproduction in any medium, provided the original author and source are credited.

ABSTRACT

Prostate cancer is diagnosed late in life, when co-morbidities are frequent. Among them, hypertension, hypercholesterolemia, diabetes or metabolic syndrome exhibit an elevated incidence. In turn, prostate cancer patients frequently undergo chronic pharmacological treatments that could alter disease initiation, progression and therapy response. Here we show that treatment with anti-cholesterolemic drugs, statins, at doses achieved in patients, enhance the pro-tumorigenic activity of obesogenic diets. In addition, the use of a mouse model of prostate cancer and human prostate cancer xenografts revealed that *in vivo* simvastatin administration alone increases prostate cancer aggressiveness. *In vitro* cell line systems supported the notion that this phenomenon occurs, at least in part, through the direct action on cancer cells of low doses of statins, in range of what is observed in human plasma. In sum, our results reveal a prostate cancer experimental system where statins exhibit an undesirable effect, and warrant further research to address the relevance and implications of this observation in human prostate cancer.

INTRODUCTION

The initiation, progression and therapeutic eradication of cancer is largely associated to the evolving mutational landscape of the tumor [1]. However, tissue-specific factors, the tumor microenvironment and the immune activation status are determinant factors of cancer cell survival and progression [2]. Critically, systemic metabolic alterations, nutrition, obesity and comorbidity-derived long-term therapies in elderly population shape the incidence and aggressiveness of cancer in our society [3-6]. Prostate cancer (PCa) is among the most frequent tumor type in men, and the main risk factors include family history, race and age [7]. Importantly, due to its predominant diagnosis in men above 60 years old, comorbidities are frequent. These include obesity, metabolic syndrome, arterial hypertension and diabetes [8]. In turn, PCa patients at the time of diagnosis are commonly subject to chronic therapies. Anti-hypercholesterolemic treatment is prescribed to millions of individuals around the globe in the form of statins, and their benefits and harms have been studied [9]. Due to their extensive and chronic use, it is of the utmost importance to carefully evaluate the impact of this long-term therapy on the biology of cancer, at doses and administration modes achieved in human subjects. In this study, we evaluated the impact of statin treatment in the pathogenesis and progression of PCa. Through the use of PCa mouse models, cellular systems and observational studies in patients we demonstrate that treatment with these compounds is associated to increased aggressive features in this disease.

RESULTS

Anti-hypercholesterolemic treatments are often prescribed in the context of overweight or obesity [16]. Therefore, in order to evaluate the impact of statins (the main family of anticholesterolemic compounds, inhibitors of the mevalonate pathway enzyme Hydroxymethyl glutaryl CoA reductase - HMGCR) in PCa biology, we first evaluated the effect of statin exposure in the context of obesity in *Pten* prostate-specific heterozygous mice (*Pten*^{pc+/-}), which exhibit a weak, non-cancerous phenotype [10, 17]. We focused on the predominant statin used in the clinic, simvastatin. It is worth noting that the hydrophilic nature differs among statins, which could lead to distinct biological consequences *in vivo* [18]. We queried the available bibliography (Supplementary Table 1) and determined a low dose of simvastatin with proven biological activity [19]. Simvastatin was loaded in food pellets and provided *ad libitum*, thus enabling the uptake of simvastatin in an administration mode and concentration comparable to human subjects, including the activation of the drug in the liver [20]. We established an experimental design in which we induced obesity by feeding the mice

with western diet (containing high fat and carbohydrates) [21], and once the obesity was achieved, simvastatin was loaded to the obesogenic diet (Figure 1a for experimental design). At the end of the experiment, the weight of the mice on western diet was significantly increased compared to mice on standard diet (45.44 ± 1.34 gr *versus* 40.72 ± 2.15 gr, $p = 0.04$), whereas simvastatin addition to western diet did not have an impact on this parameter (46.83 ± 1.05 gr, $p = 0.43$). The combination of obesity and statin treatment increased prostate mass (Figure 1b). At the histological level, obese *Pten*^{pc+/-} mice exhibited 50% incidence of prostate intraepithelial neoplasia (PIN) at 11 months of age, without the appearance of invasive carcinoma lesions (Figure 1c, d). Strikingly, simvastatin treatment administered after the onset of obesity (Figure 1a) led to invasive cancerous lesions with an incidence of 45%, a phenotype only achieved in this mouse model when both copies of *Pten* are lost in the prostate epithelium [10, 13] (Figure 1c, 1d). Molecular analysis of these prostates revealed that simvastatin treatment exacerbated cell proliferation, accounted by Ki67 positivity (Figure 1d, 1e). These results provide unprecedented evidence for an undesired consequence of the treatment with statins in obese individuals with genetic predisposition to develop PCa.

We next evaluated the impact of statin treatment on PCa initiation using a *Pten* prostate-specific knockout (*Pten*^{pc-/-}), which allows the study of proliferative burst under oncogenic signalling [13, 17]. Four-week statin treatment in *Pten*^{pc-/-} at the time of *Pten* excision and disease onset (8 weeks of age) resulted in an increased prostate mass and proliferation, without overt histological changes (Figure 2).

PCa initiation, progression and resistance to therapy depend on distinct molecular mechanisms. Advanced PCa is currently treated with androgen-deprivation therapy [22]. Previous reports have documented that *Pten*^{pc-/-} mice subject to orchiectomy exhibit overall pathological response [23]. Therefore, we performed surgical castration in order to address effects of statins on cancer cell biology beyond proliferation (Supplementary Figure 1a). In line with the undesirable effect of statin treatment observed in the other experimental systems, we observed a trend towards increased prostate mass and castration resistance in simvastatin-treated mice (Supplementary Figure 1b-d), in the absence of a significant alteration in cell proliferation (Supplementary Figure 1d, e).

In sum, the use of a faithful mouse model of PCa uncovers an unexpected effect of simvastatin that is associated to the increase of PCa cell proliferation, cancer initiation and resistance to therapy.

Our data provides evidence of the undesirable effect of simvastatin in murine PCa. To extrapolate these results to human PCa, we took advantage of a human PCa cell line, PC3, and evaluated the impact of simvastatin feeding on tumor growth in subcutaneous xenografts. In line

with our previous results, simvastatin fed mice exhibited significantly heightened tumor growth rate (Figure 3a).

Multiple reports have documented the antitumoral effect of statins *in vitro*. The majority of these studies rely on doses of these compounds in the micromolar range [24-45] (Supplementary Table 2). However, the concentration of statins found in plasma of patients subject to anti-cholesterolemic treatments is in the nM range [46]. Therefore, we sought to establish an *in vitro* experimental model that would recapitulate the concentration of statins achieved in patients. To this end, we first corroborated the reported effects of high simvastatin doses. Micromolar doses of simvastatin elicited an anti-proliferative and cytotoxic response in PCa cells (Supplementary Table 2; Supplementary Figure 2a,

b). Next, we designed an experimental approach aimed at ascertaining the cell autonomous biological consequences of low simvastatin doses in PCa cells. We pre-treated PC3 cells with 50 nM simvastatin for a minimum of 7 days, which did not result in any sign of toxicity in two-dimensional growth assays (Figure 3b, Supplementary Figure 2c). This treatment schedule did not affect cell migration (Supplementary Figure 2d), but surprisingly resulted in elevated self-renewal capacity and anchorage-independent growth (Figure 3c, 3d). Of note, the effect of simvastatin *in vitro* was recapitulated in other cell lines (LNCaP and 22RV1, Figure 3d) and with an alternative HMGCR inhibitor (fluvastatin, Supplementary Figure 2e). Moreover, moderate genetic inhibition of HMGCR with two independent doxycycline-inducible shRNAs

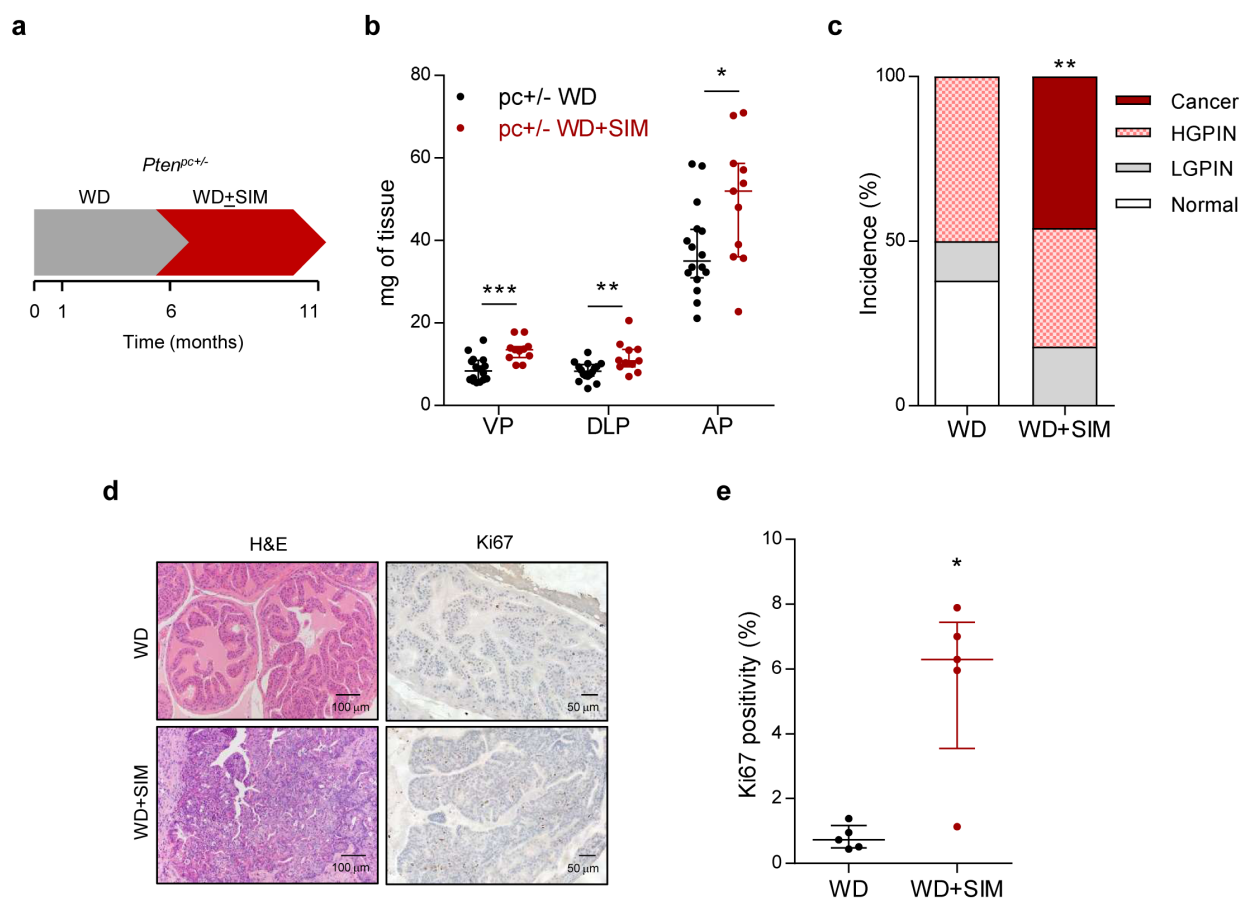


Figure 1: Simvastatin administration cooperates with obesogenic diets to drive prostate cancer. a. Schematic representation of the experimental design. 4-6 week-old prostate-specific *Pten*-heterozygous (*Pten*^{pc+/-}; *pc*^{+/-}) mice were fed with western diet (WD) to induce obesity. At 6 months of age, mice were randomly assigned to WD or WD loaded with simvastatin (WD + SIM) and fed for 5 months, and tissues were harvested and analysed. b. Prostate lobes weights of *Pten*-heterozygous (*Pten*^{pc+/-}; *pc*^{+/-}) mice fed with WD (*n* = 16) or WD + SIM (*n* = 11). VP, DLP, AP refer to ventral, dorsolateral and anterior prostates, respectively. c. Histopathological characterization of the prostate (Normal: no lesions; LGPIN: Low-grade prostatic intraepithelial neoplasia; HGPIN: High-grade prostatic intraepithelial neoplasia; Cancer: prostate adenocarcinoma) (WD, *n* = 16, WD+SIM, *n* = 11). d. Representative histological images of the prostate. Left, H&E (Haematoxylin-eosin) and right, Ki67 staining. WD shows non-cancerous tissue, WD+SIM shows adenocarcinoma. e. Quantification of Ki67 positive nuclei (%), indicating proliferating cells (WD, *n* = 5; WD SIM, *n* = 5). Statistical analysis: Mann-Whitney statistic test (b, e) and Chi Square test with 3 degree freedom (c). Error bars represent median with interquartile range. **p* < 0.05, ***p* < 0.01, ****p* < 0.001.

(Supplementary Figure 2f, g) elicited an effect comparable to simvastatin in anchorage-independent growth. Conversely, subtle HMGCR over-expression elicited the predicted opposing effect (Supplementary Figure 2f, h).

Since anchorage-independent growth and self-renewal capacity are required steps in tumor re-initiation and metastatic seeding [47], we evaluated whether PC3 cells treated for 7 days with 50 nM simvastatin would harbour elevated metastatic capacity. To this end, we injected PC3 cells pre-treated with vehicle or simvastatin in the tail vein of immunocompromised mice, and analysed the appearance of lung metastatic lesions (Supplementary Figure 2i right). Simvastatin treatment did not reduce metastatic burden, but rather resulted in increased rate of

lung metastasis, which did not reach statistical significance ($p = 0.1$) probably owing to the low number of mice (Supplementary Figure 2i). In sum, our results support the existence of a biological context where statin treatment could promote features of PCa aggressiveness.

The effect of statins could be associated to the alteration in major oncogenic signalling pathways sustaining PCa function. Therefore, we evaluated the levels and/or activity of androgen receptor (AR), Phosphoinositide 3-kinase (PI3K, using as a readout serine 473 phosphorylation of AKT) and mitogen activated protein kinase (MAPK, using as a readout tyrosine 202/204 phosphorylation of ERK - extracellular signal regulated kinase) in AR-expressing LNCaP (AR-

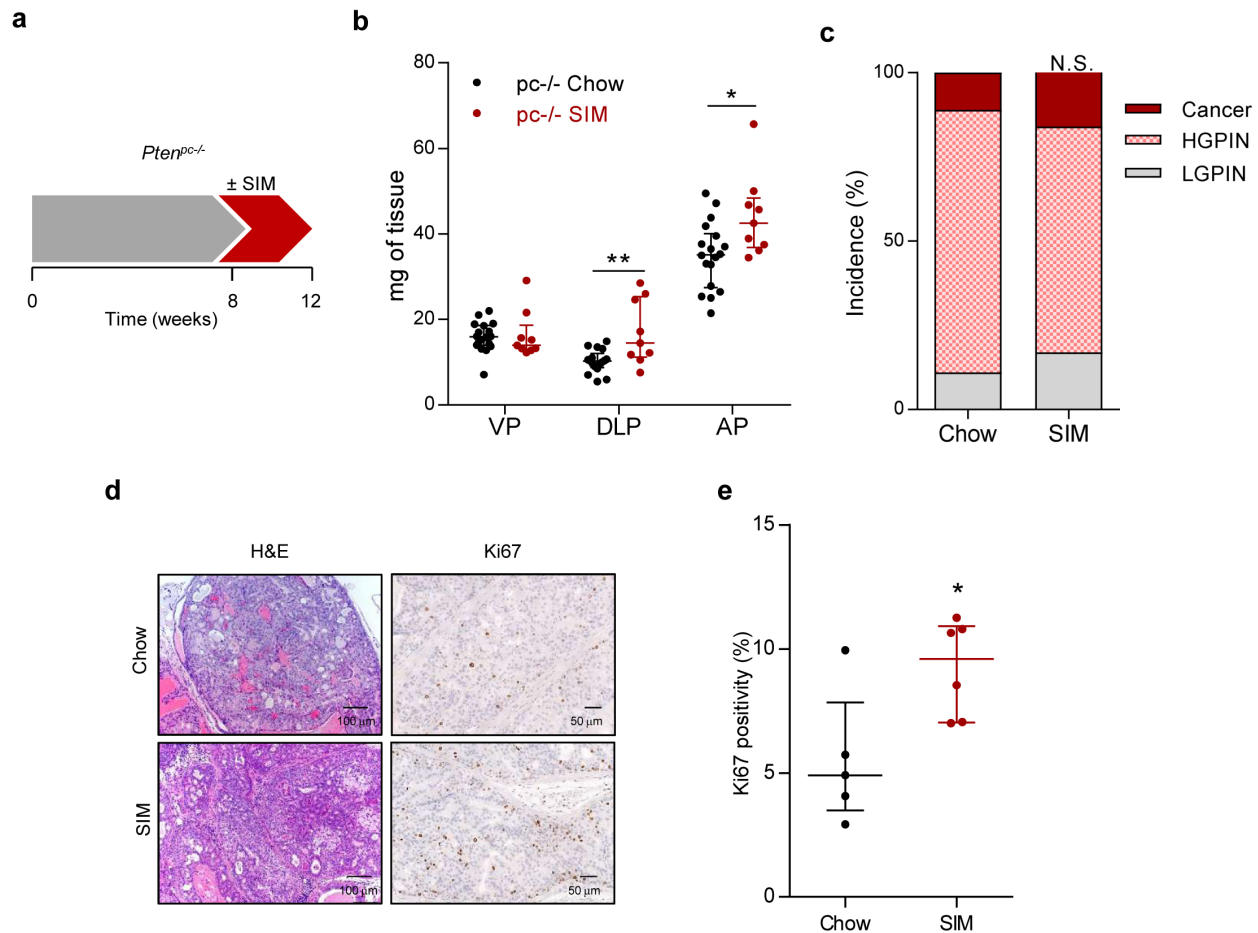


Figure 2: Simvastatin administration increases feature of aggressiveness in prostate cancer initiation. **a.** Schematic representation of the experimental design. 8 week-old *Pten*-deficient (*Pten^{pc-/-}*; *pc-/-*) mice were fed with simvastatin-loaded (SIM) diet or chow for four weeks, and tissues were harvested and analysed. **b.** Prostate lobe weights of *Pten*-deficient mice fed chow (*pc-/-* Chow, $n = 18$) and SIM diet (*pc-/-* SIM, $n = 9$). VP, DLP, AP refer to ventral, dorsolateral and anterior prostates respectively. **c.** Histopathological characterization of the prostate. (LGPIN: Low-grade prostatic intraepithelial neoplasia; HGPIN: High-grade prostatic intraepithelial neoplasia; Cancer: prostate adenocarcinoma) (Chow, $n = 9$; SIM, $n = 6$). **d.** Representative histological images of the prostate. Left, H&E (Haematoxylin-Eosin) and right, Ki67 staining, showing prostate intraepithelial neoplasia (PIN) in *Pten*-deficient mice fed with SIM or chow. **e.** Quantification of Ki67 positive nuclei (%), indicating proliferating cells, in *pc-/-* Chow ($n = 5$) and *pc-/-* SIM ($n = 6$). Statistical analysis: Mann-Whitney statistic test (b, e) and Chi Square test with 2 degree freedom (c). Error bars represent median with interquartile range. N.S.: Non-significant. * $p < 0.05$, ** $p < 0.01$.

dependent) and 22RV1 (AR-independent) cell lines. None of these parameters (AR protein levels or activity by means of the mRNA abundance of its target *KLK3*; AKT or ERK phosphorylation) was consistently altered neither *in vitro* nor *in vivo*, thus precluding their involvement as a major component of the mechanism of action of statins (Supplementary Figure 3; unprocessed scans in Supplementary Figure 5). Of note, we also monitored

the expression of cholesterol transporters and metabolic enzymes that could be altered as a consequence of statin treatment [48, 49]. We did not observe consistent changes neither in low density lipoprotein receptor (LDLR) nor in other enzymes and transporters (Apolipoprotein (APO) genes, ACAT1 (acetyl CoA cholesterol acyl transferase) and 2 and lipoprotein lipase (LPL)), precluding a major involvement of such alterations in the biological effect of

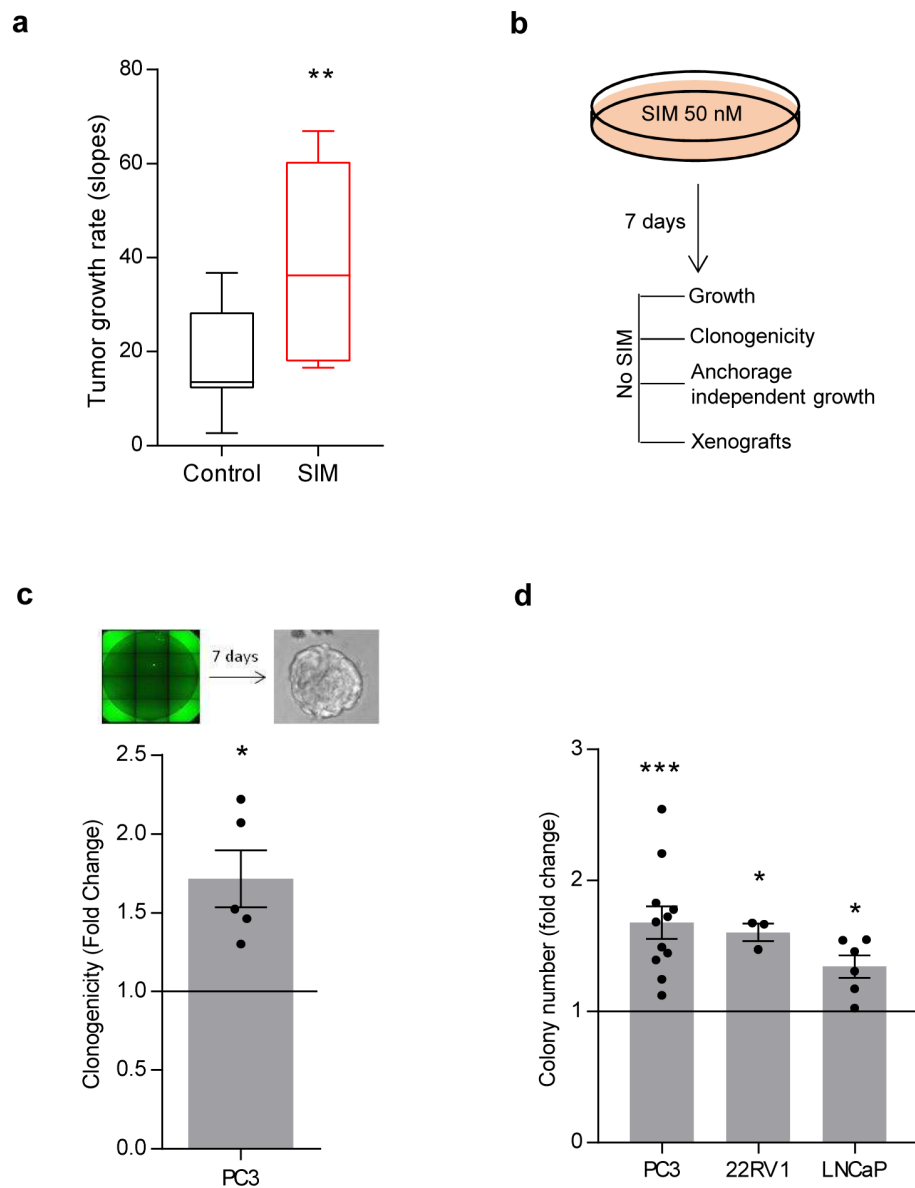


Figure 3: Low-dose simvastatin enhances features of prostate cancer aggressiveness in vitro and in vivo. **a.** Tumor growth rate from PC3 cell xenografts upon feeding nude mice with chow or simvastatin-loaded (SIM) diet. 5 mice for condition were used, 4 tumors per mouse. 100.000 PC3 cells were injected. Mice were fed with simvastatin loaded chow starting 72h before injections. Box plot representation. **b.** Schematic representation of simvastatin treatment *in vitro* in PC3 cells. Cells were pre-treated for 7 days with 50 nM simvastatin, and biological effects were evaluated. **c.** Effect of simvastatin pre-treatment on clonal self-renewal capacity ($n = 5$) in PC3 cells. **d.** Effect of 50 nM simvastatin pre-treatment on anchorage-independent growth in PC3, 22RV1 and LNCaP cell lines. Statistical analysis: Mann Whitney test (a), one sample t test (c, d. Error bars represent standard error of the mean. $*p < 0.05$, $**p < 0.01$, $***p < 0.001$.

these compounds (Supplementary Figure 4).

Observational studies have evaluated the association of statins to PCa risk and aggressiveness (Supplementary Table 3) [50, 51]. Our data suggests that there could be a subset of PCa patients where statins could exert undesirable effects. We analyzed data from a prospective study conducted in Vall d'Hebron Research Institute [15]. To carry out this analysis, 2408 men were selected, after excluding those men who were undergoing 5- α -reductase inhibitors treatment and those men who had been using statins for less than three years. In this cohort, the impact of statins was previously evaluated as part of a multivariate analysis with other factors such as age, PSA or serum cholesterol levels; or in combination with plasma cholesterol or aspirin treatment [15, 40]. 37.2% of patients passed the statin treatment criteria beyond 3 years. In the multivariate study, statins were not associated to PCa risk. PCa was detected in 848 men (35.2%), and 297 of them (35%) were classified as high grade (HGPCa, Gleason score >7; as compared to Low Grade PCa (LGPCa; Gleason score \leq 7)). In line with previous reports, treatment with this family of compounds reduced the risk of suffering from PCa (overall risk (OR) = 0.717; p = 0.006). However, 41.8% of patients treated with statins were diagnosed with HGPCa, whereas aggressive disease was less prevalent among patients not taking the cholesterol-lowering drug (32.5% of statin non-treated patients presented HGPCa, p = 0.012, OR 1.495 (1.095-2.039)) (Supplementary Table 4). To which extent the effect of statins is a predominant selective effect reducing the incidence of LGPCa, or whether it has an activity promoting the appearance of HGPCa remains to be studied, since both scenarios could lead to the results obtained in our analysis. In addition, our observational study does not account for statin dose, which, according to our experimental data, could be an important factor. Of note, these results are in line with the increased risk of high grade cancer reported in patients subject to statins that show normalized serum cholesterol levels [15], or patients with combined treatment of statins and aspirin [40]. Importantly, these results were corroborated in a multivariate analysis with other chronic pharmacological treatments (Supplementary Table 5). It should be noted that the controversy in observational studies with statins remains high [52], and additional analysis in well-annotated cohorts is granted.

DISCUSSION

Systemic metabolic alterations impact on the function and cross-talk of cells in our body. Indeed, the incidence and aggressiveness of cancer is in part associated to non-cell autonomous factors, such as nutrition, obesity or chronic therapeutic regimes [3, 53]. Statins are administered to millions of people worldwide. In turn, their consequences on tumor biology

have become a research field of great interest. We have studied the consequences of statin treatment in PCa biology, and demonstrated through the use of a wide array of pre-clinical and experimental approaches that these compounds promote features of disease aggressiveness. It should be noted that our experimental systems might reflect the existence of a sub-population of PCa patients for whom statins have undesirable effects, in line with other studies [54, 55]. Interestingly, a large study of 47294 individuals focused on the study of coronary heart disease observed that patients treated with low-dose simvastatin (5-10 mg/day) and achieving low total serum cholesterol, presented increased risk of developing cancer (OR = 3.16 for serum cholesterol < 160; OR = 1.85 for serum cholesterol = 160-179) [56]. The analysis of the available observational studies supports the existence of a context where statins could increase the aggressiveness of the disease in PCa patients. Overall, current epidemiological studies [15, 40, 50, 51, 54-68] would benefit of re-analysis taking into account this new information.

Experimental cancer systems often serve for the validation and causal demonstration of observations originated in patient studies. However, these approaches can also be employed to predict the consequences of societal or lifestyle changes. Our experimental systems provide very provocative results that still lack full clinical validation to demonstrate the potential existence of a subset of PCa patients in which statins exert an undesired activity. Our results warrant further analysis of the cell autonomous and systemic impact of statin treatment in PCa and other cancers in order to understand the biological context associated to a protective or detrimental activity of these compounds.

MATERIALS AND METHODS

Cellular and molecular assays

Human prostate carcinoma cell lines (PC3, LNCaP and 22RV1) were purchased from Leibniz-Institut - Deutsche Sammlung von Mikroorganismen und Zellkulturen GmbH (DSMZ, Germany), who provided authentication certificate. In addition, we validated their identity by microsatellite analysis. Cell lines were routinely monitored for mycoplasma contamination. Simvastatin and mevalonate (Sigma-Aldrich) for *in vitro* purposes were activated by heating (50 °C) with NaOH (0.1N) for two hours. Fluvastatin (Sigma-Aldrich) was used following manufacturers' indications.

For clonogenicity assay, PC3 cells expressing GFP were plated in poly-HEMA pretreated 384 plates at 1 cell per well in DMEM/F12 (Gibco) plus EGF (100 mg/ml), bFGF (10 mg/ml), B27 (Thermo Fisher), 8% BSA (Sigma-Aldrich). Wells with 0, 1, or >1 cells were annotated. 7

days after plating, sphere formation from wells with single cells was quantified. Crystal violet-based cell number quantification, soft-agar anchorage independent growth and western blotting were performed as previously described [10]. Antibodies used for western blotting: androgen receptor (clone D6F11, Cell Signaling #5153), phosphorylated ERK (T202/204; extracellular signal regulated kinase, clone 20G11, Cell Signaling #4376), phosphorylated AKT (S473; clone 736E11, Cell Signaling #3787), ERK (clone 3A7, Cell Signaling #9107), AKT (Cell Signaling #9272), β -Actin (clone AC-74; Sigma #A5316), LDLR (EP1553Y; Abcam #ab52818) and HSP90 (Heat Shock Protein 90, Cell Signaling #4874).

RNA was extracted using NucleoSpin® RNA isolation kit from Macherey-Nagel (ref: 740955.240C). For RNA harvesting from mouse tissue, we introduced a prior step consisting on the incubation of the tissue in RNAlater ICE (Thermo Fisher) overnight at -20°C and phenolic extraction with TRIreagent (TR118, MRC). In all cases, 1 μ g of total RNA was used for cDNA synthesis using qScript cDNA Supermix from Quanta (ref. 95048). Quantitative Real Time PCR (qRT-PCR) was performed as previously described [10]. Universal Probe Library (Roche) primers and probes employed in human samples: *HMGCR*, primers: Fw: gttcgggtggcctctagttag, Rv: gcattcgaaaagtcttgacaac; Probe: 65. *KLK3*, primers: Fw: gtgcttggcctctctgt Rv: agcaagatcacgctttgttc; Probe: 44. *LDLR*, primers: Fw: gatagtgacaatgtctaccaagc, Rv: cctcacgctactgggcttc; Probe: 6. *APOD*, primers: Fw: gagaggccagtcaccaagac, Rv: gagaaggacctggagcttt; Probe: 8. *APOA2*, primers: Fw: gagaaggtcaagagcccaga, Rv: ccttctgatcaggggtgctc; Probe: 68. *APOC1*, primers: Fw: gccttgataagctgaagga, Rv: gaaatgtctctgaaaaccactcc; Probe: 47. *LPL*, primers: Fw: caggcctttgagatttctctgt, Rv: gaaggagtagtctatttggtaa; Probe: 13. Universal Probe Library (Roche) primers and probes employed for mice: *Ldlr*, primers: Fw: gatgctatacctaccctcaa, Rv: tgctcatgccacatgctc; Probe: 64. *ApoD*, primers Fw: aatttccatcttggaaatgc, Rv: ggatcttcaatttctgaccatc; Probe: 63. *ApoC1*, primers Fw: tgggaacactttggaagaca, Rv: acttggccaaatgctctga; Probe: 46. *ApoA2*, primers Fw: tgctggtcaccatctgtagc, Rv: catatccggctcctgctgc; Probe: 12. *ApoE*, primers Fw: ttggtcattgctgacagg, Rv: agcgcaggtaatcccagaa; Probe: 32. *Lpl*, Fw: tttgtgaaatgccatgacaag, Rv: cagatgcttctctctgtttgt; Probe: 47. *Acat1*, Fw: ggctgaactcagtaaccacaca, Rv: ttggettctagccgattcc; Probe: 71. *Acat2*, Fw: attccagccataagcaagc, Rv: tttagctattggccgagaca; Probe: 88. β -*ACTIN* and *GAPDH* housekeeping assays from Applied Biosystems (β -*ACTIN*, Hs99999903_m1; *GAPDH*, Hs02758991_g1; Mm99999915_g1); showed similar results (all qRT-PCR data presented was normalized using *GAPDH*).

Lentiviral shRNA sequences targeting HMGCR (TRCN0000262852 and TRCN0000262856, Sigma Mission Library) were cloned into TET-pLKO puro vector

(gift from Dr. Dmitri Wiederschain [11], Addgene plasmid #21915). HMGCR over-expressing lentiviral plasmid (pLX304) was obtained from <https://plasmid.med.harvard.edu> (HsCD00412328).

Animals

All mouse experiments were carried out following the ethical guidelines established by the Biosafety and Welfare Committee at CIC bioGUNE. The procedures employed were carried out following the recommendations from AAALAC. Xenograft experiments were performed as previously described [12], injecting 10⁵ cells per condition in two flanks per mouse (male Hsd:Athymic Nude-Foxn1 nu/nu). For metastasis experiment, 6x10⁵ cells in 200 μ l were injected by tail vein [12]. When possible, mice were injected randomly and xenografts measured blindly to reduce bias due to caging. Western diet (SSNIFF, D12079 mod.) with high carbohydrates and fat (50% carbohydrates, 21% fat) was compared with the 4% fat of the control diet. Simvastatin was provided in the diets (both standard diet and western diet) at 12 mg/kg chow. The supplied concentration of simvastatin in mice was equivalent to 12 mg/day in humans, which corresponded to low doses for anticholesterolemic treatment (the standard dose being 40 mg/day).

The *Pten*^{loxP} conditional knockout alleles have been described elsewhere [13]. Prostate epithelium specific deletion was effected by the Pb-Cre4. Mice were fasted for 6 h prior to tissue harvest in order to prevent metabolic alterations due to immediate food intake.

Histopathological analysis

Samples of prostate gland or lungs were fixed overnight in 10% neutral buffered formalin, embedded in paraffin and sectioned 5 μ m thick and dried. Slides were dewaxed and re-hydrated through a series of graded ethanol until water and were stained with hematoxylin-eosin (H-E). Histopathological lesions of the prostate were classified according to current histological criteria [14].

Detection of PC3 in lungs metastatic foci of immunocompromised mice in the metastasis assay was assessed by immunohistochemical staining of Vimentin (NCL-L-VIM-572, Leica biosystems) using the streptavidin-biotin-peroxidase complex.

Proliferation was evaluated in paraffin embedded prostate samples by using Ki67 antibody (MA5-14520, Thermo Scientific). Five fields, at least 400 cells each field from the AP (anterior prostate) lobe were counted.

Immunohistochemical stainings of AR, pERK, pAKT and LDLR (references as in western blot analysis) were performed on deparaffinized prostate sections using the streptavidin-biotin-complex peroxidase method. Antigen retrieval was carried out by heating sections in

10 mM sodium citrate, pH 6.0. Immunodetection was performed with the Polink-2 HRP Plus Rabbit Detection System (D39-110, GBI Labs, Bothell, WA, USA) and slides were developed with the peroxidase substrate kit (SK-4105, Vector Laboratories, Burlingame, CA, USA). Staining score 0 to 3 was given by two independent investigators based on the % of stained cells and the intensity of the staining.

Patients

We analysed data from a prospective study conducted in Vall d'Hebron Research Institute [15]. To carry out this analysis, 2408 men were selected, after excluding those men who were undergoing 5- α -reductase inhibitors treatment and those men who had been using statins for less than three years. Prostate cancer (PCa) was detected in 848 men (35.2%), and 240 (28.3%) were high grade prostate cancer (HGPCa) (Gleason score > 7). The overall demographics and clinical characteristics of the men enrolled, as well as the methodological aspects have been previously reported [15].

Statistics

For patient analysis, quantitative variables were expressed as medians + semi-interquartile range. Qualitative variables were expressed as rates. Univariate analysis included the Chi-square test to analyse the association between qualitative variables and the Cochran test to evaluate their strength. Multivariate analysis using the binary logistic regression was carried out to examine the independent predictors of PCa risk and tumor aggressiveness. Odds ratios (OR) and 95% coefficient interval (CI) were calculated.

For *in vivo* studies, in the absence of normal distribution, a non-parametric Mann Whitney U test was applied for two-group comparisons. For frequency analysis, Chi-square test was used when there were more than 2 variables and Fisher F test was used for 2 variables. For *in vitro* experiments, normal distribution was assumed and one sample t-test was applied for one component comparisons with control. Error bars represent mean \pm SEM (standard error of the mean) *in vitro*, and median with interquartile range *in vivo*, unless otherwise specified. We considered $p < 0.05$ to be statistically significant.

Author contributions

AC-M performed the majority of *in vitro* and *in vivo* experiments, unless specified otherwise. LC performed *in vitro* analysis and immunohistochemistry. AZ performed the *in vivo* obesity and simvastatin treatment in *Pten^{pc+/-}* mice. VT, SF-R, KZ, LA, LV-J, NM-M contributed to

in vitro experiments and analysis. JMF provided the diagnosis of mouse prostate tissue. ARC provided Support with statistical analysis. PZ, AA-A, FG, DC, SMVL, JMF-P, AMA and AG-M provided technical support and critical discussions. MO and JM performed the human patient analysis in the VHIR cohort. AC directed the project, supervised data analysis and wrote the manuscript.

ACKNOWLEDGMENTS AND GRANT SUPPORT

Apologies to those whose related publications were not cited due to space limitations. AC-M is supported by the MINECO postdoctoral program and the CIG program from the European commission (660191). NM-M was supported by the Spanish Association Against Cancer (AECC), AECC JP Vizcaya. VT is supported by Fundación Vasca de Innovación e Investigación Sanitarias, BIOEF (BIO15/CA/052), the department of health of the Basque Government (2016111109) and the 2016 grant of the AECC (Junta provincial de Bizkaia). LA, AA-A and LV-J were supported by the Basque Government of education. The work of A.C. is supported by the Ramón y Cajal award, the Basque Department of Industry, Tourism and Trade (Etortek) and the department of education (IKERTALDE IT1106-16), ISCIII (PI10/01484, PI13/00031), FERO VIII Fellowship, the BBVA foundation, the MINECO (SAF2016-79381-R), Severo Ochoa Excellence Accreditation SEV-2016-0644) and the European Research Council (Starting Grant 336343; Proof of Concept 754627). The participation of AC, VT, NM-M, SF and AZ as part of CIBERONC was co-funded with FEDER funds.

CONFLICTS OF INTEREST

The authors declare no conflicts of interest.

REFERENCES

1. Martincorena I, Campbell PJ. Somatic mutation in cancer and normal cells. *Science*. 2015; 349: 1483-9. doi: 10.1126/science.aab4082.
2. Hanahan D, Weinberg RA. Hallmarks of cancer: the next generation. *Cell*. 2011; 144: 646-74. doi: 10.1016/j.cell.2011.02.013.
3. Calle EE, Rodriguez C, Walker-Thurmond K, Thun MJ. Overweight, obesity, and mortality from cancer in a prospectively studied cohort of U.S. adults. *N Engl J Med*. 2003; 348: 1625-38. doi: 10.1056/NEJMoa021423.
4. Bail J, Meneses K, Demark-Wahnefried W. Nutritional Status and Diet in Cancer Prevention. *Semin Oncol Nurs*. 2016; 32: 206-14. doi: 10.1016/j.soncn.2016.05.004.
5. Marosi C, Koller M. Challenge of cancer in the elderly. *ESMO Open*. 2016; 1: e000020. doi: 10.1136/

esmoopen-2015-000020.

6. Williams GR, Mackenzie A, Magnuson A, Olin R, Chapman A, Mohile S, Allore H, Somerfield MR, Targia V, Extermann M, Cohen HJ, Hurria A, Holmes H. Comorbidity in older adults with cancer. *J Geriatr Oncol*. 2016; 7: 249-57. doi: 10.1016/j.jgo.2015.12.002.
7. Hsing AW, Chokkalingam AP. Prostate cancer epidemiology. *Front Biosci*. 2006; 11: 1388-413.
8. Quagliariello V, Rossetti S, Cavaliere C, Di Palo R, Lamantia E, Castaldo L, Nocerino F, Ametrano G, Cappuccio F, Malzone G, Montanari M, Vanacore D, Romano FJ, et al. Metabolic syndrome, endocrine disruptors and prostate cancer associations: biochemical and pathophysiological evidences. *Oncotarget*. 2017; 8: 30606-16. doi: 10.18632/oncotarget.16725.
9. Collins R, Reith C, Emberson J, Armitage J, Baigent C, Blackwell L, Blumenthal R, Danesh J, Smith GD, DeMets D, Evans S, Law M, MacMahon S, et al. Interpretation of the evidence for the efficacy and safety of statin therapy. *Lancet*. 2016; 388: 2532-61. doi: 10.1016/S0140-6736(16)31357-5.
10. Torrano V, Valcarcel-Jimenez L, Cortazar AR, Liu X, Urosevic J, Castillo-Martin M, Fernandez-Ruiz S, Morciano G, Caro-Maldonado A, Guiu M, Zuniga-Garcia P, Graupera M, Bellmunt A, et al. The metabolic co-regulator PGC1alpha suppresses prostate cancer metastasis. *Nat Cell Biol*. 2016; 18: 645-56. doi: 10.1038/ncb3357.
11. Wiederschain D, Wee S, Chen L, Loo A, Yang G, Huang A, Chen Y, Caponigro G, Yao YM, Lengauer C, Sellers WR, Benson JD. Single-vector inducible lentiviral RNAi system for oncology target validation. *Cell Cycle*. 2009; 8: 498-504.
12. Martin-Martin N, Piva M, Urosevic J, Aldaz P, Sutherland JD, Fernandez-Ruiz S, Arreal L, Torrano V, Cortazar AR, Planet E, Guiu M, Radosevic-Robin N, Garcia S, et al. Stratification and therapeutic potential of PML in metastatic breast cancer. *Nat Commun*. 2016; 7: 12595. doi: 10.1038/ncomms12595.
13. Chen Z, Trotman LC, Shaffer D, Lin HK, Dotan ZA, Niki M, Koutcher JA, Scher HI, Ludwig T, Gerald W, Cordon-Cardo C, Pandolfi PP. Crucial role of p53-dependent cellular senescence in suppression of Pten-deficient tumorigenesis. *Nature*. 2005; 436: 725-30. doi: nature03918.
14. Ittmann M, Huang J, Radaelli E, Martin P, Signoretti S, Sullivan R, Simons BW, Ward JM, Robinson BD, Chu GC, Loda M, Thomas G, Borowsky A, et al. Animal models of human prostate cancer: the consensus report of the New York meeting of the Mouse Models of Human Cancers Consortium Prostate Pathology Committee. *Cancer Res*. 2013; 73: 2718-36. doi: 10.1158/0008-5472.CAN-12-4213.
15. Morote J, Celma A, Planas J, Placer J, de Torres I, Oliván M, Carles J, Reventos J, Doll A. Role of serum cholesterol and statin use in the risk of prostate cancer detection and tumor aggressiveness. *Int J Mol Sci*. 2014; 15: 13615-23. doi: 10.3390/ijms150813615.
16. Feingold KR, Grunfeld C. Obesity and Dyslipidemia. In: De Groot LJ, Chrousos G, Dungan K, Feingold KR, Grossman A, Hershman JM, Koch C, Korbonits M, McLachlan R, New M, Purnell J, Rebar R, Singer F, Vinik A, Editors. *Endotext*. South Dartmouth: Mass. Endotext.org; 2000.
17. Nardella C, Carracedo A, Salmena L, Pandolfi PP. Faithfull modeling of PTEN loss driven diseases in the mouse. *Curr Top Microbiol Immunol*. 2011; 347: 135-68. doi: 10.1007/82_2010_62.
18. Boudreau DM, Yu O, Johnson J. Statin use and cancer risk: a comprehensive review. *Expert Opin Drug Saf*. 2010; 9: 603-21. doi: 10.1517/14740331003662620.
19. Miller RA, Harrison DE, Astle CM, Baur JA, Boyd AR, de Cabo R, Fernandez E, Flurkey K, Javors MA, Nelson JF, Orihuela CJ, Pletcher S, Sharp ZD, et al. Rapamycin, but not resveratrol or simvastatin, extends life span of genetically heterogeneous mice. *J Gerontol A Biol Sci Med Sci*. 2011; 66: 191-201. doi: 10.1093/gerona/glq178.
20. Blumenthal RS. Statins: effective antiatherosclerotic therapy. *Am Heart J*. 2000; 139: 577-83.
21. Hammond CL, Wheeler SG, Ballatori N, Hinkle PM. Ostalpha-/- mice are not protected from western diet-induced weight gain. *Physiol Rep*. 2015; 3. doi: 10.14814/phy2.12263.
22. Merseburger AS, Alcaraz A, von Klot CA. Androgen deprivation therapy as backbone therapy in the management of prostate cancer. *Onco Targets Ther*. 2016; 9: 7263-74. doi: 10.2147/OTT.S117176.
23. Carver BS, Chapinski C, Wongvipat J, Hieronymus H, Chen Y, Chandralapaty S, Arora VK, Le C, Koutcher J, Scher H, Scardino PT, Rosen N, Sawyers CL. Reciprocal feedback regulation of PI3K and androgen receptor signaling in PTEN-deficient prostate cancer. *Cancer Cell*. 2011; 19: 575-86. doi: S1535-6108(11)00155-3.
24. Aberg M, Johnell M, Wickstrom M, Widunder A, Siegbahn A. Simvastatin reduces the production of prothrombotic prostasomes in human prostate cancer cells. *Thromb Haemost*. 2008; 100: 655-62.
25. Al-Husein B, Goc A, Somanath PR. Suppression of interactions between prostate tumor cell-surface integrin and endothelial ICAM-1 by simvastatin inhibits micrometastasis. *J Cell Physiol*. 2013; 228: 2139-48. doi: 10.1002/jcp.24381.
26. Babcook MA, Shukla S, Fu P, Vazquez EJ, Puchowicz MA, Molter JP, Oak CZ, MacLennan GT, Flask CA, Lindner DJ, Parker Y, Daneshgari F, Gupta S. Synergistic simvastatin and metformin combination chemotherapy for osseous metastatic castration-resistant prostate cancer. *Mol Cancer Ther*. 2014; 13: 2288-302. doi: 10.1158/1535-7163.MCT-14-0451.
27. Brown M, Hart C, Tawadros T, Ramani V, Sangar V, Lau M, Clarke N. The differential effects of statins on the metastatic behaviour of prostate cancer. *Br J Cancer*. 2012; 106: 1689-96. doi: 10.1038/bjc.2012.138.

28. Chang HL, Chen CY, Hsu YF, Kuo WS, Ou G, Chiu PT, Huang YH, Hsu MJ. Simvastatin induced HCT116 colorectal cancer cell apoptosis through p38MAPK-p53-survivin signaling cascade. *Biochim Biophys Acta*. 2013; 1830: 4053-64. doi: 10.1016/j.bbagen.2013.04.011.
29. Costa RA, Fernandes MP, de Souza-Pinto NC, Vercesi AE. Protective effects of l-carnitine and piracetam against mitochondrial permeability transition and PC3 cell necrosis induced by simvastatin. *Eur J Pharmacol*. 2013; 701: 82-6. doi: 10.1016/j.ejphar.2013.01.001.
30. Crosbie J, Magnussen M, Dornbier R, Iannone A, Steele TA. Statins inhibit proliferation and cytotoxicity of a human leukemic natural killer cell line. *Biomark Res*. 2013; 1: 33. doi: 10.1186/2050-7771-1-33.
31. Furuya Y, Sekine Y, Kato H, Miyazawa Y, Koike H, Suzuki K. Low-density lipoprotein receptors play an important role in the inhibition of prostate cancer cell proliferation by statins. *Prostate Int*. 2016; 4: 56-60. doi: 10.1016/j.pnil.2016.02.003.
32. Goc A, Kochuparambil ST, Al-Husein B, Al-Azayzih A, Mohammad S, Somanath PR. Simultaneous modulation of the intrinsic and extrinsic pathways by simvastatin in mediating prostate cancer cell apoptosis. *BMC Cancer*. 2012; 12: 409. doi: 10.1186/1471-2407-12-409.
33. Hoque A, Chen H, Xu XC. Statin induces apoptosis and cell growth arrest in prostate cancer cells. *Cancer Epidemiol Biomarkers Prev*. 2008; 17: 88-94. doi: 10.1158/1055-9965.EPI-07-0531.
34. Ingersoll MA, Miller DR, Martinez O, Wakefield CB, Hsieh KC, Simha MV, Kao CL, Chen HT, Batra SK, Lin MF. Statin derivatives as therapeutic agents for castration-resistant prostate cancer. *Cancer Lett*. 2016; 383: 94-105. doi: 10.1016/j.canlet.2016.09.008.
35. Kim JH, Cox ME, Wasan KM. Effect of simvastatin on castration-resistant prostate cancer cells. *Lipids Health Dis*. 2014; 13: 56. doi: 10.1186/1476-511X-13-56.
36. Kochuparambil ST, Al-Husein B, Goc A, Soliman S, Somanath PR. Anticancer efficacy of simvastatin on prostate cancer cells and tumor xenografts is associated with inhibition of Akt and reduced prostate-specific antigen expression. *J Pharmacol Exp Ther*. 2011; 336: 496-505. doi: 10.1124/jpet.110.174870.
37. Kureishi Y, Luo Z, Shiojima I, Bialik A, Fulton D, Lefer DJ, Sessa WC, Walsh K. The HMG-CoA reductase inhibitor simvastatin activates the protein kinase Akt and promotes angiogenesis in normocholesterolemic animals. *Nat Med*. 2000; 6: 1004-10. doi: 10.1038/79510.
38. Liang Z, Li W, Liu J, Li J, He F, Jiang Y, Yang L, Li P, Wang B, Wang Y, Ren Y, Yang J, Luo Z, et al. Simvastatin suppresses the DNA replication licensing factor MCM7 and inhibits the growth of tamoxifen-resistant breast cancer cells. *Sci Rep*. 2017; 7: 41776. doi: 10.1038/srep41776.
39. Menter DG, Ramsauer VP, Harirforoosh S, Chakraborty K, Yang P, Hsi L, Newman RA, Krishnan K. Differential effects of pravastatin and simvastatin on the growth of tumor cells from different organ sites. *PLoS One*. 2011; 6: e28813. doi: 10.1371/journal.pone.0028813.
40. Olivian M, Rigau M, Colas E, Garcia M, Montes M, Sequeiros T, Regis L, Celma A, Planas J, Placer J, Reventos J, de Torres I, Doll A, et al. Simultaneous treatment with statins and aspirin reduces the risk of prostate cancer detection and tumorigenic properties in prostate cancer cell lines. *Biomed Res Int*. 2015; 2015: 762178. doi: 10.1155/2015/762178.
41. Oliveira KA, Zecchin KG, Alberici LC, Castilho RF, Vercesi AE. Simvastatin inducing PC3 prostate cancer cell necrosis mediated by calcineurin and mitochondrial dysfunction. *J Bioenerg Biomembr*. 2008; 40: 307-14. doi: 10.1007/s10863-008-9155-9.
42. Park YH, Seo SY, Lee E, Ku JH, Kim HH, Kwak C. Simvastatin induces apoptosis in castrate resistant prostate cancer cells by deregulating nuclear factor-kappaB pathway. *J Urol*. 2013; 189: 1547-52. doi: 10.1016/j.juro.2012.10.030.
43. Rogers M, Kalra S, Moukharskaya J, Chakraborty K, Niyazi M, Krishnan K, Lightner J, Brannon M, Stone WL, Palau VE. Synergistic growth inhibition of PC3 prostate cancer cells with low-dose combinations of simvastatin and alendronate. *Anticancer Res*. 2015; 35: 1851-9. doi: 10.1007/s10863-008-9155-9.
44. Stine JE, Guo H, Sheng X, Han X, Schointuch MN, Gilliam TP, Gehrig PA, Zhou C, Bae-Jump VL. The HMG-CoA reductase inhibitor, simvastatin, exhibits anti-metastatic and anti-tumorigenic effects in ovarian cancer. *Oncotarget*. 2016; 7: 946-60. doi: 10.18632/oncotarget.5834.
45. Wang G, Cao R, Wang Y, Qian G, Dan HC, Jiang W, Ju L, Wu M, Xiao Y, Wang X. Simvastatin induces cell cycle arrest and inhibits proliferation of bladder cancer cells via PPARgamma signalling pathway. *Sci Rep*. 2016; 6: 35783. doi: 10.1038/srep35783.
46. Backman JT, Kyrklund C, Kivisto KT, Wang JS, Neuvonen PJ. Plasma concentrations of active simvastatin acid are increased by gemfibrozil. *Clin Pharmacol Ther*. 2000; 68: 122-9. doi: 10.1067/mcp.2000.108507.
47. Lambert AW, Pattabiraman DR, Weinberg RA. Emerging Biological Principles of Metastasis. *Cell*. 2017; 168: 670-91. doi: 10.1016/j.cell.2016.11.037.
48. Guillaumond F, Bidaut G, Ouaiissi M, Servais S, Gouirand V, Olivares O, Lac S, Borge L, Roques J, Gayet O, Pinault M, Guimaraes C, Nigri J, et al. Cholesterol uptake disruption, in association with chemotherapy, is a promising combined metabolic therapy for pancreatic adenocarcinoma. *Proc Natl Acad Sci U S A*. 2015; 112: 2473-8. doi: 10.1073/pnas.1421601112.
49. Vasseur S, Guillaumond F. LDL Receptor: An open route to feed pancreatic tumor cells. *Mol Cell Oncol*. 2016; 3: e1033586. doi: 10.1080/23723556.2015.1033586.
50. Bonovas S, Filioussi K, Sitaras NM. Statin use and the risk of prostate cancer: A metaanalysis of 6 randomized clinical

- trials and 13 observational studies. *Int J Cancer*. 2008; 123: 899-904. doi: 10.1002/ijc.23550.
51. Tan P, Zhang C, Wei SY, Tang Z, Gao L, Yang L, Wei Q. Effect of statins type on incident prostate cancer risk: a meta-analysis and systematic review. *Asian J Androl*. 2016. doi: 10.4103/1008-682X.190327.
 52. Schnoeller TJ, Jentzmik F, Schrader AJ, Steinestel J. Influence of serum cholesterol level and statin treatment on prostate cancer aggressiveness. *Oncotarget*. 2017; 8: 47110-20. doi: 10.18632/oncotarget.16943.
 53. Evans JM, Donnelly LA, Emslie-Smith AM, Alessi DR, Morris AD. Metformin and reduced risk of cancer in diabetic patients. *BMJ*. 2005; 330: 1304-5. doi: 10.1136/bmj.38415.708634.F7.
 54. Chang CC, Ho SC, Chiu HF, Yang CY. Statins increase the risk of prostate cancer: a population-based case-control study. *Prostate*. 2011; 71: 1818-24. doi: 10.1002/pros.21401.
 55. Wettstein MS, Saba K, Umbehr MH, Murtola TJ, Fankhauser CD, Adank JP, Hofmann M, Sulser T, Hermanns T, Moch H, Wild P, Poyet C. Prognostic Role of Preoperative Serum Lipid Levels in Patients Undergoing Radical Prostatectomy for Clinically Localized Prostate Cancer. *Prostate*. 2017. doi: 10.1002/pros.23296.
 56. Matsuzaki M, Kita T, Mabuchi H, Matsuzawa Y, Nakaya N, Oikawa S, Saito Y, Sasaki J, Shimamoto K, Itakura H, Trial JLSGJLI. Large scale cohort study of the relationship between serum cholesterol concentration and coronary events with low-dose simvastatin therapy in Japanese patients with hypercholesterolemia. *Circ J*. 2002; 66: 1087-95.
 57. Allott EH, Farnan L, Steck SE, Arab L, Su LJ, Mishel M, Fontham ET, Mohler JL, Bensen JT. Statin Use and Prostate Cancer Aggressiveness: Results from the Population-Based North Carolina-Louisiana Prostate Cancer Project. *Cancer Epidemiol Biomarkers Prev*. 2016; 25: 670-7. doi: 10.1158/1055-9965.EPI-15-0631.
 58. Allott EH, Howard LE, Cooperberg MR, Kane CJ, Aronson WJ, Terris MK, Amling CL, Freedland SJ. Postoperative statin use and risk of biochemical recurrence following radical prostatectomy: results from the Shared Equal Access Regional Cancer Hospital (SEARCH) database. *BJU Int*. 2014; 114: 661-6. doi: 10.1111/bju.12720.
 59. Bansal D, Undela K, D'Cruz S, Schifano F. Statin use and risk of prostate cancer: a meta-analysis of observational studies. *PLoS One*. 2012; 7: e46691. doi: 10.1371/journal.pone.0046691.
 60. Chen HY, Wang Q, Xu QH, Yan L, Gao XF, Lu YH, Wang L. Statin as a Combined Therapy for Advanced-Stage Ovarian Cancer: A Propensity Score Matched Analysis. *Biomed Res Int*. 2016; 2016: 9125238. doi: 10.1155/2016/9125238.
 61. Ford I, Murray H, McCowan C, Packard CJ. Long-Term Safety and Efficacy of Lowering Low-Density Lipoprotein Cholesterol With Statin Therapy: 20-Year Follow-Up of West of Scotland Coronary Prevention Study. *Circulation*. 2016; 133: 1073-80. doi: 10.1161/CIRCULATIONAHA.115.019014.
 62. Friedman GD, Flick ED, Udaltsova N, Chan J, Quesenberry CP Jr, Habel LA. Screening statins for possible carcinogenic risk: up to 9 years of follow-up of 361,859 recipients. *Pharmacoepidemiol Drug Saf*. 2008; 17: 27-36. doi: 10.1002/pds.1507.
 63. Huang BZ, Chang JI, Li E, Xiang AH, Wu BU. Influence of Statins and Cholesterol on Mortality Among Patients With Pancreatic Cancer. *J Natl Cancer Inst*. 2017; 109. doi: 10.1093/jnci/djw275.
 64. Jespersen CG, Norgaard M, Friis S, Skriver C, Borre M. Statin use and risk of prostate cancer: a Danish population-based case-control study, 1997-2010. *Cancer Epidemiol*. 2014; 38: 42-7. doi: 10.1016/j.canep.2013.10.010.
 65. Krane LS, Kaul SA, Stricker HJ, Peabody JO, Menon M, Agarwal PK. Men presenting for radical prostatectomy on preoperative statin therapy have reduced serum prostate specific antigen. *J Urol*. 2010; 183: 118-24. doi: 10.1016/j.juro.2009.08.151.
 66. Mamtani R, Lewis JD, Scott FI, Ahmad T, Goldberg DS, Datta J, Yang YX, Boursi B. Disentangling the Association between Statins, Cholesterol, and Colorectal Cancer: A Nested Case-Control Study. *PLoS Med*. 2016; 13: e1002007. doi: 10.1371/journal.pmed.1002007.
 67. Platz EA, Leitzmann MF, Visvanathan K, Rimm EB, Stampfer MJ, Willett WC, Giovannucci E. Statin drugs and risk of advanced prostate cancer. *J Natl Cancer Inst*. 2006; 98: 1819-25. doi: 10.1093/jnci/djj499.
 68. Pottegard A, Clark P, Friis S, Hallas J, Lund L. Long-term Use of Statins and Risk of Renal Cell Carcinoma: A Population-based Case-Control Study. *Eur Urol*. 2016; 69: 877-82. doi: 10.1016/j.eururo.2015.10.020.

